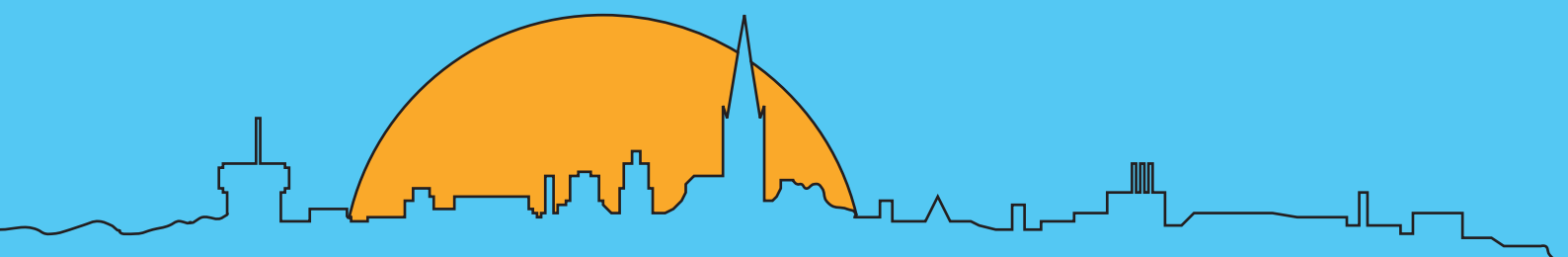


SICFP'21

The 17th Scandinavian International Conference on Fluid Power

Online, hosted from Linköping, Sweden
1 - 2 juni, 2021

Proceeding



©2021 The author(s)

Published by

Linköping University Electronic Press, Sweden

Serie: Linköping Electronic Conference Proceedings 182

ISBN: 978-91-7929-013-9 ISSN: 1650-3686 (print), 1650-3740 (online)

Proceedings of the 17th Scandinavian International Conference on Fluid Power, SICFP'21

The Division of Fluid and Mechatronic Systems (Flumes) at Linköping University, Sweden, hosted the 17th Scandinavian International Conference on Fluid Power, SICFP'21, June 1-2, 2021. The conference is arranged on a biannual basis alternating between Linköping University (LiU) and Tampere Technical University, (TUT). Due to the COVID-19 outbreak, the conference was arranged as an on-line event.

The proceedings have a table of contents with 22 peer-reviewed articles and one with 4 non-reviewed articles.

The published papers are from a wide range of fields of fluid power, such as industrial automation, machines, aircraft, mining, forest, and offshore equipment, etc. It is evident that Fluid power is in a stage of rapid transformation, as requirements on efficiency and environmental compatibility are having a real impact on component and system design. Furthermore, there is an increasing attention to the combination with electrical power systems, that can result in more energy- and cost-efficient concepts. Increased level of intelligence, sensors, connectivity and communication in machines, are also trends that will greatly influence efficiency, operations, and business models.

A few articles from the conference proceeding have been chosen to be published in a special issue in the International Journal of Fluid Power (dedicated to SICFP).

Chairman of the programme committee

Petter Krus, Linköping University, Sweden

Editors

Petter Krus, Linköping University, Sweden

Liselott Ericson, Linköping University, Sweden

Magnus Sethson, Linköping University, Sweden

Program Committee

Prof. Torben Ole Andersen, Aalborg University, Denmark

Dr. Katharina Baer, Vanderlande, Netherland

Prof. Eric Bideaux, Laboratoire Ampère INSA Lyon, France

Prof. Paolo Casoli, Università degli Studi di Parma, Italy

Dr. Alessandro Del'Amico, Saab AB, Sweden

Dr. Liselott Ericson, Linköping University, Sweden

Dr. Björn Eriksson, Parker, Sweden

Prof. Ludger Frerichs, Technische Universität Braunschweig, Germany

Dr. Emma Frosina, Università degli Studi di Napoli Federico II, Italy

Prof. Marcus Geimer, Karlsruher Institut für Technologie, Germany

Prof. Luiz Goes, ITA, Brazil

Prof. Heikki Handroos, Lappeenranta University of Technology, Finland

Dr. Kim Heybroek, Volvo AB, Sweden

Prof. Kalevi Huhtala, Tampere University of Technology, Finland

Prof. Petter Krus, Linköping University, Sweden

Prof. Roland Larsson, Luleå Technical University, Sweden

Dr. Viktor Larsson, Linköping University, Sweden

Prof. Yajun Liu, South China University of Technology, China

Prof. Jean-Charles Mare, INSA Toulouse - Institut Clément Ader, France

Prof. Massimo Milani, University of Modena, Italy

Prof. Victor Juliano De Negri, Federal University of Santa Catarina, Brazil

Prof. Jan-Ove Palmberg, Linköping University, Sweden

Prof. Luciana Pereira, UFABC, Brazil

Prof. Andrew Plummer, University of Bath, UK

Dr. Marcus Rösth, HIAB, Sweden

Dr. Magnus Sethson, Linköping University, Sweden

Prof. Rudolf Scheidl, Johannes Kepler University Linz, Austria

Prof. Katharina Schmitz, RWTH Aachen University, Germany

Prof. Nariman Sepehri, University of Manitoba, Canada

Prof. Kim A. Stelson, Center for Compact and Efficient Fluid Power, USA

Prof. Viktor Sverbilov, Samara National Research University, Russia

Prof. Andrea Vacca, Purdue University, USA

Prof. Jürgen Weber, Technische Universität Dresden, Germany

Prof. Travis Wiens, University of Saskatchewan, Canada

Prof. Ouyang Xiaoping, Zhejiang University, China

Prof. Huayong Yang, Zhejiang University, China

Invited Speakers

Astrid Mozes, Eaton Corporation, USA

Prof. Katharina Schmitz, RWTH Aachen University, Germany

Dr. Marcus Rösth, HIAB, Sweden

Prof. Jean-Charles Mare, INSA Toulouse - Institut Clément Ader, France

List of Articles

Peer-reviewed Articles	7
Hydraulic Trainer for Hands-on and Virtual Labs for Fluid Power Curriculum	8
<i>Hassan Assaf, Andrea Vacca</i>	
Comparison of Sliding Mode Controller for Classical and Direct Driven Electrohydraulic System	26
<i>Juraj Benić, Željko Šitum, Mihael Čipek, Danijel Pavković, Josip Kasać</i>	
Experimental Investigation of the Influence of Fluid Viscosity on the Efficiency of a Crawler Excavator	36
<i>Sebastian Deuster, Katharina Schmitz</i>	
Improving the Performance of Self-contained Cylinder Drives with Load-holding Capabilities	50
<i>Viktor Hristov Donkov, Søren Ketelsen, Torben Ole Andersen, Morten Kjeld Ebbesen, Lasse Schmidt</i>	
A Study of Hydraulically Actuated Oscillating Pitch to Increase Energy Production in Wind Turbines	62
<i>Daniel Escobar, John Sampson, Kim A. Stelson</i>	
Improving the Energy Efficiency of Single Actuators with High Energy Consumption: An Electro-Hydraulic Extension of Conventional Multi-Actuator Load-Sensing Systems	74
<i>David Fassbender, Tatiana Minav, Christine Brach, Kalevi Huhtala</i>	
Load Weight Estimation on an Excavator in Static and Dynamic Motions	90
<i>Mehmet Ferlibas, Reza Ghabcheloo</i>	
Experimental Investigation of New Design Concepts for the Tribological Contact between the Valve Plate and the Cylinder Block in Axial Piston Machines	104
<i>Stefan Andre Geffroy, Stephan Wegner, Stefan Gels, Katharina Schmitz</i>	
A New Degree of Freedom for Variable Axial Piston Pumps with Valve Plate Rotation	117
<i>Thomas Heeger, Liselott Ericson</i>	
Strategies to Minimize Data Sample Size for Regression-based Pump/motor Models	134
<i>Jack Johnson, José Garcia-Bravo, Pawan Panwar, Paul Michael</i>	
Pump-Controlled Actuators with Dump Valves	150
<i>Samuel Kärnell, Emil Fernlund, Fabian Lagerstedt, Liselott Ericson</i>	
Control Optimisation of a Pump-Controlled Hydraulic System using Digital Displacement Pumps	161
<i>L. Viktor Larsson, Robert Lejonberg, Liselott Ericson</i>	
Adaptive Identification and Application of Flow Mapping for Electrohydraulic Valves	173
<i>Jianbin Liu, André Sitte, Jürgen Weber</i>	
The Determination of Hydraulic Motor Displacement	188
<i>Paul John Michael, Jose Garcia-Bravo</i>	
Modelling, Simulation and Validation of the Pneumatic End-Position Cylinder Cushioning	206
<i>Fedor Nazarov, Jürgen Weber</i>	
Improving the Efficiency of Valve-controlled Systems by using Multi-chamber Actuators	224
<i>Henrique Raduenz, Liselott Ericson, Kim Heybroek, Victor J. De Negri, Petter Krus</i>	
Loss Analysis and Concept Comparison for Electrically Driven Hydraulic Loader Crane	237
<i>Amy Rankka, Alessandro Dell'Amico</i>	
Design of Pressure Control for Optimal Damping in Individual Metering Systems	252
<i>Gerhard Rath, Emil Zaev, Goran Stojanoski, Darko Babunski</i>	
Concept, Simulation Studies and Design for a Novel Concept of the Hydraulic Binary Counter	262
<i>Rudolf Scheidl, Matthias Scherrer</i>	
Simulating a High Frequency Piezo Pump with Disc Reed Valves	274
<i>Nathan P Sell, Andrew R Plummer, David N Johnston, Jonathan L du Bois</i>	
Multidimensional Trajectory Tracking for Numerically Stiff Independent Metering System	283

<i>Goran Stojanoski, Dimitar Ninevski, Gerhard Rath, Matthew Harker</i>	
Novel Hydraulically Relieved Electromechanical Direct Actuation System for Large Scale Switching Valves	294
<i>Tobias Vonderbank, Pierre Lafl Chavez, Katharina Schmitz</i>	
Non-reviewed Articles	308
The Hydraulic Infinite Linear Actuator for Efficient and Flexible Timber and Agricultural Logistics	309
<i>Magnus Landberg, Magnus Sethson, Petter Krus</i>	
Benchmarking the Performance of Hydrostatic Pumps	322
<i>Robin Mommers, Peter Achten, Jasper Achten, Jeroen Potma</i>	
Extremal Optimisation Approach to Component Placement in Blood Analysis Equipment . . .	332
<i>Magnus Sethson</i>	
Control Strategies for a Dual AC Motor Pump System in Aircraft Hydraulic Power Packages .	353
<i>Nils Trochermann and Frank Thielecke</i>	

Peer-reviewed Articles

Hydraulic Trainer for Hands-on and Virtual Labs for Fluid Power Curriculum

Hassan Assaf, Andrea Vacca

Maha Fluid Power Research Center, Purdue University, West Lafayette, IN 47907, USA
E-mail: assafh@purdue.edu, avacca@purdue.edu

Abstract

Hands-on experiences constitute a high value, perhaps unreplaceable, element of applied engineering disciplines such as fluid power. Hydraulic and pneumatic trainers have been developed over the years to expose students to applications of fluid power technology. However, the traditional approach for educating students through hands-on lab is recently under high pressure due to the following aspects: a) the outdated design of the traditional trainers that seldom integrate modern electro-hydraulic components, data acquisition systems, and visual aids; b) the increased need for online education. These factors have been endangering the number of students – already low compared to the industry needs – enrolled in fluid power programs.

This paper describes the effort made at Purdue University to develop a modern hydraulic trainer along with its digital twin that tackles the above challenges. A novel physical trainer was formulated to allow 29 lab experiences that span from basic concepts of single actuator control to more sophisticated layouts for controlling multiple actuators. The trainer largely uses electro-hydraulic components, sensors as well as a DAQ system connected with a touch base screen, aimed at maximizing the student's feeling of experiencing modern technology. A virtual trainer that replicates the physical trainer is developed and implemented with the commercial software Unity 3D. The virtual trainer uses the CAD drawings of the physical components of the actual trainer, and it allows reproducing all the main aspects of the real lab experience, including typical students' mistakes and realistic operating noise. This trainer simulator was successfully used for the first time at Purdue in Fall 2020, and it will represent a valid option for virtual hands-on experiences for distance learning students for years to come.

Keywords: Fluid Power Education, Hands-on experience, Fluid Power, Virtual Simulator, Online Learning, Object-oriented programming, Digital twin

1 Introduction

Hands-on learning is a significant portion of the learning puzzle for applied engineering disciplines such as fluid power. It does not only make the class material more enjoyable and exciting to students, but it also allows better to engage the students through an active learning process and it helps to fix the basic concepts into each student's mind. Moreover, it can give the feeling of the problem, which cannot be taught, especially for troubleshooting experiences. In fluid power (FP), hydraulic and pneumatic trainers have been successfully used over the last decades for this purpose. A hydraulic trainer is training equipment to support the teaching of hydraulic and pneumatic motion control. It is a customizable test bench with a power unit, valves, actuators, and hoses with connectors. This paper particularly aims at trainers for educating the next generation of engineers in hydraulic control technology. In addition to the development of a virtual learning tool (imitates the real experiments in the virtual world) to support online education. The need for online education was constantly growing until it became an unreplaceable necessity during the COVID19 pandemic.

Many of the existing trainers have relevant limitations with respect to the state-of-the-art applications. From one side, they are often limited with the operating pressure and flow for safety reasons. The flexibility of reproducing both resistive and overrunning loads to the circuit is limited. However, most importantly, the existing trainers usually cover a minimal spectrum of the hydraulic control circuits that are commonly used in fluid power machines. Moreover, the human interface is often too rudimental: as very seldom advanced graphical user interfaces or modern data acquisition and control systems are used to accompany the students towards the accomplishment of a specific experience.

1.1 State of the art

Another significant limitation of most of the existing trainers is on their flexibility. Trainers offered by the fluid power companies such as Amatrol [1], Bosch Rexroth [2], Eaton [3], FPTI [4], Hytech [5], Id System- didactic [6], Parker Hannifin [7], SMC [8], SAP engineers [9], come with specific modules suitable for training only specific concepts. Therefore, it can be challenging, from the point of view of cost and spatial availability, to set up a laboratory where multiple students can simultaneously run experiments in multiple stations. The pre-designed modules of most of the mentioned trainers are often designed for a specific fluid power curriculum, where the different concepts are presented following a pre-determined conceptual sequence. While this can be considered an advantage for the students that can experience well established programs, such design is a great obstacle for instructors that want to experiment with new concepts or follow educational paths different from the pre-designed one.

Many academic institutions (the list here would be very wide, involving most of the academic fluid power labs in the world) use as educational test rigs experimental setups similar to those used for research purposes. A significant example is described in [10]. Such labs constitute in-depth experiences for the students, but they are often unsuitable for providing exposure to basic concepts, circuit assembly, and troubleshooting.

From the considerations above, it is clear the convenience of having available trainers highly flexible, which can be used for training the students with both basic and advanced concepts by using the same working area. Purdue University upgraded a non-commercial version of Parker Hannifin trainers [11] by introducing some advanced experiments related to electrical control and installing a DAQ system, but it is now outdated due to technological advances in the last decade. Festo [12] offers a test bench that allows running basic and advanced labs but lacks a well-designed human-machine interface, which can be a drawback for the students and cannot simulate different loads.

An important aspect of this flexibility pertains to the ability of the trainer to demonstrate different concepts related to the main parts of a hydraulic system: the flow supply (different concepts based on either fixed or variable displacement pumps are available); the control type (pump control, or different type of valve control) different actuators (linear and rotary actuator); different loads (overrunning, resistive). A test station that can reproduce in a compact implementation all the above elements in all possible combinations, even involving multiple functions, can be considered as ideal to educate and stimulate the students to all possible fluid power concepts.

The work presented in this paper not only tackles the above-described challenges but also considers that if such implementation is possible for an actual trainer, then it could be reproduced in a virtual environment in the same fashion for online education.

In the area of online education for hydraulic control systems, there is a wide category of tools that is available to students such as [13], [14], [15], mostly built in academia, in common are limited to few basic experiences without allowing the user to build and assemble the circuit themselves. Moreover, no recent research has been done toward improvements. [16], [17] represent more recent work in that field but still does not give the user the choice of connecting a circuit themselves in real-time. The most effective and successful tools easily accessible online for both guided and self-education are those dedicated to the simulation and rendering of hydraulic machines. Here, simulation tools such as FluidSIM [18], Simcenter Amesim [19], Automation Studio [20], Simulation X [21], and hydraulic simulation software by engineering adventures [22] are among the most popular. They allow the users to build a hydraulic circuit of their own and simulate it. However, the mistake that a learner can make with such tools and the related troubleshooting is a typical debugging of a software tool. Using the above tools, the students likely miss a realistic experience of connecting physical components and visualizing the actual operation of the hydraulic system.

With this goal in mind, the authors conceived a physical trainer along with a digital twin that can be used to replicate the lab experiences in a virtual manner. The digital twin utilizes Unity 3D software and the CAD models of the components used in the physical trainer to provide the students with a realistic experience. The process of

selecting the components, connecting the component hydraulic ports with hoses, operating the system is reproduced through a graphical interface that also included the audio sounds recorded from the physical trainer. In this way, the instructor can use the virtual trainer in multiple ways to satisfy fluid power curricula of different nature: from online-only virtual lab experiences to mixed virtual and physical labs, to in presence lab where the virtual tool is used in aid of de-densifying the presence of the student at the physical station to respect social distancing rules.

The remaining sections of this paper details mostly the choices made in the design of the physical trainer (section 2). The virtual simulator is briefly presented in section 3.

2 Hydraulic Trainer

The following factors can be considered important for the design of a successful hydraulic trainer that supports a fluid power curriculum via hands-on lab experiences:

- a) Spatial requirement. The smaller is the trainer; the higher is the number of trainers that can fit a normal size classroom. This requirement was particularly taken into consideration in this work, considering a design with a flexible working area where the students can easily assemble different hydraulic circuits simply by placing and connecting components from a proper component rack (Figure 1).
- b) Cost and safety. In the proposed design, components typical of the mobile market are traditionally less expensive than those used in industrial hydraulics are selected to lower the system cost. The level of power, in terms of maximum flow rate ($< 13 \text{ l/min}$) and pressure ($< 50 \text{ bar}$) chosen for the proposed test stations allows performing all the required lab experiences but limits the typical risks of high-pressure systems and increases the longevity of the selected components. The students are always required to wear safety glasses when working at the trainer and follow the safety instructions provided by the instructor.
- c) Human experience. A well-designed test station that uses modern engineering technology increases the appeal of fluid power technology to the students. For the selected design, a touch base screen guides the students to every lab experience, allowing selecting the sensors and the control inputs to the hydraulic components. The IQAN system by Parker will also allow future development for running real-time simulations of the tested systems that can be compared to the actual experiment.
- d) Available set of lab experiences. An effective hydraulic trainer can support both basic and advanced lab experiences in such a way that the student can be exposed to the basic concepts of fluid power but also to the state-of-the-art technology present in commercial machines. As will be detailed in subsection 2.1, particular attention was put on formulating a design of the test station with respect to the experiences available to the instructor.

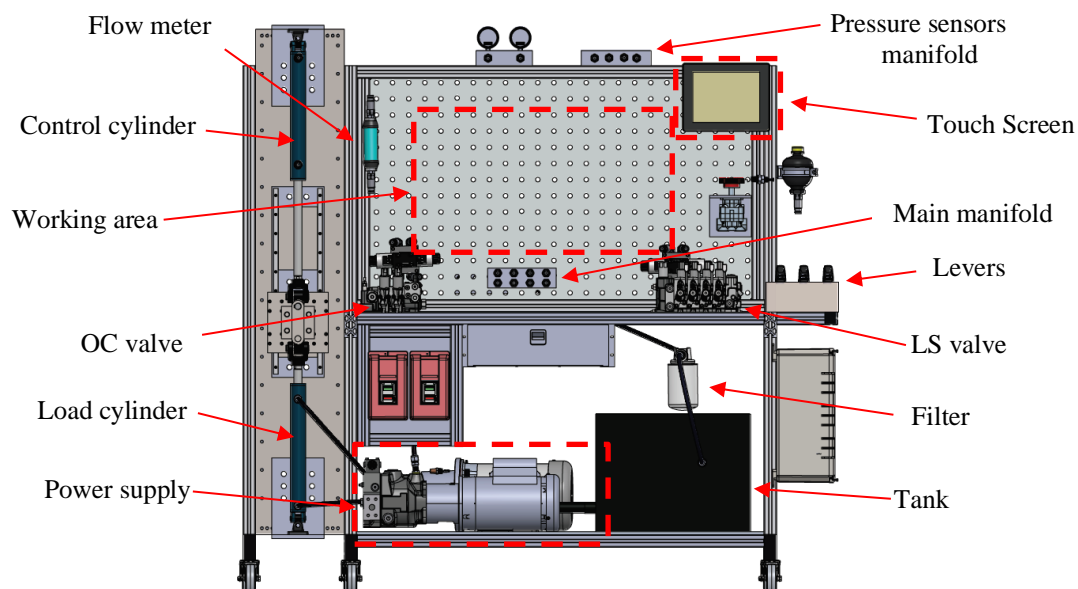


Figure 1: Trainer stand CAD drawing.

The last two points, c) and d), are not trivial for fluid power technology. As stated during SICFP95 by Rob Koski, “With a few notable exceptions, engineering colleges and universities worldwide have generally ignored fluid power as a subject.” [23]. This statement still holds in 2021, with negative consequences to: (i) the number of engineering students introduced to fluid power and (ii) the lack of established textbooks and educational curriculum available to the students interested in learning this technology. This means that, still today, there is not a commonly accepted education method in fluid power available in academia. This latter statement is also consistent with the lack of textbooks that covers the basics as well as most important aspects of the modern fluid power technology. Several textbooks, such as [24], [25], largely focus on the architecture and the operating features of important fluid power components, but lack in providing a system level approach for designing fluid power systems. Other textbooks, such as [26], [27], privilege the analysis of servo-hydraulic systems and do not cover the technology commonly used in off-road machinery. Milestones textbooks such as [28], [29], and [30] focus a lot on the basic theory behind the functioning of hydraulic control systems, but they are not up to date with the modern technology. Finally, other books, such as [31], [32], are suitable only to specific aspects of fluid power technology, such as positive displacement machines and hydrostatic transmissions. All the above textbooks are successfully used at different colleges, as an indication that an established method for teaching fluid power still does not exist. Therefore, it is intuitive how the situation as pertains to hands-on experience is even more sparse, and very often, trainers used in academia are conceived by the fluid power industry, as it appears in the references provided in the previous section.

The above premise is provided to stress the fact that the selection of a proper set of lab experiences to educate hydraulic engineers is far from being obvious. In the trainer presented in this work, the effort was put in providing a useful set of experiences that can be used to support fluid power programs that conceptualize a fluid power from the point of view of the supply type (impressed flow / impressed pressure), and actuator control type (primary control, metering control, secondary control). Therefore, the basilar elements are provided with a simple hydraulic system involving no actuations (for the demonstration of key component features) or single actuation. More advanced hydraulic circuits, such as systems with multiple actuators, are then provided as an extension of the basic circuits. This philosophy of educating engineers in fluid power is a recent trend consolidated in some recent textbooks, such as [33], [34].

2.1 Lab experiences

Hydraulic control systems offer multiple possible layout architectures to control hydraulic functions. These architectures often present substantial differences regarding the control features and hydraulic components used in the system. Hydraulic systems used to control a single actuator can be classified according to two criteria. The first criterion is the supply concept. In a hydraulic system, the supply is the pump, which can operate as a flow supply or pressure supply. Pressure supply is when the pump is adjusting its displacement to keep a given pressure. The second criterion is the control concept. Based on the control element location in the circuit, the system architecture can implement different control methods: primary control, metering control, and secondary control. Figure 2 combines in one figure all the possible configurations. By combining all possible control concepts with all possible supply concepts, 12 methods for controlling an actuator can be realized (most of these with proper variants, as discussed in [34]). Every single circuit has its own features, uses different types of components, and behaves differently according to the nature of the load (i.e., resistive vs. overrunning). The great majority of today's hydraulic systems are based on the metering control, where the control element is located in a valve between the supply and the actuator, where actuators can be placed in series or in parallel with respect to the flow supply.

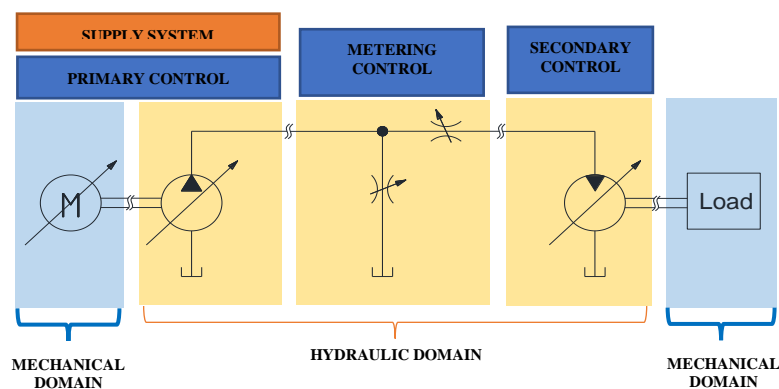


Figure 2: The basic control concepts involved in the control of a single actuator.

Following the above strategy of illustrating hydraulic control concepts, the proposed trainer offers multiple labs for both single-user and multiple-user architectures and also allows establishing different levels of load, including resistive and overrunning conditions. In addition to these labs on hydraulic control concepts, the trainer allows some component-focused or troubleshooting-related labs as detailed in Table 1 and Table 2.

The component-focused experiences are suitable to demonstrate the basic features of the lab (such as setting the maximum operating pressure while studying the behavior of the main pressure relief valve) as well as to demonstrate the basic functioning of some key components used in a hydraulic system. Of particular relevance is the pump characterization lab experience, where the flow vs. pressure performance of the main pump installed in the trainer is tested for the students.

The troubleshooting experiences are designed to expose the students to some practical troubleshooting concepts typical of real systems. Of relevance is the aeration and cavitation test, where one of the pumps installed in the rig is forced to operate in a condition of low suction pressure with the possibility of introducing entrained air into the system (see the schematic of Figure 3). Another test suitable to develop the student’s ability to use the theoretical concepts of hydraulics for troubleshooting purposes is the cylinder leak test (Figure 4), where it can be determined if the cylinder seal has internal leakages by observing the piston motion during the tests.

The single actuator tests are listed in Table 3. The table shows the tests used at Purdue to educate undergraduate students, but the flexibility of the trainer would allow for a much longer list. The majority of the circuits aim at demonstrating the metering control technology, which has a lot of variants and market applications. A test is designed for primary control systems. Secondary control is currently not implemented on the trainer, but it will be an easy extension that will be implemented in the future. The tests designed for the single actuator control permit to illustrate and tests the basic features of metering control. For this purpose, basic circuits with meter-in and meter-out orifices (needle valves) are tested on an actuator at which the load (either resistive or overrunning) can be set by the student. After these basic experiences, the trainer allows studying architectures typical of the current state of the art, based on open center circuits, load sensing circuits, or additional components such as counterbalance valves. An experience is also designed to test the capability of an accumulator to recover energy. The most significant schematics are reported in brevity in Figure 5. Each one of these experiences permits the student to build and operate the system, and most importantly, to acquire the most important data necessary to validate the theoretical equations that govern the system. These sensors are shown in the schematic of Figure 5. In many cases, the lab instructor purposely omits the location of the sensors so that this can be added as one of the learning objectives of each experience. The students must build each circuit of the experience by connecting the relevant hydraulic components with quick connectors.

Table 1: List of hydraulics troubleshooting labs experience.

Hydraulics Troubleshooting		
T1. Aeration, Cavitation, and Entrained Air	T2. Cylinder Leak Test	T3. Cylinder Cushion

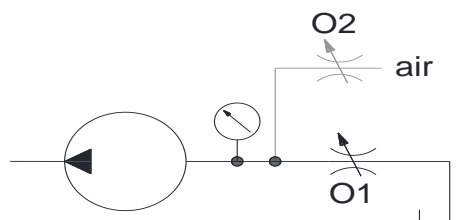


Figure 3: Aeration and Cavitation lab schematic.

Table 2: List of component characterization labs.

Component Characterization			
C1. Pump Characterization	C2. Valve Characterization	C3. Maximum Relief Pressure	C4. Proportional Hydraulics

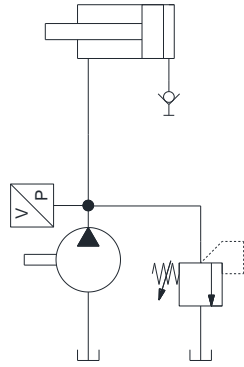
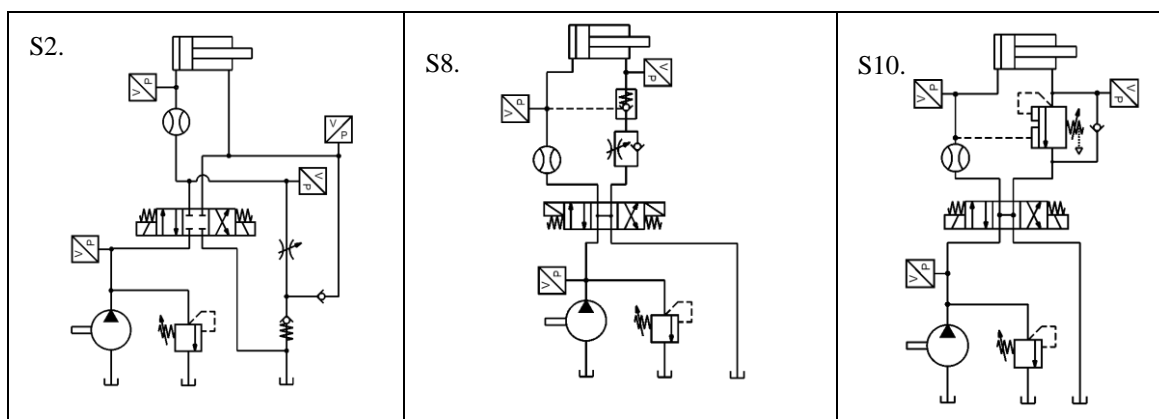


Figure 4: Cylinder leak test schematic.

Table 3: List of single user lab experiences.

Single Actuator Labs	
S1. Maximum Bleed-off	S2. Unloaded Pump Condition
S3. Pump flow rate through an orifice	S4. Sequence Circuit
S5. Basic Circuit	S6. Open Center Hydrostatic transmission
S7. Regeneration	S8. Passive Load Holding
S9. Meter-in	S10. Counterbalance Valve
S11. Meter-out	S12. Constant Pressure System
S13. Unloading Circuit	S14. Load Sensing System
S15. E-LS system	S16. Load Sensing System with a Fixed Displacement Pump



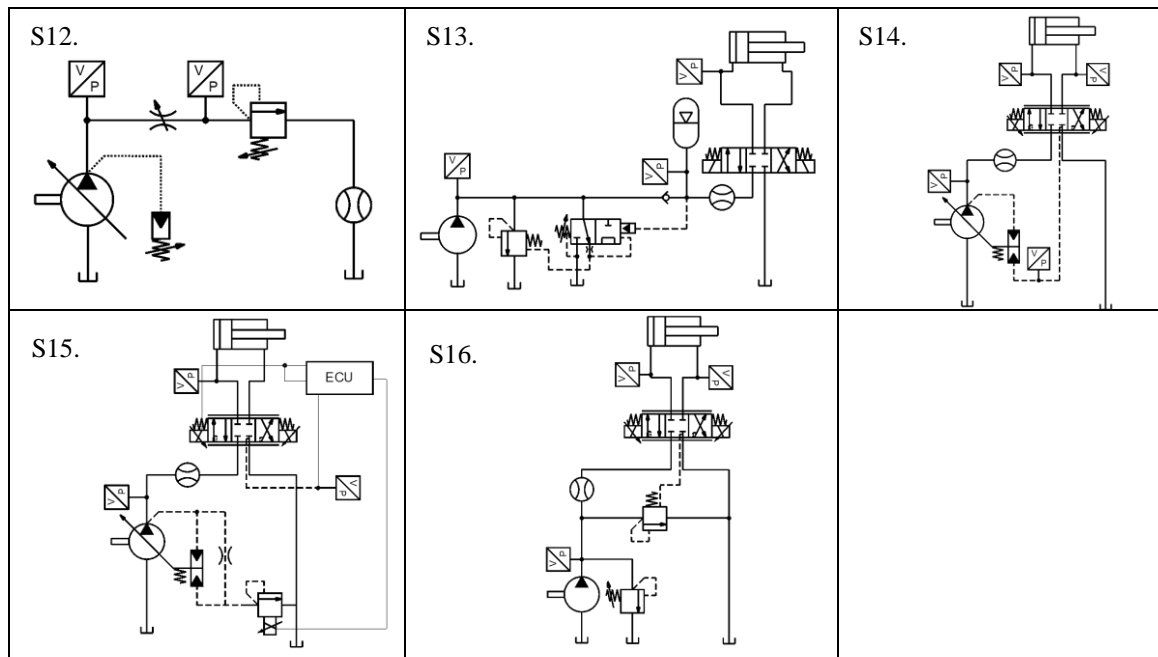


Figure 5: Simplified circuit layout of single actuators

The single actuator experiences build the basis for progressing towards the study of multi-actuator circuits. Multi-actuator circuits reflect the typical design of common fluid power machines. In multi-actuator circuits, a single flow supply – prime mover is used to drive multiple functions. Depending on the circuit layout, series or parallel, aspects of pressure summation or flow summation occur at the supply line. These aspects can be easily illustrated by using two actuators. Two actuator circuits are also used to analyze the aspect of load interference between different actuators present in the same circuit. This pressure interference causes different behaviors with respect to the synchronization between the actuator motion. These aspects of control are shown with the circuits that are summarized in Table 4. The ISO schematics for these labs are shown in Figure 6. Lab 1 represents a circuit with a cylinder and motor with two independent pressure levels, and it is suitable to demonstrate the above concepts when a pressure reducing valve is used to control one of the circuits. Lab 2 shows the aspect of synchronization and pressure amplification in the case of series configuration. Lab 3 focuses on an open center system with two cylinders and illustrates the typical load interference aspects of these circuits. Labs 5 and 6 are dedicated to the load sensing control technology that is very often used in mobile machinery. The aspects caused by different choices on the valve compensator design are shown in two separate labs. Similarly, to the single actuator experiences, also, in this case, the students, by selecting the location of the sensors, can plot pressure vs. actuator flow information to analyze the aspect of controllability and energy efficiency of each system.

Table 4: List of multiple user lab experiences.

Multiple User Mobile Hydraulics		
Fixed displacement System	Constant Pressure System	Load Sensing System
M1. Dual Pressure Circuit M2. Multiple User in Series M3. Multiple User Open Center System	M4. Multiple User Constant Pressure System	M5. Non-Compensated LS System M6. Pre-Compensated LS System

Overall, the authors selected 29 labs as effective to provide undergraduate students an optimal complement to the theoretical lectures of a traditional fluid power class (3 credits, 36 hrs). However, the flexibility of the trainer allows performing additional tests to accommodate a different selection of labs or a higher number of labs (such as in fluid power programs formed by multiple classes). 29 experience might hardly be feasible in a single class. Nevertheless, the number can accommodate different instructor preferences. Most importantly, having many experiences can open the instructor to change the traditional homework assignments from worked problems to more insightful lab experiences that the student can run in replacement to the homework.

The control valves that allow performing all these experiences can be classified into three different categories: the directional control valves, pressure control valve, and flow control valves. These components are tabulated in Table 5, Table 6, and Table 7, respectively.

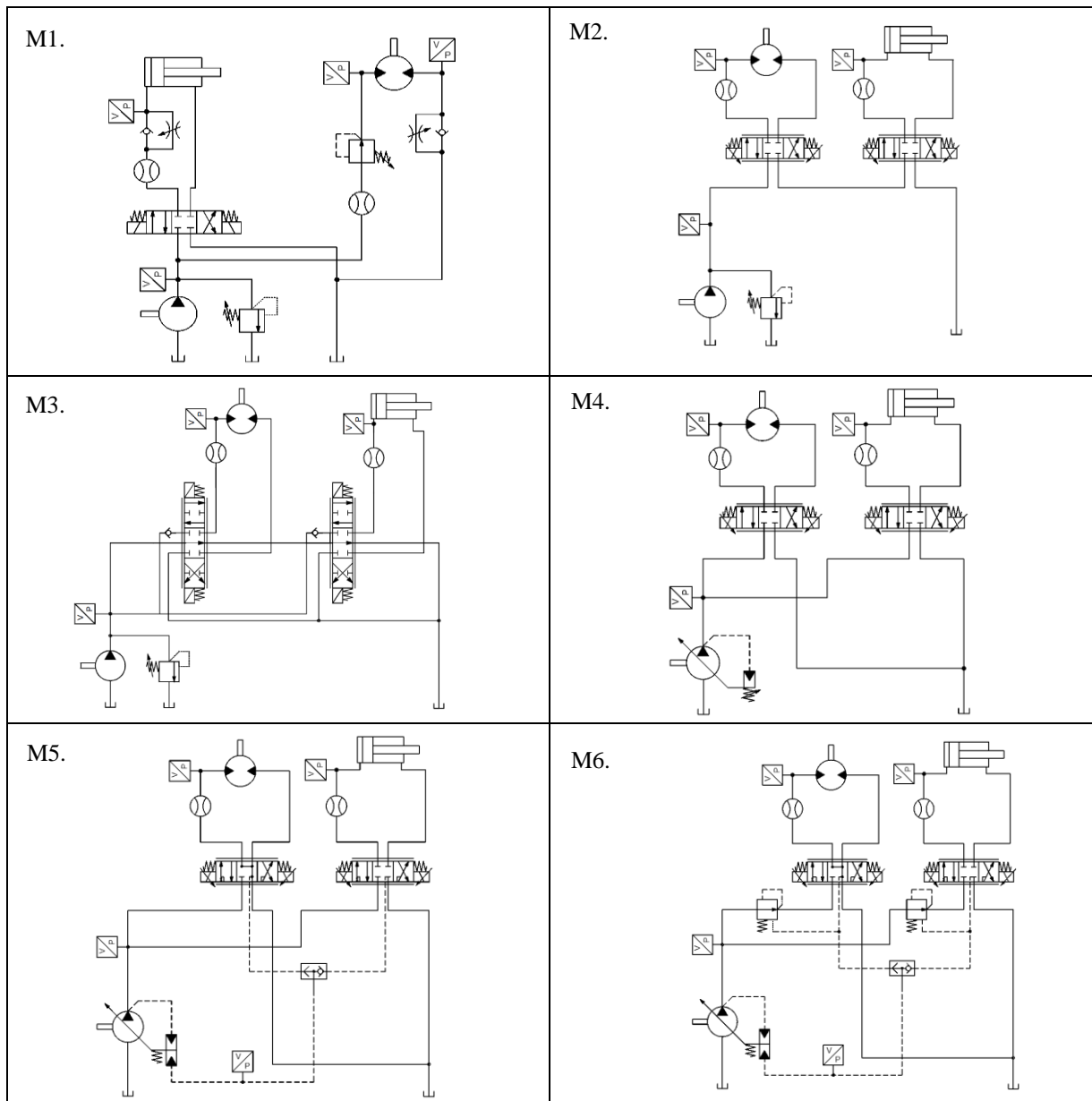


Figure 6: Simplified circuit layout of multiple actuators.

Table 5: Directional Control valve product number.

DCV	Product Number
LS valve	Parker L90LS
OP valve	Parker P70CF
Directional valve	ParkerD1FB
Directional valve	Parker D1VW
Check valve	Parker PSK20610
Loaded check valve	Parker CVH081

The LS valve and the Open Center (OP) valve are customized to meet the low flow requirements of the trainer (10.5 L/min). The LS valve consists of four sections. The first two are non-compensated valves, one is a motor

spool, and the other has a cylinder spool. The other two are pre-compensated valves with a compensator setting of 5 bar, similarly, having a motor and cylinder spool. This valve can be controlled either manually with the mechanical levers or electronically through the DAQ. The OP valve has two sections solenoid operated. Three directional valves (4-way 3 position), two of them are proportional closed center valves. The other is an ON/OFF open center valve.

Table 6: Pressure Control valve product number.

Pressure control valve	Product Number
Pressure reducing valve	Parker PSK20614
Pressure relief valve	Parker RD102K09
Counterbalance valve	Parker E2B02
Unloading valve	Parker RU104
Logic element	Parker 10SLC2-A-75
Logic element	Parker 10SLC2-A-25

Table 7: Flow control valve list.

Flow control valve	Product Number
Needle valve	Parker PSK20608
Pressure compensated Flow control valve	Parker PSK20611
Flow control valve	Parker PSK20609

2.2 Power Supply

Many considerations were put on the choice of the supply pump to be used in the trainer. The main goal was to achieve a supply that can be suitable to operate as both fixed and variable flow supply. For the case of variable flow supply, the desire was to allow the unit to operate with both pressure compensating mode, as in a constant pressure system, or flow compensating mode, as in a load sensing (LS) system. The choice was to modify the basic layout of a 16 cc/rev LS axial piston pump, as shown in Figure 8. The power supply has three ports connected to the main manifold, as shown in Figure 1, with quick disconnectors on the user's side. Next to the pump, Figure 7 shows the flow compensator of the pump, which reduces the pump displacement to set an outlet pressure equal to the pressure value at the LS port pressure plus a margin. The LS signal is connected downstream of a needle valve placed between the pump outlet and port 1 of the manifold. In this way, the pressure drop across the needle valve is always equal to the pump margin. In this way, setting the needle valve opening allows controlling the pump flow provided to the system.

$$Q = C_f \Omega_o \sqrt{\frac{2(p_p - p_{LS})}{\rho}} = C_f \Omega_o \sqrt{\frac{2s}{\rho}} \quad (1)$$

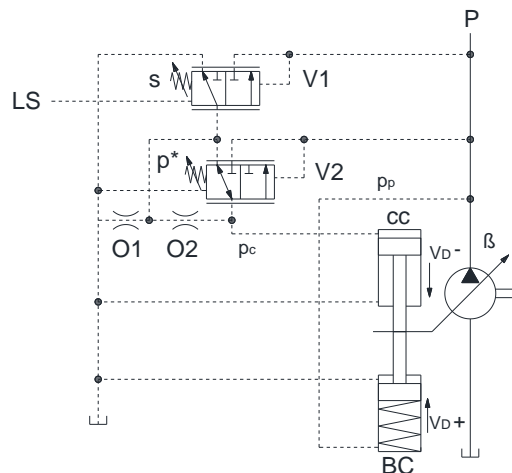


Figure 7: Detailed ISO schematic of a variable displacement pump.

This operating mode allows setting the flow rate of the pump and allows the students to “see” the flow supply as a fixed displacement pump. In this scenario, the IQAN system displays on the screen the pump volumetric efficiency as a function of the system pressure in real-time. If the user connects port 2 as an outlet and port 3 to the LS line, the pump then behaves as a traditional LS unit where the needle valve and the bidirectional ON/OFF valve are kept fully closed to avoid any interference with the LS signal. Connecting to port 2 and choosing with the DAQ to operate as a constant pressure system, that activates the bidirectional valve allowing the pressure reducing valve to control the LS signal and therefore the pump outlet pressure independently from the load information and only based on the user command to the reducing valve. In a similar fashion, an Electronic-Load Sensing flow supply is achieved by letting the user to identify which pressure sensor is transmitting the pressure information to the pressure reducing valve. Figure 9 summarized all the operating modes of the flow supply.

The pump pressure range is between 17-69 bar, but for safety reasons, the maximum pressure is set at 50 bar by adjusting the pressure limiter setting. The pump displacement is 16 cc/rev, but its maximum swashplate angle was limited to provide a maximum flow rate of 10.3 L/min at a speed of 1800 rpm of the prime mover.

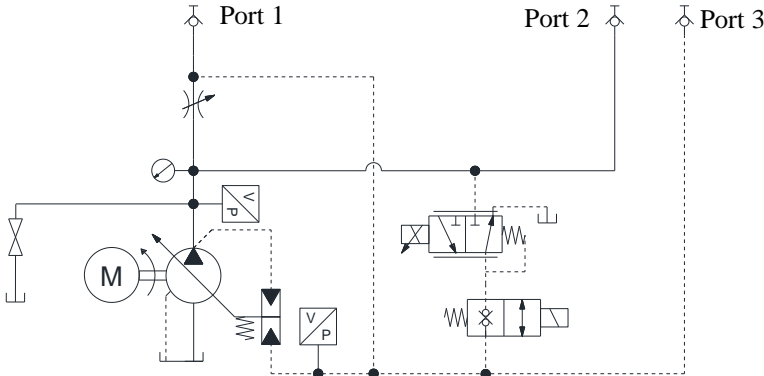


Figure 8:Trainer power supply ISO schematic.

Table 8: Power supply hardware.

Power Unit	Product Number
Axial Piston Pump	Parker PVP16102A
Pressure control valve	Parker EPR111C
Needle valve	ParkerD1FB
Bi-Directional valve	Parker GS02700NS
Shut-off valve	Parker V500CS6

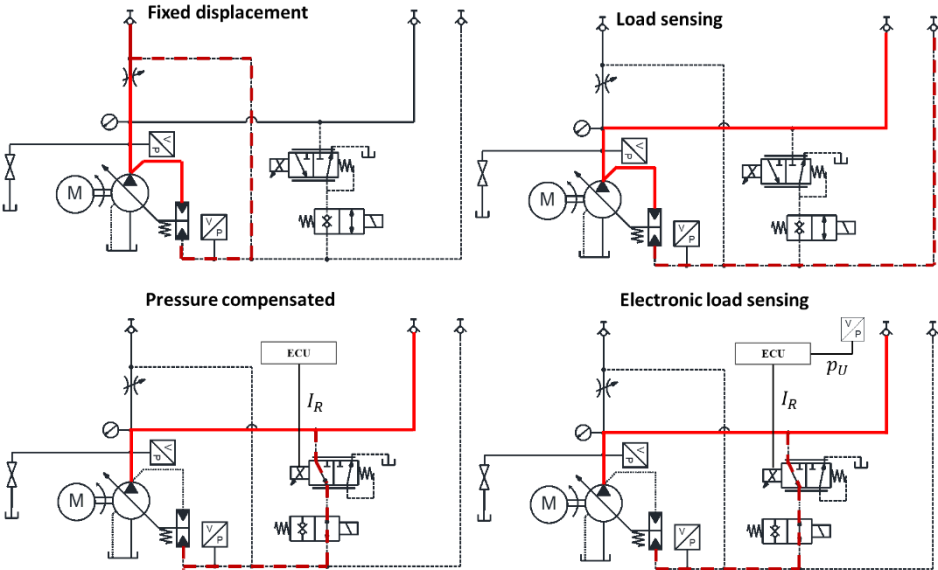


Figure 9:Different power modes of operation of the supply unit functions.

2.3 Actuator and Load module

An original feature of the presented hydraulic trainer is the capability of testing different circuits for various loads acting on the hydraulic actuators (resistive or overrunning). This is achieved by a dedicated load module which can be represented with the schematic of Figure 10. The cylinder used in the test circuit is referred to as “control cylinder”: this cylinder will be connected by the student with either one of the circuits discussed in the previous section 2.1 by using quick connectors. This control cylinder is connected to a “load cylinder,” which is connected to an auxiliary load circuit, whose components are listed in Table 9. The load cylinder is used to set the desired force acting on the control cylinder, in both directions. This is accomplished by two reducing/relieving pressure valves used to control the pressure in the cylinder chambers and, consequently, the load force. Cylinders are coupled with dual-axis aluminum roller guides to compensate for any possible side forces due to unavoidable misalignment. Users can set the load force using the DAQ. The force range varies between 0 and 3.5 KN in the case of resistive and 0 to -500 N in case of overrunning. Using two pumps allows to control each chamber pressure separately and permits the use of a smaller electrical motor.

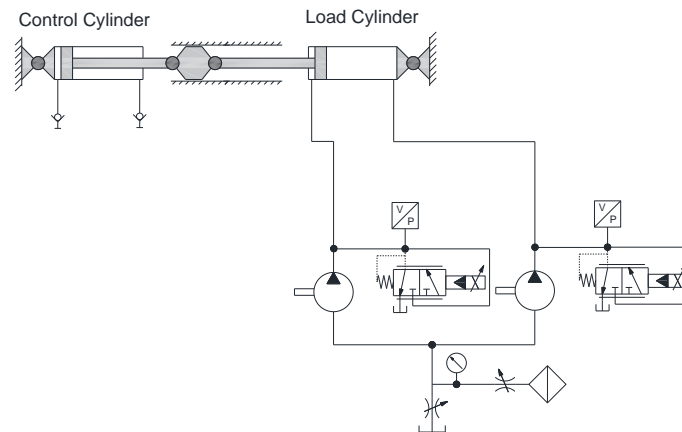


Figure 10: Load module structure.

The auxiliary circuit that supplies the load cylinder is based on a tandem gear pump. Due to the high capabilities of gear pump to handle cavitating conditions, the same unit is used in combination with a variable orifice that was installed with a tee connection having a pressure gauge and a needle valve for aeration to allow the lab experience T1 (Table 1) previously mentioned.

Table 9: Components used in the load module circuit.

Component	Product number
Tandem Gear pump	Parker PGP505
Hydraulic cylinders	Parker 1.50BBDH
Pressure control valve	Parker EPR111C
Hydraulic cylinder	Parker PSK20603
Bidirectional motor	Parker PSK20618
Needle valve	Parker N400SS
Industrial ball valve	Parker V502SS-8
Muffler	Parker EM25
Pressure gauge	Wika 0 to -30 IN HG

2.4 Trainer GUI, DAQ, and Sensors

Parker Hannifin's IQAN electro-hydraulic control system was installed on the trainer to be used as an intelligent DAQ (master control). The master control offers an interactive and intuitive human machine interface. The master control includes a 24 V DC power supply, an MD4 10.1" touch display, XC43 expansion module, levers, pressure sensors, flow meters, position sensor, and a speed sensor. Figure 11 schematically shows the instrumentation for the trainer, along with the approximated location of each sensor and valve. All the selected parts are listed in Table 10.

The Parker IQAN-MD4 serves as a touch display, interface, and controller. The XC43 expansion module allows up to 50 sensors of voltage, current, digital, and timer inputs. It permits the control of 36 valves with different outputs, either proportional or digital. The module communicates with the touch display over a CAN bus. The master control allows exposing the students to the basic features of electronic control, sensors, wiring schematics, calibration, diagnostics. The authors believe that this use of HMI, based on GUI, DAQ, and the use of electronic sensors instead of traditional gauges, contributes to stimulate the students about the learning of engineering aspects outside traditional hydraulic control systems, and at the same time provide a modern perception of the trainer.

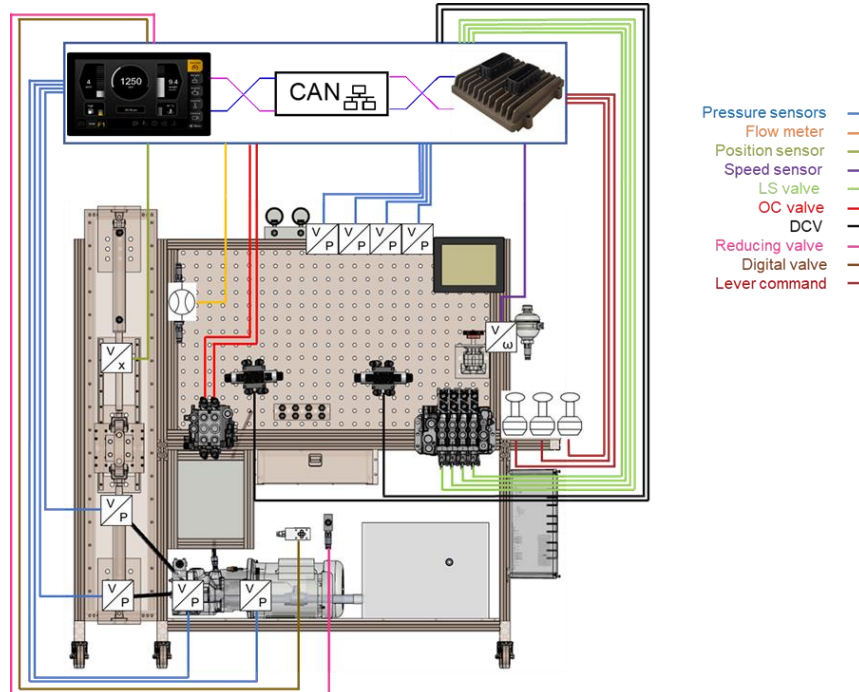


Figure 11: Master control diagram for reference trainer.

The code development and testing are done through the IQANdesign [35], which is a graphical design tool. The system allows recording the data into an excel file to facilitate an offline data analysis.

A user-friendly GUI was formulated and implemented. This GUI has a top-down structure that allows the student to navigate between the pages using the touch screen. It starts from choosing different kinds of power supply, reading the sensor's value while running the experiment, changing the units between metric and imperial if needed. The GUI provides the chosen labs list, allowing the student to visualize the hydraulic circuit to be connected, the description of the lab's experience, and the instructor questions they need to answer. This also eliminates the need for a printed handout. The user can also install Simulink models for online model validation. Another available feature is implementing and testing Simulink controllers with any hydraulic circuit opening the opportunity to teach advanced control classes. A GUI example related to the multiple user open center lab is shown in Figure 12. The GUI also allows asking multiple-choice questions at the trainer stand.

Table 10: List of master control components.

Master Control hardware	Product Number	Output type
Power Supply	120 V AC/ 24 V DC	/
Expansion module	Parker IQAN-XC43	CAN bus
Touch screen	Parker IQAN-MD4	/
Pressure sensor	Parker IQAN-SP	Voltage 0.5-4.5V
Flow meter	Parker SEN40601	CANopen
Position sensor	ASM WS31C	Voltage 0.5-10V
Speed sensor	Parker 01712ECD	Frequency
Lever	Parker IQAN-LST	Voltage 0.5-4.5V
Pressure gauge	Parker PSK20615	Visual
Flow meter	Parker PSK20612	Visual

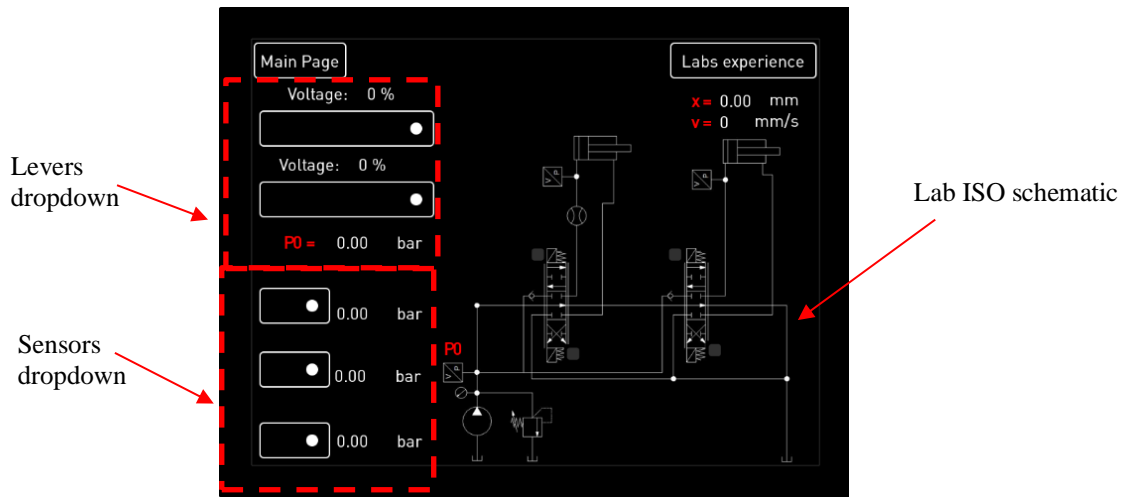


Figure 12: GUI lab experience example.

2.5 Actual Implementation

The trainer stand's design was done starting from the CAD drawing of the current Parker Hannifin trainer [7] and modified to be suitable for the new setup shown previously in Figure 1. It is a double-sided learning platform. One side is used for hydraulics, while the other is used for the pneumatic module. The frame is made with aluminum, and dimensions are 1.72 m high* 1.72 m wide* 1 m deep. The trainer stand has two power units with the corresponding motor starters, a hydraulic tank with a capacity of 75 liters, where a filter is installed at the return line. DAQ, electronically controlled valves, and the load module fixed to the frame. The electronically controlled valves are fixed and secured, so students do not need to change or connect the electrical wires while building the circuit.

The development of the proposed trainer occurred with an initial prototype, developed at the authors' Maha Fluid Power Research Center, followed by a final implementation installed at the Purdue Agricultural and Biological Engineering fluid power motion control lab sponsored by Parker Hannifin (Figure 13). Parker Hannifin also provided support and components for the implementation of the trainers. The prototype of the trainer was essential to test the supply circuit, the load module, the controls, and every single lab experience.

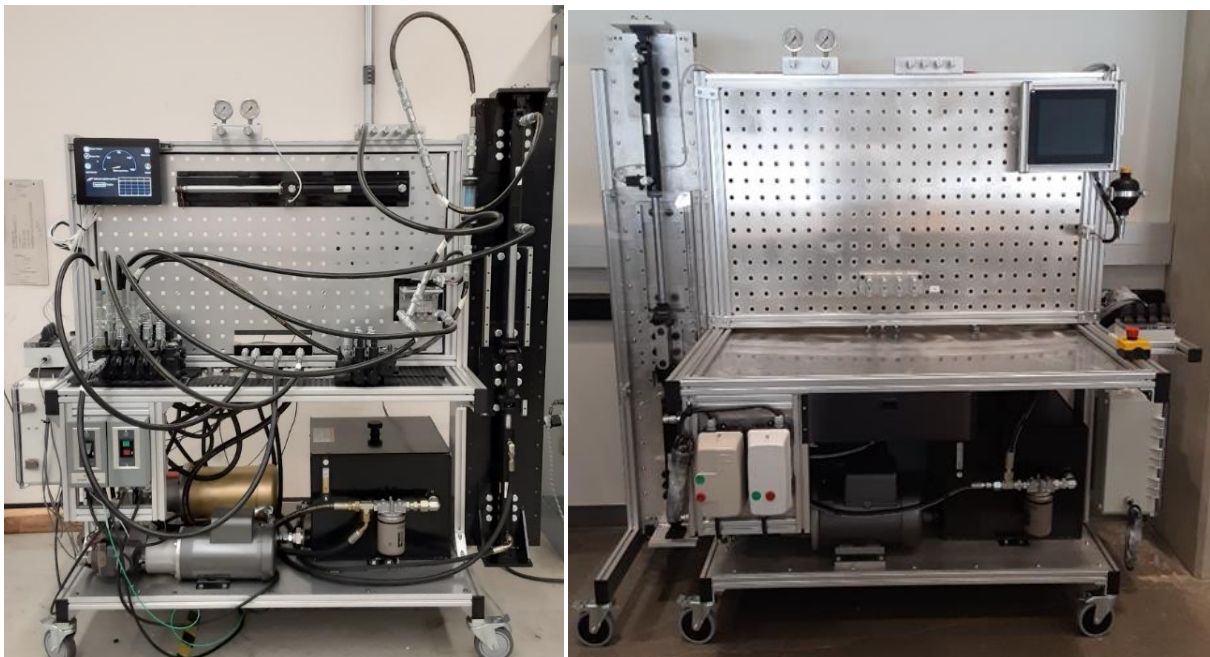


Figure 13: Actual hydraulic trainer: prototype (left); final implementation (right).

Figure 14 shows the components carrier that is double-sided, so every two trainers will need one of them—also having the hose racks as highlighted in the figure.

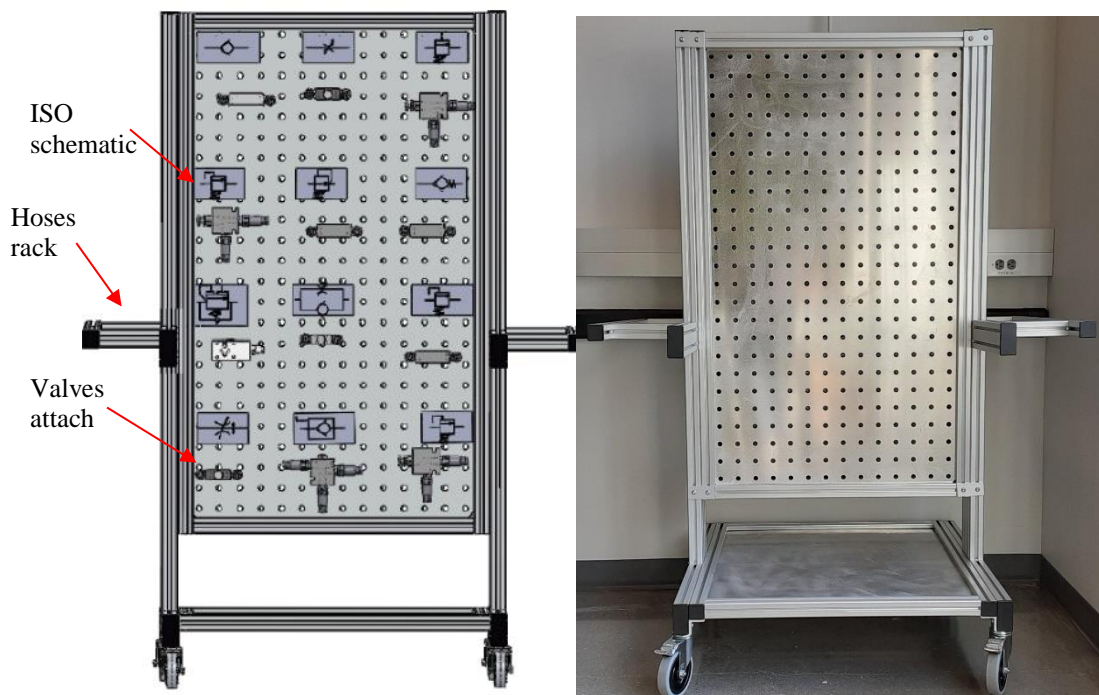


Figure 14: Component carrier CAD (left); final implementation (right).

The component carrier's spirit comes from the simulation tools, in which the user drags the valve from the library into the working area to build the circuit. Here the idea is similar the valves are attached to the component carrier while they are not in use. The user picks up the valve after looking at the ISO schematics and attaching it to the trainer stand. That will make the digital twin look realistic.

3 Virtual Simulator

As mentioned in the introductory section of the paper, the development of a digital twin of the trainer implemented in this work constitutes an essential part of this project. The modular implementation of the trainer, with a drag/drop approach for placing hydraulic components to be connected with quick couplers, was replicated in a software environment to allow the students to perform the same lab experiences using a digital platform (computer, tablet, smartphone). The simulator can be entirely operated from the web or through an App that can be installed. No additional help is needed from the instructor. Like in an actual lab with the physical trainers, the student needs to build and operate the circuit just by looking at the lab handout, inclusive of the hydraulic schematic and lab goals. Unity3D is used as the virtual simulation environment. The software is a typical game engine development tool, which permits creating a real-time 3D project in discipline fields. In the simulator, the user can drag the components rendered with actual CAD drawings from the component carrier to the trainer stand and connect them using the hoses with quick disconnectors. The tool is easy to use, especially for those who worked with the actual trainer before. Unlike the physical trainer, this does not have any safety concerns. Indeed, the virtual trainer also allows overcoming the pressure and flow limitation of the physical trainers for the execution of certain labs (such as the pump characterization, where it is desirable to exceed the 50 bar pressure limitation). The actual CAD of all components was imported from SolidWorks into Blender as STL files. Inside Unity, a universal render pipeline used for graphics optimization was implemented to improve the appearance further. After the visual part, each component was modeled with its own equations using an object-oriented programming C#. Further details on the implementation choices of the software will be provided in future publications.

A crucial aspect of the virtual trainer is the possibility of reproducing some of the mistakes that an actual student can make in the physical trainer. This usually consists of allowing an incorrect sequence for connecting the

components. The virtual trainer also uses sound clips taken from the actual trainer when components are connected or when the system is operated.

A GUI was built to reflect the master control present in the physical trainer. It is possible to switch two modes using a toggle, building, and running mode. The building mode is meant to build the hydraulic circuit where it is possible to see the component carrier with the valves and hoses, while in the running mode, these features disappear, and the master control will show up. Electrohydraulic proportional valves are also controlled differently from manual ones: the first is controlled using an electronic lever, and the last using a mechanical lever.

As an example, Figure 15 shows lab S9 from Table 3, where an orifice with a bypass check valve is used to control the motor speed. The master control is showing the hydraulic schematic along with the sensors and levers. The lever is used to control the DCV, and a slider manages the opening area of the orifice based on the user's command. While in the right, the trainer stand is shown with the circuit connected.

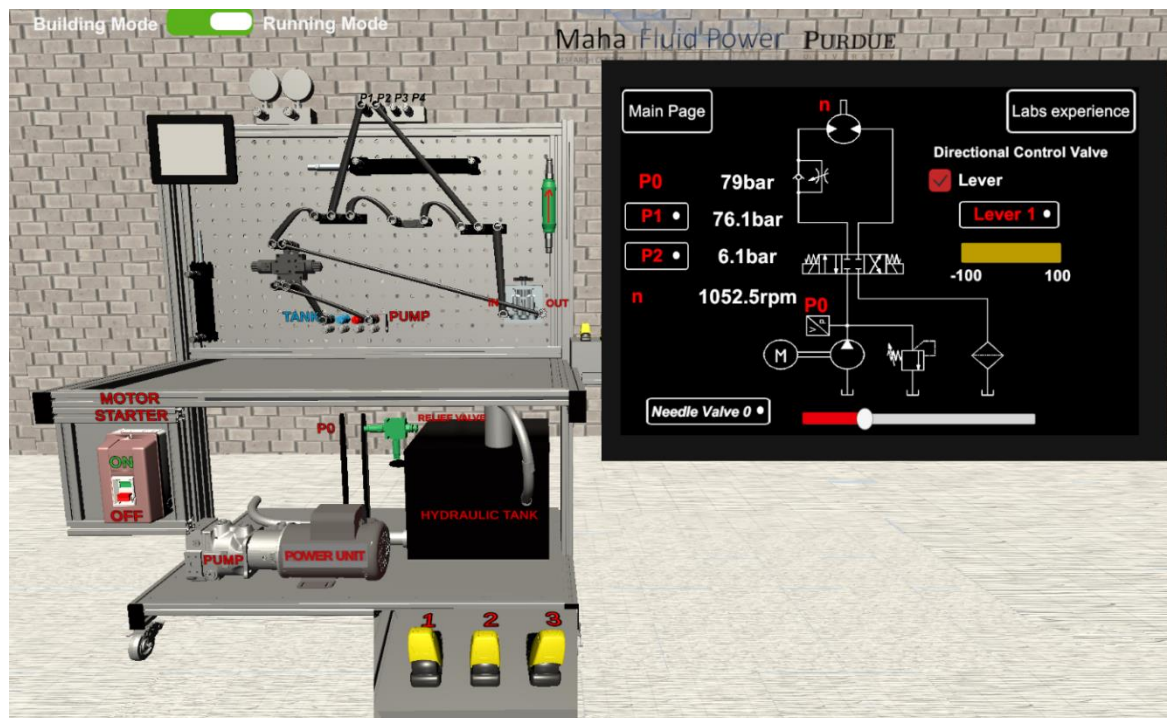


Figure 15: Virtual Simulator lab experiment setup.

4 Conclusion

This work focused on a new hydraulic trainer that was developed at Purdue to support education in fluid power classes. The trainer fulfills the needs of having a flexible structure where the hydraulic circuits can be built in a drag/drop fashion. The use of modern DAQ, such as touch screen and sensors make the trainer appealing to students. The choice of the lab experiences allowable by the trainer suits classes where hydraulic control technology is taught with respect to the basilar concepts of primary control, metering control, and secondary control. Each system is presented considering different options of flow supply (fixed or variable flow supply) or of load acting on the actuator (resistive or overrunning). A total of 29 experiences are referred to in this paper, even if a larger number is easily allowable. The trainer was successfully developed during 2020 and implemented in its final version in early 2021. It is currently successfully adopted in fluid power classes at Purdue University. To fulfill the recent needs for online education, a virtual trainer was developed in Unity 3D to replicate the physical trainer. The virtual trainer allows executing the same experiences in a realistic fashion, using a visual rendering based on 3D drawings of the actual components and sound clips recorded from the physical trainers. The virtual tool was used for the first time in Fall 2020 in a fluid power class involving 18 senior undergraduate students. The trainers and their digital twin were the main practical experience offered in the class. Under the class questionnaire “The projects or laboratories aid me in achieving the class objectives” 75% of responses were “strongly agree, and 16.67% agree”.

Future work will involve adding more lab experiences, especially on hydrostatic transmissions taking advantage of the modularity of the setup.

Nomenclature

Designation	Denotation	Unit
Q	Flow rate	L/min
p_p	Pump Pressure	bar
p_c	Cylinder pressure	bar
p_M	Motor pressure	bar
Q_p	Pump flow rate	L/min
Q_c	Cylinder flow rate	L/min
Q_M	Motor flow rate	L/min
s	Pump margin	bar
T	Troubleshooting	
C	Component	
S	Single User	
M	Multiple User	
FP	Fluid power	
LS	Load sensing	
DCV	Directional control valve	
HMI	Human machine interface	
CBV	Counterbalance valve	
E-LS	Electronic load sensing system	
OP	Open center	
V1	Differential pressure	
V2	Absolute pressure limiter	
CC	Control cylinder	
BC	Bias cylinder	
β	Swashplate angle	radian
p_c	Control pressure	bar
p_p	Pump pressure	bar
O1, O2	Dynamic office	
V_d	Pump displacement	cc/rev
p^*	Pressure setting	bar
GUI	Graphical user interface	
IQANdesign	Graphical design tool	

References

- [1] Amatrol, Hydraulic Training maintenance, Application & Troubleshooting.
<https://amatrol.com/product/fluid-power/hydraulics/>
- [2] Rexroth, Hydraulic Training Systems.
<https://www.boschrexroth.com/en/us/training/purchase-training-systems/hydraulics-training-systems/hydraulic-training-systems>.

- [3] Eaton, Hydraulics Training.
<https://www.eaton.com/us/en-us/support/education-training/hydraulics-training-.html>.
- [4] FPTI, Hydraulic Training System.
http://www.fpti.org/simulators_hydraulic.php.
- [5] Hytech, Advance Electrohydraulic Training Kits.
<http://www.hytechworld.com/advance-hydraulic-training-kit-electrohydraulic/>.
- [6] ID System-didactic, Hydraulic didactic benches.
<https://www.idsystem-didactic.com/en/hydraulic-didactic-benches/>.
- [7] Parker, Motion Control Training.
https://www.parker.com/literature/Training/Hydraulics%20Training/PH_Hydraulic%20Training%20Brochure.pdf
- [8] Static, HydroTrainer.
https://static.smc.eu/binaries/content/assets/smc_cee/trainingsystems/hydrotrainer-200_en.pdf.
- [9] SAP Engineers & Consultants, Hydraulic Trainers.
<https://www.sapengineers.com/hydraulic-trainers.html>.
- [10] N. Nervegna, *Oleodinamica e Pneumatica Esercitazioni*, Politeko, Torino, 2002.
- [11] Buckmaster D Michel J. *Improved electro-hydraulic trainers stations*, 2011 Louisville, Kentucky, August 7-10, 2011 1110740. (doi:10.13031/2013.37736).
- [12] Festo learning Systems Equipment sets.
<https://www.festo-didactic.com/int-en/learning-systems/equipment-sets/hydraulics/training-packages/?fbid=aW50LmVuLjU1Ny4xNy4yMC41NTY>.
- [13] Jesus Pagan MS. *STEM Education Using Emulation Software for Hydraulic Fluid Power Applications*. Journal of Business and Management Sciences. 2018; 6(3):86-92. doi: 10.12691/jbms-6-3-4.
- [14] Gao, Z., Liu, S., Ji, M., & Liang, L. (2011). *Virtual hydraulic experiments in courseware: 2D virtual circuits and 3D virtual equipments*. Computer Applications in Engineering Education, 19.
- [15] Pauniahio L., Hyvönen M., Erkkilä R., Vilenius J., Koskinen K.T., Vilenius M. (2005) *Interactive 3D Virtual Hydraulics*. In: Nicholson P., Ruohonen M., Thompson J.B., Multisilta J. (eds) E-Training Practices for Professional Organizations. IFIP International Federation for Information Processing, vol 167. Springer, Boston, MA. https://doi.org/10.1007/0-387-23572-8_33.
- [16] Hydac, Virtual Reality Training.
<https://www.hydac.com.au/news/post/hydac-australia-develops-virtual-training-environment-that-escapes-covid-19.html>.
- [17] LunchBox Sessions, Industrial training.
<https://www.lunchboxsessions.com/>.
- [18] Festo, FluidSIM.
<https://www.festo-didactic.com/int-en/learning-systems/software-e-learning/fluidsim/fluidsim-5.htm?fbid=aW50LmVuLjU1Ny4xNy4xOC41OTEuNzk3NQ>.
- [19] Siemens, Simcenter Amesim.
<https://www.plm.automation.siemens.com/global/en/products/simcenter/simcenter-amesim.html>.
- [20] Famic Technologies, Automation Studio.
<https://www.famictech.com/en/Products/Automation-Studio/Educational-Edition>.
- [21] SimulationX, Simulation software.
<https://www.esi-group.com/products/system-simulation>.
- [22] E4training, Hydraulic Simulation list. <https://www.e4training.com/navigate2.php>.
- [23] Koski, R.E., 1995. *Fluid power education—what went wrong?* Proceedings of 4th Scandinavian International Conference on Fluid Power, Tampere, Finland, p.71-92.

- [24] AssoFluid. *Hydraulics in Industrial and Mobile Applications*, Grafiche Parole Nuove, Milano, 2007.
- [25] A Esposito. *Fluid Power with Applications*. Pearson Prentice Hall, Columbus, Ohio, 2009. ISBN-9780135136904.
- [26] J Watton. *Fundamentals of Fluid Power Control 1st Edition*. Cambridge University, New York, 2009. ISBN-13: 9780521762502.
- [27] N D Manning, and R C Fales. *Hydraulic Control Systems 2nd Edition*. John Wileys and Sons, Chennai, India, 2020. ISBN-13: 9781119416470.
- [28] H E Merritt. *Hydraulic Control Systems*. John Wileys and Sons, Cincinnati, Ohio, 1967. ISBN 0471596175.
- [29] J Blackburn, G Reethof, and J L Shearer. *Fluid Power Control*. The MIT Press, 1966. ISBN- 13: 978-02620200060.
- [30] D McCloy, H R Martin. *Control of Fluid Power: Analysis and Design*. Ellis Horwood Ltd, 1980. ISBN-13:9780853121350.
- [31] J Ivantysyn, and M Ivantysynova. *Hydrostatic Pumps and Motors*. Akademia Books International, New Delhi, India, 2001. ISBN 8185522162.
- [32] G Costa and N Sepheri. *Hydrostatic Transmission and Actuators: Operation, Modelling and Applications 1st Edition*. John Wileys and Sons, Chennai, India, 2015. ISBN: 9781118818794.
- [33] N Nervegna, Rundo. *Passi nell'oleodinamica*. Politeko, Torino, ISBN: 9788894802153.
- [34] A Vacca, and G Franzoni. *Hydraulic Fluid Power: Fundamentals, Applications and Circuit Design*. John Wileys and Sons, 2021. ISBN: 9781119569114.
- [35] Parker Hannifin, IQANdesign.
<https://www.iqan.se/store/iqandesign.html>.

Comparison of Sliding Mode Controller for Classical and Direct Driven Electrohydraulic System

Juraj Benić, Željko Šitum, Mihael Cipek, Danijel Pavković, Josip Kasac

Department of Robotics and Production System Automation, Faculty of Mechanical Engineering and Naval Architecture
University of Zagreb, Zagreb HR-10000, Croatia
E-mail: jbenic@fsb.hr, zsitum@fsb.hr, mcipek@fsb.hr, dpavkovic@fsb.hr, jkasac@fsb.hr

Abstract

In this paper, a novel energy-efficient Direct Driven Hydraulic (DDH) drive is made in parallel with a classical valve-controlled proportional electrohydraulic system. In the proposed concept asymmetrical hydraulic cylinder is controlled with two reversible pumps directly connected to a servo motor. Due to direct control of the oil flow, such system provides higher energy efficiency in comparison to a valve-controlled hydraulic system. The experimental setup is designed with the possibility of easy switching between both systems, which enables an exact comparison of the experimental results. Sliding Mode Controller (SMC) is designed for the DDH system and also for the classical proportional electro-hydraulic system. A comparison study of two systems is done based on the experimental results obtained with the SMC while reference results are obtained with a widely used PID controller. Parameters for the PID controller are obtained with the Ziegler-Nichols method. The same parameters are used for both controllers in all test cases. The performance and energy efficiency of the proposed system is evaluated through a step and sine wave reference signal with different payloads varying from 0 to 200 kg with 20 kg increments. Additionally, system performance is evaluated based on six parameters calculated from the system response while energy efficiency is calculated based on input and output powers of the systems.

Keywords: direct driven hydraulics, classical hydraulics, sliding mode control, system dynamics, energy efficiency

1 Introduction

Today, despite lower energy efficiency in comparison to electromechanical actuators, electrohydraulic systems due to their high power-to-weight ratio, self-cooling, fast response and lower cost are widely used in many applications such as non-road mobile machinery, manufacturing industry, robotics and aircrafts. Traditionally, valve-controlled systems that are energy-inefficient due to fluid throttling are used in such applications [1]. Disadvantages of the valve-controlled systems are overcome by displacement-controlled hydraulic systems or pump-controlled electrohydraulic systems [2, 3, 4]. In comparison to valve-controlled systems, servo-driven pump-controlled systems have compact structure, higher efficiency and the advantage of speed regulation loop [5].

Novel Direct Driven Hydraulic (DDH) drive is a new concept of a cylinder pump-controlled system firstly introduced in [6] and detailed described in [7]. In [8], a compact design of a DDH drive was investigated where the oil tank was replaced with an accumulator. It was shown that the larger pressure accumulator can replace the oil tank while the smaller one compensates for the pumps displacement error due to manufacturing. The energy efficiency of the proposed system was investigated in [9]. The tests showed that lifting efficiency varies from 48 to 20% while lowering efficiency varies from 32 to 8%. Simulation results from the aspect of the energy efficiency are shown in [10] for the micro-excavator with three DDH units. Results showed that energy consumption due to the extra weight of the three DDH is 15% higher, but approximately 20% more regeneration energy is produced. In [11] comparison of energy efficiency of a 5-ton excavator with a load sensing system was compared to three

DDH units for front attachment. The simulation results showed that the overall energy efficiency of three DDH units is approximately 73.3% in comparison to 31.4% for the load sensing system. The influence of different types of oil on system efficiency is presented in [12]. It is shown that different types of oil can significantly increase system efficiency by almost 10% for temperatures below -10°C . From the aspect of the control theory in [13], a self-tuning fuzzy PID controller is used for controlling the DDH unit with the ability of online tuning making this controller more adaptive and effective in the proposed application. From the given literature it's concluded that the system dynamics between traditionally valve-controlled and DDH drive hasn't been compared yet.

In this paper, the DDH system is made in parallel with the classical proportional electrohydraulic system. An extensive analysis of the system dynamics and energy efficiency between DDH and classical system is presented. Due to nonlinear system dynamics, unknown and varying system parameters Sliding Mode Controller (SMC) is utilized for tracking the desired trajectory and stabilization of the system in a given set point. Both systems are subject to the same loads and working conditions allowing us a mutual comparison of the obtained results. Reference results are obtained with PID controller, while results obtained with an SMC are analyzed and compared to the reference results.

The rest of this paper is organized as follows. In Section 2 description of the experimental setup with used components and simplified schematic representation of the system is given. Section 3 describes used control algorithms while in Section 4 extensive analysis of the system dynamics is presented base on experimental results. In Section 5 energy efficiency is calculated based on power flow and compared. Conclusion and further work are given in Section 6.

2 Experimental setup

The experimental setup used in this research and a simplified schematics representation of the setup are shown in fig. 1. On the proposed setup, the classical valve-controlled proportional electro-hydraulic system and the DDH system are tested independently but under the same working conditions. The classical system uses a 1.1 kW AC motor with 1380 rev/min coupled with a $3.7\text{ cm}^3/\text{rev}$ gear pump for ensuring constant pressure of a 60 bar. Proportional valve PRM2 from Argo-Hytos is used for motion control of a double-acting asymmetrical hydraulic cylinder 32/22x300 mm.

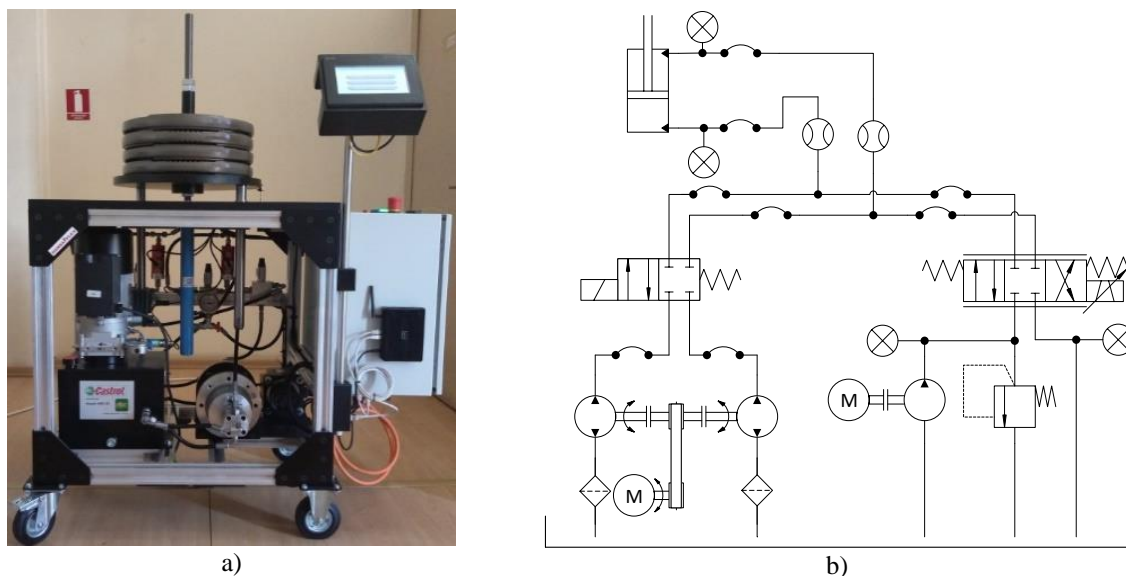


Figure 1: Experimental setup - a) front view, b) schematics representation.

The DDH drive is shown in fig. 2. It uses two reversible Argo-Hytos gear pumps with a displacement of 4.8 and $2.5\text{ cm}^3/\text{rev}$ for direct motion control of the hydraulic cylinder. The pumps are mutually interconnected with the same shaft. Mitsubishi HG-SN152JK speed controlled 1.5 kW permanent-magnet synchronous motor with a maximal rotational velocity of 2000 rev/min is used for propelling the pumps. Digital AC servo amplifier MR-JE-200A with model reference adaptive control is used as black-box speed controller based on the input voltage signal from the PLC. For the torque transfer from the servo motor to the pumps, a belt transmission is used. The A-side and B-side pumps create the inlet and outlet flow to the cylinder where the movement direction of the cylinder depends on the servo motor rotational direction while the required operating pressure is determined by the payload.

Experimental setup is designed for easy switching between both systems allowing us an exact comparison of obtained experimental results. Wire Micro-Epsilon WDS sensor is used for measuring cylinder position, while

EVS and HDA sensors from Hydac are used for measuring inlet and outlet flow from the cylinder and pressures inside cylinder chambers. Piston velocity is estimated on-line with an algebraic differentiator defined in [14]. Data logging on a 10 ms base is implemented on a Mitsubishi PLC along with the proposed control algorithms. The detailed system description is given in [15].

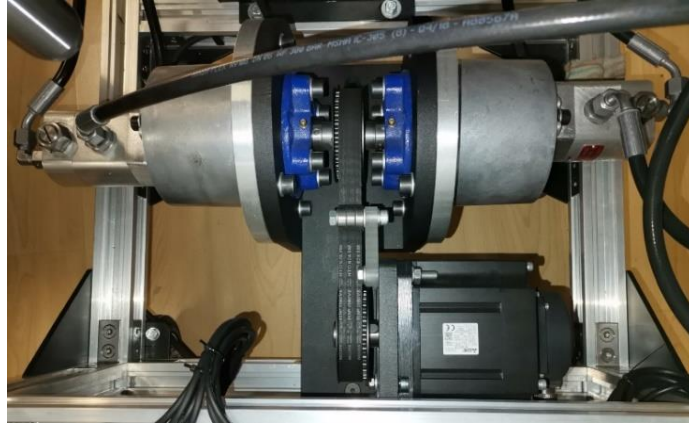


Figure 2: DDH drive

3 Control algorithms definitions

The control process of an electrohydraulic system is a tough task due to the nonlinearities that occur in the system. Because of that linear controllers, such as PID regulator, can only achieve good results around the linearization point. Nonlinear control algorithms can easily overcome nonlinearities that occur due to friction phenomena, internal and external leakages and parameter variation. An overview of the control structure for the DDH model is given in fig. 3. Input to the system is desired cylinder position and the output of the system is the cylinder position. The output of the controller is a voltage signal which is sent to a servo drive or proportional valve.

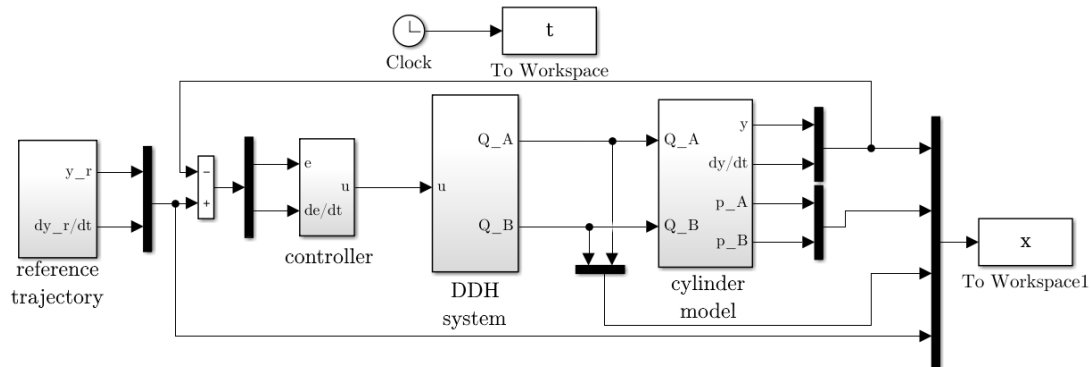


Figure 3: Overview of the control structure of the DDH system

From the defined control structure, the system error is defined as:

$$e = x_d - x_m \quad (1)$$

where x_d and x_m are desired and measured trajectories respectively.

In control theory, the PID controller is one of the most used regulators in the industry due to its simplicity and satisfying performances in a different kind of process. Today, PID controller is implemented in its discrete form and it can be found in all control devices as a stand-alone controller or as a function block in a PLC. For obtaining the reference results, PID regulator in its general form is used and it's given as:

$$u = k_p(\alpha x_d - x_m) + \int k_i e dt + k_d(\beta \dot{x}_d - \dot{x}_m) \quad (2)$$

where k_p , k_i and k_d are proportional, integral and derivative gain respectively, u is the control signal while α and β are weighting coefficients for choosing between different structures of a PID controller. With $\alpha=\beta=1$ parallel form of the PID controller is achieved while with $\alpha=\beta=0$ I-PD structure of the controller is obtained. In this paper parallel form of the PID controller is used. The controller parameters are obtained with the Ziegler-Nichols method for the step amplitude of 150 mm. The obtained parameters are used for both test signals and different payloads.

The sliding mode controller (SMC) is a nonlinear discontinuous robust controller and it is used in presence of the disturbances and system parameter variation. Proposed SMC is given as:

$$s = \dot{e} + \lambda e \quad (3)$$

$$u = k_1 s + k_2 \text{sign}(s) \quad (4)$$

where s is a sliding variable and k_1 , k_2 and λ are designed parameters and u is the control signal. Variable k_1 acts on system stability and reference tracking while k_2 acts on the unknown system dynamics and chattering. Given form of the SMC has second-order dynamics and it only requires system error for calculating the control signal.

4 System dynamics

Both systems are subject to a series of test cases in the duration of 60 seconds. The cylinder payload was increased from 0 to 200 kg with a 20kg increment. This approach allows us to test the robustness of the proposed regulators on the different payloads while maintaining the same regulator parameter. All tests are carried out with initial conditions set to zero. The robustness and system dynamics of the proposed regulator are determined through 6 parameters calculated from step and sine wave system response. Conclusions are given for a cycle duration.

4.1 Sine wave experimental results

Three parameters are calculated from the results obtained for the sine wave reference trajectory. Amplitude error (A_e) and phase shifting (ρ_e) are calculated from an optimized sine wave signal fitted over recorded data where the objective function which needs to be minimized is Moment of Error Squared (MES) defined as:

$$MES = \int te(t)^2 dt \quad (6)$$

Withal, MES criterium is used as a performance metric of a sine wave response. Reference trajectory is given as:

$$x_d(t) = 0.15 + 0.05\sin(2\pi \cdot 0.2t) \quad (7)$$

System response, error and control signal for the proposed controllers and a fully loaded cylinder are shown in fig. 4. Both controllers showed good tracking capabilities. The maximal absolute tracking error for each controller is about 10 mm. The SMC regulator showed better tracking capabilities than a PID controller and obtained a faster and smoother response.

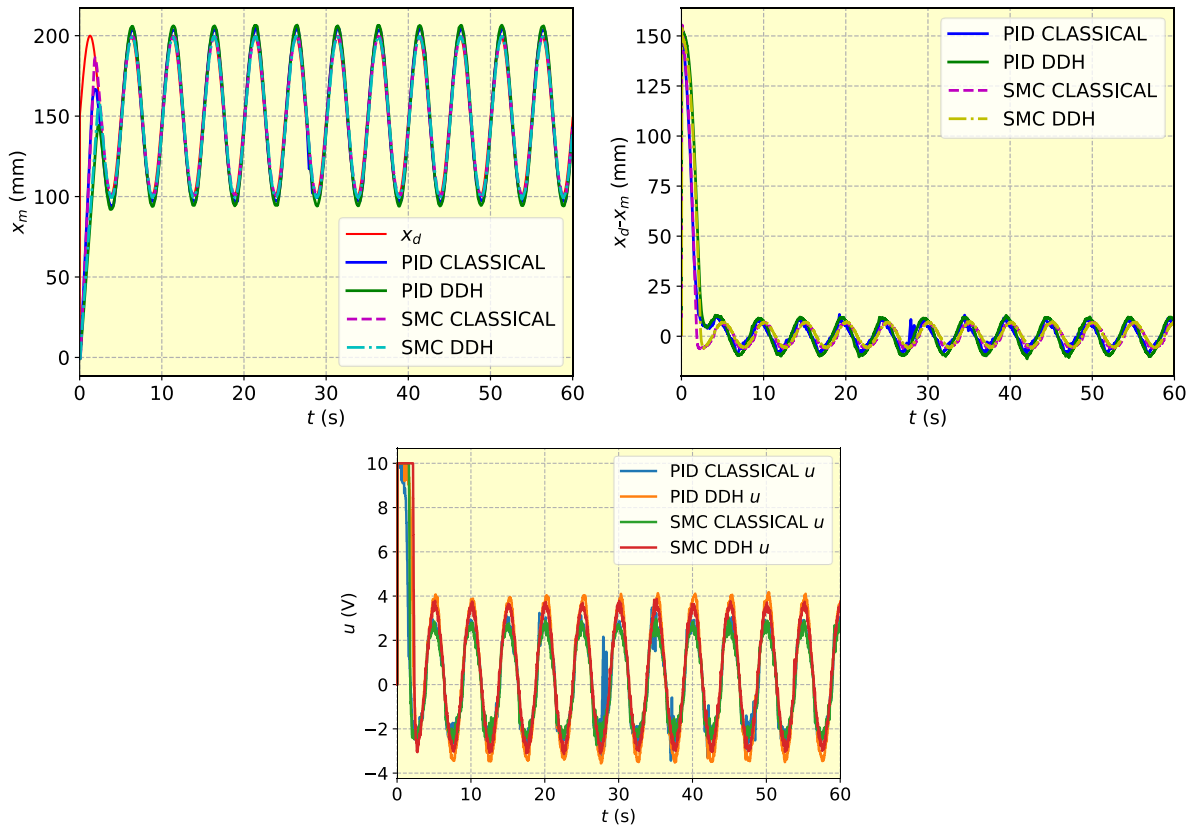


Figure 4 Sine wave experimental results for a fully loaded cylinder

Decomposition of the system response on amplitude and phase error for the sine wave reference trajectory is shown in fig. 5. The minus sign for the amplitude error means that the amplitude of system response is higher than the desired amplitude. PID controller for the classical system has amplitude error around -4.4 mm while for DDH system amplitude error is -6 mm. SCM regulator showed that both systems have amplitude error around zero while a small deviation occurred for payloads over 80 kg. This deviation is neglectable in comparison to the PID controller. The smallest phase-shifting occurred on the classical system with a PID controller and the largest on a DDH system controller with a PID regulator. For both systems, similar phase-shifting occurred with SMC. The DDH system was accelerated and phase-shifting was lower in comparison to the PID controller while classical systems showed an opposite trend. It's also shown that the PID controller is robust for the small amplitudes of sine wave signal and given payloads. That robustness comes out due to PID parameters obtained for the cylinder middle position (150 mm) and payload of 100 kg.

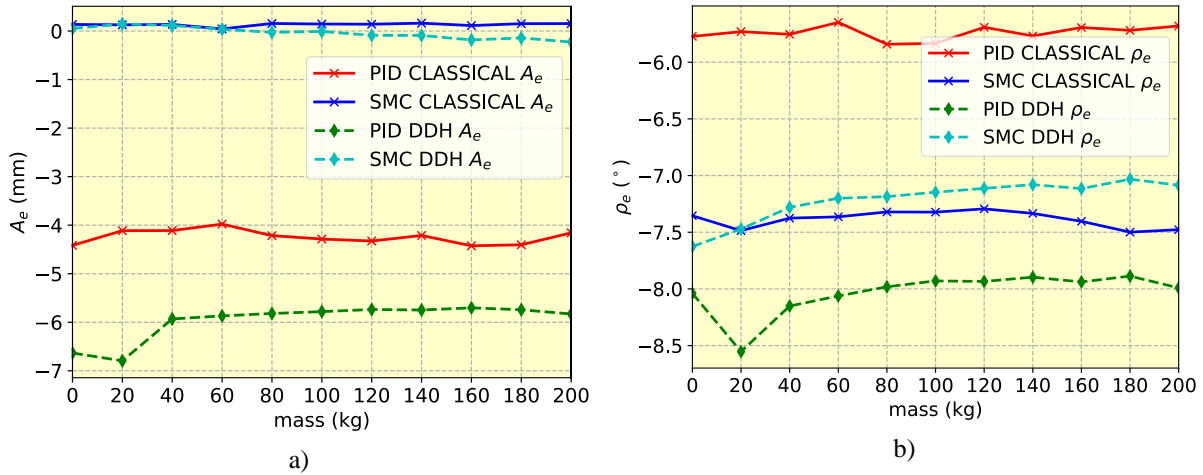


Figure 5 Sine wave decomposition: a) amplitude error, b) phase shifting

As a last performance index for the sine wave results, the *MES* criterion (6) is calculated and shown in fig. 6. Both systems obtained small cumulative errors with SMC. For the DDH system cumulative error of SMC is drastically smaller in comparison to the PID controller and it almost overlaps with results obtained with the classical system controlled with a PID controller.

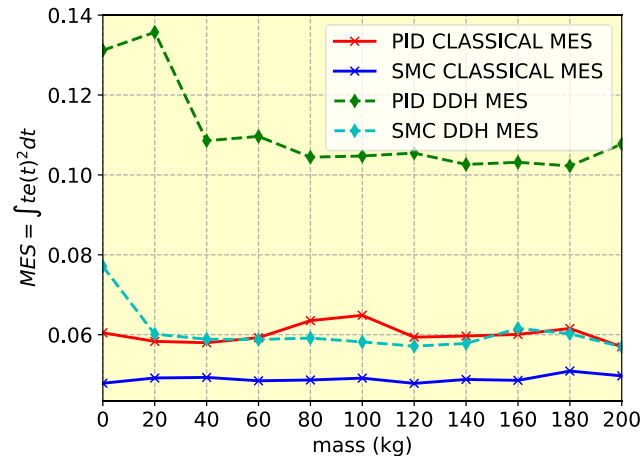


Figure 6 MES criterion for the sine reference signal

4.2 Step signal experimental results

Reference test step signal consist of a six different cylinder position set to 280, 10, 150, 22, 10 and 0 mm. The duration of each step signal is set to 10 seconds. From the obtained results, three performance indexes were calculated. Rise time (T_r) is defined as an interval that it takes for the response to rise from 10% to 90% of the steady-state value. Settling time (T_s) is the interval that takes for the error to settle between ± 1 mm of a step final value. The last performance index is the Integral of Squared Error (ISE) used as a cumulative measure for the system error and it is defined as:

$$ISE = \int e(t)^2 dt \quad (8)$$

Step results for a fully loaded cylinder and control signal are shown in fig. 7. Systems controlled with SCM showed a slightly faster response in compression to the PID controller. Due to small differences in response for both controllers detailed analysis is carried out on which conclusion are given.

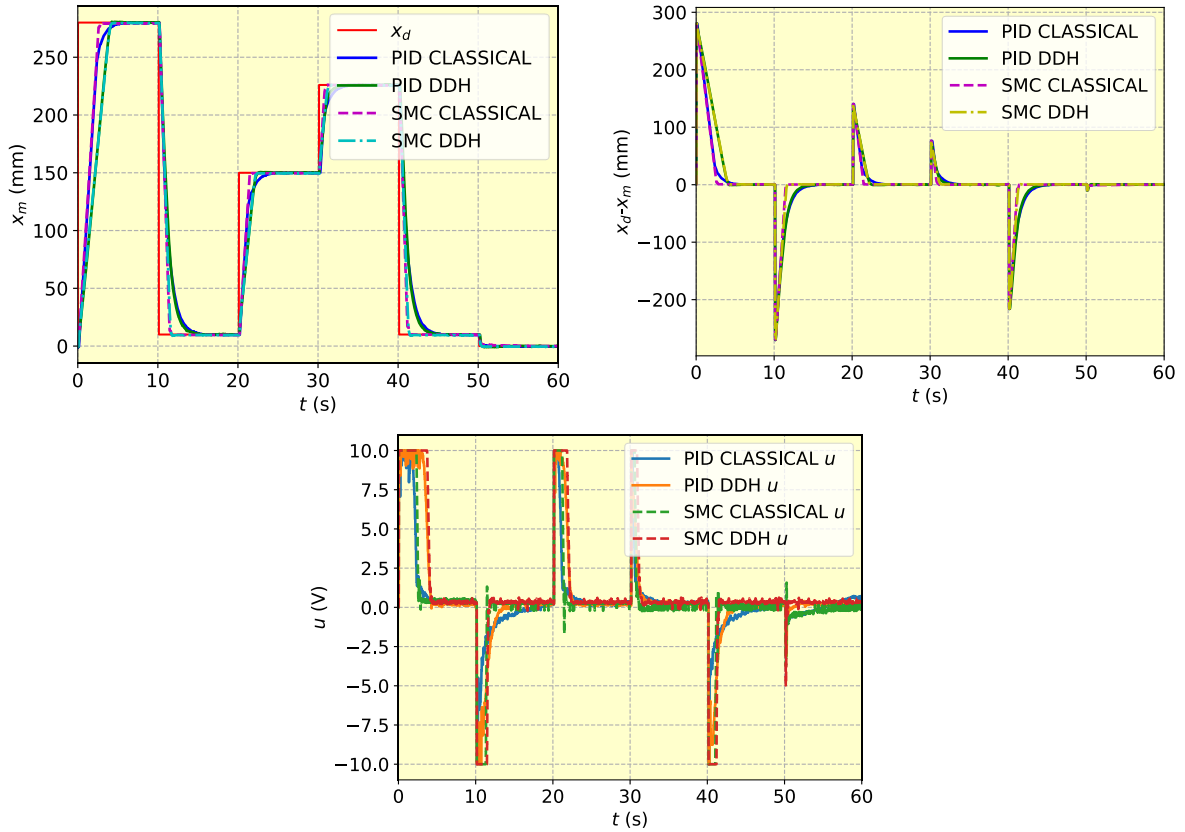


Figure 7 Step signal experimental results for a fully loaded cylinder

Mean values of the rise and settling time for all test cases and every change of the step signal are shown in fig. 8. From the aspect of rise time, the DDH system controlled with SMC show slightly better performance for lifting movements while faster dynamics is obtained for lowering movements. The SMC for the classical system showed far better results for rise time but results for the small-signal regime aren't satisfying. From the aspect of settling time, the classical system showed the same trend as for rise time. The DDH system controlled with SMC showed slightly higher results in comparison to PID for lifting movements while settling time for lowering movements was lower.

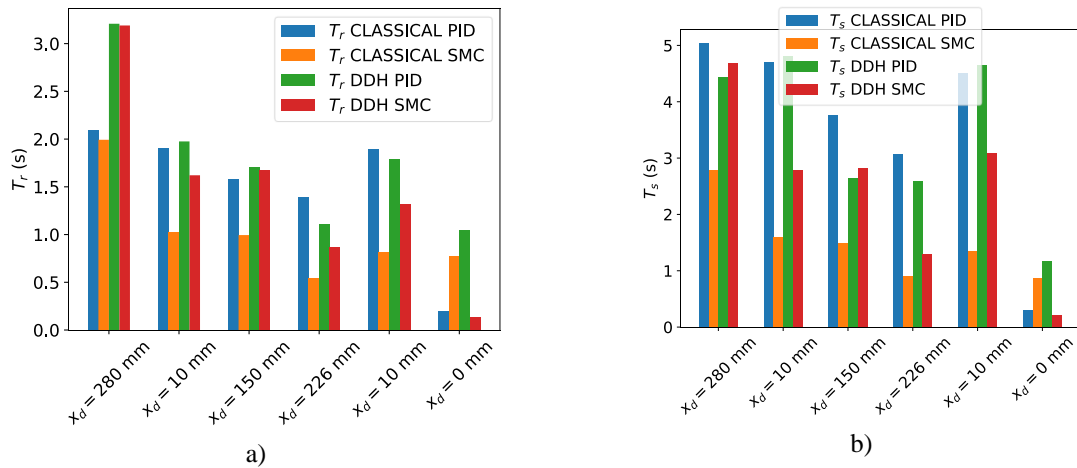


Figure 8 Mean values for: a) rise time, b) settling time

The cumulative errors of the systems based on *ISE* criterium are shown in fig. 9. There is almost no difference between results obtained with SMC and PID controller for the individual system.

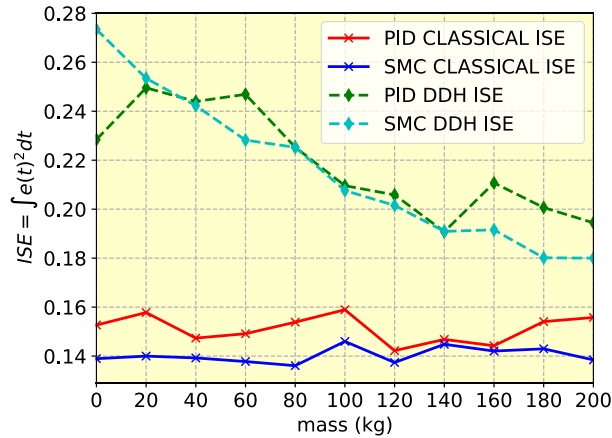


Figure 9 ISE criterion for the step reference signal

5 Energy efficiency

The input and output energy of the system is determined based on power flow direction meaning that the negative work done by the hydraulic cylinder is considered as an additional input to the system. Energy regeneration for the DDH system isn't taken into the account due to the impossibility of conducting such experiment but it's possible as presented in [9]. Based on the previous assumption, the input energy of the system is calculated as:

$$E_{in} = \int P_{el} dt + \int |P_{cyl}| \Big|_{P_{cyl} < 0} dt \quad (9)$$

where P_{el} is input electrical power consumed either by the servo motor or the AC motor and P_{cyl} is a power of the hydraulic cylinder defined as:

$$P_{cyl} = (p_A A_A - p_B A_B) v_{cyl} \quad (10)$$

where A_A and A_B are piston head and rod side areas respectively, p_a and p_b are pressures inside hydraulic chambers while v_{cyl} is the velocity of the hydraulic cylinder.

The output energy of the system is defined as:

$$E_{out} = \int |P_{cyl}| \Big|_{P_{cyl} \geq 0} dt \quad (11)$$

From (9) and (11) energy efficiency of the proposed system is given as:

$$\eta = \frac{E_{out}}{E_{in}} 100 \quad (12)$$

Input and output energies of the systems for the fully loaded cylinder are shown in tab. 1. Results showed that there is a small difference in input and output energy between different types of controllers for the same system. The main difference occurred between DDH and classical systems due to pressure used for overcoming cylinder payload. The DDH uses variable pressure determined by the payload while the classical system uses higher pressures determined by the pressure set on a safety valve. Safety pressure is set to 60 bars taking into account pressured drop across the proportional valve (10 bars) and dynamic payload forces. Pressure comparison is shown in fig. 10.

Table 1 Input and output energies of the systems for the fully loaded cylinder

		PID			SMC		
		E_{in} (kJ)	E_{out} (kJ)	η (%)	E_{in} (kJ)	E_{out} (kJ)	η (%)
DDH system	sinus	10.55	3.08	29.17	10.06	2.79	27.77
	step	8.38	1.09	13.05	9.97	1.10	11.07
classical system	sinus	77.34	2.97	3.84	78.42	2.79	3.55
	step	76.08	1.08	1.42	74.91	1.10	1.46

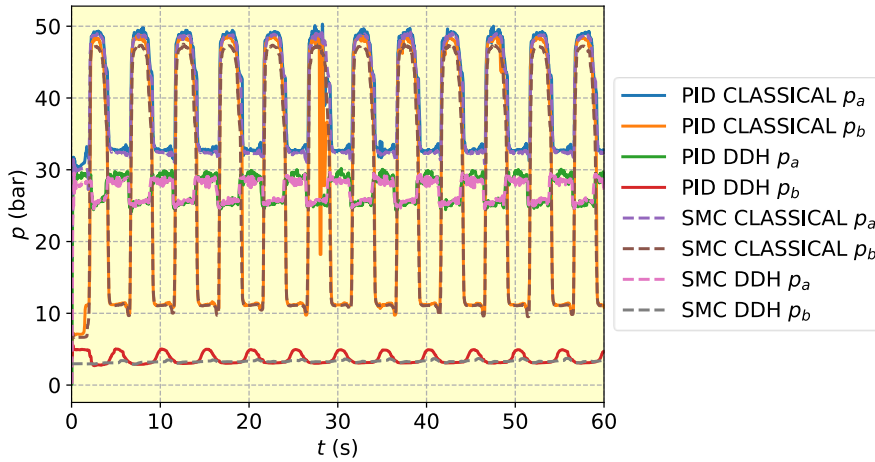


Figure 10 Pressures inside cylinder chamber

Energy efficiency calculated from (12) for a given test signal is shown in fig. 11. Results showed that the energy efficiency of a classical system is almost identical for both controllers. The DDH system controlled with a PID controller has slightly better energy efficiency in comparison to SMC but both controllers have superior efficiency in comparison to the classical electrohydraulic system.

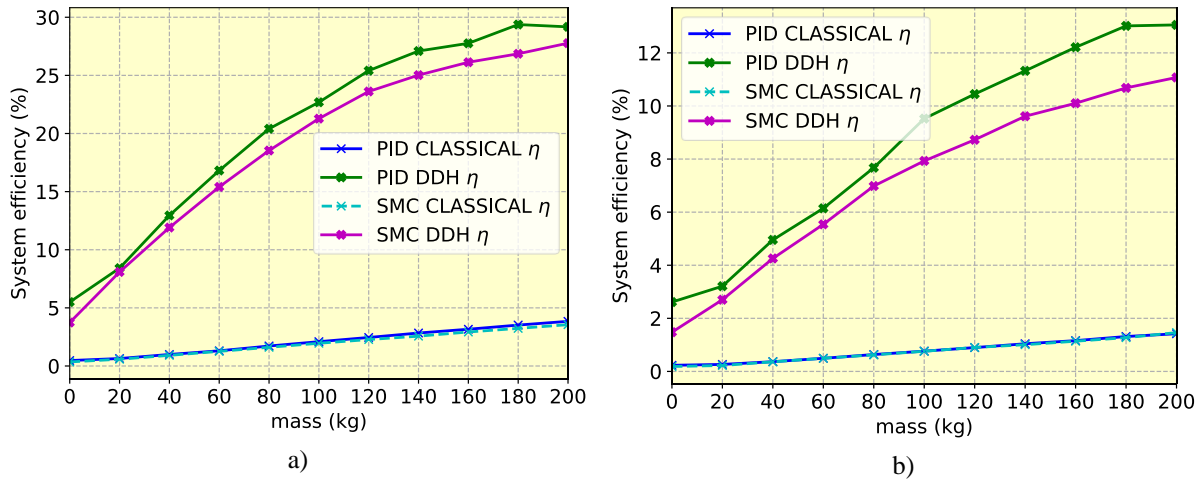


Figure 11 Energy efficiency for: a) sine wave reference signal, b) step reference signal

6 Conclusion

The DDH system controlled with SMC obtained faster dynamics in comparison to the PID controller. Such faster dynamics showed an impact on the energy efficiency which is slightly lower than one calculated from results obtained with the PID controller giving us an acceptable trade-off. Classical system controlled with SMC showed slight improvements in system dynamics and almost no impact on energy efficiency in comparison to PID controller. All overall, the SMC controller for the DDH system showed superior results in comparison to a PID controlled classical system. Furthermore, the additional energy efficiency of the DDH system can be achieved if energy regeneration is utilized for lowering movements. The system dynamics will be additionally investigated in

future work with the integrator backstepping controller. Such controller should achieve excellent tracking capabilities for sine wave reference trajectory and better results for the rise and settling time for step reference. Energy efficiency will be slightly lower, but still acceptable. Additionally, a detailed energy efficiency model will be developed. The proposed model will include hydro-mechanical, hydraulic and electrical losses.

Acknowledgments

It is gratefully acknowledged that this research has been supported by the European Regional Development Fund under the grant KK.01.1.1.04.0010 (HiSkid). The authors would like to acknowledge and thank Mr. M. Čavka from Hidromehanika d.o.o, Mr. H. Zidar from ABC maziva d.o.o. and Mrs. O. Tomić from HANSA-FLEX Croatia d.o.o. who greatly contributed to the development of this laboratory model and provided their assistance in the hardware setup.

Nomenclature

Designation	Denotation	Unit
A_A	piston head area	m^2
A_b	piston rod-side area	m^2
e	error between desired and measured trajectory	mm
E_{in}	input energy of the system	J
E_{out}	output energy of the system	J
k_1	SMC design parameter	-
k_2	SMC design parameter	-
k_d	PID controller derivate gain	-
k_i	PID controller integral gain	-
k_p	PID controller proportional gain	-
p_a	pressure on piston head side	Pa
p_b	pressure on piston rod side	Pa
P_{cyl}	hydraulic cylinder power	W
P_{el}	input electrical power to the system	W
s	sliding variable	-
T_r	rising time	s
T_s	settling time	s
u	control signal	V
U_{eff}	effective voltage of AC network	V
v_{cyl}	piston velocity	m/s
x_d	desired trajectory	mm
x_m	measured trajectory	mm
α	weighting coefficients	-
β	weighting coefficients	-
η	system efficiency	%
λ	SMC design parameter	-

References

- [1] M. Ivantysynova, "Innovations in pump design-what are future directions?," in *Proceedings of the JFPS International Symposium on Fluid Power*, 2008.
- [2] J. Siebert, M. Wydra and M. Geimer, "Efficiency Improved Load Sensing System—Reduction of System Inherent Pressure Losses," *Energies*, vol. 10, p. 941, 7 2017.
- [3] J.-m. Zheng, S.-d. Zhao and S.-g. Wei, "Adaptive Fuzzy PID Control for Switched Reluctance Motor Direct Drive Servo Hydraulic Press," in *2009 International Conference on Measuring Technology and Mechatronics Automation*, 2009.
- [4] O. D. A. Hiroyuki, K. OHTSU, S. A. T. O. Hiroshi and K. KANEHIRO, "Designing advanced rudder roll stabilization system - Using High Power with Small Size Hydraulic System," in *Proceedings of the JFPS International Symposium on Fluid Power*, 2008.
- [5] S. Kuchler, O. Sawodny, K. Schneider and K. Langer, "Vibration damping for a hydraulic driven luffing cylinder at a boom crane using feedforward control," in *2009 IEEE/ASME International Conference on Advanced Intelligent Mechatronics*, 2009.
- [6] T. Minav, C. Bonato, P. Sainio and M. Pietola, "Direct Driven Hydraulic Drive," in *The 9th International Fluid Power Conference, 9. IFK, March 24-26, 2014, Aachen, Germany*, 2014.
- [7] T. A. Minav, J. E. Heikkinen and M. Pietola, "Electric-driven Zonal Hydraulics in Non-Road Mobile Machinery," in *New Applications of Electric Drives*, InTech, 2015.
- [8] T. A. Minav, P. Sainio and M. Pietola, "Direct-Driven Hydraulic Drive Without Conventional Oil Tank," in *ASME/BATH 2014 Symposium on Fluid Power and Motion Control*, 2014.
- [9] T. A. Minav, C. Bonato, P. Sainio and M. Pietola, "Efficiency of direct driven hydraulic drive for non-road mobile working machines," in *2014 International Conference on Electrical Machines (ICEM)*, 2014.
- [10] A. Niraula, S. Zhang, T. Minav and M. Pietola, "Effect of Zonal Hydraulics on Energy Consumption and Boom Structure of a Micro-Excavator," *Energies*, vol. 11, p. 2088, 8 2018.
- [11] S. Zhang, T. Minav and M. Pietola, "Decentralized Hydraulics for Micro Excavator," in *Proceedings of 15:th Scandinavian International Conference on Fluid Power, 15th Scandinavian International Conference on Fluid Power, Fluid Power in the Digital Age, SICFP'17, June 7-9 2017 - Linköping, Sweden*, 2017.
- [12] T. Minav, J. Heikkinen, T. Schimmel and M. Pietola, "Direct Driven Hydraulic Drive: Effect of Oil on Efficiency in Sub-Zero Conditions," *Energies*, vol. 12, p. 219, 1 2019.
- [13] T. Minav, M. Pietola, D. M. Filatov, A. V. Devyatkin and J. Heikkinen, "Fuzzy control of direct-driven hydraulic drive without conventional oil tank," in *2017 XX IEEE International Conference on Soft Computing and Measurements (SCM)*, 2017.
- [14] J. Kasac, D. Majetic and D. Brezak, "An algebraic approach to on-line signal denoising and derivatives estimation," *Journal of the Franklin Institute*, vol. 355, p. 7799–7825, 10 2018.
- [15] J. Benić and Ž. Šitum, "Position Controller for Direct Driven Electro-Hydraulic System," in *International conference Fluid Power 2019: Conference Proceedings*, 2019.

Experimental investigation of the influence of fluid viscosity on the efficiency of a crawler excavator

Deuster Sebastian, Schmitz Katharina*

Institute for Fluid Power Drives and Systems (ifas), RWTH Aachen, Germany
E-mail: sebastian.deuster@ifas.rwth-aachen.de, katharina.schmitz@ifas.rwth-aachen.de

Abstract

In view of decreasing energy resources and the rising problems associated with CO₂ emissions and global warming, there is a strong interest in reducing the fuel consumption of machines in all sectors. Manufacturers of mobile machinery, such as hydraulic excavators, are also striving to develop increasingly efficient machines. Triggered by this development trend, the power density of hydraulic systems and their components continues to increase. This results in higher pressures, temperatures and lower oil volumes in the system. As a result, the hydraulic fluid used is subject to greater thermal stress and the systems thermal properties are becoming increasingly important. Further developments of tribological systems, for example in hydraulic displacement units, also create new demands on the hydraulic components and fluids. The fluid properties in particular are increasingly coming to the fore. For this reason, the content of this paper is to consider the influence of the hydraulic oil's viscosity on the efficiency of a crawler excavator and to present the viscosity dependent losses of valves and pipe/hose lines. To this purpose, experimental tests are discussed by regarding viscosity related energy losses of the hydraulic system of a crawler excavator. Therefore the results of experimental tests of a gravel cycle at different temperatures will be discussed. The results are divided into different types of energy losses. Finally, a hypothesis can be made about the dependence of the viscosity of the hydraulic fluid on the efficiency of the system.

Keywords: crawler excavator, temperature distribution, fluid viscosity, energy efficiency, energy losses

1 Introduction

In consideration of decreasing energy resources and the increasing problems associated with CO₂ emissions and global warming, there is a growing interest in reducing the fuel consumption of machines in all sectors. Triggered by this trend, the power density of hydraulic systems and their components continues to increase. This results in higher pressures and temperatures as well as lower oil volumes in the system. As a result, the hydraulic fluid is subjected to higher thermal and mechanical loads. Due to this, knowing the thermal properties of the system becomes increasingly important. High temperatures in hydraulic systems favor the mechanisms of oil ageing, hence reducing the service life of hydraulic components and precision of the machine and the intervals of changing hydraulic oil. Additionally, an important aspect is, that the temperature of the fluid in various components of a hydraulic system influences its viscosity. This affects the power losses in the hydraulic system, including hydraulic-mechanical losses such as pipe friction and volumetric losses such as leakage losses. In a complex hydraulic system such as that of a mobile excavator, these types of losses only occur simultaneously.

To evaluate the economic efficiency of a machine, the total costs of ownership (TCO) are used. The TCO is divided into costs for the acquisition and costs for the operation of the machine. An energy-efficient hydraulic system has several advantages. For example, on the one hand, less energy is needed to operate the system, and on the other

hand, less power loss has to be dissipated in the form of heat. The losses occurring in a hydraulic system can basically be divided into two types, component-dependent and system-related losses.

In mobile machinery, there is a variety of concepts for increasing functionality and energy efficiency. The component efficiencies and especially the systems architecture and its intelligent control have a significant influence on the overall efficiency of a drive system.

The concepts currently used and developed can be divided into two main categories. On the one hand, concepts that concern the systems structure and on the other hand those addressing intelligent controls. **Figure 1** shows several concepts used in hydraulic systems of mobile machinery. One example for intelligent control concepts is independent metering, where independent valves realize the inlet and outlet control edges. By decoupling the control edges, volume flow paths can be selected much more flexibly and recuperative operations can be realized.

Regarding the systems structure, in addition to the development of various hybrid structures, a trend toward the electrification and digitization of mobile machines can be observed. [1]

Furthermore, there are concepts combining multiple conceptions. The STEAM concept [2] for example uses a hydraulic system combining different concepts regarding the system structure to improve the energy efficiency of a mobile excavator.

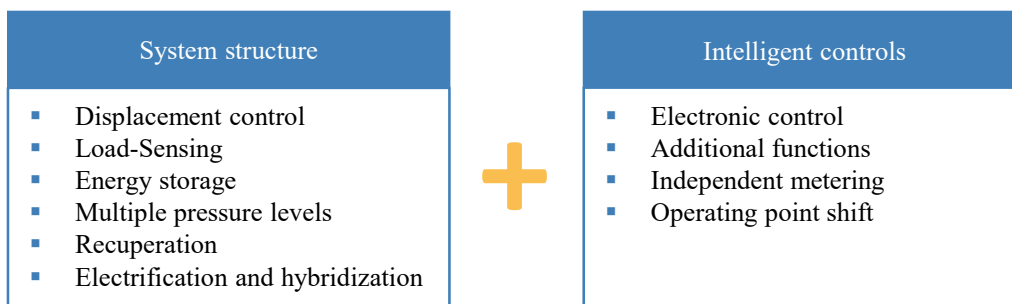


Figure 1: Concepts for increasing efficiency

This paper discusses the potential of the influence of fluid viscosity on the efficiency of a mobile working machine. The temperature distribution of the hydraulic oil during operation in a mobile machine is within a wide temperature range. In addition to the temperature deviation between the different components, temperature variations over time occur in various working applications. This paper deals with the viscosity dependent losses of valves and pipe/hose lines of a crawler excavator. For this purpose, spatially resolved temperatures and pressures in the hydraulic system during the execution of a dig and dump cycle are experimentally obtained and analyzed with respect to their influence on the efficiency of the excavator. The dig and dump cycle represents the work task mainly performed during operational life of a crawler excavator.

2 Power dissipation of mobile machines

The energy conversion and conduction in components of hydraulic systems is usually accompanied by losses. Losses are caused by individual hydraulic system components. According to these component-dependency, the losses can be divided into volumetric and hydraulic-mechanical losses. These types of losses are influenced by the viscosity of the used pressure medium, moreover they are dependent on the operating point. The selection of the main circuit configuration of the hydraulic system determines the system dependent losses for example the throttling losses in a system with resistance control.

According to [3], the power loss P_{loss} results from the drive power P_{input} and the efficiency η_{total} of the hydraulic system (Eq. (1)). It is assumed that the total power dissipation of the hydraulic system can be determined by the difference between the total power consumed by the hydraulic system and the total power used by the hydraulic system to perform work. The only heat that gets into the hydraulic oil comes from the power losses of the hydraulic system. [4]

$$P_{loss} = P_{input}(1 - \eta_{total}) \quad (1)$$

[5] presents the losses of a mobile excavator in relation to the input fuel energy. The results based on an experimental performance of a 90° digging cycle. In addition to the losses in relation to the total input power, the individual efficiencies of the various subsystems are also discussed. In **Figure 2** the results of the analysis are presented by means of a Sankey diagram. Based on the fuel energy fed into the system, only about 7.4 % is

converted into useful work for the digging cycle. Major losses occur when the chemical energy of the fuel is converted into mechanical work by the internal combustion engine (ICE). This mechanical energy is afterwards transferred to the hydraulic pump via a shaft, converting this mechanical power into hydraulic power. The control system in this case consists of valves, pipes and hoses. The work provided is implemented by the actuators. The efficiencies of the individual subsystems in relation to the energy supplied as well is shown. It is noticeable, that the individual efficiency of the control system is below the efficiency of the combustion engine. The losses occurring in the control system include, in addition to system-dependent losses, losses at valves and in piping systems, whose viscosity dependence is investigated in this paper. In the following, the viscosity dependence of volumetric and hydraulic-mechanical losses occurring in an excavator's hydraulic system will be discussed.

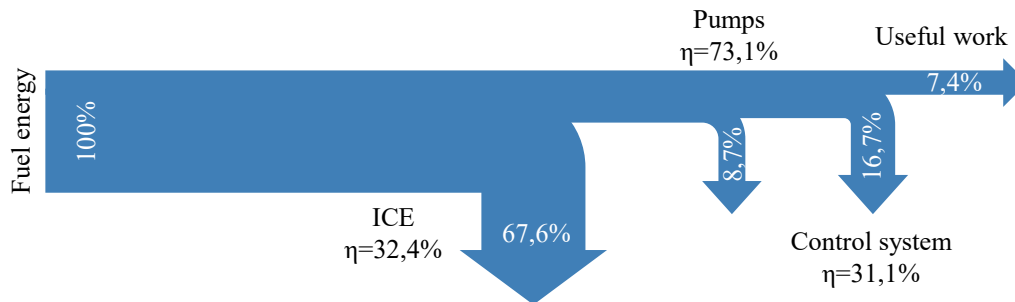


Figure 2: Energy losses of a mobile excavator [5]

2.1 Volumetric losses

Volumetric losses occur in form of internal leakage. In this case hydraulic fluid flows from the high-pressure side to the low-pressure side through function-related gaps between the components of the hydraulic unit that move relatively to each other. These gap losses occur, for example, at the ring surface of a piston-bushing contact of a pump or motor. Laminar flows through circular cross-sections are characterized by equation (2), the Hagen-Poiseuille equation. It describes the loss volume flow Q , r is the radius of the gap and l the respective length. η describes the dynamic viscosity of the fluid. Δp is the pressure difference occurring across the gap. [6]

$$Q = \frac{\pi \cdot r^4}{8 \cdot \eta \cdot l} \cdot \Delta p \quad (2)$$

At a high viscosity η , the volumetric losses decrease due decreasing gap volume flow. Conversely, filling losses occur because the pump sucks in the liquid less well due to the high friction losses. To avoid cavitation, the so-called permissible starting viscosity must not be exceeded. Cavitation can cause damage to the pump and leads to filling losses, which increase the volumetric losses. [6]

2.2 Hydraulic-mechanical losses

Friction losses in tribological contacts of hydraulic components and in flowing hydraulic fluids are called hydraulic-mechanical losses. A high viscosity, for example at low temperatures, leads to an increase in friction in the fluid. The hydraulic-mechanical losses occur in fluid-flow areas of the system, for example in hydraulic resistances. These flow losses cause pressure losses and a heating of the fluid. High flow velocities due to large volume flows and small flow cross sections increase the pressure losses. Furthermore, the flow losses depend on the geometry of the components by which fluid is leaded. It is taken into account by corresponding resistance coefficients and characteristic curves when a hydraulic system is designed.

At low relative velocities between two surfaces of tribological contacts shear stress occurs. As well as when the viscosity of the pressure fluid at high temperatures falls below the minimum required for the application, no load-bearing lubricating film can be generated and mixed friction occurs between the moving components. [7] Operation in the area of mixed friction can be minimized and the occurrence of mixed friction prevented. Thus, the viscosity influences the efficiency of the hydraulic system as well as the service life of the components and the availability of the entire hydraulic system.

2.3 Energy losses of a hydraulic system

Outgoing from the main circuit of the hydraulic system of the excavator, the power losses of the system can be divided to the different system components. **Figure 3** shows the various main loss mechanisms of a hydraulic system. Energy losses occur mainly in pumps and motors, valves and piping. Further losses are caused, for

example, by filters and coolers. The energy losses shown in Figure 3 usually occur in the system in a superimposed form. The three main loss mechanism and their dependency on the fluid viscosity are explained in more detail below.

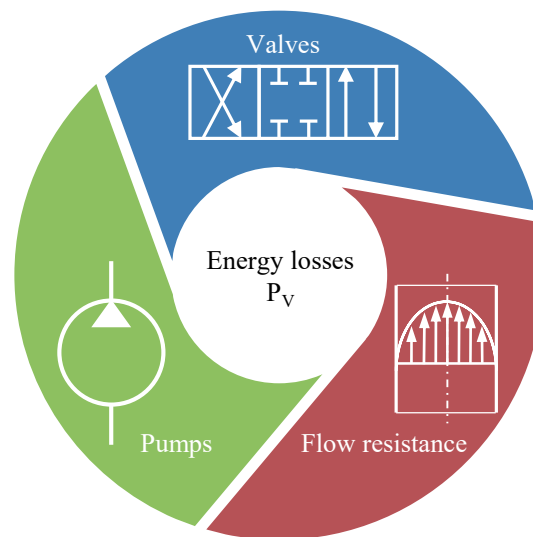


Figure 3: Energy losses

2.3.1 Pumps

Hydraulic displacement units can be characterized by volumetric, hydraulic-mechanical and total efficiency. All leakage losses in hydraulic units are summarized in the form of volumetric losses. Leakage losses are mainly caused by two fluid volumes with different pressure levels. This is the case, for example, in contacts with narrow gaps. In addition to leakage losses, hydraulic-mechanical losses occur. These losses result in the theoretical drive torque being smaller than the torque actually required. The mechanism include mixed friction, as well as pressure losses due to friction shear and throttling at cross-sectional changes. [6]

The dependence of the volumetric and hydraulic mechanical efficiency of various pump designs on the fluid viscosity was investigated by [8]. In this context, various hydraulic oils with different base oils were measured with regard to their influence on efficiency of the displacement units. A dependence of the fluid viscosity on the efficiency was found, which led to an increase of up to 3 % of the overall efficiency compared to conventional HLP mineral oils. This behavior was observed for fluids with a high viscosity index. Due to the extensive investigations of this research work, these losses are not part of the considerations of this paper. The investigations of this paper focus on the viscosity-dependent parasitic losses in valves and pipe/hose lines.

2.3.2 Valves

Energy losses in directional control valves can be divided in terms of losses due to the separation of the flow from the control edge in the turbulent range and into losses due to wall friction. For a given nominal size, this pressure loss depends on the size of the volume flow, on the design and on the operating viscosity. Approximately, directional control valves can be considered as an orifice resistance. This approach of determine the losses caused by valves excludes the consideration of viscosity on the losses via the slide valve.

In the hydraulic system of a mobile machine test excavator, spool valves are used to direct the volume flow to the desired actuator. Each hydraulic consumer is controlled by its own spool valve, so that the power losses can be assigned to the individual actuators.

2.3.3 Flow resistance

On the one hand flow resistance in straight pipes is caused by friction of the fluid near the wall and on the other hand by the internal friction of the fluid itself. The pressure losses Δp_F in pipelines can be described with equation (3). The resistance coefficient λ is function of the Reynolds number, which has a viscosity dependence. A high viscosity at low temperatures leads to increasing friction in the fluid. Hydraulic-mechanical losses increase in all areas of the system where a volume flow exists, for example in hydraulic resistances. These flow losses cause pressure losses and heating of the fluid. High flow velocities v due to large volume flows and small flow cross-sections d increase pressure losses. Furthermore, the flow losses depend on the length l of the pipe. When designing a hydraulic system corresponding resistance coefficients and characteristic curves are taken into account.

$$\Delta p_F = \lambda \cdot \frac{l}{d} \cdot \frac{\rho}{2} \cdot v^2 \quad (3)$$

In the hydraulic system of mobile machines, flow resistances result from the routing of the fluid to the consumers, from deflections of the fluid flow in the system and from rapid changes of cross-sections.

3 Test setup

The dependence of viscosity on the energy losses of a mobile machine will be discussed in this paper. The following chapter presents the test setup for the corresponding measurements.

3.1 Test excavator

The table in **Figure 4** shows the specifications of the test excavator. The crawler excavator *EC18D* [9] manufactured by *Volvo CE* belongs to the class of compact excavators. It is driven by tracks. In addition to the linear actuators, which are required for digging, the excavator has actuators for raising and lowering the blade, as well as for adjusting the travel width. The test excavator is equipped with hydraulic-mechanical one-circuit load-sensing system, which is controlled by electro-hydraulic pilot valves instead of the usually implemented hydraulic joysticks. An electro-hydraulic prototype control allows for completely automated and reproducible digging cycles. In addition, joystick signals are processed electronically to allow for manual operation. The main pump supplies the respective hydraulic actuators. During operation, the highest load pressure in the system is detected and the displacement volume of the pump is adjusted accordingly. The total weight of the machine is 1790 kg. The gross power of the diesel engine is 12 kW. The nominal bucket filling level is 36 liters. The hydraulic tank consists of 15 liters and the hydraulic system consists of 21 liters. The hydraulic system is operated with a hydraulic oil of class HLP 46.



Specification	Value	Unit
Weight	1790	kg
Gross power	12	kW
Nominal bucket filling level	36	l
Hydraulic tank	15	l

Figure 4: Specifications Excavator [9]

3.2 Test Cycle

The typical construction site activity of an excavator consists of the sum of four different load cycles. These include “grading” with a ratio of 10 %, “driving” with 20 %, “idling” with 30 % and the load cycle “digging” with 40 % of the total task. [10] The executed test cycle is based on the test cycles defined by the Japan Construction Mechanization Association (JCMA) [11] for determining the fuel consumption and energy losses of hydraulic excavators, for example. In the test a 90 degree dig and dump cycle is performed. The dimensions and the execution of the cycle is shown in **Figure 5**. With the nominal filling quantity of 36 liters and the moved basalt chips (8-16 mm grain size), the weight per transshipment is about 54 kg. After unloading the bucket the upper carriage is swung back as well as the excavator arm is lowered to the starting position. The position of the excavator remains unchanged during the entire process. The tests are carried out in an air-conditioned laboratory so that the comparability of the measurements results is ensured. In addition, the ambient temperature is recorded.

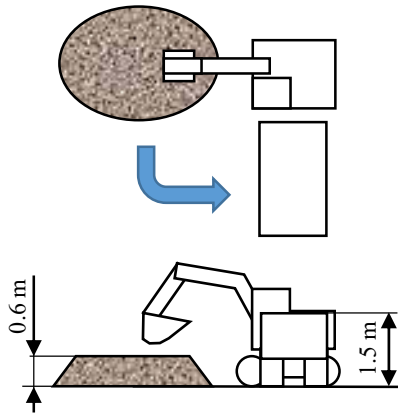


Figure 5: Dimensions dig and dump cycle

3.3 Measuring equipment

The test excavator is equipped with appropriate measurement technology to record the relevant data. **Figure 6** shows the main circuit of the hydraulic system with the installed sensors. The main circuit generally consists of the three linear actuators: The boom, stick and bucket cylinders. The swivel motor correspondingly drives the slewing gear for swiveling the upper carriage. The diesel engine drives the main hydraulic pump. Other actuators, such as the track motor, are not considered in this study because they are not activated during the executed test cycle.

3.3.1 Pressure

Pressure sensors are integrated in the system to identify the occurring losses. The main control valve consists of several proportional valves that control the volume flow to the individual actuators. Pressure losses that occur through the control edges of the valves are measured. Due to the system design of the load sensing system, the pump supplies the volume flow which provided the pressure of the major consumer in the system. This results in system-related losses at the other consumers due to the throttling of power in the direction of the tank.

The fluid is conducted to the respective consumers via hoses. Flow losses occur due to wall friction and deflections. To record the differential pressure, the test object is equipped with pressure sensors on the piston and rod side of the hydraulic cylinders. In case of the swivel motor, the differential pressure is not recorded because the hose connection from the main control valve to the motor is relatively short in comparison to the other hoses.

3.3.2 Temperature

Due to friction and throttling losses that occur in the hydraulic system of the excavator, energy is dissipated in the form of heat. This heat is transferred to the components of the system and to the hydraulic fluid, which effects a temperature increase as a result. The heating of the fluid is described by equation (4).

$$\phi = m \cdot c \cdot \Delta T \quad (4)$$

The fluid of mass m with heat capacity c heats up by temperature ΔT when it absorbs heat Φ . Part of the absorbed heat is dissipated to the environment via the hydraulic fluid and the surfaces of the tank and hydraulic lines, through heat conduction and convection. After reaching a steady-state temperature ($\Delta T = 0$), the entire power loss is dissipated to the environment in the form of heat.

The temperature is recorded at the throttling points. At these points in the system, high temperatures occur locally in the fluid, which are caused by friction. For this purpose, thermocouple is adapted into the center of the fluid flow. The identification of the temperature enables to infer the viscosity of the fluid, which is significant for the power calculation. According to Ubbelohde-Walther (Equation 5), the change in viscosity is expressed using an empirically determined equation. [12] The pressure dependence is neglected in the calculations due to the limited system pressure of 170 bar.

$$m = \frac{\lg \lg(v_1 + 0,8) - \lg \lg(v_2 + 0,8)}{\lg T_2 - \lg T_1} \quad (5)$$

Furthermore, the minimum viscosity in the hydraulic system is determined. Of particular importance is the viscosity of the hydraulic oil at the tribological contacts of the main pump. To record the leakage oil temperature, the temperature is recorded at the outlet of the leakage oil flow. If the viscosity of the hydraulic oil falls below a critical point, the parts moving relative to each other can no longer be sufficiently separated and thus there is no longer a lubricant film capable of bearing loads. The tribological system is thus operating in a state of mixed friction which leads to wear the component. In addition, the tank temperature and the ambient temperature are recorded.

3.3.3 Volume flow

The volume flow of the actuators is recorded in order to calculate the power loss occurring in the hydraulic system. The travel path of the linear cylinders is recorded by means of displacement transducers. The angular position of the upper carriage is recorded via a rotary encoder. The volume flow of the main pump is determined via a screw spindle counter.

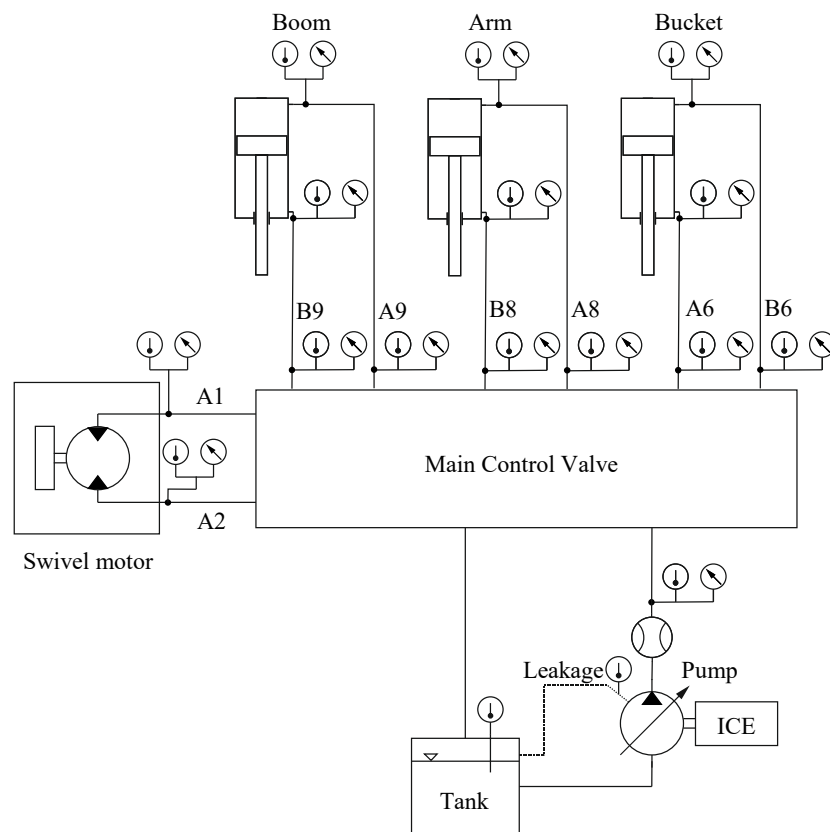


Figure 6: Main Hydraulic Circuit Excavator

4 Results

In this chapter, the results of experimental investigations will be regarded with regard to the test cycles, the pressure and temperature distribution and the dependency of the viscosity on the efficiency of the excavator. Efficiency considerations are based on energy losses of the parasitic resistances through the main control valve and the connecting lines to the actuators.

4.1 Test execution

The test sequence described in chapter 3.2 is carried out in the laboratory at the *Institute for Fluid Power Drives and Systems (ifas) of RWTH University Aachen*. The position of the bucket tip x_{tip} , y_{tip} , the rotation angle φ and the cycle time t act as reference variables. The test cycle is repeated until comparable cycles regarding the reference variables can be identified. **Figure 7** shows the geometric coordinates of the excavator with respective designations. The first test is carried out after a cold start and assessed based on the power losses in the main circuit of the hydraulic system. This test is repeated with one cycle in the warmed-up condition and the respective results

are compared. For reaching the warm cycled condition, the test cycle is repeated until the change in tank temperature before and after the cycle is stationary. This ensures that the maximum temperatures during the execution of the test cycle are reached.

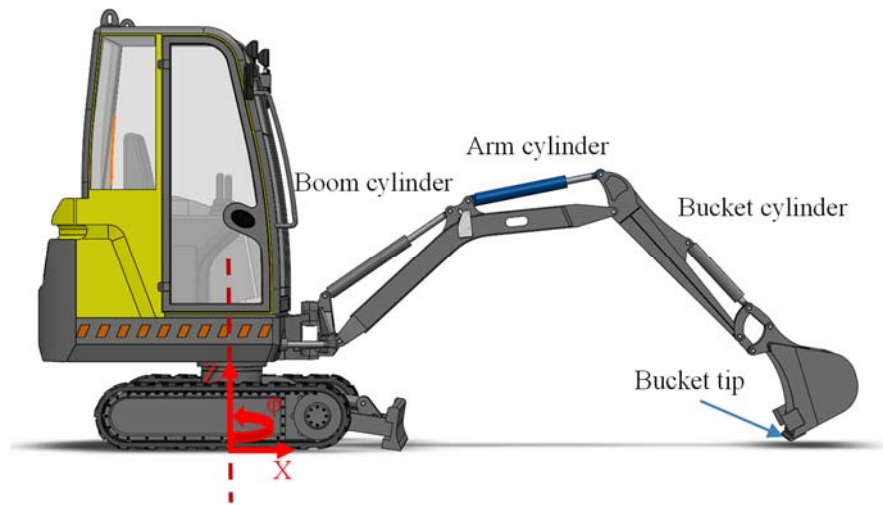


Figure 7: Geometrical description

4.2 Pressure distribution

The measurement of the pressure distribution over a dig and dump test cycle serves as the basis for the efficiency assessments of the two cycles. Thus, the energy loss at chokes and resistors can be calculated. The pressures are recorded according to the measuring points shown in Figure 6. The measured values are recorded over the entire cycle at a frequency of 1000 Hz. The cycle can be divided in four different sections shown in **Table 1**. The exact procedure of the test cycle is described in chapter 3.2. **Figure 8** shows the pressure distribution during the cycle recorded at the actuators. The pictograms illustrate the operations performed by the excavator during this period. The designations can be seen in Table 1.

Table 1: Division of the cycle

Section	Process	Time range
1	Digging	0 – 23 s
2	Rotation to unload	23 – 32 s
3	Unload	32 – 43 s
4	Rotation to the end	43 – 52 s

Before starting swiveling at a cycle time of approximately 17 seconds, a rise in the pump pressure p_{Pump} to a maximum of 170 bar can be seen, without a consumer requesting this pressure. This can be explained by the corresponding actuators moving at a low speed in the digging process. The variable displacement pump possess a minimum displacement degrees and thus continues to deliver a minimum volume flow of 20 l/min, which is, however, only used to a small extent by the actuators. There is a system-dependent power loss occurs in this section of the cycle noticeable.

The high pressures of the boom (A9/B9) or bucket (A6/B6) cylinder result from holding the excavator arm's load and the bucket loaded with grit. The load acting on the arm cylinder (A8/B8) is to a large extent absorbed by the joints of the excavator and due to this, the pressure prevailing in the boom cylinder during load holding is considerably lower. At this load, the flow to the pump is correspondingly closed by the valve spool. There is a

slight oil leakage from the pressure line to the tank. The significant sections of the cycle for energy loss calculation result from the corresponding work performed by the actuators and are explained further in the chapter 4.4.

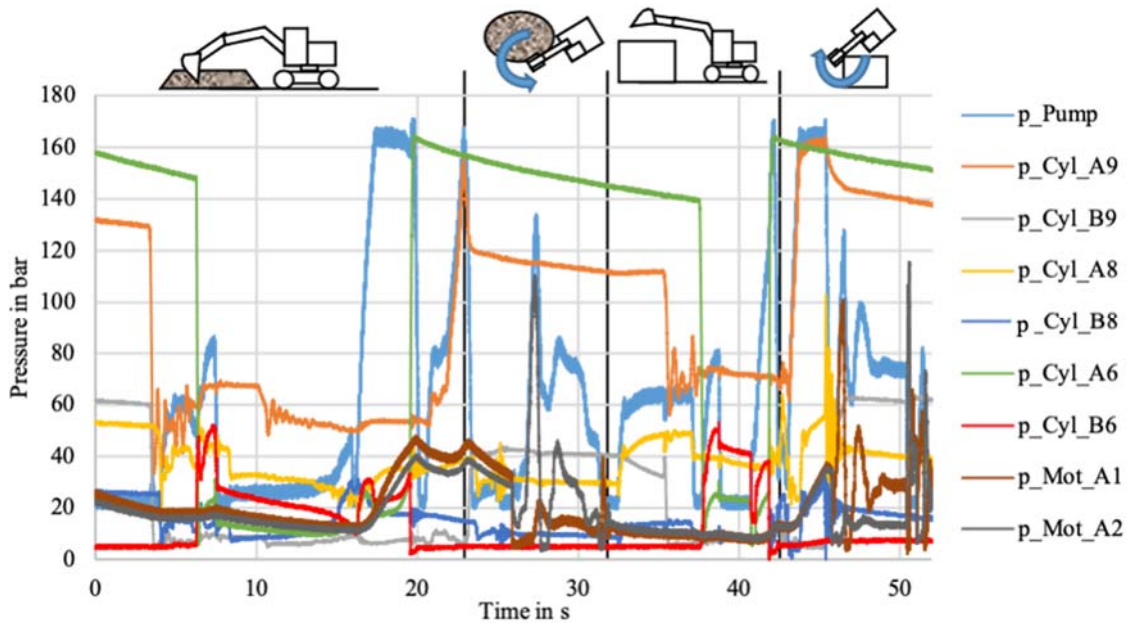


Figure 8: Pressure curves during the dig and dump cycle

4.3 Temperature distribution

The temperature distribution in the hydraulic system of the excavator during the cycle provides information about throttling points and relevant heat emissions in the hydraulic system. During the cycle, temperature distribution within the main circuit of the excavator was recorded. Based on this, the viscosity at relevant throttling points can be determined. The measuring points are located as shown in Figure 6.

An important measuring point is the tank's temperature for determining the inlet viscosity. **Figure 9** shows maximum recorded temperatures at respective measuring points of the regarded hydraulic system. The red numbers represent temperatures of the warmed-up cycle and the blue numbers those of the cold started cycle. In both cases, an ambient temperature of 23 °C was measured. On average, the temperatures are 14.21 °C apart. It should be noted that these are maximum temperatures, which are shown in the figure regardless of the time of their occurrence during the cycle.

Maximum temperatures in the respective cycle occur in both cycles on the piston side of the arm cylinder. This occurs during the retraction of the arm after unloading the grit. In this case, due to the rapid acceleration of the cylinder, friction of the fluid occurs on guide rings and seals of the cylinder, leading to a corresponding increase in temperature in the fluid.

Furthermore, minimum viscosity of fluid during the cycle can be determined from the maximum fluid temperatures in the hydraulic circuit. A minimum viscosity of 24.2 mm²/s results for the warm cycle and a viscosity of 38.9 mm²/s for the cold one.

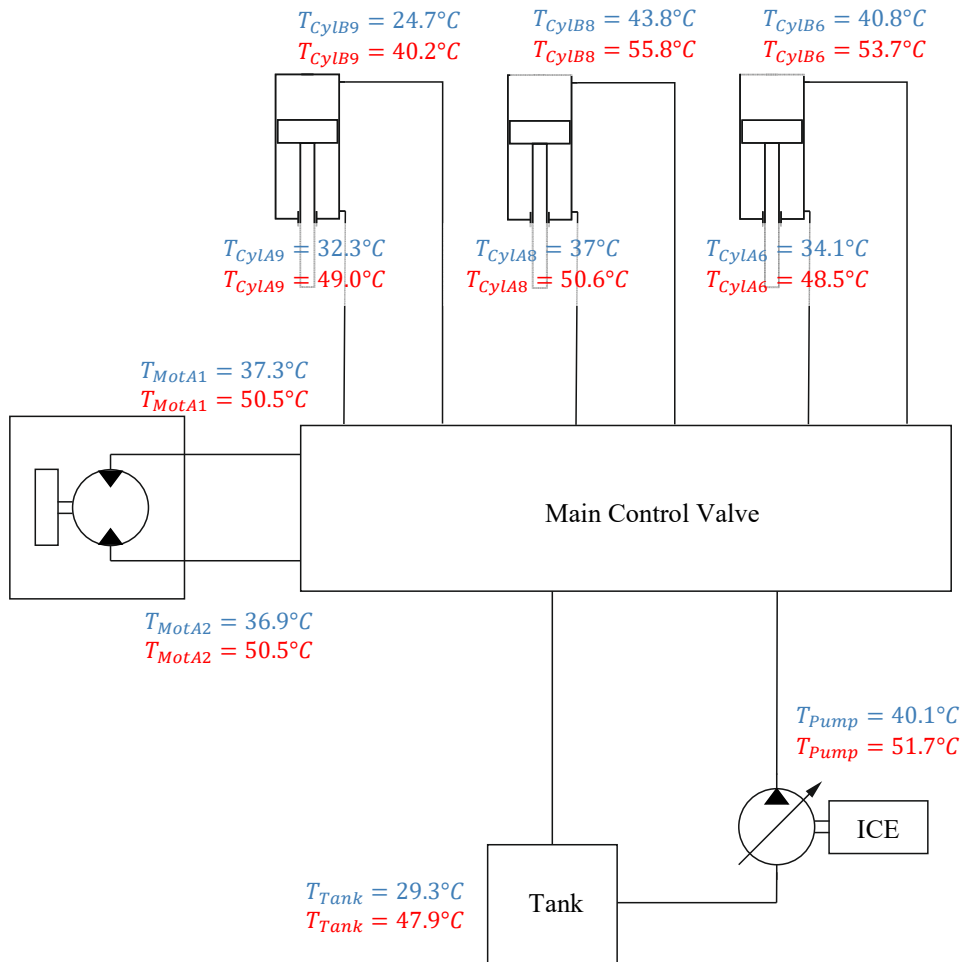


Figure 9: Max. Temperature during cycle

4.4 Efficiency

For efficiency analysis, various individual operation sectors of the cycles are considered in which the respective actuators are operated. These sectors are shown in **Table 2**. Only functions are considered in which the pump supplies the actuators with hydraulic power. The joystick is therefore deflected to its maximum so that the valve gate is fully open. No pressure is released via the load sensing system. At the operating points considered, the pump only supplies its controlled actuator. System-related losses are therefore not included in the calculations.

In the considered sectors, the respective considered consumer represents the highest consumer pressure in the system and the displacement volume of the pump is adjusted accordingly. In case of the boom cylinder, this involves functions that lift the excavator's arm. In the case of the arm, this is an analogous situation when the arm is extended. In section of the bucket cylinder, the operation sector in which the bucket is opened against weight force is considered. And the case of the swivel motor, the rotations are the focus of the considerations.

Not considered are tasks when the arm segment is lowered. Here hydraulic power is throttled accordingly through the valve's gate towards the tank. In these cases, it is hydraulic power generated by weight force of the dredging arm and thus not provided by the main pump of the hydraulic system. Thermal power generated by the throttling transferring with the fluid into the tank.

Table 2: Operation sectors

Actuator	Sector 1	Sector 2
Boom (A/B 9)	Lifting after digging	Lifting after unload
Arm (A/B 8)	Extend to the digging	Extend for unloading
Bucket (A/B 6)	Open to digging	Open to unload
Swivel Motor (A1/A2)	Rotation to unload	Rotation to the end point

Figure 10 shows the position of energy losses considered. For each sector, energy loss from the main pump via spool of the main control valve ($E_{loss,M}$) and the energy losses via the hose line from main control valve to respective actuators are calculated ($E_{loss,H}$). For this purpose, the average value of power losses over time steps are identified and multiplied by duration of the respective sector.

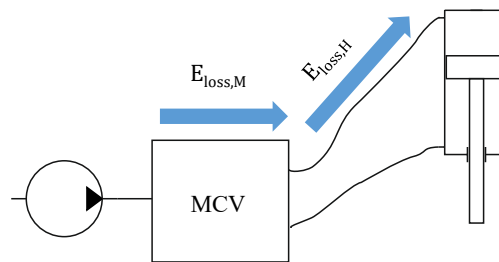


Figure 10: Position of energy losses

Table 3 shows results of the calculations for the cold and warm cycles. The column with index “M” (MCV) stands for losses from the pump via the respective spool of the main control valve. ($E_{loss,M}$ in Figure 10). The column with index “H” (Hose) represents losses from the main control valve to the respective actuator ($E_{loss,H}$ in Figure 10). The column with index “H” (Hose) represents losses from the main control valve to the respective actuator. Losses from the main control valve to the swivel motor and the main control valve to the boom cylinder were not taken into account in the calculation due to relatively short line lengths to those of the other actuators.

Table 3: Energy losses in J

	Boom				Arm				Bucket				Swivel motor			
	Sector 1		Sector 2		Sector 1		Sector 2		Sector 1		Sector 2		Sector 1		Sector 2	
	M	H	M	H	M	H	M	H	M	H	M	H	M	H	M	H
Cold cycle	116	--	25	--	529	48	531	49	554	324	241	81	282	--	273	--
Warm cycle	77	--	32	--	235	13	516	52	510	181	168	70	236	--	218	--

The data shows differences between the two regarded cycles. The largest losses are caused by the arm and bucket cylinders. This is due to relatively short travel length of the boom in relation to the other two linear actuators during the test cycle. The ratio is about 36 % for the boom and 30 % for the bucket cylinder. Furthermore, arm and bucket cylinders perform more dynamic tasks in the digging cycle than the boom cylinder, resulting in larger volume flows.

With exception of lifting the arm by retracting the arm cylinder after unloading the grit (arm/sector 2/H), the energy losses via respective hose lines (H) in the warmed-up cycle are lower than those of the cold cycle. On average, the energy losses are 46.5 J lower in the warmed-up cycle.

Losses via the main control valve (M) are also lower in warm condition of the hydraulic system for all actuators except for sector 2 of the boom cylinder (boom/sector 2/M). On average, the energy losses of the warmed-up cycle are 69.88 J below those of the cold cycle. A large deviation can be observed especially during the first retraction of the arm cylinder. This can be explained by the fact that the strokes of the two cycles differ by 50 mm in this case. If this factor is excluded from the analysis, the hot cycle is on average 37.86 J lower than the cold cycle regarding the energy losses from pump via the main control valve during the test cycle.

Table 4 shows the energy provided by the pump for both cycles considered, as well as the ratio of the sum of the losses from Table 3 to total energy of the pump during the cycle. The indices of Table 3 are also used in this table. The energy provided by the pump is 7.6 % higher in the cold cycle than in the warmed-up cycle. The amount of percentage differences in the ration of losses regarded to total energy provided by the pump point out the influence of fluid viscosity on the energy consumption of the hydraulic system of the mobile machine.

Table 4: Contribution of the energy losses to the total energy

Cycle	Pump	M	H
Cold	174340 J	1.46 %	0.29 %
Warm	161056 J	1.24 %	0.20 %

The percentage share of losses considered in total energy provided by the pump can partly be explained by inefficient control of the pump. The pump delivers a minimum volume flow of 20 l/min at minimum deflection (Chapter 4.2). This means that a not inconsiderable amount of energy is throttled back to tank due to the system structure. In addition, only individual operations of the cycle are included in the considerations. Furthermore, it is a cycle which is carried out at a relatively slow speed. With higher converted volume flows of the consumers, higher losses and a proportionally greater viscosity dependency of losses can be expected.

5 Summary and Conclusion

Current research and development is aimed at developing new concepts to increase the efficiency of mobile machines. Despite innovative developments in systems design and intelligent controls, a significant portion of the energy entering the hydraulic system is dissipated. A proportion of losses are due to volumetric and hydraulic mechanical losses. These losses depend, in part, on the viscosity of the hydraulic fluid used. In this paper, the influence of viscosity-dependent losses of a crawler excavator is considered. A central aspect of the considerations are the viscosity-dependent losses via the main control valve and the hose lines to the actuators. The joystick is therefore deflected to maximum so that the valve gate is fully open. No pressure is released via the load sensing system. At operating points considered; the pump only supplies the controlled actuator. System-related losses are therefore not included in these calculations. The focus of the considerations are two dig and dump cycles at different fluid temperatures. For this purpose, the cycle was considered once at a cold start and in a warmed-up condition. Energy considerations refer to working operations of the machine, in which the pump supplies the respective consumers. Relevant operations were considered for each actuator. Energy consumption for the operations was then determined for both cycles. This enables showing the dependence of the viscosity on energy losses of the operations. The shares of the considered losses in the respective total power are nearly identical. The percentage of the considered energy losses (MCV and hose) on the total energy input of the pump is 0.31 % ($= (M_{Cold} + H_{Cold}) - (M_{Warm} + H_{Warm})$) higher in the cold cycle than in the hot cycle (Table 4). The determined values show a dependence of viscosity on the power loss of the hydraulic system of mobile working machine of approx. 1.6 % in average. The considerations show the relevance of the allowance of the fluid properties in the design and in the efficiency of hydraulic machines. Furthermore, the observations indicate that the viscosity dependence of the parasitic losses considered is present to a relatively small extent. Former research works showed that the influence of fluid viscosity on pump efficiency has an influence of up to 3 %. This indicates that, in case of efficiency savings through adjustment of the fluid viscosity, the pump in particular shows an important role, in addition to the losses in valves and pipe or hose lines. An approach of the targeted adaptation of the fluid viscosity to the conditions of the individual hydraulic system thus offers potential for further considerations. Further researches of the influence of fluid properties on the energy losses of hydraulic systems are planned with regard

to the viscosity index. In this context, bio based hydraulic oils, which naturally have a higher viscosity index than mineral oils, are to be considered.

Nomenclature

Designation	Denotation	Unit
c	Heat capacity	J/(kg·K)
d	Diameter	m
$E_{loss,H}$	Energy loss hose	J
$E_{loss,M}$	Energy loss main control valve	J
η	Dynamic viscosity	Pa·s
η_{total}	Overall efficiency	-
l	Length	m
λ	Friction coefficient	--
m	Fluid mass	kg
m	Directional constant	-
ν	Kinematic viscosity	mm ² /s
p	Pressure	Pa
Δp_F	Pressure difference friction	Pa
P_{loss}	Power loss	W
P_{input}	Input power	W
ϕ	Heat	W·s
Q	Volume flow	l/min
r	Radius	m
ρ	Density	kg/m ³
T	Temperature	K
v	Velocity	m/s
x_{tip}	Position bucket tip on the x-axis	mm
y_{tip}	Position bucket tip on the y-axis	mm

6 References

- [1] BAUMA 2020. Will electric and driverless versions of construction machines soon be available? <https://www.bauma.de/en/trade-fair/industry-trends/efficiency/construction-machines-driverless/> (Accessed January 6, 2021).
- [2] Vukovic, M. Hydraulic hybrid systems for excavators. Dissertation, RWTH Aachen; Shaker Verlag GmbH, **2017**.
- [3] Hlawitschka, E. Zum Temperaturverhalten von Hydraulikanlagen. *Zeitschrift Agrartechnik*, **1979**, 29, 86–88.
- [4] *Proceedings of the 52nd National Conference on Fluid Power*.
- [5] Sturm, C. *Bewertung der Energieeffizienz von Antriebssystemen mobiler Arbeitsmaschinen am Beispiel Bagger*; KIT Scientific Publ: Karlsruhe, Baden, **2015**.
- [6] Schmitz, K.; Murrenhoff, H. *Grundlagen der Fluidtechnik // Hydraulik: Teil 1: Hydraulik*; Shaker Verlag: Aachen, **2018**.
- [7] Jacobs, G., Ed. *Maschinengestaltung: Band 1*; Mainz: Aachen, **2016**.
- [8] Otto, N. *Erprobung nachhaltiger Hydraulikfluide auf Ester- und Wasserbasis*, 1st ed.; Shaker: Herzogenrath, **2019**.

- [9] Volvo Construction Equipment. EC15D, EC18D, ED20D: Volvo Compact Excavators 1.54-1.95 t 16.3 hp. https://www.volvoce.com/-/media/volvoce/global/products/excavators/compact-excavators/brochures/brochure_ec15d_ec18d_ec20d_t4f_en_21_20045575_c.pdf?v=6nxHPw (Accessed January 6, 2021).
- [10] Helmus, M.; Fecke, M. *Standardisierung definierter Lastzyklen und Messmethoden zur Energieverbrauchsermittlung von Baumaschinen: Schlussbericht zum Forschungsvorhaben*, **2015**.
- [11] JCMA - Japan Construction Mechanization Association Standards Committee. JCMAS H 020:2007 - (Japan Construction Mechanization Association Standard): Earth-moving machinery – Fuel consumption on hydraulic excavator – Test procedures. <http://www.cema.or.jp/general/news/pdf/17th/17thJapanese> (Accessed December 18, 2020).
- [12] DIN Deutsches Institut für Normung e.V. *Prüfung von Mineralölen und verwandten Stoffen – Bestimmung des Viskosität-Temperatur-Verhaltens: Richtungskonstante m*; Beuth Verlag: Berlin, **04.2011**.

Improving the performance of self-contained cylinder drives with load-holding capabilities

Viktor Donkov¹, Søren Ketelsen¹, Torben Andersen¹, Morten Kjeld Ebbesen², and Lasse Schmidt¹

¹Department of Energy Technology ,Aalborg University, Aalborg, Denmark
E-mail: vhd@et.aau.dk

²Department of Engineering sciences, University of Agder, Grimstad, Norway

Abstract

A self-contained pump-driven cylinder drive system based on two electric motor and pump (TEMPO) units used for actuation of a two-link, medium-sized knuckle boom crane, is investigated. The TEMPO drive system is equipped with load holding valves and is a closed hydraulic system with a gasless self-pressurizing reservoir. Besides accommodating prescribed safety requirements, the load holding valves allow to reduce energy consumption during standstill. The transition between load holding and motion modes should be unnoticeable for the operator, hence the transition between these modes must be fast, a feature that has not been accomplished in previous attempts. An additional challenge with the system is a constant position error appearing during the locking process. By refining the hydraulic circuit and the control structure, these shortcomings are addressed. A simulation study with a realistic loading cycle is conducted in order to investigate the motion performance of the system. The simulation results demonstrate that the mentioned shortcomings are mitigated, suggesting a potential for future load carrying applications based on the proposed TEMPO drive.

Keywords: Compact Drives, Load Holding, Control

1 Introduction

Self-contained pump-driven cylinder drive systems offer an alternative to standard hydraulic cylinder systems. Standard hydraulic drives are normally based on a proportional valve which throttles the flow between the pressure source and the hydraulic cylinder. Throttling control has the benefit of being simple and robust, but it reduces the overall efficiency of the system. Pump-driven cylinder drives remove the need for throttling by decentralizing the pressure supply i.e. each cylinder has its own pump which delivers only the flow needed to move the cylinder. Pump-driven cylinder drives have been proposed for knuckle boom cranes in [1]. Furthermore, self-contained pump-driven cylinder drives were proposed in [2]. The system offers energy efficiency improvements over the standard hydraulic system and also offers other benefits such as plug-and-play capabilities i.e. only an electrical connection is needed to the self-contained drive. The two pumps driven by separate electric motors in the TEMPO drive compensate for the different flow requirements due to the cross-section area difference in the differential cylinder. The two inputs also allow for control of cylinder motion and back-pressure separately. Knuckle boom cranes require certain safety features one of which is load holding. In a classical system the safety functionality is achieved with Counter-Balance Valves (CBV). If used in pump-driven cylinder drives the CBV can prevent the recovery of energy [3]. A different system for load holding with TEMPO drives was explored in [4]. The feature allows load holding valves to lock the movement of the cylinder in case of a loss in pressure. The authors of [4] focused on the safety of the system and not on making the locking and unlocking process fast. The load holding valves can also be engaged in order to reduce energy losses during standstill, but in order for this to be done it is desired that the locking process happens as fast as possible. If the locking and unlocking happens sufficiently fast, then it can happen automatically without impeding the work flow of the operator which normally drives such a crane. In order to lock the load holding valves, the pressure in one chamber needs to be reduced rapidly which can cause a deviation in the cylinder's position [4]. A method to address this was proposed in paper [5], but it was only tested for open loop control. In this paper the controller methods from [4] and [6] will be combined to facilitate faster locking and unlocking of the TEMPO drive proposed in [2]. The error during locking is addressed

before the valves fully lock through manipulation of the references in the control structure. When the load holding valves are opened rapidly vibrations can appear due to the fast change in system parameters. A similar problem was observed in [6] and a control method based on two controllers which operate at the same time was proposed by the authors. This method has been adapted for the problem at hand. The aim of the study is to reduce the 2 s locking and unlocking time reported in [4]. The target for the locking and unlocking process is set as 250 ms, because on average, reaction time takes between 150 and 300 milliseconds for most humans. The model of the hydraulic system will be discussed in Section 2. A linear model and a coupling analysis is presented in Section 3. The control algorithm and the mode switching is discussed in 4. Simulation results are presented in section 5. These results are discussed and a conclusion is presented in Section 6.

2 Model

A knuckle boom crane is chosen for an example application, because this research is a continuation of the work done in [4]. The example crane used in this paper was also used in papers [1], [4] and [7]. An example crane with a similar scale can be seen in Fig. 1. The mechanical model is based on the Euler-Lagrange method [8], but the actual mechanical model is omitted here for brevities sake. The model can be found in [1] or one of the other papers. For convenience the general length and mass of the crane structure are presented in Tab. 1. Paper [9] shows how the inclusion of the electric motors and pumps needed for a compact drive, do not significantly affect the lifting capability of the crane.

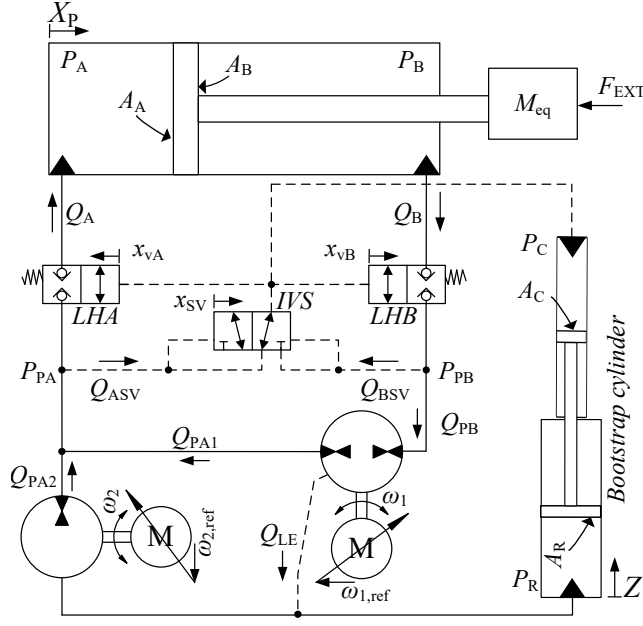


Figure 1: Knuckle Boom Crane example provided by National Oilwell Varco.©

Table 1: Sizes for example crane used.

Body	Length [m]	Mass [kg]
Inner Jib	13.75	6000
Outer Jib	9.24	3300
Cylinder 1	2.33	1500
Cylinder 2	2.84	750

The hydraulic circuit which drives the links of the crane can be seen in Fig. 2. One system is needed per link. In this case the focus is on the system driving the main boom of the crane. The TEMPO system is modelled by Eq. (1)-(16). The two valves LHA and LHB are the load holding valves which close if the pressure P_C drops below 10 bar. The inverse shuttle valve IVS always selects the lower of the two pressure P_{PA} and P_{PB} . The same pressure P_C is also supplied to the charge side of the bootstrap cylinder which provides the pressure on the supply side. Due to the area ratio A_C/A_R , a 26 bar pressure on the charge side, results in 2 bar in the reservoir side chamber. Cylinder cross port leakage is assumed negligible for both cylinders, and the following definitions are made $V_A = V_{0A} + A_A X_P$, $V_B = V_{0B} - A_B X_P$, $\alpha = A_B/A_A$, $V_R = V_{0R} + A_R Z$, $V_C = V_{0C} - A_C Z$, $\alpha_R = A_C/A_R$. The volumes V_{PB} , V_{PA} , V_{0A} , V_{0B} , V_{0R} , and V_{0C} are constant.



$$\ddot{X}_P = \frac{A_A (P_A - \alpha P_B) - F_{\text{friq}} - F_{\text{EXT}}}{M_{\text{eq}}} \quad (1)$$

$$\ddot{Z} = \frac{A_R (P_R - \alpha_R P_C) - F_{\text{friq,BS}}}{M_{\text{BS}}} \quad (2)$$

$$\dot{P}_A = \frac{\beta_A}{V_A} (Q_A - \dot{X}_P A_A) \quad (3)$$

$$\dot{P}_B = \frac{\beta_B}{V_B} (\dot{X}_P \alpha A_A - Q_B) \quad (4)$$

$$\dot{P}_{PA} = \frac{\beta_{PA}}{V_{PA}} (Q_{PA1} + Q_{PA2} - Q_A - Q_{ASV}) \quad (5)$$

$$\dot{P}_{PB} = \frac{\beta_{PB}}{V_{PB}} (Q_B - Q_{PB} - Q_{BSV}) \quad (6)$$

$$\dot{P}_C = \frac{\beta_C}{V_C} (Q_{ASV} + Q_{BSV} + \dot{Z} A_R \alpha_R) \quad (7)$$

$$\dot{P}_R = \frac{\beta_R}{V_R} (Q_{LE} - Q_{PA2} - \dot{Z} A_R) \quad (8)$$

Figure 2: Asymmetric cylinder controlled by DvSP-system.

$$Q_{PA1} = \omega_1 D_1 - K_1 (P_{PA} - P_{PB}) - K_1 (P_{PA} - P_R) \quad (9)$$

$$Q_{PB} = \omega_1 D_1 - K_1 (P_{PA} - P_{PB}) + K_1 (P_{PB} - P_R) \quad (10)$$

$$Q_{PA2} = \omega_2 D_2 - K_2 (P_{PA} - P_R) \quad (11)$$

$$Q_{LE} = K_1 (P_{PA} - P_R) + K_1 (P_{PB} - P_R) \quad (12)$$

$$Q_A = x_{vA} K_{Qv} \sqrt{|P_{PA} - P_A|} \text{sign}(P_{PA} - P_A) \quad (13)$$

$$Q_B = x_{vB} K_{Qv} \sqrt{|P_B - P_{PB}|} \text{sign}(P_B - P_{PB}) \quad (14)$$

$$Q_{ASV} = (1 - x_{sv}) K_{Qsv} \sqrt{|P_{PA} - P_C|} \text{sign}(P_{PA} - P_C) \quad (15)$$

$$Q_{BSV} = x_{sv} K_{Qsv} \sqrt{|P_{PB} - P_C|} \text{sign}(P_{PB} - P_C) \quad (16)$$

$$x_{vA} = x_{vB} = \begin{cases} 0 & \text{for } P_C \leq P_{CR} \\ \frac{P_C - P_{CR}}{P_{OP} - P_{CR}} & \text{for } P_{CR} < P_C < P_{OP} \\ 1 & \text{for } P_C \geq P_{OP} \end{cases} \quad (17)$$

$$x_{sv} = \begin{cases} 0 & \text{for } P_{PA} < P_{PB} \\ 0.5 & \text{for } P_{PA} = P_{PB} \\ 1 & \text{for } P_{PA} > P_{PB} \end{cases} \quad (18)$$

X_P is the cylinder piston position, F_{friq} is the force of friction, Z is the position of the bootstrap cylinder, and $F_{\text{friq,BS}}$ is the friction of the bootstrap cylinder. P_A , P_B , P_{PA} , P_{PB} , P_C , P_R are control volume pressures, Q_{PA1} , Q_{PB} , Q_{PA2} and Q_{LE} are pump flows modelled by the Wilson pump model using geometric pump displacements D_1 , D_2 and laminar leakage coefficients K_1, K_2 . Q_A , Q_B , Q_{ASV} and Q_{BSV} are valve flows modelled by the orifice equation, x_{vA} , x_{vB} , x_{sv} are valve poppet positions modelled as quasi static, i.e. no poppet/spool dynamics is included. P_{CR} and P_{OP} are valve cracking and full open pressures respectively. The friction model used to determine F_{friq} can be seen in Eq. (19). The same model with much smaller parameters was used for $F_{\text{friq,BS}}$. The friction parameters can be seen in Tab. 2.

$$F_{\text{friq}} = (F_c + (F_s - F_c) e^{(-\text{abs}(\dot{X}_P)/v_s)}) \tanh(\gamma \dot{X}_P) + B_{\text{cyl}} \dot{X}_P \quad (19)$$

where F_c is the Coulomb friction coefficient, F_s is the static friction coefficient, v_s is the Stribeck velocity, γ and the tanh function remove the discontinuity at zero velocity, B_{cyl} is the viscous friction coefficient. Finally, the effective bulk modulus of the oil air mixture, β_i , $i = \{A, B, PA, PB, PI, ACC\}$ is modelled being pressure dependent using Eq.

(20) according to [10].

$$\beta_i(P_1) = \frac{(1 - \varepsilon) \left(1 + \frac{m(P_1 - p_{\text{atm}})}{\beta_F}\right)^{-\frac{1}{m}} + \varepsilon \left(\frac{p_{\text{atm}}}{P_1}\right)^{\frac{1}{\kappa}}}{\frac{1 - \varepsilon}{\beta_F} \left(1 + \frac{m(P_1 - p_{\text{atm}})}{\beta_F}\right)^{-\frac{m+1}{m}} + \frac{\varepsilon}{\kappa p_{\text{atm}}} \left(\frac{p_{\text{atm}}}{P_1}\right)^{\frac{\kappa+1}{\kappa}}} \quad (20)$$

where ε is the volumetric air content at atmospheric pressure (p_{atm}), β_F is the bulk modulus of the pure fluid, m is the pressure dependent bulk modulus gradient of the pure fluid and κ is the poly-tropic constant which is set to 1.4, assuming air to behave as an ideal gas and the compression process to be adiabatic. The effective bulk modulus is limited to 7500 bar, to include some mechanical compliance. The permanent magnet synchronous motors are modelled by their current dynamics in the dq rotating reference frame according to [11]:

$$i_d = \frac{1}{L_d} (u_d - R_s i_d + \omega_{re} L_q i_q) \quad (21)$$

$$i_q = \frac{1}{L_q} (u_q - R_s i_q - \omega_{re} L_d i_d - \omega_{re} \lambda_{pm}) \quad (22)$$

where i and u are current and voltage respectively, L and R_s are the inductance and the resistance of the stator coils, ω_{re} is the electric speed of the rotor shaft, and λ_{pm} is the flux linkage of the permanent magnet in the rotor. The torque produced by these currents are:

$$T_e = \frac{3}{2} p (\lambda_{pm} i_q + (L_d - L_q) i_d) \quad (23)$$

where p is the number of pole pairs. This connects the electrical rotor speed ω_{re} and the mechanical speed of the motor shaft as $\omega_{re} = p \omega_m$. This in turn can be modelled by:

$$\dot{\omega}_m = \frac{T_e - T_p - B_s \omega_m}{J_s} \quad (24)$$

where T_p applied by the pump, B_s is a friction coefficient, and J_s in the inertia of the rotor, the shaft, and the pump. The sizes of the components can be seen in Tab. 2.

Table 2: Components

Component	Size	Component	Size
$D1$	26 [cm^3/rev]	L_s	1.2 [m]
$D2$	28 [cm^3/rev]	A_A	0.0616 [m^2]
K_{Qv}	$4.0069 \cdot 10^{-6}$ [$m^3/(sPa)$]	A_B	0.0302 [m^2]
K_{Qsv}	$1.4086 \cdot 10^{-6}$ [$m^3/(sPa)$]	A_C	0.0025 [m^2]
P_{CR}	10 [bar]	A_R	0.0629 [m^2]
P_{OP}	20 [bar]	B_s	0.01 [Nms/rad]
J_s	0.06 [kg/m^2]	L_q, L_d	20.2 [mH]
p	3 [-]	R	1.30 [Ω]
λ_{pm}	0.7857 [Wb]	B_{cyl}	30000 [Ns/m]
F_c	1401 [N]	F_s	409 [N]
v_s	0.0075 [m/s]	γ	2000 [s/m]

3 Linear model

In [2] it was found that the system as presented in the previous section is highly coupled. In order to decouple the motion of the cylinder from the back pressure a number of virtual inputs and outputs need to be designed. The equations for the linear model of system when the load holding valves are open can be defined as Eq. (25) - (29). In these equations the following definitions and assumptions hold $\beta_0 = \beta_A = \beta_B = \beta_R/\Psi$, $\rho_B = V_B/V_A$, $\rho_R = V_R/V_A$, and $\rho_C = V_C/V_A$. The assumption of equal bulk modulus in the two control volumes is justified in the fact, that in motion operation mode both chamber pressures are kept at an elevated level (e.g. above 20 bar). Ψ is the ratio between the bulk modulus of the oil in the reservoir side of the bootstrap cylinder and β_0 . This parameter is assumed to be known. A study showing how changes in the parameter will affect stability can be seen in [2] and

a study of how much the parameter actually changes can be seen in [12]. Based on these papers parameter Ψ was calculated at the linearisation point based on (20).

$$P_A = \frac{\beta_0}{V_{A0}} (\omega_1 D_1 + \omega_2 D_2 - \dot{X}_P A_A) \quad (25)$$

$$P_B = \frac{\beta_0}{V_{A0}(\rho_B + \rho_C)} (-\omega_1 D_1 - \dot{X}_P A_A \alpha + A_R \dot{Z} \alpha_R) \quad (26)$$

$$P_R = \frac{\beta_0 \Psi}{V_{A0} \rho_R} (-\dot{Z} A_R - \omega_2 D_2) \quad (27)$$

$$\ddot{X}_P = \frac{A_A (P_A - \alpha P_B) - \dot{X}_P B_C}{M_{eq}} \quad (28)$$

$$\ddot{Z} = \frac{A_R (P_R - \alpha_R P_C) - \dot{Z} B_{BS}}{M_{BS}} \quad (29)$$

3.1 Input-Output Transformation

Instead of considering the physical pressure states, [13] found it desirable to formulate an output transformation considering more appropriate pressure states. These virtual pressures were selected to be the virtual load pressure P_L , and the level pressure P_H :

$$P_L = P_A - \alpha P_B, \quad P_H = P_A + H P_B \quad (30)$$

The level pressure P_H was used to control the pressure in one cylinder chamber to a constant value in [13]. This was done in order to improve the stiffness of the system. In [2] the aim of P_B is twofold. On one hand the chamber pressure is kept constant improving system stiffness, but also the reservoir pressure P_R is controlled in order to prevent cavitation or damage to the pumps' seals. In order to be able to control P_R the following virtual pressures are defined.

$$P_L = P_A - \alpha P_B, \quad P_H = P_A + H P_B + G P_R \quad (31)$$

The load pressure is proportional to the piston force and as such closely related to the cylinder motion dynamics. The level pressure will be used to control the pressure in the reservoir side of the bootstrap cylinder. If H and G are defined properly, the virtual level pressure is decoupled from the piston motion/load pressure. This allows the motion of the cylinder and the pressure in the reservoir to be controlled separately. By inserting the non-linear pressure dynamics from Eq. (25), (26) and (27), the dynamics of the virtual outputs become:

$$\begin{aligned} \dot{P}_L &= \dot{P}_A - \alpha \dot{P}_B \\ &= \frac{\beta_0}{(\rho_B + \rho_C) V_{A0}} (-(A_A \dot{X}_P - \omega_1 D_1 - \omega_2 D_2)(\rho_B + \rho_C) + (A_A \dot{X}_P \alpha + A_R \dot{Z} \alpha_R - \omega_1 D_1) \alpha) \end{aligned} \quad (32)$$

$$\begin{aligned} \dot{P}_H &= \dot{P}_A + H \dot{P}_B + \dot{H} P_B + G \dot{P}_R + \dot{G} P_R \\ &= \frac{\beta_0}{(\rho_B + \rho_C) V_{A0}} A_A (\alpha H - \rho_B - \rho_C) \dot{X}_P - \frac{\beta_0}{\rho_R (\rho_B + \rho_C) V_{A0}} A_A (G (\rho_B + \rho_C) \Psi - \rho_R \alpha_R H) \dot{Z} + \\ &+ f_1(P_L, P_H, P_R, H, G, \dot{H}, \dot{G}, \omega_1, \omega_2) \end{aligned} \quad (33)$$

here $f_1(P_L, P_H, P_R, H, G, \dot{H}, \dot{G}, \omega_1, \omega_2)$ are the terms not affected by the velocity of the two cylinders i.e. \dot{X}_P and \dot{Z} . In order to remove the dependence of \dot{P}_H on \dot{X}_P and \dot{Z} , the term H and G are chosen as:

$$H = \frac{\rho_B + \rho_C}{\alpha} \quad (34)$$

$$G = \frac{\rho_R \alpha_R}{\Psi \alpha} \quad (35)$$

This choice is done according to [2]. That this choice removes the coupling in the system can be seen later in the subsection. With the coupling removed, two virtual inputs are established:

$$Q_L = \frac{D_1(\rho_B + \rho_C + \alpha)}{\rho_B + \rho_C} \omega_1 + D_2 \omega_2 \quad (36)$$

$$Q_H = \frac{(\alpha - 1) D_1}{\alpha} \omega_1 + \frac{(\alpha - \alpha_R) D_2}{\alpha} \omega_2 \quad (37)$$

Collecting terms in Eq. (32) and (33), and using these definitions of Q_L and Q_H results in the dynamics:

$$\dot{P}_L = \frac{\beta_0}{V_{A0}} Q_L + f_2(P_L, P_H, P_R, \dot{X}_P, \dot{Z}) \quad (38)$$

$$\dot{P}_H = \frac{\beta_0}{V_{A0}} Q_H + f_3(P_L, P_H, P_R, \dot{X}_P, \dot{Z}) \quad (39)$$

Using the virtual inputs Q_L and Q_H and the virtual outputs P_L and P_H a matrix of transfer functions can be established as:

$$\begin{bmatrix} X_P(s) & \dot{X}_P(s) & \dot{Z}(s) & P_L(s) & P_H(s) & P_R(s) \end{bmatrix}^T = \mathbf{G}_{DC} \begin{bmatrix} Q_L \\ Q_H \end{bmatrix} \quad (40)$$

As was mentioned previously the use of the virtual inputs and outputs is warranted by the coupling of the system. In order to check that the new states are decoupled a Relative Gain Array (RGA) analysis is conducted. The RGA number ($N_{\#}$) is defined for diagonal input/output pairing in Eq. (41) and off-diagonal pairing in Eq. (42), [14]:

$$N_{\#dia} = \sum_{k,j} \left| \mathbf{G} \times (\mathbf{G}^{-1})^T - \begin{bmatrix} 1 & 0 \\ 0 & 1 \end{bmatrix} \right| \quad (41)$$

$$N_{\#off} = \sum_{k,j} \left| \mathbf{G} \times (\mathbf{G}^{-1})^T - \begin{bmatrix} 0 & 1 \\ 1 & 0 \end{bmatrix} \right| \quad (42)$$

where \mathbf{G} is a two by two transfer function, \times is the element-by-element multiplication or Hadamard product. k, j is the number of row and columns in the transfer function matrix. Further details on the RGA and RGA-number can be found in [14] or [15]. If $N_{\#dia}$ and $N_{\#off}$ attains the values 0 and 4 respectively for all frequencies for a particular input/output pairing, then these can be considered ideally decoupled. In Fig. 3, the coupling analysis for the transfer function Eq. (40) can be seen. The figure shows that the motion of the cylinder can be controlled with the virtual input Q_L , while the reservoir pressure can be controlled with the virtual input Q_H . No coupling is present.

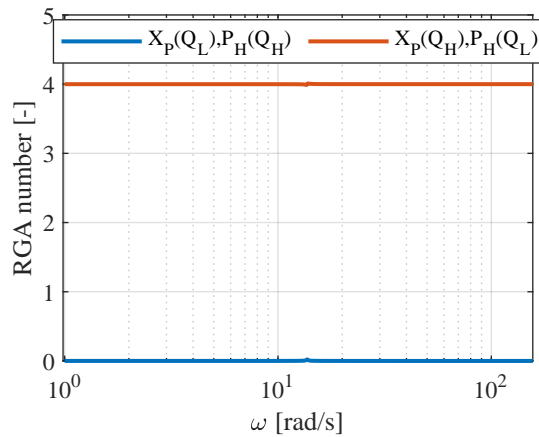


Figure 3: RGA number of motion system

4 CONTROL

A block diagram of the control structure can be seen in Fig. 4. The control structure is a cascade controller with a motion controller giving rotational velocity references for the two pumps $\omega_{1,ref}$ and $\omega_{2,ref}$. These references are then followed by the electric motors which have their own cascade control structure made up from a velocity controller which generates current references $i_{q1,ref}$ and $i_{q2,ref}$. The $i_{d1,ref}$ and $i_{d2,ref}$ are selected as zero, because that produces the largest torque. The current references are received by the Field Oriented Controller (FOC) which produces voltage references. Converters are omitted from the model, because of the computational demand which their inclusion produced. A load holding controller controls the pressures P_{PA} and P_{PB} . The output of the motion controller and the output of the load holding controller are blended together by the mode transition controller. The tuning for all these controllers is shown in the following subsections.

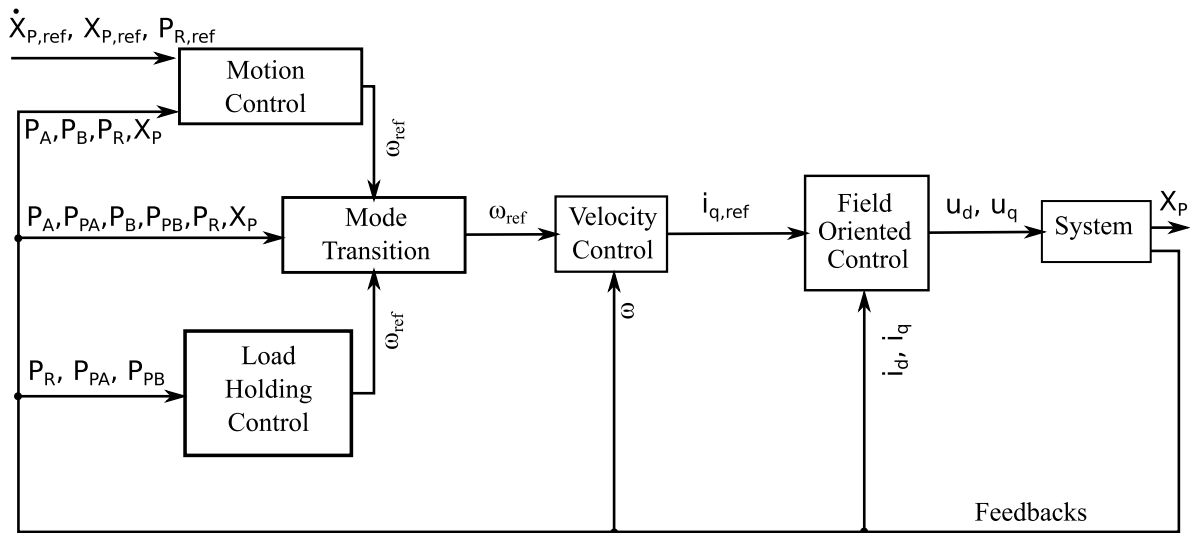


Figure 4: Block diagram of control structure

4.1 Motion control

The electric motors are controlled using FOC. A linear model for the current dynamics has been established and a Proportional-Integral (PI) controller is used to obtain a phase margin of 90 deg at 5000 rad/s. This corresponds to a bandwidth of the closed loop of ≈ 800 Hz. This value is chosen to be 10 times slower than the switching frequency of the converter. The bode plot for the open loop of the current dynamics with and without a controller can be seen in Fig. 5. The open loop dynamics of the velocity of the motors can be seen in Fig. 6. A PI controller is used again and the phase margin is selected such that the bandwidth of the motor will be ≈ 80 Hz.

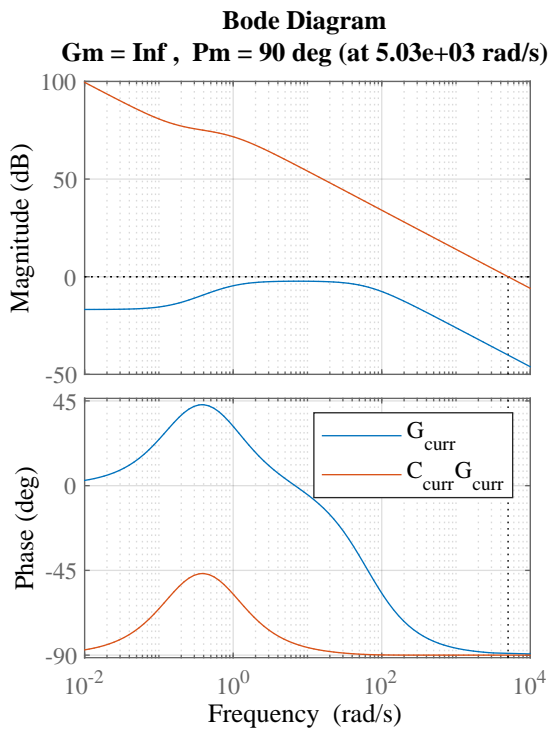


Figure 5: Current controller

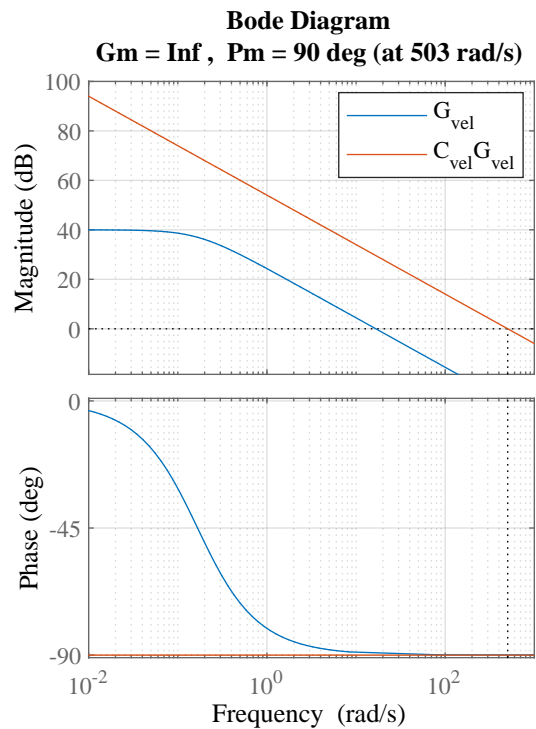


Figure 6: Motor shaft speed controller

A pressure feedback is designed to compensate the position transfer function. This feedback introduces virtual damping into the system and reduces the resonance peak at 13 rad/s. The uncompensated and compensated system can be seen in Fig. 7

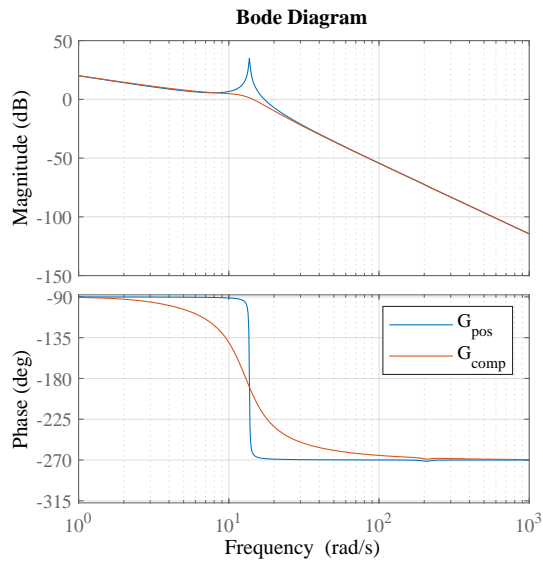


Figure 7: Pressure feedback compensation

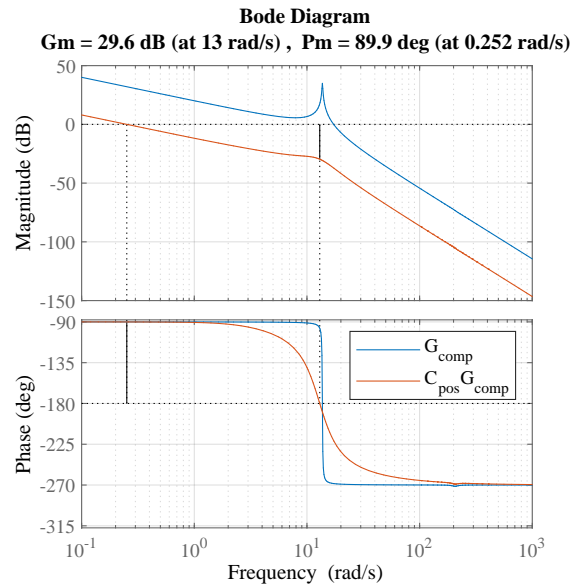


Figure 8: Cylinder position controller

The compensated system is easier to control and a simple proportional controller is used together with a velocity feed-forward. The open loop dynamics can be seen in Fig. 8.

For the P_H controller a proportional controller is used. The open loop dynamics can be seen in Fig. 9.

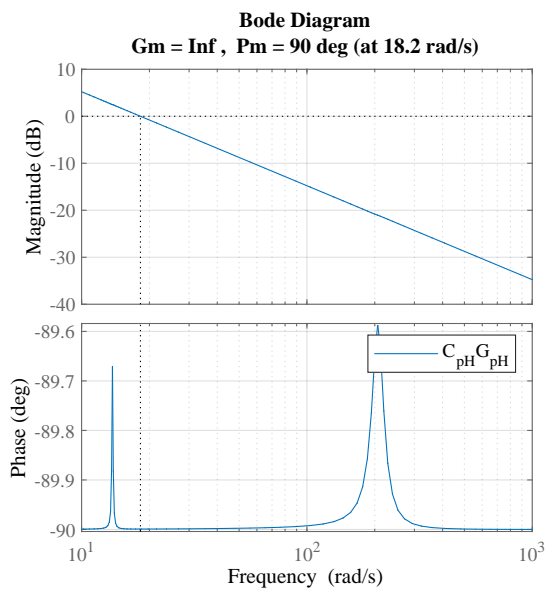


Figure 9: Level pressure controller

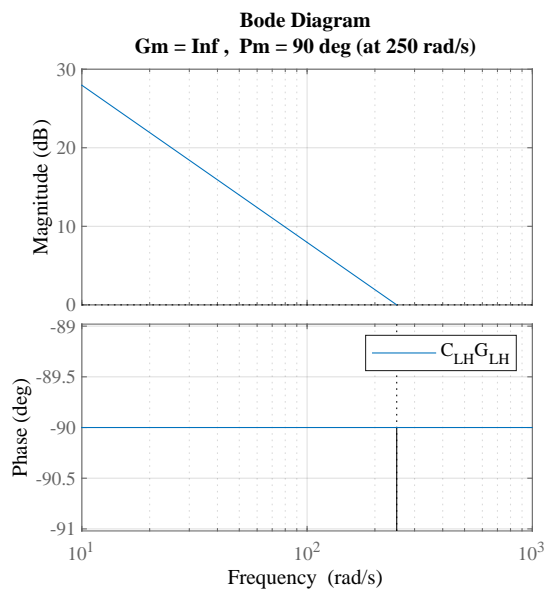


Figure 10: Load holding controller

A proportional controller is also used to control pressure P_{PA} and P_{PB} when the load holding valves are engaged. The small volumes V_{PA} and V_{PB} result in fast dynamics for the transfer function. Furthermore these controller are tuned much harder, resulting in a higher bandwidth for the closed loop. This is done in order to facilitate the fast locking and unlocking of the load holding valves. The bode plot can be seen in Fig. 10.

4.2 Transition control

It was mentioned in the introduction that the aim of this paper is to further the work done in [4]. A smooth transition was prioritised in [4] which resulted in transition times of up to 2 s. Furthermore the piston position was not controlled during the transition period, which resulted in increased position error during the locked period. In

this paper the transition is achieved through 5 distinct modes. The criteria for switching between modes is shown in Eq. (43).

$$mode = \begin{cases} 1 & \text{for } mode = 0 \text{ \& } L_{on} = 1 \\ 2 & \text{for } mode = 1 \text{ \& } P_{PB} < 10bar \\ 3 & \text{for } mode = 2 \text{ \& } L_{on} = 0 \\ 4 & \text{for } mode = 3 \text{ \& } abs(P_A - P_{PA}) < l_T \\ 0 & \text{for } mode = 4 \text{ \& } abs(P_A - P_{PA}) < l_T \text{ \& } abs(P_B - P_{PB}) < l_T/100 \end{cases} \quad (43)$$

where L_{on} is an indicator that load holding should engage and l_T is a threshold value of 1 bar. Mode 0 can be considered normal motion, while mode 2 can be considered locked mode. Modes 1, 3, and 4 are transition modes. In mode 1 the pressure P_{PB} is reduced until the load holding valves are locked. During mode 3 the pressure P_{PA} is increased until it matches P_{PA} , so when the load holding valves are opened in mode 4, the cylinder position does not change. In the current implementation L_{on} is triggered at certain time stamps and disabled in the same way. In future implementation it can be triggered according to other criteria such as a velocity reference close to zero together with a position error within a preselected limit or an inactivity timer. These could represent that the load has reached its destination. During all modes the transition controller adds the outputs of the motion controller and the load holding controller as seen in Eq. (44). The references sent to these two controllers are changed by the transition controller which facilitates the smooth transition. The two controller which are active at the same time together with filtering of reference pressures removed oscillations during locking and unlocking of a similar system in [6].

$$u = \omega_{move}(x_P, x_{ref}, P_H, P_{SetRef}) + \omega_{hold}(P_A, P_{PAref}, P_{PB}, P_{PBref}) \quad (44)$$

The reference $P_{PB,ref}$ changes in the different modes according to:

$$P_{PB,ref} = \begin{cases} P_B & \text{for } mode = 0 \\ 1bar & \text{for } mode = 1 \\ 1bar & \text{for } mode = 2 \\ 1bar & \text{for } mode = 3 \\ P_{R,ref}/\alpha_r & \text{for } mode = 4 \end{cases} \quad (45)$$

During mode 0 $P_{PB,ref} = P_B$, which means that the load holding controller outputs zero. When load holding is engaged in mode 1, $P_{PB,ref}$ drops to 1 bar. The controller starts dropping the pressure in the line, which closes *LHB*. During this time, the level pressure controller is disabled by selecting $P_{R,ref}$. This can be seen in Eq. (47). When load holding is being disengaged in mode 4 the pressure reference is set to $P_{R,ref}/\alpha_r$ so the controller can move P_{PB} to a value where the level pressure controller can take over again. The reference for $P_{PA,ref}$ changes according to:

$$P_{PA,ref} = \begin{cases} 1bar & \text{for } mode = 2 \\ P_A & \text{else} \end{cases} \quad (46)$$

In all modes except mode 2 $P_{PA,ref}$ is equal to the current value of P_A . After mode 1 has been engaged and the load holding valves have been closed, maintaining a large pressure in the line serves no purpose. During mode 2 the reference drops to 1 bar, which would reduce the torque on the pumps and motors. Before load holding can be disengaged the pressure in the line has to be raised to the load carrying pressure or the cylinder position will drop as soon as the load holding valves are opened. For this reason $P_{PA,ref}$ is set to P_A in mode 3 and mode 4.

The level pressure controller should produce zero output when load holding is engaged, so $P_{R,ref}$ is defined as:

$$P_{R,ref} = \begin{cases} 2bar & \text{for } mode = 0 \\ P_{set,ref} & \text{else} \end{cases} \quad (47)$$

In normal operation the reservoir pressure is controlled to be 2 bar. This corresponds to a P_C of 26 bar. When load holding engages, $P_{R,ref}$ is selected as $P_{set,ref}$, which is calculated according to Eq. (48). This disables the level pressure controller, because it brings the pressure error to zero.

$$P_{set,ref} = \frac{P_H - P_L}{\frac{\alpha}{\alpha_r} + \frac{H}{\alpha_r} + G} \quad (48)$$

5 Results

The controller described in the previous section was used to follow a 140 s position trajectory as can be seen in Fig. 11. The figure shows the motion of the cylinder driving the main boom of the crane. Three locking periods are commanded - one from 1 s to 6 s, a second one from 65.5 s to 74.5 s, and a third one from 138.5 until the end

of the simulation. The locking and unlocking cannot be seen clearly in Fig. 11, but can be more easily seen in the error plot seen in Fig. 12 and the plots of the pressures Fig. 13 and Fig. 14. During the second locking period the pressures P_A and P_B oscillate. No flows are coming into or out of the chamber, so these vibrations are caused by the movement of the crane structure. The vibrations can be caused by a modelling error in the friction of the cylinder, which appears to be too small. The problem could also be related to the stiffness of the Matlab solver, but no set of options was found which would provide better results. The first locking process occurs during complete standstill of the cylinder and it can be seen that the pressures do not oscillate. The simulation model should be validated with real hardware, but this was not possible for this study. Laboratory tests are planned in the future. Increasing the gain of the motion controller can be expected to reduce the error over the entire trajectory this resulted in pressure spikes during the unlocking process at 74.5 s.

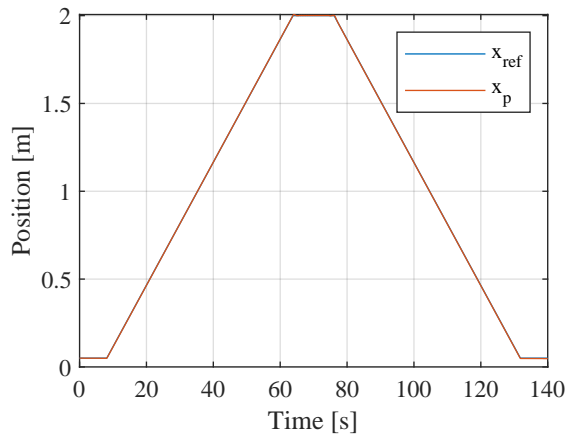


Figure 11: Motion of the cylinder.

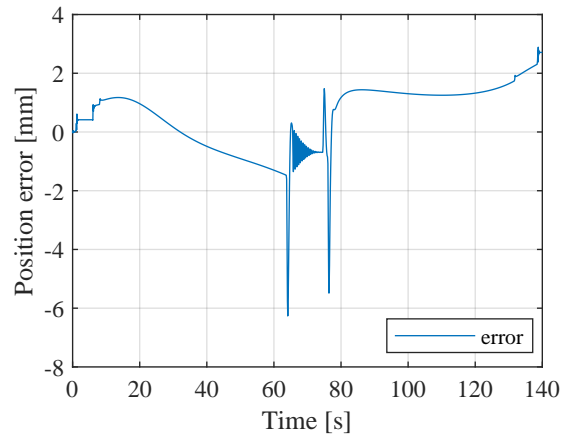


Figure 12: Position error over the trajectory.

During locking the pressure P_{PB} drops first to close the load holding valves. This can be seen in Fig. 13. As the pressure in chamber B drops the force of the cylinder increases and this would result in cylinder movement. The motion controller tries to counteract this by decreasing the pressure P_A . Once the load holding valves are locked P_{PA} drops as well. A plot showing this can be seen in Fig. 14.

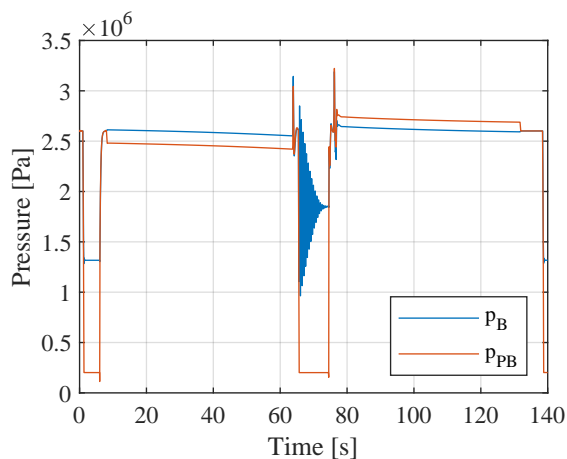


Figure 13: Pressures in line B.

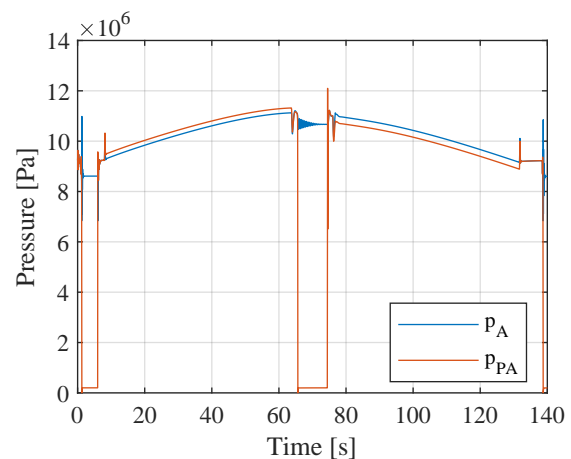


Figure 14: Pressure in line A.

A plot which shows the locking process better can be seen in Fig. 15 and Fig. 16. It takes approximately 250 ms from the locking command until the pressure P_{PB} drops below 10 bar. The unlocking process happens much slower at approximately 1813 ms. This is due to the condition for switching from mode 4 to mode 0 requiring a very small error between P_{PB} and P_B . Attempting to go into motion mode with a large pressure difference resulted in large outputs from the level pressure controller which the electric motors cannot execute. Reducing the gain of the level pressure controller could reduce this problem, but the large gain is necessary to prevent the level pressure dynamics from becoming unstable at the top of the cylinder. The same instability issue with low level pressure gain was observed in [4] and occurs due to a pole moving into the right half plane.

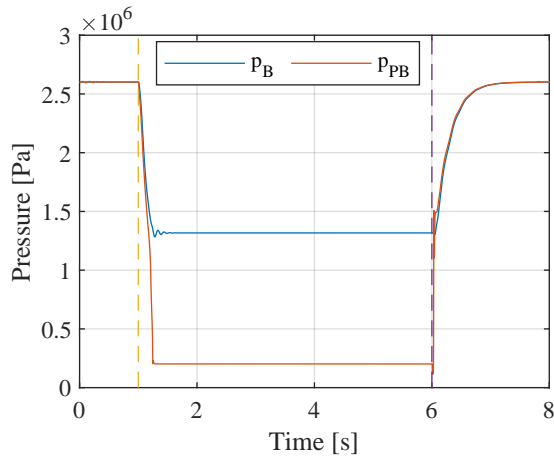


Figure 15: Pressures in line B during load holding.

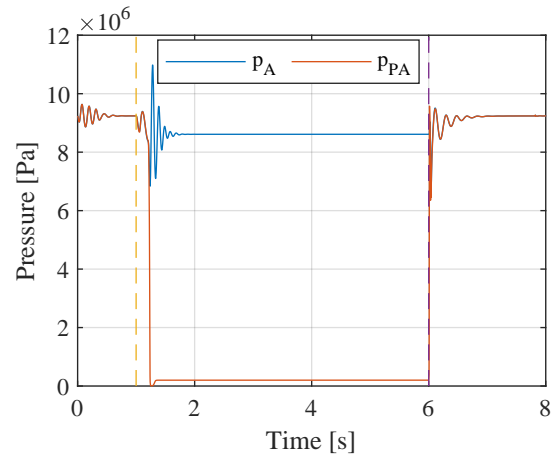


Figure 16: Pressure in line A during load holding.

A surge in the pressure P_{PB} can be seen at 6.034 s when the pressure rises above 10 bar which unlocks the load holding valves. The pressure reference $P_{PB,ref}$ is filtered with a second order filter according to [6]. Reducing the cut-off frequency of the filter removed this surge but caused other problems and a reduction in locking and unlocking time.

6 CONCLUSION AND FUTURE WORK

A simulation study of a knuckle boom crane with self-contained pump-driven cylinder system was conducted. The system has both self-locking capabilities as well as a bootstrap cylinder for a reservoir. The non-linear model is linearised and an input-output transformation is conducted in order to remove the coupling in the system. Controllers for moving, locking and unlocking of the hydraulic cylinder have been developed and explained. The aim of this paper was to reduce the locking and unlocking time from 2 s reported in [4]. Locking time has been reduced to 250 ms, but unlocking time has only been reduced to 1.8 s. This is due to limitation of the electric motors combined with large variations in system dynamics as the position of the cylinder changes. The unlocking time can be considered unsatisfactory, because it might be too long for the system to be used passively i.e. locking and unlocking every time the velocity reference is zero. For future work the vibrations occurring when the cylinder is locked at its top position need to be investigated. The possibility of choosing different virtual states or using an adaptive controller in order to be able to have a less conservative tuning should also be investigated.

ACKNOWLEDGMENT

The research in this paper has received funding from The Research Council of Norway, SFI Offshore mechatronics, project number 237896/O30.

References

- [1] Søren Ketelsen, Lasse Schmidt, Viktor Hristov Donkov, and Torben Ole Andersen. Energy saving potential in knuckle boom cranes using a novel pump controlled cylinder drive. 2018.
- [2] Søren Ketelsen, Damiano Padovani, Morten Kjeld Ebbesen, Torben Ole Andersen, and Lasse Schmidt. A gas-less reservoir solution for electro-hydraulic compact drives with two prime movers. In *Fluid Power Systems Technology*, volume 83754, page V001T01A038. American Society of Mechanical Engineers, 2020.
- [3] Ahmed Imam, Moosa Rafiq, Ehsan Jalayeri, and Nariman Sepehri. Design, implementation and evaluation of a pump-controlled circuit for single rod actuators. In *Actuators*, volume 6, page 10. Multidisciplinary Digital Publishing Institute, 2017.
- [4] Søren Ketelsen, Torben Ole Andersen, Morten Kjeld Ebbesen, and Lasse Schmidt. A self-contained cylinder drive with indirectly controlled hydraulic lock. *Modeling, Identification and Control (Online)*, 2020.
- [5] Daniel Hagen and Damiano Padovani. A method for smoothly disengaging the load-holding valves of energy-efficient electro-hydraulic systems. 2020.

- [6] Lasse Schmidt, Søren Ketelsen, Damiano Padovani, and Kasper Aa Mortensen. Improving the efficiency and dynamic properties of a flow control unit in a self-locking compact electro-hydraulic cylinder drive. In *ASME/BATH 2019 Symposium on Fluid Power and Motion Control*. American Society of Mechanical Engineers Digital Collection, 2019.
- [7] Viktor Hristov Donkov, Torben Ole Andersen, Henrik Clemmensen Pedersen, and Morten Kjeld Ebbesen. Application of model predictive control in discrete displacement cylinders to drive a knuckle boom crane. In *2018 Global Fluid Power Society PhD Symposium (GFPS)*, pages 408–413. IEEE, 2018.
- [8] Mark W Spong and Mathukumalli Vidyasagar. *Robot dynamics and control*. John Wiley & Sons, 2008.
- [9] Søren Ketelsen, Torben Ole Andersen, Morten Kjeld Ebbesen, and Lasse Schmidt. Mass estimation of self-contained linear electro-hydraulic actuators and evaluation of the influence on payload capacity of a knuckle boom crane. In *ASME/BATH 2019 Symposium on Fluid Power and Motion Control*. American Society of Mechanical Engineers Digital Collection, 2019.
- [10] Sunghun Kim and Hubertus Murrenhoff. Measurement of effective bulk modulus for hydraulic oil at low pressure. *Journal of Fluids Engineering*, 134(2), 2012.
- [11] Pragasan Pillay and Ramu Krishnan. Modeling of permanent magnet motor drives. *IEEE Transactions on industrial electronics*, 35(4):537–541, 1988.
- [12] Nikolaj Grønkær, Lasse Nørby Nielsen, Frederik Ødum Nielsen, Søren Ketelsen, and Lasse Schmidt. Multi-objective control of a self-locking compact electro-hydraulic cylinder drive. 2020.
- [13] Lasse Schmidt, Morten Groenkjaer, Henrik C Pedersen, and Torben O Andersen. Position control of an over-actuated direct hydraulic cylinder drive. *Control Engineering Practice*, 64:1–14, 2017.
- [14] Sigurd Skogestad and Ian Postlethwaite. *Multivariable Feedback Control - Analysis and Design*. Wiley, 2. edition, 2005.
- [15] Torkel Glad and Lennart Ljung. *Control Theory - Multivariable and Nonlinear Methods*. Taylor & Francis, 2000.

A Study of Hydraulically Actuated Oscillating Pitch to Increase Energy Production in Wind Turbines

Daniel Escobar, John Sampson, and Kim A. Stelson

Mechanical Engineering Department, University of Minnesota, Minneapolis, Minnesota/United States of America

E-mail: escob060@umn.edu, samps251@umn.edu, kstelson@umn.edu

Abstract

The focus of this paper is to oscillate the pitch of the wind turbine blades using hydraulic actuation to increase the power captured by a hydrostatic wind turbine. This is based on the fact that oscillating an airfoil under specific conditions increases the instantaneous lift coefficient by up to 97%. Different conditions were investigated by varying airfoil shape, waveform shape, waveform amplitude, waveform frequency and average angle of attack. The following conditions were found to give the best performance: a low camber airfoil, a lower average angle of attack than used for a non-oscillating airfoil, and an optimized waveform shape called a “tilted sinusoid.” A multi-level factorial experiment determined the most impactful variables were frequency, amplitude, and average angle of the tilted sinusoid. The best frequencies and amplitudes were studied through numerical simulations and hill climbing optimization. Results showed that oscillating the pitch of the wind turbine blades would, under all conditions tested, never outperform steady-state turbine operation, the main reason being the higher drag coefficients that are also present when oscillating the pitch of the blade.

Keywords: Hydrostatic Transmission, Wind Power, Pitch Oscillation, Energy Storage, Accumulator.

1 Introduction

Wind energy is the fastest growing energy source across the world. As climate change and irreversible environmental damage rises, wind energy is seen as a clean alternative to greenhouse gas emitting fossil fuels. It currently accounts for 6.3% of U.S. energy production and 5% of energy production worldwide [1]. Wind energy will continue to grow rapidly in the next decade. The Department of Energy (DOE) had set the goal for wind energy to comprise 10% of domestic power production by 2020, 20% by 2030 and 35% by 2050 [2]. Although we missed the goal for 2020, we are confident that we will greatly exceed the goal for 2030 and that we will achieve the goal for 2050 because of the exponential growth trend of wind power production.

There are many challenges associated with wind energy production and a major one is its energy efficiency. Most wind turbines capture roughly 0.35 to 0.45 of the energy in the wind, a ratio known as the power coefficient, C_p . A well-known theory developed in 1919 by Albert Betz sets the theoretical maximum limit of C_p as 0.593 [3], [4]. The goal of our wind turbine research is to reduce losses in wind turbines and raise efficiencies to be as close to this value as possible by implementing hydraulic systems and advanced controls. Increasing the efficiency of wind turbines will reduce the overall cost of wind energy and further increase its implementation across the world.

Wind turbine controls include torque, pitch and yaw control and they operate in four control regions, fig. 1. In our research we focus on torque control and pitch control. Conventionally, torque control is used to maximize the power in region 2 and pitch control is used to regulate the power in region 3. The control strategy in regions 1 and 4 consists of stopping the operation of the turbine because of low wind speeds in region 1 or damaging high wind speeds in region 4.

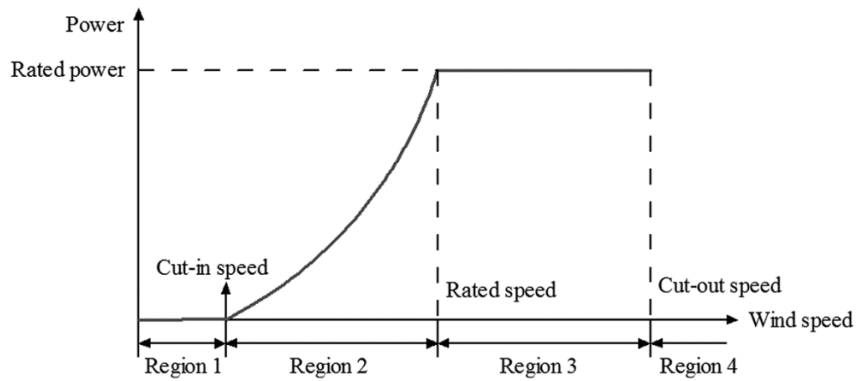


Figure 1: Control regions of a conventional wind turbine [5]

Most research approaches for improving power capture of wind turbines consist of maximum power point tracking (MPPT) in region 2. MPPT is achieved most successfully by controlling the rotor torque. Multiple approaches have been proposed and are summarized in [6] - [8]. Other approaches such as Model Predictive Control [9], and Extremum Seeking Control [10] have been proposed and also show promising results. These approaches are exclusive for traditional fixed-gearbox turbine transmissions, leaving an opportunity for researchers to investigate the performance of hydraulic transmissions for wind turbines.

The focus of our research is on hydraulic transmissions for midsize wind turbines (100 kW to 1 MW). In this sector, hydrostatic transmissions (HSTs) have many benefits over traditional fixed-gearbox turbine transmissions. For example, a higher power to weight ratio, an infinitely variable transmission ratio, and the ability to run without the need for costly power electronics [11], [12]. Also, there are off-the-shelf components that are readily available to use in this power level. Conventional gearboxes are prone to fatigue damage [13] whereas hydraulic components are not. Previous research from our group has shown that the overall efficiency of an HST turbine is comparable to a gearbox turbine [14]. Taking advantage of the hydraulics in the HST turbine, we have explored different options for improving the efficiency of the wind turbine. We have explored a hybridized HST that uses an accumulator and a secondary pump to store energy in region 3 and release it in region 2 improving the overall performance of the turbine by 4% [5], [15]. We are currently modifying an HST test stand at the University of Minnesota to experimentally validate the idea.

Oscillating the pitch to increase the lift forces and the torque on the rotor to generate more power has also been explored. Oscillating an airfoil generates a phenomenon of delayed flow separation known as dynamic stall [16], which, under very specific conditions (frequency, amplitude and average angle of attack) can increase the instantaneous maximum lift coefficient by up to 97% [17]. This concept is well described in the literature, especially for load and aeroelastic calculations. Oscillating pitch models were originally developed for helicopter applications and have been adapted for wind turbine modelling [18]. Holierhoek et al. [19] did a systematic comparison between experimental data and three of the most used models on wind turbine airfoils, but never explored the opportunity to improve power harvesting. In this study we explored through computational fluid dynamics (CFD) simulations and Blade Element Momentum Theory (BEMT) the possibility of using oscillating pitch for wind turbine applications. The paper will present the tools and methods used to perform the study and will later explain the different results obtained through simulations and optimization.

2 Design and Modeling

2.1 Blade Element Momentum Theory (BEMT)

A turbine blade has an airfoil cross-section with continuously varying chord, orientation and shape along its length as shown in fig. 2. The variation from root to mid span to tip is required so that the blade is strong and efficient. The blade is twisted so that the angle of attack is constant along its length. The product of the chord length and the radius is designed to be constant so that the Reynolds number is constant. For this reason, the chord length decreases with radius.

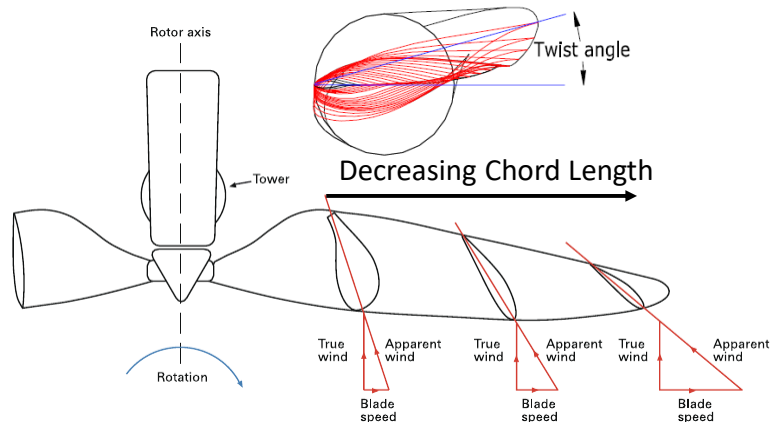


Figure 2: A typical modern horizontal axis wind turbine blade with airfoil profiles, twist and chord length variation [20]

The importance of the aforementioned aspects of wind turbine blade design is that they allow for characterization of the full 3D turbine blade from the physics of a single 2D cross-section using BEMT. BEMT is a combination of momentum theory and blade element theory. Momentum theory by itself analyses the momentum balance of the rotating annular stream tube passing through the turbine, fig. 3 [21]. Blade element theory is the study of the forces generated by the airfoil's lift and drag forces, fig. 4, at different sections along the length of the blade [22]. The combination of both allows us to obtain useful relationships that lead towards fast and simple calculations. The method assumes steady wind conditions, no interaction in between elements, nor wake expansion. Methods to include tip losses, yaw of the turbine, 3D corrections among others have been implemented to improve the analytical results [23], but are not included in this work.

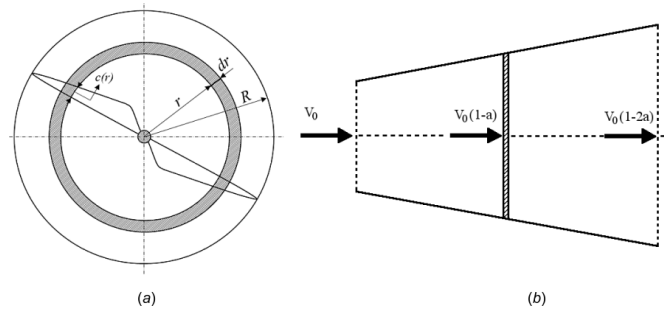


Figure 3: Typical geometry used for BEM theory analysis (a) Actuator disk (b) Fluid stream tube [23]

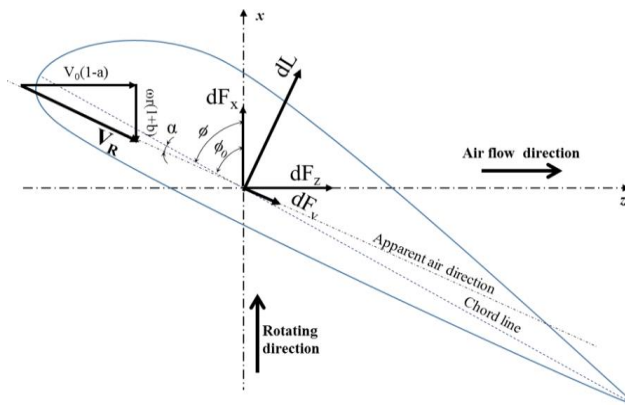


Figure 4: Forces acting on the single blade element [23]

From BEMT we can calculate the torque generated by each element of the wind turbine blade using eq. (1),

$$dT = \frac{1}{2} \rho B c(r) R(r) V_R^2 (C_L \sin(\phi) - C_D \cos(\phi)) dr \quad (1)$$

Where ρ is the density of the air, B is the number of blades, $c(r)$ is the chord length of the element at distance from the hub r , $R(r)$ is the radius of the blade at distance from the hub r , V_R is the relative velocity of the wind, C_L is the aerodynamic lift coefficient, C_d is the aerodynamic drag coefficient, and ϕ is the angle of relative velocity of the wind with respect to the axis of the rotor. The total power generated by the turbine can then be calculated using eq. (2),

$$P_r = \int_{R_{hub}}^R \omega dT \quad (2)$$

where R_{hub} is the radius of the turbine hub, R is the radius of the blade, and ω is the rotational velocity of the blades.

The net power for the static case is the power generated by the blades on the rotor, eq. (2). The net power for the blade oscillation case is the power generated by the oscillating blades minus the power needed to oscillate the blades, P_{osc} , eq. (3). To calculate P_{osc} we assume steady-state operation and no friction losses,

$$P_{osc} = \omega_p \tau_{aero} \quad (3)$$

Where ω_p is the rotational velocity of the pitching and τ_{aero} is the torque generated on the blade by the aerodynamic forces and can be calculated by,

$$\tau_{aero} = \frac{1}{2} C_{M_{osc}} \rho V_R^2 c(r)^2 dr \quad (4)$$

and $C_{M_{osc}}$ is the aerodynamic moment coefficient of the oscillating blade. The dynamic power in the rotor is,

$$P_{dyn} = P_r - P_{osc} \quad (5)$$

Taking into account that C_L and C_D in eq. (1) are the coefficients of the oscillating blade.

2.2 Variable Selection

To evaluate the performance of the oscillating pitch versus the static pitch a response variable, the power ratio, P_{ratio} , is introduced. The equation for the power ratio is,

$$P_{ratio} = \frac{P_{dyn}}{P_{sta}} \quad (6)$$

where P_{dyn} is the power captured from the dynamic simulation and P_{sta} is the power captured from the static simulation. There are five major variables that significantly impact the response variable, P_{ratio} . These variables are the airfoil shape, the waveform of oscillation, the average angle of attack, the amplitude, and the frequency. An extensive exploration of the airfoil shape and waveform oscillation was performed before running the optimization for the other three variables.

The airfoil selected for the study is the DU 96-W-180 developed at the Delft University of Technology in the Netherlands. An image of its shape is shown in fig. 5. A low camber airfoil was selected because it has a high lift-to-drag ratio [24] and its profile data is available online [25]. We also explored high camber airfoils like the S8XX series from the National Renewable Energy Lab (NREL) and the results showed much lower performances.

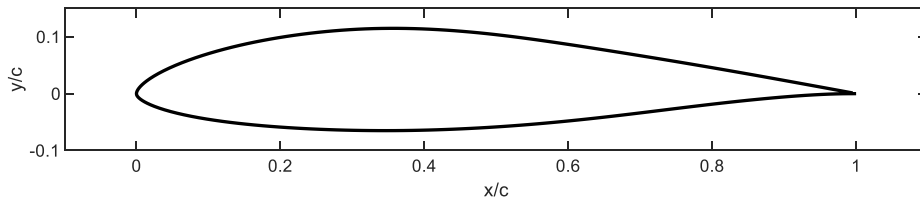


Figure 5: DU 96-W-180 airfoil outline

The waveform selected for the study is a “tilted sinusoid”, with an equation of the general form,

$$\alpha = \sum_{k=1}^n \frac{\binom{2n}{n-k}}{k 2^{2n-1}} \sin(k 2\pi f t) \quad (7)$$

where f is the frequency, t is time, and in general $\binom{2n}{n-k}$ is a combination which is defined as,

$$\binom{2n}{n-k} = \frac{(2n)!}{(n-k)!(n+k)!} \quad (8)$$

We chose a value of $n = 4$ to obtain the desired tilting as shown in fig. 6. As $n \rightarrow \infty$ the waveform becomes a sawtooth wave.

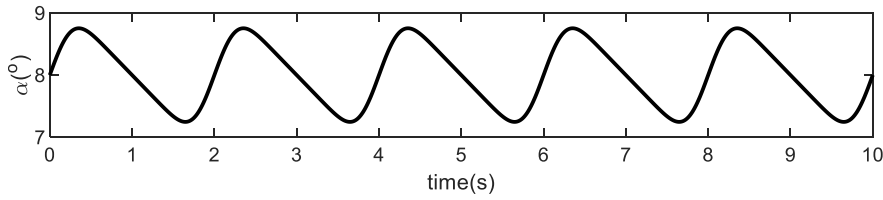


Figure 6: "Tilted sinusoid"

The benefits of a tilted sinusoid oscillation as compared to a regular sinusoid are further described in section 3.1.2 of this paper.

The three independent variables that are changed to form the solution space are the average angle of attack, amplitude, and frequency. The average angle of attack is the center angle that the airfoil oscillates around. The second free variable is the amplitude of the dynamic pitching. The only constraint on this variable is that the amplitude cannot be larger than the average angle of attack to avoid negative angles of attack during the blade's cycle. Negative angles of attack produce very poor or even negative lifts so they will be avoided. The final free variable is the frequency of the oscillation. The major constraint on this variable is that the maximum rotational speed possible with common wind turbine actuators is roughly 10 deg/s [26]. One rotational cycle for the airfoil is defined as tilting up to the highest angle, then down to the lowest angle, and then back to its starting angle; therefore, the total angular difference the airfoil travels in one cycle is four times the amplitude. Consequently, the equation for maximum possible frequency, f_{max} , is,

$$f_{max} = \frac{\omega_{max}}{4A} \quad (9)$$

where ω_{max} is the maximum rotational speed of 10 deg/s and A is the amplitude in degrees. Therefore, the maximum frequency for each simulation case is related to the amplitude of that simulation.

The power ratio values obtained from these simulations are compared to each other for finding the pitching settings that produce the highest efficiency. The static blade simulations are performed in QBlade, the dynamic pitching CFD simulations are performed in Ansys Fluent® and the BEMT calculations are performed in MATLAB®.

2.3 CFD Simulations

All the CFD Simulations are run with 2D airfoil cross-sections using the SST $k-\omega$ turbulence model as suggested by Menter [27]. The mesh size is initially 0.002 m for the factorial experiment with refinement around the edge of the airfoil. The mesh size is later enlarged to 0.01 m for the hill climbing optimization to improve the speed of the simulations after validating that the new mesh size produces accurate results. The larger mesh is shown in fig. 7. The mesh is coarse far away from the airfoil cross-section but refined in the circular region around the airfoil and even further refined at the leading edge. The average angle of attack is then set by rotating the profile in the geometry setup. Then, a user defined function (UDF) is programmed in C language to simulate the desired oscillatory movements. After loading the UDF into Ansys Fluent®, a 10 s simulation is run. For the factorial experiment, the time step is 0.002 s with 5000 time steps but this is increased to a time step of 0.01 s with 1000 time steps for the hill climbing optimization for the same reason of reducing simulation time. Ansys Fluent® reports the lift, drag, and pitching moment coefficients in the 2D simulation which can then be plugged into a series of calculations including equations (1) and (2) to calculate the overall power generated by the turbine based on BEMT.

Based on the increase of the mesh size and the time step for the hill climbing optimization to save time, a discrepancy of power ratio of around 2% is found with respect to the initial simulations. Despite the slight discrepancy between the two meshes and time steps, this is still a valid method for the purpose of finding the optimal point.

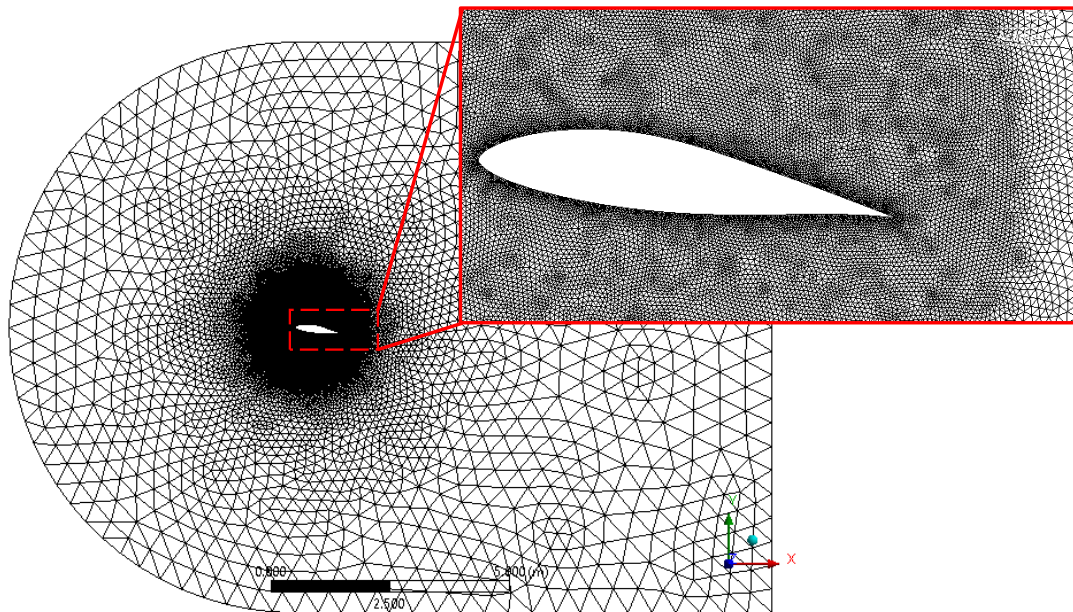


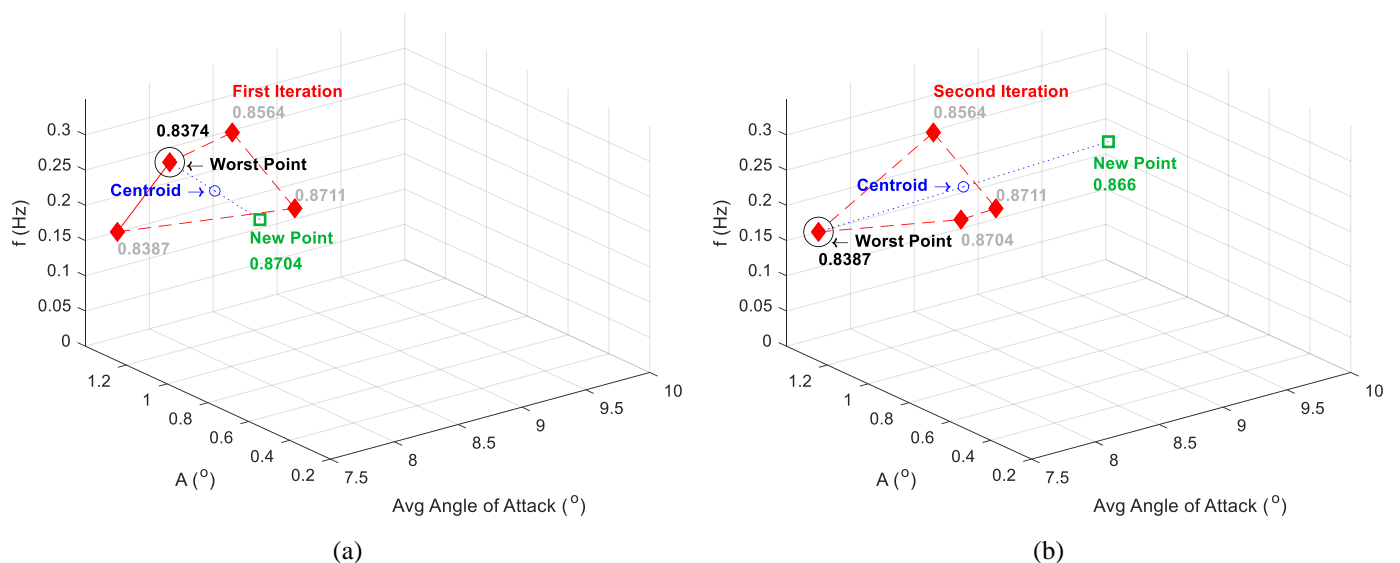
Figure 7: 2D mesh in Ansys Fluent® with detailed view of the mesh around the airfoil

2.4 Factorial Experiment

The first portion of the optimization study is based on a factorial experiment. Factorial design is an efficient method for determining the effect of multiple independent variables on a response variable. It involves selecting high and low values for each independent variable to search the solution space and determine the relative effect of each independent variable, or combinations of variables, on the output variable [28]. The only three independent variables that are adjusted are the average angle of attack, the amplitude, and the frequency. A high, low, and medium value are selected for each independent variable. This creates twenty-seven cases that are run in Ansys Fluent®.

2.5 Hill Climbing Optimization

The second portion of the optimization study is based on a hill climbing optimization. Hill climbing optimization is an iterative local search technique. For this final solution space search, a greedy approach is used. This means that the algorithm always moves in the direction of higher power ratio with the goal of finding the best solution [29]. Since it is a three-variable optimization, four initial points are required. To find the next prospect point, the centroid of a trapezoid is found, and a new point is projected from the worst point. This new point replaces the worst point from the previous iteration, then a new centroid is found, and a new point projected. This process is iterated until the optimal solution is found. Figure 8 (a), (b) and (c) illustrate the idea for the first three iterations of the optimization. Figure 12 shows the complete optimization path found for this study.



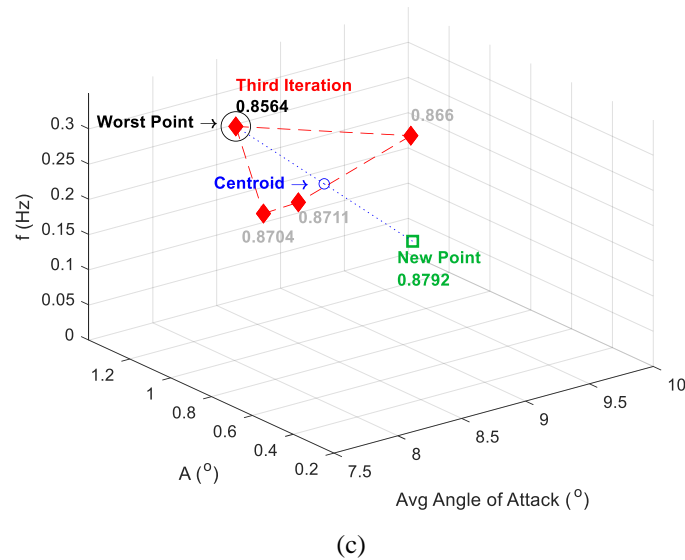


Figure 8. Step-by-step hill climbing optimization example. The numbers represent the power ratio, P_{ratio} , for the specific average angle of attack, amplitude, and frequency being evaluated.

3 Results and Discussion

The results obtained in this work are divided into two. The first set of results are related to the initial CFD simulations used to evaluate the aerodynamic forces acting on the wind turbine blade. The second set of results are related to the optimization results obtained through the factorial experiment and the hill climbing optimization to find the best conditions of oscillation.

3.1 CFD Simulations

We explored the effect of the angle of attack on both the lift and drag of airfoils. This information allowed for an educated choice of the solution space to search in the optimization process. Experimental [17] and CFD simulation data of the lift and drag coefficients are shown in fig. 9. Figure 9 (a) shows that the static CFD case, the purple line, exhibits a maximum lift coefficient around an angle of attack of 15° but in fig. 9 (b) it is clear that the drag can be orders of magnitude larger at this point than it is at low angles of attack. Both the experimental and simulation data on these plots suggest that the optimal combination of lift and drag will probably be found roughly between 5° and 11° . In that range, the lift coefficient is still high but more importantly, the drag coefficient is extremely low. The data in fig. 9 is from an NREL S809 airfoil but this is still a useful starting range for the airfoil used in the optimization.

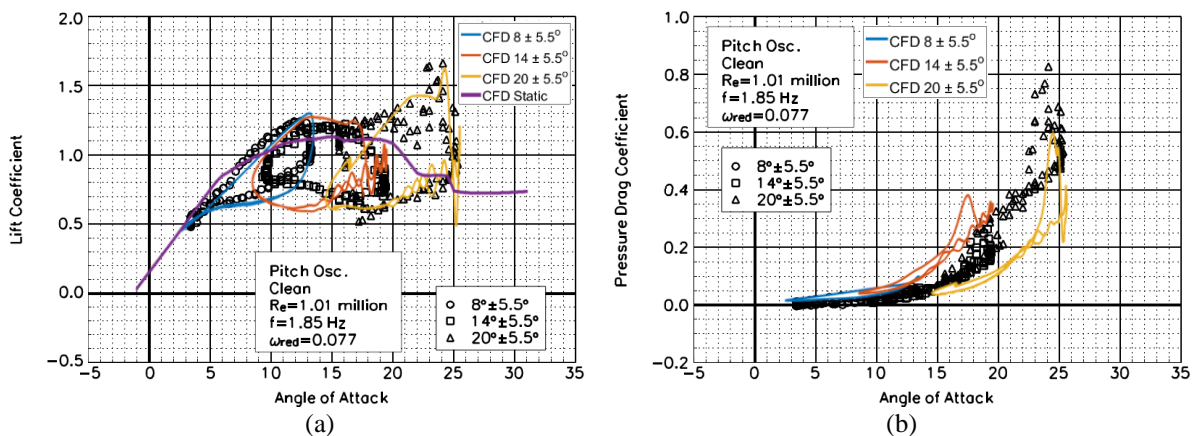


Figure 9: (a) Dynamic lift coefficients vs. angle of attack curves for S809 airfoil, experimental (black markers) vs CFD data (color lines). (b) Dynamic drag coefficients vs. angle of attack curves for S809 airfoil, experimental (black markers) vs. CFD data (color lines)

3.2 Waveform Evaluation

Simulation data shows that a tilted sinusoid oscillation waveform performs better than a regular sinusoid. Specifically, a waveform that goes up quickly and down slowly captures more power. A plot of this type of tilted sinusoid is shown in the bottom plot of fig. 10. The data in fig. 10 is from two simulations in Ansys Fluent® with the same conditions but different waveforms. It can be seen in the third plot of fig. 10 that the tilted sinusoid produces higher lift coefficient to drag coefficient ratios than a regular sinusoid. The primary reason for this is because when the airfoil moves down slowly, the lift coefficient stays higher than it does with the regular sinusoid, top plot of fig. 10. The drag coefficient is shown in the second plot of fig. 10; the peak locations differ for the sinusoids, but the average drag coefficient is about the same for both.

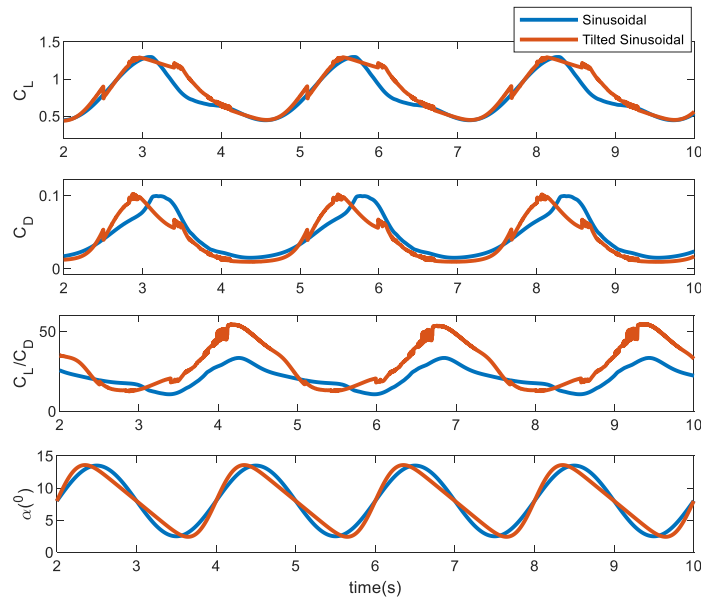


Figure 10: Comparison of C_L and C_D for regular sinusoid and tilted sinusoid waveforms. Data is from CFD simulations in Ansys Fluent®

3.3 Factorial Experiment

The only three independent variables that were adjusted were the average angle of attack, the amplitude, and the frequency. A high, low, and medium value were selected for each independent variable. This created twenty-seven cases that were run in Ansys Fluent® and the results are shown in the box diagram in fig. 11. The low, medium, and high values for each independent variable can be seen along the bottom and right edges of the solution space box in the figure and the number at each point is the power ratio value reported from applying BEMT calculations to the data.

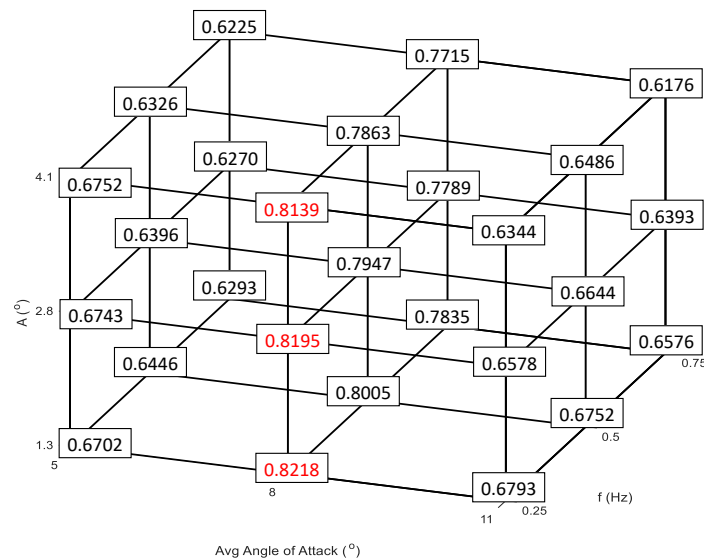


Figure 11: CFD power ratio results from the factorial experiment. Most efficient points highlighted in red

Figure 11 provides insight into how each variable affects the final power captured from the turbine. The highest power ratio values are highlighted in red. An average angle of attack of 8 degrees captures more power than higher or lower average angles of attack. This is because with an average angle of attack of 8 degrees the oscillation stays in the range of low drag but still has relatively high lift. Also, it appears that lower frequencies produce better power capture; the highest values are found at a frequency of 0.25 Hz. The reason for this mainly being that it requires less input power to pitch the blade at a lower frequency. Finally, amplitude is the variable that has the smallest effect on the power captured by the blade. For the most part, smaller amplitudes result in slightly higher power capture, but the effect is minimal compared to the effect of average angle of attack and frequency. The best result from the initial 27 simulations was used as a starting point for the hill climbing optimization.

3.4 Hill Climbing Optimization

The path of the hill climbing optimization is shown in fig. 12. The four starting points are shown as red diamonds, the optimization path is shown as a black solid line and the maximum power ratio is shown as a green star. One of the initial points was the point of highest power ratio from the factorial experiment and the other three were chosen around that with the idea to provide depth in every variable so that the algorithm could search the solution space effectively. A total of twenty-four simulations were run in this portion of the optimization. The search algorithm was reinitialized twice due to stalling and each time it was restarted the size of the search was refined around the highest value from the previous run. The first time the search stalled because the new point had a negative frequency, and the second stall was because the new suggested point had already been simulated. These are both very common problems and solutions for this type of optimization. Overall, a 9% increase in power capture was discovered with the hill climbing algorithm over the highest power ratio found from the factorial experiment with a final power ratio of 0.8977. The frequency, average angle of attack and amplitude for the highest power ratio were 0.0065 Hz, 8.6022° and 0.6486°. It is expected to see a power ratio of 1 if the algorithm reaches a frequency of 0 Hz and an average angle of 8°. However, there is a simulation mismatch that comes from calculating optimal aerodynamic coefficients with QBlade for the static case and with Ansys Fluent® for the dynamic case.

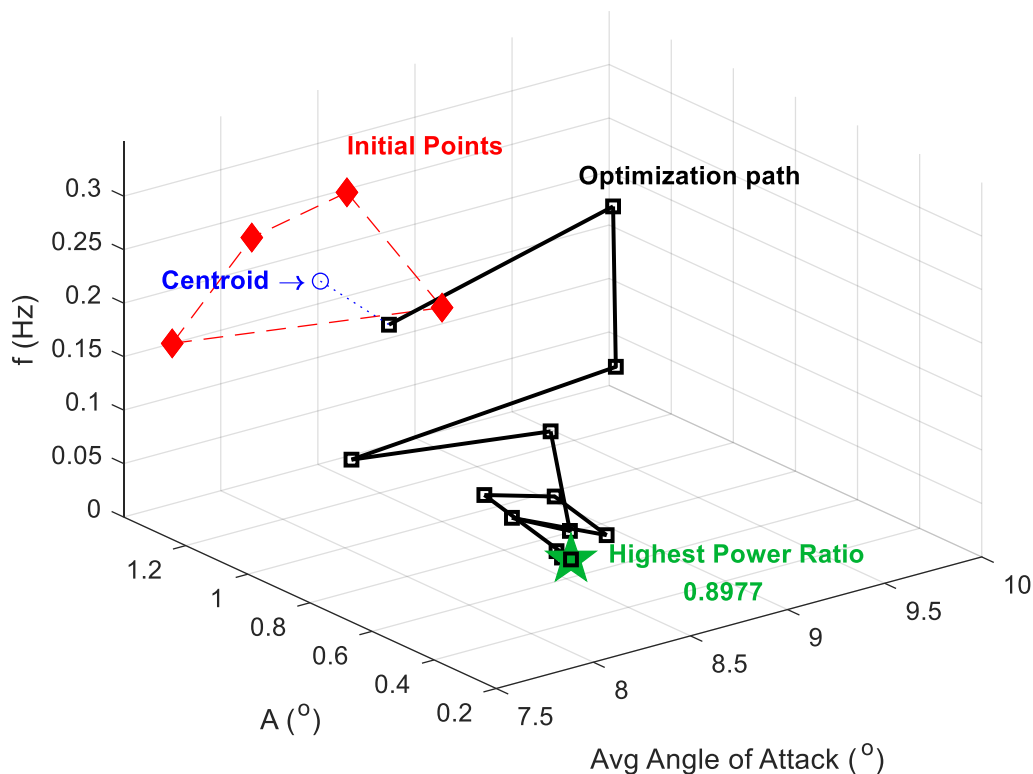


Figure 12: Path of hill climbing optimization shown in black. Initial points shown as red diamonds and point of highest power ratio shown as a green star (The optimization path is only showing the new point for each iteration)

Hill climbing does not guarantee finding the global maximum and it can end up reporting a local maximum as the final result because the greedy approach used cannot climb down hills. This is a general problem of any convex optimization technique [30]. It could get stuck on a local maximum without knowing that there is a higher power ratio value somewhere else in the solution space. A common method for overcoming this is to restart the search numerous times in random locations but there was not enough time to do this because each simulation required

intensive manual input consisting of determining the new waveform equation, rewriting the waveform code, reinitiating the CFD simulation, and after the simulation, inputting the data into the MATLAB® code to determine the next search point. However, performing the factorial experiment first allowed for a coarse search of the relevant solution space where the maximum power ratio value is almost certain to be found, so it is reasonable to believe that the hill climbing optimization started close to the global maximum. If this is the case, the final point of maximum power ratio found by this optimization can be considered to be the global maximum. Another optimization technique known as ant colony optimization was considered but not used because it also requires a large number of simulations [31].

4 Conclusion

We have explored the opportunity to harvest more power from wind by oscillating the pitch of wind turbine blades. The study compared, through simulations, the power captured by static pitch wind turbine blades to the power captured by oscillating the pitch of wind turbine blades. We used CFD analysis combined with BEMT to calculate the power ratio. For the first stage of the study, it was found that oscillating the blades with a tilted sinusoid improved the overall performance when compared to oscillating the blades with a sinusoid wave. This was evident when comparing the lift to drag ratio between the two waveform inputs. For the second stage of the study, an optimization of the oscillating conditions was proposed. The optimization showed that the overall performance of the oscillating case was never higher than the overall performance of the static case. For the optimal conditions, the oscillating blade could only produce 89.77% of the power produced by the static blade. This is mainly because of the drag forces present in the system and because you have to input extra power into the system to oscillate the blades.

References

- [1] R Wiser, E Lantz, T Mai, J Zayas, E DeMeo, E Eugeni, J Lin-Powers, R Tusing. Wind Vision: A New Era for Wind Power in the United States. *The Electricity Journal*, 28(9):120-132, 2015.
- [2] U.S. Department of Energy. Wind Vision Report by United States Department of Energy. 2008. [Online]. Available: <https://www.energy.gov/eere/wind/wind-vision>.
- [3] A Betz. Windenergie und Ihre Ausnutzung durch Windmühlen. *Vandenhoeck and Ruprecht, Göttingen*, 1926.
- [4] J F Manwell, J G McGowen, and A L Rogers. *Wind Energy Explained: Theory, Design and Application*. Wiley, New York, 2009.
- [5] R Dutta, F Wang, B F Bohlmann, and K A Stelson. Analysis of Short-Term Energy Storage for Midsize Hydrostatic Wind Turbine. *Journal of Dynamic Systems, Measurement and Control*, 136(1), 2013.
- [6] K E Johnson, L Y Pao, M J Balas, L J Fingersh. Control of Variable-speed Wind Turbines: Standard and Adaptive Techniques for Maximizing Energy Capture. *IEEE Control Systems Magazine*. 26(3):70-81, 2006.
- [7] M A Abdullah, A H Yatim, C W Tan, R Saidur. A review of maximum power point tracking algorithms for wind energy systems. *Renewable and sustainable energy reviews*. 16(5):3220-7, 2012.
- [8] L Y Pao, K E Johnson. A tutorial on the dynamics and control of wind turbines and wind farms. Proc. of the *IEEE American Control Conference*. 2076-2089, 2009.
- [9] F Wang, K A Stelson. Model predictive control for power optimization in a hydrostatic wind turbine. Proc. of the *13th Scandinavian International Conference on Fluid Power*. 92:155-160), 2013.
- [10] Y Xiao, Y Li, M A Rotea. CART3 field tests for wind turbine region-2 operation with extremum seeking controllers. *IEEE Transactions on Control Systems Technology*. 27(4):1744-52, 2018.
- [11] J Schmitz, N F Diepeveen, N Vatheuer, and H Murrenhoff. Dynamic Transmission Response of a Hydrostatic Transmission Measured on a Test Bench. Proc. of the *European Wind Energy Conference and Exhibition (EWEA)*, 2012.
- [12] C Ai, W Gao, Q Hu ,Y Zhang, L Chen, J Guo, Z Han. Application of the Feedback Linearization in Maximum Power Point Tracking Control for Hydraulic Wind Turbine. *Energies*, 13(6), 2020.
- [13] S Sheng. Report on Wind Turbine Subsystem Reliability - A Survey of Various Databases (Presentation), NREL (National Renewable Energy Laboratory). 2013.
- [14] B Mohanty, F Wang, and K A Stelson. Design of a Power Regenerative Hydrostatic Wind Turbine Test Platform. *JFPS International Journal of Fluid Power System*, 11(3):130–135, 2019.
- [15] E Mohr, B Mohanty, and K A Stelson. Short-Term Energy Storage System for Hydraulic Hybrid Wind Turbine Transmission. Proc. *2020 Bath/ASME Symposium, Fluid Power Systems Technology*, 2020.
- [16] A Choudhry, M Arjomandi, and R Kelso. Methods to Control Dynamic Stall for Wind Turbine Applications. *Renewable Energy*, 86:26-37, 2016.

- [17] M J Hoffmann, R Reuss Ramsay, and G M Gregorek. Effects of Grit Roughness and Pitch Oscillations on the S809 Airfoil. *NREL/TP-442-7817, National Renewable Energy Lab, Golden, CO (United States)*, 1995.
- [18] J G Leishman. Challenges in Modeling the Unsteady Aerodynamics of Wind Turbines. *ASME 2002 Wind Energy Symposium*, 132:141-167, 2002.
- [19] J G Holierhoek, J B de Vaal, A H van Zuijlen, and H Bijl. Comparing Different Dynamic Stall Models. *Wind Energy*, 16:139-158, 2013.
- [20] P J Schubel and R J Crossley. Wind Turbine Blade Design. *Energies*, 5(9):3425-3449, 2012.
- [21] E Kulunk. *Aerodynamics of Wind Turbines, Fundamental and Advanced Topics in Wind Power*. R. Carriveau, 2011.
- [22] F Mahmuddin. Rotor Blade Performance Analysis with Blade Element Momentum Theory. *Energy Procedia*, 105:1123-1129, 2017.
- [23] V Dehouck, M Lateb, J Sacheau, and H Fellouah. Application of the Blade Element Momentum Theory to Design Horizontal Axis Wind Turbine Blades. *Journal of Solar Energy Engineering*, 140:1-9, 2019.
- [24] L Prandtl and O G Tietjens. *Applied Hydro and Aeromechanics*. Dover, New York, 1957.
- [25] A M Halawa, B Elhadidi, and S Yoshida. Aerodynamic Performance Enhancement Using Active Flow Control on DU96-W-180 Wind Turbine Airfoil. *Evergreen*, 5(1):16-24, 2018.
- [26] M H Hansen, A Hansen, T J Larsen, S Øye, P Sørensen, and P Fuglsang. Control Design for a Pitch-Regulated, Variable Speed Wind Turbine. *R-1500, Risø National Lab, Roskilde, Denmark*, 2005.
- [27] F R Menter. Two-Equation Eddy-Viscosity Turbulence Models for Engineering Applications. *AIAA*, 32(8), 1994.
- [28] E P George, J S Hunter, W G Hunter, R Bins, K Kirlin IV, and D Carol. *Fractional Factorial Designs. Statistics for Experimenters: Design, Innovation, and Discovery*. Wiley, New York, 2005.
- [29] I P Gent and T W Alsh. Towards an Understanding of Hill-climbing Procedures for SAT. *AAAI*, 93:28-33, 1993.
- [30] D Yuret and M De La Maza. Dynamic Hill Climbing: Overcoming the limitations of optimization techniques. *The Second Turkish Symposium on Artificial Intelligence and Neural Networks*, 208-212, 1993.
- [31] M Dorigo, M Birattari, and S Thomas. Ant Colony Optimization. *IEEE Computational Intelligence Magazine*, 1(4):28-39, 2006.

Improving the Energy Efficiency of Single Actuators with High Energy Consumption: An Electro-Hydraulic Extension of Conventional Multi-Actuator Load-Sensing Systems

David Fassbender^{1,2}, Tatiana Minav¹, Christine Brach², and Kalevi Huhtala¹

¹Innovative Hydraulics and Automation, Tampere University, Tampere, Finland

²Bosch Rexroth, Elchingen, Germany

E-mail: david.fassbender@tuni.fi, tatiana.minav@tuni.fi, christine.brach@boschrexroth.de, kalevi.huhtala@tuni.fi

Abstract

A load sensing (LS) supply in combination with control valves is one of the most common solutions for the actuation of implements on heavy-duty mobile machines (HDMMs). A major drawback of this approach is its relatively low energy efficiency due to metering losses—especially for multi-actuator operation and load braking. Several novel, more efficient concepts have already been proposed but involve high component costs for each actuator, which is not acceptable for HDMMs with many actuators that have a medium to low energy turnover. Therefore, this work proposes a novel system design which is based on a conventional LS system—for cheap operation of a high number of low-energy-consuming actuators—but allows to avoid metering losses for single high-energy-consuming actuators by replacing their metering valves with electric-generator-hydraulic-motor (EGHM) units that work similar to pump-controlled concepts. The benefits of the novel concept are explained in detail by looking at the three main throttling functions of an actuator in a typical valve-controlled LS systems, which the novel concept avoids by applying pressure in the actuator return lines and recuperating energy electrically instead of dissipating it by throttling. Furthermore, advantages and challenges for the novel concept are analyzed, and ways to address the latter are presented. Before the novel concept is simulated, the required control algorithms are presented. The simulation study in Amesim and Simulink focuses on a telehandler that utilizes the novel concept for the boom, extension and tilt actuators. Simulation results show that the novel system can decrease the required input energy for typical duty cycles by up to 34% compared to a conventional LS system. At the same time, simulations show that, from an economic perspective, it seems most reasonable to utilize the novel EGHM units only for the boom and extension actuators of the studied telehandler.

Keywords: Electro hydraulics, energy efficiency, cost efficiency, heavy-duty mobile machinery, load-sensing system

1 Introduction

Hydraulics is the state-of-the-art technology for actuating the implements of heavy-duty mobile machines (HDMMs), such as excavators, wheel loaders, telehandlers or cranes. The main advantages that make hydraulics indispensable in this field are its power and force density, robustness, ease of linear actuation, and the low effort for adding multiple valve-controlled actuators to a single hydraulic supply unit.

On the downside, conventional hydraulic implement systems have the common disadvantage of low energy efficiency. Regardless of the specific type, open-center, negative-flow-control or load sensing (LS), conventional hydraulic implement systems achieve motion control by means of valves which lead to metering losses. For multiple actuators that are supplied by the same pump, the losses are especially high if the loads vary between actuators and valves need to compensate the load pressure differences by throttling. Such a system still requires energy—under bad conditions even a lot—when a load needs to be braked and energy could actually be recuperated.

Even though the low energy efficiency of these systems leads to higher energy consumption, for a long time, it has been accepted by industry for the sake of low component costs, and more efficient alternatives could only be perceived in academia. However, recently, energy efficiency or emissions, respectively, are becoming more important for industry since climate change is leading to stricter emission legislation and more extensive political programs started. An example is the European Union's Green Deal, which aims at zero net greenhouse gas emissions by 2050 and lists a "Proposal for more stringent air pollutant emissions standards for combustion-engine vehicles" in its action plan for 2021 [1]. A first approach to meet those new requirements is to design HDMMs that are still diesel-powered but use hydraulic systems with increased efficiency. A step further, HDMMs can be electrified, which allows to avoid local emissions entirely and enables zero-emission construction sites that become more and more common in cities such as Oslo for example [2]. Nevertheless, also for electrified machines, energy efficiency is highly important since the capacity of modern batteries is still rather limited and high efficient systems are the only way to achieve sufficiently long operation times.

Accordingly, there is a major interest in the development of new concepts that are more efficient than conventional valve-controlled systems but still competitive from a cost and performance perspective. So far, a concept that satisfies all demands is missing. Independent metering, for example, reduces metering losses but does not eliminate them entirely, and currently available valves do not fully satisfy the needs of such systems [3]. Furthermore, several concepts exist that can eliminate metering losses entirely and even recuperate energy from braking loads, such as hydraulic transformers, digital hydraulics, displacement control or electro-hydraulic actuators (EHAs). However, hydraulic transformer concepts are, so far, not reasonable due to the low efficiency of transformers that could be formed out of commercially available components [4]. Similarly, several digital hydraulic concepts depend on high performance valves that are, as well, commercially not available yet [5]. On the other hand, digital concepts that are based on multi-chamber cylinders proved to be feasible [6], but due to the more complex design the costs for each cylinder rise. The component costs rise as well for displacement controlled concepts or EHAs since a separate pump or pump and motor, respectively, is necessary for each actuator. Furthermore, issues with cooling, filtering, mode-switching, or low stiffness are compromising pump-controlled systems [7].

All in all, a few novel concepts appear more efficient and feasible from a technical point of view, but certain issues remain and generally the component costs per actuator are increased significantly. This might be acceptable as long as the reduction in energy costs can compensate the increased capital costs over time— in other words, if the payback time is short enough. For main actuators with high energy turnover and amounts of braking loads, such as a boom lift actuators, this might be the case; however, it is very common for HDMMs to have also several auxiliary drives that have a low energy turnover due to being rarely actuated or having low loads for most of the time. For those actuators, the potential for saving energy is rather low and increased component costs cannot be justified—the payback time of novel, sophisticated concepts would be too long. Moreover, many HDMMs traditionally offer a hydraulic power-take-off for attachments, which is a simple connection to the centralized pump supply on most conventional machines. For the aforementioned novel concepts, establishing such a power-take-off would require additional effort. Accordingly, it is advisable to keep up a conventional hydraulic supply, such as an LS pump, on the HDMM—for auxiliary actuators and flexible power take of—and apply novel concepts only for the main actuators.

Instead of having two separate hydraulic systems on the same machine, this paper proposes a novel energy-efficient concept which can be integrated into an existing LS system. That way, conventional valve-controlled actuators are still compatible with the hydraulic system and, in contrast to typical EHA concepts for example, the novel concept can benefit from the connected LS supply in terms of actuator stiffness, oil maintenance, handling of large cylinder sizes and more. In the next section, the novel concept is explained in detail, followed by a section dealing with the control of actuators that apply the novel concept. Another section is dealing with the simulation model of a telehandler that was used to compare the energy consumption with the novel concept to the consumption of a purely conventional LS system. The simulation results are discussed and followed by a conclusion and an outlook section.

2 Novel System Concept

The main idea of the novel concept is to replace the conventional control valves of single actuators in an LS system by an electric-generator-hydraulic-motor (EGHM) unit which requires only an additional directional valve for switching the direction of movement and for load holding. The energy that is conventionally throttled and lost in the form of heat can be converted into electric energy and reused this way, which leads to a significantly increased energy efficiency. In Figure 1, the difference between actuators with the novel concept (left side) and a conventional actuator (right side) can be seen. Any number of novel and conventional actuators can be connected to the same LS pump, and operation is only limited by the maximum flow that can be provided by the pump.

Ideally, the energy that is recuperated by the EGHM units is directly used again by the LS pump. Therefore, a combination of a servo electric machine (EM) and a fixed displacement pump is ideal to form the LS supply, as it was already shown in [8] or [9] for example. However, conventional variable-displacement LS pumps driven by internal combustion engines can be used alternatively if an additional EM is attached to support the engine, as shown in Figure 1 on the bottom right. Accordingly, the novel concept does not rely on a full electrification of the HDMM, and diesel can remain the primary energy source if desired.

Moreover, Figure 1 shows that the load pressures of each actuator are sensed, transmitted and processed electronically instead of electro-mechanically, which was already described as electronic LS in [10] for example. As a result, the pump pressure is still controlled in order to reach the maximum load pressure plus an LS margin, but the margin is defined in the software and can be adjusted, which is necessary for the novel concept as will be explained in Section 3. Furthermore, it should be noted that the concept is applicable for rotary actuators, such as an excavator swing, as well, but only cylinders will be discussed in this paper.

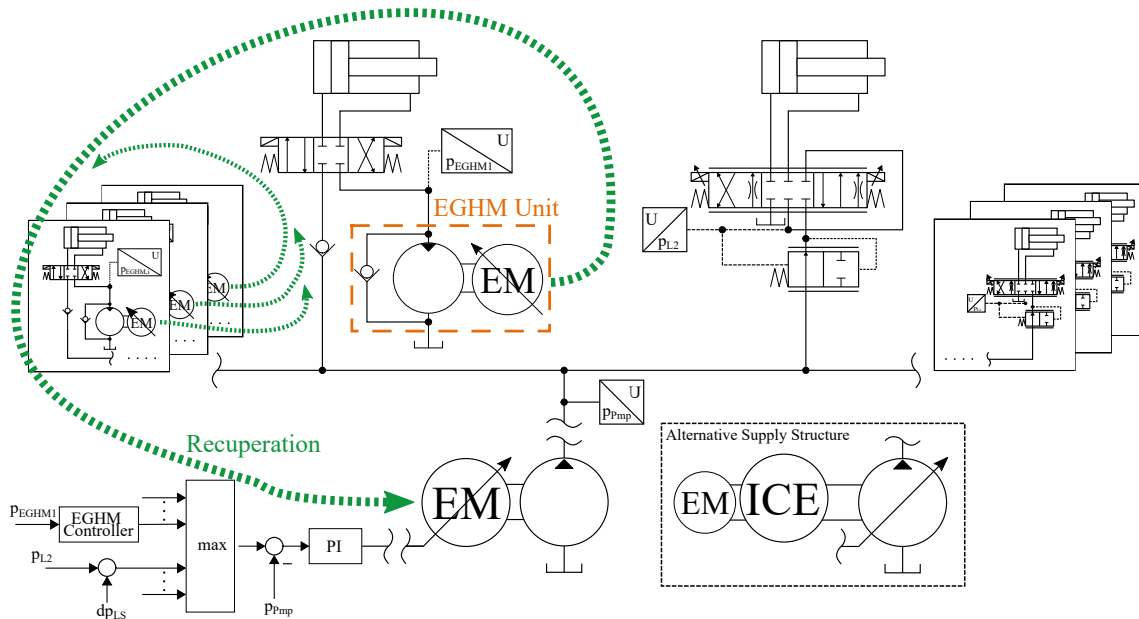


Figure 1: Simplified schematics of LS system including undefined number of actuators with novel concept on the left side and conventional valve-controlled actuators on the right side

2.1 Replacing Throttling by Electric Braking

In order to understand how the novel EGHM unit can fulfil the control functions of conventional valves and to analyse under which conditions the efficiency improvement of the novel system is most significant, the throttling mechanisms of conventional LS control valves are analysed. Three main mechanisms can be identified, each related to one valve in the schematics that are shown in Figure 2a.

2.1.1 Throttling for Speed Control

Next to controlling the flow direction, the flow control valve V1 in Figure 2 controls the actuator speed by metering the supply flow of the actuator. This is achieved by varying the relative valve spool displacement y_{vlv} , knowing that the flow across the metering edge, in this case Q_{spl} , follows the equation

$$Q_{spl} = y_{vlv} \cdot c_{vlv} \cdot \sqrt{\Delta p_{ctr}} \quad (1)$$

c_{vlv} depends on the valve geometry as well as fluid properties and can be assumed constant. In order to achieve a sufficient maximum flow with reasonably large valve sizes and maximum spool displacements, the pressure drop across the edge Δp_{ctr} must be high enough. Common are pressure drops around 20 bar, which are held constant by the pressure compensator (V2 in Figure 2) in order to obtain a proportional behavior between actuator speed and spool displacement. The resulting losses at the flow control valve equal the product of Q_{spl} and Δp_{ctr} and can be seen in Figure 3a.

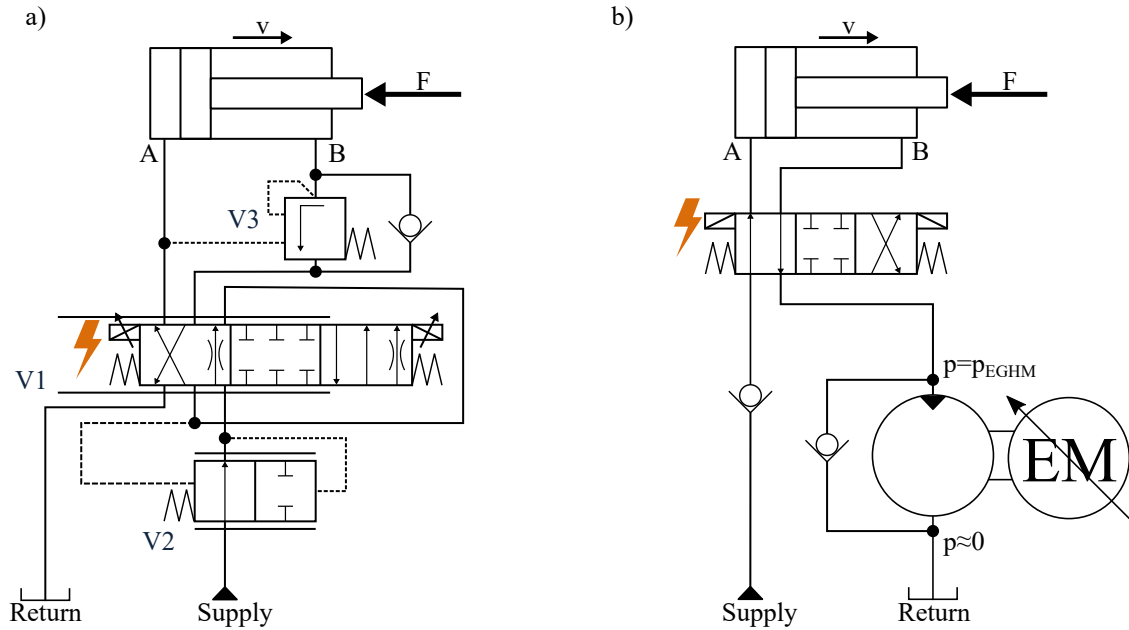


Figure 2: Schematics of two actuators during extension a) with conventional control valves b) with novel EGHM unit

Contrary to this, the novel concept controls the actuator speed by metering the return flow Q_{ret} according to the equation

$$Q_{ret} = n_{EM} \cdot V_{mot} \cdot \frac{1}{\eta_{vol,mot}} \quad , \quad (2)$$

which includes the speed of the electric machine that is working as a generator n_{EM} , and the constant displacement of the hydraulic motor V_{mot} . $\eta_{vol,mot}$ is the volumetric efficiency of the hydraulic motor. It may seem that there is no need for a pressure drop across the EGHM unit because pressure is no part of Equation 2; still, it is advisable to apply a certain minimum pressure $p_{EGHM,min}$ in order to achieve a minimum torque on the EM and improve the control behavior as will be discussed later. However, the pressure drop across the EGHM unit is transformed into electric energy which can be reused and is not dissipated like Δp_{ctr} . Accordingly, the novel concept can always increase the efficiency at least slightly due to the more efficient speed control mechanism.

2.1.2 Throttling for Pressure Compensation

If two or more actuators with different pressure requirements need to be supplied, the pressure difference between the actuators must be compensated by control elements in order to keep control of the system. Conventionally, this is done by a pressure compensator (V2 in Figure 2). The power that is dissipated at this valve equals the product of supply flow and load pressure difference and can be seen in Figure 3b.

For the novel concept, the EGHM unit fulfils the pressure-compensation function as well. Automatically, the EM applies a higher torque if the supply pressure is higher than necessary, and the pressure p_{EGHM} rises until the pressure forces at the cylinder are in balance with the load force. The higher torque leads to more electric energy which can be circulated back to the LS pump. Even though the circulation involves transformation losses, a significant amount of energy can be saved this way.

The efficiency improvement due to this mechanism is always present during simultaneous operation of an actuator that applies the novel system and another actuator with a higher pressure requirement. Furthermore, the improvement is most significant for large load-pressure differences and for high flows of the actuator(s) with lower load pressure, as can be seen by looking at the loss area in Figure 3b.

2.1.3 Throttling for Load Braking

Because the control valve V1 applies meter-in, not -out control, overrunning loads (negative load in Figure 2) bear the risk of cavitation and loss of control if no pressure can be build up in the return line to brake the load. To prevent this, counterbalance valves, such as shown in Figure 2a on the B side, can be used or the cross sections of the return

edges of the directional valve could be reduced. As a result, the actuator can still be controlled by metering the supply flow, but the pump is still required to apply pressure even though the actuator power is negative.

With the novel concept, the whole load-braking power, which is lost in conventional systems through throttling at V3 and can be seen as an area in Figure 3c, can be recuperated by the EGHM unit instead. Again, this happens automatically and can be perceived in the form of a rising pressure p_{EGHM} and torque of the EM whenever the load turns negative. This benefit of the novel concept is especially significant for actuators that frequently need to brake loads at relatively high speeds. However, for market applications, it should be noticed that the EGHM units also have to fulfil the same safety functions as conventional braking valves, such as load holding/braking whenever the energy supply fails.

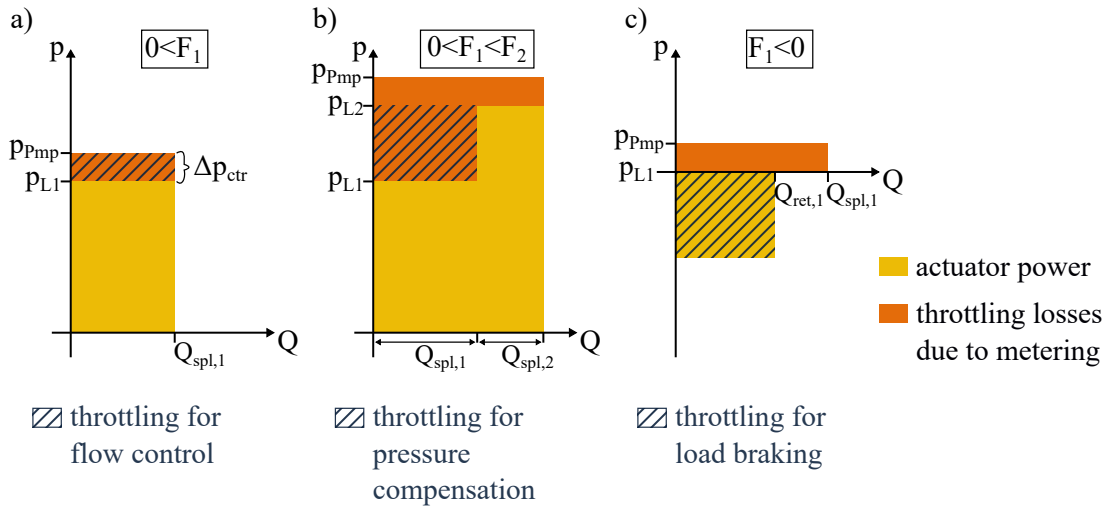


Figure 3: Pressure flow diagrams of one or two valve-controlled actuators (such as shown in Figure 2a) and shaded power-loss areas that can be reduced with the novel system a) during all operation, b) during simultaneous operation of multiple actuators, c) during load braking

2.2 Challenges for Novel Concept

The principle of metering the return flow with an EGHM unit might simplify some of the control mechanism of conventional LS systems, but it leads to new challenges as well, which are discussed here, alongside ways of addressing them.

2.2.1 Circulation Losses

As explained in the introduction, increased component costs can only be justified by an early payback time, which is also true for the novel EGHM concept. Ideally, the novel system avoids all metering losses that appear in the conventional system entirely, but in practice the recuperation and circulation of energy from electric power to hydraulic power and back to electric power involves losses as well. The hydraulic losses along lines and the directional valves cannot be neglected, and the efficiencies of hydraulic motor, EM and inverter might be high, but in sum they will lower the amount of energy that can actually be fed back significantly. Therefore, the novel concept should only be applied to actuators for which the throttling losses discussed in Section 2.1 would be especially high so that energy circulation still leads to sufficient savings. Section 4.6 will deal with the detection of actuators that are suitable for the novel system.

2.2.2 Amplified Pressures

In Section 2.1, it was already mentioned that the novel concept achieves pressure compensation as well as load braking by applying pressure in the cylinder return line. At the same time, it is possible that the full pump pressure is applied to the supply side of the cylinder. In this constellation, the hydraulic cylinder with its differential areas behaves like a pressure transformer, and high pump pressures can lead to much higher return line pressures. The transformation ratio is equal to the cylinder area ratio

$$\Phi = \frac{A_A}{A_B}, \quad (3)$$

where A_A is the piston-side area and A_B the ring area. In extreme cases, such as for the extension cylinder of the telehandler which will be investigated later, Φ can be as high as 1.9, and Figure 4a shows the pressure conditions that can appear at this cylinder. If the pump supplies a typical maximum pressure of 250 bar—because another actuator demands such a high pressure—and flow losses are neglected, the full 250 bar are applied to the piston-side of the cylinder. Without any load to counteract the pressure force, this results in a pressure of 475 bar in the return line. Even higher pressures would be obtained if a negative load is applied.

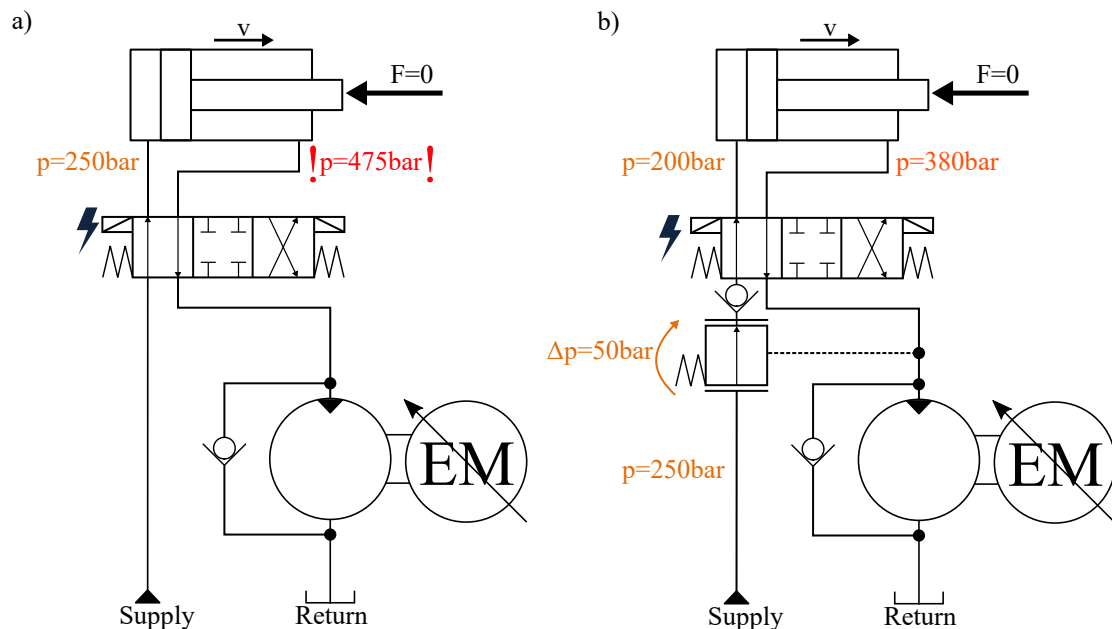


Figure 4: Pressure conditions in the novel concept at maximum pump supply pressure, no load and with a cylinder ratio of $\Phi = 1.9$; a) without pressure compensation and b) with pressure compensation. Other flow losses are neglected

Such high pressures are unacceptable as commercial mobile hydraulic components for this pressure level are not available. The highest standard mobile cylinder pressure rating that could be found by the authors was 380 bar [11], which should be the upper limit for the return line pressure. This can be achieved by adding a pressure compensating valve such as shown in Figure 4b. The valve prevents the recuperation of a part of the surplus pump power but keeps the pressure in an acceptable range at all times. However, the negative influence on the energy efficiency is expected to be less significant for cylinders with typical area ratios in the range of 1.3-1.6. Furthermore, the throttling only appears if the load pressure differences are close to the maximum and the cylinder is retracting.

2.2.3 Increased Flows

Next to high pressures, high cylinder area ratios also lead to significantly increased return line flows that need to be handled by the EGHM unit. During retraction, the return line flow is Φ -times larger than the supply flow, and, compared to the LS pump, the hydraulic motors need to be larger or spin faster in order to achieve the same retraction speeds as a convectional LS system does. However, this issue is not new and well known for other pump-controlled concepts. In [12], it was proposed to install a proportional bypass valve in order to reduce the amount of returning flow at the hydraulic unit of an EHA during retraction. Such a bypass valve could be installed in parallel to the hydraulic motor in the novel concept as well if the high return line flow cannot be handled otherwise. The downside would be a reduced efficiency during fast regenerative retraction.

2.2.4 Limited Compatibility with Conventional Valves

An important aspect of the novel concept is its compatibility with conventional LS control valves for low-cost actuation. It should be mentioned that the compatibility is limited to pre-compensated LS control valves, which can handle a varying LS margin as long as it is high enough. Post-compensated control valves would show an unstable control behavior if the margin is changing because the LS margin directly relates to the pressure drop across the metering edge Δp_{ctr} , which was discussed in Section 2.1.1. However, due to the electronic processing of the valve control signals, the behavior of post-compensated valves can also be achieved with pre-compensated valves, as will be shown in Section 3.1.

2.3 Advantages Towards Electro-Hydraulic-Actuator Concepts

After the elaborations in the previous sections it might be obvious that the novel EGHM concept can perform more efficiently than conventional valve-controlled concepts, but the last section also showed some challenges on the component side. Thus, it might seem more straight forward to choose a pump-controlled EHA concept instead of the novel concept since they usually require less hydraulic and electric machines per actuator and the issues with energy circulation and high pressures do not apply while efficiencies are high and regeneration is possible as well. However, the following part lists major benefits of novel EGHM-controlled actuators towards typical EHAs that prove the relevance of the novel concept:

- **A high minimum chamber pressure** can be achieved with the EGHM concept. EHAs typically suffer from low chamber pressures on one side or even cavitation [13]. The chamber pressures define the stiffness of the cylinder, and a low stiffness is problematic if closed-loop controls are to be applied to the cylinder, which becomes more relevant with a perceptible trend of HDMM automation [14]. Other researchers addressed this issue by adding proportional valves to the EHA [15], which introduces extra losses, or by using two electric motors per actuator [16]. Considering this, the EGHM concept with only one EM per actuator and a shared EM for the pump appears advantageous.
- **No accumulator** is needed for the novel system. Most EHAs include accumulators for differential flow compensation. The required accumulator sizes can be rather large, as discussed in [17], especially for large cylinders and high flows, which are typical for HDMMs. Thus, the EGHM concept can be used for cylinders that are too large for most EHA concepts.
- The novel concept is designed as an **open circuit**. Open circuit pumps show higher efficiencies than those for closed circuits [18], pump or motor leakages are easier to handle and oil cooling as well as filtering is more convenient, especially for a single centralized reservoir such as present in the novel concept. Open-circuit pump-controlled actuators exist as well, but issues with tilting loads and mode switching during movement were reported [13, 19], which does not apply for the EGHM concept.
- **High EM speeds** can be utilized in the novel system because the hydraulic unit, in contrast to EHAs, works solely as a motor. Medium-sized pumps usually have maximum speeds of 2,000-3,000 rpm, but hydraulic motors such as the Rexroth A2 motor [20], which is used for the simulation model in this paper, can operate at up to 5,000 rpm. This allows to select a relatively small hydraulic motor and an EM with high speed but low torque, which is more compact and potentially less expensive than an EM with higher torque and lower speed ratings.

3 Control of the Novel System

Even though the novel concept is based on an LS system, the control is not as trivial as the control of conventional LS valves because many of the functions that were previously covered by valve mechanisms need to be covered by the control software instead.

3.1 Speed Control

The relations between cylinder flows and cylinder speeds v can be expressed for extension as

$$v_{\text{ext}} = Q_{\text{spl}} \cdot A_A = Q_{\text{ret}} \cdot A_B, \quad (4)$$

and for retraction as

$$v_{\text{ret}} = Q_{\text{spl}} \cdot A_B = Q_{\text{ret}} \cdot A_A. \quad (5)$$

Q_{spl} is the supply flow going to the cylinder, and Q_{ret} the returning flow. Furthermore, it is assumed that the speed control signal, such as a joystick signal, represents the ratio of desired supply flow for the cylinder to the maximum permissible supply flow, which is common for conventional HDMM LS systems. Moreover, the maximum supply flow for each actuator is equal to the maximum pump flow in this study. In this case, the control software must assure that the sum of required supply flows for multiple active actuators is not higher than the maximum pump flow. Otherwise, the EGHM could not control the actuator speed and cause cavitation in the return lines. Accordingly, the control applies the following rule to the operator's speed control signals y_i for each actuator i out of N actuators in order to obtain the saturated control signals $y_{\text{sat},i}$:

$$y_{\text{sat},i} = \begin{cases} y_i \cdot \frac{Q_{\text{pmp,max}}}{\sum_{i=1}^N y_i \cdot Q_{\text{act,max},i}}, & \text{if } \sum_{i=1}^N y_i \cdot Q_{\text{act,max},i} > Q_{\text{pmp,max}} \\ y_i, & \text{otherwise} \end{cases} \quad (6)$$

The saturated control signals $y_{\text{sat},i}$ are used to control the valves of conventional actuators in the system and for calculating the required speeds of the EGHM units. Also, it should be noted that this control approach leads to the same behavior which is obtained with a conventional post-compensated system—even though pre-compensated valves are used. However, the rule could also be changed in order to prioritize certain actuator functions such as steering.

Finally, Equation 7 combines Equations 2, 3, 4 and 5 and shows how the control signal is transformed into a speed signal n_{des} for the EMs of each novel actuator:

$$n_{\text{des}} = \begin{cases} \frac{y_{\text{sat}} \cdot Q_{\text{act,max}} \cdot \eta_{\text{vol,mot}}}{V_{\text{mot}} \cdot \Phi}, & \text{if } y_{\text{sat}} > 0 \text{ (extension)} \\ \frac{y_{\text{sat}} \cdot Q_{\text{act,max}} \cdot \Phi \cdot \eta_{\text{vol,mot}}}{V_{\text{mot}}}, & \text{if } y_{\text{sat}} < 0 \text{ (retraction)} \end{cases} \quad (7)$$

In addition, the directional valves must be switched into extension or retraction position as soon as movement is required. Moreover, for the control of the electric generators, positive torques are permitted because otherwise they would cause cavitation when the cylinder reaches its end stops and no more flow can be received from the cylinder.

3.2 Pump Pressure Control

Because the novel concept is more complex than a conventional LS system, also the calculation of the required pump pressure has to be adjusted. Three objectives have to be considered:

- The pump pressure should only be as high as necessary in order to save energy.
- The conventional actuators should receive enough pressure to move the load and to apply the pressure drop Δp_{ctr} (Equation 1) at the control valve.
- The novel actuators should receive enough pressure to build up at least the required minimum pressure in front of the EGHM unit (without pressure, the EM cannot apply a torque and control the speed).

Figure 5 shows the signal flow diagram of the control for a system with one novel actuator (index 1) and one conventional actuator (index 2), which respects all three objectives that are mentioned above.

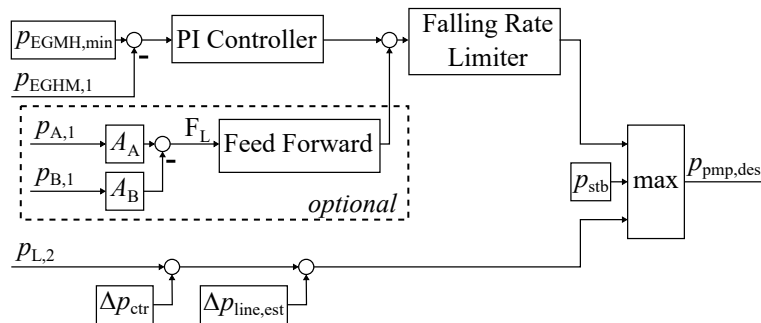


Figure 5: Signal flow for the calculation of the required pump pressure.

The pressure in front of the EGHM unit is detected by a pressure sensor and used as a feedback to control it in order to reach the minimum required pressure $p_{\text{EGHM,min}}$. The relation between the pump pressure, which is adjusted by the controller, and the pressure in front of the unit is highly nonlinear and depends on the direction of movement and amount of flow. Therefore, the parameter tuning of the controller can be difficult, especially if the attached mechanical system has a low damping ratio. The performance can be improved by adding a force feedback signal, which is done in the following simulation part, but this would also require two additional sensors for a real

application. Simulations also showed that oscillations of the mechanical system that cannot be compensated fast enough by the controller lead to pressure spikes close to zero in front of the unit. This may lead to cavitation and definitely to discontinuous movement since the EM cannot apply torque and control the speed. To prevent pressures close to zero, $p_{EGMH,min}$ should be chosen high enough as a buffer, and limiting the falling rate of the pump pressure signal can prevent low pressure peaks caused by the controller as well. On the downside, the rate limiter leads to a higher average pump pressure and potentially to higher losses which will be shown in Section 4.6.

In contrary to this, for the conventional actuator, it is sufficient to sum up the load pressure, which is sensed by a sensor at the LS port of the valve; the pressure margin Δp_{ctr} , which is required at the control edge; and a margin $\Delta p_{line,est}$ that is added to account for flow losses between the pump and the control valve.

Finally, the highest required pump pressure among all actuators defines which pressure is sent to the pressure controller of the pump. This is legitimate since all actuators can handle higher but not lower pressures. However, it should be noted that those switching as well as saturation effects make anti-windup measures in the PI-controllers indispensable. For the case that no actuator is active, also a standby pressure p_{stb} is considered, which assures that all supply lines remain pressurized for fast response.

4 Simulation Study

After explaining the concept, its characteristics, and the way of controlling it, this section deals with the simulation study that was done in order to show how much energy-efficiency improvement is feasible with the novel concept compared to a conventional LS concept. Furthermore, it will be analysed which actuators are most suitable to be controlled by the novel concept and which should remain valve-controlled. This is done by looking at the specific example of a telehandler. The different parts of the simulation model will be explained before the results are presented.

4.1 Telehandler

A 9-tonne telehandler is chosen as the platform for the simulation study because it represents a typical HDMM and its implements comprise hydraulic cylinders of significantly different sizes and functions. For this study, only the linear actuators for boom, extension and tilt are considered, which are depicted in Figure 6. However, additional actuators such as steering cylinders, stabilizers or attachments could also be connected to the LS pump of the novel system, but it seems unlikely that controlling those with the novel EGHM unit could be economical. The telehandler is typically equipped with forks or a bucket for load handling. Furthermore, it should be noticed that the reference telehandler includes compensation cylinders which can be seen in Figure 6 as well. Whenever the boom cylinders are actuated, the compensation cylinders are moving too, and their hydraulic connection to the tilt cylinders results in an almost constant fork or bucket orientation during boom lifting and lowering, even though the tilt is not actively actuated.

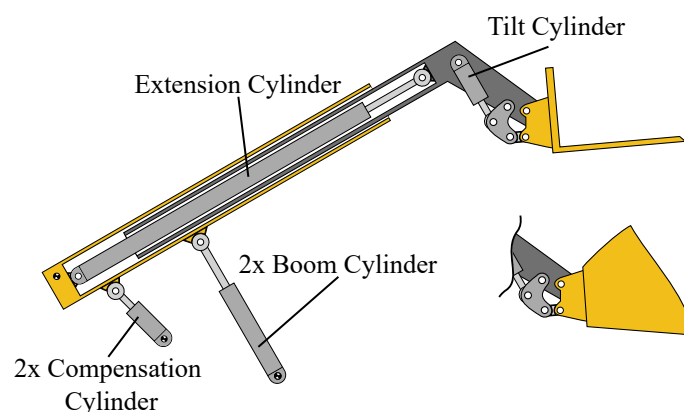


Figure 6: Mechanical parts and hydraulic cylinders of the modelled telehandler implements

The purpose of modelling the implements of the telehandler is to simulate a realistic load for the cylinders in the model of the novel concept. In order to do so, a planar mechanical model was created in the Simcenter Amesim environment, where it can be directly connected to the hydraulic model. Geometry data was obtained by measurements of the reference telehandler, and inertia data was retrieved through reverse engineering of the components with a CAD software. The exact piston and rod diameters of the cylinders are known. Gravity is included in the model, and friction was modelled for the cylinders with a viscous speed-proportional component

and a constant coulomb component. The friction parameters were adopted from the model of a similar machine and slightly adjusted according to the different cylinder sizes. The fact that the model was not validated against measurements of a real version of the telehandler is assumed to be legitimate as only simulation results will be compared to each other that were obtained with the same model.

4.2 Electro Hydraulics

The whole hydraulic system is modelled in Amesim as well, using the basic libraries. The EMs for the pump and EGHM units are modelled as perfect torque sources with PI-controllers for pressure or speed control, respectively. The controllers include maximum torque and speed limitations, anti-windup functions and feedforward terms of the required flow for the pressure controller or feedforward terms of the load pressure in case of the speed controller. Parameters were obtained from the data sheets of suitable permanent magnet synchronous motors. A further description of the controllers is beyond the scope of this paper.

Simulations are done in 5 different setups that are characterized by the choice of actuators that are modelled with the novel concept or remain valve-controlled:

- Setup 0: All actuators conventional (benchmark)
- Setup 1: EGHM units for all actuators
- Setup 2: EGHM unit for boom only
- Setup 3: EGHM units for boom and tilt
- Setup 4: EGHM units for boom and extension

Comparing duty-cycle efficiencies between the different setups will allow to assess which actuator has a high potential for efficiency improvement with the novel system and which one does not.

The modelled schematics of the novel concept correspond to Figure 4b and the schematics of the conventional actuators to Figure 2a, with the exception that the counterbalance valves are installed on both cylinder sides for the boom cylinders and on the piston side only for tilt and extension. Relief valves for the pump and all cylinder chambers were added as well; otherwise, the overall system design corresponds to Figure 1, but energy recuperation is only considered in the post processing.

The sizing of the hydraulics was done in order to meet the same performance as the original reference telehandler with a maximum pump flow capability of $150 \frac{l}{min}$. Each actuator is able to receive the entire maximum pump flow. The chosen displacements and related maximum speed limits of the hydraulic pump [21] and motors [20] can be seen in Table 1 and 2. The motors in the novel concept for boom and extension need to be larger than the tilt motor due to the higher Φ , as explained in Section 2.2.3. At the same time, this results in a lower maximum pressure (set by the compensating valve) for the EGHM units of boom and extension because the torque on the EM would be too high otherwise. The mechanical and hydraulic efficiencies of all hydraulic machines are modelled by implementing lookup tables that include reference data from measurements.

Because dynamic performance is of less importance in this study, the mechanical modelling of the valves has been omitted and mathematical equations without higher order are used to control the opening of single hydraulic edges, of which one or multiple form the pressure compensating or the directional valves. For the conventional valve-controlled actuator, the pressure drop characteristics from the data sheet of a Rexroth SB34 valve block [22] are imitated. The characteristics of the non-metering edges in the same LS valve block have been adopted for the maximum opening of the directional valve and the pressure compensating valve in the novel concept as well.

4.3 Control

The control of the electro-hydraulic system was implemented in Matlab Simulink according to the equations and signal flow diagram in Section 3. The key control parameters can be seen in Table 2. The control blocks for each actuator are chosen for each setup depending on the concept—novel or valve-controlled. The conversation between the hardware model in Amesim and the control in Simulink is achieved through discrete co-simulation with a sample time of 1 ms.

4.4 Duty Cycles

The efficiency performance of the 5 different setups should be compared for a realistic duty cycle in order to achieve meaningful results. Furthermore, simulating different cycles with varying times of actuation for each

Table 1: Key Model Parameters

Parameter	Value	Unit
$p_{EGHM,max,boom/exte}$	320	bar
$p_{EGHM,max,tilt}$	380	bar
Δp_{ctr}	20	bar
$V_{mot,boom/exte}$	56.6	cm ³
$V_{mot,tilt}$	44.9	cm ³
V_{pmp}	63	cm ³
Φ_{boom}	1.6	-
Φ_{tilt}	1.3	-
Φ_{exte}	1.9	-

Table 2: Key Control Parameters

Parameter	Value	Unit
$n_{pmp,max}$	2600	rpm
$n_{mot,tilt,max}$	5000	rpm
$n_{mot,boom/ext,max}$	5000	rpm
$p_{EGHM,min}$	20	bar
$p_{pmp,max}$	250	bar
$\Delta p_{line,est}$	10	bar

actuator and times of simultaneous operation as well as varying amounts of load braking will tell if the novel concept can perform better or worse under specific conditions.

The desired cycle movements are traced by a state-flow controller in Simulink, which separates each cycle into steps. For each step, movement commands are given to specific actuators until a desired position is reached and the next step starts. At the same time, the controller can increase or decrease the load mass in the telehandler model. All setups receive the same duty cycle tracing commands and can be compared to each other. The following cycles are implemented:

4.4.1 Loading with Bucket (Cycle A)

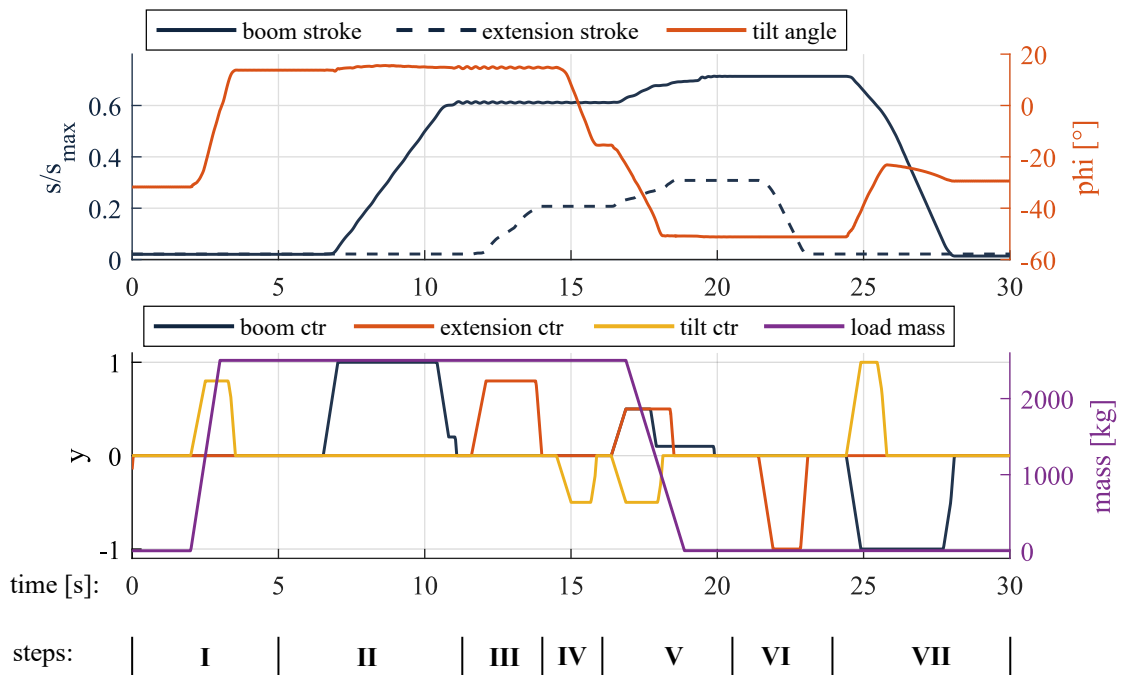


Figure 7: Load mass, control signals and resulting movement for duty cycle A

A typical telehandler task is loading a truck or a container with a relatively high opening by dumping material into the truck or container from above. Buckets with capacities of up to 4,000 l are used to handle loads such as earth or grain that are picked up from a pile. For the simulated cycle, a full bucket load of 2,500 kg is assumed, which can still be handled at low to medium extension length without the risk of tilting the whole telehandler. Figure 7 shows the command signals and resulting movements from the simulation of Setup 1. The smooth curves with only little oscillation prove the functionality of the novel concept, but further analyses of the dynamics are beyond the scope of this investigation. The single steps can be described as following:

I: Tilting the bucket up after the telehandler drove into the pile (load is applied) (→driving to the truck/container) →II: Lifting boom →III: Extending →IV: Starting to tilt bucket →V: Dumping load by tilting, extending and

lifting simultaneously (load is removed) →VI: Retracting →VII: Return to load, by lowering boom and tilting bucket back to initial position

4.4.2 High Stacking of Pallets (Cycle B)

For another cycle, positioning a pallet at a high position, such as in a warehouse, is chosen as a task with more actuation time for the extension cylinder. Two versions of the task are simulated: Cycle B1 simulates the lifting of a pallet and empty lowering of the boom back to ground, and cycle B2 simulates empty lifting and lowering of the pallet, which involves more load braking. For the load mass, 1,500 kg, the maximum weight of a EUR-pallet, is chosen. Again, control signals and modelled movement of Setup 1 are depicted in Figure 8. The steps can be described as following:

I: Lift boom until fork is at eye level →II: Tilt forks until horizontally →III: Lift boom and extend simultaneously until pallet is above drop position →IV: Lower boom and drop pallet (weight decreases) →V: Retract while slightly lifting boom to get forks out of pallet →VI: Get back to drive position by lowering boom, retracting and tilting forks back

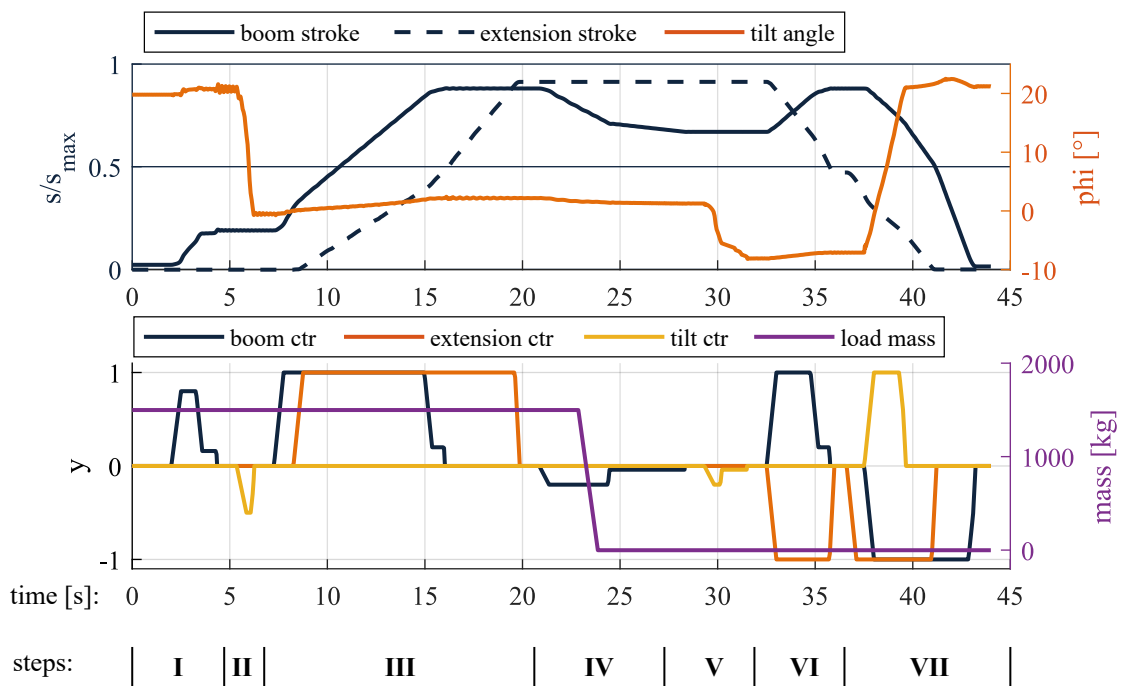


Figure 8: Load mass, control signals and resulting movement for duty cycle B1

Cycle B2 differs only slightly from the reverse cycle B1 in the way the pallet is picked up or dropped. Therefore, cycle B2 is not further described here.

4.5 Energy Analysis

In order to analyse the overall efficiency of the 5 different setups, the mechanical speed and torque of the pump and the the hydraulic motors in the novel concept are recorded and transformed into electric power input and output in the post processing. The transformation involves an assumed inverter efficiency of $\eta_{inv} = 98\%$. The value is assumed constant and adopted from [23], even though the inverter in this publication would be too small, but no specific parameters of larger inverters could be found. The efficiencies of the EMs (η_{EM}) are considered by lookup tables that were obtained from lumped parameter simulations of an permanent magnet synchronous machine. The parameters for the simulation were obtained from data sheets of EMs with matching torque and speed capability. Accordingly, the electric input power can be calculated as

$$P_{el,in} = 2\pi \cdot n_{pmp} \cdot T_{pmp} \cdot \frac{1}{\eta_{EM(n,T)} \cdot \eta_{inv}}, \quad (8)$$

and the electric output power of all N EGHM units as

$$P_{el,out} = \sum_{i=1}^N 2\pi \cdot n_{mot,i} \cdot T_{mot,i} \cdot \eta_{EM(n,T)} \cdot \eta_{inv}. \quad (9)$$

Finally, the required electric energy for the whole cycle can be calculated in the following way:

$$E_{el,in} = \int_0^{t_{end}} P_{el,in} - P_{el,out} dt \quad (10)$$

The fact that it might be necessary to store some parts of the recuperated energy temporarily in an electric storage whenever $P_{el,out}$ is higher than $P_{el,in}$ is neglected here. This is justified by the relatively high charge and discharge efficiencies of modern batteries and supercapacitors.

4.6 Results

The results of the simulations and post-processing are the amounts of electric input energy $E_{el,in}$ that are required for each setup to complete the different duty cycles—in other words, the energy consumption. Those values can be seen in Figure 9 alongside a visualization of the amounts of energy that are circulated and recuperated with the novel EGHM units. The energy amounts are normalized with reference to the required energy for Setup 0 in each cycle, which was 473.6 kJ for Cycle A, 744.7 kJ for Cycle B1 and 533.2 kJ for Cycle B2.

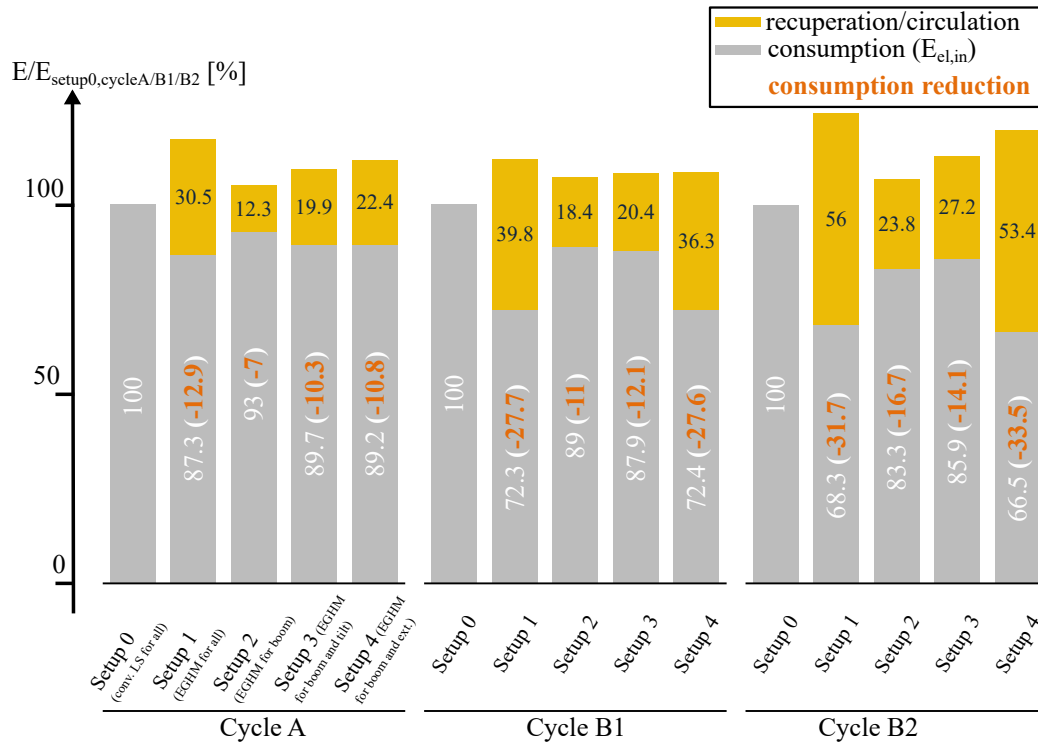


Figure 9: Electric energy consumption for each setup and cycle as well as energy that is circulated and recuperated by the novel EGHM units (the reference energy for each cycle is the energy required by the conventional Setup 0)

Figure 9 shows that applying the novel EGHM units to all three actuators can lead to significant reductions of the required energy. For cycle A, 12.9% are rather small, while 27.7% for B1 are remarkable and 31.7% for B2 even higher. The differences are most likely caused by the fact that the cycles B1 and B2 involve higher lifting and thus more potential for load energy recuperation than Cycle A. Because B2 involves lowering of the loaded forks, the potential of this cycle and thus the energy reduction is the highest. The influence of simultaneous operation, which was discussed in Section 2.1.2, can hardly be judged here since all cycles contain similar amounts of serial or simultaneous operation of the different actuators.

Furthermore, by comparing the energy bars of the different setups within one duty cycle, more statements can be made. Utilizing the novel EGHM units for all actuators (Setup 1) seems to yield the highest improvements, except for Cycle B2 which favors Setup 4. For this cycle, controlling the tilt cylinder with conventional valves is actually more efficient than using the EGHM unit. The reason might be the increased pump pressure caused by

the EGHM pressure controller which is further discussed at the end of this section. Furthermore, the tilt is only moving a little in the cycles B 1 and B 2; thus, there is not much potential for load energy recuperation, which is different for Cycle A. For this cycle, the improvement due to the novel boom actuator is most significant (see Setup 2) but a novel extension actuator (difference between Setup 4 and Setup 2) as well as a novel tilt actuator (difference between Setup 3 and Setup 2) contribute a decrease of energy of around 3% as well. For cycles B 1 and B 2, on the other hand, the contributions of a novel boom actuator and a novel extension actuator are almost the same and both between 11-16.8%. Thus, it seems reasonable to apply the novel EGHM units in any case for the boom cylinders and also for the extension cylinder if B 1/B 2-like duty cycles are common. However, the tilt actuator should remain valve-controlled. This reduces component costs but still yields a significantly improved energy efficiency.

Moreover it can be noticed, that the stacks of the grey and yellow bars in Figure 9 are higher for the Setups 1-4 than for Setup 0. The stack of the grey $E_{el,in}$ bar and the yellow recuperation/circulation bar corresponds to the energy which is transmitted by the EM of the pump during the cycle. It is increased by the novel EGHM units because their pressure controllers (depicted in Figure 5) include a pressure falling rate limiter, which increases the average pressure and thus power as well as energy of the pump. Since the increased pressure leads to more circulation losses for the EGHM units and more throttling losses for conventional valves in the system, this effect is assumed to have a significant impact on the overall efficiency of the novel systems. If the pressure controllers for the EGHM units could be improved and lead to lower pump pressures, this would earn the novel concept a further advantage towards conventional systems.

5 Conclusion and Outlook

This paper proposed a novel more efficient concept for the control of actuators in LS systems by means of units that combine an electric generator with a hydraulic motor. An analyses of the throttling losses of conventional control valves could show how the novel concept can avoid these and under which conditions. Using this knowledge, it can be estimated how significant the potential of efficiency improvement for a certain actuator on an HDMM is. Furthermore, simulations of three different characteristic implement work cycles of a telehandler could quantify the amount of energy that can be saved with the novel concept compared to conventional purely valve-controlled concepts.

The highest reduction of 34% could be achieved with a combination of valve-controlled tilt actuator and EGHM units for boom and extension. This shows how a significant efficiency improvement can be achieved by applying electro-hydraulic elements to single actuators with high energy turnover while the system remains compatible for conventional valve-controlled actuators.

In next steps, the concept could be applied to other common HDMMs and simulated as well in order to see if the results differ from the observations of the telehandler study in this paper. Moreover, the pressure control for the EGHM unit could be further improved and impacts on the efficiency as well as machine dynamic and control stability could be analysed. A step further, experiments with real HDMMs could validate the simulation results and confirm the relevance of the novel concept. Simultaneously, the additional component costs of a system with EGHMs compared to a conventional LS system could be estimated as well as the approximate amortisation time.

This project has received funding from the European Union's Horizon 2020 research and innovation programme under the Marie Skłodowska-Curie grant agreement No 858101



References

- [1] European Commission. Communication from the Commission to the European Parliament, the European Council, the Council, the European Economic and Social Committee and the Committee of the Regions - The European Green Deal, December 2019.
- [2] Bellona Foundation. Zero Emission Construction Sites: The Possibilities and Barriers of Electric Construction Machinery. Technical report, June 2018.
- [3] Jürgen Weber. Independent metering systems. *International Journal of Hydromechanics*, 1(1):91–106, 2018.
- [4] Peter A J Achten, Zhao Fu, Georges E M Vael, and Innas Bv. Transforming future hydraulics: a new design of a hydraulic transformer. In *5th Scandinavian International Conference on Fluid Power*, Linköping, Sweden, 1997.

- [5] Matti Linjama. Digital Fluid Power - State of the Art. In *12th Scandinavian International Conference on Fluid Power*, Tampere, Finland, May 2011.
- [6] Norrhydro Oy. NorrDigiTM System digital hydraulics solution and engineering services. www.norrhydro.com, accessed 22.04.2020.
- [7] Søren Ketelsen, Damiano Padovani, Torben Andersen, Morten Ebbesen, and Lasse Schmidt. Classification and Review of Pump-Controlled Differential Cylinder Drives. *Energies*, 12(7), April 2019.
- [8] Yasutaka Tsuruga, Kiwamu Takahashi, Tatsuo Takishita, and Hajime Kurikuma. Electric drive unit for construction machine, May 2016. patent number US9347203B2.
- [9] Darko Lovrec, Mitja Kastrevc, and Samo Ulaga. Electro-hydraulic load sensing with a speed-controlled hydraulic supply system on forming-machines. *International Journal of Advanced Manufacturing Technology*, 41(11/12):1066–1075, August 2009. Publisher: Springer Nature.
- [10] Ulrich Lenzgeiger, Peter Schmuttermair, and Uwe Maier. Electronic Load-Sensing for Tractors. In *11th International Fluid Power Conference*, Aachen, Germany, 2018.
- [11] Liebherr-Components AG. Liebherr Hydraulic Cylinders 380 bar Series-Production Range: Product brochure. <https://www.liebherr.com/shared/media/components/documents/hydraulics/hydraulic-cylinders/liebherr-hydraulic-cylinders-380-bar-series-production-range-product-brochure-en-web.pdf>, accessed 20.01.2021.
- [12] Shaoyang Qu, David Fassbender, Andrea Vacca, Busquets Enrique, and Uwe Neumann. A closed circuit electro-hydraulic actuator with energy recuperation capability. In *12th International Fluid Power Conference*, Dresden, Germany, October 2020.
- [13] Shaoyang Qu, Andrea Vacca, David Fassbender, and Enrique Busquets. Formulation, Design and Experimental Verification of an Open Circuit Electro-Hydraulic Actuator. In *2020 IEEE Global Fluid Power Society PhD Symposium (GFPS)*, October 2020.
- [14] Martin Frank. *A Step Towards the Design of Collaborative Autonomous Machines A Study on Construction and Mining Equipment*. PhD Thesis, Blekinge Institute of Technology, Sweden, 2019. ISBN: 978-91-7295-393-2.
- [15] Lasse Schmidt, Søren Ketelsen, Morten Helms Brask, and Kasper Aastrup Mortensen. A Class of Energy Efficient Self-Contained Electro-Hydraulic Drives with Self-Locking Capability. *Energies*, 12(10), May 2019.
- [16] Seung Ho Cho and Siegfried Helduser. Robust motion control of a clamp-cylinder for energy-saving injection moulding machines. *Journal of Mechanical Science and Technology*, 22(12):2445–2453, December 2008.
- [17] Søren Ketelsen, Giacomo Kolks, Torben Ole Andersen, Lasse Schmidt, and Jürgen Weber. Bootstrap reservoir concepts for electro-hydraulic compact cylinder drives. In *12th International Fluid Power Conference*, volume 3, pages 201–215, Dresden, Germany, October 2020.
- [18] Shaoyang Qu, David Fassbender, Andrea Vacca, and Enrique Busquets. A High-Efficient Solution for Electro-Hydraulic Actuators with Energy Regeneration Capability. *Energy*, November 2020.
- [19] Kim Heybroek. *On Energy Efficient Mobile Hydraulic Systems: with Focus on Linear Actuation*. Ph.D., Linköping University, Linköping, Sweden, October 2017. ISBN: 9789176855119.
- [20] Bosch Rexroth AG. Axial piston fixed motor A2FM/A2FE Series 70 (Data Sheet RE 91071), 2020.
- [21] Bosch Rexroth AG. Axial piston units A10FZO, A10VZO and A10FZG, A10VZG Series 10 for variable-speed drives (data sheet RE 91485), October 2016.
- [22] Bosch Rexroth AG. Load-sensing directional valves in sandwich plate design SB24-EHS, SB34-EHS (data sheet RE 66171), February 2020.

[23] Tatiana Minav. *Electric-drive-based control and electric energy regeneration in a hydraulic system*. PhD Thesis, Lappeenranta University of Technology, Lappeenranta, Finland, August 2011. Accepted: 2011-08-08T06:35:36Z.

Acronyms

EGHM	electric-generator-hydraulic-motor
EHA	electro-hydraulic actuator
EM	electric machine
HDMM	heavy-duty mobile machine
LS	load sensing

Nomenclature

Designation	Denotation	Unit
E	energy	Ws
F	force	N
n	rotational speed	rpm
N	number of actuators in system	-
p	pressure	bar
P	power	W
Q	flow	m ³ /s
s	cylinder displacement	m
T	torque	Nm
v	linear speed	m/s
V	displacement of hydraulic machine	ccm
y	control ratio	-
Φ	cylinder area ratio	-
η	efficiency ratio	-

Index	Denotation
A	at piston side of cylinder
act	for an actuator
B	at rod side of cylinder
boom	for boom actuator
ctr	for control
des	desired value
EGMH	for EGHM unit
el	electric
EM	for electric machine
est	estimated value
ext	for extension
exte	for extension actuator
i	for counting of actuators
inv	for electric inverter
L	related to load
line	for hydraulic line
max	maximum value
min	minimum value
mot	for hydraulic motor
pmp	for hydraulic pump
req	required value
ret	at return line
rtr	for retraction
sat	saturated value
spl	at supply line
stb	standby
tilt	for tilt actuator
vlv	valve specific
vol	volumetric

Load weight estimation on an excavator in static and dynamic motions

Mehmet Ferlibas and Reza Ghabcheloo

Faculty of Engineering and Natural Sciences (ENS), Tampere University, Tampere, Finland
E-mail: mehmet.ferlibas@gmail.com, reza.ghabcheloo@tuni.fi

Abstract

Excavators are one of the commonly used types of hydraulic machines in earth moving operations. The material handled is often transferred by dump trucks having a payload capacity that should not be exceeded. Payload monitoring systems are needed in order to prevent the possible problems during the delivery, increase the work efficiency, reduce the cost, and obtain the product information automatically without the requirement of truck scales. In this study, we propose a novel approach to estimate the load weight in the bucket of the excavator when the machine links are in motion. We consider the excavator as a three-revolute joint manipulator in vertical plane with the boom, the stick, and the bucket links. We rewrite the dynamic torque equations in a decoupled form as the linear combination of dynamic parameters and functions of joint angles, velocities, and accelerations. We perform least squares estimation to identify these parameters allowing us to predict the no load joint torques for any configuration of the links. We show that the most accurate torque prediction is the difference between the boom torque and the stick torque. We then derive the relation between the joint torques with and without the load, which are functions of the dynamic parameters. Using these equations, we can estimate the load weight. The relation becomes simpler when the links are stationary, since only the gravitational parameters remain present in the torque equations. The relation in dynamic case requires the parameters of the polar coordinates for the center of gravity of the bucket and we show that these parameters can be estimated with the knowledge of the empty bucket mass. We summarize our findings on load weight estimation for different cases including stationary poses and dynamic trajectories on free space and discuss the results. Although the friction is neglected throughout the modeling, the results obtained indicate that the effect of the static friction plays an important role in the accuracy of the estimated payload mass. We show that our dynamic model based solution is very promising, and exhibit only 2% error for high enough velocities.

Keywords: Load weight estimation, payload estimation, dynamic parameter estimation, hydraulic machine, excavator

1 Introduction

Excavators play a significant role in variety of work sectors such as construction industry, mining, forestry activities and agriculture. The weight of the payload on the dump trucks has to be measured since each truck has a payload capacity that should not be exceeded for safety reasons. However, the use of truck scales increase the cost, and they are not always available in every kind of work sites. Therefore, there is a need for payload monitoring systems for excavators, in order to increase the work efficiency, lower the operational cost, and eliminate the need for truck scales and automatically calculate the amount of work done. [1].

Different research works have been done in order to develop such payload monitoring systems for different hydraulically operating machines. There are existing methods proposed for wheel-loaders that use a neural network approach [2] or generate the dynamic model of the wheel loader [3]. Also, there are algorithms developed for mini excavators [4] and excavators [1, 5–8].

A research on available payload estimation systems for excavators have been presented in [9] and stated that the load weight is calculated by making a linear interpolation using a map consisting of the data with two different

load weights on a pre-defined range of motion. A method based on the static parameters of the dynamic model of the excavator is developed in [4] for stationary poses. An analytical approach for payload estimation has been presented in [8] for simulation environment and it is validated on a real excavator in [7].

In order to identify the dynamic parameters of the dynamic model of the excavators, the structural similarity of the excavators to the serial link robot manipulators has been benefited. Since the excavator links, the boom, the stick, and the bucket operate with the help of hydraulic actuators, change in the joint angles have been described as functions of the linear displacement in these hydraulic actuators [10].

Problem of parameter estimation on excavators has been studied in different research works. Inertial parameters are identified by making use of the dynamic model of the excavator with the displacement measurements of the hydraulic cylinders and pressure readings in [11]. The link parameter values and friction terms have been estimated in [12]. The dynamic parameters, gravitational parameters and Coulomb & Viscous friction parameters were estimated in [4, 13, 14] as these parameters are necessary to develop weighing algorithms.

In this paper, a load weight estimation method is developed. The problem is divided into two parts as static estimation and dynamic estimation. The static approach that is developed using a mini-excavator in [4] is tested using a larger scale Komatsu 138PC-US8 excavator and the results show that the effect of static friction has a significant effect on the estimated load masses. The dynamic weighing algorithm is developed assuming that the bucket's center of gravity is independent from the variable load weight in the bucket. The method proposed requires the dynamic parameter estimation process so that the no-load torque values could be predicted accurately as these predictions were needed in order to estimate the load mass.

The structure of this paper is as follows. Machine instrumentation is explained in the section 2 and the dynamic model of the excavator is derived in the section 3. The static estimation and dynamic estimation and the results obtained are discussed in the sections 4 and 5, respectively. Finally, the conclusion is given in the section 6.

2 Machine instrumentation

A Komatsu PC138US-8 excavator was used in data collection for this research. The CAD model of the excavator can be seen in the figure 1 below. The excavator is taken into account as a three-revolute joint manipulator in vertical plane with the boom, the stick and the bucket links. There are four IMU sensors installed on the cabin frame, the boom link, the stick link, and the bucket that is the end-effector in order to measure the angular position and angular velocity values of each link. The angular position measurements of each link are recorded with respect to the previous link. In other words, angular position of the bucket is recorded with respect to the stick, angular position of the stick is recorded with respect to the boom, and angular position of the boom is recorded with respect to the cabin frame. Furthermore, there are two pressure sensors located in each hydraulic cylinder. Therefore, there are six pressure sensors used in total, to measure the pressures inside the chambers and to calculate the actuator forces. All the sensors used operate at frequency of 200 Hz.

The boom, stick and bucket angular positions are shown in the figure 1 as θ_2 , θ_3 , and θ_4 , respectively. The constant angles β_1 and β_2 are used to calculate the joint variable q_2 and the constant angles β_3 and β_4 are used to obtain the joint variable q_3 . The constant lengths L_{11} and L_{12} from boom joint to the both ends of the hydraulic actuator are used together with the joint variable q_2 in order to obtain the actuator length z_2 . Similarly, the constant lengths L_{21} and L_{22} are used together with the joint variable q_3 to calculate the actuator length z_3 . The actuator lengths are used in calculation of cylinder Jacobians that is needed for calculating the torques exerted in each link. Since the IMU sensor on the bucket was located on the dog bone, obtaining the joint variable q_4 from the joint angle θ_4 is more difficult. The dimensions of the four-bar linkage were needed in order to convert the joint angle θ_4 to the joint variable q_4 . Note that the index 1 is reserved for the cabin frame which is kept outside the scope of this study.

Torque calculation from the pressure readings and cylinder jacobians that are obtained using the angular position measurements has been discussed in [1].

The simplest schematic diagram of the excavator is illustrated in the figure 2. The boom torque, the stick torque, and the bucket torque are represented as τ_2 , τ_3 , and τ_4 , respectively. The parameters α_i and r_i are the polar coordinates of the center of gravity (cg_i) of link i . The angular position of the links are θ_2 for the boom, $\theta_{23} = \theta_2 + \theta_3$ for the stick, and $\theta_{234} = \theta_2 + \theta_3 + \theta_4 + c$ for the bucket with respect to the horizontal plane, where c is a constant angle, that is shown in the figure 1, used in order to map the bucket angular position measurement to the bucket tip. Derivation of the constant angle c is discussed in [1].

3 Dynamic model of the excavator

Excavators are hydraulically actuating manipulators. Excluding the cabin frame from our research, and assuming that the tiltrotator is only a series of offsets and nonfunctional, the excavator can be considered as a planar three-

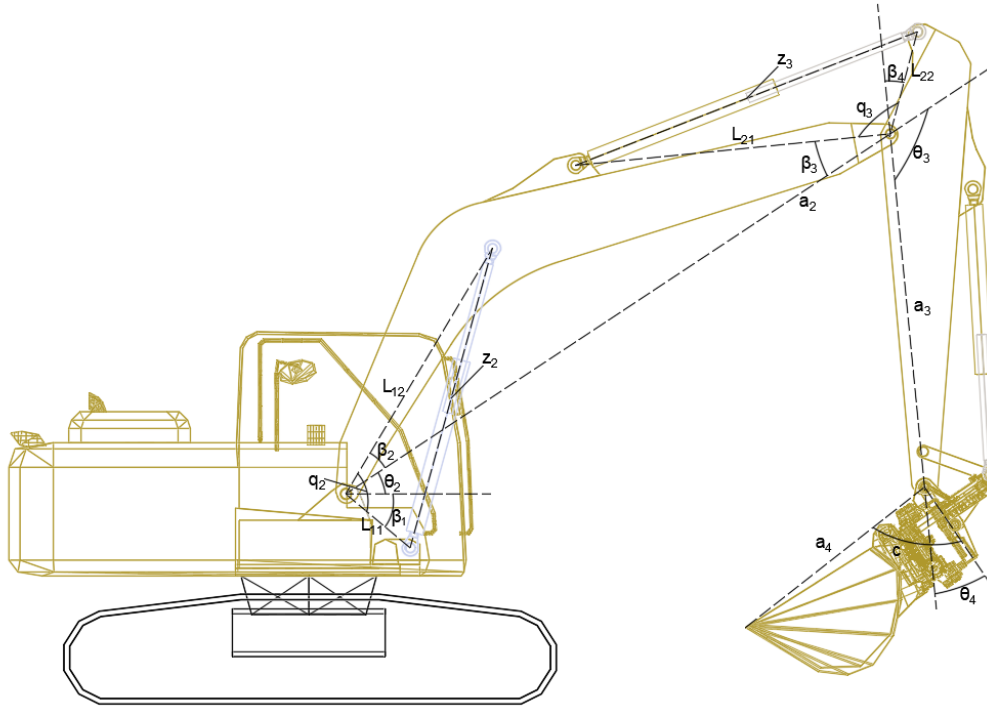


Figure 1: Excavator CAD Model [1]

revolute joint manipulator [13].

The following equation (1) describes the dynamic model of a robot manipulator [6, 15–17]:

$$\tau = D(\Theta)\ddot{\Theta} + C(\Theta, \dot{\Theta})\dot{\Theta} + G(\Theta) \quad (1)$$

Where,

- τ is the joint torque vector,
- Θ is the vector of joint angles,
- $D(\Theta)$ is the inertia matrix,
- $C(\Theta, \dot{\Theta})\dot{\Theta}$ is the vector of Coriolis and centrifugal terms,
- $G(\Theta)$ is the gravity torque vector.

As pointed out in [17], the torque equation (1) can be written as the linear combination of dynamic parameters that are assumed to be constant, π , and a matrix of functions of joint positions, velocities and accelerations $Y(\Theta, \dot{\Theta}, \ddot{\Theta})$:

$$\tau = Y(\Theta, \dot{\Theta}, \ddot{\Theta})\pi \quad (2)$$

Neglecting the friction, we can assume that the system is conservative, i.e. the summation of kinetic energy and potential energy is constant, and keeping the cabin frame stationary, the torque equations (3) were obtained using Euler-Lagrange method [13, 14]:

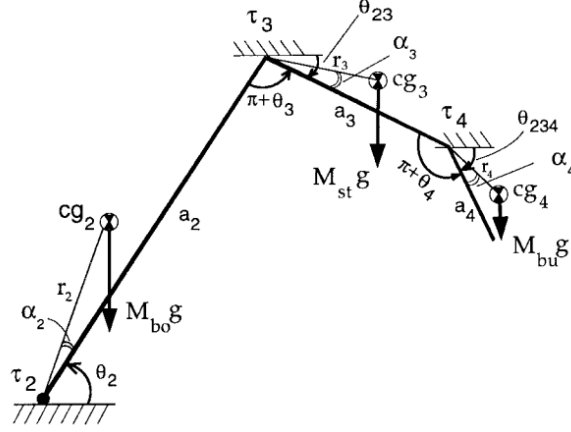


Figure 2: Excavator schematic diagram [13]

$$\begin{aligned}
\tau_4 &= (I_{bu} + M_{bu}r_4^2)\ddot{\theta}_{234} + M_{bu}a_2r_4[\ddot{\theta}_2\cos(\theta_{34} + \alpha_4) + \dot{\theta}_2^2\sin(\theta_{34} + \alpha_4)] \\
&\quad + M_{bu}a_3r_4[\ddot{\theta}_{23}\cos(\theta_4 + \alpha_4) + \dot{\theta}_{23}^2\sin(\theta_4 + \alpha_4)] + M_{bu}gr_4\cos(\theta_{234} + \alpha_4) \\
\tau_3 &= \tau_4 + (I_{st} + M_{st}r_3^2 + M_{bu}a_2^2)\ddot{\theta}_{23} + M_{bu}a_2a_3(\ddot{\theta}_2\cos(\theta_3) + \dot{\theta}_2^2\sin(\theta_3)) \\
&\quad + M_{bu}a_3r_4[\ddot{\theta}_{234}(\theta_4 + \alpha_4) - \dot{\theta}_{234}^2\sin(\theta_4 + \alpha_4)] \\
&\quad + M_{st}a_2r_3[\ddot{\theta}_2\cos(\theta_3 + \alpha_3) + \dot{\theta}_2^2\sin(\theta_3 + \alpha_3)] \\
&\quad + M_{bu}ga_3\cos(\theta_{23}) + M_{st}gr_3\cos(\theta_{23} + \alpha_3) \\
\tau_2 &= \tau_3 + [I_{bo} + M_{bo}r_2^2 + (M_{st} + M_{bu})a_2^2]\ddot{\theta}_2 \\
&\quad + M_{st}a_2r_3[\ddot{\theta}_{23}\cos(\theta_3 + \alpha_3) - \dot{\theta}_{23}^2\sin(\theta_3 + \alpha_3)] \\
&\quad + M_{bu}a_2a_3(\ddot{\theta}_{23}\cos(\theta_3) - \dot{\theta}_{23}^2\sin(\theta_3)) \\
&\quad + M_{bu}a_2r_4[\ddot{\theta}_{234}\cos(\theta_{34} + \alpha_4) - \dot{\theta}_{234}^2\sin(\theta_{34} + \alpha_4)] \\
&\quad + (M_{bu} + M_{st})ga_2\cos(\theta_2) + M_{bo}gr_2\cos(\theta_2 + \alpha_2)
\end{aligned} \tag{3}$$

Where I_{bo} , I_{st} , and I_{bu} are the moments of inertia of the boom link, the stick link, and the bucket link, respectively and the parameters M_{bo} , M_{st} , and M_{bu} represent the masses of the boom link, the stick link and the bucket link, respectively. The parameter a_2 is the linear distance between the boom joint and the stick joint. Similarly, the parameter a_3 is the linear displacement between the stick joint and the bucket link, and the parameter a_4 is the distance from the bucket link to the bucket tip.

4 Static estimation of the load weight

The torque equations given in the equation (3) are reduced to the following equation (4) when the machine links are stationary, i.e. all the velocity and acceleration terms are set to zero:

$$\begin{aligned}
\tau_4 &= M_{bu}gr_4\cos(\theta_{234} + \alpha_4) \\
\tau_3 &= \tau_4 + M_{bu}ga_3\cos(\theta_{23}) + M_{st}gr_3\cos(\theta_{23} + \alpha_3) \\
\tau_2 &= \tau_3 + (M_{bu} + M_{st})ga_2\cos(\theta_2) + M_{bo}gr_2\cos(\theta_2 + \alpha_2)
\end{aligned} \tag{4}$$

We rewrite the static torque equation (4) above in the decoupled form, that is the torque difference of the two consecutive joints and benefit from the well-known trigonometric identity, $\cos(\alpha + \beta) = \cos(\alpha)\cos(\beta) - \sin(\alpha)\sin(\beta)$, and obtain the following equation (5):

$$\begin{aligned}
\tau_4 &= M_{bu}gr_4[\cos(\theta_{234})\cos(\alpha_4) - \sin(\theta_{234})\sin(\alpha_4)] \\
\tau_{34} &= \tau_3 - \tau_4 = M_{bu}ga_3\cos(\theta_{23}) + M_{st}gr_3[\cos(\theta_{23})\cos(\alpha_3) - \sin(\theta_{23})\sin(\alpha_3)] \\
\tau_{23} &= \tau_2 - \tau_3 = (M_{bu} + M_{st})ga_2\cos(\theta_2) + M_{bo}gr_2[\cos(\theta_2)\cos(\alpha_2) - \sin(\theta_2)\sin(\alpha_2)]
\end{aligned} \tag{5}$$

The equation (5) can be converted into matrix form as stated in the equation (2):

$$\begin{bmatrix} \tau_4 \\ \tau_{34} \\ \tau_{23} \end{bmatrix} = g \begin{bmatrix} \cos(\theta_{234}) & -\sin(\theta_{234}) & 0 & 0 & 0 & 0 \\ 0 & 0 & \cos(\theta_{23}) & -\sin(\theta_{23}) & 0 & 0 \\ 0 & 0 & 0 & 0 & \cos(\theta_2) & -\sin(\theta_2) \end{bmatrix} \begin{bmatrix} \pi_{s1} \\ \pi_{s2} \\ \pi_{s3} \\ \pi_{s4} \\ \pi_{s5} \\ \pi_{s6} \end{bmatrix} \quad (6)$$

Where the vector $[\pi_{s1} \ \pi_{s2} \ \pi_{s3} \ \pi_{s4} \ \pi_{s5} \ \pi_{s6}]^T$ is named as the vector of gravitational parameters, π_s :

$$\pi_s = \begin{bmatrix} \pi_{s1} \\ \pi_{s2} \\ \pi_{s3} \\ \pi_{s4} \\ \pi_{s5} \\ \pi_{s6} \end{bmatrix} = \begin{bmatrix} M_{bu}r_4\cos(\alpha_4) \\ M_{bu}r_4\sin(\alpha_4) \\ M_{bu}a_3 + M_{st}r_3\cos(\alpha_3) \\ M_{st}r_3\sin(\alpha_3) \\ (M_{bu} + M_{st})a_2 + M_{bo}r_2\cos(\alpha_2) \\ M_{bo}r_2\sin(\alpha_2) \end{bmatrix} \quad (7)$$

Note that the equation (6) is linear in the gravitational parameters. Once the torque vector $[\tau_4, \tau_{34}, \tau_{23}]^T$ is obtained, the vector of gravitational parameters, π_s , can be found using Least Squares Estimation (LSE) as explained in the section 4.1.

The pressure readings have been used to calculate the force (F) exerted on each hydraulic actuator using the relation $F = P_1A_1 - P_2A_2$, where P_1 and P_2 are the pressures in chamber A and chamber B of the hydraulic cylinders and A_1 and A_2 are the cross-sectional areas of chamber A and chamber B, respectively.

The torque values for each joint has been calculated with the multiplication of the forces and cylinder jacobians. Figure 3 visualizes the constant β_1 and β_2 angles that are used to calculate the boom joint variable, q_2 , together with the measured boom angle, θ_2 , the constant lengths from boom joint to the both ends of the hydraulic cylinder are represented as L_{11} and L_{12} that are used to calculate the length of the actuator, z_2 . The equation (8) shows the calculation of the boom cylinder jacobian, J_{bo} . Similarly, how the stick cylinder jacobian and the bucket cylinder jacobian are derived can be seen in [1].

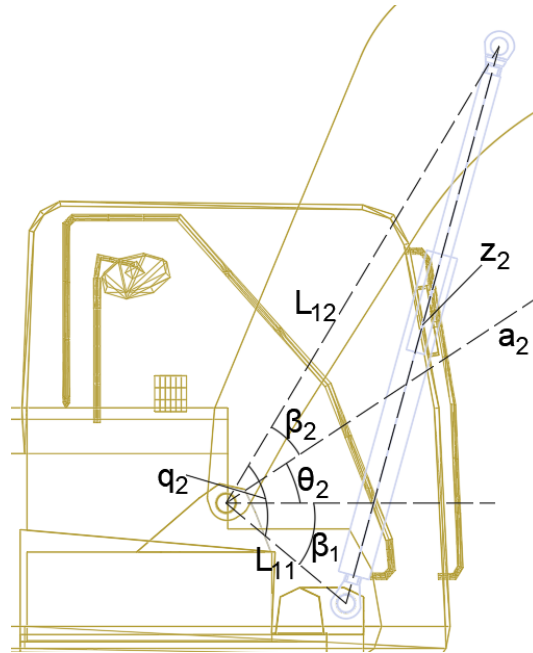


Figure 3: Boom joint angle and joint variable [1]

$$\begin{aligned}
q_2 &= \beta_1 + \beta_2 + \theta_2 \\
z_2 &= \sqrt{L_{11}^2 + L_{12}^2 - 2L_{11}L_{12}\cos(q_2)} \\
J_{bo} &= \frac{dz_2}{d\theta_2} = \frac{L_{11}L_{12}\sin(q_2)}{z_2}
\end{aligned} \tag{8}$$

After obtaining the torque values, the gravitational parameters can be found using the following equation (9):

$$\pi = (Y(\Theta)^T Y(\Theta))^{-1} Y(\Theta)^T \tau \tag{9}$$

Where $Y(\Theta)$ is the regressor matrix, and defined as follows:

$$Y(\Theta) = g \begin{bmatrix} \cos(\theta_{234}) & -\sin(\theta_{234}) & 0 & 0 & 0 & 0 \\ 0 & 0 & \cos(\theta_{23}) & -\sin(\theta_{23}) & 0 & 0 \\ 0 & 0 & 0 & 0 & \cos(\theta_2) & -\sin(\theta_2) \end{bmatrix} \tag{10}$$

4.1 Static parameter estimation

The estimation of the gravitational parameters that are given in the equation (7) allows us to predict the torque values in decoupled form, when the bucket of the excavator is empty.

In order to obtain the gravitational parameters, a training data set consisting of 38 different static postures of the machine links has been collected. In the data set, angular positions of the boom link, the stick link and the bucket link has been recorded together with the pressure readings of the hydraulic cylinders.

After gathering the data and making use of the equation (10), the gravitational parameters are estimated as given in the table 1.

Table 1: Estimated gravitational parameters

Parameter	Estimated Value (kgm)
π_{s1}	189.85
π_{s2}	318.80
π_{s3}	2753.27
π_{s4}	132.33
π_{s5}	8297.89
π_{s6}	1156.44

As can be seen from the table 1, all of the parameters are found to be positive, as expected.

The estimated gravitational parameters have been tested on a test data set consisting of 19 different static postures that are different than the ones in the training data set. The mean absolute percentage value of the error (MAPE) in the predicted torque values are reported in the table 2 below:

Table 2: Accuracy of predicted no-load torque values

Predicted Torque	MAPE
τ_4	40.98%
τ_{34}	10.25%
τ_{23}	8.31%

From the results presented in the table 2, we conclude that the most accurate torque prediction is τ_{23} , that is the difference between the boom torque and the stick torque. The highest error has been obtained for the bucket torque, τ_4 , and the possible reasons of the error are listed below:

- The effect of static friction is more dominant compared to other torque values,
- The test data of the bucket angular measurements exceeds the range of the ones in the training data.

4.2 Load weight estimation using the gravitational parameters

For an arbitrary mass in the bucket of the excavator, \hat{M} , the static torque equations given in the equation (5) can be rewritten by replacing M_{bu} with $M_{bu} + \hat{M}$ and the following equations (11) can be obtained:

$$\begin{aligned}\tau_4 &= (M_{bu} + \hat{M})gr_4\cos(\theta_{234} + \alpha_4) \\ \tau_{34} &= (M_{bu} + \hat{M})ga_3\cos(\theta_{23}) + M_{st}gr_3\cos(\theta_{23} + \alpha_3) \\ \tau_{23} &= (M_{bu} + \hat{M} + M_{st})ga_2\cos(\theta_2) + M_{bo}r_2\cos(\theta_2 + \alpha_2)\end{aligned}\quad (11)$$

These torque equations given in the equation 11 are valid for any value of the load in the bucket and can be written as the summation of the no load torque and the torque due to the load in the bucket as stated in the following equation (12) [4]:

$$\begin{aligned}\tau_{4L} &= \tau_{4NL} + \hat{M}gr_4\cos(\theta_{234} + \alpha_4) \\ \tau_{34L} &= \tau_{34NL} + \hat{M}ga_3\cos(\theta_{23}) \\ \tau_{23L} &= \tau_{23NL} + \hat{M}ga_2\cos(\theta_2)\end{aligned}\quad (12)$$

In the equation (12) above, the subscript NL represents the no load torque value and the subscript L denotes the torque with the load. We can predict the no load torque values by making use of the estimated gravitational parameters. In the light of the results presented in the table 2, the most suitable torque equation is the difference between the boom torque and the stick torque, τ_{23} . We can predict the value of τ_{23} by making use of the last two elements of the gravitational parameter vector, $\pi_{5,5}$, and $\pi_{5,6}$ and solve the equation 12 for \hat{M} as in the equation (13) below [4]:

$$\hat{M} = \frac{\tau_{23L} - \tau_{23NL}}{ga_2\cos(\theta_2)}\quad (13)$$

In order to validate the usability of this approach presented above, we collected data sets with two different reference load masses that are 250 kg and 500 kg. The collected data sets have 37 different static postures for 250 kg and 42 different static postures for 500 kg. The results of the estimated load weight are presented in the table 3 below:

Table 3: The results of static load weight estimation using the estimated gravitational parameters

Load Weight	MAPE	Standard Deviation
250 kg	13.98%	13.56%
500 kg	9.42%	6.78%

The possible sources of the error are listed below:

- The static friction is kept outside of this study and the static friction might be different even for the same static posture with different load weights in the bucket.
- The accuracy of the predicted no load torque is directly related to the gravitational parameters. Increasing the number of static postures in the training data set and covering more parts of the excavator's working space would result in better no load torque estimations; therefore, the error in the load weight estimation would be lowered.
- The used reference loads are concrete blocks. Thus, the load is not uniformly distributed in the bucket. The position of these concrete blocks in the bucket might have an affect on the pressure readings and the measured torque value, τ_{23L} in the equation (13) might change.

5 Dynamic estimation of the load weight

The dynamic torque equations given in the equation (3) can also be written in the decoupled form and using the well-known trigonometric identities $\cos(\alpha + \beta) = \cos(\alpha)\cos(\beta) - \sin(\alpha)\sin(\beta)$ and $\sin(\alpha + \beta) = \sin(\alpha)\cos(\beta) +$

$\cos(\alpha)\sin(\beta)$, we can write the dynamic torque equations in matrix form as done in the equation (14). Note that the equation is in the form of $\tau = Y(\Theta, \dot{\Theta}, \ddot{\Theta})\pi$ as mentioned in the equation (1).

$$\Delta\tau = \begin{bmatrix} \tau_4 \\ \tau_{34} \\ \tau_{23} \end{bmatrix}_{3 \times 1} = \begin{bmatrix} y_{11} & 0 & 0 & y_{14} & y_{15} & 0 & 0 & 0 & 0 \\ 0 & y_{22} & 0 & y_{24} & y_{25} & y_{26} & y_{27} & 0 & 0 \\ 0 & 0 & y_{33} & y_{34} & y_{35} & y_{36} & y_{37} & y_{38} & y_{39} \end{bmatrix}_{3 \times 9} \begin{bmatrix} \pi_{d1} \\ \pi_{d2} \\ \pi_{d3} \\ \pi_{s1} \\ \pi_{s2} \\ \pi_{s3} \\ \pi_{s6} \\ \pi_{s5} \\ \pi_{s6} \end{bmatrix}_{9 \times 1} \quad (14)$$

Where the subscripts s and d stand for static and dynamic parameters, respectively, and

$$\begin{aligned} y_{11} &= \ddot{\theta}_{234} \\ y_{14} &= a_2 \ddot{\theta}_2 \cos(\theta_{34}) + a_2 \dot{\theta}_2^2 \sin(\theta_{34}) + a_3 \ddot{\theta}_{23} \cos(\theta_4) + a_3 \dot{\theta}_{23}^2 \sin(\theta_4) + g \cos(\theta_{234}) \\ y_{15} &= -a_2 \ddot{\theta}_2 \sin(\theta_{34}) + a_2 \dot{\theta}_2^2 \cos(\theta_{34}) - a_3 \ddot{\theta}_{23} \sin(\theta_4) + a_3 \dot{\theta}_{23}^2 \cos(\theta_4) - g \sin(\theta_{234}) \\ y_{22} &= \ddot{\theta}_{23} \\ y_{24} &= a_3 \ddot{\theta}_{234} \cos(\theta_4) - a_3 \dot{\theta}_{234}^2 \sin(\theta_4) \\ y_{25} &= -a_3 \dot{\theta}_{234}^2 \sin(\theta_4) - a_3 \ddot{\theta}_{234} \cos(\theta_4) \\ y_{26} &= a_2 \ddot{\theta}_2 \cos(\theta_3) + a_2 \dot{\theta}_2^2 \sin(\theta_3) + g \cos(\theta_{23}) \\ y_{27} &= -a_2 \ddot{\theta}_2 \sin(\theta_3) + a_2 \dot{\theta}_2^2 \cos(\theta_3) - g \sin(\theta_{23}) \\ y_{33} &= \ddot{\theta}_2 \\ y_{34} &= a_2 \ddot{\theta}_{234} \cos(\theta_{34}) - a_2 \dot{\theta}_{234}^2 \sin(\theta_{34}) \\ y_{35} &= -a_2 \dot{\theta}_{234}^2 \sin(\theta_{34}) - a_2 \ddot{\theta}_{234} \cos(\theta_{34}) \\ y_{36} &= a_2 \ddot{\theta}_{23} \cos(\theta_3) - a_2 \dot{\theta}_{23}^2 \sin(\theta_3) \\ y_{37} &= -a_2 \dot{\theta}_{23}^2 \sin(\theta_3) - a_2 \ddot{\theta}_{23} \cos(\theta_3) \\ y_{38} &= g \cos(\theta_2) \\ y_{39} &= -g \sin(\theta_2) \end{aligned} \quad (15)$$

It can be realized from the parameter vector (π) that one dynamic parameter (π_{d_i}) is introduced for each torque equation and the parameter vector is given in the equation (16) below.

$$\pi = \begin{bmatrix} \pi_{d1} \\ \pi_{d2} \\ \pi_{d3} \\ \pi_{s1} \\ \pi_{s2} \\ \pi_{s3} \\ \pi_{s6} \\ \pi_{s5} \\ \pi_{s6} \end{bmatrix} = \begin{bmatrix} I_{bu} + M_{bu} r_4^2 \\ I + M_{st} r_3^2 + M_{bu} a_3^2 \\ I_{bo} + M_{bo} r_2^2 + (M_{st} + M_{bu}) a_2^2 \\ M_{bu} r_4 \cos(\alpha_4) \\ M_{bu} r_4 \sin(\alpha_4) \\ M_{bu} a_3 + M_{st} r_3 \cos(\alpha_3) \\ M_{st} r_3 \sin(\alpha_3) \\ (M_{bu} + M_{st}) a_2 + M_{bo} r_2 \cos(\alpha_2) \\ M_{bo} r_2 \sin(\alpha_2) \end{bmatrix} \quad (16)$$

The torque values have been obtained using the pressure readings and angular position measurements of the machine links as described in the section 4. After constructing the regressor matrix $Y(\Theta, \dot{\Theta}, \ddot{\Theta})$ it is possible to estimate the dynamic parameters using Least Squares Estimation as explained in the section 5.1.

5.1 Dynamic parameter estimation

In order to perform the dynamic parameter estimation using the Least Squares Estimation method, five different data sets with empty bucket over the similar trajectories have been collected. In order to avoid the contact force between the bucket and the ground, the trajectories have been generated on free space.

One of the five data sets have been used for estimating the parameters given in the equation (16), and the other four data sets have been used to compare the predicted torque values that are found using the estimated dynamic parameters with the actual torque values.

In order to construct the regressor matrix $Y(\Theta, \dot{\Theta}, \ddot{\Theta})$, the angular velocity and the angular acceleration values of the boom link, the stick link, and the bucket link are needed as can be seen in the equation (15). Due to the practical limitations, the angular acceleration values could not be recorded; therefore, these values were needed to be estimated. Using a polynomial fitting approach, the angular acceleration values have been estimated. The smoothing splines method have been utilized in MATLAB in order to fit the piece-wise polynomials on the angular position data and the angular velocities and angular accelerations have been found by taking the derivatives of the fitted polynomials. Once the angular velocity estimations matched the angular velocity measurements, the angular acceleration estimations have been assumed to be correct.

The root-mean-squared error (RMSE) values for each link are reported in the table 4 below.

Table 4: Root-mean-squared error values for estimated angular velocities

Estimated Angular Velocity		RMSE (deg/s)
Boom velocity	$\dot{\theta}_2$	0.33
Stick velocity	$\dot{\theta}_{23}$	0.35
Bucket velocity	$\dot{\theta}_{234}$	0.34

After estimating the angular velocity and angular acceleration values for all the links with acceptable error rates, the regressor matrix $Y(\Theta, \dot{\Theta}, \ddot{\Theta})$ has been constructed and the parameter estimation has been performed on the torque difference between the boom joint and the stick joint, τ_{23} that is given in the equation (17) below.

$$\tau_{23} = \begin{bmatrix} \ddot{\theta}_2 \\ a_2 \ddot{\theta}_{234} \cos(\theta_{34}) - a_2 \dot{\theta}_{234}^2 \sin(\theta_{34}) \\ -a_2 \ddot{\theta}_{234} \sin(\theta_{34}) - a_2 \dot{\theta}_{234}^2 \cos(\theta_{34}) \\ a_2 \ddot{\theta}_{23} \cos(\theta_3) - a_2 \dot{\theta}_{23}^2 \sin(\theta_3) \\ -a_2 \ddot{\theta}_{23} \sin(\theta_3) - a_2 \dot{\theta}_{23}^2 \cos(\theta_3) \\ g \cos(\theta_2) \\ -g \sin(\theta_2) \end{bmatrix}^T \begin{bmatrix} I_{bo} + M_{bo} r_2^2 + (M_{st} + M_{bu}) a_2^2 \\ M_{bu} r_4 \cos(\alpha_4) \\ M_{bu} r_4 \sin(\alpha_4) \\ M_{bu} a_3 + M_{st} r_3 \cos(\alpha_3) \\ M_{st} r_3 \sin(\alpha_3) \\ (M_{bu} + M_{st}) a_2 + M_{bo} r_2 \cos(\alpha_2) \\ M_{bo} r_2 \sin(\alpha_2) \end{bmatrix} \quad (17)$$

Parameter estimation has been performed over 10 seconds of a time interval on one of the five dynamic trajectories. In other words, 2000 data samples have been used. The values of the parameters given in the equation (17) have been found using the formula given in the equation (18), and listed in the table 5 below.

$$\pi = (Y(\Theta, \dot{\Theta}, \ddot{\Theta})^T Y(\Theta, \dot{\Theta}, \ddot{\Theta}))^{-1} Y(\Theta, \dot{\Theta}, \ddot{\Theta})^T \tau_{23} \quad (18)$$

Table 5: Estimated values of parameters appearing in the dynamic torque difference between the boom and the stick

Parameter	Estimated Value	Unit
π_{d3}	28827.71	kgm^2
π_{s1}	298.04	kgm
π_{s2}	592.86	kgm
π_{s3}	8228.37	kgm
π_{s4}	2571.05	kgm
π_{s5}	8927.32	kgm
π_{s6}	1386.54	kgm

Note that all the parameters given in the table 5 above are positive, as expected. It is possible to predict the torque difference between the boom and the stick, τ_{23} , for any position, velocity and acceleration values of the excavator links. Note also that the estimated gravitational parameters are not the same with the results obtained in the static estimation that is discussed in the section 4.1. Since the static friction is eliminated in the dynamic estimation of the parameters, the results of torque predictions on dynamic trajectories are more consistent. In order to check the

reliability of these parameters, the torque values of the remaining four data sets have been predicted and compared with the actual torque values that are calculated based on the pressure readings and angular position measurements. The mean-absolute-percentage-error (MAPE) values of torque predictions for each data set are listed in the table 6.

Table 6: Accuracy of predicted dynamic no-load torque values

Predicted $\tau_{23_{NL}}$	MAPE
Data set #1	4.20%
Data set #2	5.24%
Data set #3	5.67%
Data set #4	3.85%

The predicted torque values have an error around 5%, meaning that the parameters given in the table 5 estimated accurately. Figure 4 illustrates the predicted torque values together with the actual ones.

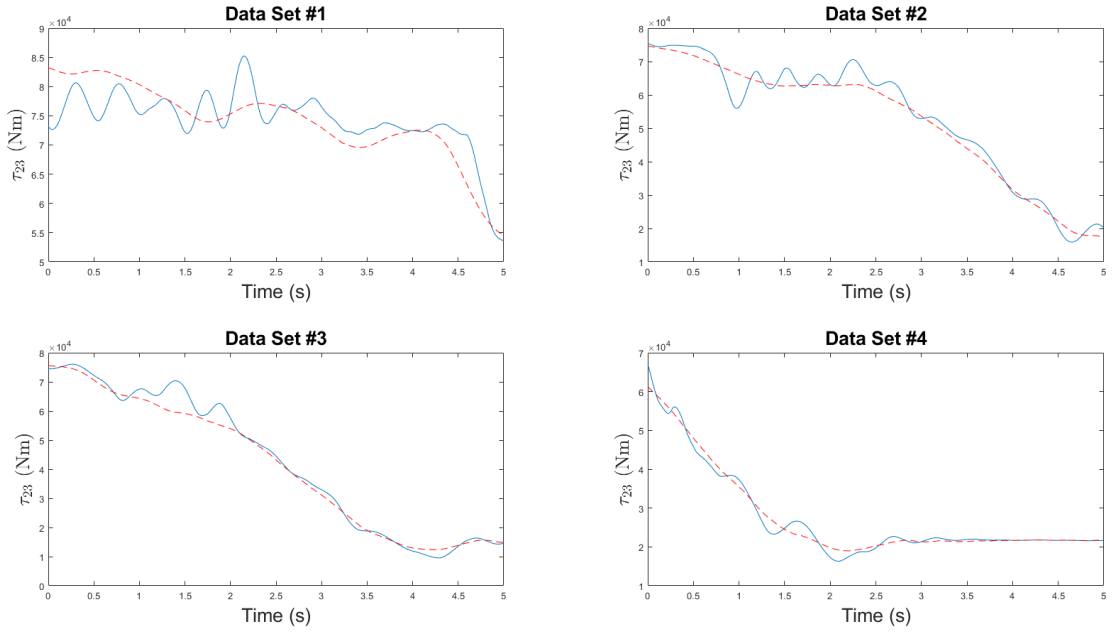


Figure 4: Measured (—) and predicted (---) torque values

5.2 Load weight estimation using the dynamic parameters

Assuming that the bucket center of gravity is fixed and does not change depending on the variable load weight in the bucket, the dynamic torque equation representing the difference between the boom torque and the stick torque, τ_{23} , can be obtained by replacing M_{bu} with $M_{bu} + \hat{M}$ where \hat{M} is the arbitrary load mass in the bucket as given in the equation 19

$$\begin{aligned}
\tau_{2L} - \tau_{3L} = \tau_{23L} = & [I_{bo} + M_{bo}r_2^2 + (M_{st} + (M_{bu} + \hat{M})a_2^2)]\ddot{\theta}_2 \\
& + M_{st}a_2r_3[\ddot{\theta}_{23}\cos(\theta_3 + \alpha_3) - \dot{\theta}_{23}^2\sin(\theta_3 + \alpha_3)] \\
& + (M_{bu} + \hat{M})a_2a_3(\ddot{\theta}_{23}\cos(\theta_3) - \dot{\theta}_{23}^2\sin(\theta_3)) \\
& + (M_{bu} + \hat{M})a_2r_4[\ddot{\theta}_{234}\cos(\theta_{34} + \alpha_4) - \dot{\theta}_{234}^2\sin(\theta_{34} + \alpha_4)] \\
& + (M_{bu} + \hat{M} + M_{st})ga_2\cos(\theta_2) + M_{bo}gr_2\cos(\theta_2 + \alpha_2)
\end{aligned} \tag{19}$$

The equation (19) above can be rearranged as the summation of the no load torque and the torque due to the load weight in the bucket. The resulting torque equation is given in the equation (20) below.

$$\begin{aligned}\tau_{23L} = & \tau_{23NL} + \hat{M}a_2^2\ddot{\theta}_2 + \hat{M}a_2a_3(\ddot{\theta}_{23}\cos(\theta_3) - \dot{\theta}_{23}^2\sin(\theta_3)) \\ & + \hat{M}r_4a_2\ddot{\theta}_{234}\cos(\theta_{34} + \alpha_4) - \hat{M}r_4a_2\dot{\theta}_{234}^2\sin(\theta_{34} + \alpha_4) + \hat{M}ga_2\cos(\theta_2)\end{aligned}\quad (20)$$

The torque value with the load (τ_{23L}) in the bucket is calculated using the pressure measurements from the cylinders and the angular position measurements of the links, as discussed earlier. Furthermore, the no load torque value (τ_{23NL}) can be predicted for the same angular position, velocity and acceleration values. Then, \hat{M} can be found using the difference between τ_{23L} and τ_{23NL} as stated in the equation (21) below [1].

$$\hat{M} = \frac{\tau_{23L} - \tau_{23NL}}{a_2^2y_{33} + r_4\cos(\alpha_4)y_{34} + r_4\sin(\alpha_4)y_{35} + a_3y_{36} + ga_2\cos(\theta_2)}\quad (21)$$

Where the parameters y_{33} , y_{34} , y_{35} , and y_{36} are given in the equation (15).

It should be noted that the polar coordinates of the bucket center of gravity, r_4 and α_4 that can be seen in the figure 2 are needed in order to estimate the payload mass in the bucket that is given in the equation (21) above. Estimation of these parameters is discussed in the section 5.2.1.

5.2.1 Estimation of the polar coordinates of the bucket center of gravity

In order to estimate the polar coordinates of the bucket center of gravity, one can use the second and the third elements of the dynamic parameter vector that is described in the equation (16), π_{s1} and π_{s2} , together with the mass of the bucket and tiltrotator assembly. Knowing the fact that the bucket-tiltrotator is 750 kg, the parameter α_4 can be found taking the inverse tangent of the division of π_{s2} to π_{s1} gives us the parameter α_4 as shown in the equation (22) below.

$$\alpha_4 = \tan^{-1}\left(\frac{\pi_{s2}}{\pi_{s1}}\right)\quad (22)$$

Once the value of α_4 is obtained, the parameter r_4 can be found using one of the following relations given in the equation (23) below.

$$\begin{aligned}r_4 &= \frac{\pi_{s1}}{M_{bu}\cos(\alpha_4)} \\ r_4 &= \frac{\pi_{s2}}{M_{bu}\sin(\alpha_4)}\end{aligned}\quad (23)$$

Once the values of the parameters α_4 and r_4 have been obtained, it becomes possible to estimate the load weight in the bucket using the equation (21) above.

5.3 Collected data sets and the results

In order to find out the usability of the method developed, five data sets with 318 kg reference load and five data sets with 618 kg reference load have been collected using similar trajectories on free space. The mass estimation formula given in the equation (21) has been used for every sample in the used data sets and an array of mass estimation is created and the mean value is reported as the final result of the estimated load weight.

Three scenarios have been generated and the load weight estimation has been performed in each scenario that are listed below:

- Load weight estimation over five seconds of time intervals where the machine links have velocities higher than 2 deg/s in magnitude.
- Load weight estimation using the dynamic parts of the data sets, i.e. the data samples when the machine links are stationary discarded.
- Load weight estimation using all the samples in the data sets including the stationary parts as well.

The load weight estimation for these three scenarios stated above are presented in the tables 7, 8 and 9, respectively.

Table 7: The results of dynamic load weight estimation over 5 seconds of time intervals

Test Data	Estimated Load Weight	Error (%)
Data set #1, 618 kg	614.22 kg	0.61%
Data set #2, 618 kg	612.39 kg	0.91%
Data set #3, 618 kg	610.89 kg	1.15%
Data set #4, 618 kg	623.53 kg	0.90%
Data set #5, 618 kg	621.33 kg	0.54%
Data set #1, 318 kg	319.24 kg	0.39%
Data set #2, 318 kg	313.99 kg	1.26%
Data set #3, 318 kg	317.19 kg	0.26%
Data set #4, 318 kg	321.68 kg	1.16%
Data set #5, 318 kg	332.69 kg	4.62%

Table 8: The results of dynamic load weight estimation using only the dynamic parts of the data sets

Test Data	Estimated Load Weight	Error (%)
Data set #1, 618 kg	630.77 kg	2.07%
Data set #2, 618 kg	642.37 kg	3.94%
Data set #3, 618 kg	621.90 kg	0.63%
Data set #4, 618 kg	606.41 kg	1.87%
Data set #5, 618 kg	612.75 kg	0.85%
Data set #1, 318 kg	336.17 kg	5.71%
Data set #2, 318 kg	310.63 kg	2.32%
Data set #3, 318 kg	310.84 kg	2.25%
Data set #4, 318 kg	349.36 kg	9.86%
Data set #5, 318 kg	323.26 kg	1.65%

Table 9: The results of dynamic load weight estimation using all the samples in the data sets

Test Data	Estimated Load Weight	Error (%)
Data set #1, 618 kg	618.87 kg	0.14%
Data set #2, 618 kg	510.55 kg	17.39%
Data set #3, 618 kg	603.33 kg	2.37%
Data set #4, 618 kg	567.38 kg	8.19%
Data set #5, 618 kg	541.41 kg	12.39%
Data set #1, 318 kg	279.24 kg	12.19%
Data set #2, 318 kg	298.28 kg	6.20%
Data set #3, 318 kg	290.09 kg	8.78%
Data set #4, 318 kg	340.66 kg	7.13%
Data set #5, 318 kg	301.64 kg	5.15%

As can be seen from the results, the best results are achieved with high velocity values and the worst results are obtained with the inclusion of the stationary parts of the data sets. The possible sources of the errors are listed below:

- The frictional parameters are neglected in dynamic modeling but the effects of the friction was present in the data sets.
- Used reference load weights were concrete blocks; therefore, the center of gravity has changed with different load weights in the bucket but it assumed to be unchanged.
- The accuracy of the dynamic parameters have an effect on the torque predictions and more accurate estimations would yield more accurate torque predictions.
- Angular velocity estimations and angular acceleration estimations were not 100% accurate. Therefore, the predicted torque values have been affected and resulted in an increase for the error of the dynamic load weight estimations.

6 Conclusion

We presented solutions for load weight estimation problem on excavators. We proposed two different methods based on static and dynamic models. The dynamic model of the excavator is developed considering the excavator as a planar robot manipulator with three-revolute joints: the boom, the stick and the bucket. The cabin frame is kept outside the scope of this research and the tiltrotator is assumed to be non-functioning and only a series of offsets. Due to the practical limitations, we were not able to record the angular acceleration measurements and we estimated these values using a polynomial fitting approach. Even though the friction is neglected throughout the study for simplicity, effects of the static friction was present in the data and it was observed in the results of static estimation of the load weight. A dynamic load weight estimation method is proposed assuming that the bucket center of gravity is independent from the load mass in the bucket and the results show that the approach can work accurately with high velocity motion trajectories. The proposed method for dynamic estimation of the load weight can be implemented real-time if the angular acceleration values can be measured together with the angular position and angular velocity values. Accurate results could be obtained real-time when the friction is not dominating. Also, the idea of dynamic parameter estimation and using the torque difference between the case when the end effector carries load and the case when the end effector is unloaded could be extended to other machines such as cranes but needs further investigation. Finally, the possible sources of the error for the estimated load weights have been discussed.

References

- [1] Mehmet Ferlibas. Load weight estimation on excavators. Master's thesis, Tampere University, 10 2020.
- [2] Jahmy J. Hindman. *Dynamic payload estimation in four wheel drive loaders*. PhD thesis, University of Saskatchewan, 2008.
- [3] Frederic Ballaire. *Dynamic, continuous, and center of gravity independent weighing with a loader*. PhD thesis, Technical University of Kaiserslautern, 2015.
- [4] S. Tafazoli, P. D. Lawrence, S. E. Salcudean, D. Chan, S. Bachmann, and C. W. de Silva. Parameter estimation and actuator friction analysis for a mini excavator. In *IEEE Int. Conf. Robot. Automat.*, pages 329–334, Minneapolis, MN, USA, 4 1996.
- [5] Artur Gawlik and Piotr Kucybała. Dynamic weighing system used in excavator. *Journal of KONES*, 24(4):31 – 38, 2017.
- [6] Anton Renner, Hannes Wind, and Oliver Sawodny. Online payload estimation for hydraulically actuated manipulators. *Mechatronics*, 66:102322, 2020.
- [7] Ashwin Walawalkar, S. Heep, Martin Frank, R. Leifeld, and Christian Schindler. Validation of an analytical method for payload estimation in excavators. In *Commercial Vehicle Technology 2018*, 03 2018.
- [8] Ashwin Walawalkar, Steffen Heep, Florian Schneider, Jan Schübler, and Christian Schindler. A method for payload estimation in excavators. *Proceedings of the 4th Commercial Vehicle Symposium*, pages 424–437, 2016.

- [9] Nureddin Bennett, Ashwin Walawalkar, and Christian Schindler. Payload estimation in excavators: Model-based evaluation of current payload estimation systems. 03 2014.
- [10] N. G. Hareesha and K. N. Umesh. Kinematic and isotropic properties of excavator mechanism. 07 2018.
- [11] Seungjin Yoo, Cheol-Gyu Park, and Seung-Han You. Inertial parameter estimation for the dynamic simulation of a hydraulic excavator. *Journal of Mechanical Science and Technology*, 32(9):4045–4056, 2018.
- [12] Yahya H. Zweiri. Identification schemes for unmanned excavator arm parameters. 5(2):185–192, 2008.
- [13] Shahram Tafazoli, Peter. D. Lawrence, and S.E. Salcudean. Identification of inertial and friction parameters for excavator arms. *IEEE Transactions on Robotics and Automation*, 15(5):966–971, 10 1999.
- [14] Shahram Tafazoli. *Identification of frictional effects and structural dynamics for improved control of hydraulic excavators*. PhD thesis, University of British Columbia, 1997.
- [15] Yunfei Dong, Tianyu Ren, Ken Chen, and Dan Wu. An efficient robot payload identification method for industrial application. *Industrial robot*, 45(4):505–515, 2018.
- [16] N. R. Parker, S. E. Salcudean, and P. D. Lawrence. Application of force feedback to heavy duty hydraulic machines. In *IEEE Int. Conf. Robot. Automat.*, pages 375–381, 5 1993.
- [17] Bruno Siciliano, Lorenzo Sciavicco, Luigi Villani, and Giuseppe Oriolo. *Robotics Modelling, Planning and Control*, chapter 7. Springer, 2009.

Experimental Investigation of New Design Concepts for the Tribological Contact between the Valve Plate and the Cylinder Block in Axial Piston Machines

Stefan Geffroy*, Stephan Wegner**, Stefan Gels***, Katharina Schmitz*

*Institute for Fluid Power Drives and Systems, RWTH-Aachen University, Campus-Boulevard 30, 52074 Aachen
E-mail: S.Geffroy@ifas.rwth-aachen.de

**Stackpole Powertrain International GmbH, Campus-Boulevard 30, 52074 Aachen

***Hydraulische Antriebstechnik P&G GmbH, Nettestraße 39, 58762 Altena

Abstract

Axial piston machines are widely used in both stationary and mobile hydraulic systems due to their efficiency and robustness in high pressure applications. Important tribological contacts in axial piston machines are between pistons and bushings, sliding shoe and swash plate, as well as between cylinder block and valve plate. The analysis of these contacts is imperative to improve the overall performance of the machine, since they influence its efficiency to a high extend. This paper focuses on the contact between the valve plate and the cylinder block.

High pressure forces acting on the cylinder block result in a tilted position, defining the shape of the interface with the valve plate. The tilted position is overlayed by the cylinder block's rotation, resulting in unfavorable lubrication conditions and high contact pressure.

Measures to actively influencing the cylinder block's position during its rotation is currently researched at ifas. Using pressure pockets in the kidney grooves of the cylinder block is one of these measures and presented in this paper. The investigation is done simulative and experimental, using a 140 cm³ pump on a special test rig, measuring the cylinder block movement. The results of this are presented in this paper.

Keywords: Axial piston pump, cylinder block, pressure pocket, tilting

1 Introduction

Axial piston machines are used in many mobile and stationary hydraulic systems, because they can deliver high volume flow rates at a high pressure with an overall efficiency of about 90 % in modern units [1]. Figure 1 shows the main components of an axial piston pump. Tribological contacts in this machine are defined as surfaces moving relative to each other, separated by a thin fluid film. Essential pairings are the pistons with their respective cylinders/bushings, the sliding shoe with the swash plate and the valve plate with the cylinder block [1]. Nearly 90 % of the overall efficiency [2] can be traced back to these contacts. The research and further development of these tribological contacts in axial piston machines is therefore of great importance in context of resource efficiency, climate protection and emission laws. In context with the goal of removing leaded materials [4], which are partially used in these contacts, several aspects need to be combined to allow for improvements coming from different stakeholders.

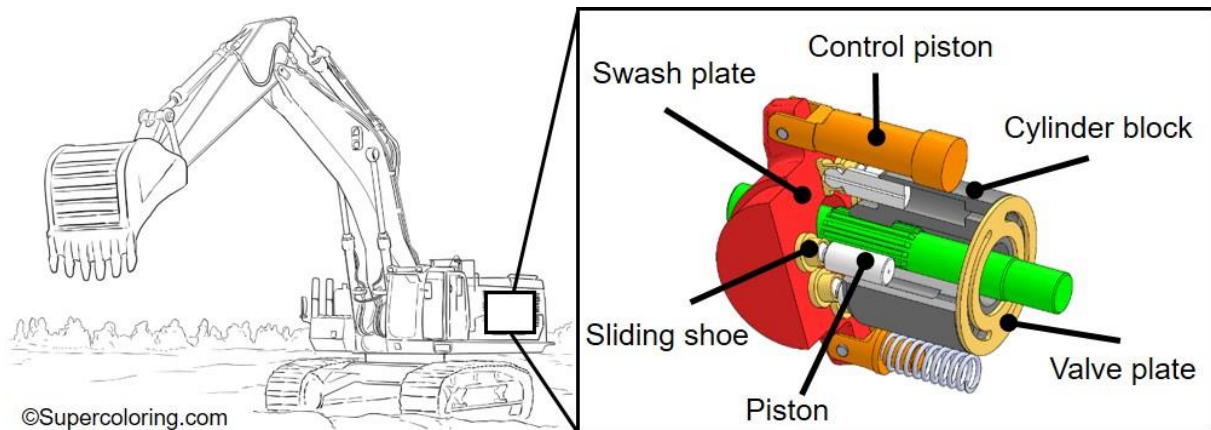


Figure 1: Main parts of an axial piston machine [3]

The here presented analysis focuses on the contact between the valve plate and the cylinder block. The cylinder block is driven by the shaft which in turn is driven by the engine. Axially it is in contact with the stationary valve plate which inherits kidney shaped openings, connected to the inlet and outlet ports of the pump. The cylinders in the cylinder block are connected via bores to the interface and due to the rotational movement, each cylinder transitions from the low pressure port to the high pressure during each rotation, synchronized with the suction and pressure stroke of the piston. Therefore, this is a forced commutation. The main task of the interface is to seal high and low pressure areas and openings against each other and the housing/ambient pressure. To reach the sealing function, the axial gap between cylinder block and valve plate must be as small as possible, however the system should not introduce unnecessary friction. Therefore, it is designed as hydrostatic/hydrodynamic axial bearing, incorporating the described functionality. Pressurized surfaces within the cylinder block are balanced against the area of the axial bearing, compensating the acting forces with a small remaining force acting as “gap-closing” force, always ensuring a safe operation. Springs acting on the cylinder block create a preload force, pressing the cylinder block against the valve plate. This creates an offset to the force balance and accounts for low-pressure operations, going along with low pressure forces and the risk of a lifting the cylinder block off the valve plate. Forces acting in gap-closing direction are designed so that a good compromise between friction and volumetric losses is established. However, a safety margin to prevent lift-off, unintended machine usage and dynamic effects must be implemented, moving the design point away from the sweet spot in the direction of higher friction. Another problem results then for self-sucking pumps. The increasing gap at low pressure side loses its function of sealing. Therefore, the pressure can collapse. This effect limits the self-sucking speed of axial piston pumps.

To account for tolerances, unfavorable lubrication conditions, high load peaks and to allow a run-in, the materials are often selected to be steel on one component, paired with a soft material on the other part (e.g., brass or bronze alloy). Lead within the alloy improves the durability and robustness, however it's use is Hence lead is a toxic heavy metal and its use is strongly regulated in the EU due to its toxicity.

Due to unbalanced forces resulting from the pressure difference between the high and low pressure apertures, the cylinder block tilts during operation. By setting up the equilibrium of the forces and moments acting on the cylinder block, P. Achten investigates the tilting effect analytically in [5]. The obtained results showed that the forces and moments are heavily unbalanced during operation, mainly due to two characteristics of axial piston machines. First, greater differences in fluid volume in each displacement chamber are caused by different rotational angles of the swash plate, thus causing uneven centrifugal forces. Also, compressive forces resulting from the narrowing of the cross-section of the cylinder block bores are very different, especially in operation points with high load pressures. Therefore, the resulting pressure difference between the low pressure side and the high pressure side grows bigger, so that the cylinder block gives in towards the high pressure side. A simulation model was built up by S. Wegner for the investigation of the cylinder block's movement. The description and validation of the model can be found in [6]. It is shown that the cylinder block tilts to the high pressure side and holds the attained position almost constantly during constant operating conditions, therefore supporting the statement of P. Achten's investigation. The position of the minimum gap height of a 9 piston machine, while 4 and 5 pistons are pressurized, is shown in fig. 2. The shown simulative results are consistent with experimental investigations [6].

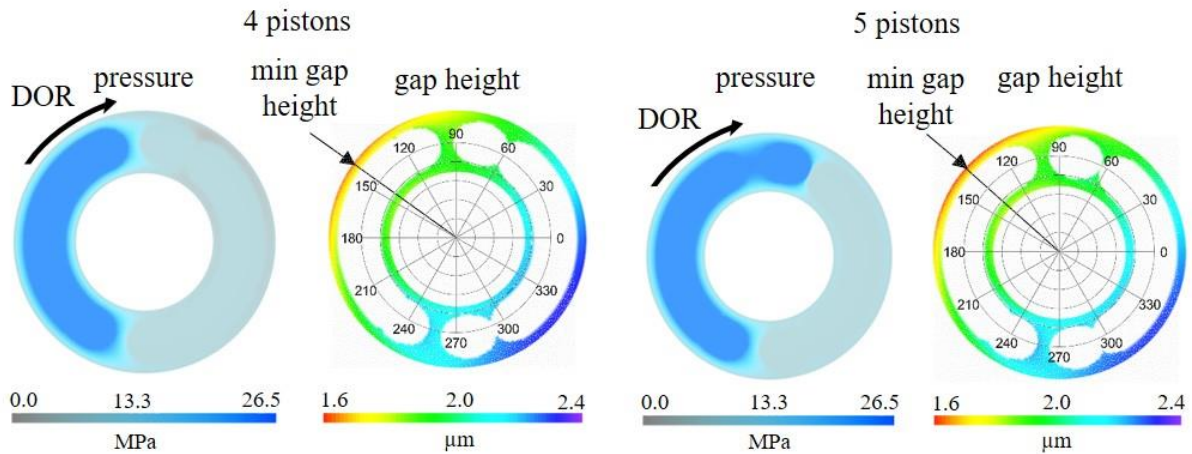


Figure 2: Position of minimum gap height [6]

Due to the negative effects named earlier, small gap heights increase the risk of high wear due to increased friction as well as local hot spots [7]. Especially the high temperature is a challenge for the material substitution. Coatings like “Diamond Like Carbon” (DLC) are very hard and have good tribology properties but are sensitive to high temperatures. Therefore, the development of design concepts with the aim to reduce tilting and temperature are of great interest.

In the context of this work, there are some interesting approaches. In [8], a concept with punctual pressure field is presented. Bores are positioned in the outer support ring of the valve plate and connected to the high-pressure kidney. The resulting pressure field reduces the cylinder block’s tilting. A speed increase of 15 % in self-priming mode of the pump results. The additional manufacturing expenditure a disadvantage of this concept. In addition to the relief bores, the connecting bores must be drilled from the outside into a round surface and must then be sealed by a plug. The manufacturing of the relief bores into a spherical valve plate is very difficult and therefore expensive and there must be enough space in the sealing gap for these bores. Due to the additional leakage, the volumetric efficiency decreases. The aim of another concept is to avoid the tilting of the cylinder block by an additional device [9]. Compensation pistons are installed and connected to the flow channel to add a moment against the tilting. In [10] a concept with externally pressurized pressure pockets in the valve plate is patented. The moment against the tilting can therefore be controlled independently of the operating point. The disadvantages are the additional manufacturing costs and that the complex application of the control for each operating point. S. Haug investigates and extends these concept [11][12] and applies it to other tribological contacts. He develops an operating point dependent control and could prevent the tilting for all investigated operation points almost completely in this way. P. Achten investigates the effect of additional pressure pockets in the barrels of a floating cup axial piston [13]. They are connected with grooves to the bores and build up a hydrostatic bearing in the contact between the barrel and the port plate.

This work presents a new design concept for the cylinder block and its experimental investigation. Pressure pockets are placed at the outlet bores of the cylinder block. The underlying idea is to add an imbalance which relieves the area of minimum gap height for a short time to avoid the local temperature hot spots.

2 Concept Development

The development process is based on a simulation study with the simulation model, described in [6], developed at ifas. After a short explanation of the program, this chapter presents the simulation study and its results.

2.1 Simulation Model

A simulation model was created set up for the detailed analysis of the tribological contact between the cylinder block and the valve plate. The simulation is a continuation of tribological simulations specialized on interfaces in hydraulic pumps [14]. A detailed explanation is given in [6], and will only be briefly described in this work. In fig. 3 the principle of the simulation is depicted. The following physical effects are included:

- Fluid behavior using the Reynolds equation discretized on finite volumes
- Lumped parameter simulation calculating the cylinder pressures in each time step

- Input of external forces, either quasi-static via look-up table or coupled to pressure variables resulting during the simulation
- Contact pressure (Greenwood and Tripp/Williamson model)
- Solid friction using the contact pressure acting on each finite volume (the interface surface)
- Fluid friction
- Solid body movement of the cylinder block
- Surface deformation

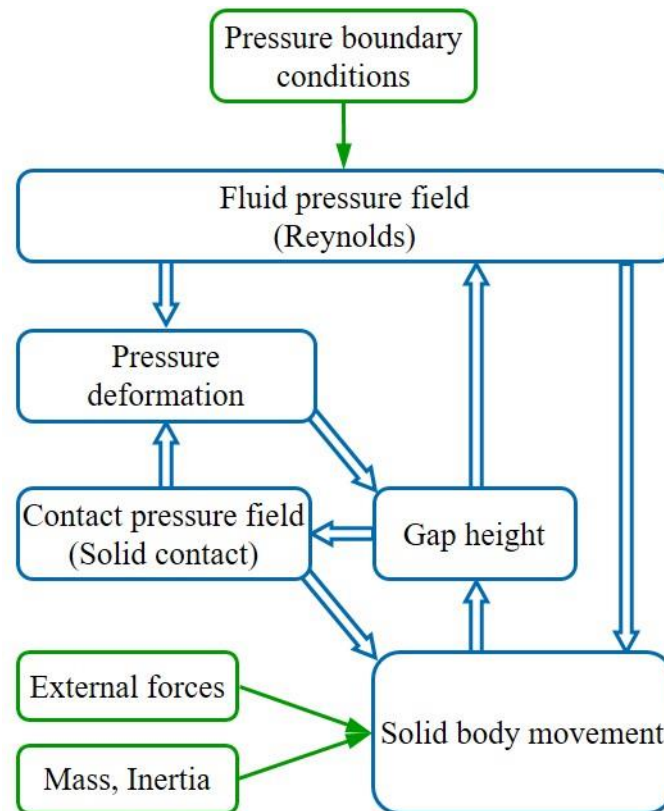


Figure 3: Chart of the Simulation model [15]

In each time step, the lumped parameter simulation is set up first, analyzing connections between cylinder block and valve plate features and creating a non-linear set of equations. The result is a defined pressure value for each feature (e.g. cylinder block piston pressure or valve plate port pressure) which is a boundary condition for the second set of non-linear equations, covering the aforementioned physical effects. The implicit Euler method is implemented as integration method, the set of equations is solved using the monolithic approach using the solver KINSOL [16].

2.2 Simulation Studies

The development process of the new design concept presented in this work starts with the simulation pre-study, which is published in [15] and is only shortly concluded in the following. This study investigated the effect of additional forces, moving with the cylinder block at a defined radius, derived from the kidney's shape. For the investigation of the effect of an additional imbalance, the forces are only active in the area of minimum gap height. With one force of 1.25 kN, acting at radius of 45.55 mm, which is the outer shape of the kidney, the minimum gap height is shortly increase of about 5 %, compared to the standard version. This leads to a reduction of the contact pressure of over 25 % and reduces therefore also the thermal load.

Additional forces can be installed by pressure pockets. In another design concept, presented in [15], these are placed at the high pressure kidney of the valve plate. The result is a static pressure field which creates a constant moment against the tilting. First experimental results show that this concept reduces the friction torque within the interface. To create the aforementioned effect of an additional imbalance, the pressure pockets are placed on the

cylinder block. In this way, the forces investigated in the pre-study can be replicated, because of the pressure pockets are at high pressure side, they have great effect. But when they are at low pressure side, they have near no influence. In the concept of P. Achten [13], the surfaces are machined separated to the bores and then connected by groves to it. Another possibility, which is more easy to machine, is to integrate the pockets direct into the shape of the kidneys. Another advantage is that the pressure build up in the pockets is immediately when the bore joins the high pressure area. The limiting factor for these surfaces is the minimum sealing gap width. It should lay in the interval between 0.125 to 0.175 times the bore diameter [17]. For the geometry of the axial piston pump the sealing land should be 3.125 mm. The maximum width is then 0.925 mm for the outer and 3.125 mm for the inner pressure pocket. Figure 4 shows the new design of the cylinder block's kidney shape in CAD and the prototype with their measured surfaces.

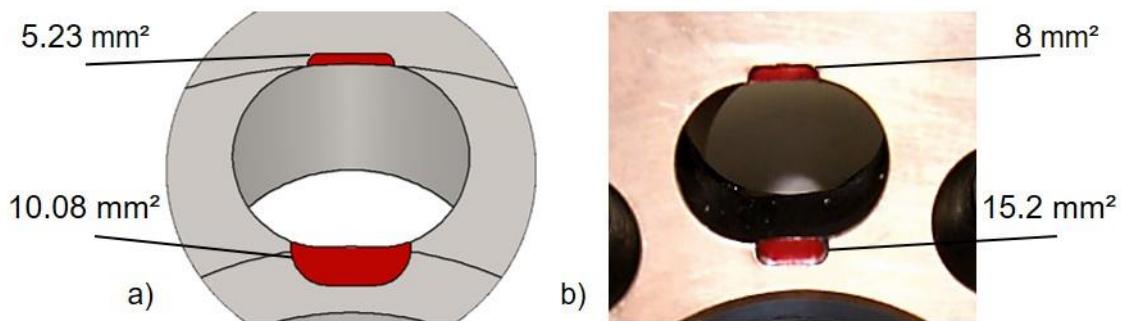


Figure 4: Additional pressure pockets a) CAD and b) prototype

The outer pocket is designed with the maximum width, while for the inner one 2 mm are used. This shape was then added to the simulation model for the analysis of this design concept. The main point of interest of the simulations was to investigate the effect of the pressure pockets in different configurations. The full study and its results are to find in [18] but are briefly explained here. The 12 different geometries, which are used are shown in fig. 5. Kidneys with the additional pressure pockets are black marked. They are measured and compared for one operation point with a rotational speed of 1500 rpm and a load pressure of 250 bar. Configuration one is the standard geometry without pressure pockets. The effect of a raising number of additional surfaces, which are asymmetrical distributed, is investigated with the versions two up to version ten. In the configurations eleven and twelve, the pockets are installed symmetrically.

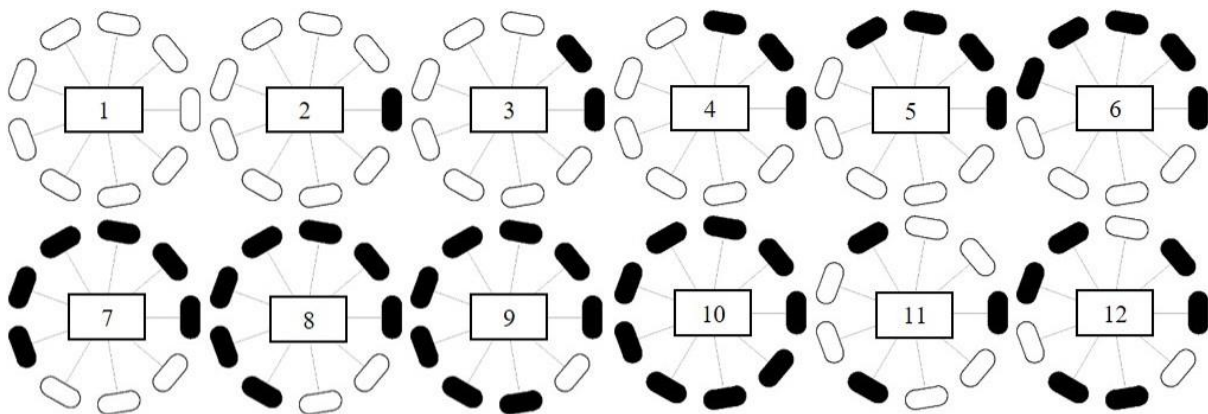


Figure 5: Investigated configurations

The simulation results show that the gap height is increased by the additional pressure pockets. Therefore, all configurations reduce the contact pressure from 17 % in case of one modified kidney to over 50 % for the version ten, where all are extended with the additional surfaces. Figure 6 shows the simulation results for the relative change of the tilt angle. The tilt angle of the cylinder block is only reduced for the configuration two and three with a small effect of less than 5 %. In the other versions with a higher number of pressure pockets, the tilting of the cylinder block increases. A possible explanation for this effect is that the increased gap height simply allows for more tilting until the contact pressure counters the movement. The concept idea to add an additional imbalance finds its maximum with the configuration six. As explained previous, there are two extrem points in an axial piston pump with nine pistons, when four or five kidney are pressurized. The maximum amplitude is reached, when five

modified cylinder block bores are pressurized, while the four cylinder block bores with standard geometry are in contact with the low-pressure kidney of the valve plate.

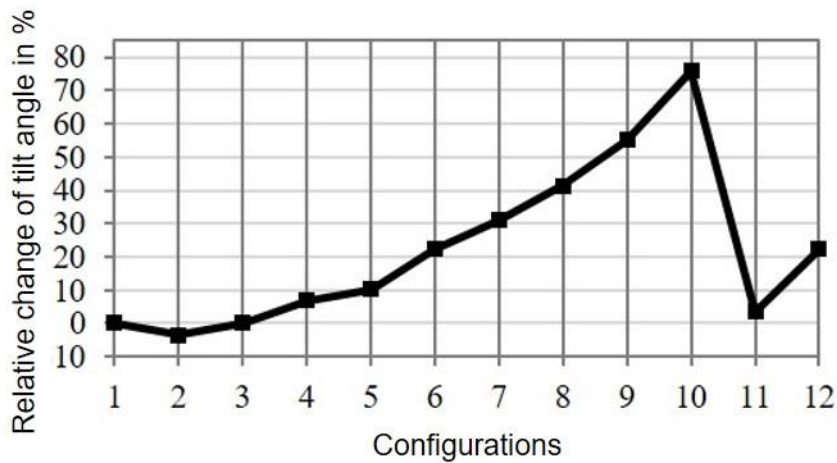


Figure 6: Relative change of the tilt angle for the considered configurations

The effect of an additional imbalance on the operating behavior of the pump cannot be estimated in advance. For this reason, a prototype was initially manufactured. For the initial test, configuration two was selected. Simulations for several operation points were carried out and evaluated. The operating points for the simulation are: speed (n) from 250 rpm to 2500 rpm in steps of 250 rpm; load pressure (p) from 50 bar to 250 bar in steps of 50 bar. The results for the minimum gap height (h) and the contact pressure (cp) are to shown in fig. 7 and fig. 8. The change of minimum gap height depends on the load pressure. This was expected. With the increasing speed, the effect of the pressure pockets is decrease by dynamical effects. The maximum reduction of the contact pressure is of near 15 % at low speed while maximum pressure.

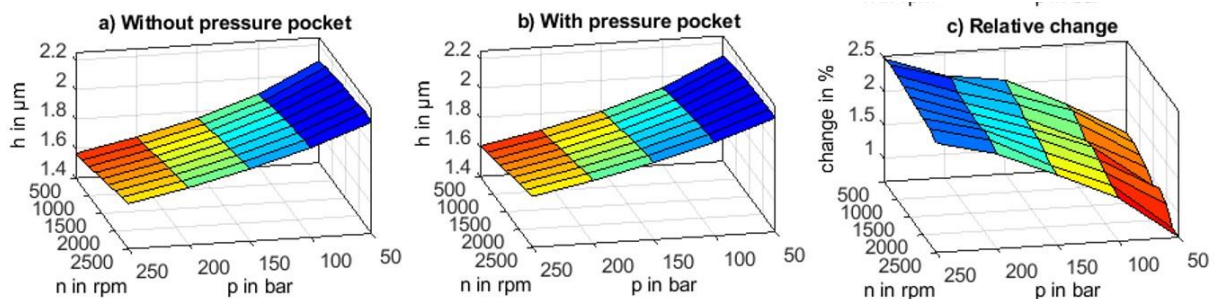


Figure 7: Minimum gap height and its relative change

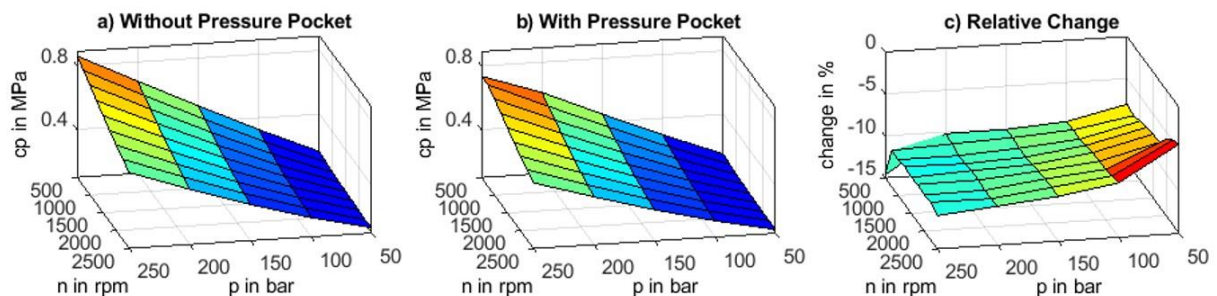


Figure 8: Contact pressure and its relative change

3 Experimental Investigation

3.1 Test Rig

For the experimental investigation of the tribological contact focused in this work, a test rig was developed and built up at the institute, shown in fig. 9. The test pump (p1) is driven by a 160 kW motor. s5 and s6 are used for torque, speed and angular position measurement. Oil delivered from the filling pump p2 is filtered through f1. At the inlet and outlet of the test pump pressure (s2 & s9) and temperature (s2 & s8) are measured, the outlet flow is measured by s10. The load pressure is controlled by the load valve block (LV). The pump p4 delivers the fluid for the hydrostatic bearing (explanation in the following). The bearing pressure is set by valve (B). The leakage of the hydrostatic bearing and the test pump is delivered to the tank by the pump p3. In the secondary circuit, which includes the pump p5, the filter f2 and the water cooler c1, the oil is conditioned.

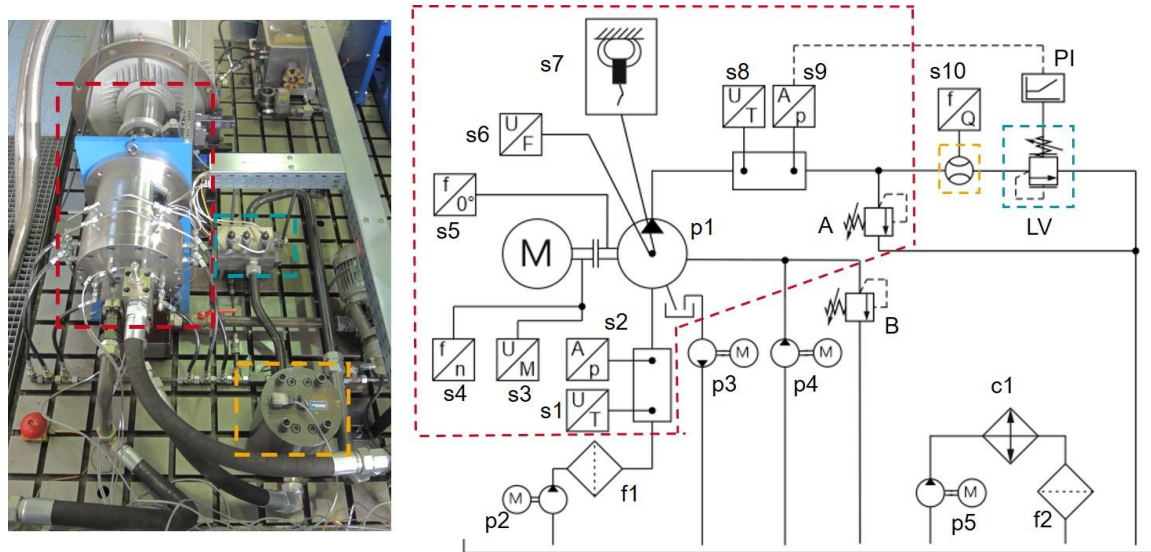


Figure 9: Test rig and hydraulic circuit diagram

The test bench was dimensioned for the analysis of a 140 cm³ axial piston pump with a maximum pressure of 340 bar and a maximum drive speed of 2400 rpm. The main drive components are placed in the test pump, which is presented in fig. 9. For the measurement of the friction torque between the valve plate and the cylinder block, a hydrostatic bearing was developed, which is also part of the test pump. The swash plate angle can be adjusted by means of spacers with the fixation bolt from 0° to 16°. The main components of the hydrostatic bearing are the housing (blue) and the inner runner (green), which is externally pressurized. Six eddy current sensors (s7 in fig. 8), three in radial direction (black arrows in fig. 10) and three in axial direction (red arrows in fig. 10) are installed for the measurement of the cylinder block's movement as well as the gap height.

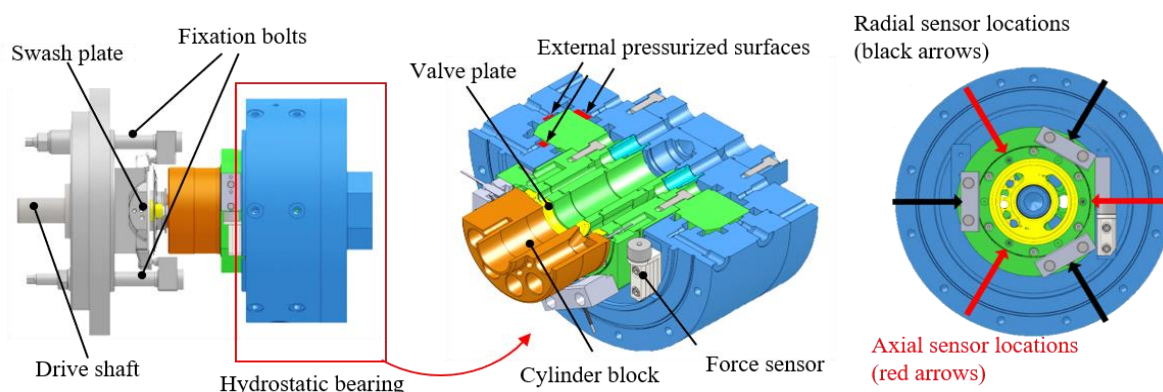


Figure 10: Drive train of the test pump and detailed view of the hydrostatic bearing [19]

3.3 Experimental Results

Due to the risk of damaging the test rig or the sensor system in the start-up of the first test series, the test pump was not fully loaded. The range of rotational speed was limited to 1000 rpm, setting measuring points every 250 rpm for the initial tests. The pressure was limited to 250 bar, increasing from 100 bar in 25 bar steps for each speed. The swivel angle was set to 8° , resulting in a displacement of 70 cm^3 . The hydrostatic bearing was pressurized to 100 bar. The suction side was set to a pre-load pressure of 8 bar. All measuring points were approached three times. Figure 10 shows the measured friction torque between valve plate and cylinder block for the standard configuration (gray) and the modified component (indicated with (Pro) in black). As expected from previous investigation, both configurations show a linear increase of the frictional torque at different pressure and speed level.

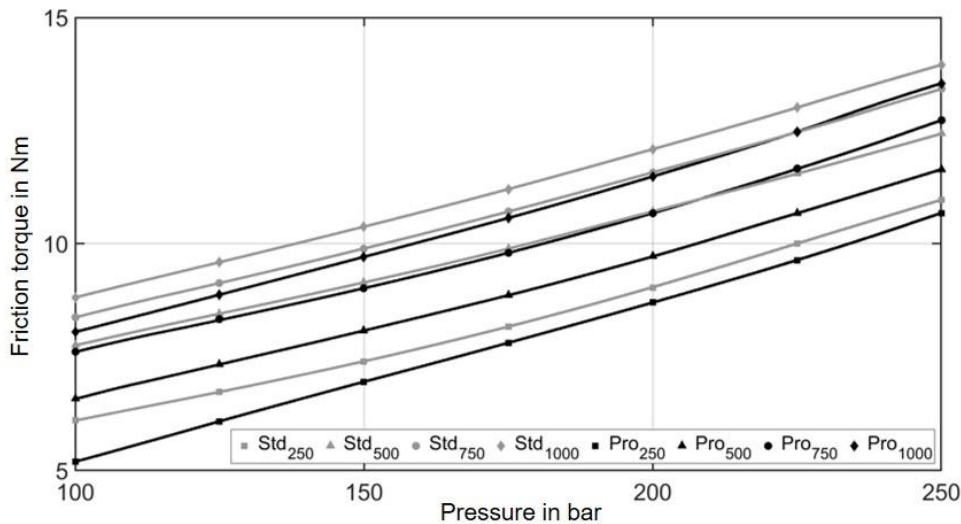


Figure 11: Friction torque for different pressure levels and rotation speeds

The relative change in frictional torque is plotted in fig. 12. In the prototype configuration, the friction torque is significantly reduced in all measuring points. At 100 bar, the largest friction torque reduction is measured over the measured speeds range, reaching a maximum reduction of about 15 % at 250 rpm and 500 rpm. With increasing load pressure, the reduction decreases almost linearly, but is still significantly reduced at 250 bar. The relative change in volumetric efficiency is shown in fig. 13. Particularly at low rotational speed, leakage increases notably, resulting in a significant reduction in volumetric efficiency. With increasing speed, this effect is less predominant, amounting to a maximum of about 2 % efficiency reduction.

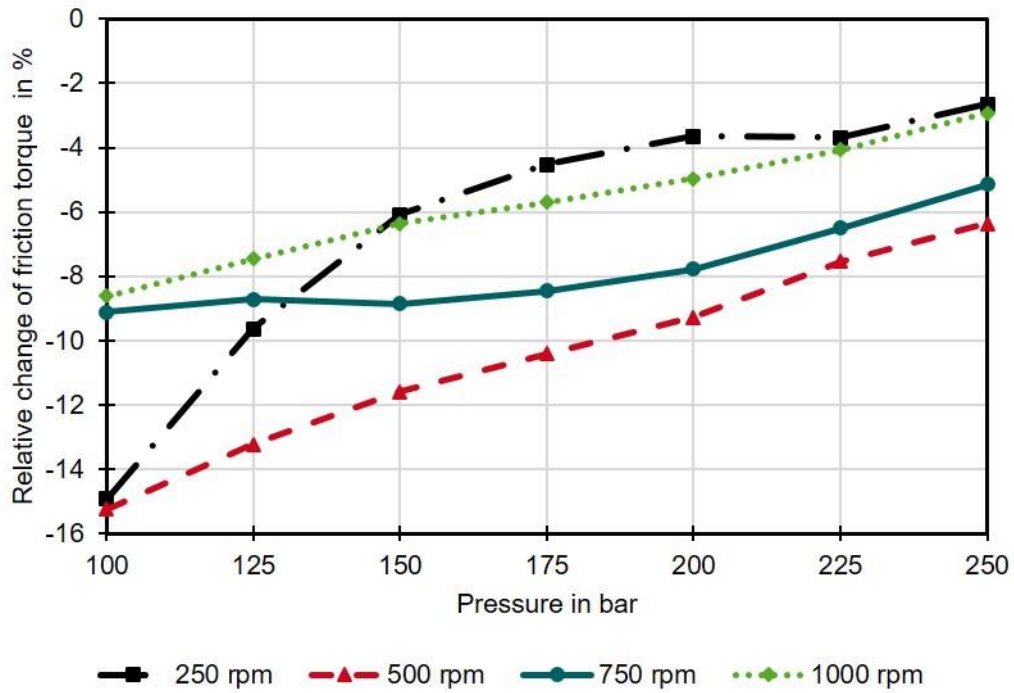


Figure 12: Relative change of friction torque

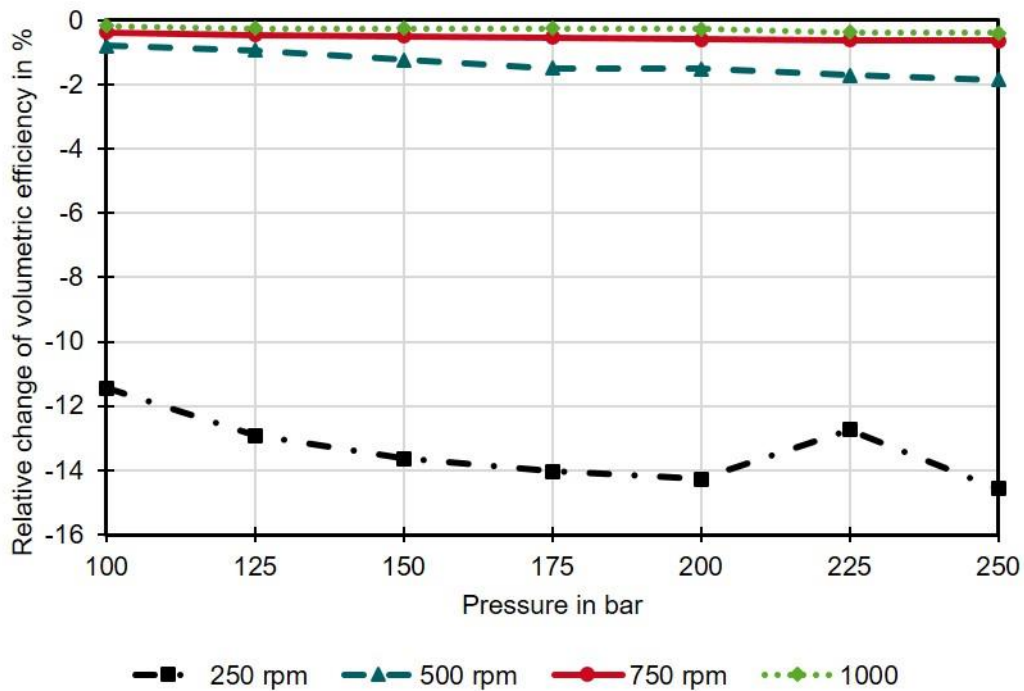


Figure 13: Relative change of volumetric efficiency

The goal of the design concept is to install an additional imbalance. Therefore, the measurements of the eddy current sensors are compared in the following. Using the same coordinate system from fig. 2, the black h1 line denotes the axial and radial sensor position at 60°, the red h2 line at 180° and the green h3 line at 300°. The sensor position is visualized in fig 14.

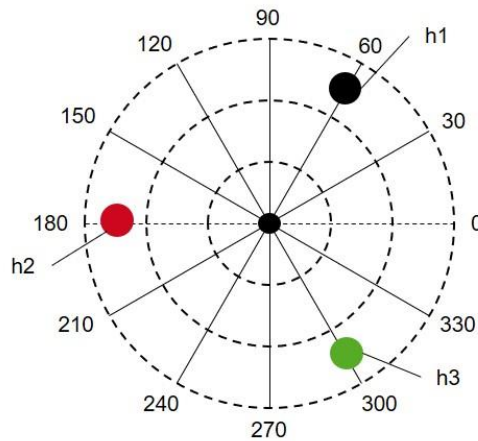


Figure 14: Sensor position of the axial and radial eddy current sensors

Different alloy compositions of the cylinder block material affecting the eddy-current sensors, machining inaccuracies of the targeted surface, differences in height adjustment of the sensors and further imperfections of the rotating system. For a better understanding, the raw sensor signal of h2, the distance to target (cylinder block), over one rotation at 100 bar (blue line) and 250 bar (red line), which therefore includes all of the pre named influences is plotted in fig. 15. However, the gap height reduction from 100 bar to 250 bar at high pressure region is clearly visible. The movement of the cylinder block depending on the pressurization of each of the nine pistons can be identified better in the red line as in the blue one.

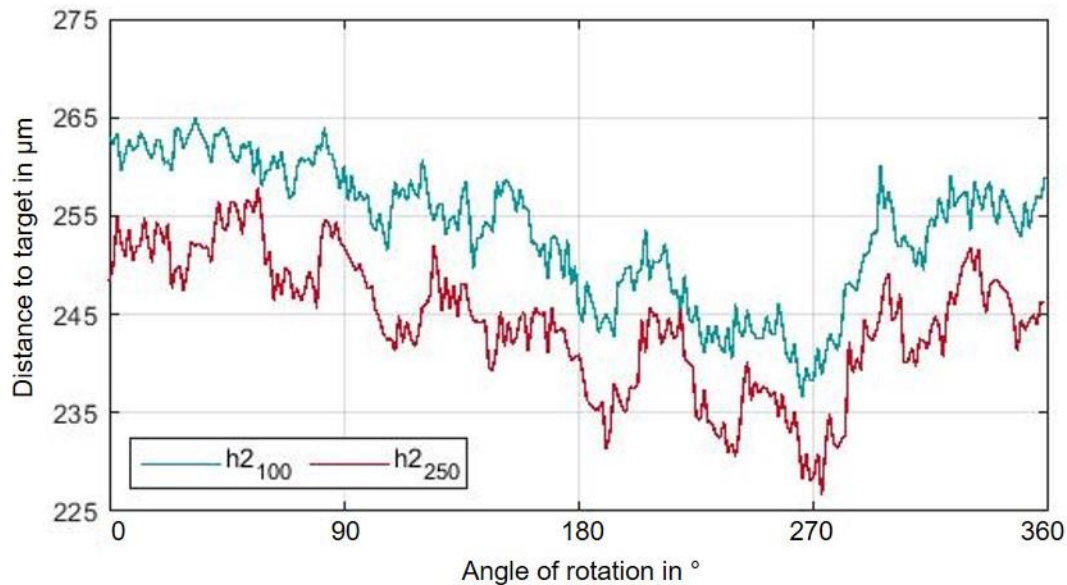


Figure 15: Raw sensor signal of h2 for 100 bar and 250 bar

For the analyzation of the influence of the new design to the movement of the cylinder block, the measured distance to target is averaged over one revolution and then compared for the operation points at 100 bar and 250 bar, by building the difference between this two points. This is done for all considered drive speeds. Figure 16 shows the change of distance for the axial eddy current sensors h1 (black), h2 (red) and h3 (green) for the prototype (full line) and the standard (dashed line) configuration. From the simulation results it was expected that the cylinder block tilts in way that a minimum gap height occurs at approx. 130° (see fig. 2). The change of distance in fig. 16 show also this trend of the tilting direction. Compared to the high pressure operation point, the distance form h1 and h2 to the cylinder block is decreased, while it is increased for h3. For the prototype configuration the calculated change of distance is different. There is a lower reduction at h2 and a higher increase at h3. Very interesting is that the distance between h1 and the cylinder block is more reduced on average over one revolution. This indicates a change in the movement and therefore the tilt angle.

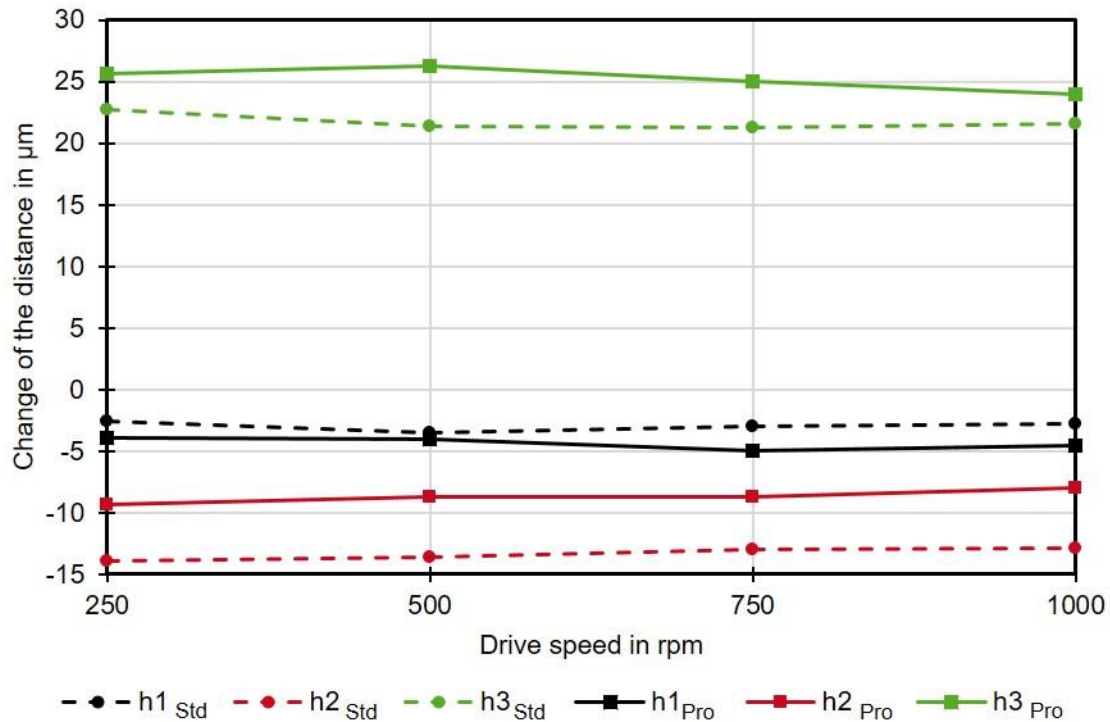


Figure 16: Change of distance from 100 bar to 250 bar for both configurations

For the understanding and visualization of the changed movement of the cylinder block, the orthogonal vector of the plane given by the measured distance of the axial sensors is calculated. Then, its direction is projected to a coordinate system. This method as well as the movement from 100 bar (origin) to 250 bar for all measurements is shown in fig. 17. The projection of the orthogonal vector lays in a very close area for the standard as well as for the prototype configuration. There is a significant change in the movement. While the cylinder block without pressure pockets tilts more to the high pressure side as expected from the simulations, the direction of the tilting for the prototype is very different.

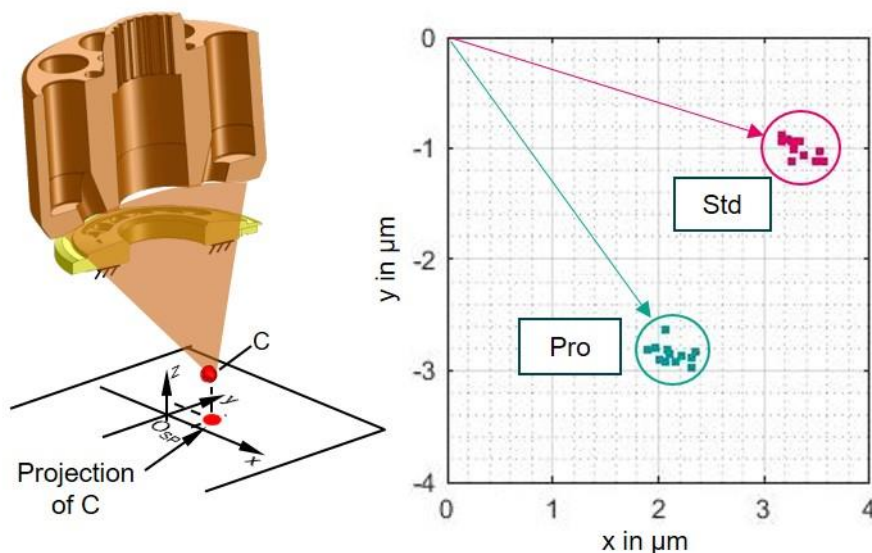


Figure 17: Projection of the orthogonal vector

4 Conclusion and Outlook

In a simulation study, fully presented in an earlier work of the author, the effect of additional pressure pockets was analyzed. Twelve configurations with a different number and position of pressure pockets are investigated in it.

The greatest reduction of the cylinder block's tilting angle was calculated for the configuration with only one optimized kidney groove. Further simulations over a wide range of operating points, which are presented in this work, show that this design increase the gap height which leads to a significant reduction of the contact pressure. A prototype was machined and tested on the test rig. The experimental results show that the new design concept with the additional pressure pockets in on kidney of the cylinder block has significant effects to the tribological contact. The friction torque is reduced up to 15% for lower speeds, 250 rmp and 500 rpm, at 100 bar. Because the part of fluid friction increases, the reduction of friction torque is lower for 750 rpm and 1000 rpm. The difference between the standard and the prototype configuration decreases linearly with increasing load pressure, but is also significant at 250 bar. As it was expected, the volumetric efficiency is reduced. The smaller gap width, due to additional surfaces, has the same effect as a throttle where the length is reduced. Therefor the additional leakage is pressure depending and more or less statically for the different speeds. Because of this, the volumetric losses are at the higher speeds less than 2 %. The evaluation of the eddy current eddy-current sensor data two different load pressure operation points show that the standard cylinder block tilts to the high pressure side, thus confirming the simulation results and the previous study in [6]. Because of the imbalance added by the additional surfaces, the prototype cylinder block show on average over one revolution another tilting direction. This validates the simulations and the effect of the new design concept. Due to this imbalance, there is no local constant area of minimum gap height. This avoids the building of high temperature hot-spot in the tribological contact. The next steps are to validate the temperature effect by simulations and experiments.

5 Acknowledgement

This work was performed in the scope of the project "Increasing the efficiency of the cylinder block/valve plate contact in axial piston machines"/"Steigerung der Leistungsfähigkeit des Kolbentrommel-Steuerspiegel Kontaktes in Axialkolbenmaschinen" (MU41225/44-1), which is funded by the German Research Foundation (DFG). The authors would like to thank the German Research Foundation for funding the project.

Nomenclature

Designation	Denotation	Unit
<i>c1</i>	Cooler 1	-
<i>cp</i>	Contact pressure	MPa
<i>DOR</i>	Direction of rotation	-
<i>fl...2</i>	Filter 1...2	-
<i>h</i>	Axial gap height	μm
<i>h1</i>	Sensor position at 60°	-
<i>h2</i>	Sensor position at 180°	-
<i>h3</i>	Sensor position at 300°	-
<i>ifas</i>	Institute for fluid power drives and systems	-
<i>LV</i>	Load valve	-
<i>n</i>	Drive speed	rpm
<i>p</i>	Pressure	bar
<i>p1...5</i>	Pump 1...5	-
<i>PI</i>	PI controller	-
<i>s1...10</i>	Sensor 1...10	-

References

- [1] M Gärtner. *Verlustanalyse am Kolben-Buchse-Kontakt von Axialkolbenpumpen in Schrägscheibenbauweise*, Dissertation, RWTH Aachen University, Aachen, 2019

- [2] B Xu, M Hu, J-H Zhang, Z-B Mao. *Distribution characteristics and impact on pump's efficiency of hydromechanical losses of axial piston pump over wide operating ranges*. Journal of Central South University, 2017
- [3] K Schmitz, H Murrenhoff. *Grundlagen der Fluidtechnik Teil 1: Hydraulik*, Shaker Verlag, Aachen, 2018
- [4] Table of restricted substances under REACH, European Chemicals Agency
- [5] P Achten, S. Eggenkam. *Barrel tipping in axial piston pumps and motors*, 15th Scandinavian International Conference on Fluid Power, Linköping, Sweden, 2017
- [6] S Wegner, S Gels, H Murrenhoff. *Simulation of the tribological contact cylinder block/valve plate and influence of geometry and operation points on the friction torque in axial piston machines*, The 9th International Fluid Power Conference, Aachen, Germany, 2014
- [7] R Ivantysyn, A Shorbaby, J Weber. *An approach to visualize limiting factors in the cylinder block/valve plate gap in Axial Piston Pumps*, ASME Symposium on Fluid Power and Motion Control, Bath, Great Britain, 2017
- [8] InLine Hydraulik GmbH, DE 198 23 353 A1, patent, Germany, 1999
- [9] Linde AG, DE 198 55 899 A1, patent, Germany, 2000
- [10] Robert Bosch GmbH, DE 10 2010 006 895 A1, patent, Germany, 2011
- [11] S Haug, M Geimer. *Optimierung von Axialkolbenmaschinen durch bedarfsangepasste Entlastung tribologischer Kontakte*, 9. Kolloquium Mobilhydraulik, Karlsruhe, Germany, 2016
- [12] S Haug, M Geimer. *Optimization of Axial Piston Units Based on Demand-driven Relief of Tribological Contacts*, The 10th International Fluid Power Conference, Dresden, Germany, 2016
- [13] P Achten, R Mommers, J Potma, J Achten. *Experimental Investigation of a Hydrostatic Bearing Between Barrels and Port Plates in Floating Cup Axial Piston Pumps*, ASME Symposium on Fluid Power and Motion Control, Bath, Great Britain, 2020
- [14] S Gels. *Einsatz konturierter und beschichteter Kolben-Buchse-Paare in Axialkolbenmaschinen in Schrägscheibenbauweise*, Dissertation, RWTH Aachen University, Aachen, 2011
- [15] S Geffroy, N Bauer, T Mielke, S Wegner, S Gels, H Murrenhoff, K Schmitz, *Optimization of the tribological contact of valve plate and cylinder block within axial piston machines*, The 12th international Fluid Power Conference, Dresden, Germany, 2020
- [16] A C Hindmarsh, P N Brown, K E Grant, S L Lee, R Serban, D E Shumaker, C S Woodward, *SUNDIALS: Suite of nonlinear and differential/algebraic equation solvers*, ACM Transactions on Mathematical Software (TOMS), 2005
- [17] J Ivantysyn, M Ivantysynova, *Hydrostatische Pumpen und Motoren*, 1. Auflage, Vogel, Würzburg, Germany, 1993
- [18] S Geffroy, S Wegner, S Gels, H Murrenhoff, K Schmitz, *New Design Concepts for the Tribological Contact of Cylinder Block and Valve Plate*, ASME Symposium on Fluid Power and Motion Control, Bath, Great Britain, 2020
- [19] S Wegner, F Löschner, S Gels, H Murrenhoff. *Validation of the physical implementation in a simulation model for the cylinder block/valve plate contact supported by experimental investigations*, The 10th International Fluid Power Conference, Dresden, Germany, 2016

A New Degree of Freedom for Variable Axial Piston Pumps with Valve Plate Rotation

Thomas Heeger and Liselott Ericson

Dep. of Management and Engineering, Fluid and Mechatronic Systems,
Linköping University, 581 83 Linköping, Sweden
E-mail: thomas.heeger@liu.se; liselott.ericsson@liu.se

Abstract

Conventionally, variable axial piston machines vary displacement by adjusting the length of the piston stroke, which can be done by adjusting the angle of the swash plate in swash plate machines or the angle of the cylinder block in bent axis machines. Another possibility to achieve variable displacement is to rotate the valve plate and thus adjust the effective use of the piston stroke. An advantage of this method is that it only requires small forces and is easier to control in comparison to conventional displacement adjustment.

This idea is not new, and the concept was studied decades ago, but unfortunately, cavitation and high pressure peaks in the bridge between the kidneys hindered a successful implementation of valve plate rotation.

Using a double pump with opposing pistons offers the potential to overcome these obstacles, as the displacement can be adjusted by joint rotation of both valve plates, and the effective bridge angles can be adjusted by relative rotation of the valve plates. This paper presents a methodology to optimise valve plate kidney angles for a double pump with rotating valve plates. Optimisation results for exemplary sets of operating points are presented. At high setting ratios, power losses and flow pulsations can be reduced. The risk of cavitation and high pressure peaks can be eliminated, but at the expense of cross-porting and increased losses at low setting ratios and high speeds.

Keywords: axial piston pump, variable displacement, valve plate rotation, bridge angles, opposing pistons

1 Introduction

Conventionally, variable axial piston machines vary displacement by adjusting the length of the piston stroke, which can be done by adjusting the angle of the swash plate in swash plate machines or the angle of the cylinder block in bent axis machines [1]. Another way to achieve variable displacement is to adjust the effective use of the piston stroke, which can be done by rotating the valve plate [2]. It is beneficial that valve plate rotation requires smaller control forces and provides easier controllability in comparison to conventional displacement adjustment [3].

This idea is not new, and the concept was already studied decades ago, but unfortunately, cavitation and high pressure peaks in the bridge between the kidneys have proven to be a major drawback of valve plate rotation [4]. Further issues that need to be considered are noise and backflow [5].

When using a double pump with opposing pistons, two rotating groups, and therefore also two valve plates, are used, see fig. 1a. When both rotating groups share a common cylinder barrel, and opposing pistons are connected through the cylinder barrel, each of the valve plates affects the effective port angles. Therefore, the ability to rotate each valve plate independently gives an additional degree of freedom, which can be used to adjust the pre- and decompression angle for different operating points and for different setting ratios, see fig. 1b. This idea has recently been presented and patented in [6].

This paper investigates whether this degree of freedom can be used to overcome the issues stated above on the example of an axial piston pump of the swash plate type. Basic considerations for port design and the state of the art for valve plate rotation (for pumps with one valve plate) are summarised in sec. 2. A double pump with

opposing pistons and rotating valve plates is simulated, and a methodology to optimise valve plate kidney angles is suggested in sec 3. In section 4, optimisation results are presented. The results are discussed in sec. 5, and the most important findings are summarised in sec. 6.

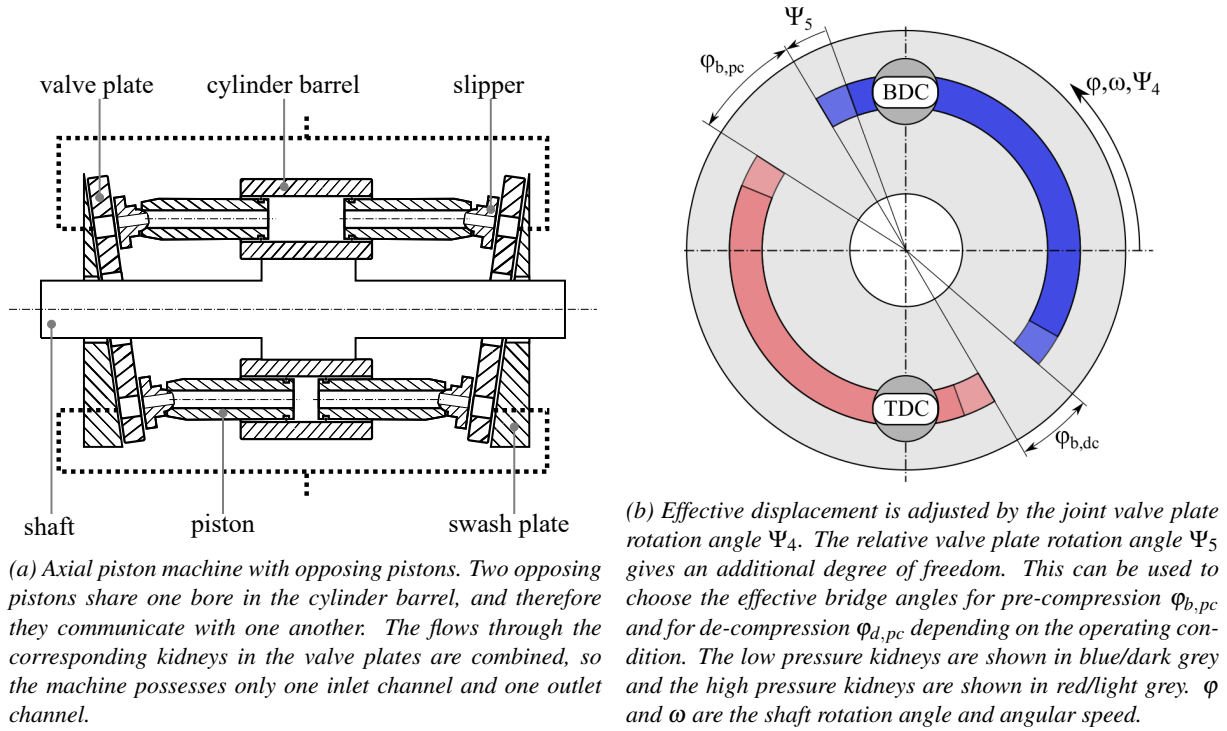


Figure 1: Sketch of double pump with opposing pistons and the additional degree of freedom due to having two valve plates.

2 State of the Art

In the following, the basics of port design (sec. 2.1) and valve plate rotation for machines with one valve plate (sec. 2.2) are summarised, so that the background for the idea of adding a degree of freedom by using a double pump with opposing pistons in sec. 3 is given.

2.1 Basics of Port Design

In positive displacement pumps, the displacement volume needs to be connected to the low pressure (LP) kidney to take in fluid and the high pressure (HP) kidney to deliver the fluid. So-called bridges separate the two kidneys and prevent cross-porting (i.e., flow from the HP kidney to the LP kidney through a direct connection provided by the displacement volume) at commutation. Typically, commutation takes place around the dead centres, where the axial piston speed is low [4]. In axial piston machines, the kidneys are located in the valve plates, which are designed to separate the inlet channel from the outlet channel and to provide a smooth pressure transition for each piston chamber. A fixed valve plate cannot provide a smooth pressure transition for all operating conditions [7]. Figure 2 shows a zero-lapped valve plate and the corresponding flow into and out of one pump chamber. In a zero-lapped valve plate, the bridge between the HP kidney and the LP kidney covers exactly the opening of one displacement volume. That means that the zero-lapped valve plate separates the HP kidney from the LP kidney, but no pre- or decompression takes place. This leads to flow pulsations due to the compressibility of the fluid.

To calculate the flow for one displacement volume (i.e., in case of axial piston pumps for each cylinder), the continuity equation can be used [8]:

$$\sum q = \frac{dV_{cyl}}{dt} + \frac{V_{cyl}}{\beta_e} \frac{dp}{dt} \quad (1)$$

The first summand of eq. 1 represents the kinematic flow, whereas the second summand represents the compressible flow, with β_e being the effective bulk modulus, $\frac{dp}{dt}$ being the rate of pressure change inside the cylinder, and V_{cyl} being the cylinder volume. For axial piston machines of the swash plate type, the cylinder volume can be calculated as

$$V_{cyl} = V_{dead} + (1 + \sin \varphi) \tan \alpha R_b A_p \quad (2)$$

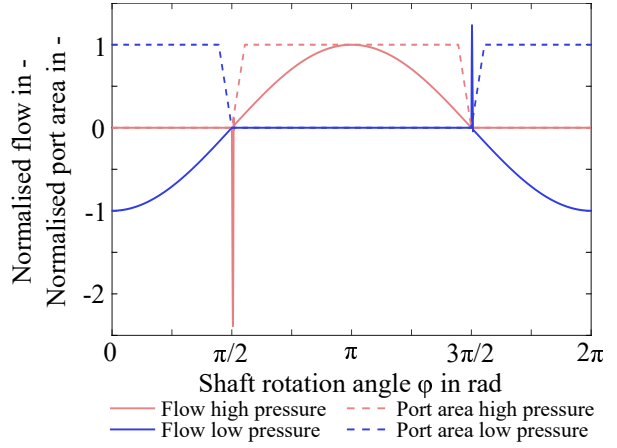
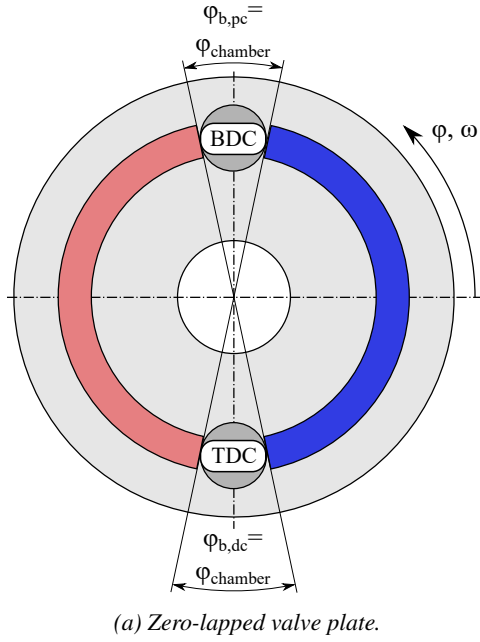


Figure 2: For a zero-lapped valve plate, the bridge angles $\varphi_{b,pc}$ and $\varphi_{b,dc}$ are identical with the swept angle over one of the openings from a displacement chamber $\varphi_{chamber}$ to the valve plate. In this figure, commutation takes place at bottom dead center and top dead center. At commutation, pressure equalisation leads to compressible flow pulsations.

with the cylinder's dead volume V_{dead} , the shaft rotation angle φ , the swash plate angle α , the barrel radius R_b and the piston area A_p . Thus, the kinematic flow is

$$\frac{dV_{cyl}}{dt} = \omega \cos \varphi \tan \alpha R_b A_p . \quad (3)$$

In order to reduce compressible flow pulsations in fluid power machines, pre-compression takes place before the displacement volume connects to the HP kidney and de-compression takes place before the displacement volume connects to the LP kidney. The angle at bottom dead center (BDC) is larger than the angle at top dead center (TDC), as the fluid volume at BDC is larger [2]. The principle design for a valve plate depending on the operating quadrant can be seen in fig. 3.

The quasi-static pressure change during pre- and de-compression with eq. 1 and $\sum q = 0$ can be calculated as

$$p_2 - p_1 = \beta_e \ln \frac{V_{cyl,1}}{V_{cyl,2}} \quad (4)$$

with the index 1 representing the state when entering the bridge and index 2 representing the state when leaving the bridge.

Equation 4 shows that pre- and decompression as shown in fig. 3 can only be customised to one pressure level. For this reason, pressure relief grooves are typically used. They provide a small channel, which smoothens the pressure transition for a wider range of pressure levels. However, the flows through the pressure relief grooves lead to undesired losses, so that pressure relief grooves are seen as a "necessary evil" [7].

2.2 Displacement Control Through Valve Plate Rotation for Pumps with One Valve Plate

In [2], the concept of displacement control through valve plate rotation has been summarised. Figures 4 and 5 visualise the principle: When the commutation is moved away from TDC and BDC, the kinematic flow while connected to the HP kidney becomes negative for some degrees of shaft rotation, and thus the effective stroke is reduced. This enables valve plate rotation to continuously adjust the effective displacement, and it is possible to switch between pump and motor mode. The setting ratio ε of the machine follows eq. 5

$$\varepsilon = \cos \varphi_{VP} \quad (5)$$

where φ_{VP} is the valve plate rotation angle.

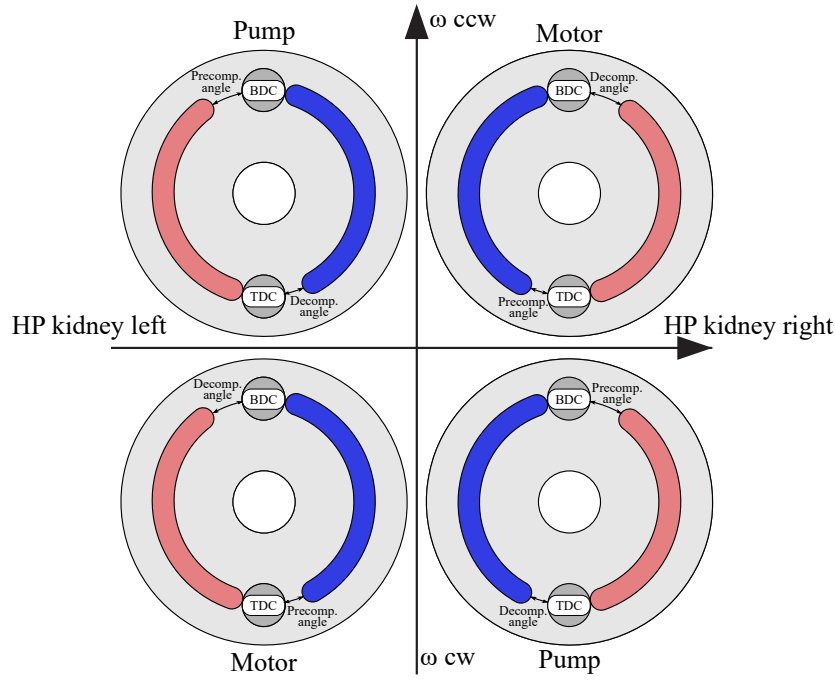


Figure 3: Principle design of optimised valve plate design for different operating quadrants for a fluid power pump/motor [2]. The bridge angles are larger than $\varphi_{chamber}$, therefore pre- and decompression take place. Compressible flow pulsations are reduced by pre- and decompression during commutation.

A challenge for displacement control via valve plate rotation is caused by the commutation and pre- and decompression angles, as the commutation does not take place around the dead centres. Differentiating eq. 2 with respect to the shaft rotation angle φ delivers the change of a chamber volume by φ :

$$\frac{dV_{cyl}}{d\varphi} = \cos \varphi \tan \alpha R_b A_p \quad (6)$$

Equation 6 shows that $|\frac{dV_{cyl}}{d\varphi}|$ is largest at $\varphi = 0$ and $\varphi = \pi$, whereas it is zero at $\varphi = \pi/2$ and $\varphi = 3/2\pi$ (where commutation usually takes place). For this reason, the same pre-/de-compression angles lead to higher maximum and lower minimum pressures, when the commutation takes place at greater distance from the dead centres (see eq. 4).

Additionally, the kidney opening/closing takes place gradually. Assuming a positive overlap, the kidney opening reduces to 0 m² when a cylinder enters a bridge. Especially during the end of the closing process, a significant throttling effect appears, which is reinforced by high axial piston velocities [4]. Due to this throttling effect,

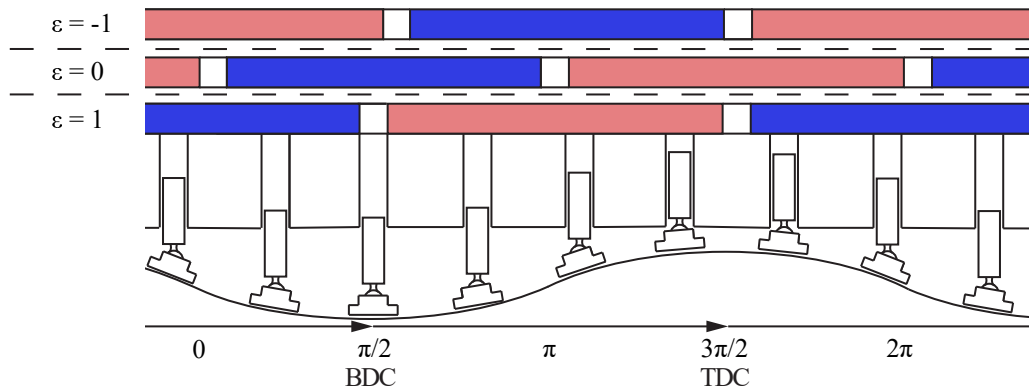


Figure 4: A valve plate in full motor-mode ($\varepsilon=-1$), no-flow-mode ($\varepsilon=0$) and full pump-mode ($\varepsilon=1$). Red/light grey rectangles symbolise the high-pressure kidney and blue/dark grey rectangles symbolise the low-pressure kidney for one full shaft rotation from 0 to 2π [2].

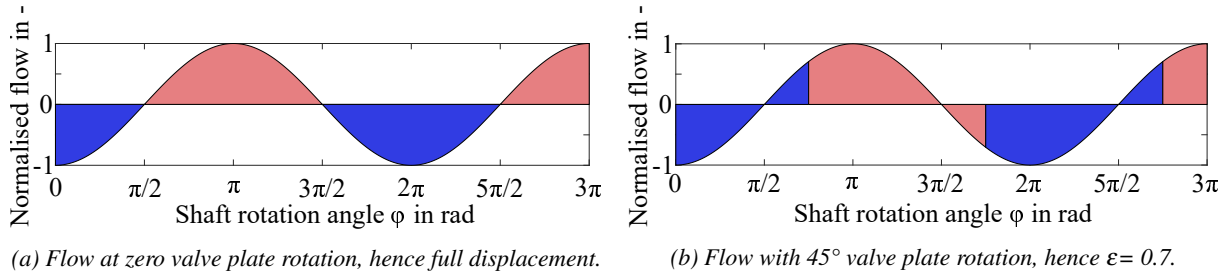


Figure 5: Normalised kinematic flow from one cylinder. Blue/dark grey areas are the volumes entering the cylinder from the low-pressure kidney and red/light grey are the volumes leaving the cylinder to the high-pressure kidney [2].

[7] states that it is "never a good idea" to even place one of the support ribs (which are typically used to improve the structural stability of the valve plate on the HP side) at the location of maximal axial piston speed.

The severity of this phenomenon is visualised in fig. 6, which shows the maximal and minimal chamber pressures occurring for zero-lapped valve plates during one shaft revolution, over the valve plate position. The maximal and minimal pressures occur at the reduced port area around commutation, due to the above described throttling effect. For a valve plate rotation of 0 or π , commutation takes place at the dead centres, hence at minimal axial piston speed. For a valve plate rotation of $\pi/2$ or $3\pi/2$, commutation is moved to a maximum distance from the dead centres, and so also to the location of maximum axial piston speeds and the maximum values of $|\frac{dV_{cyl}}{d\phi}|$. Therefore, the risk of cavitation and high pressure peaks is increased. Of course, higher pump speeds also lead to higher piston speeds, as well as increasing maximal pressures and decreasing minimal pressures.

Between π and 2π valve plate rotation, the maximal pressure is higher than between 0 and π , because the chamber is loaded with HP before the commutation between BDC and TDC (where the port restriction leads to pressure overshoots). Analogous considerations can be made for pressure undershoots in the LP kidney. When the chamber volume is increased (between TDC and BDC) around commutation, the port restrictions lead to pressure undershoots. These undershoots are more profound when the chamber is already at LP before commutation. When evaluating the pressure undershoots, it must be considered that a simplified calculation of the bulk modulus is applied. More details on the bulk modulus calculation can be found in sec. 3.1.

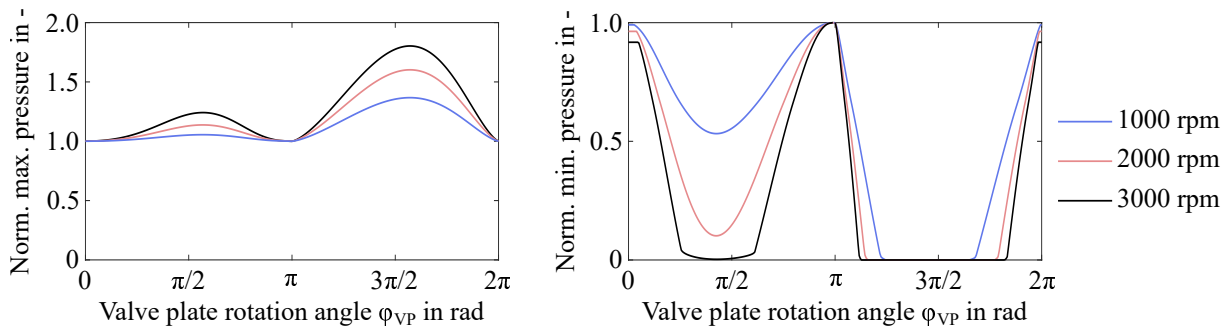


Figure 6: Throttling effect for zero-lapped valve plate: maximal and minimal pressures in chambers during one shaft revolution over angle of valve plate rotation. These graphs correspond to the machine described in sec. 3.1, with both valve plates being zero-lapped and in identical positions.

3 Valve Plate Rotation for a Double Pump with Opposing Pistons

In order to evaluate the potential of a double pump of opposing piston type with two valve plates, a simulation model is created. Optimisation is used to find the optimal kidney angles and valve plate rotation angles for given sets of operating points. Simulation results are evaluated by an objective function.

3.1 Simulation Model

A Hopsan model is used to simulate the steady-state behaviour of the pump for given kidney and valve plate rotation angles. Hopsan is a one-dimensional multi-domain simulation tool using the transmission line theory. Figure 7 illustrates the pump simulation model used in this paper. For each displacement chamber, the model consists of a volume, which is connected to the HP source resp. the LP source through orifices. As this paper investigates a double pump with opposing pistons, see fig. 1a, two pistons share one displacement volume. Each

displacement volume is connected to both valve plates, and each valve plate has two kidneys. The ends of the kidneys are rectangular, in order to provide a larger passage area than circular ends. The size of each displacement volume depends on the shaft angle, and the area and circumference of each orifice depend on the shaft rotation angle and the valve plate rotation angles.

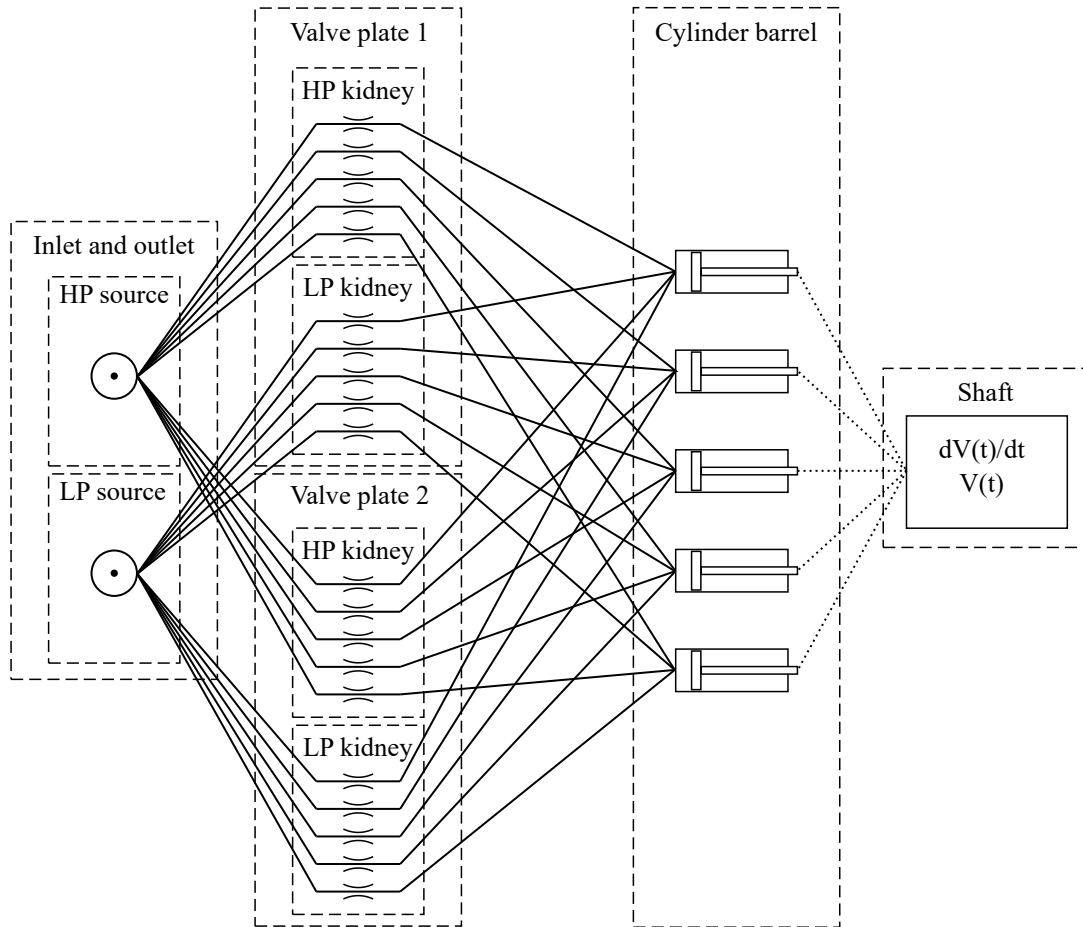


Figure 7: Illustration of pump model structure. Of course, any number of cylinders can be implemented.

The fluid's effective bulk modulus β_e for each displacement chamber is calculated as

$$\beta_e = \frac{\beta_{oil}}{1 + \frac{x_0}{\kappa p} \frac{\beta_{oil}}{1-x_0} \left(\frac{p_0}{p}\right)^{\frac{1}{\kappa}}} \quad (7)$$

with β_{oil} being the oil's bulk modulus, x_0 being the volume fraction of undissolved air at reference pressure p_0 , p being the pressure in the chamber and κ being the isentropic expansion factor of air.

Eq. 7 assumes that both the oil and the undissolved air change their volume based on the respective bulk moduli, but no air is dissolved or released. This neglects the phenomenon of cavitation, which describes the release of air from oil below ambient pressure, which reduces the bulk modulus [9]. As cavitation is neglected in this paper, the pressure undershoots are overestimated (i.e., considering cavitation would lead to higher minimum pressure levels).

The most relevant parameters of the simulated machine are shown in tab. 1.

3.2 Optimisation

In this paper, the *kidney angles* are defined by the relative position of the kidneys and their opening and closing to one another. In combination with the joint valve plate rotation angle and the relative valve plate rotation angle, the *effective port angles* are defined.

To design the valve plates, there are three degrees of freedom for the kidney angles of the valve plate, as there are three relative positions to be chosen for the kidneys' opening and closing angles. In this paper, both valve plates have the same kidney angles in order to simplify the problem. Furthermore, pressure relief grooves are not

Table 1: Parameters of simulated machine.

Quantity	Value
Type	Swash plate
Displacement volume	35 cm ³ /rev
Number of pistons	2x11
Swash plate angle	8 deg
Dead volume ratio	0.70
Swept chamber angle	26.9 deg

investigated. Additional to the three degrees of freedom for the kidney angles there are two degrees of freedom for the valve plate rotation angles (one for their joint rotation, and one for their relative rotation).

In order to solve this multi-dimensional optimisation problem, the complex-RF optimisation algorithm is used. Complex-RF is a single objective, non-gradient optimisation algorithm. It modifies Box's complex method [10] by adding a randomisation factor to avoid pre-mature collapsing of the complex and a forgetting factor which ensures that older parameter sets are replaced by more recent ones [11].

The operating points considered in this paper are shown in tab. 2. In this paper, speed and pressure are fixed, but the outlet flow is varied between different setting ratios. An explicit weighting or trade-off between the operating points does not take place in this paper, i.e., each operating point has the same weight.

Table 2: Operating points considered for valve plate optimisation. A setting ratio of 100% of the ideal flow cannot be reached due to the compressibility of the fluid. Therefore, as reference for "full" displacement, the outlet flow of non-rotated zero-lapped valve plates is used.

Quantity	Value
Setting ratio	0.9862, 0.75, 0.5, 0.25, 0
Speed	separate optimisations for: 1500 rpm, 3000 rpm
Outlet pressure	15 MPa
Inlet pressure	0.5 MPa
Volume ratio of undissolved air at 0.1 MPa	0.01
Effective bulk modulus	1.8 GPa

3.2.1 Setup of Optimisation

The preprocessing, optimisation algorithm and post-processing are implemented in MATLAB. The simulation is carried out in Hopsan through the Hopsan API. The variables $\Psi_1 - \Psi_5$ are sketched in fig. 8 and summarised in tab. 3.

The optimisation procedure is illustrated in fig. 9. The angle ϕ_{ref} is chosen arbitrarily during pre-processing. The variables $\Psi_1 - \Psi_3$ define the kidney angles and they are the optimisation variables for the outer optimisation loop. As the pressures at commutation are highly dependent on the bridge angles, Ψ_1 and Ψ_3 are chosen to explicitly represent bridge angles, rather than choosing an absolute reference for each kidney start/end angle and thus implicitly defining the bridge angles.

For a given set of kidney angles, the ideal valve plate rotational angles Ψ_4 and Ψ_5 for each operating point must be found in an inner optimisation loop. Ψ_4 represents the joint rotation of both valve plates, which mainly affects the effective displacement of the machine, whereas Ψ_5 represents the relative rotation between the two valve plates, which mainly effects the effective pre- and de-compression angles.

The objective function values of the inner loop are returned to the outer loop. The objective function value of the outer loop is the sum of the objective function values of the inner optimisation loop (one value for each operating point). Thus the potential of the kidney angles can be evaluated.

3.2.2 Formulation of Objective Function

The valve plates (in combination with their rotations) must fulfil several goals, which are combined into one objective function as Complex-RF is a single-objective optimisation method. The aim is to minimise power losses as well as flow pulsations (both in the HP channel and the LP channel). The constraints are as follows: the correct flow level must be provided in the HP channel, the minimum pressure is not to go below a defined threshold and a

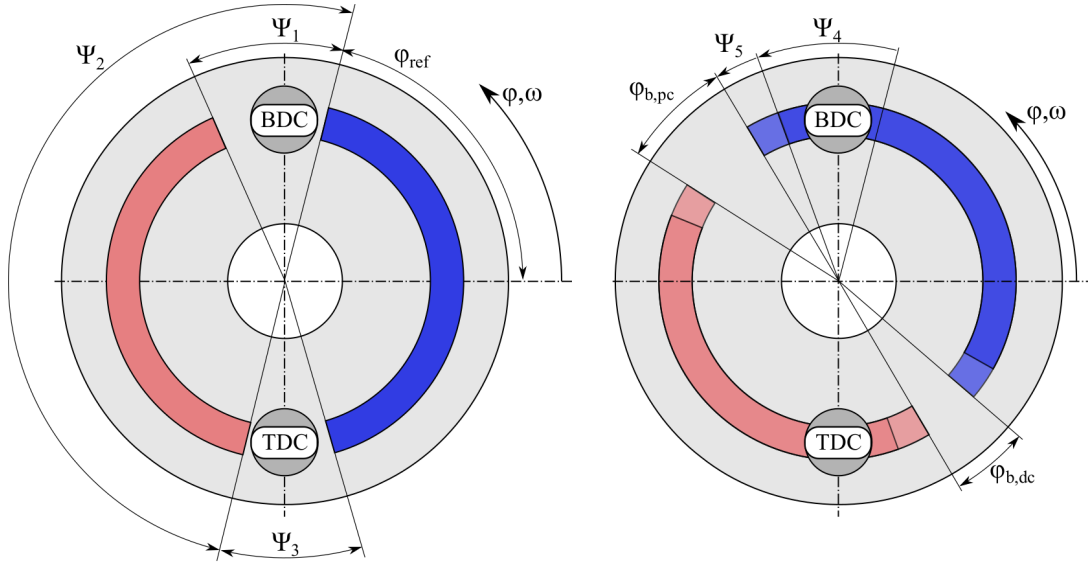


Figure 8: Sketch of optimisation variables. Left: both valve plates are in the same position. Right: Both valve plates are rotated jointly by Ψ_4 , and one valve plate is rotated further by Ψ_5 . ϕ_{ref} is set arbitrarily; Ψ_1 - Ψ_3 are optimised in the outer loop, and Ψ_4 - Ψ_5 are optimised in the inner loop.

Table 3: Optimisation variables

Symbol	Quantity	Unit
Ψ_1	Bridge angle between closing LP kidney and opening HP kidney	deg
Ψ_2	Angle between closing of LP kidney and closing of HP kidney	deg
Ψ_3	Bridge angle between closing HP kidney and opening LP kidney	deg
Ψ_4	Joint rotation angle of both valve plates	deg
Ψ_5	Relative rotation angle between the valve plates	deg

defined maximum pressure is not to be exceeded. The constraints are implemented as soft constraints, i.e., they are implemented as part of the objective function. Equation 8 shows the objective function of the outer loop, which is the sum of the inner loop objective function values of the individual operating points.

$$f_{total}(\Psi_1, \dots, \Psi_5) = \sum_{OP} f_{innerLoop} \quad (8)$$

Equation 9 is the objective function of the inner loop, which consists of the constraints as well as the objectives. The constraints are formulated with an exponential increase of objective function value when they are violated, so that the objective function value increases drastically in case of constraint violation.

$$f_{innerLoop}(\Psi_1, \dots, \Psi_5) = f_{p,losses} + f_{q,pulse,HP} + f_{q,pulse,LP} + f_{p,min} + f_{p,max} + f_{q,mean,HP} \quad (9)$$

In the following, the mathematical formulation of the inner loop's objective function and its components are explained in eq. 10 to 16. Parameters named f represent function values for the respective part of the objective function, parameters named g represent linear weighting factors and parameters named h represent weighting factors in the exponent of an exponential function.

Objectives

The power losses are calculated from the hydraulic and mechanical power. The function value for power losses increases linearly with the power losses, see eq. 10.

$$f_{p,losses}(\Psi_1, \dots, \Psi_5) = g_{p,losses}(p_{high}q_{mean,HP} - p_{low}q_{mean,LP} - T\omega) \quad (10)$$

The flow pulsations in the HP channel are calculated as the difference between the highest instantaneous flow and the lowest instantaneous flow in the HP channel. The function value for HP flow pulsations increases linearly with

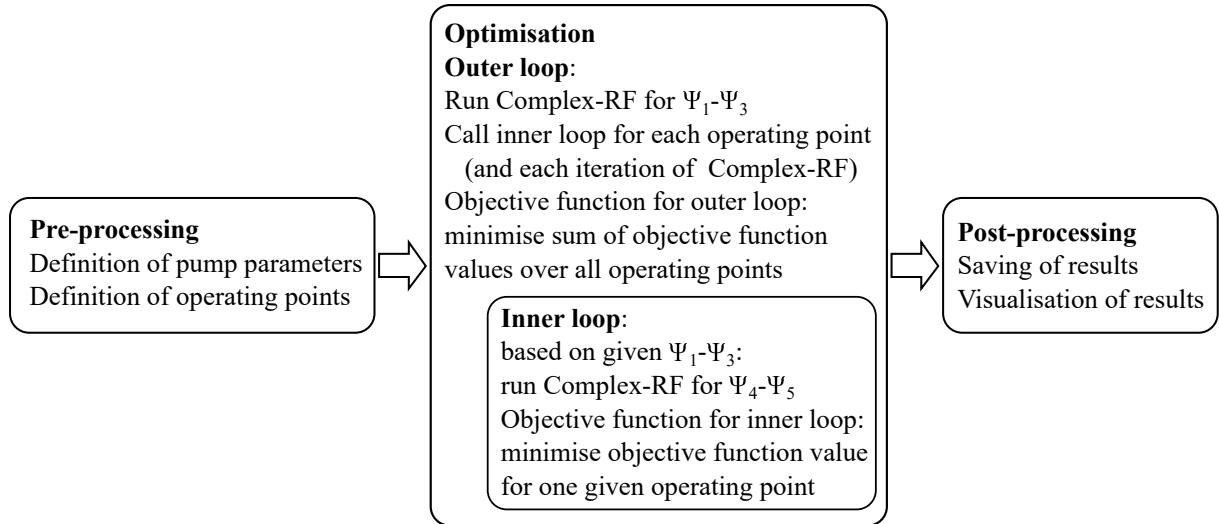


Figure 9: Setup of optimisation.

the peak-to-peak value of the flow, see eq. 11.

$$f_{q,pulse,HP}(\Psi_1, \dots, \Psi_5) = g_{q,pulse,HP}(\max(q_{HP}) - \min(q_{HP})) \quad (11)$$

The flow pulsations in the LP channel and their function value are calculated analogous to the flow pulsations in the HP channel, see eq. 12.

$$f_{q,pulse,LP}(\Psi_1, \dots, \Psi_5) = g_{q,pulse,LP}(\max(q_{LP}) - \min(q_{LP})) \quad (12)$$

In this paper, the weighting factors $g_{P,losses}$ and $g_{q,pulse,HP}$ are chosen so that the function values $f_{P,losses}$ and $f_{q,pulse,HP}$ are in the same order for a pump running at full displacement. In comparison to the HP channel flow pulsations, the energy level of LP channel flow pulsations is significantly lower. LP channel flow pulsations are therefore considered less relevant, thus $g_{q,pulse,LP} < g_{q,pulse,HP}$.

A methodological trade-off between the power losses, and the flow pulsations in the HP and LP channel is not considered in this paper.

[12] investigates Pareto fronts for the multi-objective optimisation of fluid power machines and shows that the Pareto fronts for the trade-off between two performance values (e.g., flow pulsations in the HP channel vs. the LP channel) can be quite sharp. That means that a large improvement in one performance value can be enabled without a significant deterioration of the other performance value. By including the above named quantities in the objective function, unnecessarily poor values for individual quantities can be avoided, even when no methodological trade-off is carried out.

Soft constraints

A defined minimum pressure level must be guaranteed, so that cavitation is avoided. This is necessary because cavitation causes noise and can damage the machine. To penalise cavitation, eq. 13 is implemented: When the minimum pressure is above the threshold p_{cav} , the function value $f_{p,min}$ is 0. In this paper, p_{cav} is set to 0.05 MPa. When minimum pressure is between 0 MPa and p_{cav} , $f_{p,min}$ increases exponentially with increasing distance from p_{cav} . Due to the simplified bulk modulus calculation (see sec. 3.1), it is possible that absolute pressures of 0 MPa are calculated. When a pressure of 0 MPa is provided as a simulation result, it is important that solutions that are further away from being cavitation-free have increased objective function values, so that the algorithm can find the direction to better solutions. For this purpose, the effective closing angle of the low-pressure kidney ($\varphi_{ref} + (\Psi_4 + \Psi_5)$) and the effective length of the bridge before entering the low-pressure kidney ($\Psi_3 - \Psi_5$) are used as proxies, see eq. 14.

$$f_{p,min}(\Psi_1, \dots, \Psi_5) = \begin{cases} 0, & \text{for } p_{min} \geq p_{cav} \\ g_{p,min}(e^{h_{p,min}(p_{cav} - p_{min})} - e^0), & \text{for } 0 < p_{min} \leq p_{cav} \\ g_{p,min}(e^{h_{p,min}p_{cav}} - e^0 + f_{decomp} + f_{close,LP}), & \text{for } p_{min} = 0 \end{cases} \quad (13)$$

with

$$f_{\text{decomp}}(\Psi_3, \dots, \Psi_5) = g_{\text{decomp}} e^{h_{\text{decomp}}(\Psi_3 - \Psi_5)} \quad (14a)$$

$$f_{\text{close,LP}}(\varphi_{\text{ref}}, \Psi_4, \Psi_5) = \begin{cases} 0, & \text{for } \varphi_{\text{ref}} + (\Psi_4 + \Psi_5) \geq 90^\circ - \frac{\varphi_{\text{chamber}}}{2} \\ g_{\text{close,LP}} e^{h_{\text{close,LP}}(90^\circ - \varphi_{\text{chamber}} - (\varphi_{\text{ref}} + (\Psi_4 + \Psi_5)))}, & \text{for } \varphi_{\text{ref}} + (\Psi_4 + \Psi_5) < 90^\circ - \frac{\varphi_{\text{chamber}}}{2} \end{cases} \quad (14b)$$

Pressure peaks need to be limited because they can cause noise, vibrations and damages. Pressure peaks that exceed the delivery pressure by a certain percentage are considered as acceptable and therefore receive a function value $f_{p,\text{max}}$ of 0, see eq. 15. In this paper, k_{HP} is chosen to be 1.2, i.e., a pressure overshoot of 20% is allowed. Higher pressures lead to an increasing objective function value. As pressure peaks increase aggressively when too much pre-compression takes place, no exponential function is applied here.

$$f_{p,\text{max}}(\Psi_1, \dots, \Psi_5) = \begin{cases} 0, & \text{for } p_{\text{max}} \leq k_{\text{HP}} p_{\text{high}} \\ g_{p,\text{max}}(p_{\text{max}} - k_{\text{HP}} p_{\text{high}}), & \text{for } p_{\text{max}} > k_{\text{HP}} p_{\text{high}} \end{cases} \quad (15)$$

The desired flow level needs to be provided. Therefore, any deviations from the objective flow level lead to an increasing objective function value $f_{q,\text{mean,HP}}$, see eq. 16.

$$f_{q,\text{mean,HP}}(\Psi_1, \dots, \Psi_5) = g_{q,\text{mean,HP}}(e^{h_{q,\text{mean,HP}}|q_{\text{mean,HP,expected}} - q_{\text{mean,HP}}|} - e^0) \quad (16)$$

3.3 Joint Rotation of Zero-lapped Valve Plate as Reference

In order to evaluate the quality of the results of valve plate rotation, a "benchmark" is needed. For this benchmark, the pump as described in sec. 3.1 is equipped with two zero-lapped valve plates, which are rotated jointly. The valve plate position is chosen so that the flow objectives as described in tab. 2 are met. The small deviations of the valve plate positions in comparison to eq. 5 originate from compressible flow.

4 Results

In this section, the optimisation results for both the zero-lapped valve plates and optimised solutions are presented.

4.1 Joint rotation of zero-lapped Valve Plates

As stated in sec. 3.3, joint rotation of zero-lapped valve plates is used as a comparison for each operating point. The angular positions of the kidneys are visualised in fig. 10. The corresponding objective function values are shown in fig. 14 and 15. The most important results are summarised in tab. 4 and 6.

At low speeds, the losses at full displacement are high due to insufficient pre-compression resulting in large back-flow. The objective function values at low setting ratios are relatively good, as no large pre- and de-compression angles are desired.

With increasing speeds, the performance at low displacements deteriorates due to cavitation and high-pressure peaks, which can be explained by the throttling effect as presented in sec. 2.2.

4.2 Optimised Valve Plates with Relative Rotation

The angular positions of the kidneys for each operating point are visualised in fig. 11 to 13. The corresponding objective function values are shown in fig. 14 to 15. The most important results are summarised in tab. 4 to 6.

Both at 1500 and 3000 rpm, the results show a great similarity to zero-lapped valve plates. This is motivated by the choice of operating points. Zero-lapped valve plates perform relatively well in operating points with low setting ratios, as commutation takes place at high piston speeds and low pre- and de-compression is desired. As no weighting between the displacement settings has taken place, the influence of the small displacement settings is significant. Furthermore, there is (almost) no relative rotation between the valve plates. Having both valve plates in the same position offers the advantage of being able to use the passage ways on both sides of the pump, which reduces the throttling effect in comparison to using only one passage way (which is the case when relative valve plate rotation takes place). However, the results for the optimised valve plates show reduced flow pulsations and power losses.

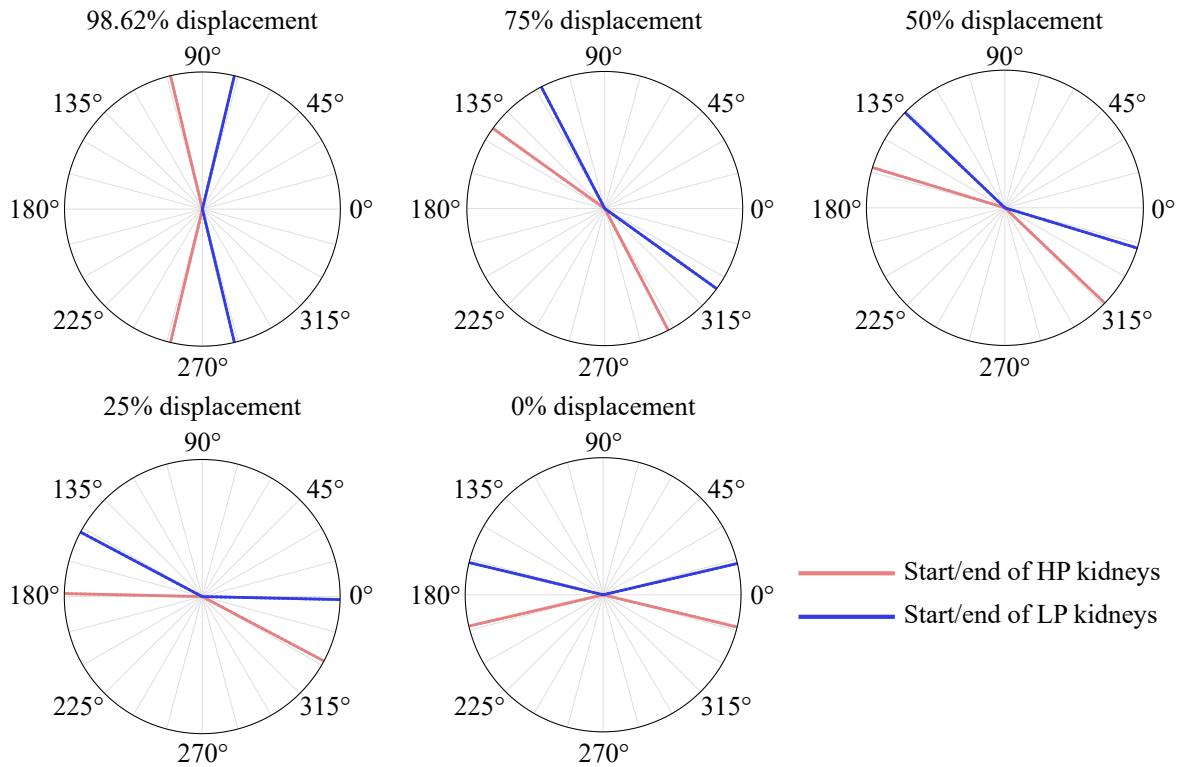


Figure 10: Visualisation of kidney positions of jointly rotated zero-lapped valve plates for each setting ratio at 1500 rpm and 15 MPa. The kidney positions differ only marginally between 1500 rpm and 3000 rpm, so no additional plots for 3000 rpm are shown. The lines indicate the angular position of the kidney's beginning and end for each setting ratio. The LP kidney is between the blue (dark grey) lines, and the HP kidney is between the red (light grey) lines. BDC is located at 90°, TDC at 270°. The direction of rotation is ccw.

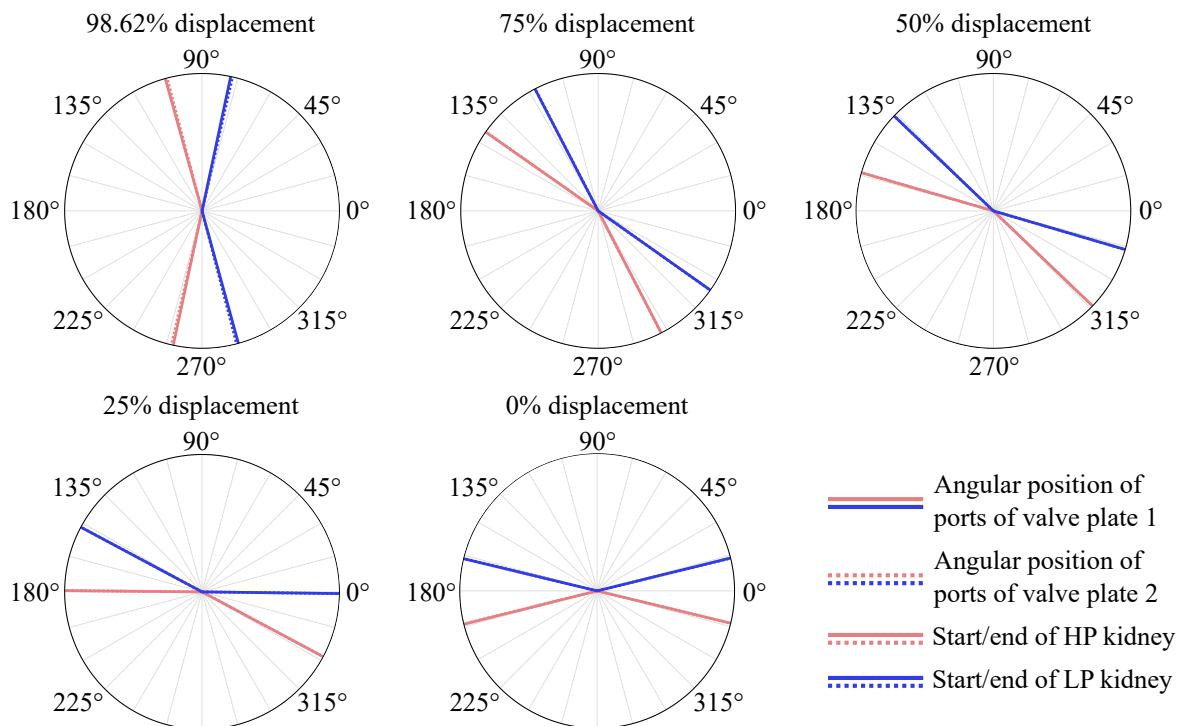


Figure 11: Visualisation of kidney positions which are optimised for valve plate rotation at 1500 rpm and 15 MPa, with setting ratios from 0 to 98.62%. The lines indicate the angular position of the kidney's beginning and end for each setting ratio. The LP kidney is between the blue (dark grey) lines, and the HP kidney is between the red (light grey) lines. BDC is located at 90°, TDC at 270°. The direction of rotation is ccw. As both valve plates are at almost the same position, only one of the can be seen.

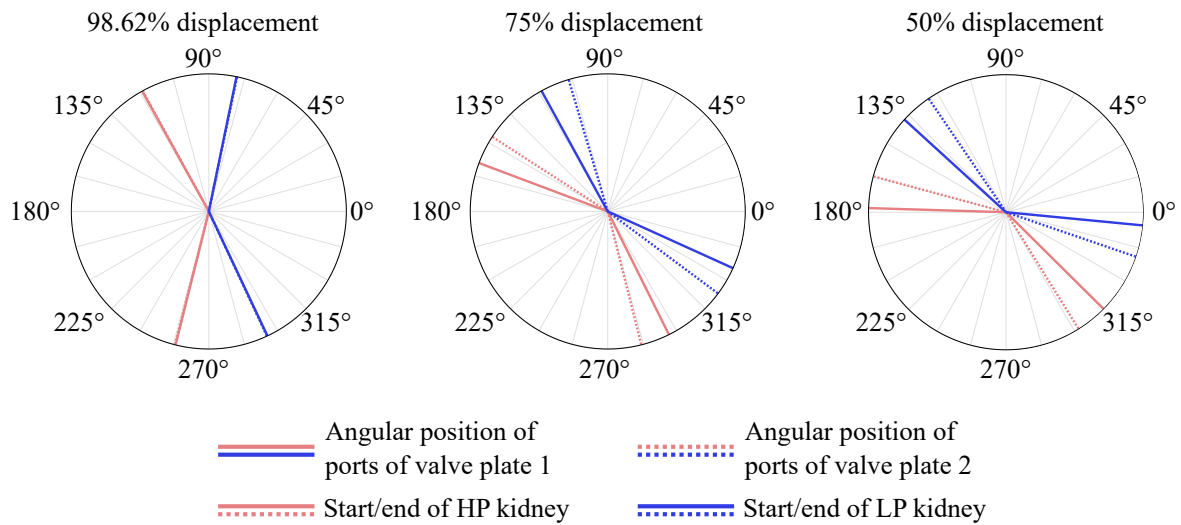


Figure 12: Visualisation of kidney positions which are optimised for valve plate rotation at 1500 rpm and 15 MPa, with setting ratios only from 50 to 98.62%. The lines indicate the angular position of the kidney's beginning and end for each setting ratio. The LP kidney is between the blue (dark grey) lines, and the HP kidney is between the red (light grey) lines. BDC is located at 90°, TDC at 270°. The direction of rotation is ccw.

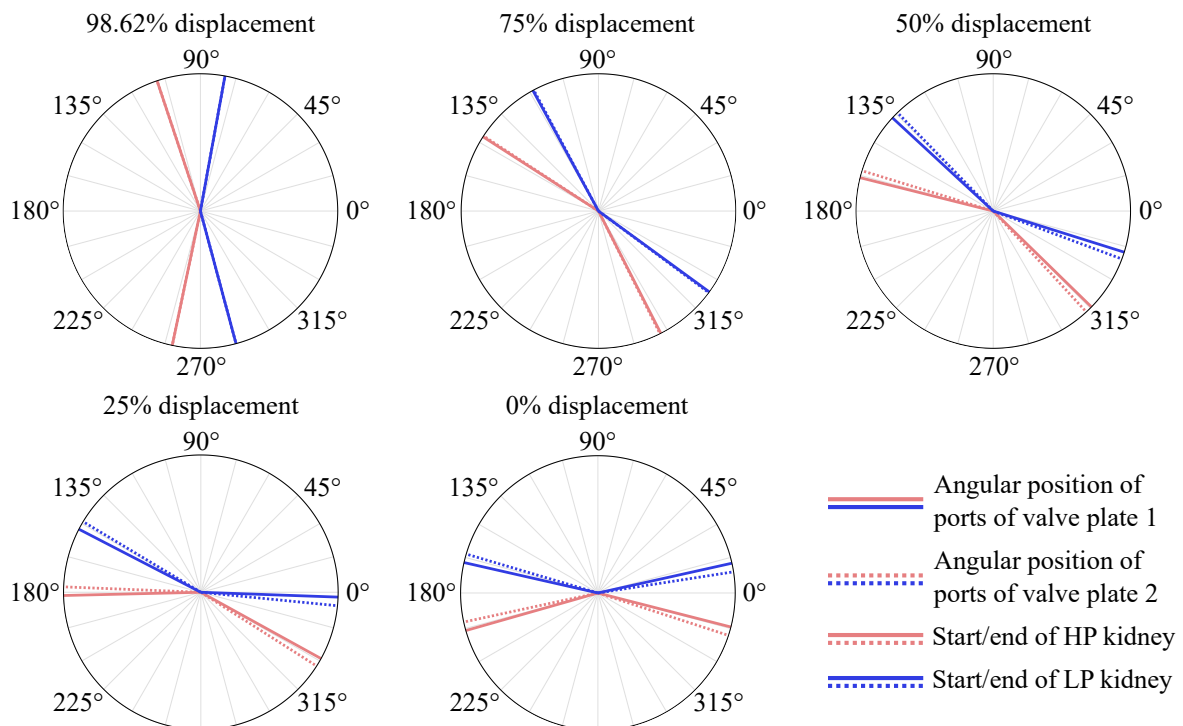


Figure 13: Visualisation of kidney positions which are optimised for valve plate rotation at 3000 rpm and 15 MPa. The lines indicate the angular position of the kidney's beginning and end for each setting ratio. The LP kidney is between the blue (dark grey) lines, and the HP kidney is between the red (light grey) lines. BDC is located at 90°, TDC at 270°. The direction of rotation is ccw.

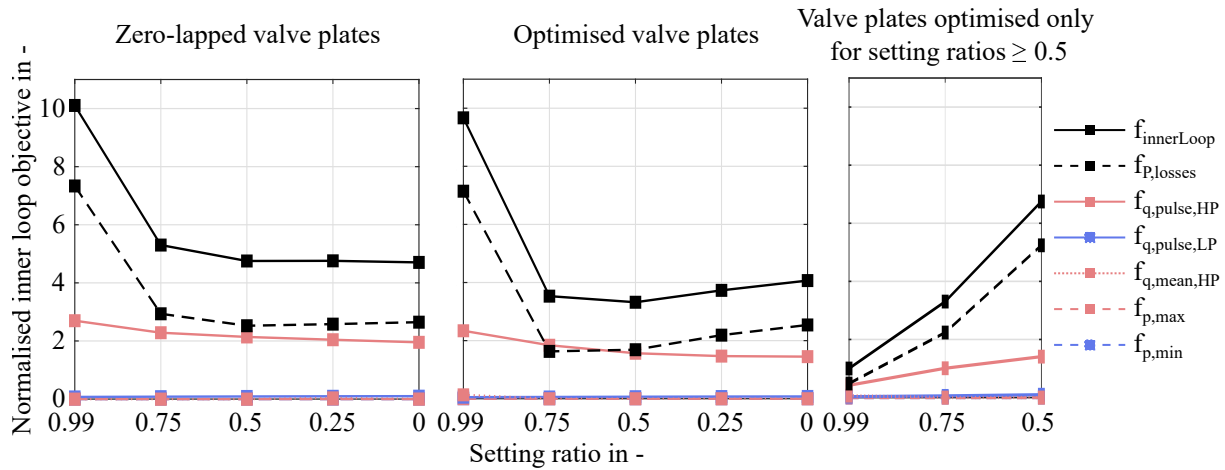


Figure 14: Visualisation of total objective function values and their compositions for each setting ratio for zero-lapped valve plates (left), for valve plates optimised for setting ratios from 0.9862 to 0 (center) and for valve plates optimised only for setting ratios from 0.9862 to 0.5 (right) at 1500 rpm and 15 MPa. The inner loop objectives are normalised with respect to the lowest inner loop objective for all results presented in this paper, i.e., the lowest normalised objective is 1 and all other objectives are relative to it.

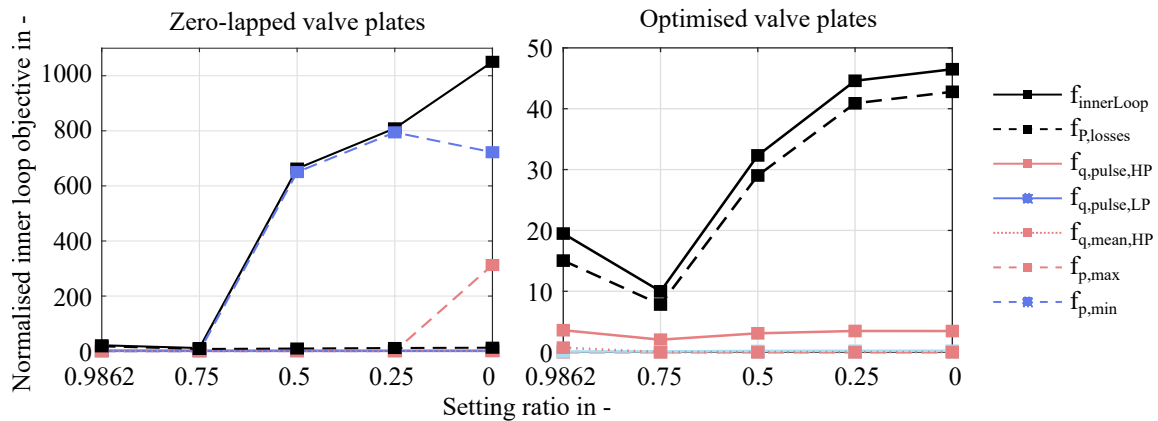


Figure 15: Visualisation of total objective function values and their compositions for each setting ratio for zero-lapped valve plates (left) and for optimised valve plates (right) at 3000 rpm and 15 MPa. Please mind the individual y-axes. The inner loop objectives are normalised with respect to the lowest inner loop objective for all results presented in this paper, i.e., the lowest normalised objective is 1 and all other objectives are relative to it.

The choice and weighting of displacement settings has a significant influence on the optimisation results. For operation at 1500 rpm and 150 bar, another optimisation is carried out omitting the lowest setting ratios and only optimising for setting ratios of 0.9862, 0.75 and 0.5 (with equal weights). Naturally, the optimisation results differ from those considering setting ratios down to 0. The optimisation results and their objective function values are visualised in fig. 12 and 14. The most important numerical values are summarised in tab. 5. The effective bridge angles at full displacement are massively increased, leading to significantly reduced power losses and flow pulsations. For partial displacement, relative valve plate rotation is increased in order to avoid cavitation and high-pressure peaks. The effective bridge angles at 50% displacement are lower than for the solution considering setting ratios down to 0.

At 3000 rpm, objective function values are generally higher than at 1500 rpm, as the absolute levels of flow pulsations and power losses are higher. The effective bridge angle used for pre-compression is larger than the effective bridge angle for de-compression. It can also be seen that the more the commutation is moved away from the dead centres, the smaller the effective bridge angles become, so increased relative valve plate rotation occurs. This aligns with the expectations based on sec. 2.1. It is noteworthy that for reduced displacement settings, the effective bridge angle for de-compression allows several degrees of cross-porting, i.e., a direct communication between the HP kidney and LP kidney through the cylinder is enabled. This is necessary, as otherwise cavitation would occur in the chamber, caused by the throttling effect as described in sec. 2.2. Naturally, cross-porting leads to increased losses. The same phenomenon occurs for the effective bridge angle for pre-compression as well, but

Table 4: Results for zero-lapped and for optimised valve plate in comparison (1500 rpm, 15 MPa).

Setting ratio in -	Zerolapped valve plate					Optimised valve plate				
	0.9862	0.75	0.5	0.25	0	0.9862	0.75	0.5	0.25	0
φ_{ref} in deg 76.6 77.2				
Ψ_1 in deg $\varphi_{chamber}=26.9$ 27.6				
Ψ_2 in deg 180 179.9				
Ψ_3 in deg $\varphi_{chamber}=26.9$ 27.4				
Ψ_4 in deg	0	40.8	59.7	75.3	89.8	0	40.2	59.1	74.7	89.2
Ψ_5 in deg 0					0.8	0.1	0.0	0.0	0.1
$\varphi_{b,pc}$ in deg $\varphi_{chamber}=26.9$					26.8	27.5	27.5	27.5	27.5
$\varphi_{b,dc}$ in deg $\varphi_{chamber}=26.9$					26.6	27.4	27.4	27.4	27.4
p_{max} in MPa	15.01	15.34	15.72	16.07	16.32	15.01	15.43	16.12	17.04	17.99
p_{min} in MPa	0.490	0.283	0.188	0.159	0.175	0.490	0.234	0.096	0.060	0.093
$q_{mean,HP}$ in l/min	51.78	39.38	26.25	13.13	0.00	51.76	39.38	26.25	13.13	0.00
$q_{pulse,HP}$ in l/min	36.9	31.2	29.3	28.0	26.7	32.0	25.2	21.4	20.1	19.8
$q_{pulse,LP}$ in l/min	19.2	21.3	23.3	24.9	26.0	13.7	15.7	17.8	19.4	20.3
P_{loss} in W	190.8	76.3	65.7	67.1	68.8	185.8	42.4	43.9	56.9	66.0
$f_{normalised}$ in -	10.1	5.3	4.8	4.8	4.7	9.7	3.5	3.3	3.7	4.1

Table 5: Results for valve plates optimised only for setting ratios from 0.9862 to 0.5 at 1500 rpm and 15 MPa.

Setting ratio in -	Optimised valve plate		
	0.9862	0.75	0.5
φ_{ref} in deg 78.1		
Ψ_1 in deg 40.6		
Ψ_2 in deg 177.6		
Ψ_3 in deg 39.2		
Ψ_4 in deg	0	28.4	46.1
Ψ_5 in deg	0.3	12.3	13.4
$\varphi_{b,pc}$ in deg	40.4	28.3	27.2
$\varphi_{b,dc}$ in deg	39.0	26.9	25.8
p_{max} in MPa	15.29	17.07	17.33
p_{min} in MPa	0.050	0.084	0.050
$q_{mean,HP}$ in l/min	51.77	39.38	26.25
$q_{pulse,HP}$ in l/min	5.8	13.8	19.3
$q_{pulse,LP}$ in l/min	7.9	15.1	25.5
P_{loss} in W	12.6	58.2	136.3
$f_{normalised}$ in -	1	3.3	6.7

less profound.

With decreasing displacement, the losses increase massively. Therefore, the objective function value of the losses dominates the optimisation for these setting ratios (see fig. 15 and tab. 6).

5 Discussion

For 1500 rpm, the optimisation results in a valve plate design which is similar to a zero-lapped valve plate, but offers slightly improved performance over the whole operating range. This is motivated by the choice and weighting of operating points. At low setting ratios, a zero-lapped valve plate performs quite well, because cross-porting is avoided, and no pre- and de-compression takes place (which could lead to cavitation and high-pressure peaks). This deteriorates the performance at high setting ratios, as pre-compression cannot be provided.

When omitting the lower setting ratios, performance at full displacement is drastically improved with decreased power losses and flow pulsations, see fig. 14 and tab. 4 and 5. This is enabled by a massive increase of the effective bridge angles. However, the performance at the 75% and 50% setting ratios slightly declines. This is caused by a more profound throttling effect due to larger relative valve plate rotation. Relative valve plate rotation reduces the passage area for the fluid around commutation, which hinders the flow into/out of the chamber. Therefore,

Table 6: Results for zero-lapped and for optimised valve plate in comparison (3000 rpm, 15 MPa).

Setting ratio in -	Zerolapped valve plate					Optimised valve plate				
	0.9862	0.75	0.5	0.25	0	0.9862	0.75	0.5	0.25	0
φ_{ref} in deg 76.6 79.7				
Ψ_1 in deg $\varphi_{\text{chamber}}=26.9$ 28.7				
Ψ_2 in deg 180 178.5				
Ψ_3 in deg $\varphi_{\text{chamber}}=26.9$ 26.9				
Ψ_4 in deg	0	41.0	60.0	75.6	90.1	0.0	38.4	54.5	69.3	83.8
Ψ_5 in deg 0					0.0	0.4	3.0	3.6	3.7
$\varphi_{\text{b,pc}}$ in deg $\varphi_{\text{chamber}}=26.9$					28.7	28.3	25.7	25.1	25.0
$\varphi_{\text{b,dc}}$ in deg $\varphi_{\text{chamber}}=26.9$					26.9	26.5	23.9	23.3	23.2
p_{max} in MPa	15.04	15.80	16.79	17.72	18.41	15.04	18.00	17.69	17.75	18.00
p_{min} in MPa	0.459	0.079	0.005	0.001	0.003	0.459	0.088	0.050	0.050	0.050
$q_{\text{mean,HP}}$ in l/min	103.55	78.75	52.50	26.25	0.00	103.49	78.75	52.50	26.25	0.00
$q_{\text{pulse,HP}}$ in l/min	52.9	43.1	41.9	41.7	41.1	49.3	28.0	42.3	47.6	47.5
$q_{\text{pulse,LP}}$ in l/min	27.4	31.3	33.4	35.6	37.4	27.2	31.1	51.5	57.8	59.3
P_{loss} in W	452.2	207.0	247.5	297.8	325.4	391.2	203.5	755.0	1063	1113
$f_{\text{normalised}}$ in -	21.4	11.3	663	809	1051	19.5	10.0	32.3	44.6	42.8

minimal pressures decrease, maximum pressures increase and higher losses occur. Due to the more profound throttling effect, cross-porting even needs to be applied at a 50% setting ratio in order to maintain the required minimum pressure level.

The results at 1500 rpm indicate that valve plate rotation is not capable of providing an efficient and silent pump from zero to full displacement. However, it can be used to improve the performance for a specific range of setting ratios.

For 3000 rpm, the optimisation also results in a valve plate design which is similar to a zero-lapped valve plate, but offers slightly improved performance at high setting ratios compared to zero-lapped valve plates. At low setting ratios, the zero-lapped valve plates suffer from cavitation and high pressure peaks. Due to relative valve plate rotation, the optimised solution can avoid cavitation and high-pressure peaks. However, several degrees of cross-porting are applied in order to maintain the required pressure levels in the chamber. This leads to very high power losses. Increased boost pressures at the pump inlet will only partially reduce the issues caused by the throttling effect. Furthermore, reducing the throttling effect by providing larger passage areas for the fluid is challenging, as the fluid flows through the piston, slipper and valve plate, see fig. 1a.

The pre-compression angles are chosen to be larger than the de-compression angles, which is in alignment with the expectations based on sec. 2.1.

Both at 1500 rpm and 3000 rpm, the mean flow level at full displacement is slightly reduced in comparison to the zero-lapped valve plates, so the soft constraint is slightly violated. This indicates that a minor reduction of the flow demand at full displacement can offer more freedom to design valve plates for reduced losses and pulsations.

6 Conclusion

Valve plate rotation can control the displacement of an axial piston machine. However, cavitation and high pressure peaks in the chamber are a drawback at low setting ratios and high speeds. This drawback can be overcome by using a double pump with opposing pistons, which has two valve plates. A relative rotation between the two valve plates leads to variable bridge angles. These variable bridge angles can eliminate the risk of cavitation and high pressure peaks, at the expense of increased power losses (and cross-porting).

Valve plate rotation seems mainly suitable for machines which mostly run at high setting ratios but need the ability to survive low setting ratios.

7 Acknowledgement

This research was funded by the Swedish Energy Agency (Energimyndigheten, Grant Number 50181-1).

Nomenclature

Designation	Denotation	Unit
f	Objective function value	-
g	Linear weighting factor	varies between equations
h	Weighting factor in exponent	varies between equations
p	Pressure	Pa
p_0	Reference pressure	Pa
q	Flow	m ³ /s
t	Time	s
x_0	Fraction of undissolved air at reference pressure p_0	-
A_p	Piston area	m ²
P_{loss}	Power losses	W
R_b	Barrel radius	m
V_{cyl}	Displacement volume of one chamber	m ³
V_{dead}	Dead volume	m ³
α	Swash plate angle	deg
β_e	Effective bulk modulus	Pa
β_{oil}	Oil's bulk modulus	Pa
ε	Machine setting ratio	-
φ	Shaft/barrel angle	rad
φ_{chamber}	Swept shaft angle covered by one displacement chamber	deg
$\varphi_{b,dc}$	Effective bridge angle at de-compression	deg
$\varphi_{b,pc}$	Effective bridge angle at pre-compression	deg
φ_{ref}	Reference angle for kidney angles	deg
φ_{VP}	Valve plate rotation angle	deg
κ	Isentropic expansion factor of air	-
ω	Shaft/barrel angular speed	rad/s
Ψ_1	Bridge angle between closing LP kidney and opening HP kidney	deg
Ψ_2	Angle between closing of LP kidney and closing of HP kidney	deg
Ψ_3	Bridge angle between closing HP kidney and opening LP kidney	deg
Ψ_4	Joint rotation angle of both valve plates	deg
Ψ_5	Relative rotation angle between valve plate 1 and valve plate 2	deg

Abbreviation	Meaning
ccw	counter-clockwise
cw	clockwise
BDC	Bottom Dead Center
HP	High Pressure
LP	Low Pressure
TDC	Top Dead Center

References

- [1] Jaroslav Ivantysyn and Monika Ivantysynova. *Hydrostatic pumps and motors : principles, design, performance, modelling, analysis, control, and testing*. New Delhi: Akademia Books International, 2001. ISBN: 8185522162.
- [2] Liselott Ericson, Samuel Kärnell and Martin Hochwallner. “Experimental Investigation of a Displacement-controlled Hydrostatic Pump/Motor by Means of Rotating Valve Plate”. In: *Proceedings of 15:th Scandinavian International Conference on Fluid Power, (SICFP’17), Linköping, Sweden*. Linköping University Electronic Press, 2017. DOI: 10.3384/ecp1714419.
- [3] P.A.J. Achten, Z. Fu and G.E.M. Vael. “Transforming future hydraulics : a new design of a hydraulic transformer”. In: *The Fifth Scandinavian International Conference on Fluid Power (SICFP ’97), Sweden, Linköping*. 1997.
- [4] Peter A. J. Achten and Zhao Fu. “Valving Land Phenomena of the Innas Hydraulic Transformer”. In: *International Journal of Fluid Power* 1.1 (2000), pp. 39–47. DOI: 10.1080/14399776.2000.10781081.
- [5] Junhee Cho, Xiaoping Zhang, Noah D. Manring and Satish S. Nair. “Dynamic Modelling and Parametric Studies of an Indexing Valve Plate Pump”. In: *International Journal of Fluid Power* 3.3 (2002), pp. 37–48. DOI: 10.1080/14399776.2002.10781146.
- [6] Andreas Tonnqvist, Jonas Forssell, Jan-Ove Palmberg, Liselott Ericson and Anders Hedebyörn. “Variable Pre and De-Compression Control Mechanism and Method for Hydraulic Displacement Pump”. Pat. US10968741B2. 2021.
- [7] Noah D. Manring. *Fluid Power Pumps and Motors: Analysis, Design and Control*. McGraw Hill Book CO, 2013. ISBN: 0071812202.
- [8] Herbert E. Merritt. *Hydraulic Control Systems*. New York: John Wiley and Sons, Inc., 1967. ISBN: 0471596175.
- [9] Maria Pettersson. *Design of fluid power piston pumps : with special reference to noise reduction*. Dissertation. Linköping: Division of Fluid Power Technology, Department of Mechanical Engineering, Linköping University, 1995. ISBN: 917871592x.
- [10] M. J. Box. “A New Method of Constrained Optimization and a Comparison With Other Methods”. In: *The Computer Journal* 8.1 (1965), pp. 42–52. DOI: 10.1093/comjnl/8.1.42.
- [11] Petter Krus and Johan Andersson. “Optimizing Optimization for Design Optimization”. In: *Volume 2: 29th Design Automation Conference, Parts A and B*. ASMEDC, 2003. DOI: 10.1115/detc2003/dac-48803.
- [12] Liselott Ericson, Johan Ölvander and Jan-Ove Palmberg. “On optimal design of hydrostatic machines”. In: *Proceedings of the 6th International Fluid Power Conference, IFK, Vol WS*. 2008, pp. 273–286.

Strategies to Minimize Data Sample Size for Regression-Based Pump/Motor Models

Jack L. Johnson^{1*}, Jose Garcia-Bravo,² Pawan Panwar³ and Paul Michael⁴

¹IDAS Electrohydraulics, Waukesha, WI., U.S.A. *Corresponding author

² School of Engineering Technology, Purdue University, West Lafayette, IN., U.S.A.

³ Department of Mechanical Engineering, University of California – Merced, Merced, CA., U.S.A.

⁴ Fluid Power Institute, Milwaukee School of Engineering, Milwaukee, WI., U.S.A.

E-mail: jack@idaseng.com, jmgarcia@purdue.edu, ppanwar@ucmerced.edu, michael@msoe.edu

Abstract

This work presents an analysis for tracking the evolution of regression coefficients and the Root-Mean-Square of their residuals on a test dataset for a hydraulic pump. The method starts by iteratively regressing data points that are undergoing sequencing by adding one new data sample at a time, then regressing with each iteration. This process was named Progressively Sequenced Regression Analysis, shortened to “PSR analysis” in this paper. The motivating and guiding postulate of PSR analysis is based on the belief that a plateau of the regression coefficients and statistical figures of merit had to exist if sampling theory is accepted to be real. It was anticipated at the outset that both the regression coefficients and the Residual RMS would converge on respective plateau values; however, it was discovered that the coefficients were very volatile, with some, more volatile than others. Tracking the Residual RMS was found to produce the more reliable measure of information saturation because the convergence is more obvious, provided that the sample sequencing was done with the experience learned from performing PSR analysis. This document is focused on explaining how orthogonally sequenced data can be mined for the limits or hyperspace vertexes of the sampled data, and the source data optimally sequenced (rearranged) to produce results that are as efficacious as Latin Hypercube (LHC) sampling for achieving information saturation at a predictable number of samples. PSR analysis has led to an objective method for verifying that the proper arrangement, i.e., optimized sequencing, of the source data set can predict the condition of information saturation and minimum useful sample size. It ends with a postulate of how this can be achieved using a combination of LHC sampling and vertex pre-test planning, or vertex mining of legacy data. The content of this paper has concentrated solely on the output flow model of hydraulic, positive displacement pumps.

Keywords: RMS of Residuals, Progressively Sequenced Regression Analysis, Latin Hypercube sampling, minimum sample size, vertex mining, vertex sequencing, hyperspace vertexes, convergence plateau, pump flow model

1 Introduction

Hydraulic pumps and motors are widely used in industrial and mobile applications requiring relatively high torque and shaft speed. In many systems, these components are preferred for their high power density, flexibility and simple operation. Unfortunately, despite being ubiquitous in countless applications, the average hydraulic system using pumps and motors presents efficiencies as low as 26% [1]. A solution to improve the efficiency of such machines is to develop accurate and reliable models that predict the behavior of pumps, valves, conductors and actuators. These models are used in industry to develop and engineer highly productive and efficient hydraulic systems through the selection of meticulously analyzed components. However, these systems can only be effective if the models are reasonably accurate.

The means for modeling hydraulic pumps and motors vary in the reported literature. Concerning hydraulic pumps and motors, the most notable means for describing the characteristic performance of a pump correspond to the

flow model and the torque model. For an ideal pump or motor, the displaced fluid is proportional to the velocity of the shaft speed, eq.1 shows this relationship.

$$Q_T = V \cdot N \quad (1)$$

Where, Q_T is the theoretical (ideal) flow, V represents the volumetric displacement of the pump or motor, and N is the shaft speed. Various methods are found in the literature for obtaining the volumetric displacement of a pump or motor [2]-[5]. And all of these seek to determine the derived displacement, a proportional constant for estimating the flow output of a pump at a given shaft speed. More sophisticated methods like the one presented by Eggers, et al. [6] were used to describe a mathematical interpolation procedure called POLYMOD, which was used for developing a torque and flow model based on a polynomial fit of experimental test data. Similarly, Conrad et al. [7] developed a loss model where the flow losses could be obtained from fitting experimental data to a line. Whether the aim is to obtain a complete flow model or simply for determining the volumetric displacement of the pump or motor, a set of experimental data points is required. However, determining how accurate the chosen method is, remains a question of not only the principles on which the method itself is based, but also the quality and volume of the data, that is, the number of experimental data points needed to obtain a useful model. The aim of this work is to present a methodology for determining an optimal sample size for the creation of models based on experimental data, which in turn, will improve testing performance. The motivation for this project was to reduce the amount of time on the test stand while at the same time increasing the amount of production hardware that would be subjected to complete mathematical modeling. Original Equipment Manufacturers (OEM) such as manufacturers of agriculture, construction, forestry equipment, etc., and researchers increasingly expect component manufacturers to supply accurate performance information and models of their components for their own system simulations and performance predictions. The single most important criterion for successful and complete creation of minimal and efficacious test data is to collect the samples in the proper order. The following sections explain how to achieve proper sampling order, and a sequenced regression method presented in this work, herein described as PSR analysis needed to estimate the number of test samples.

1.1 Overview of the PSR Procedure

Progressively sequenced regression analysis was first introduced by Johnson [8] as a method for verifying that a given number of test samples would be sufficient to reach information saturation for the creation of a mathematical pump or motor model. That study explained how Latin Hypercube (LHC) [9] experiment design was crucial to discovering the importance of data order. He also made the case for using PSR analysis as a research method that could lead to minimization of sample size for modeling purposes. Earlier Progress Reports by Johnson to the International Organization for Standardization [10]-[12] showed how the success or failure of PSR analysis is a matter of the order in which the samples are regressed. When sample order is arranged properly (skillfully), information saturation is revealed reliably, but more importantly, the number of samples needed to reach that saturation is controllable through the order used to collect the data in the laboratory, or alternately, the post-lab reordering of the data by optimal analysis, such as with data mining and vertexing.

The PSR process begins with a thoroughly ordered and nominally large source dataset called in this document the genesis file. The regression starts with only the first few samples taken from the genesis file and, placing them into a matrix to be regressed called the PSR matrix. The PSR matrix is subjected to evaluation using an ordinary, linear, multiple regression program to fit test data to a pump or motor model. eq. 2, below presents a simple flow model to be used for the linear regression, this model contains only three regressor terms, and was used in the study at hand.

$$Q_T = A_0 + A_1 N + A_2 \frac{p}{\nu} + A_3 N p \quad (2)$$

Where Q_T represents the theoretical flow estimation for this proposed mathematical model, A_n correspond to the regression coefficients for this model, N is the pump shaft speed, p is the pump differential pressure and ν is the kinematic fluid viscosity This model is adapted from the flow model first presented by Toet [5]. Other pump or motor flow equations may be used for the regression, allowing for performing studies on the effect of other operating parameters or combinations of them. Other, more complex functions were used, such as the one for fig. 2 and fig. 3. and are shown for reference.

After the regression algorithm was evaluated with the first sample points from the dataset, the regression coefficients and chosen figures-of-merit (FoMs) were stored in an output file for later viewing and processing. Examples of FoMs include; sample mean, sample standard deviation, RMS error, etc. Each iteration of the PSR

analysis added one more observation to the output data file, which contained all the regression coefficients and chosen FoMs. In this way, the evolving coefficients for the math model and FoMs could be tracked as the number of samples grew by one sample per iteration. The term “information saturation” is defined as the point at which a sufficient number of samples was reached. It was observed that when information saturation was attained no substantial changes in the RMS Residual Error followed after adding samples and iterations.

Skillful or optimal selection of the data sequencing means that the order of the first samples in the original experimental dataset or genesis file, have been selected by means that are described in this paper in the subsection below. The aim is to demonstrate that the data set can be reduced to bring about information saturation with the fewest number of data samples and furthermore, the number of samples needed to obtain information saturation is predictable as a result of implementing those optimized methods. Some details of these procedures are discussed in later sections of this paper.

1.2 The Progressively Sequenced Regression Algorithm

Figure 1 shows the basic PSR analysis flow chart that outlines the overall procedure of Progressively Sequenced Regression Analysis. The authors’ algorithm used multivariate linear regression in an iterative process, where a new data sample from the genesis file is added with each new iteration until all samples in the genesis file were processed in the analysis.

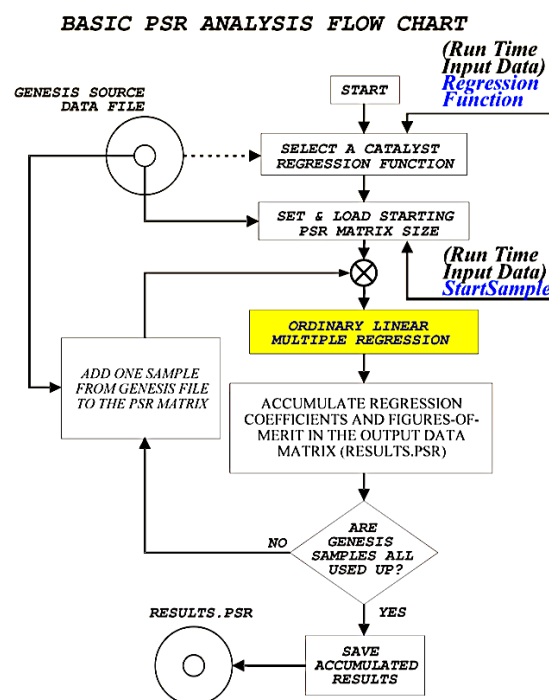


Figure 1: Basic flow chart of the PSR algorithm

Specifically, once the PSR algorithm is fed the input data, two other essential pieces of Run Time Input Data are required by the PSR analysis software. The algorithm begins with the Regression Function corresponding to any form as exemplified in eq. 2. In the first step the desired regressor columns are picked from the genesis file. In the case study presented here, these regression coefficients correspond to the following physical variables which reside in generated columns in the genesis file (data matrix):

- a. Shaft Speed (rad/s) or (rpm), N , for the A_1 term
- b. Pressure/viscosity ratio (Pa.s/m²) or (bar/cSt), p/ν , for the A_2 term
- c. Speed · pressure product, (rad/s·Pa) or (rpm·bar), Np , for the A_3 term

1.3 Review of previous findings of PSR analysis

Data crowding is a term used to stress the detrimental effects caused by consecutive samples that contribute little change from one sample to the next. They will most likely occur in the opening regions of PSR analysis, that is, when the regressed sample count is the smallest (smallest PSR Matrix). When using the orthogonal sequencing as obtained from ISO 4409 data, the effects of data crowding create problems in PSR analysis. Changes in measured speed, for example, at one sample to the measured speed at the next sample are small. The changes in the speed variable are so small as to create a near zero value of the regression determinant and will result in coefficient values that are very large and changing rapidly from data sample to data sample (coefficient volatility). Such effects are apparent in the estimation of A_0 coefficient for the regression function as shown in fig. 2.

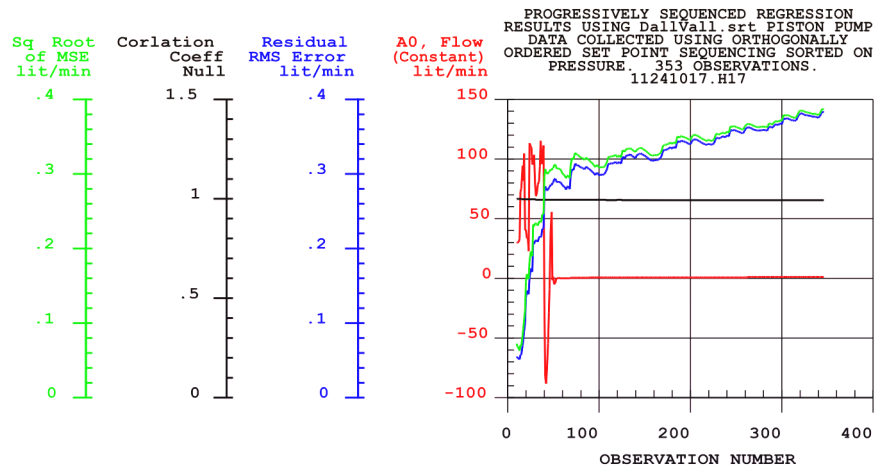


Figure 2: Example of failure to reach information saturation and coefficient volatility for an axial piston pump.

Figure 2 shows that the A_0 coefficient has gone “flat line” at just over 50 observations, suggesting that information saturation has been reached. This is a false positive because it is the extreme swings in A_0 in this region that expand graph scaling such that information saturation appears to have occurred. The existence of the flat region is a result of graphical scaling and not true arrival at the convergence zone. The failure to reach convergence becomes apparent only after the most volatile region is suppressed as is shown in fig. 3. Suppression was done simply, by setting PSR’s internal StartSample variable to 52 samples at the opening of this example PSR analysis.

Setting the SampleStart internal variable to a larger value does not ignore or discard valid data, it merely suppresses the volatile output data caused by those samples and thus avoids the graph scaling problem caused by volatility in A_0 . This becomes apparent in fig. 3 in which the volatility of the first 52 data samples has been suppressed. That is, the very first regression in the PSR analysis (fig. 3) used a PSR matrix with 52 data samples. They are valid data points taken in accordance with an ISO standard procedure, however, putting them first in the inputting sequence created the volatility due to data crowding. It takes 52 regressed samples to “flush out” the influences of the data crowding. After that, the A_0 coefficient is “better behaved” and the output is more meaningful and can be correctly interpreted. Fig. 2 and Fig. 3 show an example of a failed PSR analysis.

It was further observed that data order or data sequencing is paramount and holds the solution to successful PSR analysis. The genesis file used to generate the PSR analysis output of fig. 2 and Fig. 3 was subjected to a conventional ordering on the independent variable, differential output pressure. Early in the research, while trying to determine the processes that might control the ability to reach information saturation, sorting was done on pressure to assess the effects. The sorting based on pressure was done in ascending order, resulting in all of the lowest pressures occupying the first data samples right at the beginning of the genesis file. Along with orthogonal sequencing and its accompanying data crowding per the recommendations provided in ISO 4409, there was no worse way to prearrange the data. Sorting using the pressure was a clear way to invite data crowding problems in a worst case way, fig. 2 demonstrates this fact, and fig. 3 reinforces it. Covered in later sections of this paper are the discoveries that Latin Hypercube sequencing and orthogonal data vertexing can result in a minimization/reduction of number of samples needed for useful models because they give to the regression process the extremities of the tested hyperspace in the earliest samples, assuring attainment of information saturation.

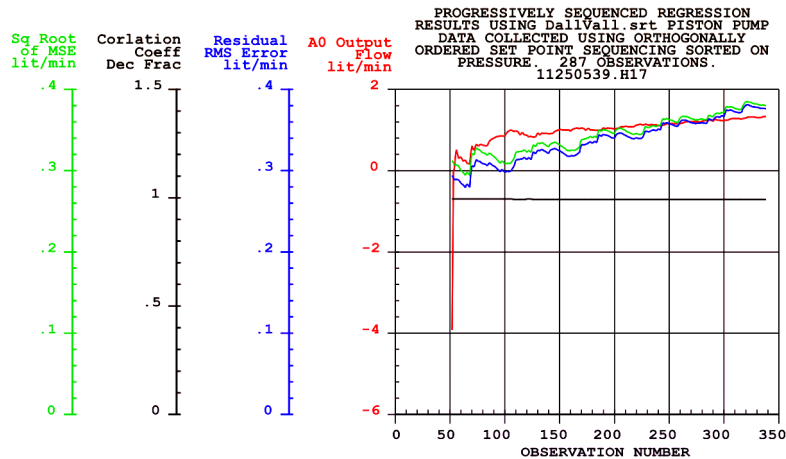


Figure 3: Detail of the A_0 coefficient for an axial piston pump without first 52 samples.

2 Methodology

The plots shown in fig. 3 contain the same curves as in fig. 2, but with the A_0 volatile data removed from the display. The reader is urged to observe the similarities in the curves of fig. 2 and fig. 3 by first seeing the large differences in the scaling of the A_0 axes in the two figures. In fig. 2 the A_0 spans from -100 to +150 lt./min (-0.00167 m³/s to 0.0025 m³/s) while the range in fig. 3 is from -6 to +2 lt./min (-0.0001 to 0.00033 m³/s). In fig. 3 the most volatile range of A_0 data has been removed from the display for the purpose of exposing A_0 's real trends with the volatility removed. The similarities in the two graphs lie in the other three variables beyond 52 observations. They have the same scaling and the same shapes in the two respective figures. It is clear in both figures that information saturation was never reached because the Residual RMS Error the Square Root of MSE both rise steadily as the PSR analysis sample count increases toward the end value of 353 samples. There is no convergence plateau. This, too, is a direct consequence of the sorting of the genesis file using pressure as the variable. Later sections of this paper show that the data can be re-sequenced so that information saturation does occur, and the number of samples needed to reach it can be controlled. Likewise, PSR analysis reveals many anomalies of regression analysis. For example, there is likely to be more volatility in the individual coefficients A_0 shown in fig. 2, than there is in the Residual RMS Error leading the researchers to adopt it as the FoM of choice.

PSR analysis is a way to exhibit the volatility graphically. Users of regression might not otherwise be aware of this volatility. Unfortunately, regression cannot extract coefficients from data with the same certainty of, say, Fourier analysis can extract harmonic components from a cyclic waveform of arbitrary shape. A given regression coefficient value depends upon the makeup of other companion regressors in the same catalyst regression function. In other words, the coefficient volatility is affected by the form of the catalyst regression function, but information saturation is affected by the order in which samples are presented to regression.

For many modelers the conventional FoM for the quality of a model is the R^2 value. In output flow modeling of a positive displacement pump, the nominal uncertainty in the independent and dependent variables is about $\pm 0.5\%$, subjectively speaking. This means that the total uncertainty in a model is probably in the range of $\pm 1\%$ or $\pm 2\%$. This means further, that about 98% of the pump performance is predictable by that amount. The random variations are only one or two percent. But it also means that the discrimination of one model to the next with the R^2 value is in the 6th or 7th decimal place, making R^2 a poor discriminator of model quality. Residual RMS Error is a far better discriminator, a reality that led the authors to adopt it as the FoM of choice.

Additionally, and just as importantly as selecting the correct FoM is the fact that sequencing must be such that the extremities of the tested hyperspace (vertexes and/or Latin Hypercube experiment design) must be present in the earliest samples in order to achieve information saturation. Any future data points that are beyond the hyperspace limits of past data points is probably going to create a rise in the Residual RMS Error and lead to a new, higher plateau. The remainder of this paper reports on the means by which the outer limits of the testing hyperspace can be controlled and information saturation can be reached.

2.1 Preparation of the dataset using an LHC experiment design

LHC sampling was used by Panwar and Michael [13] to create a designed sampling experiment using the sampling strategy followed by McKay et al. [9], their goal was to build a set of test set points to guide and sequence data collection in the laboratory. Johnson [8] used this data to carry out a PSR analysis. The results of the analysis revealed unambiguous information saturation that coincided almost perfectly with the number of samples chosen for the Latin hypercube data set (25, 50 and 100 samples), which was set to be first in each of the several genesis files and thus became the PSR learning zone as suggested in fig. 4. The learning zone is a term used in this work to explain and separate that early evolutionary region in PSR analysis where the Residual RMS Error has not yet settled on a convergence value. It is introduced graphically in the idealized graph of fig. 4. Not all data behaves this way, but is similar when sequencing is enhanced to achieve information saturation. The quest of the researchers was to find data sequencing that produced similar outcomes and unambiguous information saturation in the evolution of the FoM. Johnson [8] observed that the results produced an optimized minimum sampling requirement when using the Latin Hypercube test plan because the information saturation was obtained with a lower sample count. In this document finding this minimum requirement is referred to as optimality.

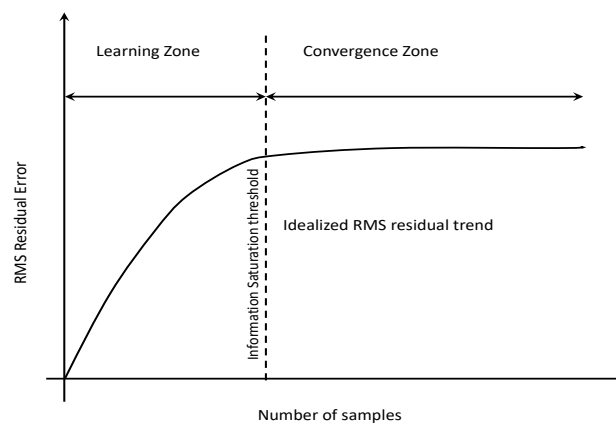


Figure 4: Ideal trend of the RMS value for a regression model.

2.2 Input Data for the LHC Algorithm

The data for the PSR analysis for this work was obtained from testing a hydraulic pump and following the standardized test procedure described in ISO 4409 [14]. The test set point sequence consisted of the aforementioned Latin Hypercube designed experiment of 25, 50 and 100 samples respectively, to serve as learning zones in several test sequences. These learning zones were followed by generally larger LHC sequences to serve as convergence zones with assurances that the hyperspace limits were the same in all LHC sequences regardless of being positioned for a learning zone or for a convergence zone, an absolutely necessary requirement as the experiment was designed using Matlab®. The subject test specimen was a variable, positive displacement hydraulic pump producing an approximate flow, Q , of 100 lt/min ($0.00167 \text{ m}^3/\text{s}$) at the maximum test speed, N , of 2200 rev/min (230 rad/s). The test set point sequence consisted of the specified number of data samples to be used as test set points in the laboratory and were constrained by the specified ranges given for the three independent test variables shown in eq.1, output pressure p , shaft input speed N , fluid viscosity ν . The LHC algorithm function from Matlab® was used for creating pre-laboratory test set points for the independent variables to be measured. Whether a test set point sequence is a learning zone or a convergence zone is a matter of placement in the genesis file plus the successful reaching of a convergence plateau.

After implementing the laboratory test plan which produced the measured data, and followed by calculating candidate independent regressors, a viable genesis data file was built, from which PSR analysis could then be performed. It was the integration of LHC sampling verified with PSR [8] that revealed the efficacy of such sampling.

Optimality was obtained in all cases because the number of samples specified in the creation of the LHC learning zone predicted almost perfectly the number of samples needed to reach information saturation. Current research now points to inclusion of hyperspace vertexes along with LHC sampling to create a more effective and optimally improved learning zone. This will in turn yield a better representation of the population of test data.

2.3 Definition of learning and convergence zones using LHC sampling

The LHC algorithm had to be invoked at least two times to create a single designed experiment: once for the “learning zone” and a second time for the expected “convergence plateau” to appear during PSR analysis iterations [8]. The learning zone samples form the first part of the test plan and the convergence plateau samples follow, and they must be in that order. If, after PSR has analyzed those learning zone samples, the RMS Residual Errors remain nominally constant, then that is a necessary and sufficient condition to confirm that information saturation has occurred (fig. 4). No instances of actual constant RMS residual error in the convergence plateau were reported. Instead, and as expected, the error varied slightly in the convergence plateau, however, Johnson [8] did not recommend objective estimates of acceptable variation limits. It is postulated now, in this paper, that a reasonable limit in the plateau zone be set equal to, or less than, the allowable measurement error that applies to the dependent variable being modeled, or a specified fraction thereof. It would be a starting point, and an assistance to the objective determination of minimum sample size for accurate models.

2.4 Definition of the start of the convergence zone

Figure 5 contains the results of the three different PSR analyses with test data from a single axial piston pump. The designed experiment explored the consequences of using LHC sampling with the three different learning zone sample counts in order to see the effects on the number of samples used, or PSR iterations, needed to reach information saturation. The terms "25's Curve", "50's Curve" and "100's Curve" in fig. 5 refer to the three genesis files with 25, 50 and 100 LHC sample sets as learning zones, with each followed by larger convergences zone sample sets.

However, this was accomplished by manually shifting data samples so the total number of samples was always 300 and all 300 were the exact same total set, but with the leading samples being comprised of the 25, 50 and 100 LHC samples respectively.

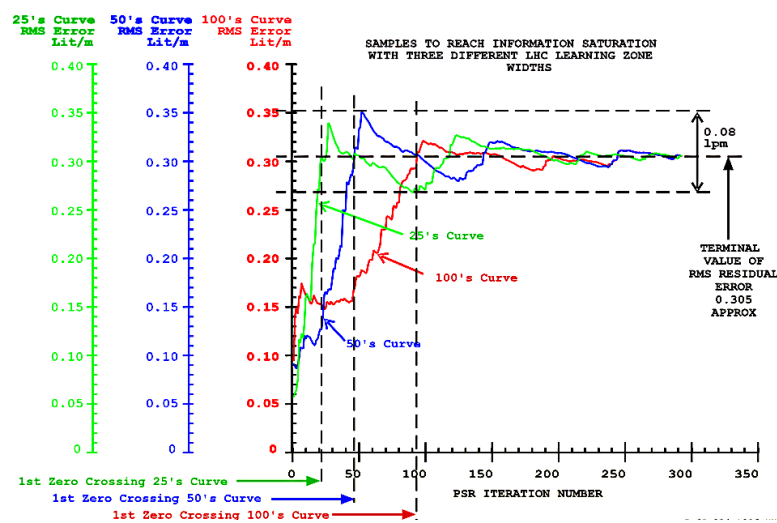


Figure 5: RMS error of predicted flow for various learning zone sample sizes.

With the semi-random nature of LHC sampling, this was the only fair way to compare the efficacy of the three learning zones. This explains why all three graphs converge on the same final value of Residual RMS Error. The criterion for having reached information saturation is the crossing of the final value of the RMS Residual error that is reached after a much longer convergence zone. fig. 5 identifies this final value as approximately 0.305 lt/min ($5.083 \times 10^{-6} \text{ m}^3/\text{s}$) for the chosen catalyst regression function presented in eq.2. An exact mathematical function to model a pump is not known, however, it is known that experimentally validated models can have 6 variable terms plus the constant [13]. This means there were seven unknown coefficients, thus the regression needed a minimum of eight samples as the absolute minimum. PSR analysis started with the eighth sample. This starting sample count, StartSample, corresponds to a PSR iteration count of one. fig. 5 is constructed with PSR iteration count as the horizontal axis so the first entry on the graph occurs at the value of 1. The iteration count in fig. 5 is what statisticians refer to as “degrees of freedom” which takes into account the number of unknowns in the catalyst regression function, however, in general, the iteration count can be independently controlled when PSR analysis starts in order to achieve some special graphical display effects and as demonstrated in comparing fig. 2 and fig. 3.

The designed experiment was used to generate the convergence zone samples as well as the learning zone samples. For all three analyses in Fig. 5, there was a total of 300 samples, therefore, the graph ends at 292 iterations. The three PSR analyses were carried out with a different number of samples each. The “25's Curve” meaning that its first 25 samples were taken from a complete LHC designed experiment set up to generate 25 designed samples. It led to a first crossing point at approximately 21 iterations corresponding to 28 data points. The “50's Curve” meaning that its first 50 samples were taken from a complete LHC designed experiment set up to generate 50 designed samples. It led to a first crossing point at approximately 46 iterations corresponding to 53 samples. Lastly, the “100's Curve” meaning that its first 100 samples were taken from a complete LHC designed experiment set up to generate 100 designed samples. It led to a first crossing point at approximately 92 iterations corresponding to 100 samples.

Additional data has been identified in fig. 4, notably the final value of the RMS Residual error, which is estimated to be about 0.305 lt/min ($5.083 \times 10^{-6} \text{ m}^3/\text{s}$). It is evident that the residual error does not reach a constant value, but instead fluctuates. The ultimate limits after first crossing, which take into account not just the peak-to-peak value of one curve, but the composite peak-to-peak of all three curves, is indicated by the span of about 0.08 lt/min ($1.33 \times 10^{-6} \text{ m}^3/\text{s}$) on the graph of fig. 5. The interpretation of the convergence zone can be estimated as 0.305 ± 0.04 lt/min ($5.083 \times 10^{-6} \pm 6.667 \times 10^{-7} \text{ m}^3/\text{s}$). This is a trivial amount of variation in light of the maximum measured output flow which is just under 100 lt/min ($0.00167 \text{ m}^3/\text{s}$) for this pump as tested. The authors believe that the minimum number of samples for this pump is 25 samples, that is the learning zone width, provided those 25 samples are collected using a 25 sample LHC-designed test set point sequence. There is every reason to believe, that a fewer number of samples will produce a useful model, provided the LHC, or equivalent, algorithm is used to establish the test's set point sequence. It will be shown shortly that when the learning zone is built using the hyperspace vertexes of an orthogonal test point sequencing, as is dictated by ISO 4409, that the ability to predict and reach information saturation is just as efficacious as is the LHC algorithm. For purposes of this paper, hyperspace vertexes are the upper and lower extremities of the independent variable ranges, that is, no test points exist outside the tested hyperspace, of the independent variables in all their combinations.

It can be concluded that with the LHC design of experiment method, the minimum sample size is an independent variable because modeling of hydraulic pumps and motors is concerned with known physics used for the mathematical model or catalyst function as shown in eq. 2. This model carries an “ideal flow term”, $A_1 \cdot N$, and an internal laminar leakage term, $A_2 \cdot p/\nu$, both of which are well known hydromechanical phenomena occurring in hydraulic pumps and motors, plus the so-called Couette/compressibility effect, i.e., the last term in eq 2. fig. 5 shows that the LHC sampling algorithm can produce a designed experiment that will always produce information saturation within the number of samples requested of the LHC algorithm. That is, the points of the first crossings coincide almost perfectly with the numbers of samples used for each respective LHC learning zone width, i.e., 25, 50 and 100.

2.5 LHC Sampling for prediction of information saturation

The authors sought to explain why when using an LHC experiment design, the point of first crossing of the final RMS residual error always coincided regardless of the number of samples selected for reaching the learning zone. It was hypothesized that because LHC is a randomization method for selecting the data, a better sampling of the pump performance can be obtained for the regression used in PSR. Therefore, the following statements can be made:

- Latin Hypercube sampling strategically spreads sample points evenly throughout the chosen data hyperspace.
- The stratification of the data used in LHC layering of the sample points creates assurances that all regions of the hyperspace are fairly sampled,
- Randomization distributes the sample test points throughout the defined hyperspace.

However, the authors recognized that conventional LHC sampling always falls short of the tested hyperspace limits, therefore the hyperspace vertexes became new possible candidates for populating the learning zones. This paper validates the vertexing strategy. Given these statements, LHC is found to be an efficient method for sampling of the entire universe of points within the hyperspace of the pump's performance. PSR analysis verifies adequacy of the sample size by reaching information saturation within the sample count used in the learning zone. In PSR analysis the adequacy of the small sample is referred to as efficacy of sampling. To the best of the author's knowledge, statisticians have not given a name to that phenomenon which allows a small number of samples to serve as a model for a much greater population of samples. PSR analysis using LHC sampling has shown empirically that even sample sizes as small as 25 provide and predict that information saturation will be reached.

LHC sampling has been producing its sufficiency in sampling since McKay first introduced it in 1979 [9], however, the sufficiency was not known until PSR analysis was used to verify it. The virtues of LHC design of experiments have been lauded by other authors [15]-[17], however, the laudits are not universal. For example, Vose [18] argues against the value of LHC sampling but, does so in the original intent and context of McKay [9]. The original intent was aimed at efforts to minimize the number of iterations needed to draw conclusions from simulations with scores or hundreds of parametric combinations. PSR analysis with LHC sampling in this current context is used to minimize data samples needed to create useful physical models drawn from the data. PSR analysis revealed, and verified, the original postulate by Johnson [8], that there must come a point where additional sample counts contribute little or nothing to the quality of the model.

2.6 The role of rearranging the genesis file

The authors investigated the beneficial effects of randomizing an orthogonally collected genesis file after having failed to reveal information saturation without ambiguity. Randomizing was carried out using a reordering algorithm which in turn made use of the semi-random number generator in their compiler. The results created an unambiguous RMS error plateau as seen on fig. 6, but it lacked the predictability of LHC sequencing. That is, LHC sequencing provided the sample count to reach information saturation, by inspection, while at best, some statistical theories likely have to be applied to make sense of the saturation sample count with random reordering of the data. Nevertheless, this data randomized sorting appears to be reliable in demonstrating information saturation, provided there are a sufficient number of data samples. But the uncertainty in predicting sample count for saturation precluded investing any further time into a search for a predictor. No further investigations were made using rearranging beyond the five corroborating analyses for a fixed displacement gear pump shown in fig. 6 and a variable displacement piston pump fig.5. For the gear pump the ideal shape suggested in fig. 4 emerged in fig. 6 and it leaves no doubt that information saturation occurs at about 30 or 40 samples. In order to use the model associated with the first observations below 30, the sorting of independent variables and the PSR analysis on unaltered orthogonally sequenced data will not work. Randomization of the data will provide models from fewer samples, however, there is no reason to believe that fig. 6 depicts a condition of optimality.

2.7 PSR and optimal sampling efficiency Discussion

In an ideal scenario, measurements would be made with zero error. Of course, a zero-error experiment is impossible, but a discussion of such an ideal scenario helps to point out the challenges in the real world scenario. The requirements for modeling an ideal, perfect, zero-error data set are listed below:

- The smallest possible PSR matrix must have only one more sample than there are unknown regression coefficients in order to satisfy this well-known requirement of regression, and,
- There must be some variation in each and all of the independent variables within the selected M+1 samples, where M is the number of unknown coefficients in the known regression function.

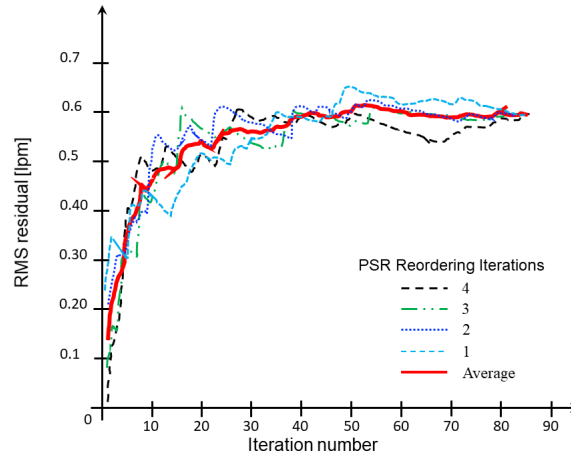


Figure 6: Effect of iterative data rearranging on RMS residuals for a gear pump

In this ideal case, assuming a perfect pump model, $M+1$ samples are all that are needed, provided both principles are met, then the perfect regression function and the perfectly measured data will absolutely guarantee a perfect set of coefficients. All error-based FoMs i.e., the RMS error, will be exactly 0.0. Perhaps more importantly, if there are more than $M+1$ samples collected by the laboratory, it makes no difference which $M+1$ samples are selected. Any $M+1$ samples, or more, within the entire assortment of collected samples will absolutely produce the exact same coefficients and will absolutely produce zero error between model and measured data. More samples are needed in the real laboratory because all of the data has errors, and the real regression function is therefore not knowable.

3 Results and discussion

A summary of the results of the research to date suggests that information saturation could not occur until the sample set included the full range of all the independent variables, from minimums to maximums in the designed test program. In all of the successful demonstrations of information saturation, it can be seen that the RMS residual error FoM begins at a low level with the very first, while regressing the fewest samples, and then gets larger as the PSR matrix sample count increases. The very first PSR model dataset (PSR matrix) is for a sample count of one more than the number of unknown coefficients in the catalyst regression function. With so few unknowns and so few samples, a low error between model and data is expected, especially when using accepted first principles to select the regressor terms [12]. There is a natural reaction to conclude that this low error produces the best model. This is not assuredly true, and such assumption leads to poor models. As more samples are added in the PSR process, the errors grow as the model misses more data points. Eventually, and at times with very low sample counts, information saturation is reached, and the learning zone samples are consumed by the growing PSR matrix and the PSR analysis enters the convergence plateau. That growth of the error leads to a better model is counterintuitive, unless information theory is applied to the principles of regression. Regression can optimally fit only those samples that are given to it. Information saturation occurs because each new sample contributes no new information, and the error reaches its plateau. If new data points were to be obtained outside the hyperspace used for creating the model, there will likely be a rise in the convergence plateau and different regression coefficients. In short, there would be a new model based upon a new set of hyperspace vertexes. On the other hand, if a user of the model entered independent variables that are outside the tested modeled hyperspace, they would be extrapolating beyond the verified limits of the model. PSR analysis helps to explain why extrapolation of any empirical model is discouraged by those who use models based on regression.

3.1 Vertexing

Vertexing is a multi-step process, it begins with finding the best candidate data samples of vertexes. This can be at test planning stage, before entering the laboratory, or it can be done on legacy data that was collected orthogonally per ISO 4409. Vertexes are the outer corners that define the ultimate limits of the tested hyperspace. Vertexes consist of all possible combinations of minimums and maximums of the independent variables: pressures, speeds, viscosities, displacements. All four are not variables in all cases, e.g., fixed displacement machines.

Regarding vertexing, there are 2^n possible vertexes in a given test, where n is the number of actual independent variables that are implemented in a test program. Arrangement of the data samples is necessary so that all the vertexes are the first samples in the genesis file. The application of strategies for the arrangement within the vertex data samples is required to avoid data crowding and variables that have not undergone actual change within the beginning small sample counts of PSR analysis. This was caused by data crowding and volatility of the A_0 coefficient in fig.2. In a fixed displacement test, there are only three independent variables, so there are 2^3 vertexes. A simple binary truth table can quickly construct all eight combinations of minima and maxima. This is a three-dimensional hyperspace and can be visualized [8]. In a variable displacement test, there can be four independent variables and the hyperspace is four dimensional and has 16 vertexes, and so on.

Each vertex is a data sample. When the data is sequenced into the PSR matrix such that the vertexes are the first 2^n points in the matrix, the resulting PSR analysis reaches information saturation at the conclusion of regressing those samples. The efficacy of starting PSR analysis with the vertexes is every bit as good as LHC sequencing. In fact, the most significant conclusion of this paper is that the optimal dataset for PSR analysis will have 2^n vertex samples followed by an LHC sequence with 2^n samples to form a super efficacious learning zone.

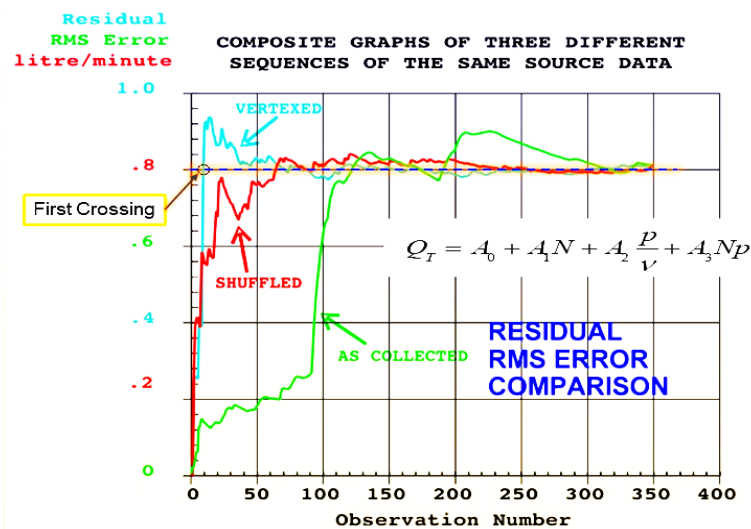


Figure 7: Overlay of compared data sequences.

The vertexes assure that all extremities of the hyperspace will be reached and represented while the LHC samples will assure that the interior of the hyperspace is considered. In the case of a two-dimensional test program, with only pressure and speed as variables, there are only four vertexes. It is recommended that the LHC sample set contain at least 8 samples in the case of a two dimensional hyperspace. Figure 7 is an example of how quickly the information saturation takes place with eight vertexes leading the genesis file to PSR analysis. The attainment of information saturation is identified as the point of “first crossing” in the figure. The resolution of the graph with 350+ data samples cannot display the gap between the vertical axis and the start of the two curves with a catalyst regression function with only four unknowns. That catalyst function was one that the authors examined as part of the many trial-and-error analyses during the early months of the project.

The authors’ software for vertex mining has a min or max strategy as options. The min strategy arranges the vertex samples so that there is the smallest amount of hyperspace distance in going from one vertex to the next. The max option is just the opposite. It sets the order of adjacent samples so that the greatest amount of hyperspace distance separates vertex neighbors in the genesis file. There has not been enough exploration of these options and results to draw any conclusions, however, the authors lean toward the max as being preferred. It is known that both data crowding and non-varying parameters can occur within the vertex learning zone. By rearranging the vertexes so that there is a maximum change from one sample to the next, it is reasoned that both data crowding and non-varying parameters are broken up.

Figure 8 shows that the A_0 coefficient is more volatile than the RMS Residual error. This is to be expected, and is the reason that coefficients are not good indicators of the success or not of reaching information saturation. However, the peak-to-peak volatility in A_0 is small, ranging from about -0.5 to about -1.05 a spread of about 1

litre/minute. Given that the maximum measured flow from this pump was nearly 100 litre/minute, the volatility of A_0 is only about $\pm 0.5\%$ of maximum measured value. The second issue examines the final value of the RMS Residual error. It is nominally about 0.8 litre/minute, or about 0.8% of maximum measured flow. In comparing the RMS value to the graphs of fig. 2 the terminal error was only 0.38 litre/minute. Both curves began with the same source data, however, the catalyst regression function for fig. 2 had seven unknown coefficients, while the function for fig. 8 used only four unknown coefficients. It is well known among modelers of physical processes that the number of terms, that is, function complexity, will affect the data fit. Figure 3 displays the better fit of the two because the RMS Residual error is less.

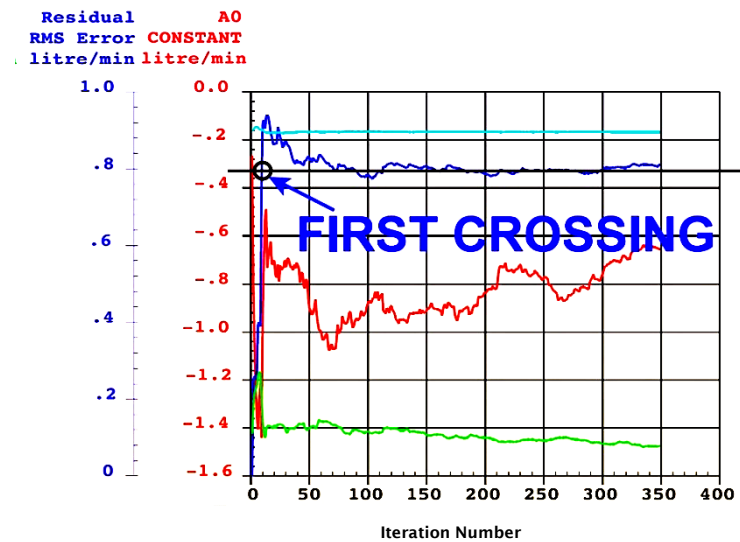


Figure 8: PSR Analysis results for an eight vertex sample dataset.

Vertex mining can be used on orthogonally collected data after the fact. It was used on legacy data for this paper. Several steps are required, and some special programming is needed in order to make the correct calculation of hyperspace distance. The steps are:

- 1) Set up a binary truth table listing all combinations of minimums and maximums based on the number of independent variables in the test program, i.e., 4, 8, 16, 32, etc. total combinations.
- 2) Search the existing data file for the absolute mins and maxes for each one of the independent variables in all samples of the data and save it in its own matrix.
- 3) Normalize each independent variable so that its maximum is 1.0 and all other values are less.
- 4) Normalize all corresponding values in the binary table so that each max value is 1.0 but each normalized minimum is whatever the normalization produces.
- 5) Taking each combination from the binary table, compare its proximity to each one of the data points in the total data array and save the one with the smallest hyperspace hypotenuse as the real vertex in a totally new matrix. Place that value at the front of the data array, but use the un-normalized original values. Then move to the next binary table entry and repeat the search for closest proximity.
- 6) When all binary table entries are completed, move all of the remaining samples into the new vertexed array making sure that the vertexes are not included because they have already been placed at the front of the new vertexed matrix.

From Johnson's progress reports [10]-[12], this phenomenon was seen clearly when the laboratory test sequence used LHC sampling strategy which also reliably and repeatably predicted the number of samples needed to reach information saturation. The results of shuffling the data to break up data crowding and non-varying independent variables, produced similar results, that is, information saturation was demonstrated, using the same data that failed in its original orthogonal order. Shuffling, however, had no predictor indications about how many samples were needed for information saturation. Genesis files for a gear pump and variable displacement piston pump were both shuffled. The PSR results are subject to interpretation, but the gear pump required about 30 to 40 samples to reach information saturation while the piston pump needed about double that number of samples. In another analysis of the piston pump by the authors, data was subjected to simple sorting on pressure. That is, the lowest pressure samples were first in the genesis file and progressively grew to maximum pressure with the last sample. The PSR results showed no clear information saturation. Instead, the RMS residual error continued to rise to the very end of the total 353 samples. This observation led to the conclusion that the learning zone needed to be populated with samples that had representation from the extremes of the independent variables. This was supported by the

demonstrated reality that LHC sampling forced the test points to range over the extremes of the independent variables. The natural outcome was the postulate that the best representatives for the learning zone would be the vertexes of the actual tested hyperspace. A variable displacement pump tested at two or more viscosities and several displacements has four independent variables, and therefore 16 vertexes are needed to define the boundaries of its hyperspace, while a gear pump, with its fixed displacement, would have only 8 vertexes in three dimensions.

A case study was carried out with a simple, and non-algorithmic, test sequence starting with the eight vertexes of a piston pump test. The goal of this case study investigated if sampling the vertexes of the hyperspace alone formed the learning zone with a consistent minimum sampling size. For example, a sample size of 16 vertexes for a four-variable test and eight vertexes are required for a three-variable test. Because the data from the pump was already obtained before the case study additional testing was not convenient, so a peripheral program was written to harvest the vertexes from the existing orthogonal legacy test data by applying a basic data mining strategy. A learning zone consisting of the vertexes of the test program hyperspace would assure that the full ranges of all independent variables would be present in the learning zone, fig. 7. A new test program with a learning zone comprised of only the hyperspace vertexes was not practical at the time, thus the synthetic process of harvesting vertexes from existing legacy orthogonally sequenced data was the only timely approach, under the circumstances. The mining and harvesting involved scanning the source data file for the extremes of all independent variables that were used to formulate an ideal set of vertexes. Next, the ideal vertexes were used to locate the real data samples that were closest to the ideal vertexes. In the first use of the method, there were three independent variables, requiring eight vertexes. When the nearest samples were found, they were extracted from the original genesis data set and reattached, but as the opening eight samples. Performing PSR analysis on the modified (re-sequenced) data set produced efficacy that rivaled the results of LHC sample sequencing. Because they represent the samples with the greatest spread in data, the eight mined vertexes were used as a learning zone in order to test the idea that the vertexes will be as efficacious as is produced by LHC sampling. The vertex data sequence has been referred to as a “synthetic” learning zone, but only because the first efficacious learning zone used LHC sampling in a more or less conventional design of experiment process. “Synthetic” in this context, suggests that the vertexes were not part of a pre-laboratory designed test plan.

Given that the StartSample variable was set to 5 (refer to the 4-unknown catalyst regression function displayed in Fig. 7 and Fig. 8) which makes the actual number of regressed samples at the first crossing point about 10 or 13, depending on the readers’ interpretation of the graph, it is unambiguous evidence that indeed, vertexes produce learning zone efficacy that is similar to, if not better than that of LHC sampling. Perhaps a combination of the two could produce even better results. The opportunities to improve efficacy have only been explored to a very limited degree. This has led the authors to postulate that a more optimal designed test sequence will use both LHC and vertexes in the learning zone. Other variables are typical of what would be expected with the efficacy of LHC sampling. The A_0 coefficient in fig. 8 has some opening volatility, but it’s not excessive and settles down reasonably well. Beyond the learning zone, the RMS peak-to-peak value is about 0.6 lpm, and with a maximum measured output of about 100 lpm, it calculates to about 0.5% of maximum output total spread ($\pm 0.25\%$), which is only half of the $\pm 0.5\%$ uncertainty limit required for the output flow per ISO 4409 (ISO, 2019) when claiming Class A Measurement uncertainty. To this point all the presented individual PSR analysis results are from a data file that was originally collected using classical orthogonal data sequencing. This is the method suggested by the recommendations of standard method ISO 4409 [14]. The results are shown in graphical form in fig. 8.

It is well known that the results of classical regression, that is, using all samples to produce a single model, will always be identical when using the same data, but in various sequences. That is, the terminal, or final coefficients, and FoMs will be exactly the same, regardless of data order. This truth is borne out in figs. 5, 6 and 7 in the fact that all traces converge on the same final value for the Residual RMS Error regardless of data order, however, the trajectories taken to get to the plateau depends on the data order. The data can be rearranged manually, especially at the beginning of the PSR analysis, so that information saturation is reached at a lower sample count. Two reliable and predictable means to achieve information saturation are now known, vertexing and LHC sampling.

4 Conclusions

Research results to date demonstrate that PSR analyses are affected by the order in which data is presented to PSR’s iterative regression process. In setting up a genesis file, it is the skill with which the samples are arranged that control whether or not information saturation is demonstrated more so than the numbers of samples. The same research has identified three different means for establishing efficacious sample sequencing that are objective and

predictive: The first is through the use of LHC experiment design to create the pre-laboratory test program for both the learning zone and the convergence zone. The second is to include the vertexes of the hyperspace extremities to guide the collection of first data samples, and the third is to randomly rearrange legacy data that was collected using the conventional orthogonal sequencing that is recommended in ISO 4409. The first two of these methods will assure that information saturation is reached within the number of samples requested of the LHC algorithm and the number of vertexes needed to define the test hyperspace. Random rearrangement of legacy orthogonal data shows promise of assuring information saturation, however, it is less predictive in the number of samples required. A fourth method, sample randomization by shuffling, produce information saturation, however, it was not predictive and was abandoned. Incorrect data sequencing (sample order) has a negative effect on the results. False negatives and false positives can occur in PSR Analysis, as illustrated in Fig. 2 and Fig. 3. The PSR analysis paradox is that one needs to have many samples in order to conclude that fewer samples would have sufficed. This makes PSR analysis a research tool and a means of verifying the efficacy of a given learning zone strategy to reach and display information saturation. PSR analysis will continue to be a useful tool in mathematical model development as a means for evaluating and validating conclusions about model quality.

5 Future Research

Future research efforts are aimed at finding a means for converging on the actual number of samples needed to achieve information saturation in the learning zone and to improving the information that can be gleaned from a data set, aside from the quest for sample size. It is postulated that a combination of LHC and vertexed learning zones will give test labs the tool to predict minimum sample count for producing reliable and useful math models. This theory needs additional testing that consists of designing the test programs with LHC and vertexing combined into a single learning zone. There needs to be one more round of testing to evaluate the efficacy and expected optimality of a combined LHC and vertexed learning zone. All research to date regarding PSR analysis has not given a means for positively calculating the minimum number of samples needed to achieve a useful model. The next step in this continuing research program aims to correct that shortcoming. The new research must investigate the nature of the learning zone data samples by comparing the sequencing that produces information saturation in the learning zone to those which don't devise a discrimination theory and then test it. This could lead to a practical Efficacy Index. At the same time, the models themselves, that are taken from the limited data sets, must be compared to ensure that they produce accurate projections of such quantities as output flow and input torque as well as overall efficiency.

6 Acknowledgments

The authors wish to thank Mr. John Montague for providing his comments and editorial revisions to this article.

7 Nomenclature

Designation	Denotation	Unit
F_i	Force	N
p	Pressure	Pa
<i>LHC</i>	Latin Hypercube	
<i>PSR</i>	Progressively Sequenced Regression	
ν	Kinematic viscosity	
N	Rotational shaft speed	rpm
p	Pressure differential	
A_n	Regression coefficients	
q	Volumetric flow rate	lpm

8 References

- [1] Love, L., Lanke, E., Alles, P. (2012), “Estimating the Impact (Energy, Emissions and Economics) of the U.S. Fluid Power Industry,” Oak Ridge National Laboratory: 2012, Report No. ORNL/TM-2011/14.
- [2] International Organization of Standardization ISO, (2008). “ISO 8426 - Hydraulic fluid power — Positive displacement pumps and motors — Determination of derived capacity.” ISO copyright office.
- [3] Society of Automotive Engineers (2019), “Hydraulic Power Pump Test Procedure J745_201911.” DOI: https://doi.org/10.4271/J745_201911
- [4] Wilson, W. E. (1950). Positive-displacement pumps and fluid motors. Pitman Publishing Corporation.
- [5] Toet, G. Die Bestimmung des theoretischen Hubvolumens von hydrostatischen Verdrangerpumpen und Motoren aus volumetrischen Messungen. *Olhydraulik Pneum.* 1970, 14, 185–190.
- [6] Eggers, B., Rahmfeld, R., & Ivantysynova, M. (2005). An energetic comparison between valveless and valve controlled active vibration damping for off-road vehicles. In *Proceedings of the JFPS International Symposium on Fluid Power* (Vol. 2005, No. 6, pp. 275-283). The Japan Fluid Power System Society.
- [7] Conrad, F., Trostmann, E., & Zhang, M. (1993). Experimental identification and modelling of flow and torque losses in gerotor hydraulic motors. In *Proceedings of the JFPS International Symposium on Fluid Power* (Vol. 1993, No. 2, pp. 677-682). The Japan Fluid Power System Society.
- [8] Johnson, J.L., (2018a). “Design of experiments and progressively sequenced regression are combined to achieve minimum data sample size”, *Int. J. Hydromechatronics*, Vol. 1, No. 3, pp.308–331.
- [9] McKay, M. D., Beckman, R. J., & Conover, W. J., (1979). “Comparison of three methods for selecting values of input variables in the analysis of output from a computer code.” *Technometrics*, 21(2), 239-245.
- [10] Johnson, J. L., (2018b). “Progressively Sequenced Regression Helps to Establish Minimum Sample Size at Test Time.” Unpublished report, 1 of 4, distributed to active members ISO\TC131\SC8\WG13, Mathematical Modeling Ad Hoc Project, January, 2018.
- [11] Johnson, J. L., (2018c). “A Sequel - Progressively Sequenced Regression Helps to Establish Minimum Sample Size at Test Time.” Unpublished report, 2 of 4, distributed to active members ISO\TC131\SC8\WG13 Mathematical Modeling Ad Hoc Project, February, 2018.
- [12] Johnson, J. L., (2018d). “Progressively Sequenced Regression Is Useful When Coupled with Efficacious Set Point Randomization.” Unpublished report, 3 of 4, distributed to active members ISO\TC131\SC8\WG13 Mathematical Modeling Ad Hoc Project, March, 2018.
- [13] Panwar, P., and Michael, P., (2018). “Empirical modelling of hydraulic pumps and motors based upon the Latin hypercube sampling method.” *Int. J. Hydromechatronics*, Vol. 1, No. 3, pp. 272–292.
- [14] International Organization of Standardization ISO, (2019). “ISO 4409 - Hydraulic fluid power - Positive displacement pumps, motors and integral transmissions - Methods of testing and presenting basic steady state performance data.” ISO copyright office.
- [15] Viana, F., Venter, G., Balabanov, V., (2010). “An Algorithm for Fast Optimal Latin Hypercube Design of Experiments.” *International Journal for Numerical Methods in Engineering*; 2010.
- [16] Helton, J.C., and Davis F.J., (2002). “Latin Hypercube Sampling and Propagation of Uncertainty in Analyses of Complex Systems.” Sandia Report, SAND2001-0417, Sandia National Laboratories, New Mexico (November 2002).
- [17] Zubarev, D. I., (2009). “Pros and Cons of Applying Proxy-models as a Substitute for Full Reservoir Simulations.” Society of Petroleum Engineers. doi:10.2118/124815-MS.

- [18] Vose, D., (2014). “The pros and cons of Latin Hypercube sampling.” Vose LinkedIn channel. Accessed 2018, url: <https://www.linkedin.com/pulse/20140708131747-483951-the-pros-and-cons-of-latin-hypercube-sampling>.

Pump-Controlled Actuators with Dump Valves

Samuel Kärnell¹, Emil Fernlund², Fabian Lagerstedt³, and Liselott Ericson¹

¹Division of Fluid and Mechatronic Systems, Linköping University, Linköping, Sweden

E-mail: samuel.karnell@liu.se, lislott.ericson@liu.se

²Hudiksvalls Hydraulikkuster, Hudiksvall, Sweden

E-mail: emil.fernlund@huddig.se

³Huddig, Hudiksvall, Sweden

E-mail: fabian.lagerstedt@huddig.se

Abstract

The electrification trend means an increased focus on the energy efficiency of mobile hydraulic systems. In turn, this means an increased focus on so-called pump-controlled systems, where actuators are controlled by pump flow rather than valve throttling. However, one of the main problems with pump-controlled systems is matching the flow into the pump with its outlet flow. There are many ways of solving this problem, but the solutions tend to be rather bulky and not ideal from a service perspective, since they often rely on accumulators. This paper presents simple but novel pump-controlled concepts, without accumulators. The energy consumption of the presented concepts is analysed and compared to other concepts. The analysis is based on measurements taken on a backhoe loader and the results show that implementation of the presented concepts on the backhoe's boom actuator can reduce the total power consumption by 50-60 % compared to the original load sensing system. This can be compared with 55-65 %, which is the yield for an ideal, accumulator-based, pump-controlled system on the boom.

Keywords: Pump-controlled systems, Backhoe loader, Electrification, Mobile Hydraulic systems

1 Introduction

Electrification of mobile machines is leading to a stronger focus on energy efficiency, not least because batteries tend to be heavy and expensive. To obtain high energy efficiency on a system level, it is important to minimise throttling losses due to differences in load pressures. This is usually an issue for linear actuators in particular, but there are several solutions, including use of hydraulic transformers [1] or multi-chamber cylinders [2]. Another alternative is to isolate consumers by using multiple pumps. The use of so-called pump-controlled actuators, where one pump is dedicated to a specific actuator, is therefore of great interest. Another appealing feature of pump-controlled systems is that they generally offer energy recuperation possibilities, which can reduce energy consumption significantly for applications where high loads are often lowered.

In other words, pump-controlled systems are promising, yet they are not commonly found on mobile machines.

1.1 Contributions

Many pump-controlled systems have been presented over the years. The focus has generally been on making the systems as efficient as possible and this has had a negative impact on the systems' complexity and maintenance requirements. In this paper, the trade-off between simplicity and energy efficiency is considered. Simple, low-maintenance concepts for pump-controlled asymmetric actuators are presented and analysed. Results on energy consumption from a case study conducted on a backhoe loader are presented, with the presented concepts compared to other system concepts.

1.2 Pump-controlled systems

The term pump-controlled system has already been mentioned plenty of times. It derives from the fact that the pump flow is used to control the motion of the actuator in such systems, unlike in conventional valve-controlled systems. The flow can be controlled by either the pump speed, the pump displacement or both. Previously, there was much focus on displacement-controlled concepts, but the electrification trend of the last years has shifted the focus towards speed control. However, both controls are principally very similar and a circuit for one control type can generally be applied to the other type as well. The main difference is that a boost pump, required for the displacement control, is often included in displacement-controlled circuits.

Pump-controlled systems have been in use for decades in the aircraft industry, [3]. The actuators used in that context are symmetrical. However, the compactness of asymmetrical cylinders generally makes them the preferred choice in mobile machines. The problem with pump-controlled asymmetrical cylinders is that the flow in to the cylinder is different from the flow that comes out. There are many solutions to this problem and an overview of the work that has been done can be found in [4]. That article presents a huge number of possible solutions to the differential flow problem, but also outlines common problems with mode switching oscillations and accurate flow matching, for example.

It is clear that the solution to the differential flow problem has not converged. However, a generalised schematic of one of the most studied pump-controlled architectures is illustrated in Fig. 1. The control valve block in the figure is often built up from passive components. It can represent an inverse shuttle valve or pilot operated check valves, for example, but there are also recent instances where active valves have been used [5]. Regardless of the control valve design, the basic idea is that an accumulator is used to take care of the differential flow. The accumulator either provides or receives flow to/from the pump or the cylinder, depending on the mode of operation. During an extension, the accumulator provides energy to the system, but during retraction, the energy flow moves in the other direction. If the components are assumed to be lossless and pressure drops over the control valves are neglected, this system is ideal from an energy point of view. It is therefore used as a reference system in this paper.

Unfortunately, there are drawbacks related to the circuit presented in Fig. 1. To minimise problems with cavitation and to increase the stiffness of the system, some kind of pressurised reservoir is required. Typically, an accumulator is used. Note that multiple actuators can share an accumulator [6]. However, this requires installation space as well as maintenance and it complicates servicing. Filtering and cooling can also be problematic. It is therefore relevant to consider other alternatives.

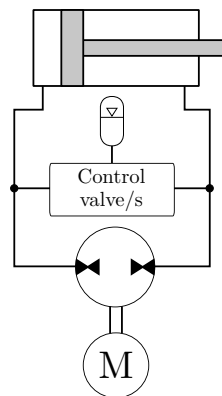


Figure 1: Common architecture for pump-controlled systems.

2 The proposed concepts

Instead of using an accumulator to handle the differential flow, the concepts that are presented in this paper share the feature that the required differential flow during extension comes from a *pressure source* and that the differential flow during retraction is directed to a tank through *dump valves*. The general architecture is illustrated in Fig 2. The dump valves are here built up from a pressure relief valve connected in series with an on/off-valve. The pressure relief valve takes care of the proportional control, and the on-board computer controls the on/off-valve. The opening pressure of the pressure relief valve is set slightly higher than the pressure source to avoid short circuit between the pressure source and dump valves. Regarding the pressure source, it can be either external or internal, which will be described more in section 2.1 and 2.2. The operation of the concepts in different modes is illustrated in Fig. 3. It can be seen how the pressure source supplies the low-pressure side of the system with flow during extension. During retraction, one of the dump valves is active instead.

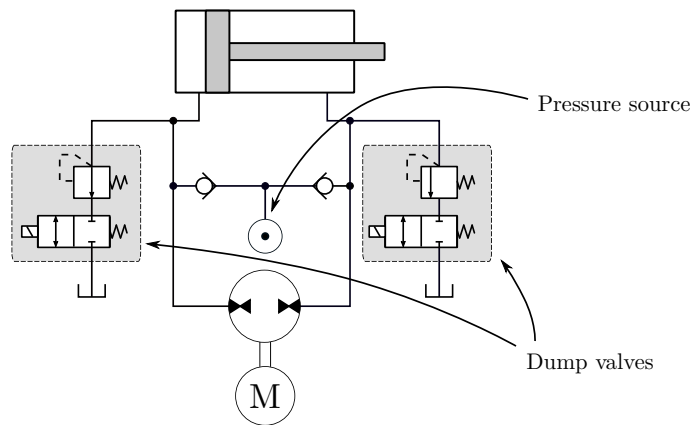


Figure 2: Generalised pump-controlled concept presented in this paper.

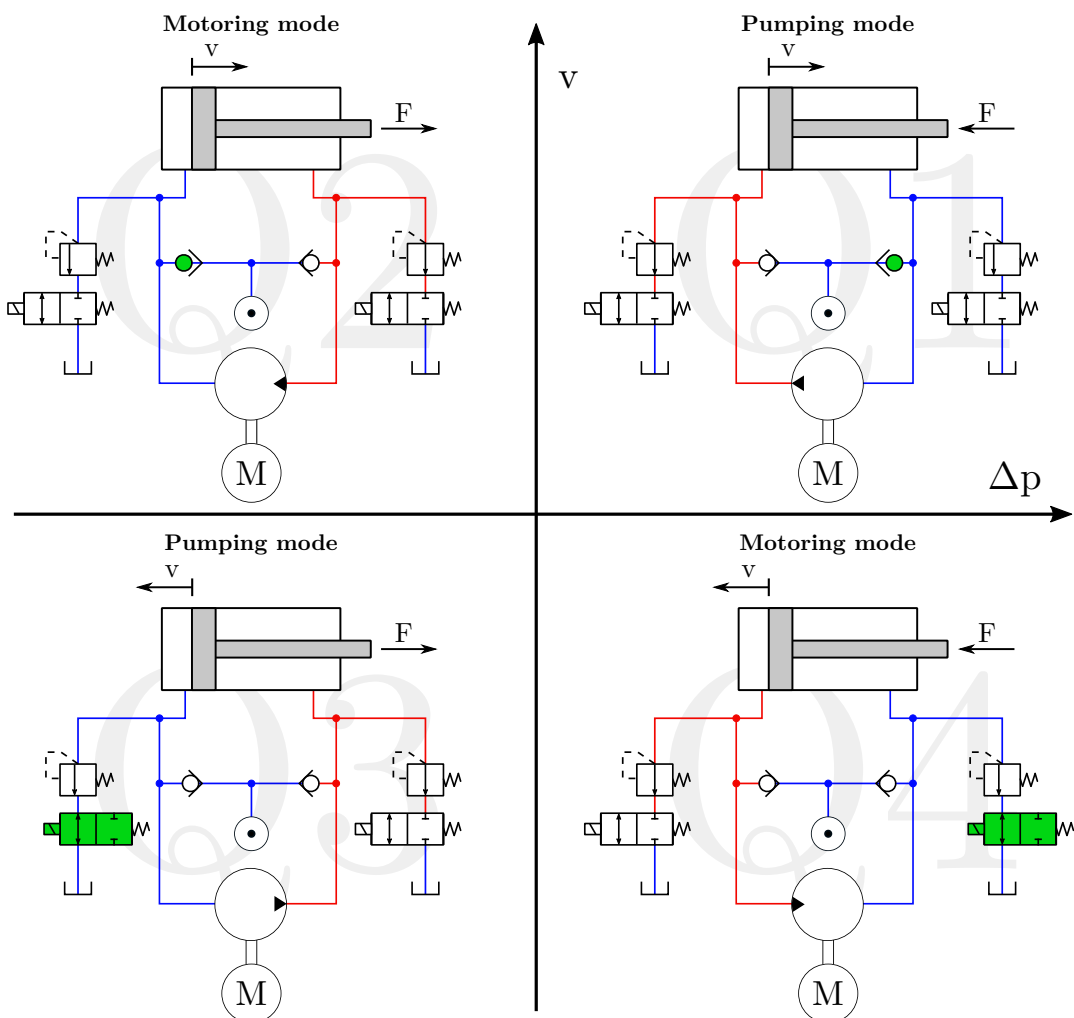


Figure 3: Working modes for the presented concept. The active control element for the differential flow is coloured.

2.1 Internal pressure supply

The dumping process is equal to energy losses and the flow that is dumped during retraction must be refilled during extension. Figure 4 shows a system where *internal pressure supply* is used to supply flow during extension. This means that an internal charge pump is used to provide the required differential flow. Note that the required components for this concept are usually included in a traditional closed-circuit pump. However, it is important to remember that the charge pump is only allowed to pump fluid in one direction in this concept. This means that the direction of the cylinder must be controlled by means of the displacement or that the charge pump must be able to handle rotations in both directions without changing flow direction, which a wobble plate pump with check valves, for example, can do. Furthermore, for optimal efficiency, the ratio between the charge pump and the main pump must match the cylinder ratio, but also the flow required for displacement control might have to be considered. Also note that the ratio will vary a great deal if displacement control is used on the main pump, which is not the case when speed control is applied. In the analysis presented in section 3, the two controls are therefore separated.

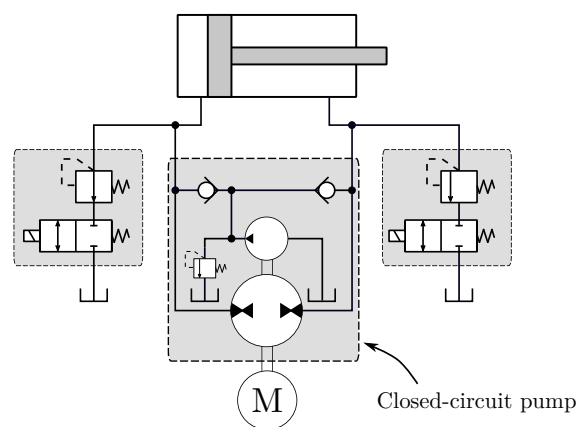


Figure 4: The presented concept with internal pressure supply.

This concept is similar in principle to displacement-controlled concepts that have been researched through the years (see e.g. [6–8]). The difference, apart from the lack of the accumulator, is that dump valves in combination with check valves are used instead of pilot operated check valves.

2.2 External pressure supply

For many mobile machines, it is only reasonable to implement pump-controlled actuators on a limited number of functions. This is mainly due to reasons of space and cost, for example, but it can also be due to limited energy saving possibilities for certain functions. Therefore, it is still relevant to power some functions with a more conventional valve-controlled system. This system can then be used as an *external pressure supply* for one or more pump-controlled systems. Pressure reducing valves can be used in-between the external pump and the pump-controlled systems to provide constant pressures to the latter. This is illustrated in Fig 5. The system within the block called *Conventional system* can be of any type, as long as it can provide the minimum pressure for the low-pressure side of the pump-controlled system. In this paper, a load sensing (LS) system is considered.

The usage of a pressure reducing valve can also be applied in systems that use pilot operated check valves or shuttle valves instead of check valves in combination with dump valves. This is because the pressure reducing valve can dump the excess flow to the tank. Efficiency-wise, the results are expected to be similar to the presented concept since they are only different ways of throttling the same flow. The difference is the pressure drop, which is set slightly higher in the dump valve.

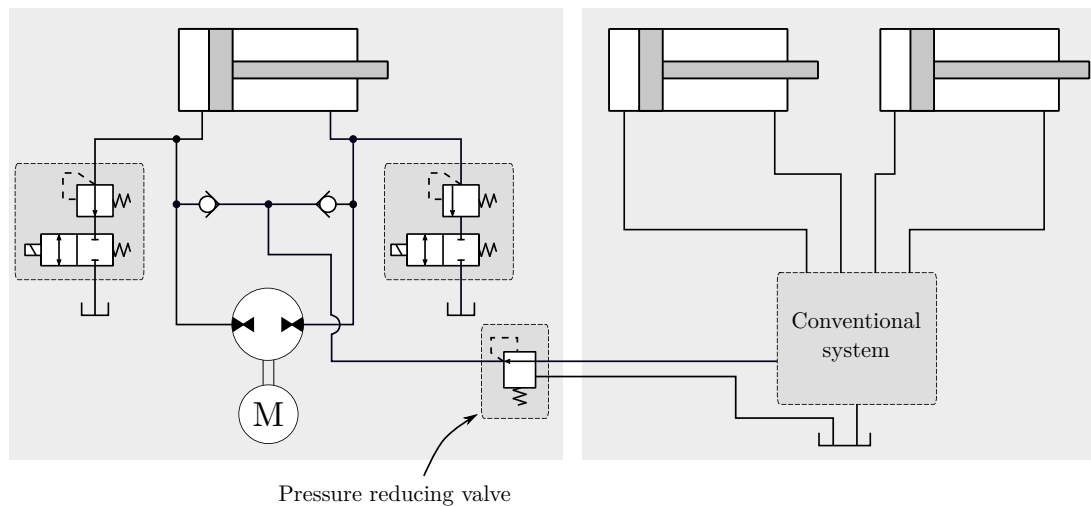


Figure 5: The presented concept with external pressure supply.

3 Energy analysis

This section contains an energy analysis, where the presented concepts are compared to other system architectures. The analysis is based on pressure and flow measurements taken on a backhoe loader in action for two different work tasks: excavating and grading. During the tasks, three of the backhoe's cylinders were used. An illustration of the backhoe loader and the cycles is presented in Fig. 6 and the measured pressure and flow requirements can be read from Fig. 7.

The energy consumption for the following systems is included in the analysis:

- **Conventional LS**

A conventional load sensing system is used for all three actuators. This is how the commercial backhoe loader is built today.

- **Separated LS**

The boom cylinder is powered by a separate LS system.

- **No recuperation**

The boom cylinder is pump-controlled, but no recuperation is possible. The arm and bucket are controlled by a conventional LS system. This system is included in the analysis to pinpoint the recuperation possibilities and does not represent any presented architecture.

- **Ideal pump-controlled system**

The boom cylinder is working in an ideal pump-controlled system according to system presented in Fig. 1. The arm and bucket are controlled by a conventional LS system.

- **Internal supply, speed-controlled**

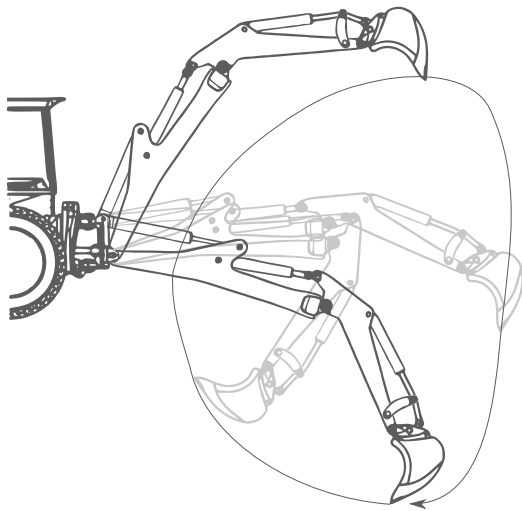
The boom cylinder is working in a pump-controlled system with dump valves and internal pressure supply according to Fig. 4. The pump for the boom cylinder is speed-controlled, which means that the flow from the charge pump is proportional to the flow from the main pump. The arm and bucket are controlled by a conventional LS system.

- **Internal supply, displacement controlled**

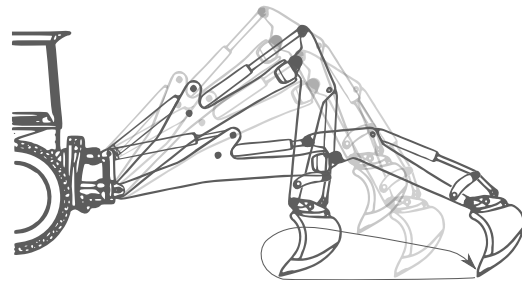
The boom cylinder is working in a pump-controlled system with dump valves and internal pressure supply according to Fig. 4. The pump for the boom cylinder is displacement controlled, but the charge pump is fixed which means that the flow from the charge pump is constant and dimensioned for the maximum required differential flow. The arm and bucket are controlled by a conventional LS system.

- **External supply**

The boom cylinder is working in a pump-controlled system with dump valves and external pressure supply according to Fig. 5. The arm and bucket are controlled by a conventional LS system.



(a) Excavating cycle. Gravel was picked up from a low position and dropped from a high position.



(b) Grading cycle with no additional load in the bucket.

Figure 6: Illustration of the example machine and its motion during the two analysed cycles. The cylinders for the boom, the arm and the bucket were operative during the cycles.

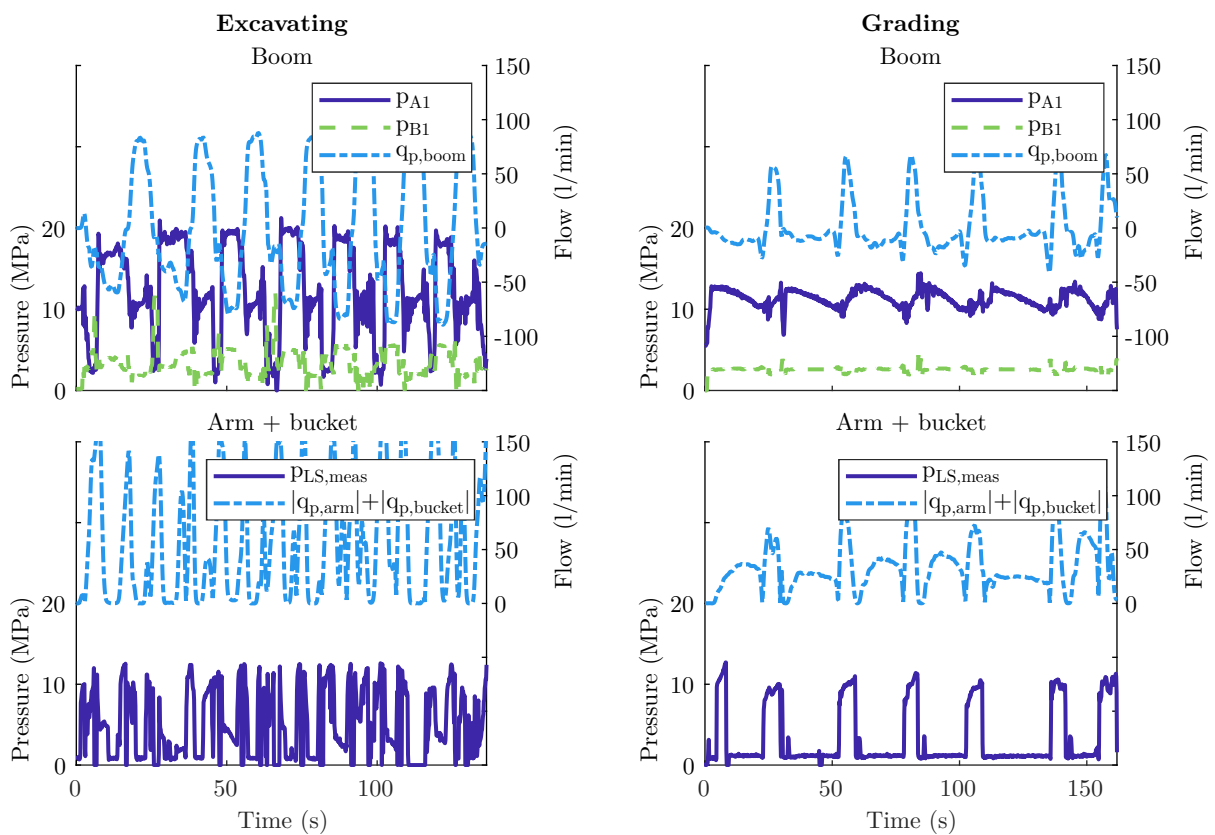


Figure 7: Measured pressure and flow for the two drive cycles. The left figures are for the excavating cycle and the right for the grading cycle. The labels correspond to the nomenclature in Fig. 8 and 9.

3.1 Measurement setup

The measurements have been taken on a machine with the internal pressure supply concept implemented on the boom cylinder. The system architecture and positioning of sensors is illustrated in Fig. 8. For more information about the test machine, see [9].

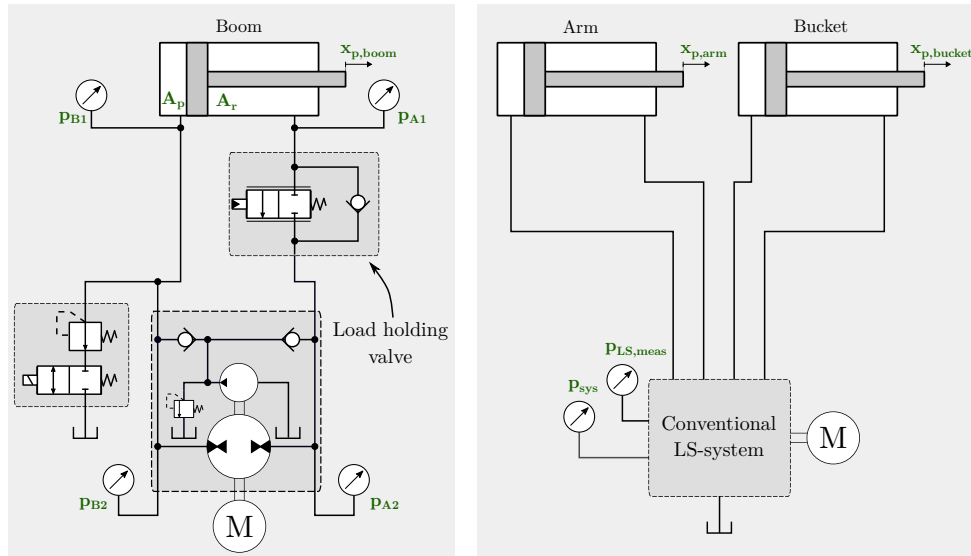


Figure 8: Measurement setup consisting of two separate circuits; one for the boom cylinder and one for the arm and bucket cylinders.

Note that the measurement setup only has one dump valve. This limits operation in *quadrant 4*. However, that has not been considered a problem for the analysed test cases. Furthermore, the machine was equipped with a load holding valve, which is required for safety related reasons. This valve was controlled with pilot pressure and opened from joystick commands.

3.2 Power calculations

The approach for the power calculations is illustrated in Fig. 9.

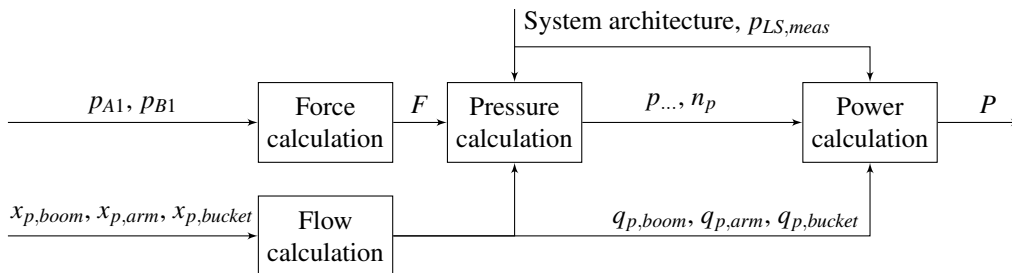


Figure 9: Power calculation process. The nomenclature relates to figure 8.

From the conducted measurements, an equivalent boom cylinder force was calculated according to Eq. (1).

$$F = p_{B1}A_p - p_{A1}A_r \quad (1)$$

This force was then used to recalculate pressures for the different system architectures. For the pressure calculations, the pressure on the low-pressure side was defined by the system concept itself, with consideration given to pressure drop over the load holding valve. The flow rates were calculated from the measured cylinder positions and the required pump speed was determined based on the flow rates. The power consumption for the different system concepts could then be calculated as follows.

$$P_{conv.LS} = \left(\max(p_{LS,boom}, p_{LS,meas}) + \Delta p_{LS} \right) \cdot |q_{p,boom}| + \left(\max(p_{LS,boom}, p_{LS,meas}) + \Delta p_{LS} \right) \cdot (|q_{p,arm}| + |q_{p,bucket}|) \quad (2a)$$

$$P_{sep.LS} = (p_{LS,boom} + \Delta p_{LS}) \cdot |q_{p,boom}| + (p_{LS,meas} + \Delta p_{LS}) \cdot (|q_{p,arm}| + |q_{p,bucket}|) \quad (2b)$$

$$P_{noRecup} = \max \left((p_{B2} - p_{A2}) \cdot q_{p,boom}, 0 \right) + (p_{LS,meas} + \Delta p_{LS}) \cdot (|q_{p,arm}| + |q_{p,bucket}|) \quad (2c)$$

$$P_{ideal} = (p_{B2} - p_{A2}) \cdot q_{p,boom} + (p_{LS,meas} + \Delta p_{LS}) \cdot (|q_{p,arm}| + |q_{p,bucket}|) \quad (2d)$$

$$P_{int.Sup} = (p_{B2} - p_{A2}) \cdot q_{p,boom} + (p_{LS,meas} + \Delta p_{LS}) \cdot (|q_{p,arm}| + |q_{p,bucket}|) + p_{supply} \cdot |n_p D_{cp}| \quad (2e)$$

$$P_{ext.Sup} = (p_{B2} - p_{A2}) \cdot q_{p,boom} + (p_{LS,meas} + \Delta p_{LS}) \cdot (|q_{p,arm}| + |q_{p,bucket}|) + \max \left((p_{LS,meas} + \Delta p_{LS}), p_{supply} \right) \cdot \max \left(q_{diff}, 0 \right) + \max \left(p_{supply} - (p_{LS,meas} + \Delta p_{LS}), 0 \right) \cdot (|q_{p,arm}| + |q_{p,bucket}|) \quad (2f)$$

The first row in (2a) to (2f) corresponds to the power related to the boom and the second to the power related to the arm and bucket. The additional rows, which exist in equations (2e) and (2f), corresponds to the power that relates to the pressure supply. A description of different parameters in the equations follows:

- $q_{p,x}$ represents the flow that the machine/machines must handle to correspond to the speed and load of cylinder x .
- $p_{LS,boom}$ (not relevant for pump-controlled systems) is the calculated required LS pressure for the boom. When this pressure is calculated, it is assumed that the pressure in the low-pressure side of the cylinder is constant.
- $p_{LS,meas}$ is the measured LS pressure for the arm and bucket.
- Δp_{LS} is the pump pressure margin for the LS pump/pumps.
- $p_{B2} - p_{A2}$ (only relevant for pump-controlled systems) is the pressure differential over the pump-controlled machine.
- p_{supply} is the pressure setting for the charging of the pump-controlled actuator.
- $n_p D_{cp}$ corresponds to the flow from the charge pump in a system with internal pressure supply.
- $q_{diff} = (A_p - A_r) \cdot v_{boom}$ is the differential flow for the boom cylinder.

4 Results

Figure 10 shows the power consumption integrated over the cycles for the different system architectures. It also shows how the energy is distributed. The results are for $p_{supply} = 2.5$ MPa and $\Delta p_{LS} = 1.5$ MPa. For the architectures with internal pressure supply, the charge pumps are optimally sized.

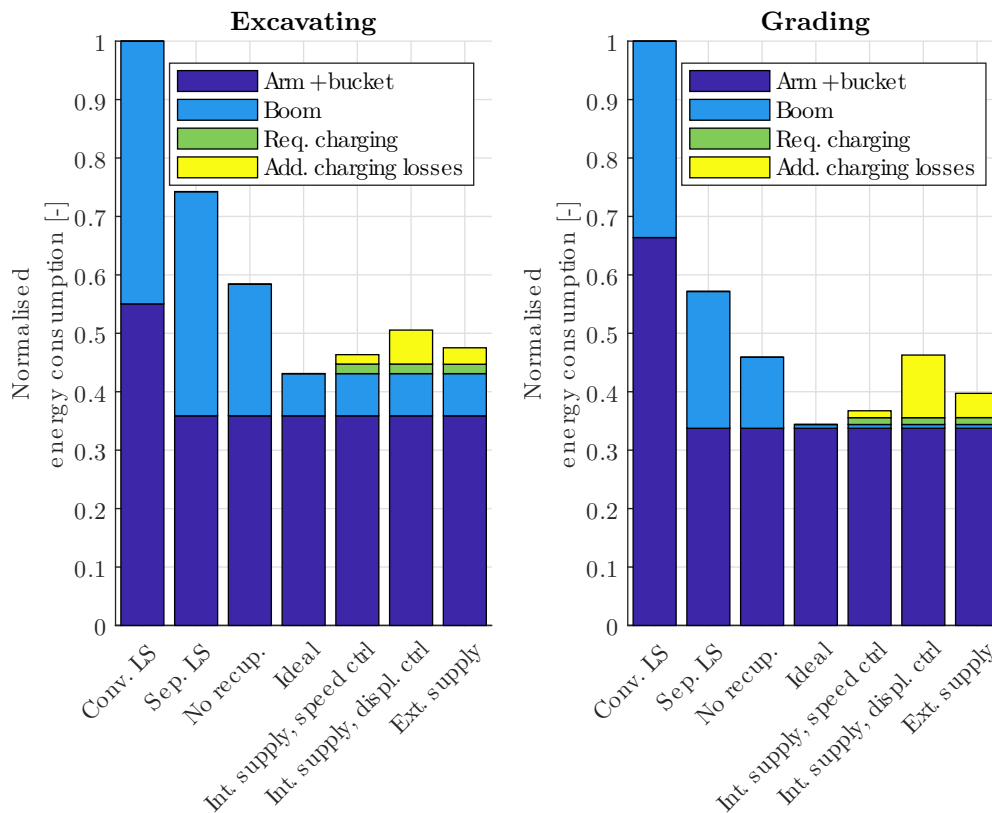


Figure 10: Normalised energy consumption for an excavating and a grading cycle for different system architectures.

The large differences between the conventional LS system and the separated LS system show that 25-40 % of the energy consumption is related to the mismatch in boom pressure and the pressure for other actuators. It can also be seen that the consumption for both the boom and arm + bucket decreases since the highest load alternates between the different functions during the cycle.

When comparing the separated LS system with the pump-controlled system with no recuperation, losses that relate to the pump pressure margin for the boom as well as losses related to the pressure in the low-pressure chamber can be seen. These losses correspond to about 10-15 % of the total consumption for the conventional LS system. Of this 10-15 %, the elimination of pump pressure margin losses corresponds to 30-40 %.

The difference between the no-recuperation system and the ideal pump-controlled system shows the recuperation possibilities. The results show that the relative recuperation possibilities are smaller for the excavating cycle than in the grading cycle. In the latter, the energy consumption for the boom is almost eliminated. That is, however, not the case for the excavating cycle since the load is dropped from a high vertical position. Still, it corresponds to more than 10 % of the total energy consumption for the conventional system.

When it comes to the energy consumption for the internally and externally supplied systems, which are the concepts that this article is orbiting around, it can be seen that the charging-related losses can reach up to 10 % of the consumption for the conventional system, but that the losses actually required only corresponds to 1-2 %. The required charging energy corresponds to the flow that is supplied to the system times the supply pressure. For concepts with internal pressure supply, the additional losses are related to the flow from the charge pump that is not delivered to the system. For external pressure supply, the additional losses are instead related to pressure drops. This means that concepts with internal pressure supply have losses that are proportional to the supply pressure setting (see Eq. (2e)), whilst the losses in the external pressure supply concept mainly depends on the drive cycle of the external pump. If it is working on pressure levels similar to the supply pressure setting, the losses are small.

5 Discussion

The intention with this paper is to present concepts for pump-controlled systems based on dump valves. The dump valve concepts were developed to be simple, which means that they should be easy to implement and require low maintenance. It was obvious that the concepts would have worse efficiency than state of the art, accumulator-based, pump-controlled systems, but there is usually a trade-off between efficiency and simplicity. A quantification of the energy losses that comes with the concepts is therefore of interest. However, since mobile machines generally have widely varying drive cycles, this study shall only be considered as an example.

Regarding the simplicity, it is considered an advantage that no accumulator is needed in dump valve concepts. This is because accumulators are bulky, not free of maintenance and can complicate servicing in the field. Another advantage is that the concepts are not completely closed, which reduces problems related to e.g., air-bleeding, cooling, and filtering. The intention with the concepts was also that they were supposed to be built from common off-the-shelf components. That intention is, however, only partly fulfilled due to problems in finding optimal closed-circuit pumps for the concepts with internal pressure supply, which is described further below.

When it comes to energy efficiency, it could be seen that the displacement-controlled internal pressure supply system had the worst performance. The speed-controlled alternative was far better, but the problem with the speed-controlled system is that the charge pump must be able to handle speeds in both directions. The availability of pumps is therefore very limited, and the complexity of the system is increased. A solution could be to use combined speed- and displacement control, which would result in losses in-between pure speed- and displacement control. Nevertheless, it is important to mention that the charging- related energy consumption is proportional to the supply pressure in concepts with internal pressure control. In the example above, the supply pressure was set to 2.5 MPa, which is rather high. This could be reduced without any problem. A high supply pressure is, however, preferable from a controllability perspective since it means higher stiffness. Another way to reduce the losses is to address the losses that relates to the charge flow that is not supplied to the system. These could be reduced by adding a by-pass valve in the charging system that is activated in quadrant 3 and 4, but this solution would increase the complexity further and is therefore not considered as relevant.

The concept with external pressure supply is of considerable interest since it only requires a few, simple components, assuming that a conventional LS system is installed on the machine. No size matching between cylinder ratio and any charge pump needs to be considered, which makes the process of finding components simple compared to the internal pressure supply concepts. It will also have very good efficiency if the external pump mostly operates at pressures close to the supply pressure setting. That was, however, not the case in the analysed cycles.

When it comes to the design of the dump valves, it should be made clear that actively controlled proportional valves can be used instead of the solution with a pressure relief valve in series with an on/off-valve, which has been presented here. In fact, with an actively controlled proportional valve, the dump valve used in quadrant 4 can be omitted since high-pressure oil can be dumped on the piston side instead. Unfortunately, this would mean slightly worse efficiency, since less fluid will pass through the hydraulic machine, and also increased complexity.

Lastly, it should be stated that a demonstrator has been built as a proof of concept for a dump valve concept [9]. This machine used internal pressure supply. The drivability of the machine was considered to be satisfactory. Mode switching oscillations have not been analysed in detail, but it has not been considered an issue during the tests that have been performed. It should, however, be mentioned that switching between quadrant 1 and 2 is passive whilst switching between quadrant 3 and 4 is actively controlled. Oscillations in the latter case is therefore expected to be easier to avoid. Once again, it should also be stated that the presented solution with dump valves in combination with check valves can be replaced by pilot operated check valves, shuttle valves, or actively controlled valves. This would mean similar efficiency to the presented concepts, but with switching behaviour similar to earlier studied concepts [8, 10, 11]. Here, we do not make any statement on which is preferable.

6 Conclusions

Pump-controlled systems based on dump valves are not optimal, but they can offer a good trade-off between efficiency and implementability. The concept with external pressure supply is considered highly interesting since it is easy to implement and since the efficiency is high if the external pressure supply usually operates at pressures similar to the supply pressure. Internal pressure supply concepts are less attractive since it can be hard to find a pump with the desired charge pump characteristics.

Nomenclature

Designation	Denotation	Unit
D	Displacement	$[m^3/rev]$
n	Rotational speed	$[rpm]$
P	Power	$[W]$
p	Pressure	$[Pa]$
q	Flow	$[m^3/s]$

References

- [1] Vael Georges E. M., Achten Peter A. J., and Fu Zhao. The innas hydraulic transformer the key to the hydrostatic common pressure rail., 2000.
- [2] Viktor Hristov Donkov, Torben Ole Andersen, Matti Linjama, and Morten Kjeld Ebbesen. Digital hydraulic technology for linear actuation: A state of the art review. *International Journal of Fluid Power*, 21(2), December 2020.
- [3] Dominique Van Den Bossche. More electric control surface actuation; a standard for the next generation of transport aircraft. In *Proceedings of the 10th European Conference on Power Electronics and Applications*, pages 2–4, 2003.
- [4] Søren Ketelsen, Damiano Padovani, Torben Ole Andersen, Morten Kjeld Ebbesen, and Lasse Schmidt. Classification and review of pump-controlled differential cylinder drives. *Energies*, 12(7):1293, 2019.
- [5] Petter H. Gøyttil, Damiano Padovani, and Michael R. Hansen. A novel solution for the elimination of mode switching in pump-controlled single-rod cylinders. *Actuators*, 9(1):20, Mar 2020.
- [6] Monika Ivantysynova. Displacement controlled linear and rotary drives for mobile machines with automatic motion control. *SAE transactions*, pages 125–132, 2000.
- [7] Christopher Williamson and Monika Ivantysynova. Pump mode prediction for four-quadrant velocity control of valveless hydraulic actuators. In *Proceedings of the JFPS International Symposium on Fluid Power*, volume 2008, pages 323–328. The Japan Fluid Power System Society, 2008.
- [8] Longke Wang, Wayne J. Book, and James D. Huggins. A hydraulic circuit for single rod cylinders. *Journal of Dynamic systems, Measurement, and Control*, 134(1), 2012.
- [9] Emil Fernlund. A novel pump-controlled asymmetric cylinder with electric regeneration: Implementation and evaluation of a closed hydraulic system on a backhoe. Master's thesis, 2020.
- [10] C Williamson and M Ivantysynova. Stability and motion control of inertial loads with displacement controlled hydraulic actuators. In *Proceedings of the 6th FPNI-PhD Symposium, West Lafayette, IN, USA*, pages 15–19, 2010.
- [11] Hakan Çalışkan, Tuna Balkan, and Bülent E Platin. A complete analysis and a novel solution for instability in pump controlled asymmetric actuators. *Journal of Dynamic Systems, Measurement, and Control*, 137(9), 2015.

Control Optimisation of a Pump-Controlled Hydraulic System using Digital Displacement Pumps

L. Viktor Larsson, Robert Lejonberg*, and Liselott Ericson

Division of Fluid and Mechatronic Systems (Flumes), Department of Management and Engineering (IEI), Linköping University, Linköping, Sweden

E-mail: viktor.larsson@liu.se; robert.lejonberg@epiroc.com; liselott.ericson@liu.se

*Epiroc Rock Drills AB, Örebro, Sweden

Abstract

When dealing with electrification of working machines, energy-efficient operation is key to maximise the usage of the limited capacity of on-board batteries. Previous research indicate that plenty is gained by reducing component and system losses by means of design. In contrast, this paper focuses on how to maximise energy efficiency by means of control optimisation. Dynamic programming with backward-facing simulation is used to find the optimal electric motor speed trajectory for a scooptram machine equipped with pump control, using digital displacement pumps with dynamic flow sharing as enabling technology. The results show that low shaft speed is preferred to minimise drag losses from parasitic components, partly facilitated by the relatively high and operation point-independent efficiencies of the pumps and electric motor. The results indicate energy reduction of 5 - 9 %, where higher figures could be expected for other, more hydraulic-intense applications, such as excavators.

Keywords: Control Optimisation, Pump Control, Digital Displacement Pump, Mobile Hydraulics

1 Introduction

Mining machines are mobile working machines used to move ore and other granular material in mines. Currently, these machines are subject to electrification, with decreased global use of energy and fossil fuels as primary motivators. For mining machines, a lowered energy consumption is directly related to cost for the user, but electrification also has positive side effects. By replacing the conventionally used combustion engine with an electric power source, local emissions such as exhaust gases, heat and noise are reduced. This reduction, or even elimination, improves the working environment for the machine operator and reduces the need for ventilation, which is a major energy consumer in a mine.

For electrified system solutions with on-board batteries, limited energy capacity compared to diesel fuel puts high requirements on the energy efficiency of the machine's motion system. This aspect is challenging in particular for the work functions, that conventionally are powered by a hydraulic system with throttle control. In pump-controlled hydraulic systems, valve throttling is minimised by powering each function with an individual pump [1].

Traditionally, pump-controlled systems have been difficult to motivate as they require the pumps to be dimensioned for the maximum flow of each function. With several functions, this results in an expensive system with multiple large pumps that primarily operate at part load with poor efficiency [2]. In this paper, the use of a digital displacement pump (DDP) is considered as a measure to mitigate the above-mentioned drawbacks of pump control.

1.1 Scope and Delimitations

The aim of the paper is to, in terms of energy efficiency, evaluate the potential of the concept presented in section 2 applied to the Epiroc ST14 Battery, and to investigate the gains of optimally controlling the electric motor shaft speed. The work functions considered are boom, bucket and steering while the component sizing and the driveline are not within the scope of the paper. The current available DDP version from Danfoss is considered, which operates in pump-mode only [3]. Energy recuperation from the loads is thus not considered.

1.2 Scooptram

The mining machine considered in this paper is referred to as *scooptram*. Similar to a wheel loader, a scooptram uses articulated steering and has a loader with boom and bucket. In contrast to the wheel loader a scooptram is, however, designed to be used under ground, and therefore has stricter space requirements, which results in a rather compact design. The specific machine model studied in this paper is the Epiroc ST14 Battery [4], shown in figure 1. It has a battery (Li-Ion NMC) as primary energy source, which is swapped to a recharged battery when empty. This concept allows battery charging from the grid and machine operation to occur simultaneously. The ST14 Battery uses one electric motor (traction motor) for propulsion and another (auxiliary motor) to power the work functions (boom, bucket and steering). Today, the work functions are implemented with a conventional load sensing system with two axial-piston pumps connected in parallel. This paper explores the potential of replacing each axial-piston pump with a Danfoss Digital Displacement Pump (DDP) [3], shown in figure 2.



(a) Epiroc ST14 Battery.

Property	Value	Unit
Mass	42	Tonnes
Nominal power (traction motor)	200	kW
Nominal power (auxiliary motor)	160	kW

(b) Machine Data [4].

Figure 1: Scooptram application considered in the paper.

1.3 Digital Displacement Pump

A DDP is a piston pump where the flow is controlled by individually connecting and disconnecting each piston to the pump's high and low pressure sides, enabled by actively controlled high-speed solenoid valves [5]. The pump displacement is then varied by controlling the number of active and non-active pump cylinders during one or several shaft revolutions [3]. Within the scope of this paper, it is assumed that this property is equivalent to a continuously variable displacement in a conventional pump.

A benefit with the DDP design is that it results in significantly higher part load efficiencies compared to conventional axial piston pumps. This benefit was showcased in the 16-tonnes DEXTER excavator, where the conventional pumps were replaced with DDPs. This swap resulted in fuel savings of up to 20 % with maintained productivity [6].

Another attractive feature of the DDP is that its physical layout facilitates access to the individual pistons. One pump can thus be treated as several pumps connected in parallel on the same shaft. Each pump, referred to as *pumplet*, can in turn be dedicated to an individual function [7]. If each pumplet flow is individually controlled, a system solution classified as a centralised pump-controlled system with mechanical power distribution [1] can thereby be achieved. In this paper, in contrast to [7], the DDPs are powered by an electric motor with variable speed, which presents a degree of freedom.



(a) Danfoss Digital Displacement Pump (DDP).

Property	Value	Unit
Max displacement	D_p 96	$\text{cm}^3/\text{revolution}$
Number of pumplets	4	
Pumplet displacement	D_p 24	$\text{cm}^3/\text{revolution}$
Pistons per pumplet	3	
Piston volume	8	cm^3

(b) Size data (one unit) [3].

Figure 2: Danfoss Digital Displacement Pump (DDP).

From a control perspective, a pump with variable speed and variable displacement has a degree of freedom since the pump flow is the product of these two variables. Traditionally, this freedom has been locked by considering either constant speed or constant displacement, primarily due to cost reasons [1]. One recent exception is [8], where a speed-controlled pump with discretely variable displacement is considered. As previously mentioned, this paper assumes continuously variable pumplet displacements.

1.4 Dynamic Programming

To lock the degree of freedom, optimal control is considered in this paper, using deterministic Dynamic Programming (DP). With DP, the control problem is discretised in state-time, where a recorded drive cycle is used to find the optimal control decision for each discrete time instant of the cycle, proceeding backward in time. The primary benefit with DP is that it yields the globally optimal solution (for a given discretisation). This benefit does, however, come with two important drawbacks. The first is a high computational cost, that increases exponentially with the number of states and control signals considered. The other is that it requires knowledge of the complete cycle, which means that the obtained control strategy is not implementable in practice. Rather, the results from the DP optimisation can be used to develop and evaluate causal control strategies. This is common practice within research of hybrid vehicles, where a DP result is commonly used as benchmark when evaluating energy management strategies, see for instance [9]. In this paper, the use of DP serves primarily two purposes:

- To explore the maximum potential of the considered system concept.
- To provide knowledge on how to optimally control the concept in a future implementation.

2 System Concept

Figure 3 shows the concept investigated in the paper. The conventional pumps in the ST14 Battery are replaced with DDPs (P_1 and P_2) connected to two valve blocks, while the rest of the system is unchanged. The three loads are controlled with directional valves (V_1 - V_3) that are assumed fully open when the load cylinders are in motoring mode and are used for meter-out throttling when the load cylinders are in pumping mode. The boom and bucket functions have bypass valves that are assumed to be controlled simultaneously with the directional valve of each function, to redirect some of the flow from the piston side chamber to the piston rod side chamber when the cylinder is in pumping mode, thereby reducing the required pump flow.

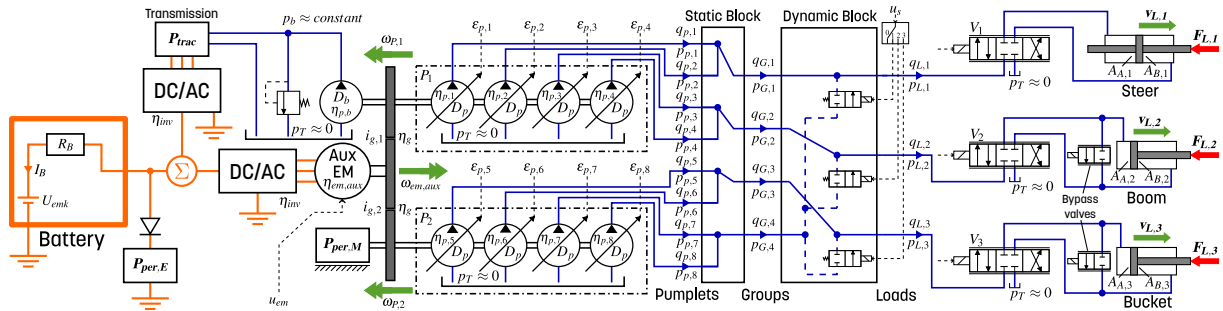


Figure 3: Layout of the system to be optimised. States that are determined directly by the drive cycle in the optimisation are highlighted in **bold**. Any check valves for load holding purposes are omitted in the figure.

The pumplets are connected to a *static* block which combines the pumplets into *groups*. The *dynamic* block connects the pumplet groups to the loads. In contrast to the static block, the dynamic block can change during use of the system, thereby enabling dynamic flow or pumplet allocation [7]. The idea of the concept is to dedicate group 1, 2 and 3 to load 1, 2 and 3, respectively, and have group 4 available as a shared resource. For instance, if 100 l/min is required by load 1, but group 1 can only provide 50 l/min, group 4 can provide the remaining 50 l/min. This enables moderate pumplet sizes as the loads seldom require their maximum flow simultaneously for the considered application.

The DDPs are powered by the auxiliary electric motor (Aux EM) which also powers peripheral mechanical functions ($P_{per,M}$, e.g. brakes, cooling) and the transmission clutch boost circuit, which consists of a fixed displacement gear pump (D_b) connected to a pressure relief valve. The auxiliary and traction (P_{trac}) electric motors are powered by the battery which also powers peripheral electric functions ($P_{per,E}$, e.g. A/C, battery cooling).

As previously discussed, the speed of the auxiliary electric motor is a free variable, and there is a compromise to make between shaft speed and flow sharing. This compromise is found using control optimisation in this paper.

3 Problem Formulation

The control optimisation problem for the considered concept is formulated as:

$$\begin{aligned}
& \underset{u_{em}(t)}{\text{minimize}} && E_B(u_{em}(t), \bar{\Lambda}(t)) \\
& \text{subject to} && 0 \leq \varepsilon_{p,k}(t) \leq 1, \quad k = 1, 2, \dots, z_p, \\
& && u_s(t) = j, \quad j \in [0, 1, \dots, z_L], \\
& && u_{em,min} \leq u_{em}(t) \leq u_{em,max}, \\
& && I_{B,min}(t) \leq I_B(t) \leq I_{B,max}(t), \\
& && \omega_{em,aux,min}(t) \leq \omega_{em,aux}(t) \leq \omega_{em,aux,max}, \\
& && \dot{\omega}_{em,aux}(t) = u_{em}(t), \\
& && \omega_{em,aux}(t_0) = \omega_{em,aux,min}(t_0), \\
& && \omega_{em,aux,min}(t_f) \leq \omega_{em,aux}(t_f) \leq \omega_{em,aux,max}
\end{aligned} \tag{1}$$

where $u_{em}(t)$ is the control signal, which is the angular acceleration of the auxiliary electric motor. This choice of control signal is made to enable limitation in shaft acceleration and thus avoid solutions with undesired and unrealistic shattering of the motor speed. It may also be noted that the introduction of the angular acceleration defines the angular speed as a state, which makes the optimal solution time-dependant. From a strict mathematical perspective, $u_{em}(t)$ may also be interpreted as an additional degree of freedom. $\bar{\Lambda}(t)$ is the drive cycle:

$$\bar{\Lambda}(t) = \begin{bmatrix} F_{L,i}(t) \\ v_{L,i}(t) \\ \vdots \\ F_{L,z_L}(t) \\ v_{L,z_L}(t) \\ P_{trac}(t) \\ \omega_{em,aux,min}(t) \end{bmatrix}, \text{ with } t \in [t_0, t_f] \tag{2}$$

where $F_{L,i}(t)$ and $v_{L,i}(t)$ is the force and velocity of load i , respectively. $P_{em,trac}(t)$ is the power to the driveline and $\omega_{em,aux,min}(t)$ is the minimum speed of the auxiliary motor as required from the driveline transmission to obtain sufficient flow to its boost circuit. t_0 and t_f are the starting time and final time of the drive cycle, respectively. The cost to minimise is the total energy consumed by the battery during the cycle:

$$E_B = \int_{t_0}^{t_f} -P_{B,ch}(t) dt \tag{3}$$

where $P_{B,ch}(t)$ is the battery charging power ($P_{B,ch} > 0$ for charging, $P_{B,ch} \leq 0$ for discharging).

4 Model

The DP algorithm uses a backward-facing simulation model to evaluate the cost-to-go at each time step. The input to this model is thus the drive cycle, $\bar{\Lambda}(t)$, and the grid of states and control signals. In the following equations, this means that $\omega_{em,aux}$ is regarded as given.

Some important modelling assumptions:

1. Constant tank pressure, $p_T \approx 0$.
2. Each control valve ($V_{1,2,3}$) and on/off valve in the dynamic valve block yield a constant pressure drop Δp_v .
3. Lossless cylinders.
4. When active, the bypass valves are controlled so that the full piston rod chamber flow is supplied by the piston chamber flow.
5. The pumplets' displacements are continuously variable.
6. Lossless static valve block.

4.1 Cylinders

The steering motion of the machine is actuated with two identical asymmetric cylinders connected in parallel. This arrangement is modelled as an equivalent symmetric cylinder. Similarly, the boom function's two cylinders are modelled as an equivalent asymmetric cylinder. Assumptions 1 - 3 yield the load pressure $p_{L,i}$ for load i :

$$p_{L,i} = \begin{cases} \frac{F_{L,i} + \Delta p_v A_{A,i}}{A_{B,i}} + \Delta p_v & P_{L,i} > 0, v_{L,i} > 0 \\ \frac{\Delta p_v A_{A,i} - F_{L,i}}{A_{B,i}} + \Delta p_v & P_{L,i} > 0, v_{L,i} \leq 0 \\ \Delta p_v & P_{L,i} \leq 0 \end{cases} \quad (4)$$

where $P_{L,i}$ is the power consumed by load i :

$$P_{L,i} = F_{L,i} v_{L,i} \quad (5)$$

The load flow $q_{L,i}$ for load i is:

$$q_{L,i} = \begin{cases} v_{L,i} A_{A,i} & v_{L,i} > 0 \\ -v_{L,i} A_{B,i} & v_{L,i} \leq 0 \end{cases} \quad (6)$$

For the boom and bucket functions, assumption 4 yields:

$$q_{L,i} = 0 \quad \text{for } P_{L,i} \leq 0, v_{L,i} \leq 0, i \in [2, 3] \quad (7)$$

4.2 Dynamic valve block

The configuration of the dynamic valve block is a function of the control signal u_s , which is implicitly defined by $\omega_{em,aux}$ after the introduction of the following rules:

1. Flow sharing is only used when a group is saturated,
2. When flow is shared, the load flow is divided equally between the saturated and shared pumplet groups,
3. The flow of each pumplet group is divided equally between the pumplets connected to this group,

To decide if sharing should occur, the maximum flow available at each group can first be calculated as:

$$\bar{q}_{G,max} = \begin{bmatrix} q_{G,max,1} \\ \vdots \\ q_{G,max,z_G} \end{bmatrix} = \bar{M}_{PG,q} \bar{q}_{p,max} = \bar{M}_{PG,q} \begin{bmatrix} q_{p,max,1} \\ \vdots \\ q_{p,max,z_p} \end{bmatrix} \quad (8)$$

where z_G is the total number of groups and z_p is the total number of pumplets. $\bar{M}_{PG,q} = \bar{M}_{GP,p}^T$ is a $[z_G \times z_p]$ matrix with zeros and ones that correspond to the connections in the static valve block (see further details in section 4.3). For the considered concept:

$$q_{p,max,k} = \begin{cases} D_p \omega_{p,1} & 1 \leq k \leq 4 \\ D_p \omega_{p,2} & 5 \leq k \leq 8 \end{cases} \quad (9)$$

where $\omega_{p,l}$ is the shaft speed of pump l :

$$\omega_{p,l} = i_{g,l} \omega_{em,aux} \quad (10)$$

where $i_{g,l}$ is the gear ratio of the gear connecting pump l to the auxiliary electric motor. Define j_{sat} as the group index at which group flow is saturated:

$$q_{L,j_{sat}} > q_{G,max,j_{sat}}, j_{sat} \in [1, 2, \dots, z_L] \quad (11)$$

where z_L is the total number of loads. According to rule 2 the flow, $q_{G,j}$, at group j is then determined as:

$$q_{G,j} = \begin{cases} q_{L,i} & i \neq j_{sat} \\ \frac{\sum_{i=1}^{z_p} \bar{M}_{GP,p}(i,j)}{\sum_{i=1}^{z_p} \bar{M}_{GP,p}(i,j) + \sum_{i=1}^{z_p} \bar{M}_{GP,p}(i,z_G)} \cdot q_{L,i} & i = j_{sat} \end{cases}, j \in [1, 2, \dots, z_L] \quad (12)$$

For the considered configuration:

$$\frac{\sum_{i=1}^{z_p} \bar{M}_{GP,p}(i,j)}{\sum_{i=1}^{z_p} \bar{M}_{GP,p}(i,j) + \sum_{i=1}^{z_p} \bar{M}_{GP,p}(i,z_G)} = \frac{1}{2}, j \in [1, 2, \dots, z_L] \quad (13)$$

The flow at the shared group is:

$$q_{G,4} = \begin{cases} 0 & i \neq j_{sat} \\ q_{L,i} - q_{G,i} & i = j_{sat} \end{cases} \quad (14)$$

and finally the group pressures are:

$$p_{G,j} = \begin{cases} p_{L,j} & j \in [1, 2, 3] \\ 0 & i \neq j_{sat} \\ p_{L,i} + \Delta p_v & i = j_{sat} \end{cases} \quad j = 4 \quad (15)$$

4.3 Static Valve Block

To determine the pumplet flows and pressures, the group flows and pressures are first collected in the vectors \bar{q}_G and \bar{p}_G , respectively:

$$\bar{q}_G = \begin{bmatrix} q_{G,1} \\ \vdots \\ q_{G,z_G} \end{bmatrix}, \bar{p}_G = \begin{bmatrix} p_{G,1} \\ \vdots \\ p_{G,z_G} \end{bmatrix} \quad (16)$$

Similarly, the pumplet flows and pressures are collected as:

$$\bar{q}_p = \begin{bmatrix} q_{p,1} \\ \vdots \\ q_{p,z_p} \end{bmatrix}, \bar{p}_p = \begin{bmatrix} p_{p,1} \\ \vdots \\ p_{p,z_p} \end{bmatrix} \quad (17)$$

Ignoring pressure losses in the static valve block, the pumplet pressures can then be determined by:

$$\bar{p}_p = \bar{M}_{GP,p} \cdot \bar{p}_G \quad (18)$$

where $\bar{M}_{GP,p}$ is a $[z_p \times z_G]$ matrix with ones and zeros that corresponds to the connections in the static valve block. For the configuration considered in this paper (figure 3):

$$\bar{M}_{GP,p} = \begin{bmatrix} 1 & 0 & 0 & 0 \\ 1 & 0 & 0 & 0 \\ 0 & 1 & 0 & 0 \\ 0 & 1 & 0 & 0 \\ 0 & 0 & 1 & 0 \\ 0 & 0 & 1 & 0 \\ 0 & 0 & 0 & 1 \\ 0 & 0 & 0 & 1 \end{bmatrix} \quad (19)$$

Ignoring leakage and obeying rule 3, the pumplet flows are determined as:

$$\bar{q}_p = \bar{M}_{GP,q} \cdot \bar{q}_G \quad (20)$$

where $\bar{M}_{GP,q}$ is a $[z_G \times z_p]$ matrix with each element:

$$\overline{M}_{GP,q}(k, j) = \frac{\overline{M}_{GP,p}(k, j)}{\sum_{i=1}^{z_p} \overline{M}_{GP,p}(i, j)} \quad (21)$$

For the configuration considered in this paper:

$$\overline{M}_{GP,q} = \frac{1}{2} \cdot \overline{M}_{GP,p} \quad (22)$$

4.4 Pumps

The relative displacement, $\varepsilon_{p,k}$, of pumplet k connected to pump l can then be determined according to:

$$\varepsilon_{p,k} = \frac{q_{p,k}}{D_p \omega_{P,l}} \quad (23)$$

The total efficiency, $\eta_{p,k}$, of pumplet k connected to pump l is then calculated with linear interpolation in an efficiency map obtained from the pump manufacturer:

$$\eta_{p,k} = f(\omega_{P,l}, p_{p,k}, \varepsilon_{p,k}) \quad (24)$$

The efficiencies are then used to calculate the input power to each pumplet:

$$P_{p,k} = \frac{q_{p,k} P_{p,k}}{\eta_{p,k}} \quad (25)$$

The power input to each pumplet can then be used to calculate the torques of pump 1 and 2:

$$T_{P,1} = \frac{\sum_{k=1}^4 P_{p,k}}{\omega_{P,1}}, \quad T_{P,2} = \frac{\sum_{k=5}^{z_p} P_{p,k}}{\omega_{P,2}} \quad (26)$$

4.5 Mechanical Losses

The boost circuit for the driveline transmission is modelled as a constant torque, assuming ideal pressure relief valve characteristics:

$$T_{b,trac} = \frac{p_b D_b}{\eta_{p,b}} \quad (27)$$

where p_b is the boost pressure, D_b the boost pump volumetric displacement and $\eta_{p,b}$ the boost pump hydromechanical efficiency (assumed constant, $\eta_{p,b} \approx 0.8$). Other peripheral mechanical losses are modelled as a constant power loss, estimated from the drive cycles:

$$T_{per,M} = \frac{P_{per,M}}{\omega_{P,2}} \quad (28)$$

4.6 Auxiliary Electric Motor

The total torque on the auxiliary electric motor is then:

$$T_{em,aux} = \frac{T_{P,1} + T_{b,trac}}{\eta_g} i_{g,1} + \frac{T_{P,2} + T_{per,M}}{\eta_g} i_{g,2} \quad (29)$$

where η_g are the gear efficiencies (assumed constant, $\eta_g \approx 0.98$). The efficiency, $\eta_{em,aux}$, of the auxiliary electric motor is calculated with linear interpolation in an efficiency map obtained from the electric motor manufacturer:

$$\eta_{em,aux} = f(T_{em,aux}, \omega_{em,aux}) \quad (30)$$

which yields the input power to the auxiliary electric motor:

$$P_{em,aux,in} = \frac{T_{em,aux} \omega_{em,aux}}{\eta_{em,aux}} \quad (31)$$

4.7 Electric circuit

The battery output power is calculated as:

$$P_B = -P_{em,trac} - \frac{P_{em,aux,in}}{\eta_{inv}} - P_{per,E} \quad (32)$$

where $P_{per,E}$ is electric peripheral losses, which are assumed constant and were estimated from the drive cycle. η_{inv} is the inverter efficiency (assumed constant). $P_{em,trac}$ is the power to the driveline electric motor:

$$P_{em,trac} = \begin{cases} \frac{P_{trac}}{\eta_{inv}} & P_{trac} \geq 0 \\ P_{trac}\eta_{inv} & P_{trac} < 0 \end{cases} \quad (33)$$

where P_{trac} is the power to the driveline recorded during the drive cycle. The battery current, I_B , is then obtained as:

$$I_B = \frac{-U_{emk}}{2R_B} + \sqrt{\left(\frac{U_{emk}}{2R_B}\right)^2 + \frac{P_B}{R_B}} \quad (34)$$

where U_{emk} and R_B are the electromotive force voltage and the internal resistance of the battery, respectively, which are both assumed to be constant and which values were obtained from the battery manufacturer. This finally yields the battery charge power:

$$P_{B,ch} = P_B - R_B I_B^2 \quad (35)$$

5 Drive Cycle

The drive cycle used in the optimisation is a short loading cycle (two repetitions, with total time $t_f = 140$ seconds, $t_0 = 0$) that was recorded with a ST14 Battery operated by a professional operator. In the recorded cycle, the machine fills the bucket in a gravel pile, reverses, turns, drives to another pile and empties the bucket. After the recording, the results were post-processed to obtain some of the states used in the optimisation (see equation (2)). The piston forces were calculated from the logged cylinder pressures and the cylinder dimensions, assuming lossless cylinders. The boom piston position was first calculated from the logged boom angle and geometrical data and then differentiated and filtered with a moving average filter to obtain the piston velocity. Similarly, the steer piston velocity was obtained from the steer angle while the bucket velocity was calculated from the logged piston position. The driveline power was calculated from the logged torque and speed of the driveline electric motor.

6 Results and Discussion

The optimisation problem in section 3 was solved with DP using the implementation in [10] with the settings in table 1. The time discretisation was made with a time step of 0.2 seconds, which is regarded as the minimum actuation time of the on/off valves used in the dynamic valve block.

Table 1: Optimisation settings.

Parameter		Value	Unit
Time step		0.2	seconds
Max motor speed	$\omega_{em,aux,max}$	3000	rpm
Motor speed grid size		200	points
Minimum motor shaft acceleration	$u_{em,min}$	-100	rad/s ²
Maximum motor shaft acceleration	$u_{em,max}$	100	rad/s ²
Motor shaft acceleration grid size		49	points

The resulting state trajectory (auxiliary motor shaft speed), the shared group load dedication ($u_s(t)$) and the pumplet group pressures for the optimised cycle are shown in figure 4 while the group and load flows are shown in figure 5. The optimisation maximises the shared group use to minimise the auxiliary motor speed. Parts of the cycle require higher shaft speed to match the required flow. These parts can be observed in figures 4-5 as the bucket filling phases (20-40 seconds and 80-100 seconds) and the boom raising phases (50-70 seconds and 110-120 seconds).

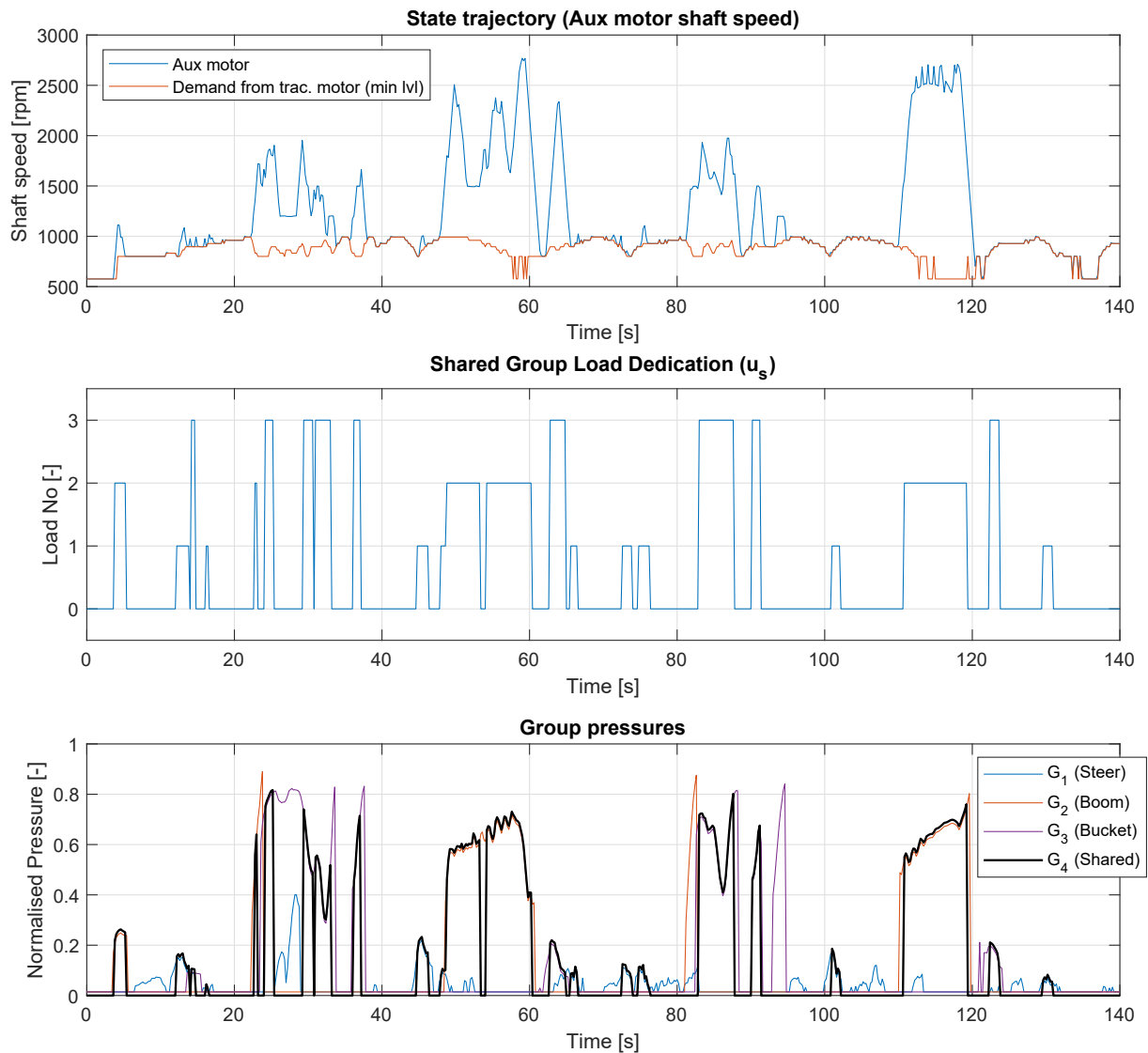


Figure 4: Auxiliary motor speed, flow sharing control signal and normalised group pressures for the optimised cycle.

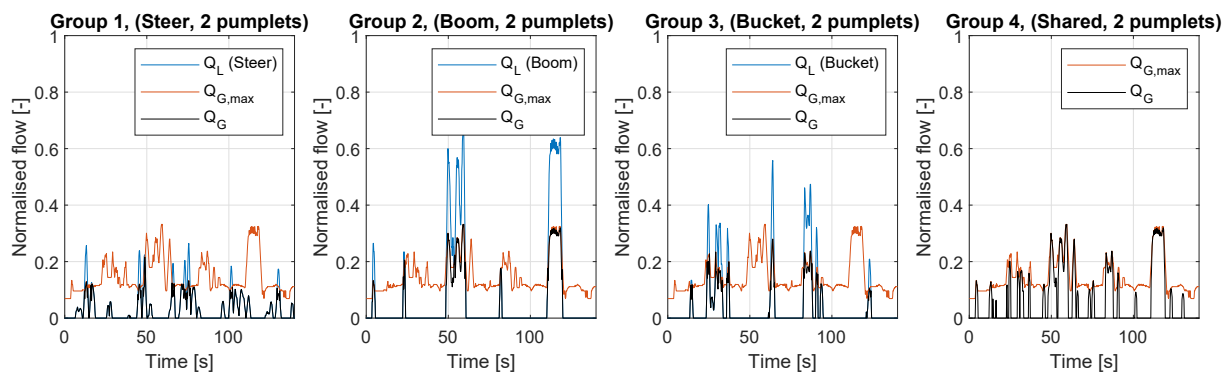
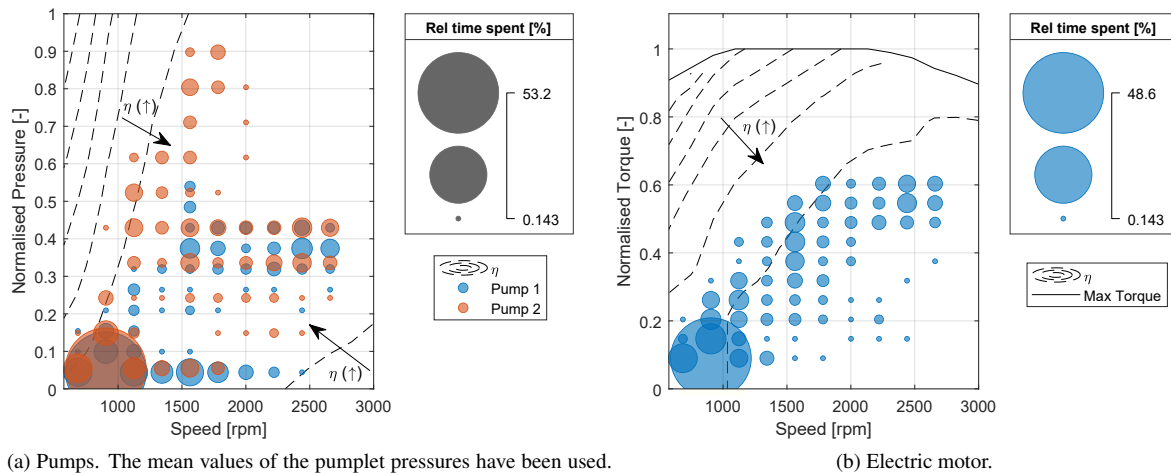


Figure 5: Normalised group and load flows for the optimised cycle.

Figure 6 shows bubble plots for the pumps and the auxiliary electric motor. In these figures as well, it is clear that low speed is preferred, since around 50 % of the cycle is spent near 900 rpm. It may be noted though, that maximum efficiency of the pumps and the electric motors is not prioritised, as the efficiency-optimal speeds for both these components are significantly higher (around 2000-3500 rpm). It was found that the reason for this was the power loss due to the transmission boost circuit. This loss increases proportionally to the electric motor shaft speed and is significantly larger (approximately a factor 2) than the losses in the pumps and the electric motor. These results highlight the benefits of considering the complete system rather than the individual components when evaluating energy efficiency, and of having high and relatively flat (operation point-independent) efficiencies in the pumps and electric motors. For the ST14 Battery machine, the results also suggest that an alternative solution for the boost circuit could be interesting.



(a) Pumps. The mean values of the pumplet pressures have been used. The efficiency map is shown for 50% of full pump displacement.

(b) Electric motor.

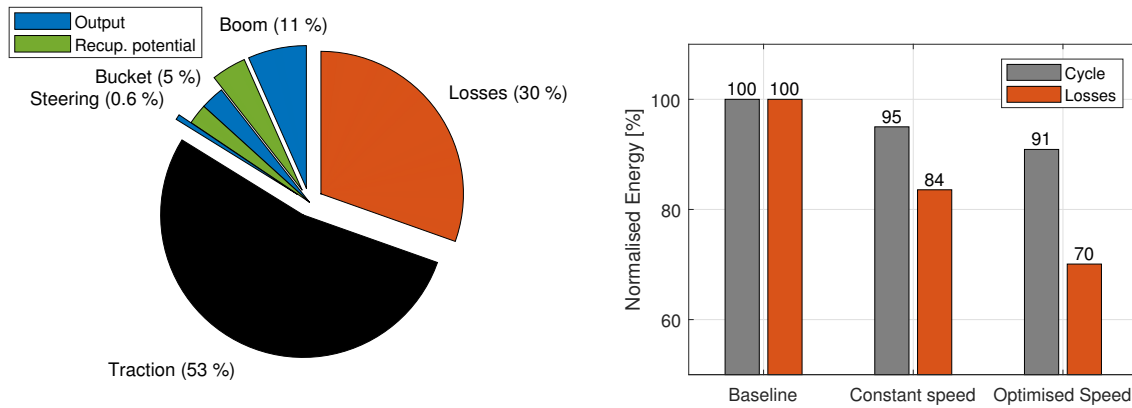
Figure 6: Bubble plots for the pumps and the auxiliary electric motor for the optimised cycle.

To investigate the gains of optimally controlling the motor speed, an optimisation with constant speed, chosen as the highest value in figure 4 (2800 rpm), was carried out. The resulting cycle energy is shown in figure 7, where the energy for the baseline case (load-sensing with axial-piston pumps) and the optimised case are also shown for comparison. Compared with the baseline case, the total cycle energy was decreased with 5 % using constant speed, while optimal speed control added an additional drop of 4 %. The losses decreased with 16 % with constant speed with an additional drop of 14 % with optimally controlled speed. The primary cause for the improvements were found to be reduced pump losses and reduced valve throttling losses. One important source of error are the peripheral electrical losses ($P_{per,E}$), which were difficult to estimate accurately and stands for approximately 7 - 8 % of the cycle's total energy consumption. This indicates a need to investigate these losses in more detail.

Compared to [6, 7], the obtained improvements may be considered surprisingly small. In [6, 7], the application is, however, an excavator with a diesel engine, where parts of the savings were achieved by selecting a more fuel-optimal point of the engine. In addition, all power is actuated with the hydraulic system in an excavator while the driveline represented 53 % of the energy consumption for the scooptram in the considered cycle (see figure 7a). Moreover, in contrast to an excavator, simultaneous use of multiple hydraulic functions is rare in a scooptram, which results in low pressure-compensating losses in the baseline case. The gains from introducing pump control in the considered application are therefore relatively low compared to the excavator considered in [7].

The results indicate that approximately 4 % extra energy savings are gained by optimally controlling the electric motor speed, where the gains are almost exclusively due to the lowered losses in the transmission boost circuit. This improvement is in the same order of magnitude as was found for the truck loader crane considered in [8], and may be seen as moderate. One important reason for this improvement being moderate is that the pumps and the electric motor both have relatively high efficiency for a large operational domain, which therefore makes the speed parameter of less importance (efficiency-wise) for these components. The fact that scooptrams often operate non-stop in short loading cycles still, however, makes 4 % a desirable improvement. On that same topic, all the presented results are based on one cycle, and other cycles may lead to a different number.

Furthermore, it may be noted that the boom and bucket functions have high amounts of energy that potentially be recuperated, which could further lower the energy losses.



(a) Cycle energy distribution (Baseline). The function energies were calculated as the integrated mechanical power ($F_{L,i} \cdot v_{L,i}$) for each function. The green fields indicate negative power that potentially could be recuperated. The losses were calculated as the difference between the logged battery input power and the total output power (functions plus traction).

(b) Cycle energy and energy losses for different cases.

Figure 7: Cycle energy. The baseline cycle energy was calculated from the recorded battery current and voltage.

7 Conclusions and Outlook

The Digital Displacement Pump facilitates the implementation of pump control in a mobile working machine. By using control optimisation, the maximum potential of the considered pump control concept with dynamic flow sharing could be evaluated. The optimal control results show that a strategy with minimised electric motor speed is preferred, primarily due to drag losses from the boost circuit of the transmission clutch actuation system. This strategy is facilitated by the high and relatively operation point-independent efficiencies of the pumps and electric motor. The results indicate a 5 % decrease in total system energy use for the considered short loading cycle, with an additional 4 % drop if the electric motor speed is optimally controlled. The improvements primarily come from reduced pump and valve throttling losses.

The low amount of simultaneous function use in the considered application suggest that greater loss reductions is to be expected for a more hydraulic-intense application, such as an excavator. Moreover, the obtained results depend on the considered concept, load cycle and the component sizes. It should also be emphasised that the obtained optimal strategy is not implementable in a causal controller, which indicate lower savings in a final application. Other applications, load cycles, concepts, combined control and component sizing optimisation and development of causal control strategies are, consequently, subjects for future work.

8 Acknowledgements

This research was funded by the Swedish Energy Agency (Energimyndigheten, Grant Number 50181-2), Volvo Construction Equipment AB and Epiroc AB. The authors would particularly like to thank Simon Magnusson and Markus Bagge at Eiproc for their input concerning the ST14 Battery machine, and Kim Heybroek at Volvo Construction Equipment for valuable input on working machines.

Nomenclature

Designation	Denotation	Unit
$A_{A/B}$	A/B-side piston area	m^2
D	Volumetric displacement	m^3/rad
Δp_v	Valve pressure drop	Pa
E	Energy	J
ε	Relative displacement	-
η	Efficiency	-
F	Force	N
I	Current	A
i_g	Gear ratio	-
Λ	Drive cycle	(vector)

$\bar{M}_{GP,p/q}$	Static valve block pressure/flow matrix (Groups->pumples)	(matrix)
$\bar{M}_{GP,p/q}$	Static valve block pressure/flow matrix (Groups->pumples)	(matrix)
v	Velocity	m/s
E	Energy	J
ω	Rotational speed	rad/s
P	Power	W
p	Pressure	Pa
q	Flow	m ³ /s
R	Resistance	Ohm
T	Torque	Nm
t_0	Cycle start time	seconds
t_f	Cycle end time	seconds
U	Voltage	V
$u_{em/s}$	Electric motor/flow sharing control signal	rad/s ² (-)
z_G	Total number of groups ($z_G = 4$ here)	-
z_L	Total number of loads ($z_L = 3$ here)	-
z_p	Total number of pumples ($z_p = 8$ here)	-
Subscripts		
aux	Auxiliary	i Load number
B	Battery	inv Inverter
b	Boost	j Group number
E	Electric	k Pumplet number
em	Electric motor	L Load
emk	Electromotive force	l Pump number
G	Group	M Mechanical
		P Pump
		p Pumplet
		per Peripheral
		sat Saturated
		T Tank
		$trac$ Traction

References

- [1] Søren Ketelsen, Damiano Padovani, Torben O. Andersen, Morten Kjeld Ebbesen, and Lasse Schmidt. Classification and review of pump-controlled differential cylinder drives. *Energies*, 12(7), 2019.
- [2] Kim Heybroek. *On Energy Efficient Mobile Hydraulic Systems: with Focus on Linear Actuation*. PhD thesis, Linköping University, 2017.
- [3] Danfoss Power Solutions. Digital Displacement Pump, User Guide <https://assets.danfoss.com/documents/149654/BC306384089197en-000102.pdf>. Last visited on: 2021-02-17.
- [4] Epiroc. Scooptram ST14 Battery <http://www.podshop.se/Epiroc/epiroc/Products/DownloadLowres/?productRef=83685>. Last visited on: 2021-02-17.
- [5] Niall Caldwell. Review of Early Work on Digital Displacement® Hydrostatic Transmission Systems. volume BATH/ASME 2018 Symposium on Fluid Power and Motion Control of *Fluid Power Systems Technology*, 09 2018. V001T01A061.
- [6] Matthew Green, Jill Macpherson, Niall Caldwell, and W. H. S. Rampen. DEXTER: The Application of a Digital Displacement® Pump to a 16 Tonne Excavator. volume BATH/ASME 2018 Symposium on Fluid Power and Motion Control of *Fluid Power Systems Technology*, 09 2018.
- [7] Matteo Pellegrini, Matthew Green, Jill Macpherson, Callan McKay, and Niall Caldwell. Applying a Multi-Service Digital Displacement® Pump to an Excavator to Reduce Valve Losses. In *12th International Fluid Power Conference (IFK'20)*, Dresden, Germany, 2020.
- [8] Samuel Kärnell, Amy Rankka, Alessandro Dell'Amico, and Liselott Ericson. Digital Pumps in Speed-Controlled Systems - An Energy Study for a Loader Crane Application. In *12th International Fluid Power Conference (IFK'20)*, Dresden, Germany, 2020.
- [9] Michael Sprengel and Monika Ivantysynova. Neural network based power management of hydraulic hybrid vehicles. *International Journal of Fluid Power*, 18(2):79–91, 2017.
- [10] Olle Sundstrom and Lino Guzzella. A generic dynamic programming matlab function. In *2009 IEEE Control Applications, (CCA) Intelligent Control, (ISIC)*, pages 1625–1630, 2009.

Adaptive Identification and Application of Flow Mapping for Electrohydraulic Valves

Jianbin Liu, André Sitte, Prof. Dr. -ing. Jürgen Weber*

Institute of Mechatronic Engineering - Chair of Fluid-Mechatronic Systems, Technical University of Dresden, Germany
E-mail: jianbin.liu@tu-dresden.de, andre.sitte@tu-dresden.de, fluidtronik@mailbox.tu-dresden.de

Abstract

Good estimates of flow mapping for electrohydraulic valves are important in automation of fluid power system. The purpose of this paper is to propose adaptive identification methods based on a recursive least squares method (RLSM), a recursive maximum likelihood method (RMLM) and radial basis function neural network (RBFNN) to estimate the uncertain parameters in flow mapping for electrohydraulic valves. In order to reduce the complexity and improve the identification performance, model structures derived from prior knowledge are introduced. The methods are applied to map the pressure-flow characteristic of an electrohydraulic valve. With the help of simulation results, the accuracy and efficiency of these algorithms are demonstrated. Some issues like invertibility of flow mapping are discussed and suggestions to apply these methods are made.

Keywords: adaptive identification, flow mapping, electrohydraulic valve, RLS, RML, RBF

1 Introduction

For many years, hydraulic-mechanical control systems have been characterized by extremely high requirements for good operability, high reliability, robustness and a favorable cost-benefit ratio. However, an increase in efficiency and productivity for control systems can only be achieved through the use of electrohydraulic components in combination with electronics, sensors and software. Among the many components that contributed to the success of electrohydraulic control systems, the proportional valve elements are of considerable importance. The flow rate of valves cannot be described precisely enough by simple physics-based equations because of highly non-linear characteristic. Offline-Identification of flow mapping is an efficient way to compensate the complex non-linearity in valves partially. Though offline-Identification cannot adapt to changes in the system properties over time, e.g. the influences of temperature, erosion on the valve edges and wear of valve spool. Therefore, a self-learning system for adaptive identification of flow mapping for proportional valve elements in electrohydraulic system is crucial, in which not only the complex non-linearity can be compensated, but also the flow mapping can be adapted to the varying system parameters. Numerous system identification methods are now available, but the suitability of adaptive identification for valve elements has not been sufficiently investigated. In addition, it is necessary to make a prediction based on limited data about flow mapping at some cases. As for the application of flow mapping, various fields can be found such as demand-based flow rate control for energy-efficient operation, high precision control, autonomous control, maintenance and fault detection, condition monitoring and diagnostics. The present paper aims to analyze different adaptive methods for (inverse) flow mapping which could be acted as feedforward controller. If the flow rate characteristic relationship $Q = f(U, \Delta p, \dots)$ is inverted to $U = f(Q, \Delta p, \dots)$, the inverse flow mapping could also be used for feedforward control instead of traditional lookup table method. Compared with the direct mapping for $U = f(Q, \Delta p, \dots)$, the inverse flow mapping can effectively reduce the complexity of computational effort while ensuring accuracy.

Starting with research and comparison of different adaptive identification methods, suitable for an adaptive identification of flow mapping in electrohydraulic valves, considering online-processing capability, signal-to-noise ratio, model fidelity and amongst others. Different adaptive identification method based on RLSM, RMLM and

RBFNN are chosen for flow mapping of electrohydraulic valves. Examples of adaptive identification with RLSM can be found in the work by Vahidi et al. [1], C. Kamali et al. [2], S. Dong et al. [3] and M. Kazemi et al. [4]. Similarly, RMLM is also the popular adaptive parameter estimation in the field of parameter identification. The origin of the RMLM can be traced back to R. A. Fisher [5]. L. Ma et al. [6] have applied the RMLM for the identification of Hammerstein ARMAX system and compared with RLSM in detail. In order to combine the advantages of Maximum Likelihood and RLSM, J. Li et al. [7] have used a maximum likelihood recursive least squares method for multivariable systems. Chen et al. [8] derived a filtering based maximum likelihood recursive least squares algorithm for reducing computational efforts. O. Nelles et al. [9] presented a comparison between RBF networks and classical methods for identification of nonlinear dynamic systems. RBFNN has wide applications in many areas such as computer science, aircraft and mathematics [10-14].

Besides the identification methods, the source data types play an important role in identification. Figure 1 proposes different source data types for identification. Static data are time independent. On the contrary, dynamic data are time dependent and the inertial effects have to be taken into account. The transition data type between them are quasi-static data, which are time dependent but slow enough to neglect its inertial effects. Usually, structured data characterize the flow behavior of throttle valves. These data are determined at discrete input signals, representing the operating range. There is a high resolution along the x-axis, whereas only a few data point exist along the y-axis. The data-gap increases the requirements for the training procedures (optimization) and eventually creates great deviations between model and estimation. A comprehensive scatter data-set appears to be advantageous in terms of coverage. However, arbitrary data is difficult to interpret and to evaluate, which is why the use of such data is not very widespread. Limited and noisy flow data are more common. The restrictions mostly result from limited capacities of the test rig or system setup. Noise is inherent to measurement data, which requires filtering of data or smoothing capabilities of the approximation procedures. Operating point data contain operating point resulting from a typical working cycle of machine. In this paper, quasi-static data combined with structured data and scattered data are used for identification.

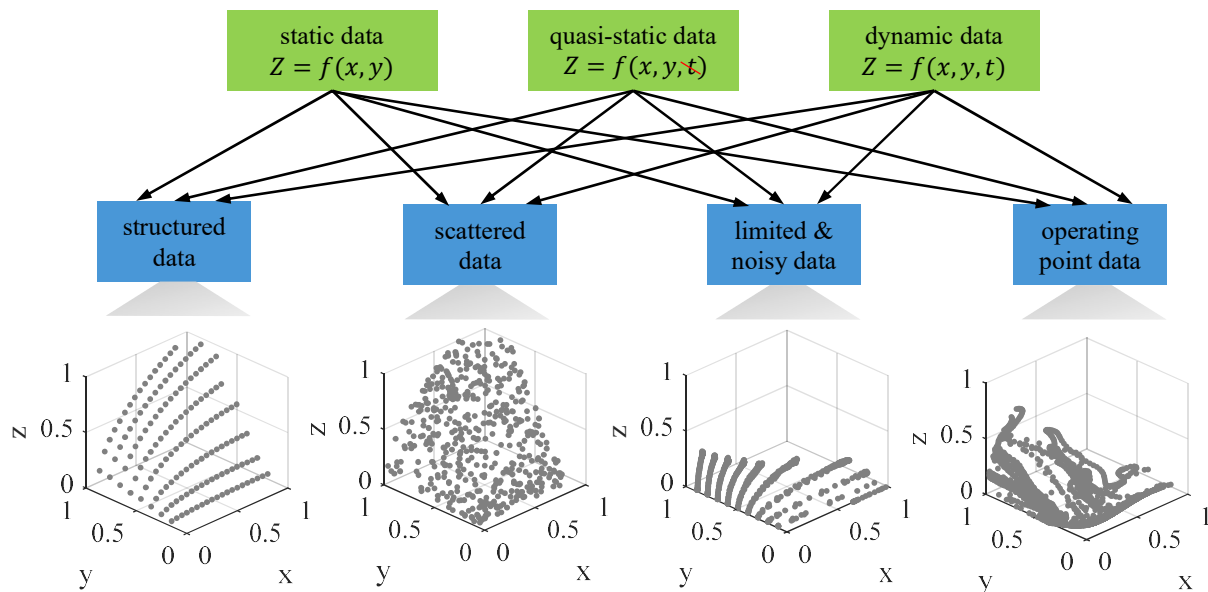


Figure 1: combination of source data types for identification [17]

The subsequent paper is organized as follows: In Section 2, to be acquainted with the static characteristics of the electrohydraulic valve, a test rig in laboratory has been set up. After that, a virtual demonstrator with real-time and streaming OPC UA data has been completed, which was carried out in simulation environment to validate the adaptive parameter identification methods. Then the suitable adaptive identification methods are chosen and derived in Section 3, including LSM, RLSM, RMLM and RBF. In Section 4, the previously developed, adaptive identification methods have been applied and exemplified in order to obtain the evolving flow mapping of a piloted proportional valve, which belongs to the test rig. The results demonstrate that the adaptive identification methods have convincing performance for the flow mapping of electrohydraulic valves. Finally, conclusions are drawn and some issues to be solved are discussed in Section 5.

2 Modelling and Test Rig of Electrohydraulic Valve

2.1 Modelling of Electrohydraulic valve

Figure 2 shows the construction of proportional seat valve “Valvistor”, which is based on hydraulic position feedback.

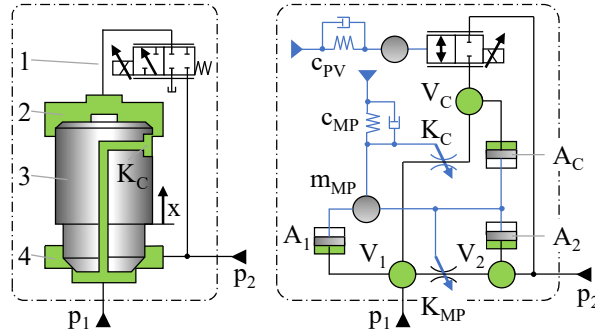


Figure 2: Construction for flow direction p_1 to p_2 (left) / simplified simulation model structure (right) [17]

Due to a negative overlap of the variable orifice between control chamber (2) and main poppet (3), the pressure p_c in the control chamber V_c is equal to the pressure p_1 at the valve inlet V_1 . Because of the upper area of the main poppet is greater than the area facing p_1 , the closing position of seat valve is ensured. Opening the pilot valve (1), pressure drop enables the pilot flow Q_{PV} and reduces the control pressure p_c in the control chamber. The main poppet starts moving until the equilibrium of forces is established. Neglecting flow- and friction forces and rearranging the force balance equation for the main poppet leads to:

$$p_c = \frac{p_1}{\varphi} + \left(\frac{\varphi-1}{\varphi}\right) p_2 \text{ with } \varphi = \frac{A_1+A_2}{A_1} \quad (1)$$

The flow rate across control-orifice K_c results in:

$$Q_c = Q_{PV} = K_c(x_0 + x_{MP})\sqrt{\Delta p_{1c}} \quad (2)$$

Where x_{MP} is the displacement of main poppet and x_0 is the negative overlap. According to eq. (1) and (2), the following interrelation can be obtained:

$$x_{MP} = \left(\frac{Q_{PV}}{K_c} \sqrt{\frac{(\varphi-1)}{\varphi(p_1-p_2)}}\right) - x_0 \quad (3)$$

The flow rate across main poppet is given as:

$$Q_{MP} = K_{MP}x_{MP}\sqrt{\Delta p_{12}} \quad (4)$$

Neglecting the negative overlap x_0 in eq. (3) and substituting eq. (3) into eq. (4), results in following equation:

$$Q_{MP} = \left(\frac{K_{MP}}{K_c} \sqrt{\frac{\varphi-1}{\varphi}}\right) Q_{PV} \quad (5)$$

The total flow rate is given as:

$$Q_T = Q_{MP} + Q_{PV} \quad (6)$$

From eq. (5) and (6), it can be seen that Valvistor amplifies a small flow rate Q_{PV} through the pilot valve, which is similar to a transistor. Therefore, the name “Valvistor” is derived from valve and transistor. More about the Valvistor can be found in [15], [16] and [17].

2.2 Test Rig and Results

Figure 3 shows the hydraulic plan and corresponding test rig built in laboratory. It consists of hydraulic reservoir, adjustable pump, pressure relief valve, test valve (Valvistor), pressure control valve (load valve) and cooling system, which is not shown here. The instrumentations installed in the system are various pressure sensors, temperature sensor, a flow meter and displacement sensor, to measure the displacement of main poppet. For the static measurements, the hydraulic system could be seen as constant pressure system with $p_0 = 200$ bar. Because of limited power of pump, max. flow rate is restricted to $Q_{max} = 200$ l/min. Furthermore, in order to reduce

influence factor, the oil temperature in tank is set to $\vartheta_T = 40^\circ\text{C}$. To acquire the static characteristics of the electrohydraulic valve, the control signals for test valve are given in the manner of discrete values. At the same time, with the help of load valve, the outlet pressure p_2 varies between maximum and minimum so that the flow rate through test valve is changed in a quasi-static manner.

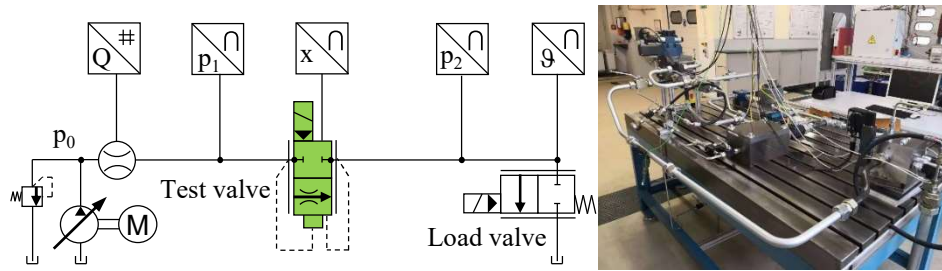


Figure 3: hydraulic plan for test rig (left) [17] Test rig in laboratory (right)

Figure 4 presents the flow rate-pressure drop characteristic curves of test valve at different control voltages. As a whole, the simulation results are in good agreement with the measured results. Based on the validated model, it's convenient to apply the adaptive identification methods in next section.

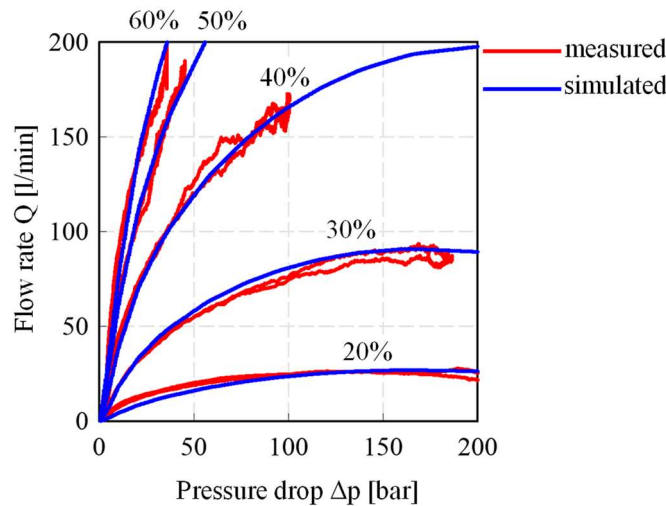


Figure 4: flow rate- pressure drop characteristic curves at different control voltages U_{rel}

3 Adaptive Identification Algorithm

3.1 Outline of Adaptive Identification

Figure 5 shows the simplified basic sequence of the identification. The first step is to define the purpose of identification. The purpose of this paper is to identify the relationship among flow rate Q , control voltage U and pressure drop Δp for electrohydraulic valves. With the help of a priori knowledge, it can be presented as:

$$Q = f(U, \Delta p)$$

The next step is determination of model structure. Model structure identification is based on the purpose of identification and the application of mathematical models in practice. Most of the mathematical model structures of linear systems can be easily identified by input and output data. However, since the static characteristics of electrohydraulic valves are more complex, which contain nonlinear factors, the model structures would mainly get through prior knowledge, assumptions and experiments. Based on these, there are two ways to determine the model structure.

The first way is to linearize the nonlinear system at first. Then use the linear system identification methods. This method will be adopted with RLSM and RMLM in the following. After trial tests, with the help of prior knowledge and algebraic polynomials [17], following approximation for the Valvisor valve can be given:

$$Q = f(U, \sqrt{\Delta p}) = a_1 + a_2 U + a_3 \sqrt{\Delta p} + a_4 U \sqrt{\Delta p} + a_5 (\sqrt{\Delta p})^2 \quad (7)$$

Where a_1, a_2, \dots, a_5 are the parameters, which should be identified. Pressure drop Δp is replaced by $\sqrt{\Delta p}$ in eq. (1). The reasons for that are closer to the theoretical flow rate formula and a kind of simple and efficient order-reduction means. By means of this linearization, it can greatly expand the scope of identification methods.

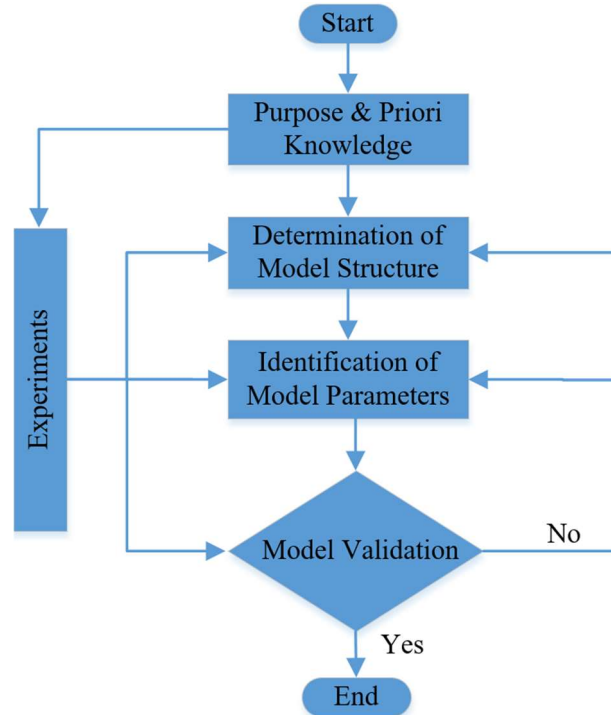


Figure 5: basic sequence of the identification [18]

Then the system approximation can be simplified as:

$$Q = X^T \theta \quad (8)$$

With $\theta = [a_1 \ a_2 \ a_3 \ a_4 \ a_5]^T$ and $X = [X_1 \ X_2 \ X_3 \ X_4 \ X_5]^T = [1 \ U \ \sqrt{\Delta p} \ U\sqrt{\Delta p} \ (\sqrt{\Delta p})^2]^T$.

The second method is to directly identify the nonlinear system model structure. For certain types of nonlinear system, models can be formulated that match well with the requirements on the model structure of known identification methods [18]. A nonlinear system identification using RBFNN will be covered in the following.

The following task is applying of suitable identification methods to identify model parameters. By means of a weighted point evaluation on the basis of the criteria suitability for linear or nonlinear process, allowable signal-to-noise ratio, suitability for offline or online processing, ability for time variant system and resulting model fidelity, preferred adaptive identification methods could be determined. At the end, least squares method (RLSM), recursive maximum likelihood method (RMLM) and radial basis function neural network (RBFNN) are therefore used for flow mapping of electrohydraulic valves and further investigated. Non-recursive least squares method (LSM) is introduced simply for derivation and comparison purposes in paper.

3.2 Non-Recursive Least Squares Method (LSM)

The non-recursive least squares method (LSM) can be utilized for linear systems. In general, the model estimation of electrohydraulic Valves is given as:

$$Q_M = a_1 X_1 + a_2 X_2 + \dots + a_n X_n \quad (9)$$

The error ε between measured output Q_P and model estimation Q_M is determined as:

$$Q_P = Q_M + \varepsilon = a_1 X_1 + a_2 X_2 + \dots + a_n X_n + \varepsilon \quad (10)$$

At different time $t = 1, 2, \dots, t$, it is easy to get the measured inputs X_i and output Q_P , which can be noted as $X_i(t)$ and $Q_P(t)$. Similarly, the error ε can be defined as $\varepsilon(t)$. Then the system equations can be written as:

$$\begin{cases} Q_p(1) = a_1X_1(1) + a_2X_2(1) + \dots + a_nX_n(1) + \varepsilon(1) \\ Q_p(2) = a_1X_1(2) + a_2X_2(2) + \dots + a_nX_n(2) + \varepsilon(2) \\ \vdots \\ Q_p(t) = a_1X_1(t) + a_2X_2(t) + \dots + a_nX_n(t) + \varepsilon(t) \end{cases} \quad (11)$$

If the vector θ and $X(t)$ are defined as $\theta = [a_1 \ a_2 \ \dots \ a_n]^T$ and $X(t) = [X_1(t) \ X_2(t) \ \dots \ X_n(t)]^T$. Then the system equation can be reduced to matrix form:

$$Q_p(t) = [X_1(t) \ X_2(t) \ \dots \ X_n(t)][a_1 \ a_2 \ \dots \ a_n]^T + \varepsilon(t) = X^T(t)\theta + \varepsilon(t) \quad (12)$$

If the vector $\mathbf{Q}_{p,t}$, \mathbf{X}_t and $\boldsymbol{\varepsilon}_t$ are defined as: $\mathbf{Q}_{p,t} = [Q_p(1) \ Q_p(2) \ \dots \ Q_p(t)]^T$, $\mathbf{X}_t = [X^T(1) \ X^T(2) \ \dots \ X^T(t)]^T$ and $\boldsymbol{\varepsilon}_t = [\varepsilon(1) \ \varepsilon(2) \ \dots \ \varepsilon(t)]^T$. Then the system equations (11) can be reduced to matrix form:

$$\mathbf{Q}_{p,t} = \mathbf{X}_t\theta + \boldsymbol{\varepsilon}_t \quad (13)$$

Where θ is the parameter vector, which should be identified. According the principle of least square, the cost function:

$$J(\theta) = \sum_{t=1}^L \varepsilon(t)^2 = \sum_{t=1}^L (Q_p(t) - X^T(t)\theta)^2 = \boldsymbol{\varepsilon}_t^T \boldsymbol{\varepsilon}_t = [\mathbf{Q}_{p,t} - \mathbf{X}_t\theta]^T [\mathbf{Q}_{p,t} - \mathbf{X}_t\theta] \quad (14)$$

To find the minimum of cost function, the first derivative with regard to the parameter vector θ is set to zero:

$$\left. \frac{\partial J(\theta)}{\partial \theta} \right|_{\hat{\theta}_{LS}} = -2\mathbf{X}_t^T(\mathbf{Q}_{p,t} - \mathbf{X}_t\theta) = 0 \quad (15)$$

This equation can be solved to provide an estimation for parameter vector $\hat{\theta}_{LS}$ as:

$$\hat{\theta}_{LS}(t) = (\mathbf{X}_t^T \mathbf{X}_t)^{-1} \mathbf{X}_t^T \mathbf{Q}_{p,t} = \left[\sum_{t=1}^L X(t)X^T(t) \right]^{-1} \left[\sum_{t=1}^L X(t)Q_p(t) \right] \quad (16)$$

Where L is the length of data.

3.3 Recursive Least Squares Method (RLSM)

The precondition for non-recursive least squares method (LSM) requires all the measured data had first been stored then estimates the parameter in one pass. Such a method requires also a lot of computational efforts, especially the matrix inversion in eq.(16). Therefore, the non-recursive least squares method (LSM) is not suitable for real time identification. In order to overcome these deficiencies, recursive least squares method (RLSM) is introduced. Furthermore, with appropriate modifications and forgetting factor, it's easy to realize the adaptive identification and solve the data saturation problem at the same time. With

$$P^{-1}(t) = \mathbf{X}_t^T \mathbf{X}_t = \sum_{t=1}^L X(t)X^T(t) = \sum_{t=1}^{L-1} X(t)X^T(t) + X(t)X^T(t)|_{t=L} \quad (17)$$

The following equation can be given:

$$P^{-1}(t) = P^{-1}(t-1) + X(t)X^T(t), \quad P(0) = P_0I > 0 \quad (18)$$

In order to reduce the error in matrix inversion of $P(t)$, according to matrix inversion lemma:

$$(A + BC)^{-1} = A^{-1} - A^{-1}B(I + CA^{-1}B)^{-1}CA^{-1}$$

The eq. (18) can be given as:

$$\begin{aligned} P(t) &= (P^{-1}(t-1) + X(t)X^T(t))^{-1} \\ &= P(t-1) - P(t-1)X(t)(1 + X^T(t)P(t-1)X(t))^{-1}X^T(t)P(t-1) \\ &= \left(I - \frac{P(t-1)X(t)X^T(t)}{1 + X^T(t)P(t-1)X(t)} \right) P(t-1) = (I - L(t)X^T(t))P(t-1) \end{aligned} \quad (19)$$

Where $L(t)$ is the gain vector:

$$L(t) = \frac{P(t-1)X(t)}{1 + X^T(t)P(t-1)X(t)} \quad (20)$$

Together with eq. (19) and (20), one then obtains:

$$P(t)X(t) = \left(I - \frac{P(t-1)X(t)X^T(t)}{1 + X^T(t)P(t-1)X(t)} \right) P(t-1)X(t) = \frac{P(t-1)X(t)}{1 + X^T(t)P(t-1)X(t)} = L(t) \quad (21)$$

According to the definition of $\mathbf{Q}_{P,t} = [Q_P(1) \ Q_P(2) \ \dots \ Q_P(t-1) \ Q_P(t)]^T = [\mathbf{Q}_{P,t-1} \ Q_P(t)]$ and $\mathbf{X}_t = [X^T(1) \ X^T(2) \ \dots \ X^T(t-1) \ X^T(t)]^T = [\mathbf{X}_{t-1} \ X^T(t)]$, the eq. (16) can be transformed as:

$$\begin{aligned} \hat{\theta}_{LS}(t) &= (\mathbf{X}_t^T \mathbf{X}_t)^{-1} \mathbf{X}_t^T \mathbf{Q}_{P,t} = P(t) \begin{bmatrix} \mathbf{X}_{t-1} \\ X^T(t) \end{bmatrix}^T \begin{bmatrix} \mathbf{Q}_{P,t-1} \\ Q_P(t) \end{bmatrix} = P(t) \left(\mathbf{X}_{t-1}^T \mathbf{Q}_{P,t-1} + X(t)Q_P(t) \right) \\ &= P(t) \left(P^{-1}(t-1)P(t-1)\mathbf{X}_{t-1}^T \mathbf{Q}_{P,t-1} + X(t)Q_P(t) \right) = P(t) \left(P^{-1}(t-1)\hat{\theta}_{LS}(t-1) + X(t)Q_P(t) \right) \end{aligned} \quad (22)$$

Base on eq. (18), one can substitute $P^{-1}(t-1) = P^{-1}(t) - X(t)X^T(t)$ in eq. (22) and obtains

$$\hat{\theta}_{LS}(t) = \hat{\theta}_{LS}(t-1) + P(t)X(t) \left(Q_P(t) - X^T(t)\hat{\theta}_{LS}(t-1) \right) \quad (23)$$

Which combined with eq. (21), one can write:

$$\hat{\theta}_{LS}(t) = \hat{\theta}_{LS}(t-1) + L(t) \left(Q_P(t) - X^T(t)\hat{\theta}_{LS}(t-1) \right) \quad (24)$$

From eq. (19), (20) and (24), recursive least squares method (RLSM) can be described by:

$$\begin{cases} L(t) = \frac{P(t-1)X(t)}{1 + X^T(t)P(t-1)X(t)} \\ \hat{\theta}_{LS}(t) = \hat{\theta}_{LS}(t-1) + L(t) \left(Q_P(t) - X^T(t)\hat{\theta}_{LS}(t-1) \right) \\ P(t) = (I - L(t)X^T(t))P(t-1) \end{cases} \quad (25)$$

If the estimation parameters of an electrohydraulic valve change abruptly, for example, damage of valve, RLSM can't capture the new values in time. The estimation parameter from RLSM will vary continuously but slowly, this is co called data saturation. With some modification, RLSM can be changed to RLSM with forgetting factor, in which less weight is given to older data and more weight to recent information. With new definition:

$$\mathbf{X}_t = \begin{bmatrix} \lambda^{\frac{1}{2}} \mathbf{X}_{t-1} \\ X^T(t) \end{bmatrix}$$

Where λ is the forgetting factor and $\in (0,1]$. The eq. (17) can be modified as:

$$P^\lambda(t) = \mathbf{X}_t^T \mathbf{X}_t = \sum_{t=1}^L X(t)X^T(t) = \frac{1}{\lambda} \sum_{t=1}^{L-1} X(t)X^T(t) + X(t)X^T(t)|_{t=L} = \frac{1}{\lambda} P^{-1}(t-1) + X(t)X^T(t) \quad (26)$$

Thus, it follows:

$$P^\lambda(t-1) = \frac{1}{\lambda} P^{-1}(t-1) \quad (27)$$

If one substitutes the eq. (27) in eq. (25), RLSM with forgetting factor is given as:

$$\begin{cases} L^\lambda(t) = \frac{P^\lambda(t-1)X(t)}{\lambda + X^T(t)P^\lambda(t-1)X(t)} \\ \hat{\theta}_{LS}(t) = \hat{\theta}_{LS}(t-1) + L^\lambda(t) \left(Q_P(t) - X^T(t)\hat{\theta}_{LS}(t-1) \right) \\ P(t) = \frac{1}{\lambda} \left(I - L^\lambda(t)X^T(t) \right) P^\lambda(t-1) \end{cases} \quad (28)$$

3.4 Recursive Maximum Likelihood Method (RMLM)

Unlike the deterministic parameters in RLSM, the parameter and output can be seen as random variables. In RMLM, the parameter vector θ has the probability density function $p(\theta)$ and the output vector $\mathbf{Q}_{P,t}$ is based on the conditional probability density function $p(\mathbf{Q}_{P,t}|\theta)$. According to the statistical property, RMLM can derive a solution to the parameter identification problem. Because of the space limitations, this paper can't give the derivation of recursive maximum likelihood method (RMLM). More Information about the derivation please to refer to [6] and [18]. RMLM for flow mapping is obtained as follows [6]:

$$\begin{cases} L(t) = P(t-1)h_f(t)(1+h_f^T(t)P(t-1)h_f(t))^{-1} \\ \hat{\varepsilon}(t) = z(t) - h^T(t)\hat{\theta}_{ML}(t-1) \\ \hat{\theta}_{ML}(t) = \hat{\theta}_{ML}(t-1) + L(t)\hat{\varepsilon}(t) \\ P(t) = (I - L(t)h_f^T(t))P(t-1) \end{cases} \quad (29)$$

With

$$\begin{cases} h(t) = [-z(t-1) \quad \dots \quad -z(t-n_a) \quad u(t-1) \quad \dots \quad u(t-n_b) \quad \hat{\varepsilon}(t-1) \quad \dots \quad \hat{\varepsilon}(t-n_d)]^T \\ h_f(t) = [-z_f(t-1) \quad \dots \quad -z_f(t-n_a) \quad u_f(t-1) \quad \dots \quad u_f(t-n_b) \quad \hat{\varepsilon}_f(t-1) \quad \dots \quad \hat{\varepsilon}_f(t-n_d)]^T \\ z_f(t) = z(t) - \hat{d}_1 z_f(t-1) \dots - \hat{d}_{n_d} z_f(t-n_d) \\ u_f(t) = u(t) - \hat{d}_1 u_f(t-1) \dots - \hat{d}_{n_d} u_f(t-n_d) \\ \hat{\varepsilon}_f(t) = \hat{\varepsilon}(t) - \hat{d}_1 \hat{\varepsilon}_f(t-1) \dots - \hat{d}_{n_d} \hat{\varepsilon}_f(t-n_d) \end{cases}$$

3.5 Radial Basis Function Neural Network (RBFNN)

RBFNN has recently drawn much attention due to their good generalization ability and a simple network structure that avoids unnecessary and lengthy calculation as compared to the multilayer feed-forward neural network (MFNN). RBFNN has three layers: the input layer X_i , the hidden layer H_j and the output layer Q_M , which are shown in Figure 6.

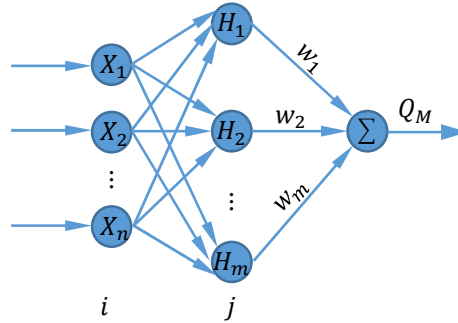


Figure 6: typical RBFNN structure

The input vector \mathbf{X} and radial basis function vector \mathbf{H} in RBFNN are defined as: $\mathbf{X} = [X_1 \quad X_2 \quad \dots \quad X_n]^T$ and $\mathbf{H} = [H_1 \quad H_2 \quad \dots \quad H_m]^T$ with $i = 1, 2, \dots, n$ and $j = 1, 2, \dots, m$. Where H_j is the Gaussian function value, which is given as:

$$H_j = \exp\left(-\frac{\|\mathbf{X} - C_j\|^2}{2b_j^2}\right) \quad (30)$$

Where $C_j = [c_{j1} \quad c_{j2} \quad \dots \quad c_{jn}]^T$ is the center vector of neural net j and b_j is the width of Gaussian function for neural net j . The width vector of Gaussian function can be given as $B = [b_1 \quad b_2 \quad \dots \quad b_m]^T$ & $b_j > 0$. Furthermore, the weight vector is $w = [w_1 \quad w_2 \quad \dots \quad w_m]^T$.

The output of RBFNN is:

$$Q_M(t) = Hw^T = H_1w_1 + H_2w_2 + \dots + H_mw_m \quad (31)$$

The cost function of RBFNN can be defined as:

$$\varepsilon(t) = \frac{1}{2}(Q_p(t) - Q_M(t)) \quad (32)$$

According to gradient descent method, RBFNN is given as:

$$\Delta w_j(t) = -\eta \frac{\partial \varepsilon(t)}{\partial w_j} = \eta(Q_p(t) - Q_M(t))H_j \quad (33)$$

$$w_j(t) = w_j(t-1) + \Delta w_j(t) + \alpha(w_j(t-1) - w_j(t-2)) \quad (34)$$

$$\Delta b_j(t) = -\eta \frac{\partial \varepsilon(t)}{\partial b_j} = \eta(Q_p(t) - Q_M(t))w_j H_j \frac{\|X - C_j\|^2}{b_j^3} \quad (35)$$

$$b_j(t) = b_j(t-1) + \Delta b_j(t) + \alpha(b_j(t-1) - b_j(t-2)) \quad (36)$$

$$\Delta c_{ji}(t) = (Q_p(t) - Q_M(t))w_j \frac{x - c_{ji}}{b_j^2} \quad (37)$$

$$c_{ji}(t) = c_{ji}(t-1) + \eta \Delta c_{ji}(t) + \alpha(c_{ji}(t-1) - c_{ji}(t-2)) \quad (38)$$

Where $\eta \in (0, 1)$ is the learning rate and $\alpha \in (0, 1)$ is momentum factor.

4 Results Analysis and Verification

The last step is the performance evaluation of the identified methods, the so-called verification by comparison of measured plant output Q_p and predicted model output Q_M . In order to identify the parameters of the electrohydraulic valve, following structured data in Figure 7 are used. To get the system excited enough, the signals cover the total operating range $U \in [0, 100]\%$ and $\Delta p \in [0, 200]$ bar.

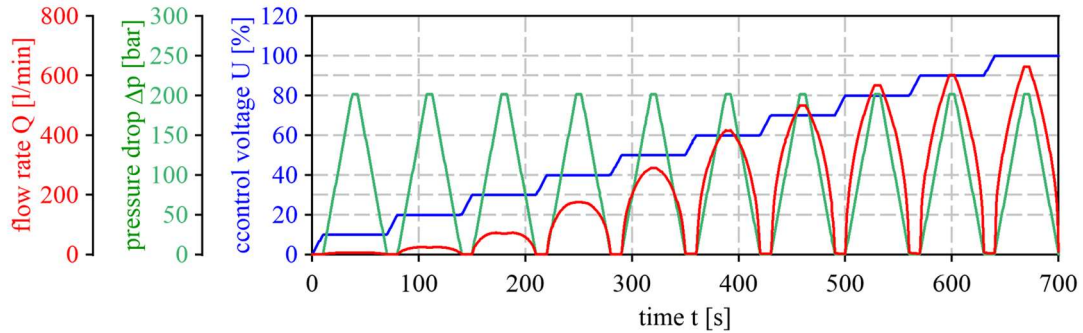


Figure 7: process of structured data to identify

In order to identify the parameters of the electrohydraulic valve, following scattered data in Figure 8 can be also utilized. For a better comparison, the signals cover the same range $U \in [0, 100]\%$ and $\Delta p \in [0, 200]$ bar like in structured data.

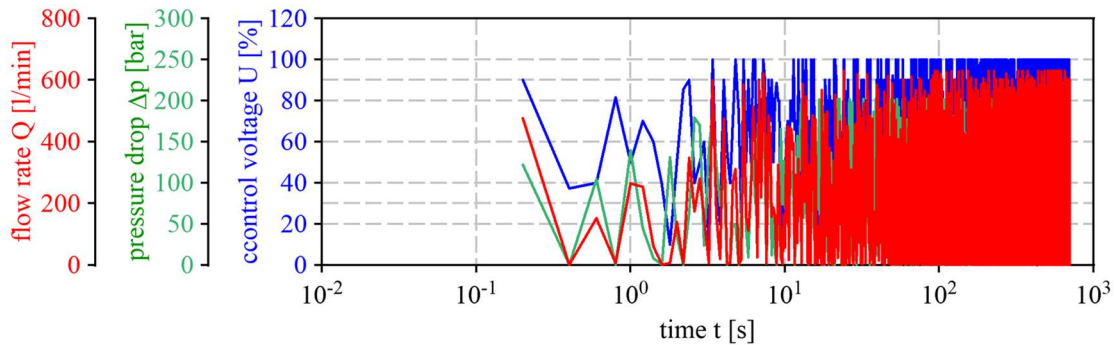


Figure 8: process of scattered data to identify

In order to illustrate the merit of the above-mentioned methods, it is appropriate to use the following signals for verification purposes. The test data include data that does not exist in the training data.

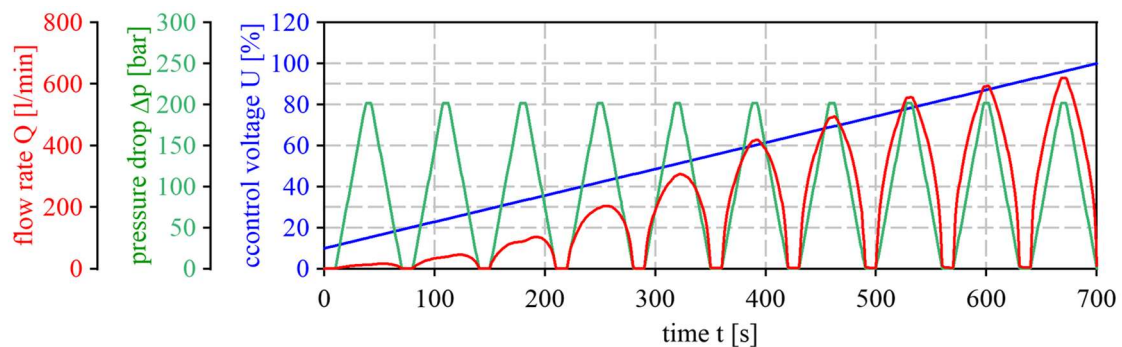


Figure 9: process of input and output data to verify

Table 1 shows verification of RLSM using different forgetting factors and RBFNN with structured data. In order to compare the goodness of identification for the different methods, the estimated flow rate Q_M are plotted against the real flow rate Q_P from test data. With an ideal identification, all points would lie exactly on the 45° red diagonal curve. For RLSM with different forgetting factors, the well-known phenomenon of parameters “fluctuation” can be deduced during increase of forgetting factor. It is noted that decreasing the forgetting factor will only worsen the situation. It could be found that RLSM with $\lambda = 0.995$ cannot get convergence at the end. If the forgetting factor is set to 1 ($\lambda = 1$), RLSM with forgetting factor will be degenerated as classical LSM, which will eliminate the fluctuation. However, classical LSM deals with all the past data equally and can result in data saturation problem. Therefore, it is necessary to select suitable forgetting factors in practice. Under the premise of predicted accuracy guarantee, the parameters fluctuation should be controlled at reasonable area at the same time. Compared with RLSM, the merit of RBFNN is the best fitting results regarding accuracy at the end, although the rate of convergence is slow. From these comparisons in Table 1, the conclusion can be drawn that RLSM with forgetting factor shows better extrapolating behavior than RBFNN. Both methods show suitable identification results. Furthermore, to use the identified flow mapping of valve, the characteristic interrelation $Q = f(U, \Delta p)$ needs to be inverted to $U = f(Q, \Delta p)$. In terms of invertibility, it's obvious that RLSM with model structure in eq.(7) is easy to transform. Whereas, it is very hard to get explicit mathematical description directly from RBFNN. A feasible way is to reidentify and change the inputs, output and model structure at the same time. As for RMLM, this method with structured data cannot converge to desired results. Therefore, it doesn't show up in the table. About the reasons for non-convergence, please refer to problems of convergence of maximum likelihood iterative procedures in multi-parameter situations by N. Mantel et al. [19].

Table 2 shows verification of RLSM under different forgetting factors and RMLM with scattered data. For RLSM with different forgetting factors, problems of convergence can also be seen during increase of forgetting factor. Compared with structured data, a wider range of forgetting factors is tolerable with scattered data. Without consideration for difficulty in data acquisition, methods with scattered data are much faster than methods with structured data in terms of the rate of convergence. Compared to RLSM, RMLM shows almost the same results regarding accuracy at the end, although the rate of convergence is slower. Regarding of RMLM, previous non-convergence problem in structured data seems to have been solved with scattered data. In conclusion, both of methods show good identification results. As for RBFNN, this method with scattered data cannot converge to desired results. Therefore, it doesn't show up in the Table 2. In RBFNN, the parameters of c_{ji} and b_j must be adjusted according to the scope of the input values. For arbitrary scattered data, the parameters are adjusted inappropriately, Gaussian function will not be effectively mapped and RBF network will be invalid [20]. Summarizing, the gradient descent method is not suitable to adjust c_{ji} and b_j in RBFNN with scattered data.

By contrast, RLSM with forgetting factor is more suitable for real application. At first, RLSM with forgetting factor is able to deal with all kinds of data types. Furthermore, another advantage of RLSM with forgetting factor in contrast to other methods is that it enables to integrate multi-dimensional dependencies with a reduced set of parameters in the software development for embedded systems. Unlike RLSM, an implementation of RBFNN in embedded systems could be problematic, since massive floating-point calculations are inevitable. Regarding to the fitting quality of RLSM, one way to improve the accuracy is to adopt partition identification for local area. The second way is to increase order in eq. (7) until the accuracy meets the requirements.

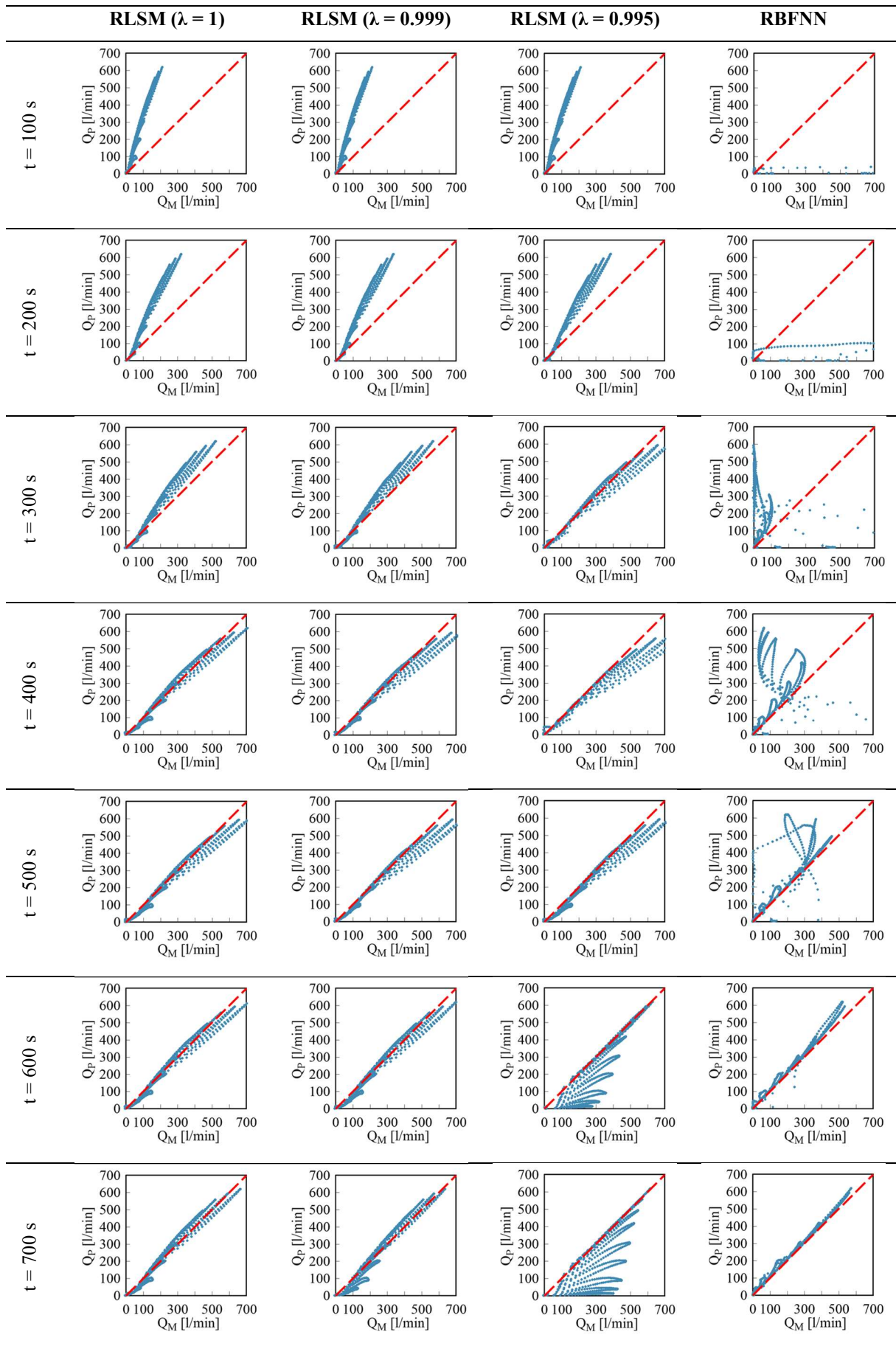


Table 1: Verification of RLSM and RBFNN with structured data

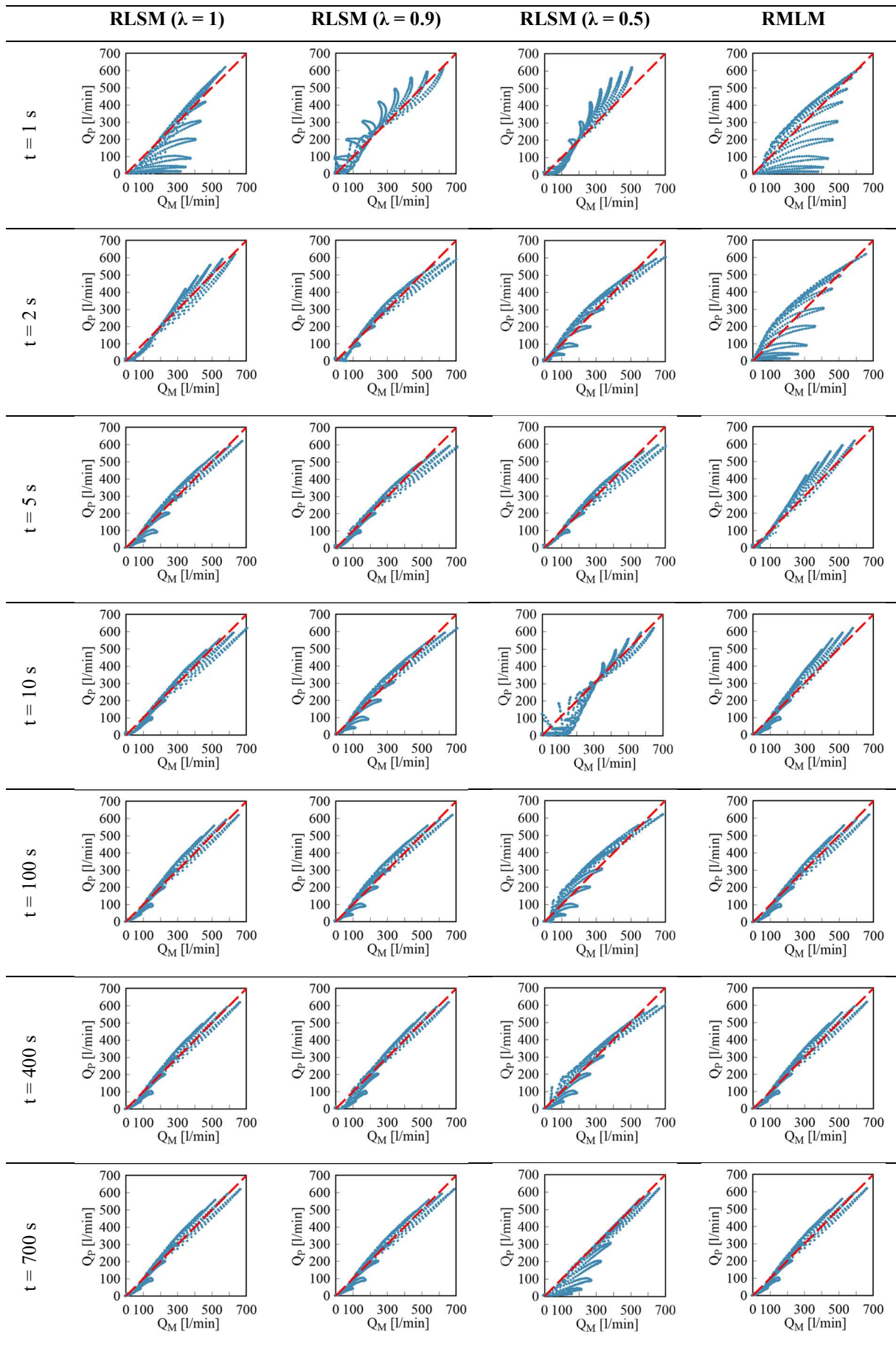


Table 2: Verification of RLSM and RMLM with scattered data

5 Conclusion and Outlook

In this research, the different flow mapping identification methods for electrohydraulic valves are proposed. This paper presented an analysis and comparison of different identification methods and data structures for 3D-flow mapping. The proposed methods can be applied to adaptive identification for real machines in the future and occupies small memory capacity at the same time. Moreover, their identification accuracy and convergence property have been sufficiently investigated.

So far, the flow mapping identification methods have been applied for only one valve with little hysteresis and at a constant temperature. In order to improve the generalization of the methods and obtain a flow mapping with higher precision, the next investigation steps are concerned with the further development of the proposed methods with respect to 4D-flow mapping or even more such as temperature and hysteresis. After that, the inverse multidimensional flow mapping in precision motion control applications should be further tested. At last, it is worth mentioning that some research on dynamic characteristics of the electrohydraulic valve with help of same test rig has been done. Identification for dynamic characteristics of electrohydraulic valves as the next challenging task would be further studied.

Nomenclature

Designation	Denotation	Unit
F_i	Force	N
a_1, a_2, \dots, a_n	Estimated parameters	-
A	Matrix	-
A_1	Piston area of main poppet in inlet	mm ²
A_2	Ring area of main poppet in outlet	mm ²
b_j	Width vector	-
B	Matrix	-
c_{ji}	Parameter in center vector	-
C	Matrix	-
C_j	Center vector	-
d_i	Coefficient for error vector	-
\hat{d}_i	Estimated Parameter in Parameter vector for noise	-
$h(t)$	Data vector	-
$h_f(t)$	Revised data vector	-
\mathbf{H}	Radial basis function vector	-
H_1, H_2, \dots, H_m	Gaussian function value	-
I	Index	-
I	Unit Matrix	-
L	Gain vector	-
j	Index	-
$J(\theta)$	Cost function	-
K_C	Flow coefficient of control-orifice	l/min·bar ^{-0.5} ·mm ⁻¹
K_{MP}	Flow coefficient of main poppet	l/min·bar ^{-0.5} ·mm ⁻¹
p_0	Constant system pressure	bar
p_1	Pressure in valve inlet	bar
p_2	Pressure in valve outlet	bar
p_c	Pressure in the control chamber	bar
$P(t)$	Data matrix	-
P_0	Initial data matrix	-
Q	Flow rate through valve	l/min
Q_C	Flow rate through control-orifice	l/min
Q_{max}	Max. Flow rate through main poppet	l/min
Q_M	Estimated flow rate for valve(model)	l/min
Q_{MP}	Flow rate through main poppet	l/min
Q_P	Measured flow rate for valve(plant)	l/min
$\mathbf{Q}_{P,t}$	Measured flow rate vector	-
Q_{PV}	Flow rate through pilot valve	l/min

Q_T	Total flow rate through valve	l/min
t	Time	s
$u(t)$	Input data	-
$u_f(t)$	Revised input data	-
U	Input voltage for valve	V
V_1	Valve chamber in inlet	mm ³
V_2	Valve chamber in outlet	mm ³
V_C	Control chamber in valve	mm ³
w_1, w_2, \dots, w_m	Weight vector	-
x	Input variable	-
x_{MP}	Displacement of main poppet	mm
x_0	Negative overlap of control-orifice	mm
X	Matrix for inputs	-
\mathbf{X}	Input vector	-
X_1, X_2, \dots, X_n	Input parameters in input matrix	-
\mathbf{X}_t	Input parameters matrix	-
y	Input variable	-
$z(t)$	Output data	-
$z_f(t)$	Revised output data	-
Z	Output variable	-
Δp	Pressure drop through valve	bar
Δp_{12}	Pressure drop between inlet and outlet	bar
Δp_{1C}	Pressure drop between inlet and control chamber	bar
α	Momentum factor	-
ε	Error	-
$\hat{\varepsilon}_f$	Estimated Error	-
ε_t	Error matrix	-
φ	Area ratio	-
ϑ	Temperature	°C
ϑ_T	Temperature in tank	°C
θ	Vector for estimated parameter	-
$\hat{\theta}_{LS}(t)$	Estimated parameter vector in LSM	-
$\hat{\theta}_{ML}(t)$	Estimated parameter vector in MLM	-
λ	Forgetting factor	-
η	Learning rate	-
<i>ARMAX</i>	Autoregressive moving average with exogenous	
<i>MFNN</i>	Multilayer feed-forward neural network	
<i>OPC UA</i>	Open Platform Communications Unified	
<i>RLSM</i>	Recursive least squares method	
<i>RMLM</i>	Recursive maximum likelihood method	
<i>RBNN</i>	Radial basis function neural network	

References

- [1] A Vahidi, A Stefanopoulou and H Peng. *Recursive least squares with forgetting for online estimation of vehicle mass and road grade: theory and experiments*. Mechanical Engineering Dept., University of Michigan, Ann Arbor
- [2] C Kamali, A A Pashikar and J R Raol. *Evaluation of recursive least squares algorithm for parameter estimation in aircraft real time applications*. *Aerospace Science and Technology* 15, P. 165-174, 2011.
- [3] S Dong, L Yu, W A Zhang and B Chen. *Robust extended recursive least squares identification algorithm for Hammerstein systems with dynamic disturbances*. *Digital Signal Processing* 101, 102716, 2020
- [4] M Kazemi and M M Arefi. *A fast iterative recursive least squares algorithm for Wiener model identification of highly nonlinear systems*. *ISA Transaction*, 2016

- [5] R A Fisher. *On the mathematical foundations of theoretical statistics*. Fellow of Gonville and Caius College, Cambridge, P. 309-368, 1922
- [6] L Ma and X Liu. *Recursive maximum likelihood method for the identification of Hammerstein ARMAX system*. Applied Mathematical Modelling 000, P. 1-13, 2016
- [7] J Li, F Ding, P Jiang and D Zhu. *Maximum Likelihood Recursive Least Squares Estimation for Multivariable Systems*. Circuits, Systems and Signal Processing 33, P. 2971-2986, 2014
- [8] F Chen and F Ding. *The filtering based maximum likelihood recursive least squares estimation for multiple-input single-output systems*. Applied Mathematical Modelling 000, P. 1-13, 2015
- [9] O Nelles and R Isermann. *A Comparison Between RBF Networks and Classical Methods for Identification of Nonlinear Dynamic Systems*. IFAC Adaptive Systems in Control and Signal Processing, P 233-238, 1995
- [10] M Y Mashor, *Some properties of RBF network with applications to system identification*. IJCIM Volume 7, P. 1-37 1999
- [11] H Yijun and N Wu. *Application of RBF Network in System Identification for Flight Control Systems*. 2010 International Forum on Information Technology and Applications (IFITA), P. 67-69, 2010
- [12] C Pislaru and A Shebani. *Identification of Nonlinear Systems Using Radial Basis Function Neural Network*. International Scholarly and Scientific Research & Innovation, Vol. 8, P. 1528-1533, 2014
- [13] J B d A Rego, A d M Martins and E d B Costa. *Deterministic System Identification Using RBF Networks*. Mathematical Problems in Engineering, Vol. 2014, P. 1-10, 2014
- [14] S Khan, I Naseem, R Togneri and M Bennamoun. *A Novel Adaptive Kernel for the RBF Neural Networks*. Circuits Systems and Signal Processing. Band 36. P. 1639-1653, 2017
- [15] B R Andersson. *On the Valvistor, a proportionally controlled seat valve*. Linköping Studies in Science and Technology. Dissertations. No. 108, 1984
- [16] E Prasetyawan, R Zhang, und A Alleyne. *Fundamental performance limitations for a class of electronic two-stage proportional flow valves*. Proceedings of American Control Conference, P. 3955-3960, 2001
- [17] A Sitte, O Koch, J Liu, R Tautenhahn, J Weber. *Multidimensional flow mapping for proportional valves*. 12th International Fluid Power Conference, Dresden, Group F, P. 231-240, 2020
- [18] R Isermann, M Münchhof. *Identification of Dynamic Systems – An Introduction with Applications*. ISBN 978-3-540-78878-2, P. 324-332, 2011
- [19] N Mantel, M Myers. *Problems of convergence of maximum likelihood iterative procedures in multiparameter situations*, Journal of the American Statistical Association, Vol.66, No.335, P. 484-491, 1971
- [20] J Liu, *Radial Basis Function (RBF) Neural Network Control for Mechanical Systems*, Springer Berlin Heidelberg, P. 24, 2013

The Determination of Hydraulic Motor Displacement

Paul Michael¹, and Jose Garcia-Bravo²

¹Fluid Power Institute, Milwaukee School of Engineering, Milwaukee, WI. United States
E-mail: michael@msoe.edu
²School of Engineering Technology, Purdue University, West Lafayette, IN. United States
E-mail: jmgarcia@purdue.edu

Abstract

Because the geometrical displacement of a pump or motor is very difficult to measure directly, the derived capacity of motors is used to assess the efficiency of positive displacement machines. The current internationally accepted method for deriving the displacement of hydraulic pumps and motors is ISO 8426:2008. Difficulties in accurately assessing derived displacement via ISO 8426:2008 have been reported by several authors. These inaccuracies can lead to efficiency results that exceed 100% in ISO 4409:2019 performance tests. In the presented work, fixed axial, variable axial, and radial piston motors were evaluated at 50°C and 80°C in dynamometer tests. Linear, orthogonal, and semi-randomized data sets were collected. The Wilson, Toet, and an analytical form of the Toet were compared with ISO 8426:2008. In general, the differences between the various methods for deriving displacement were not statistically significant, except in the instance of the axial piston motor. In the axial piston motor, the ISO 8426:2008 derived displacement was approximately 1% lower than the other methods. Use of this lower ISO 8426:2008 displacement in efficiency calculations produced values exceeding 100%. The error in the ISO 8426:2008 derived displacement determination was attributed to difficulties in detecting speed-dependent factors that affect displacement when testing is conducted at a single speed. The ISO 8426:2008 method does not provide instructions for calculating derived displacement when data is collected at more than one speed. It is proposed that the One-Step Toet method be incorporated into ISO 8426 as a method for calculating the derived displacement when users opt to measure performance at multiple speeds. This revision will reduce the potential for speed-dependent errors in the determination of derived displacement.

Keywords: Hydraulic Components, Efficiency, Test methods.

1 Introduction

Hydraulic fluid power is used in a wide range of industries including transportation, construction, mining, agriculture, the production of basic metals, and manufacturing. In a typical fluid power system, the mechanical energy of an electric motor or internal combustion engine is transferred to the fluid medium by a positive displacement pump and the controlled motion of the fluid is used to actuate valves, cylinders, and hydraulic motors. Flow and pressure losses due to internal leakage, fluid compressibility, and friction can compromise the efficiency and productivity of fluid power systems. In a 2012 publication the US Department of Energy (DOE) estimated that an average of 21% of the input power from prime movers is converted to work by a typical fluid power system [1]. These findings have spurred improvements in hydraulic pump and motor efficiency. A thorough analysis of the current understanding of the efficiency of pumps and motors was carried out by Achten et al. [2] where the effect of the changes in the internal energy of the fluid due to the compressibility effect, was found to be a significant contributor to discrepancies found while estimating the hydromechanical and overall losses of a pump or a motor. These differences were demonstrated experimentally to be higher than 10% when compared to the traditional method proposed in ISO 4409. Likewise, Williams [3] devised a methodology for estimating the volumetric efficiency based on a hydraulic resistance model, such model lumped specific performance characteristics of the pump into a hydraulic parameter that could be used to evaluate the efficiency of the machine at various operating conditions.

Hydraulic motor efficiency is a critical factor in the design of off-highway machines because it affects the maximum vehicle payload and the top propulsion speed. Since motor output shaft speed and output torque are proportional to motor displacement, an accurate estimate of the amount of fluid displaced per machine revolution is necessary to model hydraulic system performance and assess component efficiency and dynamic performance. Conceptually, hydraulic pumps and motors are positive displacement machines and the volume of fluid transferred from component inlet to the outlet per revolution is assumed to be constant, unlike for instance a centrifugal pump or torque converter. In practice however, the displacement volume of positive displacement machines can be affected by pressure, speed, and fluid viscosity. While these changes may be relatively small, they introduce complexity into the determination of displacement volumes. In the following, several methods for sample selection and determination of derived displacement are experimentally investigated. This exploration is unique, insofar as it focuses on motors and the effect of temperature on motor displacement.

2 Description of methods for determining displacement

2.1 Geometric displacement

The most basic method for determining the volume displacement of a machine is to measure the volume of fluid it takes to fill cylinders using a burette or calculating it based upon dimensional drawings. The resulting geometric displacement V_g is limited in accuracy because it does not account for changes in tolerances, clearances, and deformation that occur when the unit is operating [7]. In many cases this technique is impractical because it requires disassembly of the component. Determination of displacement without disassembly may be accomplished by measuring the volumetric flow per shaft revolution. Various methods for determining the volumetric flow per revolution have been discussed in earlier publications [8]-[10]. These methods define derived displacement as the volume displaced per revolution at zero differential pressure ($\Delta p=0$). Based upon Newtonian physics, flow or displacement of fluid is not possible at $\Delta p=0$. Hence derived (V_i) is conceptual and not a physical property of a component.

2.2 ISO 8426:2008 method

In the ISO 8426:2008 standard test method, the motor inlet flow rate is measured as a function of pressure at constant speed, temperature, and commanded displacement [11]. The derived displacement, V_i , is found by calculating the ratio of the actual flow q_{ve} and the shaft speed N at each measured pressure. The flow volume per revolution is plotted as a function of pressure and the zero intercept, that is, when Δp is equal to zero, and it is determined via linear regression. The value of V_i is defined to be the zero-pressure intercept of the line as shown in fig. 1. The key parameter that is measured in the determination of derived displacement is the flow rate. Since flow depends upon speed in a positive displacement machine, limiting the data set to a single speed produces a very narrow range of flow measurements. The narrow range of the sample set amplifies small errors in the flow measurements and neglects the effects of speed-dependent forces and cross-port leakage on displacement. Thus the use of ISO 8426:2008 displacements in ISO 4409:2019 performance tests occasionally produces efficiency values that exceed 100% [4]-[6]. Alternative methods for determining the derived displacement are presented below.

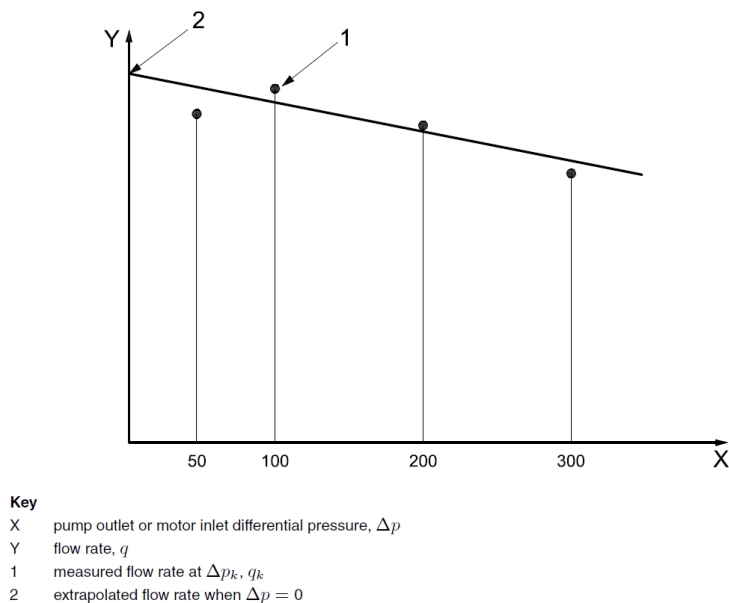


Figure 1: Graphical representation of the ISO 8426 method for deriving the displacement of a hydraulic pump [11].

2.3 Toet two-step graphical method

The Toet method was first introduced in 1970 [9], and it investigated the effects of shaft speed on the delivery of a pump at various pressures. In an ideal positive displacement machine, inlet and outlet flow rates are unaffected by pressure. However, gaps are required between moving surfaces within the pressure envelope to create a wear- and friction-reducing lubrication film. These gaps provide a path for pressure-driven leakage flow within a pump or motor. Due to pressure-driven and compressibility flow losses, the delivery of a positive displacement machine is not exactly coincident with its geometrical displacement. Furthermore, Toet explicitly discussed how the delivery of a positive displacement machine is affected by changes in pressure and temperature. The Toet method, which was produced after studying the behavior of 200 pumps, postulated that because the relationship between the effective volumetric flow rate and the shaft speed are highly linear, the derivative of flow with respect shaft speed should be constant. Thus, the Toet method calls for the measurement of effective flow rate at a minimum of five different shaft speeds. These measurements are to be repeated at different pressure levels under constant temperature conditions. For each pressure case a fitted line between effective flow and shaft speed is graphically determined and the slope of the line is obtained. The second step of the method calls for a fit of a line through the data relating the previously obtained slopes to the measured pressure. The zero-intercept of this second line corresponds to the derived displacement of the positive displacement machine according to Toet.

2.4 Wilson method

The Wilson method [8] resembles the Toet method but differs in the definition of the procedure to estimate the derived capacity of a positive displacement machine. In the first step of the Wilson method, linear relationships between the effective flow rate versus pressure are established at various shaft speeds. The intercepts of the various lines at zero pressure are then used in the second step to produce a linear relationship between the effective flow rate and the shaft speed. The slope of the resulting line from the second step corresponds to the derived capacity. According to Post [10] the two methods, Toet and Wilson, produce comparable results. Post also concluded that the displacement of pumps and motors is not a constant value because it varies with pressure, temperature, and shaft speed.

2.5 One-step Toet method

Because the above-mentioned methods are based on experimental data, one can use a statistical procedure to fit said data to predict the flow output or input of a pump or motor. In the One-Step Toet method, all of the data is fitted to a line and one of the linear coefficients is used for determination of the derived displacement. The presented method is based on the original Toet procedure [9] and synthesized into a single analytical method that uses multiple linear regression to determine the displacement [12].

The One-step Toet method can be derived by recognizing that the flow model for a pump or motor can be described by a linear relationship between the pump or motor flow q_{v_e} and the shaft speed N (eq.1).

$$q_{v_e} = V_i \cdot N \quad (1)$$

Other variables of less influence may be considered as part of this relationship, as seen in [12], these may include temperature, viscosity, modulus of elasticity, bulk modulus of the fluid, etc. The constant of proportionality in the linear relationship accompanying the rotational speed of the pump or motor corresponds to the derived capacity V_i of the hydrostatic machine.

Taking the partial derivative of the flow equation, eq.1 above with respect to the shaft speed and assuming a different line at various pressures yield the expression shown in eq. 2 below:

$$(\partial q_{v_e} / \partial N)_{p_i} = m_i \quad (2)$$

Where m_i is the slope of the line. A family of lines can be generated to represent the slope of the flow versus shaft speed relationship shown in eq.1. This is known as the first step of the Toet method [9]. The second step of the method requires the calculation of the slope of the values generated from the first step with respect to the pressure values. Hence, a second partial derivative expression can be developed to represent the second step shown in eq. 3 below. Where β_3 corresponds to the slope of the line made from the various m_i values obtained in step one. The expression for determining the flow may be obtained by integrating twice the partial derivative from eq.3. Assuming that the correspondence of the variables in the two previous partial derivatives is linear, one may say that the result from the derivative of a line is a constant value β_3 .

$$\frac{\partial \left(\frac{\partial q_{v_e}}{\partial N} \right)}{\partial p_i} = \beta_3 \quad (3)$$

Rearranging eq.3 and integrating with respect to pressure, p_i produces the expression:

$$\frac{\partial q_{v_e}}{\partial N} = \beta_3 p_i + \beta_2 \quad (4)$$

Where β_2 is an integration constant. Rearranging terms in eq. 4 and integrating a second time with respect to the shaft speed produces a linear flow equation as presented in eq.5.

$$q_{v_e} = \beta_3 p_i N + \beta_2 N + \beta_1 p_i + \beta_0 \quad (5)$$

The goal of the One-step Toet method is to fit the experimental data to a target function for the flow exiting or entering the pump or motor in the form presented in eq. 5. With the One-step Toet method, the experimental data used for fitting the flow model of eq. 5 is the same required for the two step Toet method, that is, the effective flow rate at various shaft speeds and at different pressure levels. The shaft speed coefficient, β_2 corresponds to the derived displacement of the component and has shown to yield the same value produced by the Toet graphical method as presented in section 4 below.

2.6 Latin Hypercube Sampling (LHS)

The ISO 8426:2008, Toet and Wilson methods for determining the derived displacement are based upon orthogonal sample plans. That is, each sample point is either in-line (ISO 8426:2008) or at a right angle (Toet and Wilson) to each other. Latin Hyperspace sampling (LHS) is a pseudo-randomized methodology for selecting experimental test points. It has been found to produce higher fidelity results than orthogonal methods in terms of identifying test points to populate empirical flow and torque models [13]. The scheme requires the test data to be acquired using an algorithm where the probability distribution of the variables to be measured is used to obtain the data points in a randomized way. In order to maximize sampling efficiency, none of the data points are orthogonal, in other words only one data point is collected for any given pressure or speed. Once the pseudo-randomized data points are captured, these values are fit using a multivariate linear regression algorithm like the one used for the One-step Toet method presented above. Similarly, the regression coefficient accompanying the shaft speed corresponds to the derived displacement.

3 Methods and materials

The displacements of the three motors listed in tab.1 below were evaluated in this study. These specific units were selected because they are representative of motors used in a variety of off-highway vehicle applications. Each motor was run-in according to manufacturer-specified conditions prior to testing in order to stabilize tribological conditions and efficiency. The radial piston motor is designed for low-speed high-torque duty and incorporates 8620 and 52100 steel elements to withstand high surface contact pressures. The fixed and variable displacement axial motors are designed for higher speed applications. The pistons are constructed of steel while piston slippers, valve plates and cylinder blocks incorporate alloys of copper to enhance lubrication and heat transfer.

Table 1: Test motor specifications

Motor type	Radial piston	Axial piston	Variable axial piston
Nominal displacement, cc/rev	213	100	45.2/135.6
Rated speed, RPM max	570	3300	3200
Rated pressure, Bar max	400	420	450

The displacement measurements of all three motors were collected using a dynamometer consisting of a pressure-compensated axial piston pump, twin Variable Frequency Drives (VFD), pressure, temperature, and torque transducers, and an 18-channel data acquisition system. The VFD controllers were programmed for semi-automatic testing. A simplified hydraulic circuit diagram is shown in fig. 2. A 93 kW electric load motor that was rated for a maximum speed of 1800 rpm provided the resistive load. The axial and variable motors were not evaluated at their full rated speeds due to this limitation. Fifteen seconds of data were collected for each set point at a sampling rate of 100 Hz. The input flow rate for each motor was measured at various speeds and pressures according to requirements for each derived displacement method. The results were compared using the two-sample t test at a 95% confidence interval ($\alpha=0.05$) as described in Eq. 6.

$$100 * (1-\alpha)CI = V_i \pm \left(t_{n-(k-1), \alpha/2} \right) * SE(V_i) \quad (6)$$

The null hypothesis is that different methods produce the same derived displacement results ($H_o: V_{ij}=V_{ik}$). When 95% confidence intervals for the derived displacement methods overlap, the t test fails to reject the null hypothesis and the difference between the derived displacement results is said to be *not statistically significant*. The alternative hypothesis is the methods are not equal ($H_a: V_{ij} \neq V_{ik}$). When the t test rejects the null hypothesis, H_a is accepted and the difference between the derived displacement results is said to be *statistically significant*.

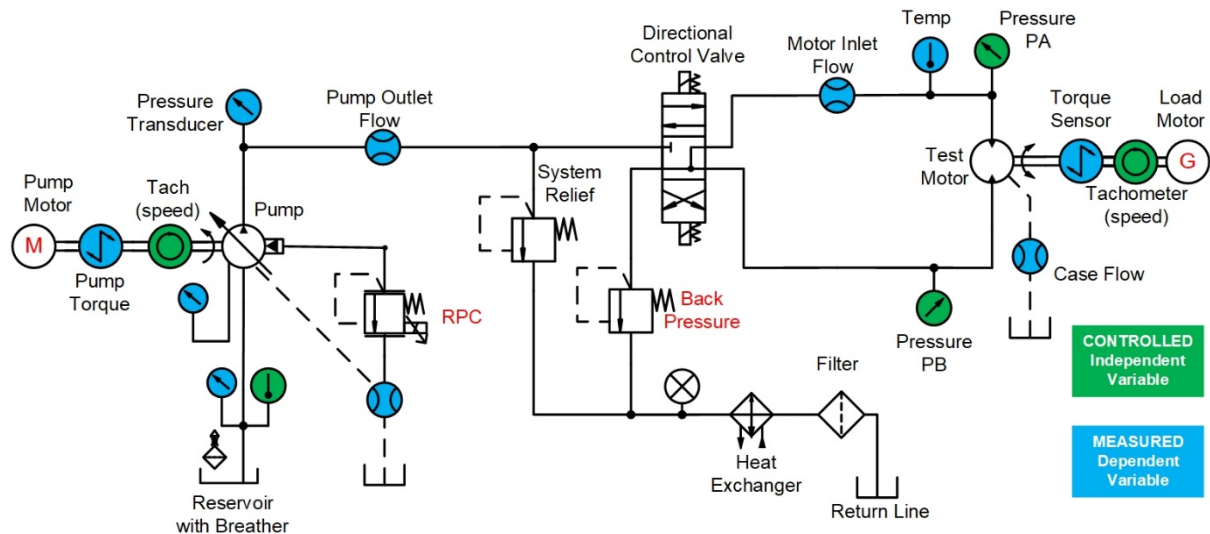


Figure 2: Hydraulic circuit schematic for motor derived displacement determinations.

4 Results and discussion

According to ISO 4409:2019, “tests shall be carried out at a stated test fluid temperature. The test-fluid temperature shall be measured at the inlet port of the unit under test and be within the range recommended by the manufacturer. It is recommended that measurements are made at two temperature levels, 50°C and 80°C.” [15] The dynamometer testing below was conducted with the pump inlet temperature at 50±1°C and 80±1°C. As in a normal hydraulic system, motor inlet temperatures tend to be several degrees higher due to the fluid temperature rise caused by the pump. As shown in fig. 3, the inlet mean temperature of the three motors was 1°C to 3°C higher than the pump inlet temperature. ISO 8426 specifies that the temperature at the inlet of the test article be reported. In the discussion below, the pump inlet temperature is used to nominally describe the motor inlet temperature. The results reported in section 4.6 show that a 1°C to 3°C variation in temperatures is unlikely to produce a statistically significant change in the derived displacement.

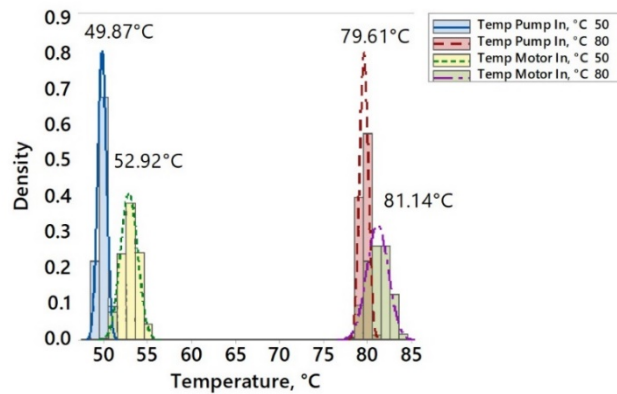


Figure 3: Histogram of the pump and motor inlet temperature measurements for the 3 test motors

4.1 Axial piston motor

The test plan for the axial piston motor is shown in fig. 4. The pressure ranged from 6.89 to 27.58 MPa and the shaft speed ranged from 50 to 1285 RPM. The lower limit of the rotational frequency for the motor was established to ensure that the flow meter was operating well above the lower detection limit of the sensor. The ISO 8426:2008 method specifies that data for 10 or more test pressures must be collected in equal increments to achieve measurement accuracy class “A.” Eleven measurements were collected between 6.89 and 27.58 MPa at 1000 RPM. Forty-five non-orthogonal data points were collected for the One-step Latin Hypercube method. Thirty-two orthogonal data points were collected for the Toet and Wilson methods (4 pressures and 8 speeds). Hence, a total of 89 data points was collected for the axial piston motor.

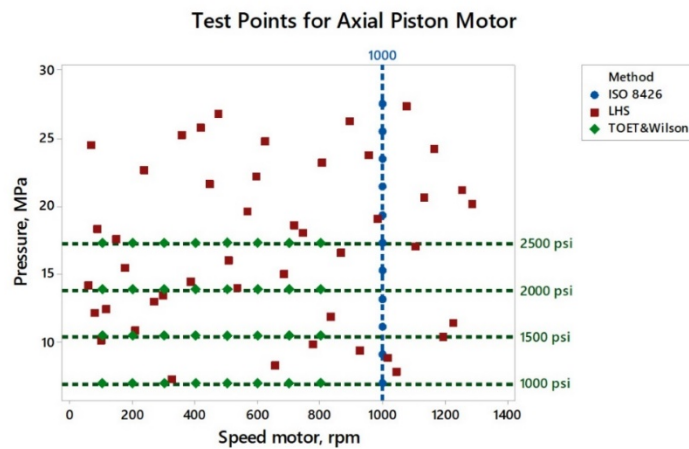


Figure 4: Test points for evaluating the derived displacement of the axial piston motor via ISO 8426, Toet, Wilson, and Latin Hypercube methods.

The results for the estimation of the derived displacement using the graphical Toet method are shown in fig. 5 and fig. 6 below. The flow rate versus speed plot in fig. 5 shows that the results overlap at the 4 test pressures. As can be seen from the regression equations in the figure, the slope is highest for the 6.89 MPa (1000 psi) results. Hence the effective displacement per revolution was highest at the lowest pressure, as expected.

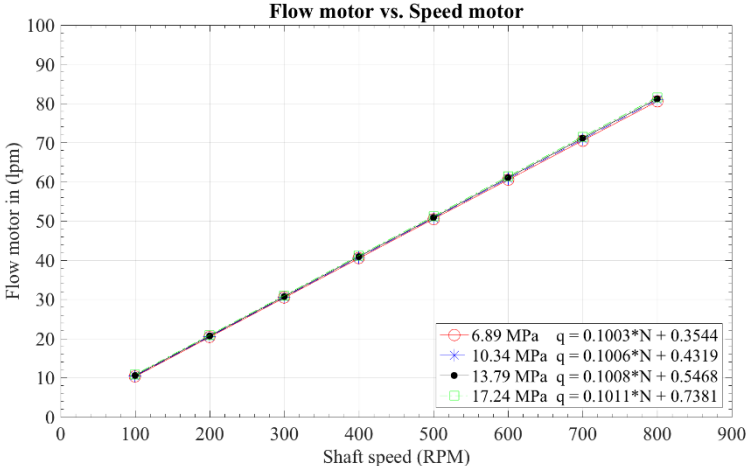


Figure 5: Step 1 of the Toet method; plot of axial piston motor inlet flow rate versus speed at four different pressures.

The second step in the Toet analysis is to plot slope versus pressure. When displayed this way, the slope of the line is in units of liters/MPa while the zero intercept is the derived displacement in liters/revolution. The derived displacement was 99.74 cc/rev. The data exhibited good linearity with an R^2 value of 0.994. An R^2 value of 0.994 means that 99.4% variation in the regression equation derived from the data can be accounted for by motor displacement and the incremental leakage flow per MPa. The pressure driven leakage flow rate was less than 0.2 cc/MPa.

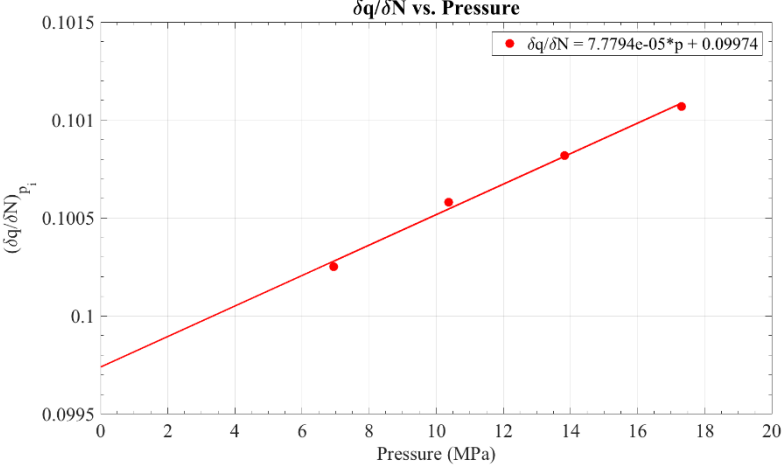


Figure 6: Step 2 of the Toet method; plot of the slope of flow with respect to speed versus pressure measurements for the axial piston motor.

The results of the derived displacement determination for the axial piston motor via the Wilson method are shown in fig. 7 and fig. 8. In fig. 7, plots of the motor inlet flow rate versus pressure are shown for eight different rotational frequencies.

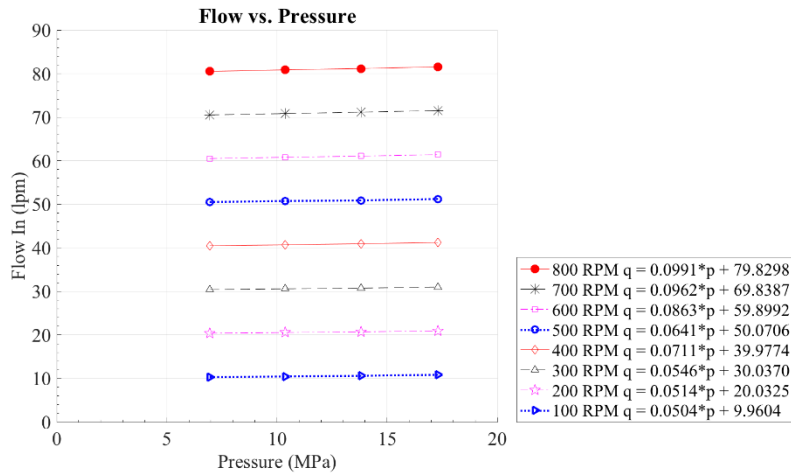


Figure 7: Step 1 of the Wilson method; plot of inlet flow rate versus pressure at four different pressures for the axial piston motor.

As can be seen from the regression equations, the pressure-driven leakage flow rate coefficient increased linearly as the speed was stepped up. The zero intercept values were a distinct function of the rotational frequency as expected.

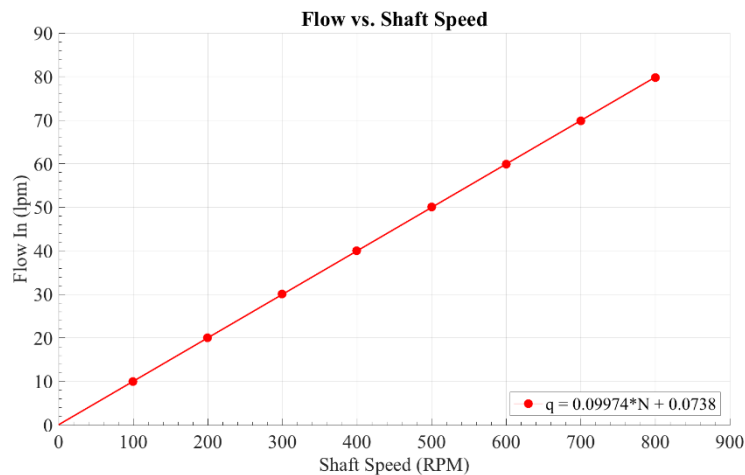


Figure 8: Step 2 of the Wilson method; plot of the flow versus speed measurements for the axial piston motor.

The second step in the Wilson method is to plot the intercept versus shaft speed as shown in fig. 8. The slope of the regression line is the displacement per revolution. As with the Toet method, the motor displacement was 99.74 cc per revolution. Since the Toet and Wilson methods used the same data, equal values for derived displacement were expected.

The orthogonal data that was used in the Toet and Wilson determinations was evaluated using multiple linear regression, (hereafter referred to as the One-step Toet method). The use of multiple linear regression to model experimental data assumes that there is a linear relationship between the independent and dependent variables, that the residuals are normally distributed, and that multicollinearity is absent. Equation 5 was used in the regression analysis.

The resulting ANOVA analysis for the One-step Toet method is shown in tab. 2. The motor inlet effective flow rate (q_{ve}) was the dependent variable in the equation. Thus, the constant term β_o was determined to have units of cubic centimeters per minute (cc/min). The estimated value of β_o was 75.1 cc/min with a standard error of 55.3 cc/min and a p-value of 0.186. Since the p-value is greater than 0.05, the relationship between β_o and the motor inlet flow rate is not statistically significant at a 95% confidence level. Essentially this means that the constant term could be omitted from the regression equation without negatively affecting the model integrity. In order to maintain mathematical equivalence to the graphical Toet method, it was necessary to include the constant term.

With respect to determining derived displacement, the coefficient β_2 is the key value. β_2 is in units of volume per revolution and as can be seen in tab. 2, the estimated derived displacement of the motor was found to be 99.74 cc/rev. Hence the determination of the derived displacement using this method yielded the same results as the graphical Toet and Wilson methods up to four significant figures. The standard error of the derived displacement V_i , which is equivalent to the standard error of the β_2 coefficient, was 0.11 cc/rev. To put this in perspective, the average volume of one droplet of hydraulic fluid at 50°C is 0.03 cubic centimeters. 0.11 cc/rev is less than 4 droplets of oil per revolution. The coefficient β_1 corresponds to a pressure dependent leakage flow coefficient. Hence the pressure-driven leakage flow rate was found to be 36.7 cc/MPa per minute. Unlike in a hydraulic pump, this leakage term is positive because the internal flow losses of a motor increase the inlet flow rate. The constant β_3 is in units of displacement over pressure. While the (Variance Inflator Factor) VIF for the N^*p term was high, the physics and mathematics of determining derived displacement demand inclusion of this term in the flow model. The correlation coefficient (R^2) of the regression equation was >99.99% with a Standard Error (SE) 43.3 cc/min. Using linear regression to determine the derived displacement from the orthogonal data yielded the same results as the two-step graphical Toet and Wilson methods, with the advantage of generating an analysis of variance (ANOVA) for estimating the uncertainty of the derived displacement values.

Table 2: ANOVA analysis for the axial piston motor displacement determination base on linear regression of orthogonal test data (One-Step Toet Method).

Term	Symbol	Coeff.	SE Coeff.	p-Value	VIF
Constant	β_o	75.1	55.3	0.186	
Derived displacement, cc/rev	β_2	99.74	0.11	0.000	10.78
Leakage flow coefficient	β_1	36.7	4.37	0.000	4.86
N^*p coefficient	β_3	0.078	0.009	0.000	14.64
Coefficient of Determination	R^2	>99.99%			
Standard Error	SE	43.3 cc/min			

Latin Hypercube sampling

In a previous investigation we found that the Latin Hypercube sampling method yielded higher fidelity torque and flow models than orthogonal sampling [13]. Test points were selected using the Latin Hypercube Sampling (LHS) procedure. The LHS data set covered a higher range of operating speeds and pressures. (This data was collected to develop motor flow and torque models for system simulation.) Non-orthogonal LHS data sets were evaluated using multiple linear regression per eq. 5. The ANOVA results are shown in tab. 3. Unlike the preceding orthogonal data, the p-value for the constant term β_o was less than 0.05 and there is a statistically significant association between the β_o and the motor inlet flow rate at a 95% confidence level. The derived displacement β_2 obtained from the LHS data was 99.73 cc/rev. This value was 0.01 cc/rev lower than that obtained from the orthogonal data. The standard error was also 0.01 cc/rev lower (0.10 cc/rev vs. 0.11 cc/rev). Since the sum of the products of the coefficient standard error (SE_{coef}) and critical t value (t^*) for each method is greater than the difference between the LHS and One-step Toet derived displacements, the null hypothesis is not rejected. The relationship SE , t^* and CI is shown in eqn. 7 and eqn. 8 below. Thus, the difference between the results produced by the two methods (LHS and One-step Toet) was not statistically significant.

$$[(SE_{Toet})(t^*_{Toet}) + (SE_{LHS})(t^*_{LHS})] > |V_{iToet} - V_{iLHS}| \quad (7)$$

$$CI_{Toet} + CI_{LHS} > |V_{iToet} - V_{iLHS}| \quad (8)$$

Table 3: ANOVA analysis for the axial piston motor displacement determination base on linear regression of Latin Hypercube data over a wider range of pressures and speeds.

Term	Symbol	Coef.	SE Coef.	p-Value	VIF
Constant	β_0	240.7	728.2	0.004	
Speed motor, RPM	β_2	99.73	0.10	0.000	9.91
Leakage flow coefficient	β_1	34.52	4.56	0.000	4.55
N*p coefficient	β_3	0.078	0.006	0.000	14.42
Coefficient of Determination	R ²	>99.99%			
Standard Error	SE	84.6 cc/min			

The above analysis of the LHS data included a wider range of speeds and pressures than was used to collect the orthogonal data as indicated by the red squares in fig. 4. The question arises, would LHS data from the same hyperspace as the orthogonal data yield the same results? In a previous investigation, Johnson reported that it is advantageous to include the hyperspace vertices when analyzing LHS data [14]. The hyperspace vertices for the axial piston motor corresponded to 50 and 800 RPM, and 6.895 and 17.24 MPa. The ANOVA for the LHS hyperspace data with vertices is shown in Table 4. The results indicate that the displacement (99.82 cc/rev) differs from the One-step Toet results by 0.08 cc/rev. Since the difference between the LHS hyperspace and One-step Toet derived displacements was less than the sum of the products of (SE_{coef}) and (t^*) for each method, the null hypothesis is not rejected. In other words, the difference between the results produced by the two methods (LHS hyperspace and One-step Toet) was not statistically significant.

Table 4: ANOVA analysis for the axial piston motor displacement determination base on linear regression of Latin Hypercube data in the same hyperspace as the orthogonal data, including vertices.

Term	Symbol	Coef.	SE Coef.	p-Value	VIF
Constant	β_0	205.0	156.0	0.214	
Speed motor, RPM	β_2	99.82	0.29	0.000	10.04
Leakage flow coefficient	β_1	31.1	12.1	0.025	3.52
N*p coefficient	β_3	0.075	0.023	0.006	11.91
Coefficient of Determination	R ²	>99.99%			
Standard Error	SE	120.7 cc/min			

For the ISO 8426:2008 standard test method, the motor inlet flow rate was measured as a function of pressure at constant speed, temperature, and commanded displacement. Eleven measurements were collected using this method and the motor displacement value was calculated to be 98.72 cc/rev as shown in fig. 9. The results indicate that the displacement differs from the orthogonal results by 1.02 cc/rev. The SE_{coef} for the ISO 8426:2008 method was smaller than the SE_{coef} for the One-step Toet method. (0.01 cc/rev versus 0.11 cc/rev). The t^* for the ISO 8426:2008 method was 2.262. The t^* for the One-step Toet method was 2.048. Since the sum of the products of SE_{coef} and t^* for each method was less than the difference between the One-step Toet and ISO 8426:2008 displacement determinations, the null hypothesis was rejected. In other words, the difference between the One-step Toet and the ISO 8426:2008 method was statistically significant in the axial piston motor.

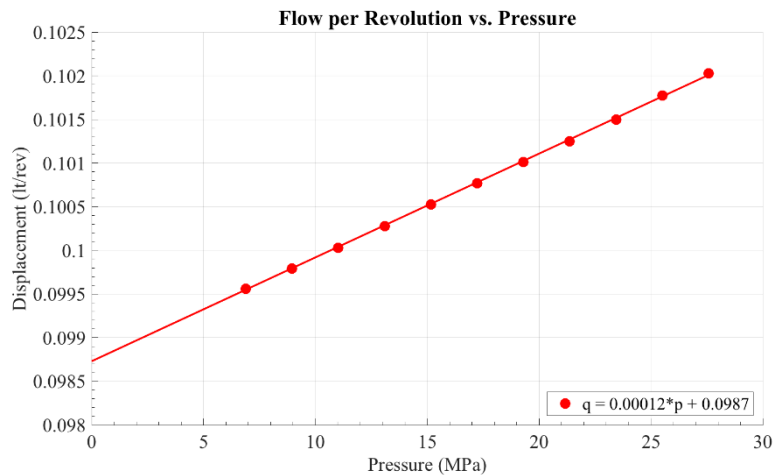


Figure 9: Plot of the flow per revolution versus pressure for the axial piston motor as specified in the ISO 8426:2008 method.

A comparison of the results for the different methods for determining the derived displacement is shown in fig. 10. Error bars illustrate the 95% confidence intervals for each data set from the axial piston motor. The graphical Toet and Wilson methods are not included because they yield the same results as the One-step Toet method but do not provide an error estimate. The differences in the derived displacement were not statistically significant in three out of four methods. The only method that generated a different derived displacement was ISO 8426:2008. The ISO 8426:2008 was 1% lower, which means that based upon the ISO 8426:2008 displacement, the theoretical torque output of the motor would also be 1% lower. As has been noted elsewhere, this can lead to efficiency determinations greater than 100% [5]. It has been hypothesized that discrepancies in ISO 8426:2008 results are due to speed-dependent cross-port leakage effects [16]. It should be noted that the 95% confidence interval for the ISO 8426:2008 method was narrower than that of the other methods. This is an artifact of measuring flow at a single speed; the resulting measurement yielded a narrow range of flow rates which obscured variations in the flow meter precision and motor speed control. Hence, collection of data points at multiple speeds is advantageous when determining the derived displacement.

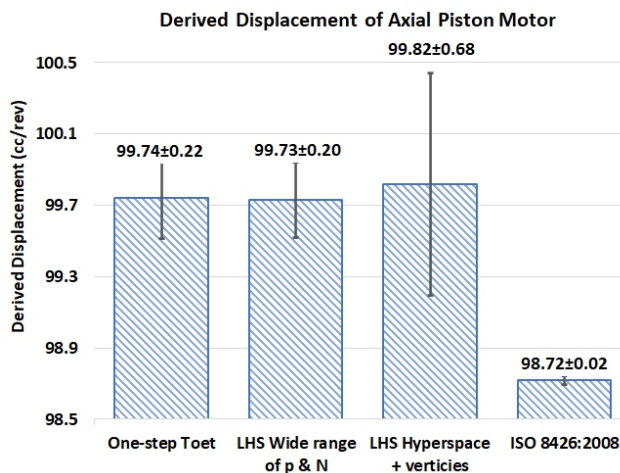


Figure 10: Results of the derived displacement of axial piston motor for the various methods tested.

As mentioned above, ISO 8426 displacement was 1% lower, and the difference was statistically significant at a 95% confidence level. More importantly than quantifying how different these methods are, it seems appropriate to determine which method yields a more accurate result. As mentioned earlier, it is not possible to directly measure derived displacement. However, the examination of the efficiency results for the motor can provide insights regarding the accuracy of the method for determining the derived displacement. Fig. 11 below shows a plot of mechanical efficiency versus volumetric efficiency for the ISO 8426:2008 derived displacement results (left), and the Toet method (right). Note that the ISO method yielded mechanical efficiency results above 100% for low values of volumetric efficiency. This is a consequence of underestimating the derived displacement of a motor where volumetric efficiency, which has V_i in the denominator, is underestimated, and mechanical efficiency,

which has V_i in the numerator, is overestimated. Efficiency results greater than 100% contradict first physics principles yet, have been reported in the literature by previous authors [4]-[6]. Hence the reader is invited to value the importance of accurately evaluating the derived displacement of pumps and motors so that accurate estimates of power loss and energy consumption may be reported.

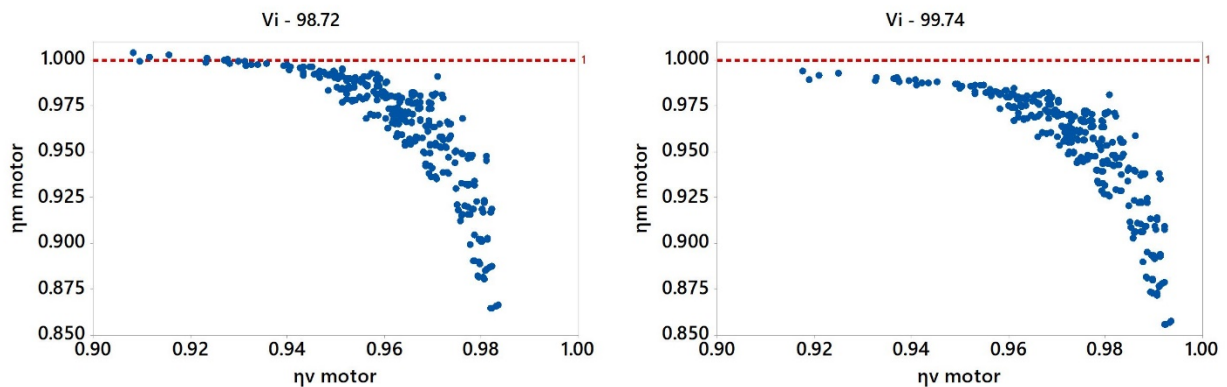


Figure 11: Mechanical and volumetric efficiencies of the axial piston motor based upon derived displacement via the ISO 8426:2008 method (left) and Tout method (right). Note that mechanical efficiency exceeded 100% when using the ISO 8426:2008 method.

4.2 Radial piston motor

The test plan for the radial piston motor is shown in fig. 12. The pressure ranged from 6.89 to 27.58 MPa and speed ranged from 50 to 564 RPM. Eleven measurements were collected between 6.89 to 27.58 MPa at 500 RPM. Forty-six semi-randomized data points were collected for the Latin Hypercube Sampling method. Thirty-two orthogonal data points were collected for the Toet and Wilson methods (4 pressures and 8 speeds). Hence 89 data points were collected for the radial piston motor.

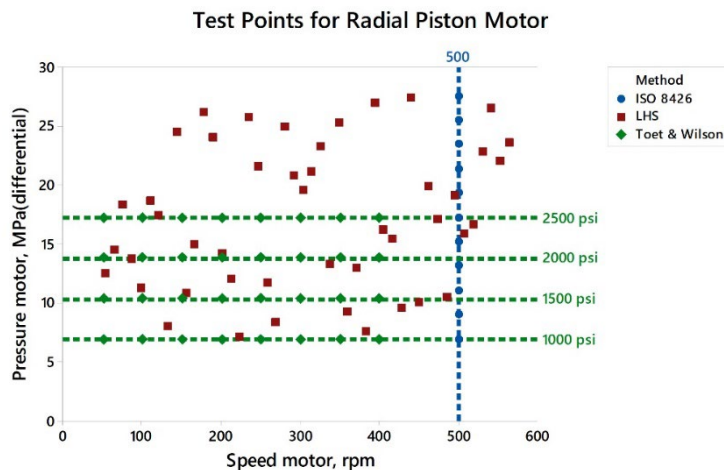


Figure 12: Test points for evaluating the derived displacement of the radial piston motor via ISO 8426:2008, Toet and Latin Hypercube methods.

The derived displacement for the radial piston motor was determined using the methods described in section 2. A summary of the results is shown in fig. 13. The Wilson and Toet methods yielded a derived displacement of 211.82 cc/rev. Likewise, the One-step Toet method yielded 211.82 cc/rev. The standard error for the displacement coefficient (β_2) was 0.20 cc/rev. The (t^*) for a two-tailed $\alpha=0.05$ was 2.05. Hence the 95% CI for the One-step Toet method was ± 0.40 cc/rev. The ISO 8426:2008 method produced a derived displacement of 211.49 cc/rev with a 95% CI of ± 0.17 cc/rev. The net difference between the ISO 8426:2008 and Toet method was 0.33 cc/rev. The sum of the confidence intervals was 0.47 cc/rev. Since the difference between the displacement values was less than the CI, the disparity between the One-step Toet and ISO 8426:2008 methods was not statistically significant. The LHS hyperspace plus vertices data yielded similar results to the One-step Toet and ISO 8426:2008 methods. The LHS data from a wider range of pressures and speeds yielded a derived displacement that was 0.94

cc/rev higher than that of the ISO 8426:2008 method. The sum of the confidence intervals for the two methods was 0.97 cc/rev. Therefore, the null hypothesis was not rejected and the difference in the derived displacement measurements was not significant in the radial piston motor.

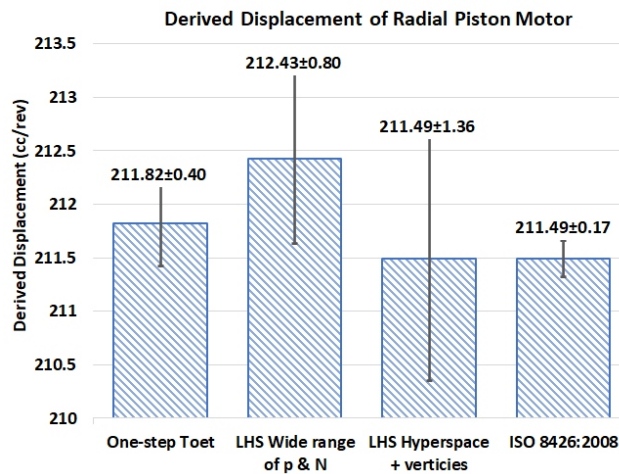


Figure 13: Results of the derived displacement of radial piston motor for the various methods tested.

4.3 Variable displacement axial piston motor

The test plan for the variable displacement motor is shown in fig. 14. The pressure ranged from 6.89 to 27.58 MPa and speed ranged from 50 to 1285 RPM. Eleven measurements were collected between 6.89 to 27.58 MPa at 400 RPM and 1000 RPM to determine the derived displacement at the minimum and maximum swashplate angle. Forty-five non-orthogonal data points were collected for the One-step Latin Hypercube method. Twenty-four orthogonal data points were collected for the Toet and Wilson methods (4 pressures and 6 speeds). Hence 91 data points were collected for the variable displacement motor.

In the following analysis, full and partial displacements were determined from a single data set. The LHS hyperspace with vertices data set had only 6 degrees of freedom at partial displacement and 5 degrees of freedom at full displacement. Consequently, the coefficient SE and t^* values were high, resulting in confidence intervals of ± 5 cc/rev and ± 10 cc/rev at minimum and maximum displacement respectively. LHS hyperspace results are not included below because the required scaling would obscure meaningful differences in the other derived displacement methods.

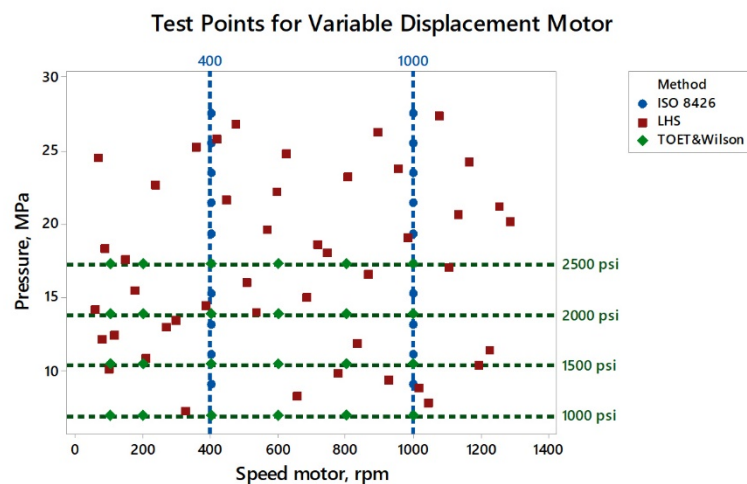


Figure 14: Test points for evaluating the derived displacement of the variable displacement motor via ISO 8426:2008, Toet and Latin Hypercube methods.

4.3.1 Variable motor partial displacement (high speed)

The derived displacement of the variable displacement motor was evaluated using the methods described in Section 2. A summary of the partial- and full-displacement results is shown in fig. 15. The high-speed One-step Toet and ISO 8426:2008 displacements were 38.49 and 38.56 cc/rev respectively. The difference was 0.07 cc/rev while the CI for the methods was ± 0.29 cc/rev. Since the One-step Toet results differed from the ISO 8426:2008 results by less than the CI, the two methods did not yield a statistically significant difference. Likewise, the LHS data from a wider range of pressures did not show a statistically significant difference in derived displacement values at high speeds.

4.3.2 Variable motor full displacement (low speed)

The One-step Toet and ISO 8426:2008 derived displacements ranged from 138.6 to 138.9 cc/rev. Since the 95% CI for the One-step Toet included the ISO 8426:2008 result, these two methods cannot be said to produce a statistically significant difference in derived displacement. The LHS data at a higher range of pressures yielded a displacement of 137.9 cc/rev with a CI of ± 0.38 cc/rev. The difference between the LHS and the ISO 8426:2008 derived displacement appears to be statistically significant. Non-linear changes in gap flow at high pressures may be a factor in the lower derived displacement value produced by the LHS data set. Alternatively, the narrow CI of the 8426:2008 method may be an underestimate of SE_{coef} . When one considers that the ISO 8426:2008 confidence interval represents less than 0.06% of the derived displacement, the possibility that this method underestimates SE_{coef} seems plausible.

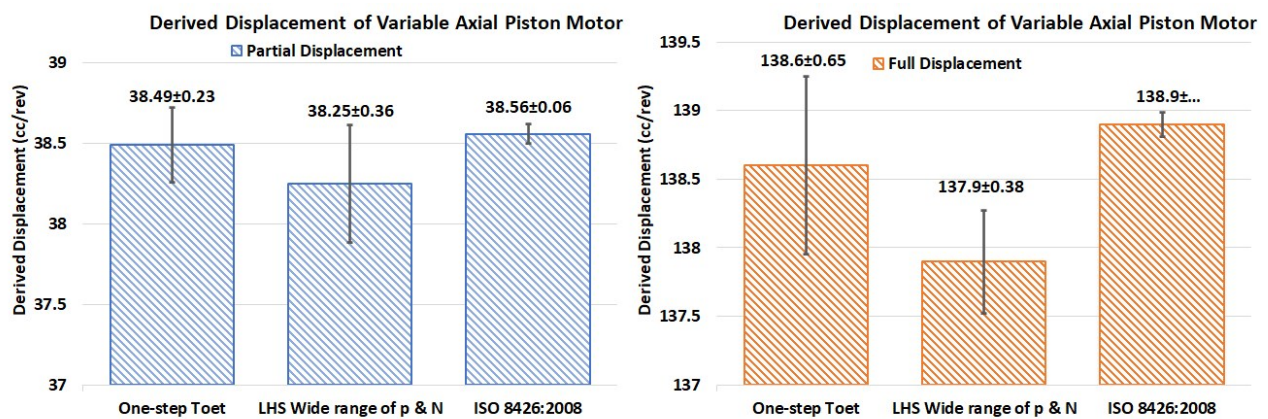


Figure 15: Results of the derived displacement of variable axial piston motor for the various methods tested.

4.4 Temperature Effects

The ISO 8426:2008 method was only investigated for pump inlet temperatures of 50°C. The ISO 8426:2008 method was not evaluated at other temperatures. However, the effects of temperature and viscosity on derived displacement were investigated using LHS data from a wide range of pressures and speeds at 50°C and 80°C. The two ISO VG 46 fluids described in tab 5 were compared. (Up to this point all of the derived displacement tests have been based upon Fluid “A” at 50°C.) Fluids “A” and “B” had a viscosity index above 140 and therefore are categorized as ISO HV46 oils in the ISO 6743-4 classification system. Fluid “A” was on the low range of this standard, both in terms of kinematic viscosity at 40°C and viscosity index. Fluid “B” had a midrange viscosity at 40°C and a relatively high viscosity index. As shown in tab. 5, the fluids differed in density as well. This is due to a difference in base oil composition. From the perspective of an oil formulator, these fluids would be substantially different in cost and quality. However, it should be noted that the dynamic viscosities of the fluids at 50°C and 80°C (shown in bold type) are quite similar.

Table 5: Properties of hydraulic fluids

Hydraulic Fluid	A	B
Kinematic Viscosity at 40°C, cSt	41.8	46.0
Kinematic Viscosity at 100°C, cSt	7.23	8.70
Viscosity Index	142	170
Density at 15°C, g/cc	0.867	0.832
Coefficient of Thermal Expansion, /°C	0.000687	0.000728
Dynamic Viscosity at 50°C, cP (calc.)	23.9	25.9
Dynamic Viscosity at 80°C, cP (calc.)	9.4	10.6

In the analysis below, data from the axial and radial piston motors was used to probe for the effects of temperature and fluid selection on derived displacement. The variable displacement motor was not evaluated in this stage because it was evaluated at two displacements, which effectively reduced the number of LHS data points to draw from by half.

The axial and radial piston motor LHS data from a wider range of pressures and speeds (red symbols in fig. 4 and fig. 12) was evaluated using eq. 5. As shown in fig. 16a, displacement of the axial piston motor ranged from 99.78 cc/rev to 100.06 cc/rev. Fluid “A” at 50°C produced the lowest derived displacement and Fluid “B” at 80°C produced the highest derived displacement result. The difference between these measurements was 0.28 cc/rev or less than 0.3%. The sum of the 95% confidence intervals was 0.27 cc/rev. Since the data spread and confidence intervals are nearly equal, the authors are hesitant to draw conclusions about the statistical significance of the difference between the derived displacement of Fluid “A” at 50°C and the derived displacement of Fluid “B” at 80°C in the axial piston motor. However it is clear that for a given fluid, the differences between the 50°C and 80°C results were not statistically significant.

Likewise, LHS data for the radial piston motor was evaluated via eq. 5. As shown in fig. 16b, the derived displacement of the radial piston motor ranged from 211.87 cc/rev to 212.30 cc/rev. The difference was 0.43 cc/rev or roughly 0.2%. The sum of the 95% confidence intervals for the top and bottom derived displacement values was 0.77 cc/rev. Since the span of the confidence interval was greater than the spread in the results, the null hypothesis is not rejected. In other words, varying the fluid temperature and composition did not produce a statistically significant change in the estimated derived displacement for the radial piston motor. These results show that the One-step Toet method provides a robust method for determining the derived displacement even when the fluid temperatures differ by 30°C.

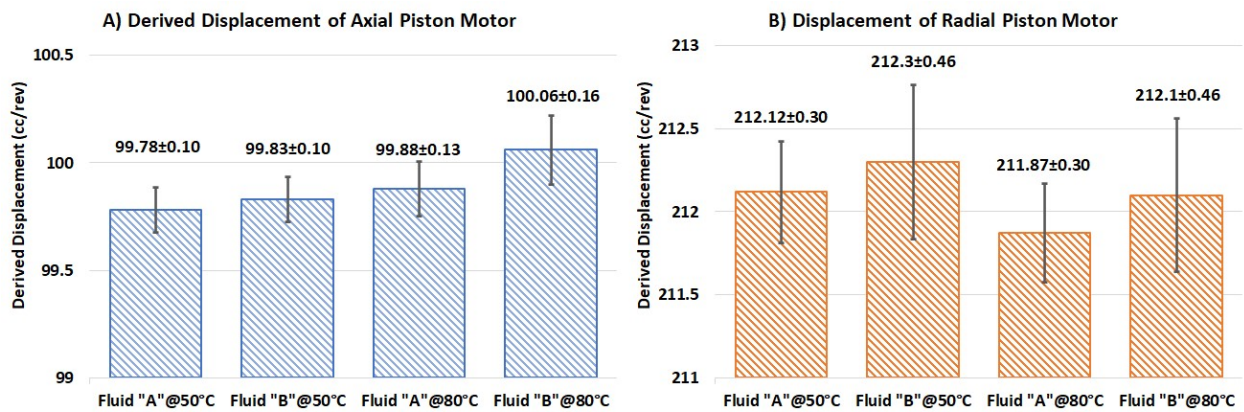


Figure 16: Comparison of derived displacement results for two fluids at 50°C and 80°C in the axial and radial piston motors.

4.5 Viscosity Effects

Gap flow or internal leakage in positive displacement machines is proportional to pressure and inversely proportional to viscosity [14]. Hence, it has been proposed that a viscosity term be used in the One-step Toet equation to account for this effect. In the analysis below, the dynamic viscosities of the fluids were used to determine if modifying the One-step Toet equation to include a viscosity term improves the fidelity of the derived

displacement determination. The kinematic viscosities of the oils at the motor inlet temperature were calculated using the Walther equation. The density of the fluid at the motor inlet temperature was calculated using the coefficient of thermal expansion listed in the fluid property table. (The density was not pressure corrected.) The product of kinematic viscosity and density was used to convert to dynamic viscosity (μ) of the fluid. Finally, the term p_i/μ was used in place of p_i in the modified One-step Toet equation as shown in eq. 9.

$$q_{ve} = \beta_3 p_i N + \beta_2 N + \beta_1 p_i / \mu + \beta_0 \quad (9)$$

A comparison of the results in fig. 16a and 17a reveals that inclusion of the pressure/viscosity ratio had a minimal effect on the derived displacement in the axial piston motor (<0.02 cc/rev). The standard error was nearly unchanged as well. Likewise inclusion of the pressure/viscosity ratio had a minor impact on the derived displacement of the radial motor as shown in fig. 16b and 17b. These results indicate that the inclusion of a viscosity term did not enhance the integrity of the derived displacement determination when individual fluid and temperature combinations are evaluated independently.

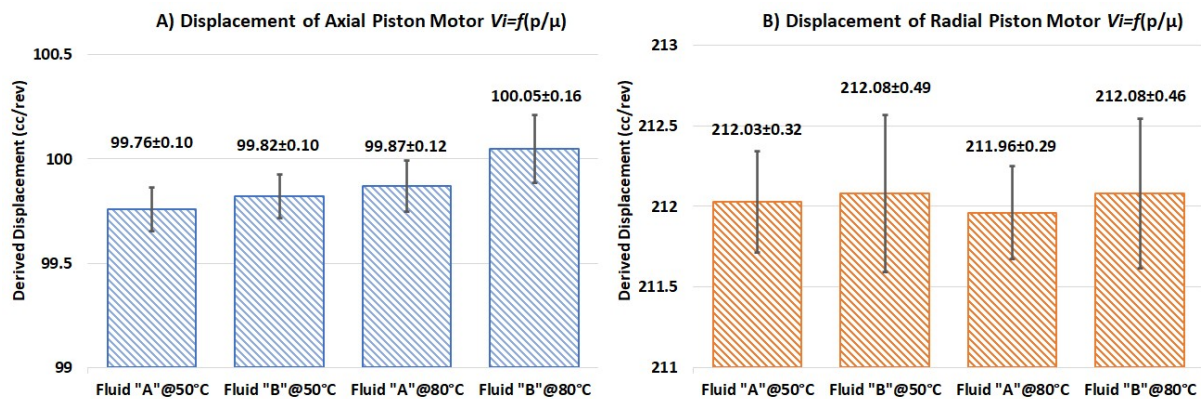


Figure 17: Derived displacement for axial piston (A) and radial piston motor (B) as a function of the viscosity/pressure ratio

5 Summary and conclusions

This paper examines alternative methods for determining hydraulic motor displacement and compares the results with the current ISO 8426:2008 procedure. Fixed axial piston, variable axial piston, and radial piston motors were evaluated at 50°C and 80°C in dynamometer tests. Linear, orthogonal, and semi-randomized data sets were collected. The linear (single speed) data was used to determine displacement via ISO 8426:2008. The orthogonal data (a matrix of pressures and speeds) was used to determine displacement using the Toet and Wilson methods. Displacement was determined from the Latin-Hypercube Semi-randomized (LHS) data by way of an analytical form of the Toet method. The analytical Toet method was derived to facilitate the estimation of uncertainty in the displacement using statistical software in a single step (One-step Toet). The One-step Toet method was shown to produce results that are identical to the graphical Wilson and Toet methods.

In general, the differences between the various derived displacement methods were not statistically significant, except in the instance of the axial piston motor. In the axial piston motor, the ISO 8426:2008 derived displacement was approximately 1% lower than the other methods. Use of the lower ISO 8426:2008 displacement value in mechanical efficiency calculations produced values exceeding 100%. This phenomena has been reported in previous publications [4]-[6]. Underestimating the derived displacement of a motor skews mechanical efficiency high because V_i is used to calculate theoretical torque, which is in the denominator of the mechanical efficiency equation. This did not occur using the other methods where displacement was determined at multiple speeds. The error in the ISO 8426:2008 derived displacement determination was attributed to difficulties in detecting speed-dependent factors that affect displacement when testing is conducted at a single speed. The ISO 8426:2008 method does not prohibit testing at multiple speeds, nor does it provide instructions for calculating derived displacement when data is collected at more than one speed. The One-step Toet method produced consistent results for various combinations of pressures, speeds, fluids, and temperatures. It is proposed that the One-Step Toet method be incorporated into a revised version of ISO 8426 as the means for calculating the derived displacement when users opt to measure performance at multiple speeds. This modification will help reduce the potential for speed-dependent errors in the determination of derived displacement.

6 Nomenclature

Property	Symbol	Units
Shaft speed	N	rpm
Pressure	p	MPa
Differential pressure	Δp	MPa
Derived Displacement	V_i	cc/rev
Geometric Displacement	V_g	cc/rev
Volumetric Flow Rate	q_{ve}	L/min
Dynamic Viscosity	μ	Centipoise (cP)
Analysis of Variance	<i>ANOVA</i>	
Linear Regression Coefficient	$\beta_0, \beta_1, \beta_2, \beta_3$	
Confidence Interval	<i>CI</i>	
Latin Hypercube Sampling	<i>LHS</i>	
Correlation Coefficient	R^2	
Standard Error of the Regression Coefficient	SE_{coef}	
Critical t statistic	t^*	

Acknowledgments

The authors gratefully acknowledge Shukai Zhang, graduate research assistant at Milwaukee School of Engineering, for collecting, processing, and organizing the experimental data used in this study.

References

- [1] Love, L., Lanke, E., and Alles, P., “Estimating the Impact (Energy, Emissions and Economics) of the U.S. Fluid Power Industry,” Oak Ridge National Laboratory: Report No.:ORNL/TM-2011/14. (2012)
- [2] Achten, P., Mommers, R., Nishiumi, T., Murrenhoff, H., Sepehri, N., Stelson, K., ... & Schmitz, K. (2019). Measuring the losses of hydrostatic pumps and motors: A critical review of iso4409: 2007. In *ASME/BATH 2019 Symposium on Fluid Power and Motion Control*. American Society of Mechanical Engineers Digital Collection.
- [3] Williams, L. T. (2020, September). Methodology for the Evaluation of Gear Pump Performance. In *Fluid Power Systems Technology* (Vol. 83754, p. V001T01A030). American Society of Mechanical Engineers.
- [4] Williamson, C., and Manring, N. “A More Accurate Definition of Mechanical and Volumetric Efficiencies for Digital Displacement® Pumps.” In *ASME/BATH 2019 Symposium on Fluid Power and Motion Control*. ASME Digital Collection Paper FPMC2019-1668 (2019).
- [5] Bramer, J. Puzzuoli, A. Michael, P. and Wanke, T. “Hydraulic Fluid Efficiency Effects in External Gear Pumps,” Proceedings of the 53rd National Conference on Fluid Power – National Fluid Power Association, Paper NCFP I14-13.3, Las Vegas, NV (2014)

- [6] Garcia-Bravo, J., Nicholson, J., “What is the real size of a pump? Revisions to ISO 8624: A standard for determination of the derived capacity of hydraulic pumps and motors”, Fluid Power Journal Magazine, June 2018. Vol. 25 Issue (6), pp. 74-75.
- [7] ISO 4391:1986. “Hydraulic fluid power – Positive displacement pumps, motors and integral transmissions – Parameter definitions and letter symbols.” International Organization for Standardization, Geneva, Switzerland (1986).
- [8] Wilson, Warren Elvin. "Performance criteria for positive displacement pumps and fluid motors." Trans. ASME 71, no. 2: 115-120. (1949)
- [9] Toet, G., “Die Bestimmung des theoretischen Hubvolumens von hydrostatischen Verdränger-pumpen und Motoren aus volumetrischen Messungen,” Ölhydraulik und Pneumatik 14. Nr. 5, 185–190. (1970)
- [10] Post, W. J. A. E. M., “Models for steady-state performance of hydraulic pumps: determination of displacement,” In C. R. Burrows, & K. A. Edge (Eds.), Fluid power systems: 9th international workshop, University of Bath, England, 9-11 September 1996 (pp. 339-353). (Fluid power series; Vol. 9). Chichester: Research Studies Press. (1997)
- [11] ISO 8426:2008. “Hydraulic fluid power – Positive displacement pumps and motors – Determination of derived capacity.” International Organization for Standardization, Geneva, Switzerland (2008).
- [12] Toet, G., Johnson, J., Montague, J., Torres, K. and Garcia Bravo, J. “The Determination of the Theoretical Stroke Volume of Hydrostatic Positive Displacement Pumps and Motors from Volumetric Measurements.” Energies, 12, 415 (2019).
- [13] Panwar, P. and Michael, P., “Empirical Modelling of Hydraulic Pumps and Motors based upon the Latin Hypercube Sampling Method,” International Journal of Hydromechatronics, Vol. 1, No. 3, pp.272-292 (2018)
- [14] Johnson, J., “Design of experiments and progressively sequenced regression are combined to achieve minimum data sample size,” International Journal of Hydromechatronics, 2018 Vol.1 No.3, pp.308 - 331 (2018)
- [15] ISO 4409:2019 “Hydraulic fluid power — Positive-displacement pumps, motors and integral transmissions — Methods of testing and presenting basic steady state performance”. International Organization for Standardization, Geneva, Switzerland (2019).
- [16] Kim, T., Kalbfleisch, P. and Ivantysynova, M. “The effect of cross porting on derived displacement volume,” International Journal of Fluid Power, 15:2, 77-85, (2014)
- [17] Wilson, Warren. E., *Positive Displacement Pumps and Fluid Motors*, Pitman Publishing, NY, Chap. 6. (1950)

Modelling, Simulation and Validation of the Pneumatic End-Position Cylinder Cushioning

Fedor Nazarov, Jürgen Weber

Chair of Fluid-Mechatronic Systems, TU Dresden, Helmholtzstraße 7a, 01069 Dresden, Germany
E-mail: fedor.nazarov@tu-dresden.de (c/o), fluidtronik@mailbox.tu-dresden.de

Abstract

In this paper a model of the pneumatic cylinder with an integrated pneumatic end cushioning is presented. This model is needed to simulate and analyze the thermodynamical processes in the pneumatic end cushioning and to elaborate a novel design strategy for damping systems with a higher capability on kinetic energy absorption and robust performance even with fluctuating operational conditions, such as supply pressure, inertial load or travel speed. To validate this model, the results of the experimentally based parametrization of the friction force in the cylinder sealings are compared for a Stribeck friction model and its modifications. A new approach suitable for an accurate approximation of the measured friction data within a wide range of pressure (2...8 bar_{rel}) and piston speed (0...0.8 m/s) is proposed. In the next step a flow rate characteristic of the integrated end cushioning throttle is experimentally obtained and analyzed. These data are used to parametrize the lumped parameters model of the cylinder with an end cushioning. Pressure and temperature in the cushioning volume and piston displacement are measured for different openings of the cushioning throttle to prove the validity of the model. The model will be used further for sensitivity analysis and robust optimization of the cushioning system design.

Keywords: pneumatic cylinder, end cushioning, thermocouple, friction, pneumatics, Stribeck curve, throttle

1 Introduction

Pneumatic drives find a widespread application in the modern industry. They are used as a cheap and reliable alternative to electric drives and as a front runner in some special industrial sectors. Pneumatic applications are essential in food, medical and diverse explosion-hazardous technologies, where they have gained a reputation of hygienic, safe, and reliable systems.

Within the last decades an integration of electronic control systems has made pneumatics smarter, safer, and simpler in both operation and design. However, time-costly manual works are still needed when setting up or adjusting some basic pneumatic components, as throttles or damping devices. Especially pneumatic end-position cylinder cushioning is very sensitive to any changes in operational conditions, setup and environment. Whenever one of those parameters has been changed, manual readjustment is usually needed. The latter has usually a trial-and-error nature. In parallel, a maximum quantity of energy, absorbed by the end-cushioning, often appears as a limitation factor when sizing the pneumatic cylinder designed to handle heavy objects. An engineer would rather prefer a larger-scaled cylinder with a proportionally higher damping capability to bring the moving mass softly and safely to the end position, even if a smaller cylinder is enough to perform the task. Large-scaling results directly in an increase in energy consumption whilst performing the same net work. For instance, the large-scaling is typical for nearly 80 % of all applications and avoiding the can contribute to reduction in energy consumption up to 40 % [1].

Having said that, the classical concept of pneumatic end-position cushioning needs to be investigated and revised to decrease its sensitivity against the operational conditions and enhance the energy absorption without enlarging the system or pushing up the costs. The first step towards this global goal is a development and validation of an accurate mathematical model of a pneumatic cylinder with a pneumatic end-position cushioning, which is discussed within this paper.

This accurate model is further needed to perform the sensitivity analysis and figure out the parameters with a highest impact on the damping capability of the end cushioning. These parameters, such as cushioning length, cushioning volume in a cylinder head, cushioning throttle conductivity as a function of the throttle opening, are accessible for the engineers on the design phase of a pneumatic cylinder. Hence, the global goal of the investigation of pneumatic end cushioning system is to find the optimal values of these design parameters corresponding to the maximum damping capability and simultaneously to guarantee a high robustness against the fluctuating operational environment, i. e. volatile supply pressure, alternating mass load or friction force.

This paper focuses only on the development, parameterization and validation of a simulation model of pneumatic cushioning device.

2 State of the art

In general, there are different ways to decelerate a moving mass within some limited stroke. The highest damping capability usually possess hydraulic shock absorbers that are also widely applied beyond pneumatic and hydraulic applications. They are reliable in operation and simple in modelling due to only a viscous term and spring force must be considered [2]. Hydraulic shock absorbers are very costly and need to be installed out of the cylinder. This increases the axial dimensions of the drive. A further approach of an external non-pneumatic cushioning is an elastic mechanical shock absorber. Such absorbers may have a good damping performance due to a sophisticated geometry and materials. That guarantees a constant deceleration within a short stroke [3]. However, mechanical dampers usually have a lower damping capability and durability when compared to hydraulic devices and can be applied only within a limited pressure range. External pneumatic damping devices that are free from the drawbacks of the integrated pneumatic cushioning are also present in the market, as for example [4]. As in case of the hydraulic shock absorbers they have high acquisition costs and need installation space out of the cylinder.

Having said that, is obvious, why the integrated pneumatic end cushioning is so widely used in the pneumatic cylinders. The main advantages are low costs, full integration into the cylinder head, reliability and ease of use. Several studies are devoted to the problematic of their simulation, adjustment and applicability. Wang et al. have developed a mathematical model of pneumatic end cushioning under assumption of an isentropic compression process in the end cushioning volume. The simulation of the piston speed, deceleration and pressure have shown good correlation with experiments. The inertial load was varied, and the other parameters were kept constant. The authors stated further potentials of model improvement with regards to consideration of the friction, fluid damping, leakage and discharge coefficients of pneumatic ports [5]. Beater has comprehensively studied the damping processes in the pneumatic cushioning as well. For this purpose, a Modelica-based simulation environment PneuLib was used. In this paper, damping capability as a function of the meter-out throttle and cushioning throttle conductance is studied. The author underlined a drawback of pneumatic cushioning in terms of its limited ability to absorb the kinetic energy at the end of the stroke. Especially crucial is a cylinder operation at a high speed. Besides this, the cushioning must be readjusted manually if the inertial mass is changed. The author also concludes a strategy for manual adjustment of the cushioning throttle [6].

Summing up, there are already some mathematical models of the pneumatic end cushioning existing, as well as some experimental studies are present. Nevertheless, none of them considers a thermal interrelation between the gas and the cylinder body in detail. Friction force model is also simplified or missing. In contrast, the present study aims for a more detailed consideration of the physical phenomena that may have a sufficient impact on the thermodynamical and mechanical parameters, relevant for the investigation and further optimization of the pneumatic cushioning system performance.

3 Mathematical model

Simulation of the physical processes, involved into deceleration of a cylinder piston, is essential for understanding the interrelations between the domains mechanics, tribology, fluid mechanics and thermodynamics. The mostly used approach for studying and designing pneumatic systems is a lumped parameter modelling, also known as a one-dimensional modelling. The simulation of one-dimensional models is commonly used to investigate the behavior of components, groups of components and complex pneumatic systems. This approach is used in this study as well. The model is implemented in the software SimulationX by ESI ITI GmbH. In the following paragraphs the implemented mathematical model of pneumatic cylinder is presented and discussed.

3.1 Force balance in a pneumatic cylinder

A typical example of a pneumatic cylinder with an integrated end cushioning is shown in the fig. 1. The functionality of the cushioning device is the same for the head and for the rod end. Due to a simpler geometry only the head end and therefore only the pull-in stroke is considered here. The speed of the piston (travel speed) is assumed to be controlled with a meter-out throttle, which is a very common industrial solution.

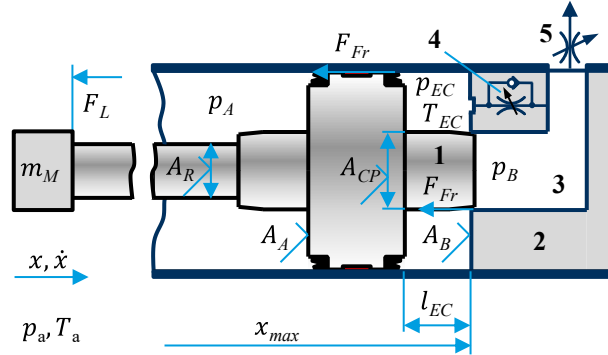


Figure 1: Simplified scheme of the pneumatic cushioning unit and its properties: 1 – cushioning plug, 2 – cylinder head, 3 – main outflow channel, 4 – end cushioning throttle (bypass channel), 5 – meter-out throttle.

The force balance is different for the main stroke ($l_{EC} < x < x_{max} - l_{EC}$), cushioning zone ($l_{EC} \geq x$ or $x \geq x_{max} - l_{EC}$) and the end position ($x = 0$ or $x = x_{max}$). For the main stroke eq. (1) applies:

$$m_M \cdot \ddot{x} = p_A \cdot A_A + p_a \cdot A_R - p_B \cdot A_B - F_L - \text{sign}(F_{Fr}) \quad (1)$$

Gravity force is not considered in eq. (1). If cylinder is mounted non-horizontally, the gravity force term can be considered implicitly as a part of for the load force F_L . After passing the main part of the stroke, cushioning plug overlaps the main outflow channel in the cylinder head. The air, constrained between the piston and cylinder head, shapes the cushioning volume with pressure p_{EC} , acting on the piston surface $A_B - A_{CP}$. The force balance for the cushioning region ($l_{EC} \geq x$ or $x \geq x_{max} - l_{EC}$) therefore differs from that for the main stroke:

$$m_M \cdot \ddot{x} = p_A \cdot A_A + p_a \cdot A_R - p_B \cdot A_{cp} - p_{EC} \cdot (A_B - A_{CP}) - F_L - \text{sign}(F_{Fr}) \quad (2)$$

In the end position ($l_{EC} = x = x_{max} - l_{EC}$) the resulting pressure force is balanced by so-called end force F_{end} acting on the cylinder head:

$$0 = p_A \cdot A_A + p_a \cdot A_R - p_B \cdot A_{cp} - p_{EC} \cdot (A_B - A_{CP}) - F_L - \text{sign}(F_{Fr}) - F_{end} \quad (3)$$

The value of the friction force in equations (1)-(3) can be defined using different approaches. Mostly used in pneumatic applications are dynamic LuGre and Dahl models [7, 8] and static Stribeck model [9, 10], polynomial speed-dependent function [11] and tangent function [2]. In this study the Stribeck model was used due to its simplicity and possibility to take into account the pressure and piston velocity dependence of the friction. According to [9] Stribeck friction model can be determined as:

$$F_{Fr} = F_{FC} + (F_{FS} - F_{FC}) \cdot e^{(-|\dot{x}|/v_S)} + k_v \cdot |\dot{x}|^a + k_p \cdot p_{AB-} \quad (4)$$

Hereinafter differential pressure will be often mentioned in the text and therefore referred as a variable p_{AB-} :

$$p_{AB-} = |p_A - p_B| \quad (5)$$

Jianfeng applies a modified version of eq. (4) where F_{FC} , F_{FS} and k_v are linearly dependent on supply pressure and differential pressure in the cylinder chambers [12]. The function has three independent variables and 12 approximation coefficients and was verified by [13]. Depending on particular friction problem, available measured data and relevant range of operational pressures, speeds and forces, Stribeck model can be simplified, and the pressure-dependent term can be neglected [10, 14, 15]. For a wide variety of pneumatic applications, e. g. point-to-point tasks, the friction model can be reduced to a static and Coulomb friction forces or even assumed as a constant value, without significant decrease in the model quality. In such case parametrization turns out to be simple. Some cylinder producers provide values of static or Coulomb friction forces for their products. Alternatively friction can be evaluated with empirical studies.

For more elaborated problems, for example servo-pneumatic systems, where piston position and speed must be computed precisely, the eq. (4) cannot be further simplified and often advanced dynamic friction models, e. g. LuGre-model are applied.

3.1.1 Approximation of the friction force within the main piston stroke with a Stribeck function

For the studied problem of pneumatic end cushioning a friction model plays an important role for two reasons. Firstly, it impacts the dynamical behaviour of the piston according to eq. (1)-(3) and thus influences the quantity of kinetic energy that is absorbed by the cushioning device when decelerating the moving mass. Secondly, friction force, especially its viscous component, performs a dissipative work itself, that is it “helps” to decelerate the mass. All in all, the friction model for the stated problem must cover a wide variety of pressures and speeds that are peculiar for pneumatic applications. When talking about the relevant speed range, should be considered that over 90 % of all industrially applied cylinders have a stroke under 200 mm and thus have a short acceleration phase. Thus, they are unlikely to be operated at speed, sufficiently exceeding 1 m/s [16, 17]. With regards to the pressure, most of the pneumatic components are usually designed to operate at the maximum pressure of 10 bar_{rel}. In terms of energy efficiency, it also makes sense to decrease the supply pressure and use a larger cylinder, if high force is required [1]. Usually, pressure range up to 8 bar_{rel} and speed range up to 0.5 m/s are addressed in the literature [18].

The coefficients v_s , k_p , k_v and a in the eq. (4) are onerous to calculate analytically and keep under control during the experiment. They are impacted by such factors as cylinder temperature, properties of the sealing lubrication and sealing materials, sealing wear and quality of the frictional surfaces [19]. For this reason, these coefficients are usually determined experimentally to parametrize the friction function for the simulation model.

There are different concepts of test rigs for friction measurement existing. Many of them are comprehensively discussed in [17, 19]. For the given problem, a test rig according to the circuit in the fig. 2, A, was assembled. A cylinder Festo DSBF with diameter of Ø32 mm and stroke of 100 mm was studied. Pressure in cylinder chambers A and B, rod coordinate and acceleration were measured at various supply pressures $p_0 \in [2, \dots, 8]$ bar_{rel} and 28 values of piston speed for each pressure. The horizontally moved mass amounted 3.7 kg. Additionally, pressure p_{EC} and temperature T_{EC} in the by-pass channel of the cushioning throttle were measured to obtain the friction force in the cushioning region and to have a reference for validation of the thermal part of the cylinder model respectively (fig. 2, B).

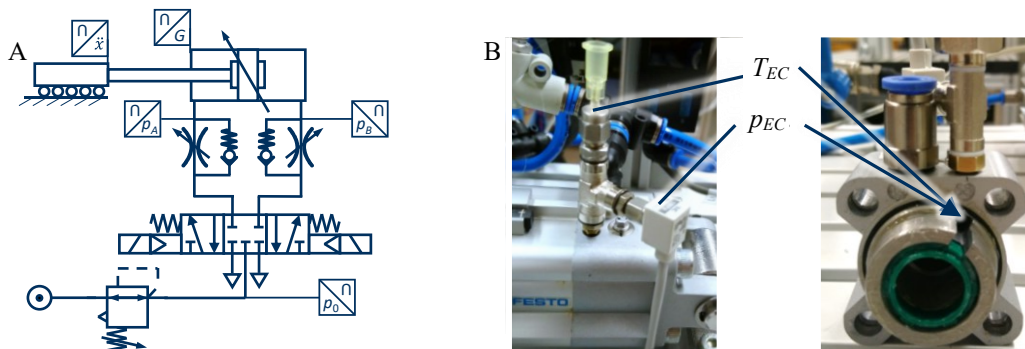


Figure 2: Circuit of the rig with tested cylinder with diameter of Ø32 mm and stroke of 100 mm (A, left) and adapter for the temperature and pressure sensors and their sensing point in the channel (B, right)

The maximum pressure was limited by 8 bar_{rel} due to the design of a directional valve (pressure limitation for internal supply of a pilot stage). Friction force of all friction pairs (i. e. piston and rod sealings and the rail housing) was estimated from eq. (1) on the part of the main stroke after reaching the quasistatic condition, i. e. constant travel speed, but before the piston enters a cushioning zone [19]. It must be noticed that the frictional phenomena and flow resistances between the pressure regulator and cylinder chambers result in a discrepancy of pressures p_A and p_B at various speed values. Besides, pressure drop between the p_0 and p_A sensing points is sufficient at high speed. Therefore, actual chamber pressures p_A and p_B must be used when fitting the model to the experimental data, and not the supply pressure p_0 . Moreover, p_A and p_B fluctuate slightly even at the above-mentioned quasistatic condition. Figure 3 shows the effect of the pressure drop in the cylinder chamber when opening the meter-out throttle (i. e. setting the speed) as well as their variance for each speed value. Further in the study the median values of p_A and p_B were used to calculate the experimental friction force.

The experimental data were merged into a 28×7 -matrix (number of throttle openings \times supply pressures) and fitted to a Stribeck function (eq. (4)) with a nonlinear least square algorithm and plotted in the fig. 4, A, as a function of speed and pressure difference in cylinder chambers p_{AB} . The obtained approximation coefficients are attached in Annex A.

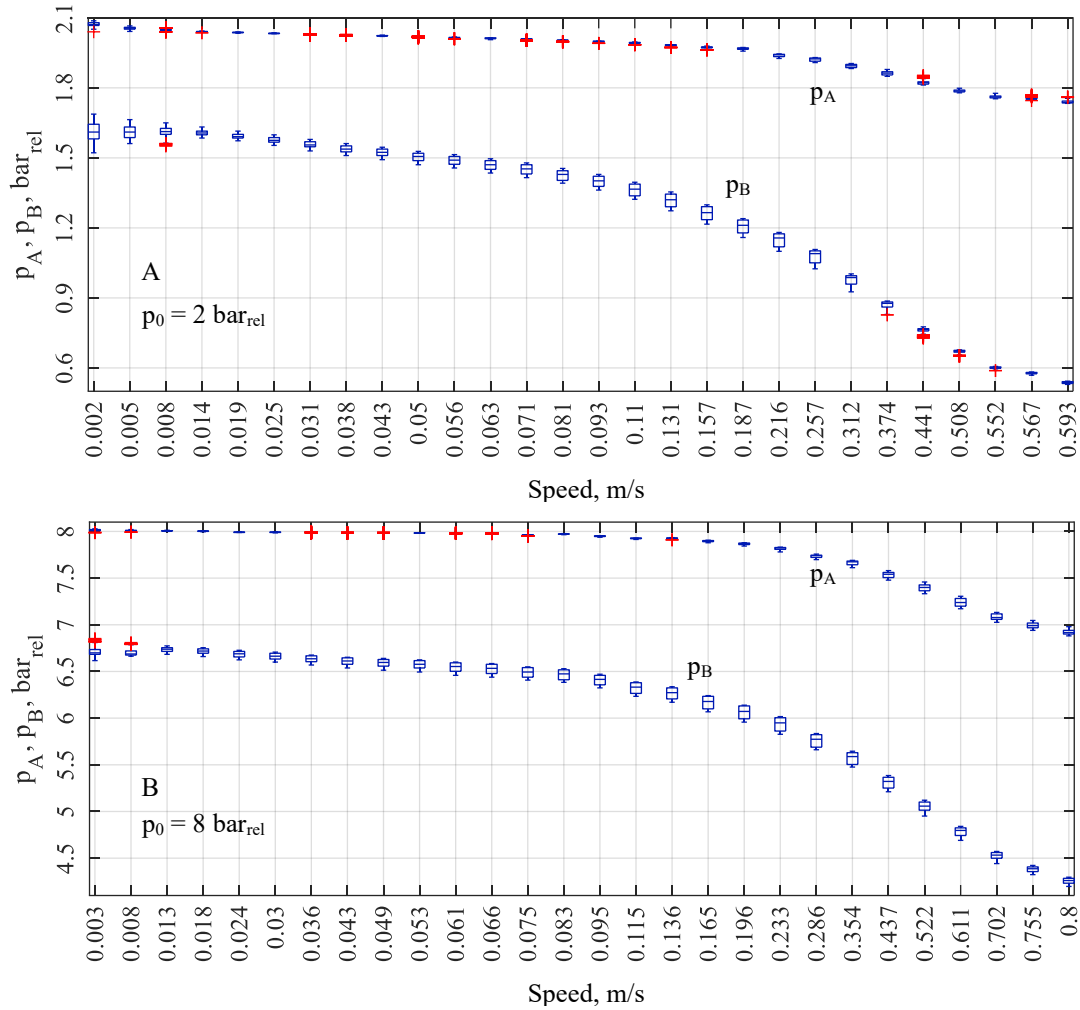


Figure 3: Variance of cylinder pressures p_A and p_B during the quasistatic part of the stroke depending on speed for supply pressure $p_0 = 2 \text{ bar}_{\text{rel}}$ (A, top) and $p_0 = 8 \text{ bar}_{\text{rel}}$ (B, bottom). Boxes correspond to the data between 25th and 75th percentile and are crossed by a median value. Outliers that are more than 1.5 times the interquartile range away from the body of the box are marked as “+”.

It is obvious that eq. (4) has a constant gradient k_p along the pressure axis. The measured friction values tend to have a convex form along the pressure direction, whereas eq. (4) results in a stiff surface that does not cover the data, measured at a high pressure difference. Significant differences in the pressure slope by piston speed of 0.1, 0.3 and 0.5 m/s were also measured by [18] and [19]. The constancy of the pressure gradient k_p affects considerably the total performance of the approximation, measured as a residual sum of squared estimates of errors RSS and as a coefficient of determination R^2 (Annex A). The low-speed region is covered unsatisfactory as well. Stribeck speed v_S that determines a transition area between the dry and viscous friction, tends to be decreased by the nonlinear least-squares algorithm and meets the lower constraint at 0.001 m/s. The Coulomb friction is also restricted by the lower constraint at 2 N. Decreasing these bounds can result in a slightly better approximation performance but contradicts the engineering experience about the typical values of F_{FC} and v_S .

Further discussion of the eq. (4) leads to an unobviousness of the pressure difference $|p_A - p_B|$ in the last term. It implies that friction forces are equal when the piston is sliding with the same speed but different pressures p_A and p_B while the differential pressure is kept the same. For example, if in one case $p_A = 7 \text{ bar}$ and $p_B = 5 \text{ bar}$, and in another case $p_A = 3 \text{ bar}$ and $p_B = 1 \text{ bar}$, friction force would be the same at equal travel speed according to (4). However, the higher the pressure is, the tighter sealing lips are pressed to the frictional surfaces and the higher the frictional force is [19]. Hence, in the next step the pressure-dependent term in eq. (4) was modified to $k_p \cdot p_{AB+}$, where p_{AB+} is a summarized chamber pressure:

$$p_{AB+} = |p_A + p_B|. \quad (6)$$

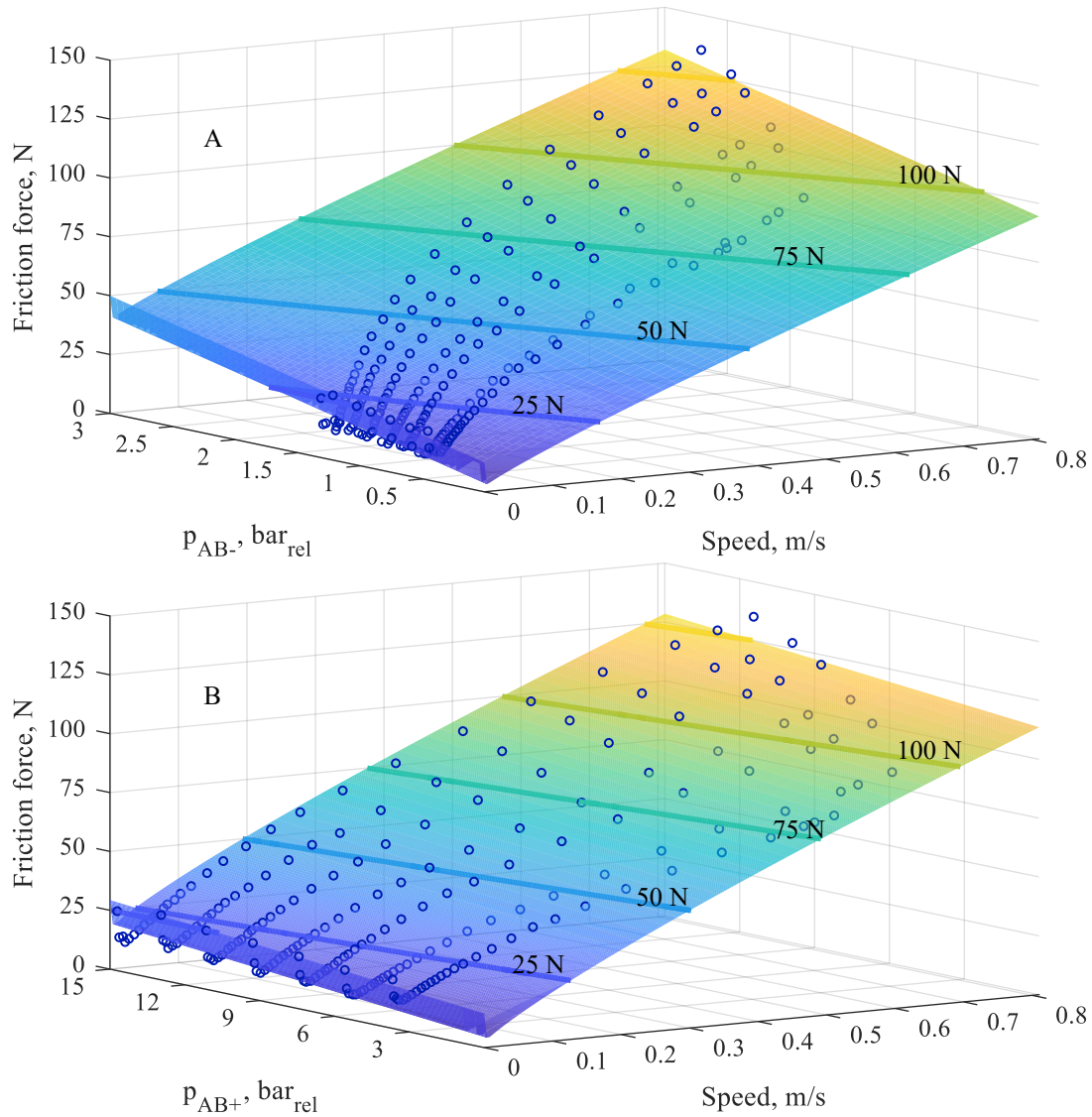


Figure 4: Experimental data (dots \circ) fitted with approximation function (4) using differential p_{AB-} (A, top) and summarized p_{AB+} (B, bottom) pressures in the cylinder chambers.

Although the results of this substitution (fig. 4, B) may look slightly better in the low-speed area, the function is still linear in the pressure direction and cannot be applied for an accurate simulation of pneumatic end cushioning due to its low accuracy. The approximation coefficients for eq. (4) with $k_p \cdot p_{AB+}$ term are grouped in the Annex A.

3.1.2 Approximation of the friction force within the main piston stroke with a modified Stribeck function

To elaborate a handy and accurate function for a wide range of slide speeds and cylinder pressures, a simple approach is proposed here. In the first step, the measured data are fitted separately for each supply pressure p_0 with eq. (7). The real cylinder pressures p_A and p_B are not taken into account in this step.

$$F_{Fr} = b + (F_{FS} - F_{FC}) \cdot e^{-|\dot{x}|/v_S} + k_v \cdot |\dot{x}|^a \quad (7)$$

In contrast to the eq. (4) a bias b appears in the first term instead of the Coulomb friction F_{FC} . Uncoupling the bias from the Coulomb friction significantly improves the quality of an approximation. The results are shown in the fig. 5 (pressure $p_0 = 7 \text{ bar}_{rel}$ is skipped). The estimated coefficients and approximation performance are attached in the Annex B.

It is noticeable that the form of the curves in the viscous region ($\dot{x} \gg v_S$) may be not convex as in the given case, but also concave for some larger cylinders, as for example, the cylinders with diameters of $\text{Ø}40$, $\text{Ø}50$ and $\text{Ø}80 \text{ mm}$ measured by [18]. Basically, this form depends on the sealing material, their form, the rheological properties of the lubrication and the testing methodology [19]. All in all, the eq. (7) approximates the measurements very accurately.

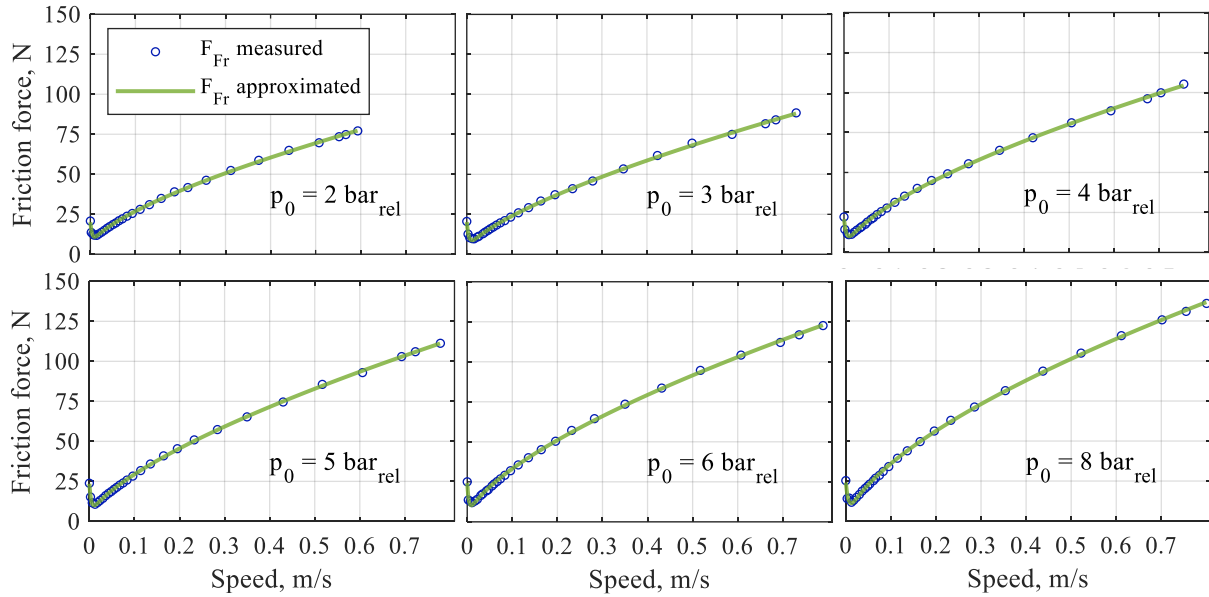


Figure 5: Friction force for supply pressure $p_0 \in [2,3,4,5,6,8] \text{ bar}_{rel}$.

In the second step, the correlation between the coefficients b , F_{FS} , F_{FC} , v_s , k_v , a and supply pressure p_0 must be analysed. For v_s , F_{FC} and a no obvious correlation can be derived, whereas for the other coefficients a descending or ascending trend is observed with an increase of p_0 . It is important to repeat that chamber pressures p_A with p_B and not p_0 are relevant for the real frictional behaviour of the cylinder. However, at high slide speed and constant p_0 , chamber pressures vary noticeably, as was shown in the fig. 3. Nevertheless, p_A and p_B do correlate with p_0 . An increase of p_0 results inevitable in an increase of p_A and p_B . Thus, p_0 can be treated as a variable that correlates implicitly with the friction force, provided that the test circuit and is not changed and no new forces appear in the system.

Considering this, the pressure-dependent coefficients b , F_{FS} , and k_v are linearised with a function $i_0 + p \cdot i_1$, where i corresponds to each of these three coefficients and p is some pressure value, used to estimate the friction. In the following, differential pressure p_{AB-} and summarized pressures p_{AB+} are used as this pressure value in the friction function. Here again, p_0 should not be applied as a variable p , because it does not reflect any changes in the external load force F_L or inertial force $m_M \cdot \ddot{x}$ (see eq. (1)) that affect p_A and p_B and thus real pressure-dependent frictional forces. In the given case, load force and inertial mass remained constant during the friction measurements, but they will be varied in the further steps and thus p_0 is not considered for friction calculation. Applying the pressure-linearized coefficients to eq. (7) following two-dimensional function is obtained:

$$F_{Fr} = b_0 + b_1 \cdot p_{AB-} + (F_{FS,0} + F_{FS,1} \cdot p_{AB-} - F_{FC}) \cdot e^{(-|\dot{x}|/v_s)} + (k_{v,0} + k_{v,1} \cdot p_{AB-}) \cdot |\dot{x}|^a \quad (8)$$

The results of approximation with eq. (8) are plotted in the fig. 6, A. Figure 6, B, corresponds to the same function, but with p_{AB+} applied instead of p_{AB-} . Both versions perform greatly in the whole range of pressures and piston speeds with coefficients of determination R^2 of 0.9975 and 0.9969 respectively (see Annex C).

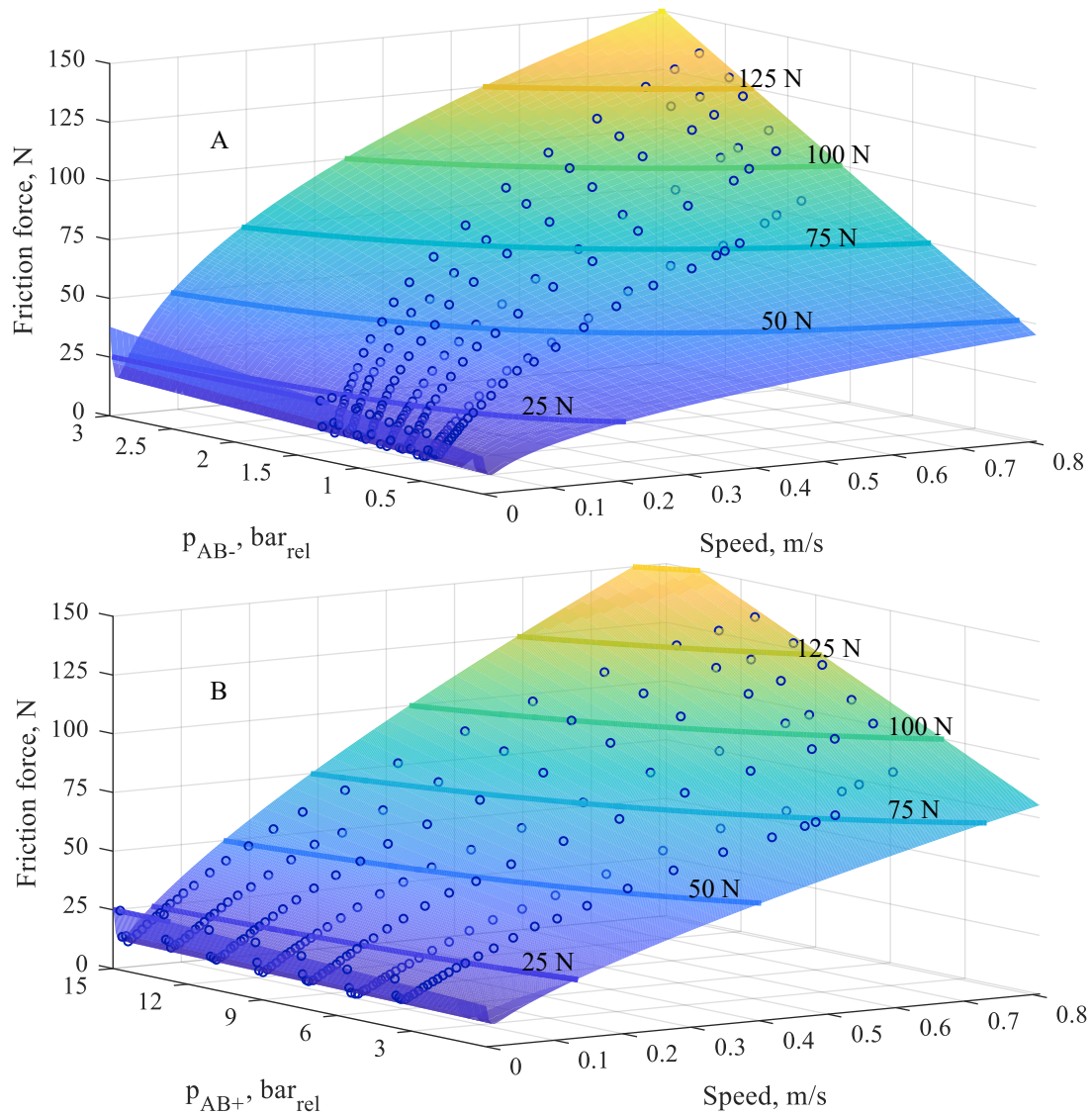


Figure 6: Experimental data (dots \circ) fitted with approximation function (8) using differential p_{AB-} (A, top) and summarized p_{AB+} (B, bottom) pressures in the cylinder chambers.

One of the advantages of the proposed method and function (8) is that the terms $i_0 + p \cdot i_1$ preserve their physical meaning. This is handy when seeking out an error or setting the constraints and initial values for the least-square algorithm. In the following study the model with summarized pressures p_{AB+} is used.

3.1.3 Approximation of the friction force in the end cushioning zone with a modified Stribeck function

For the end cushioning region friction force must be obtained separately. Friction force in the end cushioning differs from the friction within the main stroke because of the additional tribological pair between the damping plug and the damping sealing as shown in the fig. 1. When the cushioning length is reached, cylinder piston starts to decelerate, and its speed is not constant anymore. Therefore, to derive the p - v -dependence of the friction there, speed values as differentials dx/dt between each neighbour points were divided into some groups, which are defined by speed levels. All the calculated speed values that are laying between some two following levels are asserted to the group. Then, the speed values and friction forces, calculated for them from eq. (2) using the measured pressure in the cushioning volume p_{EC} , are statistically evaluated to estimate the median value of the friction and its variation for each speed group. An example for 13 levels and 12 groups of speed at $p_0 = 4 \text{ bar}_{rel}$ is shown in the fig. 7, A. On the boxplot each speed group corresponds to the mean value of its levels. As to be seen, the median values of the friction force tend to form some kind of Stribeck curve. For this reason, all the points measured in the end cushioning region were fitted with eq. (8) for various pressures p_{EC} in the cushioning volume. The results are plotted in the fig. 7, B, and the estimated coefficients are attached in the Annex C.

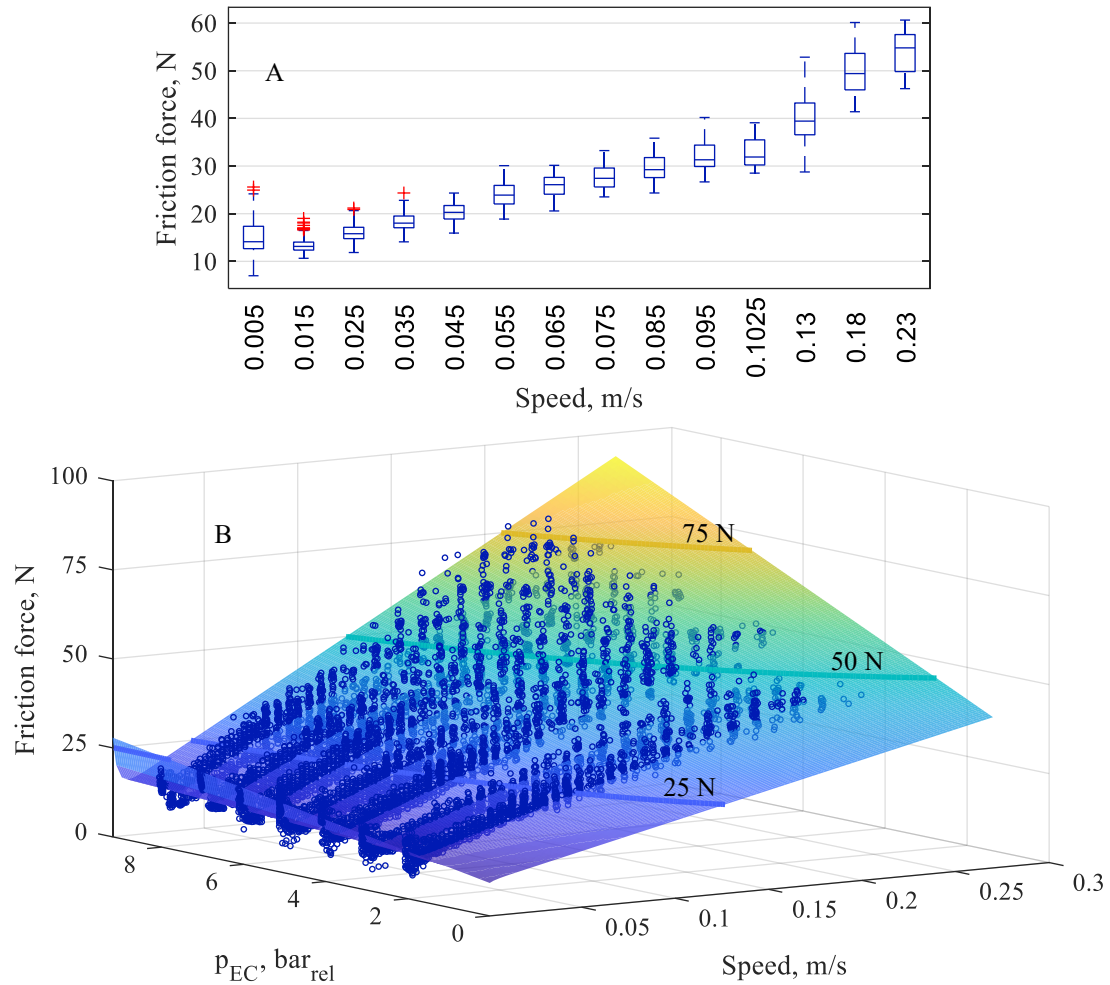


Figure 7: Measured friction forces for 12 groups of speed values in the cushioning zone at supply pressure $p_0 = 4 \text{ bar}_{\text{rel}}$ (A, top) and approximation of the friction in the end cushioning with eq. (8) (B, bottom).

Summing up the results of this paragraph, the proposed mechanical model is used for simulation of the piston movement subject to the presence of the end cushioning. The piston coordinate appears as a switch between the values of the coefficients for the main stroke and for the end cushioning zone. It is important to use separate models for the main stroke and for the end cushioning zone because of the different pressure forces acting on the piston and the different tribological pairs due to the presence of the end cushioning sealing.

3.2 Thermodynamic model of the air flow

To model the air flow and the transient pressure changes, following equations (9)-(12) for a one-dimensional control volume are numerically solved in the simulation environment. Variables with the low-case “1” correspond to the inlet parameters of the volume, with low-case “2” to the outlet, and without index to the volume itself.

As mentioned before, most pneumatic applications are limited by pressure of 10 bar_{rel}, in some rare cases of 16...20 bar_{rel}. Air temperature in pneumatic systems may oscillate in a range of $\pm 20...60 \text{ }^\circ\text{C}$ around the ambient conditions, and usually for a very short time, i. e. for few milliseconds or seconds. Within this temperature and pressure range, a dry compressed air may be treated as an ideal gas because of only a slight variation of specific heats (less than 3.5 % for c_p and less than 1 % for c_v) [20]. When talking about the applications of a high-pressure-pneumatics, or systems exposed to extreme temperature amplitudes, this simplification may result in a high error. However, when talking about the vast majority of industrial pneumatic systems, ideal gas law is applicable:

$$p \cdot V = m \cdot R \cdot T \quad (9)$$

Conservation of momentum:

$$\Sigma F = \frac{d}{dt}(\rho \cdot v \cdot V) + \dot{m}_2 \cdot v_2 - \dot{m}_1 \cdot v_1 \quad (10)$$

Conservation of mass:

$$\dot{m}_1 = \rho_1 \cdot v_1 \cdot A_1 = \frac{d}{dt}(\rho \cdot V) + \rho_2 \cdot v_2 \cdot A_2 \quad (11)$$

Conservation of energy with neglected leakages and potential energy of the air:

$$\dot{Q} + \dot{W} = \dot{U} + \dot{m}_2 \cdot \left(h_2 + \frac{v_2^2}{2} \right) - \dot{m}_1 \cdot \left(h_1 + \frac{v_1^2}{2} \right) \quad (12)$$

Heat transfer equation:

$$\dot{Q} = \alpha \cdot A \cdot (T_W - T) \quad (13)$$

From the eq. (9)-(13) equations for the transient pressure and temperature changes in the considered volume can be derived [2]. Another important relation concluded from the (9) and (12) is an isentropic flow rate equation:

$$\dot{m} = A_2 \cdot \sqrt{2 \cdot p \cdot \rho} \cdot \sqrt{\frac{\kappa}{\kappa - 1} \cdot \left[\left(\frac{p_2}{p} \right)^{2/\kappa} - \left(\frac{p_2}{p} \right)^{(\kappa+1)/\kappa} \right]} \quad (14)$$

It can be approximated with an elliptic function (15), which is widely used in pneumatics to calculate subsonic mass flow rate streaming out of the volume with constant pressure p through a pneumatic resistance with back-pressure p_2 . When the air flow reaches the sonic speed in the smallest cross-section of the resistance, the mass flow rate remains constant (choked) even if p_2 is reduced further. For this part of the flow diagram eq. (16) applies [21]:

$$\dot{m} = C \cdot \rho_a \cdot p \cdot \sqrt{\frac{T_a}{T_1}} \cdot \sqrt{1 - \left(\frac{p_2/p - b}{1 - b} \right)^2} \quad \text{for } \frac{p_2}{p} \geq b \quad (15)$$

$$\dot{m} = C \cdot \rho_a \cdot p \cdot \sqrt{\frac{T_a}{T_1}} \quad \text{for } \frac{p_2}{p} \leq b \quad (16)$$

Air density ρ_a and temperature T_a correspond to the atmospheric conditions according to the ISO 6358.

3.2.1 Parametrization of the meter-out throttle

Sonic conductance C and critical back-pressure ratio b from eq. (15)-(16) are properties of some particular pneumatic resistance. Usually, they are given explicitly or implicitly (i. e. can be derived from the flow diagrams) in the datasheets of throttles and valves. They also can be estimated experimentally on a test rig with standardized dimensions as stated in the ISO 6358. Because the meter-out and end-cushioning throttles are settled manually it is worth to assess the value of the random error caused by inaccurate throttle adjustment. In the fig. 8 a polynomial approximation of the meter-out throttle sonic conductance C_{MO} is plotted versus the number of the knob revolutions z_{MO} . The experiment was repeated 8 times, the inlet pressure was kept constant at $p = 7 \text{ bar}_{\text{abs}}$.

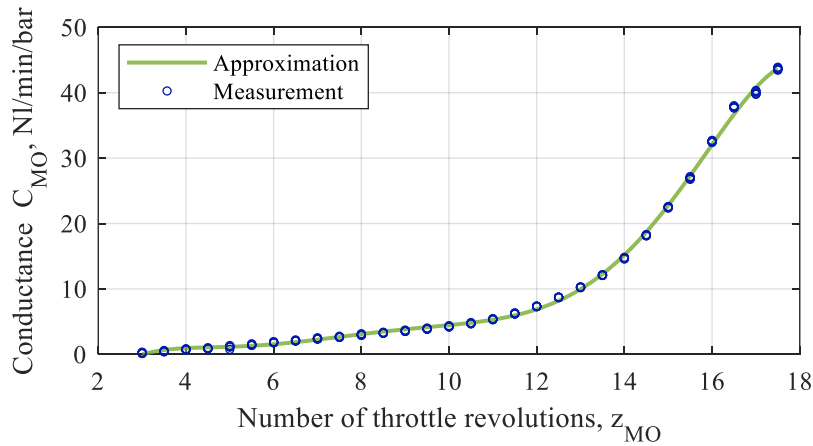


Figure 8: Sonic conductance of the meter-out throttle as a function of the number of throttle revolutions: 8 measurements and their polynomial approximation.

Generally, the absolute difference between the measured median conductance and its approximation is very low. But at small openings (under 6 revolutions) approximation error and random error can cause considerable relative error. This results in speed deviation between experiment and simulation. However, the low-speed range at $z_{MO} < 6$, which corresponds to ca. 2.5 cm/s at $p_0 = 8 \text{ bar}_{\text{rel}}$, is less relevant for the end cushioning problem because kinetic energy is proportional to the speed squared. In this context more important is an impact of the deviations in C_{MO} at a higher opening range over 16 revolutions.

Applying the estimated characteristic $C_{MO}(z_{MO})$ and critical pressure ratio of $b_{MO} = 0.45$ (measured for a fully opened throttle with two 90°-angle pneumatic fittings) to equations (15)-(16) the mass flow rate through the throttle can be calculated. The pressure p before the throttle is estimated from the force balance equations (1)-(8) and the back-pressure p_2 depends on the conductance of the pneumatic hose and the directional valve. For the simulation of pneumatic hoses, the model by Bala validated by Hepke was used [9, 22]. The directional valve can be considered using the same C - b -model. This step as well as the parametrization of the circuit segment “air source → cylinder chamber A” is analogous and therefore skipped here.

3.2.2 Investigation and parametrization of the end cushioning throttle

In the contrary to throttles, directional and servo-valves, the data about the conductance of the end cushioning throttles are not given in any of the catalogues known to the authors. By this reason the flow characteristic of the end cushioning throttle was measured experimentally in this study. For this measurement the piston of the tested cylinder was fixed at the position $x = x_{\text{max}} - l_{\text{ec}} - 4 \text{ mm}$. In this position the cushioning volume V_{EC} is connected with the cylinder outflow channel only through the end cushioning throttle. The air supply to the V_{EC} was carried out through the bore in the cylinder wall at the coordinate $x = x_{\text{max}} - l_{\text{ec}}/2$ (half the cushioning length from the cylinder head). The static pressure $p = p_{EC}$ in the cushioning volume was controlled with a sensor through another bore and kept constant at $7 \text{ bar}_{\text{abs}}$. The air temperature before the studied throttle was controlled with a thermocouple shown in the fig. 2, B. Back-pressure p_2 was adjusted with another throttle and measured in the outlet of the cylinder head. Figure 9 shows the measured and approximated characteristic $C_{EC}(z_{EC})$ and the flow rate characteristics for $C_{EC} = 24, 16$ and 8 NI/min/bar .

The approximated conductance function (fig. 9, A) slightly deviates from the measurements at throttle openings under 1.5 rev. The curvature is characterized with three different gradients: low gradient within the first 1.5 rev., high gradient between 1.5 and 3.5 rev. and a less sloping part above 3.5 rev. The use of a low and high conductance gradients is convenient to enable the fine throttle adjustment for low and high piston speeds.

A particular feature of the measured flow rate diagram in the fig. 9, B, is a high value of the critical ratio b at the full opening. For two-atomic gases and above-mentioned pressure and temperature boundaries of pneumatic applications this value is limited by $b = 0.528$, if the pneumatic resistance is treated closely to an ideal nozzle. However, the geometry of the cushioning throttle differs from that of the ideal nozzle. In the most pneumatic cylinders, the cushioning throttle is implemented as a needle throttle, and not as a common throttle with an axial gap. At a small opening the length of the gap in the needle throttle is sufficient compared to its height [20]. Therefore, the friction losses along this gap length are not negligible anymore, and the equation (14) cannot be derived from the energy conservation (12) in this case. Regardless of that fact, according to ISO 6358-1:2013 the equations (15) and (16) are applied as approximation functions to characterize various pneumatic components with non-negligible friction losses, such as pneumatic tubes, that may also have high critical ratio b .

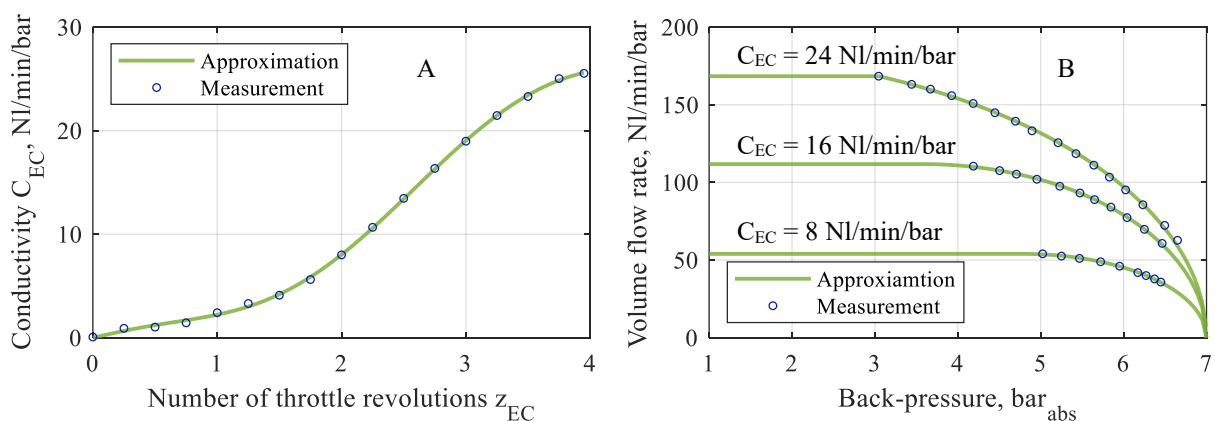


Figure 9: Measured and approximated conductance characteristic $C_{EC}(z_{EC})$ (left, A) and the flow rate characteristics for different openings of the end cushioning throttle at constant inlet pressure $p_{EC} = 7 \text{ bar}_{\text{abs}}$.

In case of the studied end cushioning throttle, parameter b_{EC} was specified in the model as a linear function of the pneumatic conductance C_{EC} . As discussed above for the meter-out throttle, the approximated measured data for $C_{EC}(z_{EC})$ and $\dot{m}(p_2/p_{EC})$ describe an interrelation between the pressure in the cushioning volume and the mass flow rate through the cushioning throttle and hence the speed of the piston in cushioning region.

3.3 Heat transfer model

Heat transfer between the compressed air, cylinder wall and environment is not negligible in pneumatic systems and must be considered to achieve the results comparable with reality. Temperature changes in a pneumatic cylinder are usually caused by pressurizing or discharging the cylinder chambers. For instance, Hassan et al. has measured the temperature fluctuations between 0 and 60 °C in a Ø50 mm cylinder with a stroke of 200 mm [23]. Hepke has compared experimentally the temperature response of three air reservoirs made of polyvinylchloride (PVC), aluminium alloy and stainless steel when charging them from 1 to 7 bar_{abs}. He figured out that the temperature rises in the PVC-reservoir up to 120 °C and drops down within several seconds. In case of aluminium and steel, which are more relevant materials for pneumatic cylinders and reservoirs, the temperature increases up to 55 and 75 °C respectively. Carneiro and Almeida have proposed a new method for the calculation of the heat transfer coefficient based on the measurements of the pressure response when charging different cylinders [24]. The authors concluded that the cylinder material, whether it is a stainless steel or an aluminium alloy, is not relevant for modelling of the thermal processes in such an extent as the inner cylinder geometry, i. e. the area exposed to the heat transfer, is. Further, De Giorgi et al. proposes an accurate method for comprehensive modelling of the thermal domain in pneumatic systems and underline an inapplicability of often used polytropic, adiabatic, or isothermal models for accurate calculations [25].

Consideration of thermal interrelations in pneumatic cylinder is very important when talking about the calculation of energy consumption. Usually, energy consumption is calculated for cylinder as an isothermal system, and gas temperature in the chambers is assumed to be equal to the environmental temperature. However, when a cylinder with a small stroke is operated at a high frequency, the air may not cool down completely and fills the cylinder chamber at higher temperature and thus at a lower density at the same pressure. This results in a lower air consumption compared to an isothermal system. In terms of pneumatic end cushioning, an ability of a cylinder body to carry the heat away during the damping phase has an impact on a total energy absorption capability of the cushioning system.

To estimate the heat transfer coefficients in a one-dimensional model of pneumatic cylinder, the approach used by Michel for modelling the thermal behaviour of compact electrohydraulic drives [26] was transferred to the pneumatic systems. According to this approach, a cylinder body can be decomposed into heat capacities with a simple geometry, such as the cylinders, rods or plates, which are streamered with an air flow longitudinally or orthogonally. These capacities are connected with each other and with pneumatic part of the model via thermal resistances, each characterized by heat conductance or heat transfer coefficient for free or forced convection. For simple geometries heat transfer coefficients can be easily estimated with low computation costs.

4 Results and discussions

To validate the simulation model of pneumatic end cushioning, static pressure p_{EC} and temperature T_{EC} in the cushioning volume as well as cylinder rod coordinate were measured. The sensing point for both temperature and pressure is shown in the fig. 2, B. For temperature measurements a thin K-type thermocouple Omega CHAL-0005 was used. It has a bare sensor head, and with diameter of 12.5 µm its cross-sectional area is about 25 times smaller than that of a human's hair. Low thickness results in a low heat capacity of the sensor head and consequently in a short response time. Unfortunately, no exact data about the response time of this model can be obtained from the datasheets. Besides, the heat transfer from the gas to a sensor head via convection depends on air density and flow speed. Thus, the time constant may be defined only for one operational point, whereas the measured air parameters in the cushioning channel vary significantly. To estimate at least a rough value of the time constant, the sensor head was exposed to a temperature change with an amplitude of 40 °C within under 2 ms at upstream velocity of 5 m/s. From the exponential response plots the time constant of about 15 ms was determined. That means, the sensors head is expected to take the temperature of the air within about 75 ms. The reaction time of the signal amplifier of 0.5 ms is therefore negligibly small when considering the entire measuring circuit. Using this time constant in the model, a signal from the thermocouple can be simulated as a PT1-element and its output is expected to be comparable with the measured temperature. The data were acquired with an oscilloscope. Time constant of the sensor Omega 5TC-TT-KI-40-1M used by [9] with diameter of Ø75 µm was measured by 90 ms and thus has reaction time of ca. 450 ms. Sensors used by [23] have the same diameter and thus are expected to have the similar dynamic properties.

A significant drawback of the $\text{\O}12.5\text{-}\mu\text{m}$ -thermocouples is their fragility. The thermocouples were glued into a G20 syringe needle, and the needle was sealed with an industrial feedthrough. For pressure measurement small sensor SMC PSE540 with response time of 1 ms and M3-connection was used. The aim was to minimize the infliction of an additional dead volume brought about by the sensors, bore in the cylinder head and an adapter. The results of the measurements for supply pressures $p_0 = 5 \text{ bar}_{\text{abs}}$ and $p_0 = 7 \text{ bar}_{\text{abs}}$ for 16 meter-out throttle revolutions (almost full throttle opening) and three openings z_{EC} of the end-cushioning throttle are shown in the fig. 10-11.

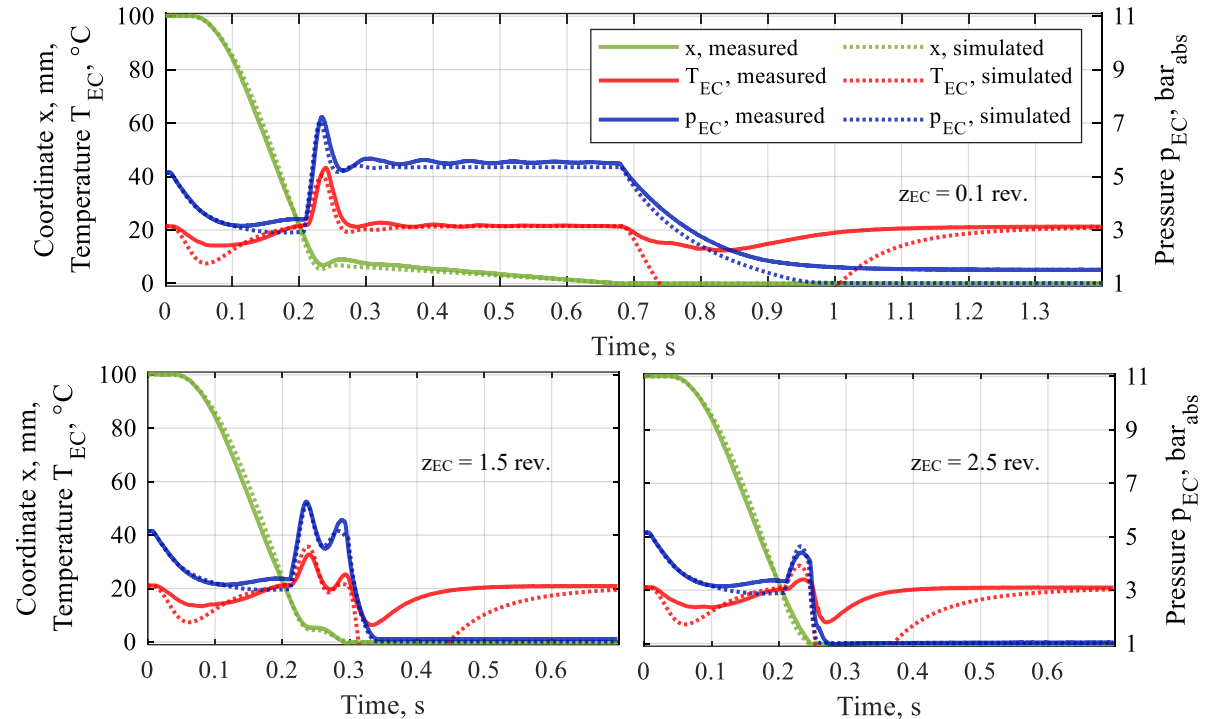


Figure 10: Piston stroke x (green), cushioning temperature T_{EC} (red) and pressure p_{EC} (blue) measured for different openings of the end cushioning throttle at $p_0 = 5 \text{ bar}_{\text{abs}}$ and moving mass $m_M = 3.7 \text{ kg}$.

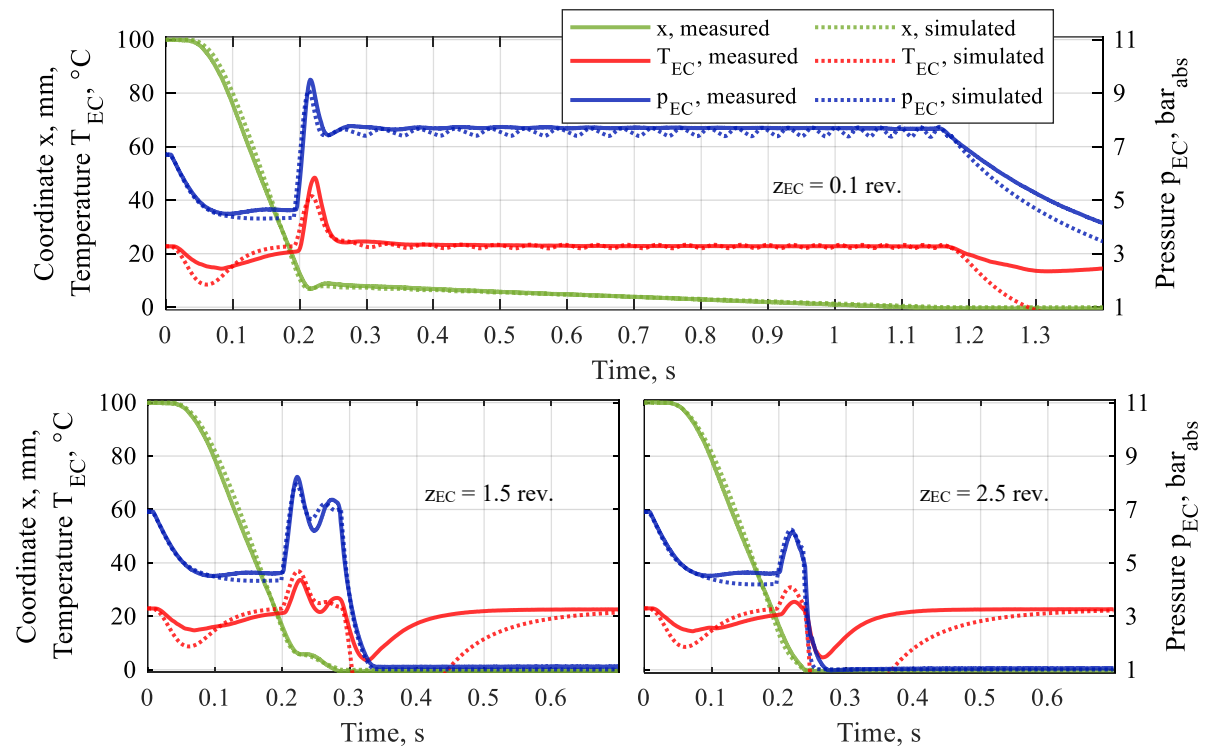


Figure 11: Piston stroke x (green), cushioning temperature T_{EC} (red) and pressure p_{EC} (blue) measured for different openings of the end cushioning throttle at $p_0 = 7 \text{ bar}_{\text{abs}}$ and moving mass $m_M = 3.7 \text{ kg}$.

Each of the three subplots in the fig. 10-11 depicts distinctive cushioning processes that typically occur in industrial applications. At very small cushioning throttle opening $z_{EC} = 0.1$ rev. (top subplots), the pressure rises significantly as soon as the cushioning region is reached by the piston. The piston springs back, but without touching the cylinder head. Because the most part of its kinetic energy is already absorbed and the throttle conductance is very low, the piston travels to the end position slowly. This is an example of a cushioning process with an overdamping. If there is no strict limitation on travel time, this setting is rather harmless because no shock, noise or vibration occur. It is worth mentioning that an increase of the moving mass above 10 kg leads to a situation, when inertia pushes the piston through the damping volume, and it reaches the cylinder head in the first oscillation phase whilst not being completely decelerated. That means that kinetic energy exceeds the maximum damping capability of the integrated cushioning for a given cylinder because no further closing of the cushioning throttle is possible. Either mass or speed must be reduced.

Another important issue must be noted, when comparing travel time in both top subplots of the fig. 10-11. In both cases the cushioning throttle was adjusted manually and was supposed to be the same. However, even a small error in the manual adjustment results in considerably different travel time. In one case the piston passes the cushioning zone within 0.48 s, in another case within this time doubled. This phenomenon illustrates well the sensitivity of the pneumatic end cushioning on the manual adjustment.

Discussing the plots for further throttle openings, is important to emphasize that in the most pneumatic applications travel time plays a major role and must be reduced to a minimum to enhance the output machine productiveness. Having said that, an optimal adjustment of the cushioning throttle is usually sought to keep the cushioning time as short as possible. A relative example is shown in the left subplots of the fig. 10-11 for cushioning throttle opening $z_{EC} = 1.5$ rev. Damping pressure increases not as significant as in the first case, piston does not rebound, but the pressure is sufficient to slow down the mass before it reaches the end position. A small amount of the rest energy may be buffered by an elastic shock absorber installed in the cylinder. No harmful vibration appears, but a quiet, soft knock may be heard. Travel time in the cushioning zone decreases to 0.08...0.09 s. Further opening of the cushioning throttle, e. g. up to 2 revolutions leads to an increase of the piston speed at the very last part of the stroke of ca. 5-8 mm: being once decelerated, piston accelerates again and hits the cylinder head. Stacking the mass up to total maximum of 10 kg is not crucial at $z_{EC} = 1.5$ revolutions and only changes the form of the stroke-time-profile closer to a monotonous sine-like deceleration.

The example of an underdamped cushioning setting is shown in the right subplots of the fig. 10-11. The conductance of the throttle is so high that the air flow out of the cushioning volume meets almost no resistance and no braking pressure is built up. As a result, piston reaches the cylinder head at almost full speed, rebounds slightly from the elastic shock absorber and stops. A long operation in this mode is fraught with a high vibration and may result in a machine damage. A noise emission level becomes uncomfortable.

5 Summary and outlook

The conductance of the end cushioning throttle is usually the once parameter that a user can adjust to reach the desirable damping quality and travel time, when taking a pneumatic drive into operation or maintaining it. The quality of the cushioning process can be quantified using an integral criterion of cushioning time, peak deceleration, and the maximum capability on energy absorption. The damping quality is not equal for the same throttle opening when operating the cylinder drive under various supply pressures, travel speeds and inertial loads. Hence, the global aim of the analysis of integrated pneumatic end cushioning systems is to figure out, how the geometry of the cushioning throttle and cylinder can be designed to guarantee a fast and repeatable deceleration and to minimize the sensitivity against fluctuating operation parameters, such as pressure, moving mass, friction and load forces. This problem can be solved by the multiparametric robust optimization of the end cushioning.

For this purpose, a one-dimensional simulation model of the pneumatic cylinder with an integrated pneumatic cushioning system was developed and is presented in this paper. Different aspects, mainly the parameterization of the friction model and the end cushioning throttle of a real cylinder are discussed in detail. A more accurate alternative to the classical Stribeck-function is proposed to calculate the friction force over a wide range of pressures and speeds.

The simulated piston stroke, pressure and temperature in the end cushioning volume are experimentally validated. The comparison plots, presented in the fig. 10-11, show consistency of the stroke and pressure profiles. In the positive region (above 0 °C) temperatures match good as well. However, the amplitude of simulated temperature in the negative range appears to be higher (up to -20...-30 °C) than it was really measured. That can be caused by a little-known transient behaviour of the temperature sensor under varying flow conditions. Another reason can be a simplification of the cylinder geometry and its thermal model that hides the complex thermal interrelations between the cylinder body and the gas flow. Hence, this approach is a compromise between the high detail degree, which can be enhanced by coupling the present one-dimensional model with a two- or three-dimensional model

solved with finite element and finite volumes methods, and the simulation time. Simulation time is essentially important for sensitivity analysis and robust optimization within the further steps because it may require up to 100,000 number of model runs. Thus, the designed one-dimensional model with simulation time varying between some tenths of the second up to few seconds is considered to be proper for both sensitivity analysis and robust optimization whilst having an acceptable level of representativeness of the real matter.

Funding sources

This research is funded by the European Social Fund and co-financed by tax funds based on the budget approved by the members of the Saxon State Parliament.

Diese Maßnahme wird mit Mitteln aus dem Europäischen Sozialfonds gefördert und mitfinanziert durch Steuermittel auf Grundlage des von den Abgeordneten des Sächsischen Landtags beschlossenen Haushaltes.

Annex

Annex A: Results of a two-dimensional approximation of measured friction force with eq. (4).

related pressure	F_{FC} , N	F_{FS} , N	v_S , m/s	k_v , kg/s	a , -	k_p , N/bar _{rel}	RSS	R ²
p_{AB-}	2 (constraint)	12.32	0.001 (constraint)	111.5	0.8914	12.56	$4.29 \cdot 10^3$	0.9797
p_{AB+}	2 (constraint)	14.45	0.00151	133.5	0.8497	0.994	$5.99 \cdot 10^3$	0.9716

Annex B: Results of a one-dimensional approximation of measured friction force with eq. (7).

p_0 , bar _{rel}	b , N	F_{FS} , N	F_{FC} , N	v_S , m/s	k_v , kg/s	a , -	RSS	R ²
2.07	5.447	20.46	5.94	0.00367	102.5	0.6796	9.85	0.9993
3.127	2.824	22.59	5.273	0.004483	106.1	0.7018	9.28	0.9995
4.115	1.468	25.78	6.407	0.004925	123.7	0.6513	17.08	0.9993
5.14	2.776	25.05	4.31	0.004033	128.7	0.6843	7.07	0.9998
6.13	2.509	25.51	3.855	0.003434	140.8	0.662	23.72	0.9993
7.085	1.274	32.95	7.864	0.005579	147.6	0.6468	28.9	0.9992
8.075	-1.17	31.08	5.856	0.005311	158.8	0.6317	26.59	0.9994

Annex C: Results of a two-dimensional approximation of measured friction force with eq. (8) for the main stroke and the end cushioning zone

related pressure	b_0 , N	b_1 , N/bar _{rel}	$F_{FS,0}$, N	$F_{FS,1}$, N/bar _{rel}	F_{FC} , N	v_S , m/s	$k_{v,0}$, kg/s	$k_{v,1}$, kg/s/bar _{rel}	a , -	RSS	R ²
p_{AB-}	-0.67	-4.4	21.64	11.78	5.08	$4.16 \cdot 10^{-3}$	49.9	43.41	0.429	526	0.9974
p_{AB+}	5.63	-0.1	17.06	0.714	5.4	$3.98 \cdot 10^{-3}$	87.46	6.1	0.746	654	0.9969
p_{EC}	9.66	0.26	8.8	2.197	8.8	$2.96 \cdot 10^{-3}$	121	19.61	1	$1.73 \cdot 10^5$	0.9292

Nomenclature

Designation	Denotation	Unit
κ	Isentropic exponent	-
ρ	Density	kg/m ³
a	Speed exponent	-
A	Cross-section area	m ²
b	Friction force bias	N
C	Sonic conductance	s·m ⁴ /kg
F	Force	N
h	Specific enthalpy	J/kg

m	Mass	kg
\dot{m}	Mass flow rate	kg/s
l	Length	m
k_p	Pressure-dependent friction coefficient	N/bar
k_v	Speed-dependent friction coefficient	kg/s
p	Pressure	bar
\dot{Q}	Heat flow	W
t	Time	s
R	Specific gas constant	J/kg/K
T	Temperature	°C, K
\dot{U}	Inner energy change	W
v	Speed	m/s
V	Volume	m ³
\dot{W}	Power	W
x	Coordinate	m
\dot{x}	Speed	m/s
\ddot{x}	Acceleration	m/s ²
z	Number of throttle revolutions	-

Index

Designation	Relation to
1	Inlet conditions
2	Outer conditions
a	Atmospheric conditions acc. to ISO 6358
A	Cylinder chamber A
$AB-$	(Pressure) difference in A and B
$AB+$	Sum (of pressures) in A and B
B	Cylinder chamber B
CP	Cushioning plug
EC	End cushioning
FC	Coulomb friction
Fr	Friction
FS	Static friction
L	Load
M	Moving (mass)
MO	Meter-out (throttle)
R	Rod

References

- [1] EnEffAH Energy efficiency in production in the drive and handling technology field: Basic principles and measures. EnEffAH Project Consortium, Stuttgart, 2012. Last access on February 12, 2021: https://www.eneffah.de/EnEffAH_Broschuere_engl.pdf.
- [2] M Doll. *Optimierungsbasierte Strategien zur Steigerung der Energieeffizienz pneumatischer Antriebe*. Dissertation, Shaker Verlag, Aachen, 2016.
- [3] White paper: ACE NoCushion Serie. Externe Endlagendämpfung für Pneumatikzylinder.
- [4] White paper: AIRTECs InnoMotix®-System. Pneumatik ohne Dämpfer.
- [5] Y T Wang et al. Computer Simulation of a Shock-Absorbing Pneumatic Cylinder. *Journal of Sound and Vibration*, 93(3):353-364, 1984.
- [6] P Beater. Endlagendämpfung pneumatischer Zylinder. *O+P Ölhydraulik und Pneumatik*, 47 (2003), No. 3: 163-167, 2003.
- [7] X B Tran et al. A new Mathematical Model of Friction for Pneumatic Cylinders. *Proceedings IMechE, Part C: J Mechanical Engineering Science*, Vol. 230(14):2399–2412, 2016.
- [8] A C Valdiero et al. Nonlinear Mathematical Modeling in Pneumatic Servo Position Applications. *Hindawi Publishing Corporation: Mathematical Problems in Engineering*, Vol. 2011, Article ID 472903:1-16, 2011. doi:10.1155/2011/472903.
- [9] J Hepke. *Energetische Untersuchung und Verbesserung der Antriebs-technik pneumatischer Handhabungssysteme*. Dissertation, Shaker Verlag, Aachen, 2017.
- [10] S Klotzbach, H Henrichfreise. Ein nichtlineares Reibmodell für die numerische Simulation reibungsbehafteter mechatronischer Systeme. *Proceeding of 16. Symposium Simulationstechnik in Rostock, 10.-13. September 2002*, pp. 1-13, 2002.
- [11] L Endler et al. Compressed air saving in symmetrical and asymmetrical pneumatic positioning systems. *Proceedings IMechE, Part I: J Systems and Control Engineering*, Vol. 229(10):957-969, 2015.
- [12] C Jianfeng. Study on Friction Characteristics of Pneumatic Cylinders Base on LuGre Model. *The 6th national fluid drive and control conference proceedings*, 2010:1-5.
- [13] Y Zhan et al. Study on Friction Characteristics of Energizing Pneumatic Cylinders. *Advanced Materials Research*, Vol. 904:306-310, 2014. doi:10.4028/www.scientific.net/AMR.904.306.
- [14] A Krämer, J Kempkes. Modellierung und Simulation von nichtlinearen Reibungseffekten bei der Lageregelung von Servomotoren, *FHWS Science Journal*, Jg. 1, No. 2:47-57, 2013.
- [15] H Watter. *Hydraulik und Pneumatik*. Friedr. Vieweg & Sohn Verlag | GWV Fachverlage GmbH, Wiesbaden, 2007.
- [16] T Radermacher et al. *Potenzialstudie Energie-/Kosteneinsparung in der Fluidtechnik*. Final Report. Umweltbundesamt, Reihe Climate Change 19/2021, 2021. Last access on April 30, 2021: https://www.umweltbundesamt.de/sites/default/files/medien/5750/publikationen/2021-04-26_cc_19-2021_fluidtechnik.pdf.
- [17] O P Heipl. *Experimentelle und numerische Modellbildung zur Bestimmung der Reibkraft translatorischer Dichtungen*. Dissertation, Shaker Verlag, Aachen, 2013.
- [18] G Belforte et al. Measurement of Friction Force in Pneumatic Cylinders. *Tribotest Journal* 10-1, September 2003. (120):33-48, 2003.

- [19] A Muth. *Reibkraftermittlung an pneumatischen Ventilen und Zylindern*. Dissertation, Shaker Verlag, Aachen, 1998.
- [20] F M White. *Fluid Mechanics*. 8th edition in SI units, McGraw-Hill Education, 2016.
- [21] L Pasięka. The applicability of the mass-flow-model according to iso 6358 with the parameter critical conductance c and critical pressure ratio b for gases in high-pressure range up to 300 bar. *Proceeding of 12th International Fluid Power Conference (12. IFK), Dresden*, Vol. 1:541-550, 2020.
- [22] H P Bala. Durchflussmessungen und strömungstechnische Kenngrößen. *O+P Ölhydraulik und Pneumatik*, 45 (2001), No. 4:246-255, 2001.
- [23] J M Hassan et al. Experimental investigation of a temperature change inside pneumatic cylinder chambers. *Al-Nahrain Journal for Engineering Sciences (NJES)*, Vol. 20 No.1:1-4, 2017.
- [24] J F Carneiro, F Gomes de Almeida. Heat transfer evaluation of industrial pneumatic cylinders. *Proceedings IMechE, Part I: J. Systems and Control Engineering*, Vol. 221:119-128, 2007.
- [25] R De Giorgi et al. Dynamic thermal model of a discharging process of a pneumatic chamber. *Proceedings of 4th FPNI-PhD Symposium, Sarasota*, pp. 571-583, 2006.
- [26] S Michel, J Weber. Prediction of the thermo-energetic behaviour of an electrohydraulic compact drive. *Proceeding of 10th International Fluid Power Conference (10. IFK), Dresden*, pp. 219-233, 2016.

Improving the efficiency of valve-controlled systems by using multi-chamber actuators

Henrique Raduenz, Liselott Ericson, Kim Heybroek*, Victor J. De Negri**, Petter Krus

Division of Fluid and Mechatronic Systems, Linköping University, Linköping, Sweden
E-mail: henrique.raduenz@liu.se, liselott.ericson@liu.se, kim.heybroek@volvo.com,
victor.de.negri@ufsc.br, petter.krus@liu.se

*Volvo Construction Equipment, Eskilstuna, Sweden

**Federal University of Santa Catarina, Florianópolis, Brazil

Abstract

This paper outlines how multi-chamber actuators can improve the efficiency of valve-controlled systems. Resistive control is a major source of energy losses in valve-controlled systems that share the same pump to drive multiple loads. In the proposed concept, by selecting different chambers, the load on the multi-chamber actuator can be transformed into different pressure and flow rate levels, allowing the adaptation of its load to the loads on other actuators. This can lead to a reduction of resistive control energy losses that occur between pump and actuators when driven simultaneously. Such systems are seen as an intermediate solution between resistive conventional hydraulics and throttle-less digital hydraulics. As a case study to highlight the possible efficiency improvement, a concept of a load sensing system with a conventional and a multi-chamber actuator is analysed. To determine its efficiency, the equations that describe its static behaviour are presented. Evaluating them for a set of load forces and speeds demonstrates how the load transformation occurs and how it can improve efficiency.

Keywords: Digital fluid power, multi-chamber actuators, throttling losses

1 Introduction

The study presented in this paper is motivated by the fact that the introduction of throttle-less digital hydraulics into a valve-controlled hydraulic system architecture might result in increased system efficiency without requiring a significant redesign. Although the full potential of throttle-less digital hydraulics to increase efficiency might not be achieved, it could still result in a considerable reduction of the system energy losses.

So far, most of the concepts for linear actuation in hydraulics have been designed with either a conventional resistive approach in mind or with a digital hydraulics approach in mind. One of the most common approaches of digital hydraulics for linear actuation was presented by Linjama *et al.* in [1], where the concept of a secondary controlled multi-chamber actuator is proposed. By using a parallel configuration of on/off valves, different connections between pressure sources and actuator chambers are obtained, resulting in discrete force levels. When the authors compare this concept to a conventional load sensing system, a 60% reduction in power losses is achieved. The authors also mention that because the typical load sensing system has several actuators, the supply pressure is optimized for one actuator only, resulting in significant throttling losses on the valves controlling other actuators. This is not the case for the secondary controlled actuator, since the loads are decoupled.

In [2] the energy efficiency of a three-chamber actuator controlled by on/off valves is evaluated. At each control edge there is a set of on/off valves with different flow areas. At each control mode (combination of actuator areas to pressures sources) the pressure of one of the chambers is controlled resistively through the selection of different valves, resulting in a different total flow area. The control objective is to find the mode that can drive the load but also reduce the pressure drop on the controlling valves, therefore reducing the losses due to the resistive control.

A similar concept as the one present in [1] is presented in [3] for the control of an excavator arm. The main difference is the additional pressure source, which results in a higher number of available force levels to be chosen. The same concept is investigated in Belan *et al.* [4], but applied to the control of flight control surfaces of aircrafts. In [4] the authors presented a detailed investigation of how the areas of the actuator chambers can be determined together with efficiency analysis. For the same load cases, the digital hydraulic actuator would result in an 80% reduction in energy losses in comparison to traditional servo-proportional control.

It is observed that the switching nature of these systems imposes a major challenge on the development of controllers and is also a significant source of losses due to the compressibility of the fluid. As mentioned in [1] compressibility losses are caused by the fact that the energy stored in hydraulic capacitance is lost when the chambers switch between pressure levels. Other researchers proposed alternative architectures that contain means of throttling control to improve mainly the control performance in detriment of a reduction in system efficiency.

In [5] the authors mention about the limited finite number of discrete force levels that can be generated by pure digital hydraulic configurations with parallel valves. To improve the force resolution, aiming to achieve an accurate control of the actuator, the authors propose that a proportional valve should be connected to one of the chambers. Results show that controllability can be improved while still maintaining high energy efficiency.

In [6] the authors present a model predictive control strategy for a four-chamber actuator connected to a common pressure rail through proportional valves, a Variable Displacement Linear Actuator (VDLA). It is similar to the concept presented in [1] except for the use of proportional valves which allow throttling control between the different force levels, resulting in smoother control while still maintaining high efficiency. In a simulation study presented in [7] the effectiveness of the VDLA is also shown at a system level for a hydromechanical hybrid motion system for a wheel loader. In [8] results show a 34-50% fuel efficiency reduction for an excavator with a hydraulic system architecture based on the VDLA. Although the high efficiency results motivate a change to the architecture of hydraulic systems in mobile machines, it is noted that a significant redesign is required.

Aiming to be an intermediate solution between valve-controlled architectures and architectures based on digital control, the goal of this paper is to show that the use of multi-chamber actuators in a valve-controlled system can result in an increase in system efficiency. The main purpose of the multi-chamber actuator is to adapt its required pressure and flow rate to reduce throttling losses that arise when multiple loads are driven simultaneously. During the literature review, the authors did not find any similar approach to the combination of valve-controlled and digital hydraulics. In this sense, another contribution of this paper to the research area is a different way of using the principles of digital hydraulics.

This paper is organized as follows: Section 2 presents a description of the proposed combination of multi-chamber actuator and valve-controlled systems; Section 3 provides a discussion on how a controller could be designed for this system; In Section 4 the concept selected for the case study is described in more detail. Section 5 presents the equations used for the efficiency analysis; Section 6 presents the analysis and efficiency results; Section 7 presents a discussion about the main points extracted from the results; and Section 8 contains the conclusions.

2 Concept Description

Figure 1a is a diagram of a secondary controlled actuation system, where the actuators are controlled by the switching of the on/off valves to establish different connections between pressure sources and actuator chambers. The combination of pressures and chamber areas results in different force levels, which can be used to perform the control action against the load. Since the valves operate either closed or fully open, the throttling losses are significantly reduced. It can be assumed that the pressures of the pressure sources remain constant and, therefore, such a system does not suffer from load interference, which means that the control of one actuator does not interfere with the control of the other actuators.

Figure 1b is a diagram of a valve-controlled load sensing actuation system with a single pump driving two loads. It is known that a major efficiency drawback in such systems arises from the throttling losses that occur between pump output and the actuators. Since the pump pressure is governed by the highest load pressure, the pressure losses on the valves controlling the other actuator are significant. In order to reduce the losses due to throttling, this paper proposes to change a conventional actuator for a multi-chamber actuator.

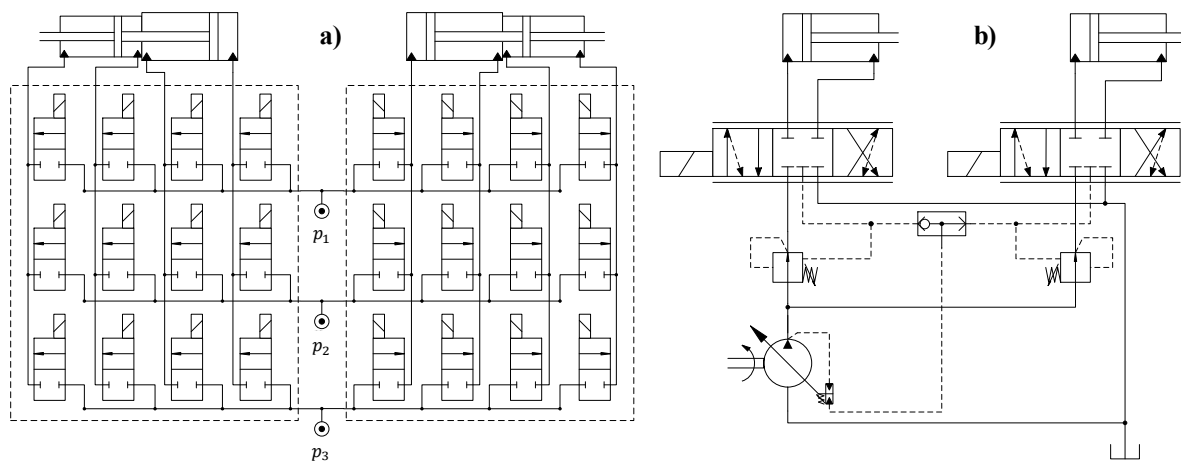


Figure 1 - a) Secondary controlled actuation system; b) Valve-controlled load sensing system.

Figure 2a is an example of the application of a multi-chamber actuator to a valve-controlled open-centre architecture. Figure 2b is an example of the application of a multi-chamber actuator to a valve-controlled load sensing architecture.

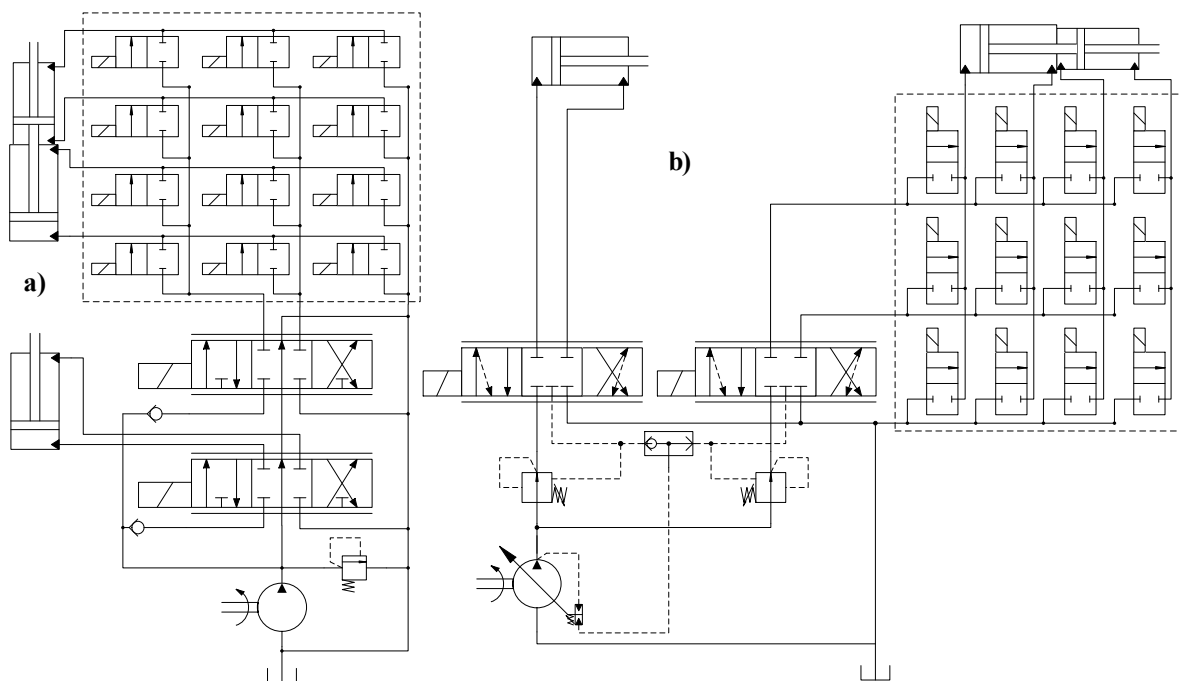


Figure 2 - a) Open-centre actuation system; b) Load sensing closed-centre actuation system.

The load on the multi-chamber actuator can be transformed into different pressure and flow rate levels through the combination of different chambers area. By selecting a combination that results in a match of load pressures between the two actuators, the throttling losses on the control valves can be reduced.

One interesting aspect of such concepts is that they do not require significant changes to the existing valve-controlled architectures. The third line that is connected between the on/off valves and the reservoir is seen as necessary to prevent the flow for expanding chambers that are not connected to the pressure supply from going through the proportional valves.

3 System Control

With the large number of possibilities to connect the proportional valve to the actuator comes the challenge of which combination to select for the different loads on the actuators and how to perform the switching between them. This is not the main topic of discussion of this paper, but some comments are made on how to select a combination to be implemented.

In a usual application of a multi-chamber actuator in a secondary controlled system, the main objective is for the actuator to achieve the desired control goal, and that would be position, speed or force. For the current concept, the objective is not just to achieve the control goal, but also to select a combination that minimizes system energy losses. In this sense, the selection of a combination is also driven by the current force and speed states on other loads. The proportional valves are still responsible for controlling position, speed or force.

It is not a trivial task to map all possible system states to the best combination. It could be found through the development and implementation of an intelligent and optimization-based controller. This would be treated as a multi-objective optimization, where a trade-off between control accuracy of the multi-chamber actuator and system efficiency should be made. As part of the study carried out by the research group, a controller based on reinforcement learning is being studied and will be presented in future publications. In this paper the focus is on the advantage of having combinations to select from, and so establishing which combination is the best for a certain system state is a topic for further research, as mentioned.

It is also important to add that each combination represents a different actuator, so the dynamic characteristic of the system is also changed. This will impact on the controller of the proportional valve, since it is controlling different actuators. Such changes should be considered when designing the controller.

4 Selected Concept for the Case Study

The architecture proposed in fig. 2b was selected to perform an analysis of its efficiency and describe in more detail how it could be increased. A schematic diagram of the selected architecture with the main variables used in the analysis is presented in fig. 3.

The configuration of multi-chamber actuator and on/off valves is the same as for the concept presented in [3]. However, the difference lies in the power supply which, for the current concept, is a load sensing architecture rather than constant pressure sources. Therefore, for this current study no sizing of components is carried out. This does not affect the analysis presented, since the principle of how the efficiency can be improved can also be demonstrated.

The connection between the multi-chamber actuator and reservoir is considered to be necessary to avoid a high imbalance of flow rates in the ports of the proportional valve and also for when a flow from the reservoir is needed to fill the expanding chambers that are not connected to the proportional valve. Although this is not considered in this paper, it would be necessary to have a pressurized reservoir.

The original system as presented in [3] was designed to be operated as a secondary controlled system, which would result in 81 force steps. For the current application not all combinations that would be available for a secondary-controlled actuator are feasible. Most of the possible combinations are excluded due to at least one of the reasons listed in the sequence:

- **No flow through the proportional valve**

Certain combinations would result in no flow at one of the ports of the proportional valve and, therefore, they have been removed. Table 1 shows an example of such a situation, where no chamber is connected to the B port of the proportional valve. Depending on the position of the proportional valve, either the supply or the return port would experience a no-flow situation.

Table 1 - Example of infeasible connection due to no flow at one of the proportional valve ports.

Ports	A	B	T
<i>Connected chambers</i>	AC	-	BD

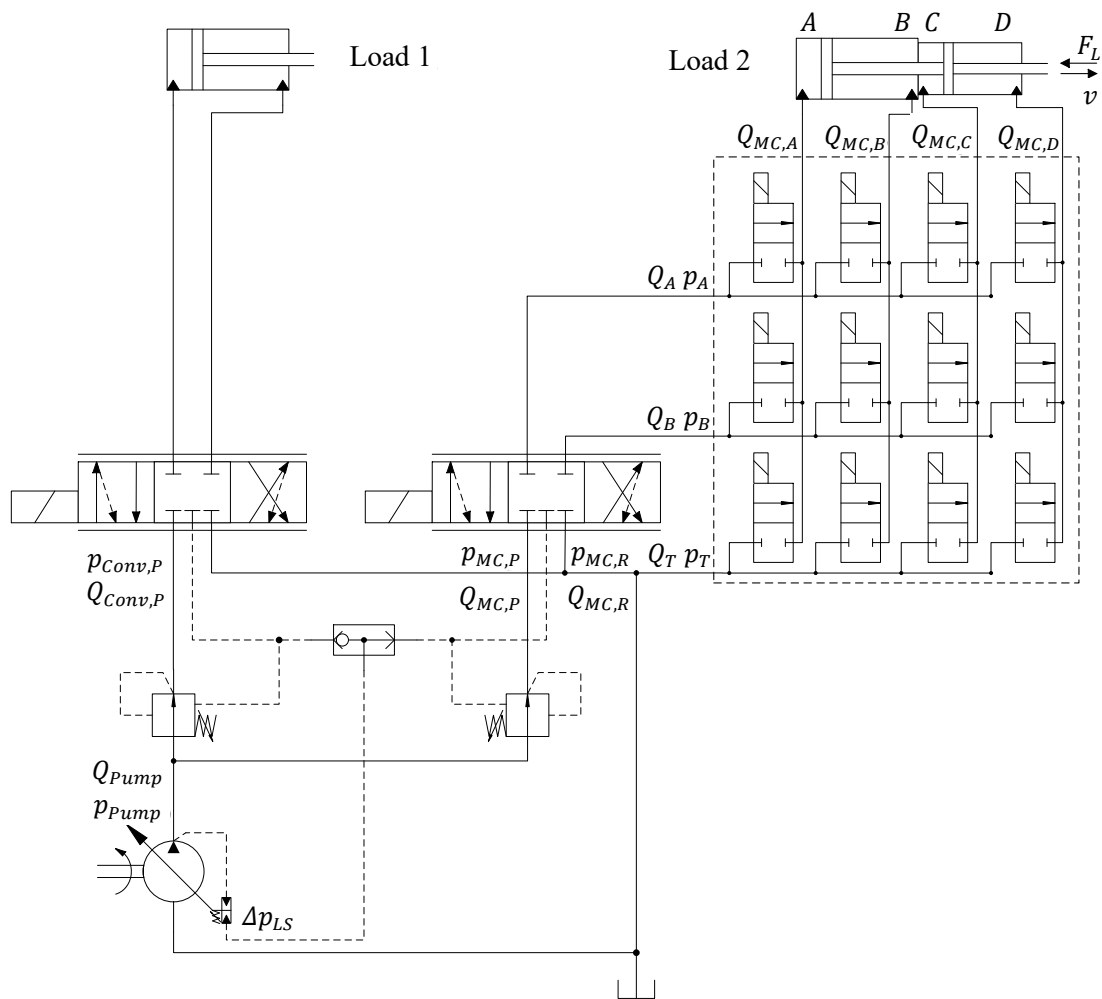


Figure 3 - Selected architecture for case study.

- **Flow with same direction in both ports of the proportional valve**

Certain combinations would result in flow in the same direction in both ports of the proportional valve, and so they have also been removed. In simple terms it means, for example, that it would result in suction of flow from reservoir through the proportional valve. One example of such a situation is presented in tab. 2.

Table 2 - Example of infeasible connection due to same flow direction in the ports of the proportional valve.

Ports	A	B	T
Connected chambers	A	C	BD

Chambers A and C are always expanding or contracting at the same time. For the given example, if the pump was supplying flow rate to chamber A then chamber C would require flow from the reservoir through port B. It is the areas of the actuator that determine which combinations are excluded for this reason, which motivates an additional study on how the selection of areas would impact the number of feasible combinations.

- **Redundant combinations when defining the actuator movement direction**

The manifold of on/off valves allows each of its input ports (A/B/T) to be connected to any of the chambers, while the proportional valve can switch direction. This results in two possibilities of operating the proportional valve and digital manifold to achieve the same actuator motion.

For example, to make the actuator retract or extend, one possibility would be to maintain the proportional valve in one side, e.g. P→A and B→T and let the on/off valves change combination to achieve the different movement direction. This situation is presented in tab. 3.

Table 3 - Example of redundant combination when operating the proportional valve in one direction.

Ports	A	B	T	Proportional valve	Actuator movement
Connected chambers 1	A	B	CD	P→A and B→T (+ position)	Extend
Connected chambers 2	B	A	CD	P→A and B→T (+ position)	Retract

An advantage of this approach is that a 4/2 instead of a 4/3 proportional valve could be used. However, another possibility is to work with a smaller number of combinations and allow the proportional valve to operate to both sides. It would also result in retraction or extension of the actuator, but for the same combination of the on/off valves. This second case would involve a number of combinations that are redundant and, therefore, can also be excluded. One example of such a situation is shown in tab. 4.

Table 4 - Example of redundant combination when operating the proportional valve in both directions.

Port	A	B	T	Proportional valve	Actuator movement
Connected chambers 1	A	B	CD	P→A and B→T (+ position)	Extend
	A	B	CD	P→B and A→T (- Position)	Retract
Connected chambers 2	B	A	CD	P→B and A→T (- Position)	Extend
	B	A	CD	P→A and B→T (+ position)	Retract

For this example, combinations 1 and 2 are redundant, since it is the proportional valve that changes the actuator's direction of movement. This approach seems to be a more natural one to adopt because fewer combinations are needed, which facilitates the process of selection of combinations when designing a controller. Another positive point is that the proportional valve does not need to be changed or its control structure significantly modified.

In terms of selecting which of the redundant combinations to use, the decision was taken to select the ones that, for a given load in one of the four quadrants of force and speed direction of the actuator, make the proportional valve always operate to the same side for all combinations. This avoids a need for the proportional valve to change the operating side if the load changes in magnitude but not the operating quadrant. In the end, sixteen combinations are thought to be feasible for this system configuration. They are presented in tab. 5.

Table 5 – Selected combinations of chambers.

Combination	A	B	T	Combination	A	B	T
1	A	B	CD	9	ABC	D	-
2	A	BD	C	10	ACD	B	-
3	A	D	BC	11	BC	D	A
4	AB	D	C	12	C	B	AD
5	AC	B	D	13	C	BD	A
6	AC	BD	-	14	C	D	AB
7	AC	D	B	15	CD	B	A
8	AD	B	C	16	-	-	-

As will be shown in the results section, even though all these combinations are available to be chosen, not all of them are feasible for all load conditions. For certain load speed and force, some would result in too high pump pressure and/or might result in a requested flow rate above the maximum capacity of the pump. In this way, such considerations would be required when making the selection of a combination by a controller.

5 System Model

For the selected system, the pressure losses on the on/off valves are considered negligible. The subscript *MC* refers to multi-chamber actuator and *Conv* to conventional actuator. The flow rate at the port of each chamber of the multi-chamber actuator is given by

$$\begin{bmatrix} Q_{MC,A} \\ Q_{MC,B} \\ Q_{MC,C} \\ Q_{MC,D} \end{bmatrix} = v \begin{bmatrix} A_{MC,A} \\ -A_{MC,B} \\ A_{MC,C} \\ -A_{MC,D} \end{bmatrix}, \quad (1)$$

where v is the actuator speed and the negative sign tells that it is an contracting chamber for a positive speed. The flow rates at the input ports of the digital valve manifold are

$$\begin{bmatrix} Q_A \\ Q_B \\ Q_T \end{bmatrix} = \begin{bmatrix} D_{AA} & D_{AB} & D_{AC} & D_{AD} \\ D_{BA} & D_{BB} & D_{BC} & D_{BD} \\ D_{TA} & D_{TB} & D_{TC} & D_{TD} \end{bmatrix} \begin{bmatrix} Q_{MC,A} \\ Q_{MC,B} \\ Q_{MC,C} \\ Q_{MC,D} \end{bmatrix}, \quad (2)$$

where D_{ij} are binary variables that determine whether the valve that connects input port i to the j chamber of the multi-chamber actuator is closed or open. The sum of the chambers area connected to A, B and T are given by

$$\begin{bmatrix} A_A \\ A_B \\ A_T \end{bmatrix} = \begin{bmatrix} D_{AA} & D_{AB} & D_{AC} & D_{AD} \\ D_{BA} & D_{BB} & D_{BC} & D_{BD} \\ D_{TA} & D_{TB} & D_{TC} & D_{TD} \end{bmatrix} \begin{bmatrix} A_{MC,A} \\ -A_{MC,B} \\ A_{MC,C} \\ -A_{MC,D} \end{bmatrix} \quad (3)$$

Whether port A or B of the digital manifold is connected to supply or return of the proportional valve depends on its position. In this way, the flow rate from the supply port ($Q_{MC,P}$) and to the return port ($Q_{MC,R}$) of the proportional valve is given by

$$Q_{MC,P} = \begin{cases} Q_B & \text{if } v < 0 \\ Q_A & \text{if } v > 0 \end{cases}, \quad (4)$$

$$Q_{MC,R} = \begin{cases} Q_A & \text{if } v < 0 \\ Q_B & \text{if } v > 0 \end{cases}. \quad (5)$$

The next step is to calculate the pressures on the proportional valve ports connected to supply ($p_{MC,P}$) and to return ($p_{MC,R}$). As for the flow rate, they are dependent on the proportional valve position and are calculated as

$$p_{MC,P} = \begin{cases} \frac{F_L}{A_A} & \text{if } F_L > 0 \text{ and } v > 0 \\ 0 & \text{if } F_L > 0 \text{ and } v < 0 \\ \frac{F_L}{A_B} & \text{if } F_L < 0 \text{ and } v < 0 \\ 0 & \text{if } F_L < 0 \text{ and } v > 0 \end{cases}, \quad p_{MC,R} = \begin{cases} 0 & \text{if } F_L > 0 \text{ and } v > 0 \\ \frac{F_L}{A_A} & \text{if } F_L > 0 \text{ and } v < 0 \\ 0 & \text{if } F_L < 0 \text{ and } v < 0 \\ \frac{F_L}{A_B} & \text{if } F_L < 0 \text{ and } v > 0 \end{cases}, \quad (6)$$

where F_L is the load force. The pressure on the reservoir port of the digital valve manifold is considered to be zero. To simplify the analysis, the load on the conventional actuator is considered to result in a pressure ($p_{Conv,P}$) and flow rate ($Q_{Conv,P}$) at the supply port of the proportional valve. With this information one can determine the pump pressure (p_{Pump}) and flow rate (Q_{Pump}) as

$$Q_{Pump} = Q_{MC,P} + Q_{Conv,P}, \quad (7)$$

$$p_{Pump} = \max(p_{MC,P}, p_{Conv,P}) + \Delta p_{LS}, \quad (8)$$

where Δp_{LS} is the additional pressure difference for the load sensing system. The hydraulic power required by each load is calculated as

$$P_{MC} = Q_{MC,P} p_{MC,P}, \quad (9)$$

$$P_{Conv} = Q_{Conv,P} p_{Conv,P}. \quad (10)$$

The hydraulic power supplied by the pump is calculated as

$$P_{Pump,hyd} = Q_{Pump} p_{Pump}. \quad (11)$$

The power to drive the pump is calculated as

$$P_{Pump} = \frac{P_{Pump,hyd}}{\eta_{vol} \eta_{mech}}, \quad (12)$$

where the mechanical and volumetric efficiencies are considered to be functions of pressure and flow rate only, since a constant pump speed is adopted for this analysis. Knowing the power to each load and the power supplied by the pump, the throttling losses in the control valves between pump and actuators ($P_{Ctrl,Loss}$) are calculated as

$$P_{Ctrl,Loss} = P_{Pump,hyd} - P_{MC} - P_{Conv}. \quad (13)$$

By applying eq. (9) to (11) into eq. (13) and by evaluating eq. (8) for the two possible cases, the analysis can be further extended to

$$\text{if } p_{Pump} = p_{MC,P} + \Delta p_{LS} \quad P_{Ctrl,Loss} = (Q_{MC,P} + Q_{Conv,P}) \Delta p_{LS} + Q_{Conv,P} (p_{MC,P} - p_{Conv,P}), \quad (14)$$

$$\text{if } p_{Pump} = p_{Conv,P} + \Delta p_{LS} \quad P_{Ctrl,Loss} = (Q_{MC,P} + Q_{Conv,P}) \Delta p_{LS} + Q_{MC,P} (p_{Conv,P} - p_{MC,P}). \quad (15)$$

From eq. (14) and (15) it is straightforward to evaluate how the selection of different chambers can affect the system efficiency. The first term of both equations indicates that the flow rate of the multi-chamber actuator should be small to obtain a reduction of those terms, which means selecting a combination with smaller areas connected to supply. The second term of both equations indicates that having similar pressure levels would also result in a reduction of those terms, which means selecting a combination that results in as close a pressure as possible to the pressure on the conventional actuator.

It must be noticed that each combination of areas affects the flow rate and pressure, so both terms of eq. (14) and (15) are affected, which means a reduction in the first term might result in an increase in the second term. In this sense, for every different force and speed on the actuators eq. (13) should be re-evaluated. However, the combination will also affect the efficiency of the pump, for which the power loss ($P_{Pump,Loss}$) is calculated as

$$P_{Pump,Loss} = P_{Pump} - P_{Pump,hyd}. \quad (16)$$

The total efficiency of the hydraulic system is then calculated as

$$\eta_{Syst} = 1 - \frac{P_{Pump,Loss} + P_{Ctrl,Loss}}{P_{Pump}}. \quad (17)$$

These equations allow the pressure and flow diagrams for the two loads to be plotted, where for the multi-chamber actuator there will be different flow rates and pressures for the different combinations of areas that are connected to the ports of the proportional valve, as defined in eq. (4) to (6).

6 Results

As show in eq. 1 and 2, flow rates at the proportional valve ports are calculated directly from the actuator speed and combination of chambers. Results for a positive and negative actuator speed are presented in fig. 4. The opening position of the proportional valve is also shown in fig. 4, where -1 means P→B and A→T, and +1 means P→A and B→T.

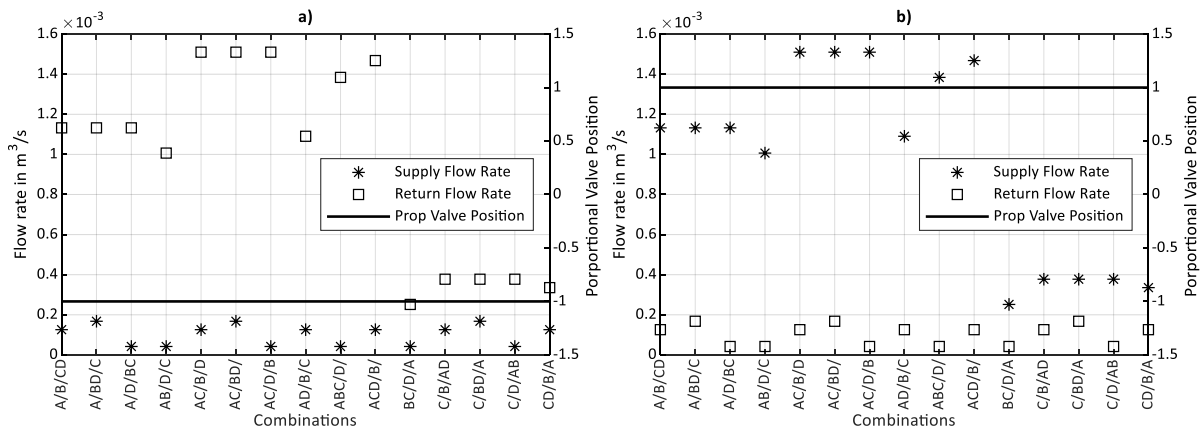


Figure 4 - Flow rate at supply and return ports of the proportional valve; a) $v = -0.2 \text{ m/s}$; b) $v = 0.2 \text{ m/s}$.

For most of the combinations there is a noticeable difference in flow rate between the two ports, which is caused by the asymmetry in the chamber areas. Further consideration of this difference is provided in the discussion section.

By considering a load on each actuator, it is possible to analyse in which conditions the selected concept could result in lower throttling losses. To show representative examples, two cases of actuator loads and speeds are presented that result in a regular load where the load is driven by the power supply, and an overrunning load where the actuator is driven by the load instead.

To establish a comparison with a conventional system, the same calculations are performed for a conventional actuator instead of a multi-chamber actuator driving Load 2 (fig. 3). The conventional actuator areas are $A_{Aconv} = A_A + A_C$ and $A_{Bconv} = A_B + A_D$ which is equivalent to combination 6 in tab. 5. In this configuration it would be capable of exerting the same force as the multi-chamber actuator. The results for this conventional actuator are always shown in the right-most position on the x-axis of the plots with the name *ConvL2*. The left-most position on the x-axis of the plots presents the conventional actuator driving Load 1, named *ConvL1*.

Figure 5 shows the resultant pressure and flow diagrams calculated with eq. (1) to (6) for each of the combinations. In both plots the load force on the multi-chamber actuator is 35 kN, speed is -0.2 m/s for the overrunning load and 0.2 m/s for the regular load, flow rate and pressure of the conventional actuator are $4.2 \times 10^{-4} \text{ m}^3/\text{s}$ (25 L/min) and 15 MPa. The width of the bars for each combination is the flow rate required from the pump and the height is the load pressure. The dash-dotted line represents the pump pressure calculated with eq. (8). In these plots, the throttling losses can be visualized as the area between the pump pressure curve and the loads.

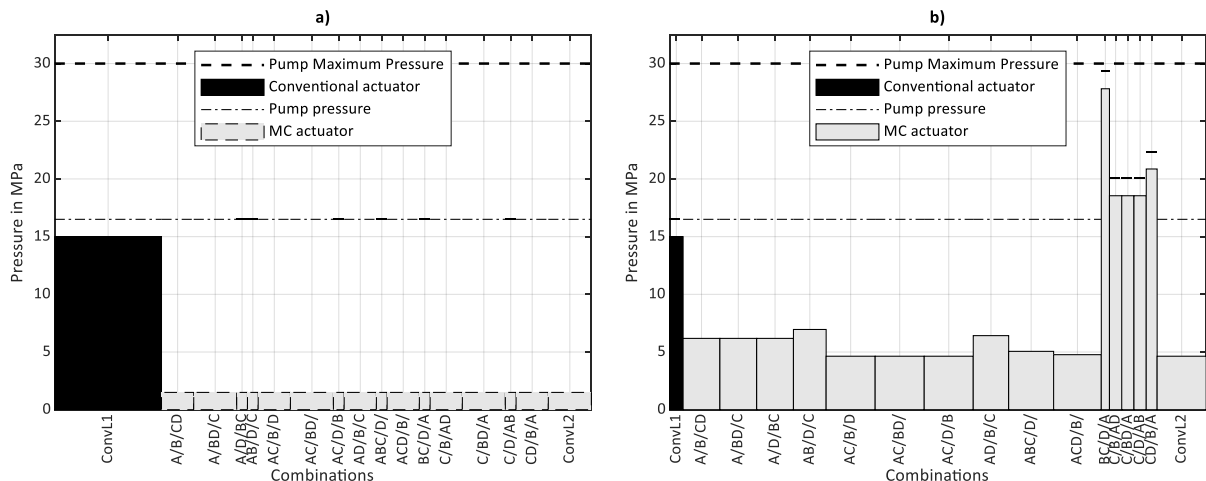


Figure 5 - Proportional valve supply port flow rate vs pressure: a) Overrunning load; b) Regular load.

Figure 5a shows the results for the overrunning load, where the pressure in the chambers connected to supply would be very small. In the calculations they were considered to be zero but to enable the visualization, in the plot they were assigned a small value. Independent of the pressure, the pump must supply the flow rate to fill up the chambers. In such situations the combination could be chosen to minimize the flow rate required from the pump

to reduce the throttling losses. For example, combination $A/D/BC$ has lower throttling losses than combination $A/B/CD$.

Figure 5b shows the results for a regular load, where it is seen that certain combinations have the potential to reduce the throttling losses. For this load situation, the combination that would result in a higher pressure and lower flow rate, like combination $CD/B/A$, would have an advantage over a low pressure and high flow combination like $A/B/CD$. This will become clear when the efficiency plots are shown. For loads higher than the one evaluated, it is likely that certain combinations would result in too high pressure, rendering them infeasible. This is because the chambers connected to supply result in a small combined area. Figure 6 presents the pressure and flow diagrams for the return port of the proportional valve.

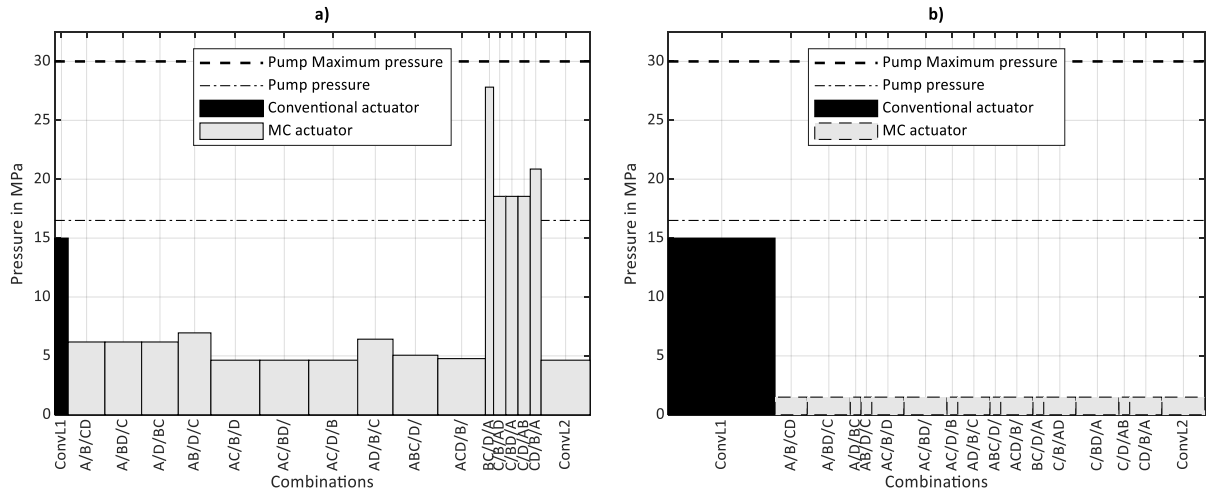


Figure 6 - Proportional valve return port flow rate vs pressure: a) Overrunning load; b) Regular load.

Figure 6a presents the return flow and pressure diagrams for the overrunning load, where the movement is controlled by the meter-out edge of the proportional valve. This diagram shows that, if one would like to recover this available energy and has the means for that in terms of installed components, it would be possible to also modulate the pressure and flow rate to the energy recuperation and storage system as well.

Figure 6b highlights the flow rate on the return port for a regular load. In the calculations the pressure is assumed to be zero since it would be connected to a reservoir, but in the plot a small value is assigned to it to enable the visualization.

Figure 7 presents the results for the calculation of pump and throttling power losses and the required hydraulic power according to eq. (9) to (16).

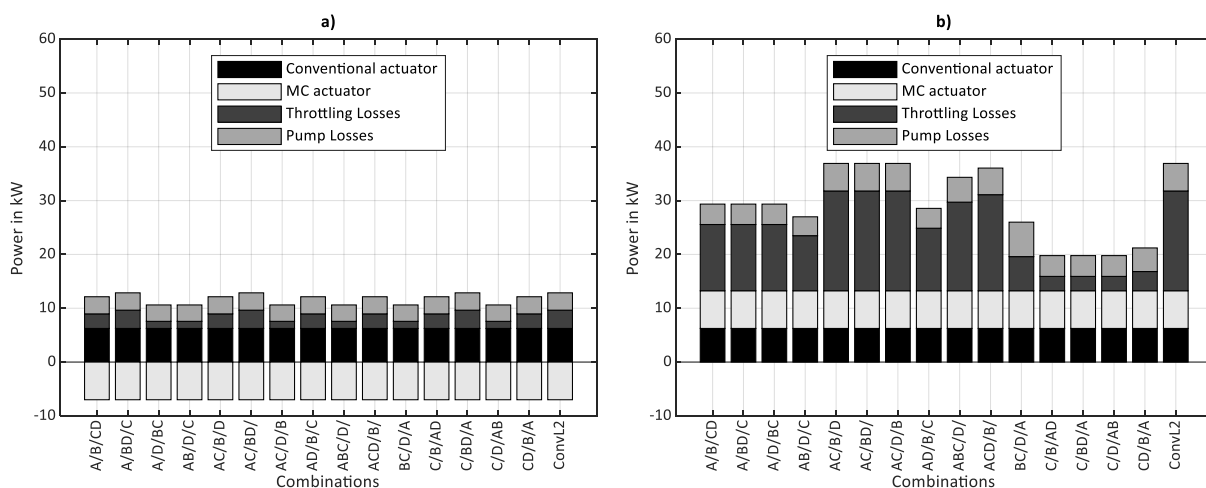


Figure 7 - Power supply and power loss: a) Overrunning load; b) Regular load;

Figure 7a shows the power supplied to and lost by the system for the case of an overrunning load. The load on the multi-chamber actuator is lost when throttling the flow back to the reservoir, since in the presented architecture it is not possible to recover this energy. Although it is an overrunning load, the throttling losses can be affected by

which combination is selected. This is because the combination affects the flow rate supplied to the unpressurized chamber of the overrunning actuator, which still result in throttling losses over the control valves. By selecting a combination with smaller chambers connected to supply, the throttling losses are minimized. Although it is an overrunning load, the compensation valve must control the same pressure drop upon the proportional valve.

Figure 7b shows the power supplied to and lost by the system for the case of a regular load. It is clear that some combinations would result in less power supplied by the system to perform the movement. Although the pump losses are not constant for all combinations, the largest difference is caused by the reduction in throttling losses.

Figure 8 shows the system efficiency for both conventional and multi-chamber actuators calculated by eq. (17). It is notable that most of the combinations of chambers would result in a higher efficiency than if the same load was driven by a conventional actuator with equivalent areas. The increased efficiency is very clear for both cases of regular and overrunning load.

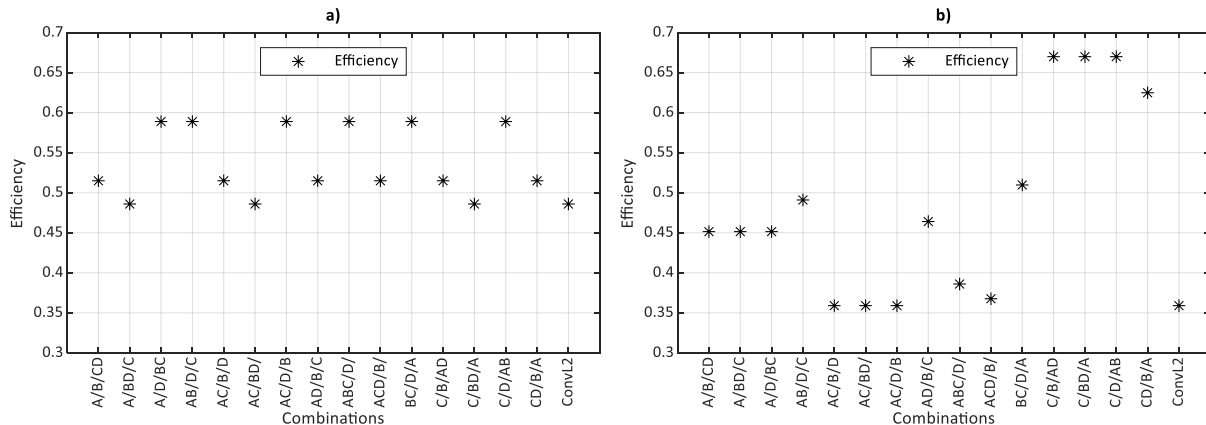


Figure 8 - System efficiency: a) Overrunning load, $v = -0.2 \text{ m/s}$; b) Regular load, $v = 0.2 \text{ m/s}$.

7 Discussion

Figure 4 shows a considerable difference between the magnitudes of flow rates at the ports of the proportional valve. This flow rate disparity is an issue since the pressure drops in the control edges of the proportional valve would be significantly different. However, when selecting combinations from the redundant ones, the larger flow rates for the different chambers can be assigned to the same ports, where the opposite is also true. In this sense, the asymmetry of the proportional valve could be designed/selected with the aim of having as close a match as possible to the asymmetry of the chamber areas. A study on matching the area ratio of actuators and areas of control edges of proportional valves is presented in [9].

The ratio between the chamber areas has a significant effect on the available combinations to be chosen from – on the one hand because more combinations can be made feasible with respect to flow direction in the proportional valve, as discussed in Section 4. On the other hand, they could be chosen to not result in many infeasible pressures or flow rates, e.g. when subjected to loads with high speed and/or force. The choice of areas would also affect the overall efficiency of the system, where a wider choice of combinations would be available depending on the load. This is a topic for further research, possibly by defining an optimization problem for the system parameters.

An argument against such concept is that it requires more hydraulic lines to establish the connections between actuator, digital manifold, proportional valve and reservoir. Another argument against it is that the return line, port T, would need to be pressurised to avoid cavitation in the actuator.

As mentioned in [10], an important feature of the parallel connected systems is that no switching is needed in order to maintain any of the combinations. Switching the valves is needed only when a different output is desired. In this sense, the current system can operate according to the load expected for a particular operation, for example a grading operation of an excavator. For the whole duration of that operation, it could maintain the same actuator set-up since no major load variations would exist. If another operation has larger load variations then switching can be executed more frequently as well.

Although in this study a multi-chamber actuator with four chambers was studied, the same concept could be applied to a three-chamber actuator. This would result in a smaller number of available combinations, but likely also reduced component costs, as a consequence of having fewer on/off valves and simpler cylinder construction.

8 Conclusions

This paper presented a possible solution to reduce throttling losses of valve-controlled hydraulic systems with the use of multi-chamber actuators. A case study was presented for a load sensing system used to drive two loads with the same pump. It was shown that the different combinations of areas of the multi-chamber actuator can be used to adapt the resultant pressure and flow rate from its load to the pressure and flow rate resultant from the load on the other actuator. In this way, throttling losses that occur due to resistive control can be reduced significantly. It was also suggested that a smart selection of the available combinations can lead to a simpler controller, since the number of combinations is reduced and possibly fewer changes to the control of the proportional valve are required. Further research should be directed towards the evaluation of design parameters and design of the controller.

9 Acknowledgements

This research is supported by the Brazilian Coordination for the Improvement of Higher Education Personnel (CAPES), the Brazilian National Council for Scientific and Technological Development (CNPq) and the Swedish Energy Agency (Energimyndigheten) Grant Number P49119-1.

Nomenclature

Designation	Denotation	Value	Unit
v	Multi-chamber actuator speed	-	m/s
F_{load}	Multi-chamber actuator load	-	N
$p_{Conv,P}$	Conventional actuator prop. valve load pressure	-	Pa
$Q_{Conv,P}$	Conventional actuator prop. valve flow rate	-	m^3/s
p_{Pump}	Pump pressure	-	Pa
Q_{Pump}	Pump flow rate	-	m^3/s
Δp_{LS}	Load sensing pressure differential	1.5e6	Pa
$Q_{MC,P}$	Multi-chamber actuator prop. valve supply flow rate	-	m^3/s
$p_{MC,P}$	Multi-chamber actuator prop. valve pressure of the port connected to supply	-	Pa
$Q_{MC,R}$	Multi-chamber actuator prop. valve return flow rate	-	m^3/s
$p_{MC,R}$	Multi-chamber actuator prop. valve pressure of the port connected to return	-	Pa
$Q_{MC,A}$	Multi-chamber actuator prop. valve port A flow rate	-	m^3/s
$p_{MC,A}$	Multi-chamber actuator prop. valve port A pressure	-	Pa
$Q_{MC,B}$	Multi-chamber actuator prop. valve port B flow rate	-	m^3/s
$p_{MC,B}$	Multi-chamber actuator prop. valve port B pressure	-	Pa
$Q_{MC,T}$	Multi-chamber actuator port T flow rate	-	m^3/s
$p_{MC,T}$	Multi-chamber actuator port T pressure	0	Pa
$Q_{MC,A}$	Multi-chamber actuator port A flow rate	-	m^3/s
$Q_{MC,B}$	Multi-chamber actuator port B flow rate	-	m^3/s
$Q_{MC,C}$	Multi-chamber actuator port C flow rate	-	m^3/s
$Q_{MC,D}$	Multi-chamber actuator port D flow rate	-	m^3/s
$[A_A A_B A_C A_D]$	Multi-chamber actuator chambers areas	$[27\ 3\ 9\ 1] A_D$	m^2
A_D	Multi-chamber actuator chamber D areas	2.097e-4	m^2

References

- [1] M Linjama, H-P Vihtanen, A Sipola, M Vilenius. Secondary controlled multi-chamber hydraulic actuator. In: The 11th Scandinavian International Conference on Fluid Power, SICFP09, 2009. Linköping, Sweden.
- [2] M Huova, A Laamanen, M Linjama. Energy efficiency of three-chamber actuator with digital valve system. International Journal of Fluid Power 11.3, pp. 15-22. 2010. DOI: 10.1080/14399776.2010.10781011
- [3] A Dell'Amico, M Carlsson, E Norlin, M Sethson. Investigation of a digital hydraulic actuation system on an excavator arm. The 13th Scandinavian International Conference on Fluid Power SICFP2013, pp. 505-511, 2013, Linköping, Sweden. DOI: 10.3384/ecp1392a50

- [4] H C Belan, C C Locateli, B Lantto, P Krus, V J De Negri. Digital secondary control architecture for aircraft application. In: The 7th Workshop on Digital Fluid Power, 2015, Linz, Austria.
- [5] E Heemskerk, R Bonefeld, H Buschmann. Control of a semi-binary hydraulic four-chamber actuator. In: The 14th Scandinavian International Conference on Fluid Power, SICFP2015, Tampere, Finland. 2015.
- [6] K Heybroek, J Sjöberg. Model predictive control of a hydraulic multichamber actuator; A feasibility study. In: IEEE/ASME Transactions on Mechatronics, Vol. 23, No. 3, June 2018.
- [7] K Pettersson, K Heybroek, P Mattsson, P Krus. A novel hydromechanical hybrid motion system for construction machines. In: International Journal of Fluid Power, Vol. 18, Issue 1, pp. 17-28, 2017. DOI: 10.1080/14399776.2016.1210
- [8] K Heybroek, M Sahlman. A hydraulic hybrid excavator based on multi-chamber actuators and secondary control – design and experimental validation. In: International Journal of Fluid Power, Vol. 19, Issue 2, 2018. DOI: 10.1080/14399776.2016.1210423
- [9] M C Destro, V J De Negri. Method for combining valves with symmetric and asymmetric actuators for hydraulic systems. In: International Journal of Fluid Power. Vol. 19, pp.1-14, 2018. DOI: 10.1080/14399776.2018.1483164
- [10] M Linjama. Digital fluid power – state of the art. In: The 12th Scandinavian International Conference on Fluid Power, Tampere, Finland, 2011.

Loss Analysis and Concept Comparison for Electrically Driven Hydraulic Loader Crane

Amy Rankka^{1,2} and Alessandro Dell'Amico¹

¹ Division of Fluid and Mechatronic Systems, Linköping University, Linköping, Sweden

² Control Systems, Hiab AB, Hudiksvall, Sweden

E-mail: amy.rankka@liu.se, allessandro.dellamico@liu.se

Abstract

The load-sensing system has for a long time been the most energy efficient hydraulic system widely used for mobile machines. When replacing the combustion engine drive with an electric drive with a battery as energy source an incentive for using more energy efficient systems arise. Some promising examples of more energy efficient systems are independent metering systems, pump controlled systems and open flow control systems. Before getting to deeply involved in a specific design, an investigation of the intended application is of importance. The objective of this study is to present a large number of energy efficient designs for the hydraulic system of an electrified loader crane by the means of a loss analysis and a high level concept comparison. To be able to cover a large design space all systems are modeled based on static pressure-flow relations for their components.

Based on measurements, the losses from simultaneous operation, backpressure losses and load holding valve losses are found to be the largest loss contributors in the hydraulic system. If an electrical supply system is added to the reference load sensing system, the overall efficiency is found to be 23 %. The hydraulic system it is found to account for 62 % of the losses and the drive system for 38 %.

The concept comparison shows that a two or four pump system with recuperation possibilities can decrease the energy consumption of the complete system on the studied working pattern by about 50 %.

Keywords: loss analysis, energy study, concept development, electrified mobile hydraulics

1 Introduction

Conventional mobile hydraulic systems are known to suffer from large losses [1] and with the ongoing electrification the losses become more evident as they directly affect the size of the heavy and costly battery. The load sensing system, which will be used as reference in this study, is the most energy efficient system widely used but still suffers from losses due to e.g. different pressure levels of active hydraulic functions. There are different ideas on how to decrease the losses, see e.g. [2], [3], [4] and [5], but this study investigates which ideas are best suited for the reference application. A loss analysis is performed on the reference system to sort out the largest loss contributors. An energy analysis on different concept systems based on real life working patterns is then performed to find the design changes that have the greatest impact on the power consumption. Static energy calculations are used to cover a large number of systems.

All concepts in this study will be driven by electrical motors. The control possibilities of the electrical motor open up for a number of concepts that are not motivated when a combustion engine is considered as the power source.

The reference system for this study is the hydraulic system of a loader crane with four hydraulic functions; slew, 1st boom, 2nd boom and extension. The slew function is driven by a symmetric cylinder and the other functions by asymmetric cylinders. A figure of the crane with placing of the cylinders is displayed in fig. 1 and a simplified view of the hydraulic system can be found in fig. 2. The hydraulic system consists of a pressure compensated directional valve and pilot operated load holding valves connected to each cylinder for safety. The cylinder design will not be investigated in this study and will consequently be left out of the analysis. The pump together with an electric motor will be included in the analysis to show the relation between drive system and hydraulic system

losses and to allow systems with different number of pumps and different capabilities of recuperation of energy to be compared. In order to make the new concepts commercially interesting, the study aims at presenting concept systems that reduce the energy consumption as much as possible with as little changes to the reference system as possible.

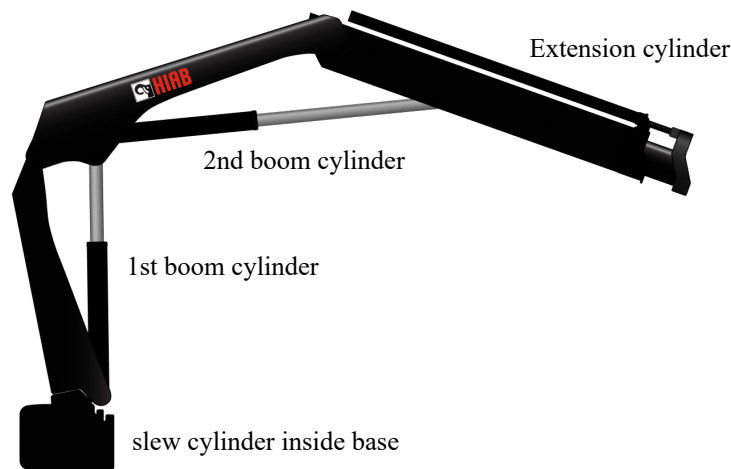


Figure 1: Reference system crane with placement of four hydraulic cylinders.

2 Method

Loss analyses are good foundations to design new systems on and done on hydraulic machines e.g. by [5], [6] and [7]. Some of the same ideas are applied to a loader crane in this study and load holding valves and components of the electric drive are added to the analysis. This work aims at investigating a much larger design space of new systems than what has been done in the above mentioned studies. The aim is not to propose one solution over another but to provide the basis for deciding which systems to investigate further. In order to minimize the time spent on each system before a first selection can be done, a method of modeling static pressure-flow relations for each component in the hydraulic system that can be used both to build the reference system and new systems is used. Dynamic properties of different systems will thus not be considered. The method can be summarized by the following steps:

- Step 1: Data gathering of reference system to get data for modeling and energy analyses.
- Step 2: Modeling of components in reference system.
- Step 3: Loss analysis of reference system. Hydro-mechanical and volumetric losses are considered for the pump but only pressure drop losses will be considered in the rest of the hydraulic system. Flow losses are mainly the flows required for valve actuation and the load sensing control but left out of the analysis. No frictional losses in the cylinders are included.
- Step 4: Concept screening.
- Step 5: Modeling of components for new concept systems.
- Step 6: Energy analysis of new concept systems. As in the loss analysis, only pressure drop losses will be considered and power consumption for valve actuation and sensors will thus not be compared for different systems.

3 Measurements and Reference System Mathematical Modeling

A model of the reference system based on pressure drop models for different components is needed for the loss analysis. The component models are also needed for the energy analysis of new concept systems where some parts of the reference system will be kept. All components in fig. 2 with arrows indicating the loss energy flow are modeled and described more thoroughly in sec. 3.1 to 3.5.

The input to the analysis will be demanded cylinder pressures and flows and to get relevant data measurements of cylinder pressures and spool positions of a crane in the field have been done during several months. The spool

$$P_{loss,pump\Delta p} = (\Delta p_{pump} - \Delta p_{spool} - f_{pumpline}(q_{pump}))q_{pump} \quad (2)$$

$$P_{loss,spool\Delta p} = \Delta p_{spool} \cdot q_{pump} \quad (3)$$

The relation between the actual pressure drop in the pumpline, $f_{pumpline}(q_{pump})$, and the constant pressure margins for different flow levels is displayed in fig. 3.

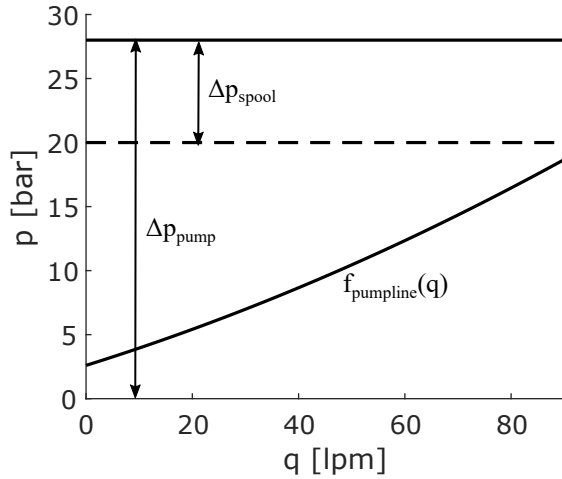


Figure 3: Actual pressure drop in pumpline and constant pressure margins for pump and spool. For high flows the actual pressure drop in the pumpline plus the spool pressure margin almost matches the pump pressure margin but for low flows the losses are much higher than needed. $f_{pumpline}(q)$ is estimated using measurement data.

3.2 Definition of Losses from Simultaneous Operation

Since all functions share the same pressure source losses occur when two or more functions with different pressure levels are active. These losses are defined according to eq. 4 where i denotes slew, 1st boom, 2nd boom or extension and $p_{i,1}$ and $p_{i,2}$ are defined according to fig. 2.

$$P_{loss,sim.op.} = \sum_{i=1}^4 (p_{ls} - p_{i,v})q_i \quad (4)$$

where

$$p_{i,v} = \max(p_{i,1}, p_{i,2})$$

$$p_{ls} = \max(p_{1,v}, \dots, p_{4,v})$$

3.3 Mathematical Models and Definitions of Losses from Load Holding Valves and Cylinder Hoses

The function of the load holding valves (LHV) is to only allow motion of the cylinder when this is requested by the operator. This is, somewhat simplified, achieved by a check valve on each side of the cylinder that can be piloted open by the pressure on the opposite side. For the 1st and 2nd boom this pilot pressure is the only pressure required to lower the cylinders. If one of these functions is the only active function and performing a lowering motion, all the pressure that has to be built up by the pump is defined as a loss. During lifting motions the check valves give rise to a pressure drop that is determined by the pressure required to open the valve and the flow passing through the restriction. Models for this relation are produced for each of the four functions and can be found in fig. 4 together with models for the pressure drops in the hoses between the main valve and the load holding valves. Note that no losses are assumed in the hoses between the main valve and load holding valves for the slew function since the valves are closely connected in the crane base.

The losses from the load holding valves are divided in losses during lifting, $P_{loss,LHV,lift}$, and losses during lowering of 1st and 2nd boom, $P_{loss,LHV,lower}$, according to eq.5 and 6. The losses from the hoses, $P_{loss,hoses}$, are defined according to eq. 7. $i = 1$ denotes slew, $i = 2$ 1st boom, $i = 3$ 2nd boom and $i = 4$ extension.

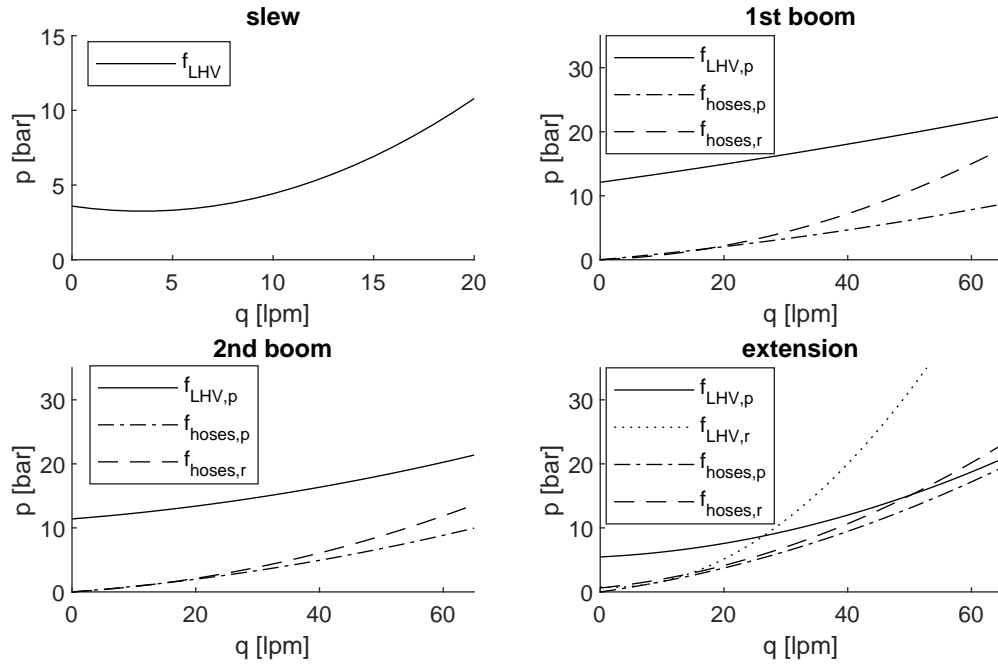


Figure 4: Models for flow-dependent pressure drop in LHV and hoses for each of the four functions. p denotes piston side and r rod side. Note that the LHV is symmetrical for the slew and that the pressure drop over the LHV on the rod side is constant for 1st and 2nd boom due to gravitation aided lowering and thus not displayed here.

$$P_{loss,LHV,lift} = \sum_{i=1}^4 f_{LHV,i}(q_i)q_i \quad (5)$$

where

f_{LHV} is from piston or rod side depending on cylinder movement direction

$$P_{loss,LHV,lower} = \sum_{i=2}^3 p_{i,loss}q_i \quad (6)$$

where

$p_{i,loss} = p_{pump}$, if i is the only active function

$p_{i,loss} = p_{i,2}$, otherwise

$$P_{loss,hoses} = \sum_{i=2}^4 f_{hoses,i}(q_i)q_i \quad (7)$$

where

f_{hoses} is from piston or rod side depending on cylinder movement direction

3.4 Definition of Losses from Backpressure

When performing a lifting motion with a cylinder the pressure in the opposite cylinder chamber would ideally be equal to the tank pressure. The different valves and restrictors between the cylinder and the tank together with an incorrect matching of in and out flow of the cylinder result however in that the pressure can be quite high. The additional pressure in the active cylinder chamber that has to be built up to overcome this backpressure is defined, multiplied with the input flow, as the backpressure losses, $P_{loss,backpressure}$, see eq. 8 where A_{active} and A_{back} are the cylinder areas on the active and back side respectively and $p_{i,3}$ and $p_{i,4}$ are defined according to fig. 2. i denotes slew, 1st boom, 2nd boom or extension

$$P_{loss,backpressure} = \sum_{i=1}^4 (p_{i,back} \frac{A_{active}}{A_{back}} - p_{tank}) q_i \quad (8)$$

where

$$p_{i,back} \in [p_{i,3}, p_{i,4}]$$

3.5 Drive System Mathematical Models

The models for pump and motor used both for the reference system and new concept systems are based on the, by the manufacturers supplied, efficiency maps in fig. 5. The torque axis of the motor maps is scaled based the maximum torque required for different systems. To maximize the efficiency of the pump and motor the size of the motor is chosen so that 60 % of the maximum torque is the torque required to get maximum pressure at 2000 rpm. Fixed pumps are assumed and the displacement is set so that maximum flow is achieved at 2000 rpm. In cases the electric motor is operated as a generator or the pump as a hydraulic motor the same efficiency maps are used. The model for the efficiency of the inverter is displayed in fig. 6 and based on data for a typical inverter [9]. The power rating of the inverter is set to correspond to the maximum power rating of the motor.

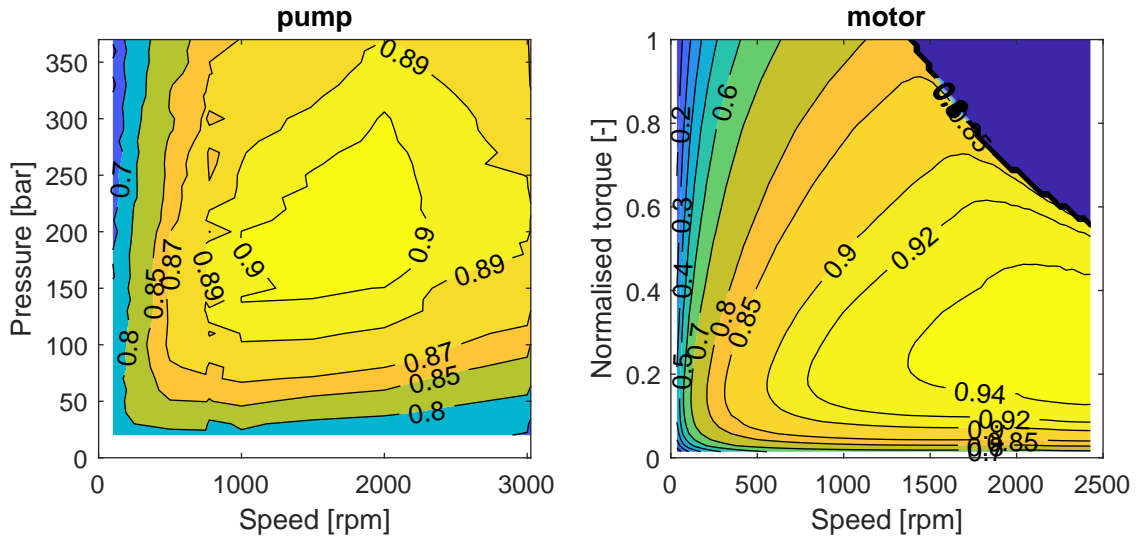


Figure 5: Efficiency maps of pump and electric motor used for reference model and new concept models.

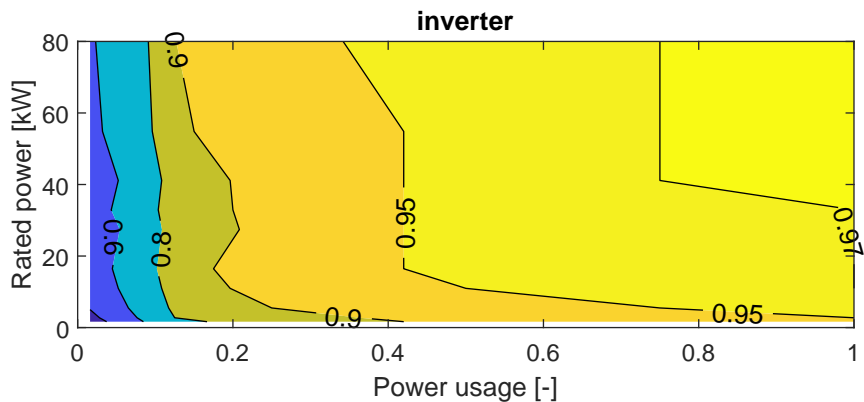


Figure 6: Efficiency map of inverter used for reference model and new concept models.

4 Reference System Energy Loss Analysis

In order to get a deeper knowledge of where the large energy losses in the system are a loss analysis is made based on the model of the reference system. Calculations are done using the models from sec. 3 and the input is the cylinder pressures and flows from the measurements of the field crane described in sec. 3. The required power at different points in the system is calculated and the resulting distribution between losses in the drive system ($P_{loss,drive}$), losses in the hydraulic system ($P_{loss,hyd}$) and useful cylinder power (P_{out}) is presented in fig. 7 a. To get an indication of the size and usage of the application the distribution of the calculated pump states are displayed in fig. 8. The pump power is equal to the sum of the hydraulic system losses and the cylinder power. The concept analysis will be focused only on improving the hydraulic system and the distribution of losses on its different components is presented in fig. 7 b.

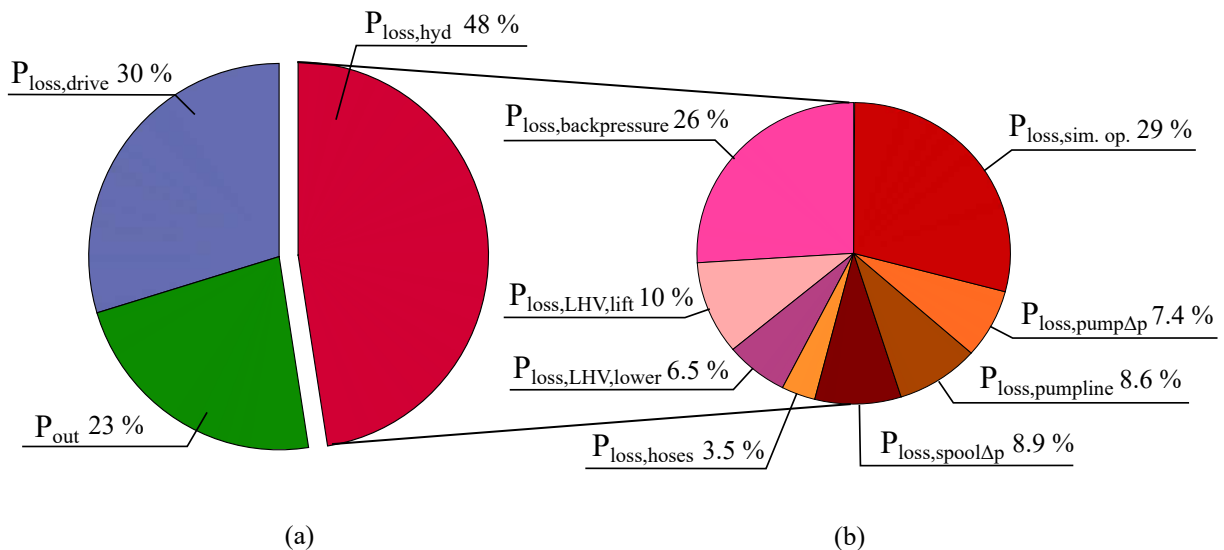


Figure 7: Distribution of power on drive system losses, hydraulic system losses and output power (a) and distribution of losses in hydraulic system (b). The denominations are taken from fig. 2.

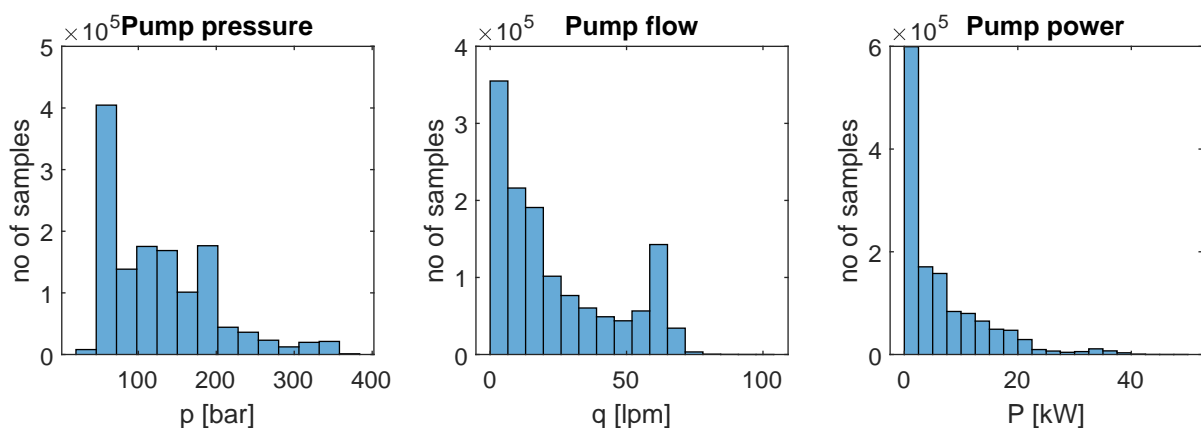


Figure 8: Distribution of pump pressure, pump flow and pump power calculated from input cylinder data and reference system model.

5 Concept Screening and Concept Mathematical Models

The energy efficiency of the hydraulic system can be improved by reducing the losses described in previous sections or make use of lowering energy. Different basic concepts are presented in tab. 1 together with what losses they can reduce. The concepts are described in sec. 5.1 to 5.5. Additionally, the concept of recuperating energy is described in sec 5.6. It can be noted that none of the concepts reduce the losses in the hoses on the crane or the pumpline. The

hoses on the armsystem can only be removed if the power pack is mounted directly onto the cylinders, a concept known as electro-hydraulic actuator. This solution is not investigated since is not considered to be plausible to mount large motors and pumps on the armsystem. The increase in energy consumption from lifting the additional weight, which can be quite significant [10], is considered to be higher than the decrease from removing the hoses. The losses in the pumpline could be reduced by a shorter line, different filter design etc., but will not be discussed further in this study.

Table 1: Loss reduction capabilities of basic concepts.

Concept	$P_{loss,sim-op}$	$P_{loss,pump\Delta p}$	$P_{loss,spool\Delta p}$	$P_{loss,LHV}$	$P_{loss,backpressure}$
Electric load holding valves				x	(x)
Flow control		x			
Open flow control		x	x		
Independent metering	x				x
Multiple pumps	x				

The basic concepts can be seen as means that solve different requirements in the system design and that can be combined into a complete system setup according to the function-means tree in fig. 9.

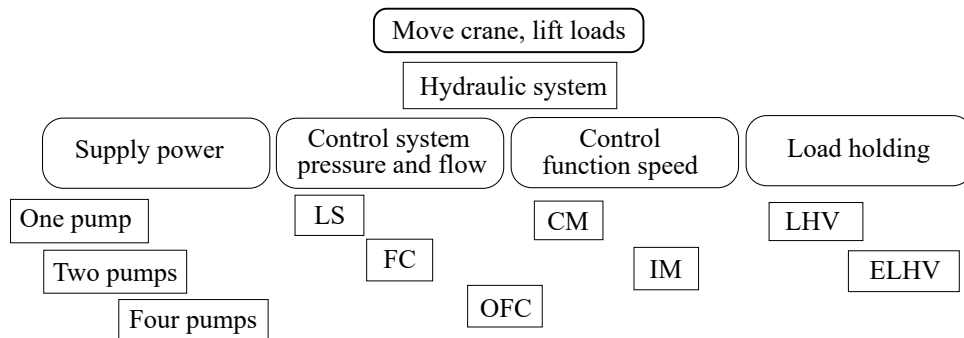


Figure 9: Function-means tree describing the four main functions of the hydraulic system of the crane and different means that can solve the functions. Every system design needs to be compiled by one of the means for each function.

The calculations of the energy consumption of the concepts is done using a combination of the models from the reference system and models of new components described in sec. 5.1 to 5.6 . Since static calculations are used, the input data can be the same working point data from the long-term log of operation from the field crane as in the loss analysis.

5.1 Electrically Controlled Load Holding Valves (ELHV) Mathematical Model

The pilot pressure controlled load holding valves could be replaced with electrically controlled valves. There are not yet any electrically controlled valves on the market designed specifically for load holding of mobile machines. On-off valves are assumed in the calculations in this study but proportional poppet valves could also be considered. These valves can be selected to have a quite low pressure drop across them when they are fully open, both on the active and on the back side, and no pilot pressure will have to be built up by the pump to perform a lowering motion. Characteristics of an on-off valve according to fig. 10 is used to calculate the pressure drop during lifting motions and on the backside of the cylinder for systems with ELHV. Ideal switching of the valve is assumed in the calculations but in a real system pressure equalizing before opening the valve might be needed [11] to prevent a drop of the load when starting a lowering motion.

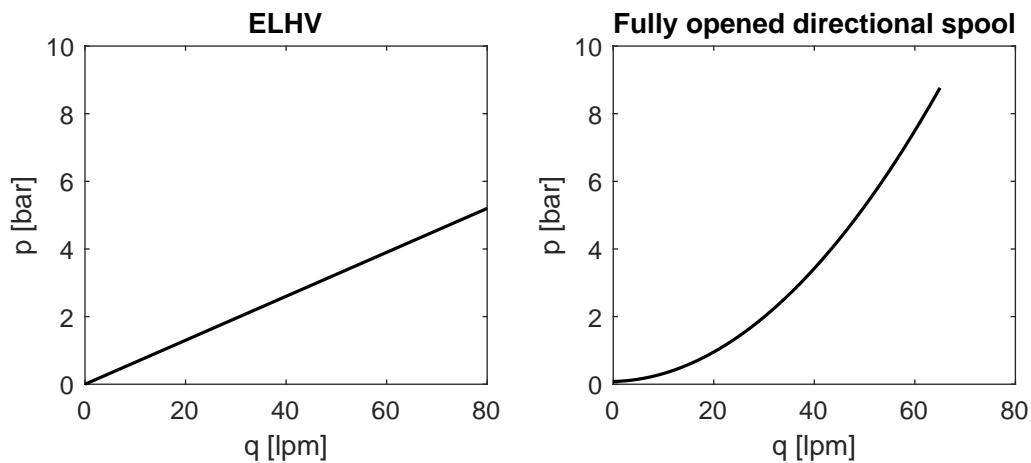


Figure 10: Models of pressure drop for on-off valves used as ELHV (left) and fully open directional spool during OFC (right). Models are taken from supplier data.

5.2 Flow Control (FC) Mathematical Model

With an electric drive, speed control is easy to implement and the flow demand of the system can be calculated from the operator commands and fed forward to the controller that calculates the required motor speed. The control aim is to keep the required velocity instead of keeping a constant pump pressure margin and the pump pressure will not be higher than needed to overcome the losses in the pumpline according to eq. 1 and to keep the pressure drop over the valve. The pressure drop over the valve is assumed to be Δp_{spool} plus an additional 2 bars over the inlet section and compensator valve.

A small overestimation of the flow demand might be needed to make up for the electrical motor being slower than a variable pump to alter the flow. The delivered flow could also be too high due to model errors and some modification is needed for a valve designed for load sensing with conventional pressure compensators to avoid high losses in these cases. Flow sharing compensators can be used [12], or a shunt valve that senses the highest load pressure. Another possibility is to introduce more sensors to the system and either measure the position of the conventional compensators and lower the flow if none of the compensators is close to fully opened [13] or measure and compare the inlet pressure to the highest load pressure. However, the calculations in this study assume a perfect match of the delivered flow.

Flow control software under the name of Flow on Demand is offered by Bucher [14] and the concept is marketed by Bosch by the name Electrohydraulic Flow Matching [15].

With a pump with electronically controlled displacement flow control can also be achieved with a fixed speed prime mover. Such a system with a combustion engine has been developed [16] and the system solution is offered by Weiss Mobiltechnik GmbH [17].

5.3 Open Flow Control (OFC) Mathematical Model

In addition to flow control of the total pump flow the flow to the heaviest load can be controlled directly by the pump flow after lighter functions have taken their required flow controlled by the directional spools. The directional spool for the heaviest function is kept fully open and thus the pressure drop over the valve is minimized instead of controlled to a constant value. The pressure drop in that case is calculated using the characteristics of an off-on valve according to fig. 10 since measurement of the spool on the reference crane was not possible. The spool is assumed to be opened fully by an electric command as soon as a function becomes the heaviest one. In a real system the spool might have to be ramped from partially closed to fully open [18] to avoid oscillations.

Open flow control could also be partially realized hydraulically with a three-way pressure compensator at the valve inlet [19].

5.4 Independent Metering (IM) Mathematical Models

As opposed to the conventional coupled metering (CM) independent metering system have independently controlled spools for meter in and meter out of the cylinders. This type of system offers several possibilities of energy consumption reduction and is further divided into three categories:

- IM 1: The backpressure in the cylinder can be controlled to be as low as possible. If combined with electric load holding valves, it is assumed that the backpressure can be minimized to the pressure to overcome the losses in the load holding valve, a fully opened directional spool and the hoses between these two valves. In a real system, a higher backpressure might be needed to get acceptable dynamic properties. Especially the slew function might suffer from heavy oscillations if not sufficiently braked.
- IM 2: A regeneration circuit that transforms the pressure up and flow down can be opened for asymmetrical cylinders that are extending. This reduces the pressure difference between functions and thus lowers the losses from simultaneous operation.
- IM 3: Circuits connecting cylinders and allowing for regeneration from a lowering cylinder to a lifting could also be possible which lower the input energy needed.

Recuperation to an energy storage, further described in sec. 5.6, is facilitated since the meter out flow can be throttled or controlled by the braking electric motor to get a safe lowering motion without the meter in flow disturbing. There are many different valve architectures for independent metering systems. One example of a setup that could lower the losses from all three categories is displayed for a circuit with two functions in fig. 11 (a).

A large number of valves is needed to get full regeneration capacity. Calculations with regeneration between functions has only been made for the two-pump setups since the architecture and number of valves are considered to be too complex in relation to the time the functionality might be possible to use for a single-pump setup.

The calculations assume ideal switches between different modes of operation. Smooth switching of modes with different flow paths for a single cylinder seems to be possible to achieve [2], [20], but such control will always come with some losses. Regeneration between functions introduces more switching and after ramps or other modification to the switches have been applied there might not be so much more time left when functions are in the states where regeneration is possible.

An independent metering valve, marketed as CMA, is available at the market by Eaton [21].

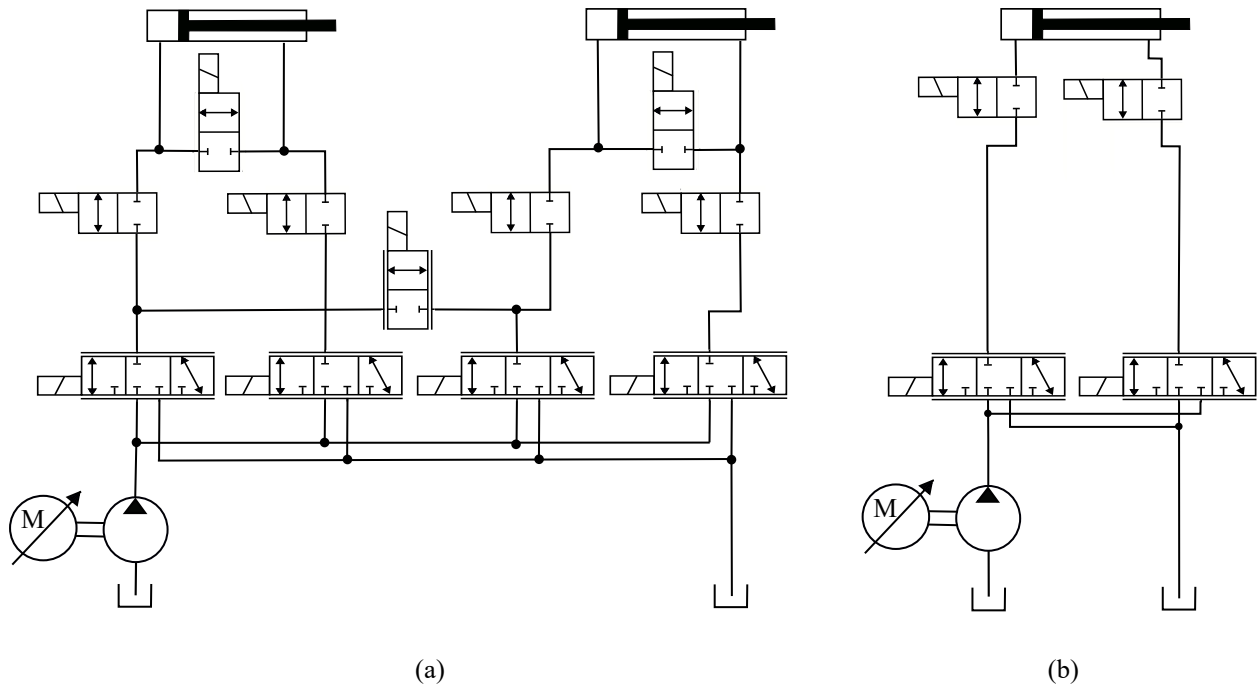


Figure 11: Examples of new system designs. (a): IM system for one of the circuits in a two pump system with ELHV and possibility to regenerate both on cylinders and between functions and recuperate energy back to the battery. (b): Open circuit for one of the circuits in a four pump system. ELHV and IM are selected for this configuration

5.5 Multiple Pump Systems

Using a system with more than one pump reduces the losses from simultaneous operation and reduces the number of mode switches required for open flow control, regeneration between functions and recuperation. A four and a two pump system are investigated. The two-pump system uses the most energy efficient fixed configuration calculated on a system with LS-CM-LHV, the slew and 1st boom connected to one pump and the 2nd boom and extension connected to the other. In a four pump system, the flow to each function can be controlled directly from its pump. In order to stay as close to the reference system as possible open circuits are assumed which means that directional valves are required to direct the flow from the pump and tank, see fig. 11 (b). Ideal swithing of different modes of operation is assumed in the calculations but in a real system, it should be considered that the rotational direction of the pump in an open circuit will be dependent both on force and velocity direction of the cylinder which can cause speed interruptions when a load goes over center [22].

5.6 Recuperation to Energy Storage

An electric drive offers the possibility of recuperating energy back to the battery. Since this does not require any additional components this alternative will be investigated rather than one using another energy storage. In a system with one pump per function the recuperation can be fully exploited. If functions are sharing a pump, recuperation is only possible when no function is requiring power from the battery. It is only assumed that recuperation is possible from the 1st and 2nd boom during lowering motions.

6 Energy Analysis

Different system setups are created by combining one mean for each function according to fig. 9 and recuperation possibilities are added to some systems. The new basic concepts are combined to clearly show the reduction in energy consumption when moving from the reference system to more complex systems. The reduction is shown both for the hydraulic system and for the hydraulic and drive system combined. Calculations are done using combinations of the models from sec. 3 and 5. The cylinder power demand from the field measurements is used as input and the results for 30 different systems are presented in tab .2.

Table 2: Energy consumption reduction for the hydraulic system (energy from pump) and for the complete system (energy from battery) with regards to the reference system for different system setups.

Supply power	Control system pressure and flow	Control function speed	Load holding	Recup.	$E_{pump,red}$	$E_{bat,red}$
1 pump	LS	CM	LHV	-	-	-
1 pump	LS	IM2	LHV	-	4 %	3 %
1 pump	FC	CM	LHV	-	6 %	6 %
1 pump	OFC	CM	LHV	-	9 %	9 %
1 pump	LS	CM	ELHV	-	8 %	11 %
1 pump	OFC	CM	ELHV	-	17 %	18 %
1 pump	LS	IM1	ELHV	-	20 %	20 %
1 pump	LS	IM1+2	ELHV	-	24 %	23 %
1 pump	FC	IM1+2	ELHV	-	29 %	28 %
1 pump	OFC	IM1+2	ELHV	-	32 %	31 %
2 pumps	LS	CM	LHV	-	22 %	11 %
2 pumps	LS	IM2	LHV	-	22%	11 %
2 pumps	FC	CM	LHV	-	29 %	18 %
2 pumps	OFC	CM	LHV	-	33 %	22 %
2 pumps	LS	CM	ELHV	-	33 %	26 %
2 pumps	LS	IM1	ELHV	-	39%	32 %
2 pumps	LS	IM1 +3	ELHV	-	44 %	39 %
2 pumps	OFC	IM1	ELHV	-	48%	41 %
2 pumps	OFC	IM1+2	ELHV	-	49 %	41 %
2 pumps	OFC	IM1+2	ELHV	x	-	45 %
2 pumps	OFC	IM1+2+3	ELHV	-	53 %	47 %
2 pumps	OFC	IM1+3	ELHV	x	-	53 %
2 pumps	OFC	IM1+2+3	ELHV	x	-	54 %
4 pumps	LS	CM	LHV	-	26 %	10 %
4 pumps	FC	CM	LHV	-	34 %	19 %
4 pumps	OFC	CM	LHV	-	37%	23 %
4 pumps	LS	CM	ELHV	-	39 %	32 %
4 pumps	LS	IM1	ELHV	-	45%	37 %
4 pumps	OFC	IM1	ELHV	-	54 %	45 %
4 pumps	OFC	IM1	ELHV	x	-	51 %

7 Discussion

The losses from the load holding valves are found to account for 11 % of the input energy to the hydraulic system, the energy analysis of new single pump systems shows that a significant part of these losses can be removed by electrically controlled valves that reduce the energy consumption of the hydraulic system by 8 %. A significant part of the backpressure losses (18 % of the input energy to the hydraulic system) can be reduced by combining the electrically controlled load holding valves with independent metering of the meter in and meter out spools which gives an additional reduction of 12 percentage points. Implementing flow control reduces the energy consumption by 6 % but the additional reduction in going from flow control to open flow control is only 3 percentage points and open flow control is perhaps not worth the effort of implementing. To add regenerative valves on asymmetric cylinders is also questionable since they have a very small impact on the losses from simultaneous operation and only reduce the energy consumption by 4 %. On a 2-pump system, there is no gain at all in adding regenerative

valves.

The energy analysis shows that a 2-pump system could have a better energy performance than a 4-pump system even though the losses from simultaneous operation can only be completely removed by the latter. This result shows the impact of over dimensioned, with regards to mean power, components in the drive system. However, in order for the most energy efficient 2-pump system to work a complex control scheme of regeneration between functions must be implemented. The question then becomes whether to invest in developing such a complex control or whether to optimize the hardware layout of a drive system with four pumps.

It is clear that a suitable component selection and control strategy for the drive system is important, a lot of the energy gained in the hydraulic system of 2- and 4-pump systems is lost in the drive system due to poor part load efficiencies. In a real life scenario it might be even worse when the available sizes of pumps and motors are limited. One way to improve the efficiency of the drive system is to put power limits on functions and thus being able to select smaller components that will be used more in the regions of high efficiency. For some applications the power limitation might only affect a short portion of the operation time and it might be acceptable to get reduced speed for heavy loads.

In addition, weight and volume of the components will be issues for a commercial product. It is also important to keep in mind that while an electric drive to a hydraulic application on truck or other machine is an add-on today this does not have to be the case in the future when the machine itself will be electrified. The possible interfaces to the driveline will be important to consider, especially if developing a multi-pump system.

8 Conclusions

The loss analysis makes it clear that there are several large contributors to the energy losses in the reference system, the losses due to simultaneous operation and backpressure in the cylinders being the two largest. The load holding valves and constant pressure margins are also large loss contributors.

If only a minor reduction in energy consumption is required there are many different ways of reaching the target reduction. The energy analysis of new concept systems shows that changing to electrically controlled load holding valves has the single greatest impact on power consumption without adding any extra components. It can also be noted that it is possible to reach up to 9 % reduction with one pump or 22 % with two pumps while keeping the valve setup of the reference system. If the aim is to reduce the energy consumption as much as possible it can be noted that a 2-pump system can achieve about the same energy performance as a 4-pump system, 54 % and 51 % reduction respectively.

Acknowledgment

The authors would like to thank Hiab AB for their contribution to this paper. The work in this paper was sponsored by the Swedish Energy Agency and is part of STEALTH, Sustainable Electrified Load Handling, App. no 44427-1.

Nomenclature

Designation	Denotation	Unit
$p_{i,3}, p_{i,4}$	Cylinder pressures, function i	Pa
$p_{i,5}, p_{i,6}$	Pressures at LHV inlets, function i	Pa
$p_{i,2}, p_{i,2}$	Pressures at valve outlets, function i	Pa
p_{inlet}	Pressure at valve inlet	Pa
p_{pump}	Pressure at pump outlet	Pa
p_{ls}	Load sensing pressure	Pa
$p_{i,v}$	Pressure at active valve output, function i	Pa
$p_{i,loss}$	Pressure defining LHV lowering losses	Pa
$p_{i,back}$	Cylinder backside pressure, function i	Pa
p_{tank}	Pressure in tank	Pa
Δp_{pump}	Pump pressure margin	Pa
Δp_{spool}	Spool pressure drop	Pa
q_{pump}	Total flow from pump	m ³ /s
q_i	Flow to function i	m ³ /s
A_{active}	Area of active side of cylinder	m ²
A_{back}	Area of back side of cylinder	m ²
P_{in}	Electric power at battery	W
P_{out}	Hydraulic power at cylinder	W
$P_{loss,drive.}$	Power loss in drive system	W
$P_{loss,pumpline}$	Power loss in pumpline	W
$P_{loss,sim.op.}$	Power loss due to simultaneous operation of functions	W
$P_{loss,pump\Delta p}$	Power loss due to constant pump pressure margin	W
$P_{loss,spool\Delta p}$	Power loss due to constant pressure drop over spool	W
$P_{loss,hoses}$	Power loss in hoses between main valve and load holding valve	W
$P_{loss,LHV,lift}$	Power loss in load holding valve during lifting motions	W
$P_{loss,LHV,lower}$	Power loss in load holding valve during lowering motions	W
$P_{loss,backpressure}$	Power loss due to backpressure in cylinders	W
$E_{pump,red}$	Energy consumption reduction for hydraulic system (energy taken from pump)	-
$E_{bat,red}$	Energy consumption reduction for complete system (energy taken from battery)	-

References

- [1] Wolfgang Burget and Jürgen Weber. Mobile Systems - Markets , Industrial Needs and Technological Trends. In *8th International Fluid Power Conference (IFK)*, pages 23–54, Dresden, Germany, 2012.
- [2] Björn Eriksson. *Mobile Fluid Power Systems Design with a Focus on Energy Efficiency*. PhD thesis, Linköping University, 2010.
- [3] Mikael Axin. *Fluid Power Systems for Mobile Applications with a Focus on Energy Efficiency and Dynamic Characteristics*. Licentiate thesis, Linköping University, 2013.
- [4] Karl-Erik Rydberg. Energy Efficient Hydraulics - System Solutions for Minimizing Losses Energy Efficient Hydraulics - System solutions for loss minimization. In *National Conference on Fluid Power*, Linköping, Sweden, 2015.

- [5] Jan Siebert, Marco Wydra, and Marcus Geimer. Efficiency Improved Load Sensing System - Reduction of System Inherent Pressure Losses. *Energies*, 10:941, 2017.
- [6] Arnold Hiebl and Rudolf Scheidl. Methodical loss reduction in load sensing systems based on measurements. In *BATH/ASME 2016 Symposium on Fluid Power and Motion Control*, Bath, UK, 2016.
- [7] Milos Vukovic, Roland Leifeld, and Hubertus Murrenhoff. Reducing Fuel Consumption in Hydraulic Excavators - A Comprehensive Analysis. *Energies*, 10:687, 2017.
- [8] Amy Rankka, Alessandro Dell'Amico, and Petter Krus. Drive Cycle Generation for a Hydraulic Loader Crane. In *The 16th Scandinavian International Conference of Fluid Power*, Tampere, Finland, 2019.
- [9] U.S. Department of Energy. Adjustable Speed Drive Part-Load Efficiency, 2012.
- [10] Abinab Niraula, Zhang Shuzhong, Tatiana Minav, and Matti Pietola. Effect of Zonal Hydraulics on Energy Consumption and Boom Structure of a Micro-Excavator. *Energies*, 11(8):2088, 2018.
- [11] Johan Edén and Fabian Lagerstedt. *An Electro-Hydraulically Controlled Cylinder on a Loader Crane*. Master thesis, Linköping University, 2018.
- [12] Mikael Axin, Björn Eriksson, and Jan-Ove Palmberg. Energy Efficient Load Adapting System without Load Sensing - Design and Evaluation. In *The 11th Scandinavian International Conference on Fluid Power*, Linköping, Sweden, 2009.
- [13] Mikael Axin, Björn Eriksson, and Petter Krus. Flow versus pressure control of pumps in mobile hydraulic systems. *Proceedings of the Institution of Mechanical Engineers. Part I: Journal of Systems and Control Engineering*, 228(4):245–256, 2014.
- [14] Bucher Hydraulics. Overall Efficiency Optimized, 2020.
- [15] Christoph Latour. Elektrohydraulisches Flow-Matching (EFM) - Die nächste Generation von Load-Sensing-Steuerungen. Mobile 2006 - International Mobile Hydraulics Congress, Ulm, 2006.
- [16] Martin Scherer, Marcus Geimer, and Björn Weiss. Forestry Crane with Electrohydraulic Flow-on-Demand System. In *71th Conference "LAND.TECHNIK - AgEng 2013"*, Hannover, 2013.
- [17] Weiss Mobiltechnik GmbH. WMT part eBSS, 2019.
- [18] Johan Nyman and Amy Rankka. *Energy-efficient, Electro-Hydraulic Power Pack*. Master thesis, Linköping University, 2015.
- [19] M Djurovic and S Helduser. New Control Strategies for Electro-Hydraulic Load-Sensing. In *Fluid Power and Motion Control (FPMC)*, pages 201–210, Bath, UK, 2004.
- [20] Ruqi Ding, Bing Xu, Junhui Zhang, and Min Cheng. Bumpless mode switch of independent metering fluid power system for mobile machinery. *Automation in Construction*, 68:52–64, 2016.
- [21] Eaton. Dynamic performance Empowering intelligent & adaptable platforms, 2020.
- [22] Samuel Kärnell. *Fluid Power Pumps and the Electrification*. Licentiate thesis, Linköping University, 2020.

Design of Pressure Control for Optimal Damping in Individual Metering Systems

Gerhard Rath , Emil Zaev* , Goran Stojanoski , and Darko Babunski*

Department product engineering, Montanuniversität Leoben, Leoben, Austria

E-mail: gerhard.rath@unileoben.ac.at, emil.zaev@mf.edu.mk, goran.stojanoski@unileoben.ac.at, darko.babunski@mf.edu.mk

*Faculty of mechanical engineering, SS. Cyril and Methodius University of Skopje, Skopje, North Macedonia

Abstract

Modern oil-hydraulic systems for moving heavy payloads are designed for optimised motion, but also for minimal energy loss. Individual metering technique, using separate control of the two actuator chambers, offers some advantages. A common strategy when moving the load is to control the incoming oil flow to obtain a desired speed, and the pressure at the downstream side for good efficiency. In this work analysis and design of PI (proportional-integral) pressure control is done. The adjustment of the control parameters of this loop is usually uncritical. In the worst case, the damping of the mechanical system is the only contribution. It is shown in this work, that pressure control can increase the damping of load oscillations. The influence of the P and I parameters to the system properties is investigated using the poles of the transfer function of the system. It is shown, that there is a point, where the damping factor of the system has its maximum value, and a design method for this optimisation is given. The problem ends up in a system of two equations of fourth order. A method is shown how to reduce the problem to solving one third-order equation, which is done numerically. Finally, the results are verified using simulation.

Keywords: hydraulic actuator; pressure control; individual metering

1 Introduction

Hydraulic actuators are often equipped with proportional valves. Oil flows for both chambers are controlled with orifices located on a single valve spool. The distribution of pressures and flows is designed with the geometric shape. Individual metering technique uses separate control for meter-in and meter-out. This gives an additional degree of freedom and enables several strategies for control, especially for the increasing demand of energy efficiency [1].

A standard method for individual metering is to control the oil flow to the first cylinder chamber in order to maintain a defined velocity, and concurrently to control the pressure in the tank side chamber low enough for small power loss, but high enough to have a margin to cavitation [1], [2]. Such strategies may be implemented in the embedded controller of a valve [3]. It is important, but difficult to know the system parameters, in particular the oil properties [4]. For example, additional sensors together with a model for the viscosity can help to improve the control results [5].

Beside the energy efficiency the damping of vibrations and oscillations can be an important design goal [6] [7]. With electronic control, acceleration or pressure feedback are preferred method [8]. A thorough guide how to design pressure feedback can be found in [9], an application example is shown in [10].

A completely different approach to reduce oscillations is to avoid those that are induced with command signals. The basic working principle is to filter out frequencies that could excite resonances in the physical system. An early work on this topic is found in [11]. These techniques are usually subsumed under the terms *input shaping*, *signal shaping* or *preshaping*. Successful implementation was done in electrical servo drives and in hydraulic systems as well [12]. A possible implementation in an individual metering system can be found in [13]. With a few exceptions, such filters are not often implemented in industrial controllers. The reason could be, that the

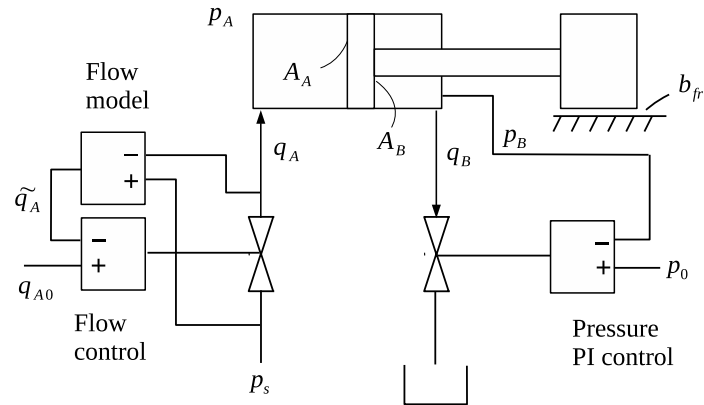


Figure 1: Scheme of the hydraulic system

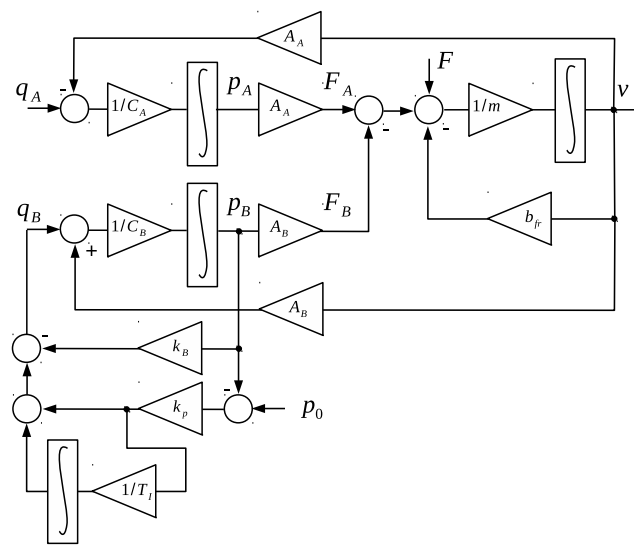


Figure 2: Block diagram of the system

dimensioning needs the work of experts. Additionally, the design requires good knowledge about the physical parameters. Furthermore, the performance is prone to changes of the parameters, like drift during operation or non-linear behaviour.

The pressure information from the downstream chamber can be used for two purposes: For active damping and for level control with respect to energy efficiency. The actual work takes a look on both aspects of pressure feedback. In the following it is shown that a PI (proportional, integral) pressure feedback loop can have an essential damping contribution to an oscillating load. A design procedure to optimise the controller is presented. Finally, it is shown by simulation, that beside the damping effect, the controller still is doing well what it is originally intended for, to keep a desired pressure level.

2 Modelling

2.1 Description of the System

Figure 1 shows a scheme for independent metering, where the oil flow into the upstream cylinder chamber is regulated with the purpose to obtain a desired motion speed. The pressure difference over an orifice is measured to calculate the flow. This flow model can be improved using oil temperature and viscosity data [5]. With the help of a control loop, a desired value for the oil flow and further for the motion speed is obtained. For the second chamber on the downstream side, a pressure controller is used to keep a constant pressure.

2.2 Dynamic Model

To model the dynamic behaviour, a linear system is used, fig. 2 shows the block diagram. The payload is modelled with a mass and linear friction, the cylinder has two chambers with compliant oil, and the electronic pressure

feedback loop is a PI controller. Of course all elements in the model interact with each other, so does the flow controller. The assumption of a constant input flow, which is not affected by system dynamics, must be justified first.

The dominating elements are the mass and the compliance of the oil in the cylinders, acting as a spring. For heavy machines, the resonant frequency will be quite low, maybe up to ten Hertz. With control system, the motion is controlled up to this frequency. Usually, higher frequencies are not a goal for control, since this would require too much hydraulic power, and would lead to wear of the mechanical components.

The pressures inside the cylinders are subjected to the dynamics of the mechanical system and hence cannot change fast, even if the sensors can measure up to some kHz. Only the supply pressure can change fast according to the pump dynamics, this property is important for the flow controller.

In the model, fig. 2, flow is regarded as a constant input without any dynamics. Pressure sensors are quite fast, having upper border frequencies of several kHz. In the case of a valve with embedded electronic control the sensors are mounted inside the valve close to the metering orifices [3]. Flow control, also integrated in the valve, is done by measuring the pressure difference. The control loop finally actuates the valve spool to change the orifice. Since the characteristic frequency of the spool motion is at least ten times higher than the resonant frequency of the mechanical system, the dynamics of flow control can be neglected, and flow may be assumed to be constant at the desired level. Under this conditions, the model in fig. 2 will be a good approximation of the actual system.

The results of this work are only valid in combination with an accurate and fast flow control, like provided by the previously mentioned configuration. We did not consider other solutions like mechanical load balancing valves.

The block diagram fig. 2 contains also non-linear elements. Friction does not influence the results much, if load forces are high. The oil flow q_B depending on the pressure p_B is modelled with two factors: The feedback gain k_p that is resulting from the design procedure and the factor k_B , which models the flow change by the pressure through the orifice of the valve. This contributes an additional damping. In order to find the factor k_B for a linear model, a linearisation about the working point has to be done first. Assuming a steady motion of v_0 , the oil flow on the B-side will be

$$q_{B0} = A_B \cdot v_0. \quad (1)$$

With an opening factor η and the nominal data of the valve, denoted by the index N , the oil flow is

$$q_{B0} = \eta \frac{q_N}{\sqrt{p_N}} \sqrt{p_{B0}}. \quad (2)$$

The pressure p_{B0} will be the setvalue of the pressure controller p_0 , then the required valve opening can be found with

$$\eta = \frac{q_{B0}}{q_N} \sqrt{\frac{p_N}{p_0}}. \quad (3)$$

For a small change of flow follows

$$\delta q_B = \left. \frac{\partial q_B}{\partial p_B} \right|_{p_B=p_0} \cdot \delta p_B, \quad (4)$$

where

$$\left. \frac{\partial q_B}{\partial p_B} \right|_{p_B=p_0} = -\eta \frac{q_N}{\sqrt{p_N}} \frac{1}{2\sqrt{p_0}}. \quad (5)$$

For a linear model, the factor is found with

$$k_B = \eta \frac{q_N}{\sqrt{p_N}} \frac{1}{2\sqrt{p_0}}. \quad (6)$$

Now the basic differential equations for the system in fig. 2 can be formulated,

$$\dot{p}_A(t) = \frac{1}{C_A} (q_A(t) - A_A v(t)), \quad (7)$$

$$\dot{p}_B(t) = \frac{1}{C_B} \left(k_p p_0 - (k_B + k_p) p_B(t) + \frac{k_p}{T_i} \int (p_0 - p_B(t)) dt + A_B v(t) \right), \quad (8)$$

and

$$\dot{v}(t) = \frac{1}{m} (F(t) - b_{fr} v(t) + A_A p_A(t) - A_B p_B(t)). \quad (9)$$

2.3 Transfer Function

For the present work, a transfer function representation was chosen, where the input is the disturbing force $F(t)$, and the output the velocity $v(t)$ of the cylinder piston. For this purpose, it is required to find the transfer function

$$G(s) = \frac{v(s)}{F(s)}. \quad (10)$$

Applying Laplace transform to eq. (7), (8) and (9) yields

$$p_A = \frac{1}{sC_A} (q_A - A_A v), \quad (11)$$

$$p_B = \frac{A_B v s + \left(k_p s + \frac{k_p}{T_i}\right) p_0}{s^2 C_B + s(k_B + k_p) + \frac{k_p}{T_i}}, \quad (12)$$

and

$$v = \frac{F + A_A p_A - A_B p_B}{ms + b}. \quad (13)$$

The pressures in eq. (13) are substituted using eqs. (11) and (12). After setting the inputs of no interest, p_0 and q_A , to zero, the transfer function for the motion speed reacting to a disturbing force input F follows

$$\frac{v(s)}{F(s)} = \frac{1}{mC_B} \cdot \frac{s^3 C_B + s^2(k_B + k_p) + s \frac{k_p}{T_i}}{s^4 + s^3 p + s^2 q + sr + t} \quad (14)$$

with the abbreviations

$$\begin{aligned} p &= \frac{k_B + k_p}{C_B} + \frac{b}{m} \\ q &= \frac{A_B^2}{mC_B} + \frac{A_A^2}{mC_A} + \frac{k_p}{C_B T_i} + \frac{b}{m} \cdot \frac{k_B + k_p}{C_B} \\ r &= \frac{b}{m} \cdot \frac{k_p}{C_B T_i} + \frac{A_A^2}{mC_A} \cdot \frac{k_B + k_p}{C_B} \\ t &= \frac{A_A^2}{mC_A} \cdot \frac{k_p}{C_B T_i}. \end{aligned} \quad (15)$$

The reaction of the system to a disturbing force, eq. (14), includes also the controller parameters and is of fourth order. To study the behaviour, the poles of the transfer function are to be found. The algebraic solution leads to very complex expressions, hence a numerical approach is used to find the roots of the transfer function.

3 Discussion of the Poles

At first the effect of pure proportional control without integrator is studied. Letting T_i go to infinity in eq. (14) leads to the third order transfer function

$$\frac{v(s)}{F(s)} = \frac{s^2 C_B + s(k_B + k_p)}{s^3 m C_B + s^2 (m(k_B + k_p) + b C_B) + s \left(A_B^2 + A_A^2 \frac{C_B}{C_A} + b(k_B + k_p) \right) + A_A^2 \frac{k_B + k_p}{C_A}} \quad (16)$$

with one pair of conjugate complex poles and one real pole. Figure 3 shows one complex pole, the others are not of interest. It can be seen, that with small values of k_p (weak control) the natural frequency is higher. Both cylinder chambers contribute with their stiffness. With strong control (high values for k_p) the natural frequency goes down, since a perfect constant pressure level in chamber B offers no stiffness.

At a certain value of k_p the real part has a minimum, this is the leftmost point of the graph displayed in fig. 3. This point is the starting point for the next step, adding the I portion of control.

If PI control is applied, again eq. (14) is to be used, which has four poles. One complex conjugate pair is mainly determined by k_p . Introducing an I portion means starting with high values of T_i . The two poles that are introduced with T_i are initially real. With decreasing values of T_i , the real poles walk along the real axis until they meet and split up into conjugate complex poles, shown in fig. 4. The first pair of poles walk towards negative real parts and meet the second pair at a certain point. This point is the goal of the design procedure, where the real part of any pole has its minimum. This means, that all transients have a fast decay. Further decreasing T_i causes one pair going to negative real values, the other pair into positive direction, which means, damping decreases again.

It can be seen that the the loop does not get unstable, but can lose the damping effect. Of course this is valid only with the assumption, that the friction is linear [9]. This can be assumed, when friction force is low compared to the dynamic load forces.

The minimal real part for all poles is obtained, when the pairs meet at the same point. Hence this point is a goal for the design of the control parameters k_p and T_i .

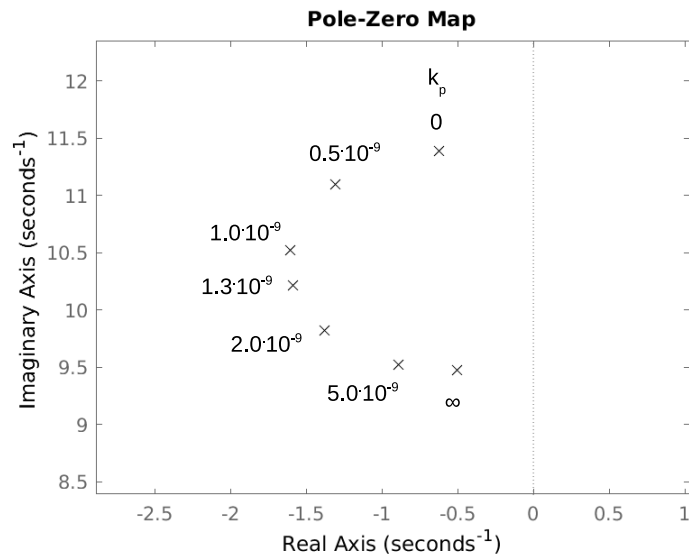


Figure 3: Pole-zero map of P-controlled system, 'x' denote the poles

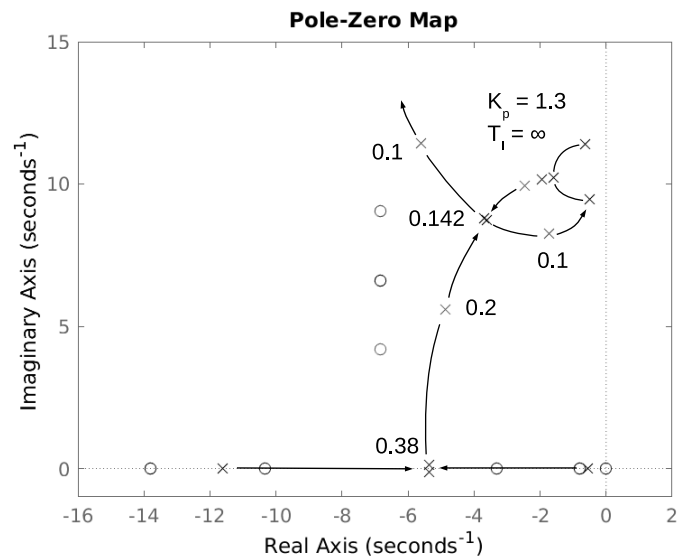


Figure 4: Root locus of PI-controlled system, 'x' denote the poles, 'o' the zeroes

4 Controller Design for Optimal Damping

The controller design problem is to find values for k_p and T_i , such that the real parts of the poles have minimal values. From fig. 3 it can be seen that there exists a solution with two identical conjugate complex pairs of poles

$$s_{01} = s_{02} = a \pm bj. \quad (17)$$

Then the denominator of a transfer function of fourth order will have the form

$$D(s) = s^4 - 4as^3 + s^2(6a^2 + 2b^2) - 4as(a^2 + b^2) + (a^2 + b^2)^2, \quad (18)$$

which can be used to compare coefficients with the denominator of eq. (14). The comparison yields two non-linear equations for k_p and T_i , one of them is of fourth order. An algebraic solution can be found with a proper tool, but delivers an extremely complicated formula as result. In order to make the work easier, this problem can be solved in two steps. Then the resulting terms are acceptable simple, and experimenting is easier.

By comparing the coefficient of s^3 , the real part of the poles can be found as a function of k_p ,

$$a = -\frac{1}{4} \left(\frac{k_B + k_p}{C_B} + \frac{b_{fr}}{m} \right). \quad (19)$$

Equation (19) shows, that the proportional gain contributes to the damping in the same way like friction b_{fr} . Both terms have the dimension t^{-1} , they are time constants of a first order system, as it can be seen in the block diagram (fig. 2). Equation (19) further shows, that even a frictionless system with $b_{fr} = 0$ could be stabilised.

A control loop for the pressure is also a kind of pressure feedback, which is often used for damping of oscillations [9]. Unfortunately eq. (19) is only a necessary condition for the optimum, but not sufficient. We cannot increase the gain, and the damping associated with it, arbitrarily.

4.1 Integral Reset Time T_i as a Function of Proportional Gain k_p

Without algebraic solution for the poles, an additional condition for the integral reset time T_i can be found. Comparing the second order coefficient yields

$$q = 6a^2 + 2b^2, \quad (20)$$

the first order coefficient

$$r = -4a(a^2 + b^2). \quad (21)$$

Eliminating b^2 in eq. (21) using eq. (20) delivers

$$r = 8a^3 - 2aq. \quad (22)$$

Substituting q with the physical parameters from eq. (15) gives a condition for the I part,

$$T_i = -\frac{k_p(2am + b_{fr})}{\frac{A_A^2}{C_A}(k_B + k_p) - 8a^3mC_B + 2a\left(A_B^2 + A_A^2\frac{C_B}{C_A} + b_{fr}(k_B + k_p)\right)}. \quad (23)$$

With a given k_p , a is known from eq. (19), and further, T_i can be found with eq. (23).

4.2 Numerical Approach for Gain k_p

At this point, any value assumed for k_p yields the real part a of a double pair of poles with eq. (19), then eq. (23) finds the corresponding value for T_i . It turns out, that only if k_p with the minimal real part is chosen, the value for T_i is an optimal solution. A numerical solution for the poles of eq. (14) can be found easily with numerical tools, e.g. Matlab™ or with the function *solve* from the Python package *sympy*. Given a value for k_p , the value for T_i and the poles are available now. This allows experiments for creating a map of poles, or to find a good pole placement.

To find the solution faster, an iterative approach can be used. The optimal solution are two pairs of poles with the same real parts and imaginary parts. As criterion, the sum of the *Manhattan* distances of the poles from the point with the mean real and mean imaginary parts of the poles is used,

$$\sigma = \sum_{i=1}^4 (|a_i - \bar{a}| + |b_i - \bar{b}|) \quad (24)$$

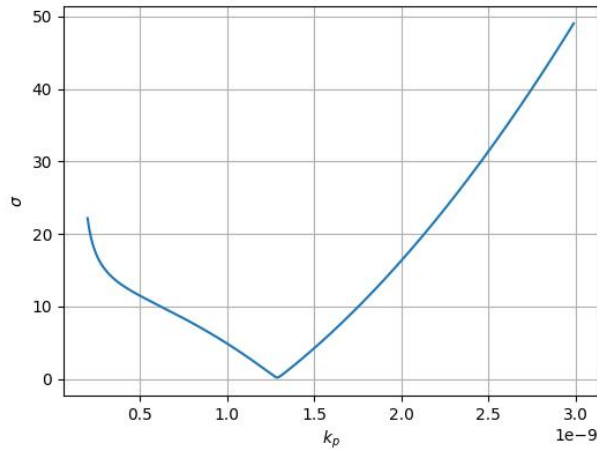


Figure 5: Manhattan distances of the poles with minimum of zero at the optimal solution

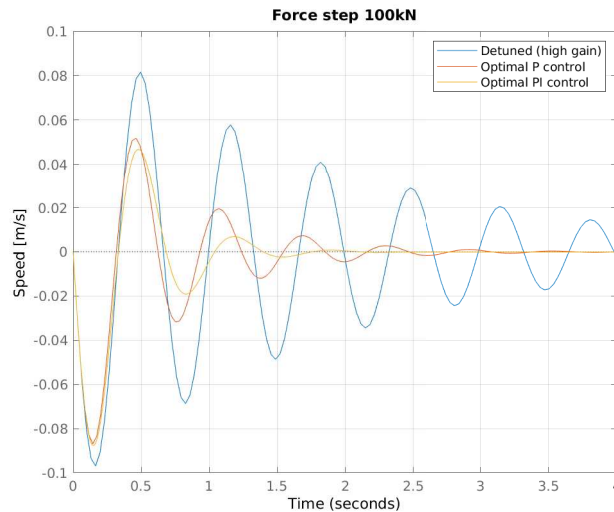


Figure 6: Step response of transfer function

with

$$\bar{a} = \sum_{i=1}^4 a_i, \quad \bar{b} = \sum_{i=1}^4 b_i. \quad (25)$$

In order to prove, that eq. (24) is a suitable measure, the values of σ over k_p are displayed in fig. 5. The graph shows clearly a minimum at zero, which means, that there is a point, where all poles meet, and that the Manhattan distance can be used to find this optimum with a numerical procedure. This can be done in *Python* with the *minimize_scalar* function of the *scipy.optimize* package in *Scipy*, or with *Matlab*TM.

5 Simulation Results

For the verification of the proposed design procedure an example hydraulic system was assumed. The mass m is chosen with 100000kg, the cylinder areas are $A_A = 0.03\text{m}^2$ and $A_B = 0.02\text{m}^2$, the chamber capacitances are $C_A = C_B = 10^{-10}\text{m}^3\text{Pa}^{-1}$ and the friction is assumed to be viscous with $b_{fr} = 100\text{kNsm}^{-1}$. A steady speed v_0 was chosen with 41 mm/s, which causes a steady oil flow q_B of 50 l/min. From this follows the factor k_B with $8 \cdot 10^{-11}\text{m}^3\text{Pa}^{-1}\text{s}^{-1}$. A disturbing force step is applied with $F = 100\text{kN}$. For the optimal pressure control gain k_p a value of $1.3 \cdot 10^{-9}\text{m}^3\text{Pa}^{-1}\text{s}^{-1}$ was found, and for the integrating part a T_i of 0.142 s.

The first experiment is to simulate the linear model according to eq. (14). Figure 6 shows the optimal solution with high damping, a result with proportional control only, and a detuned solution with very high controller gain k_p .

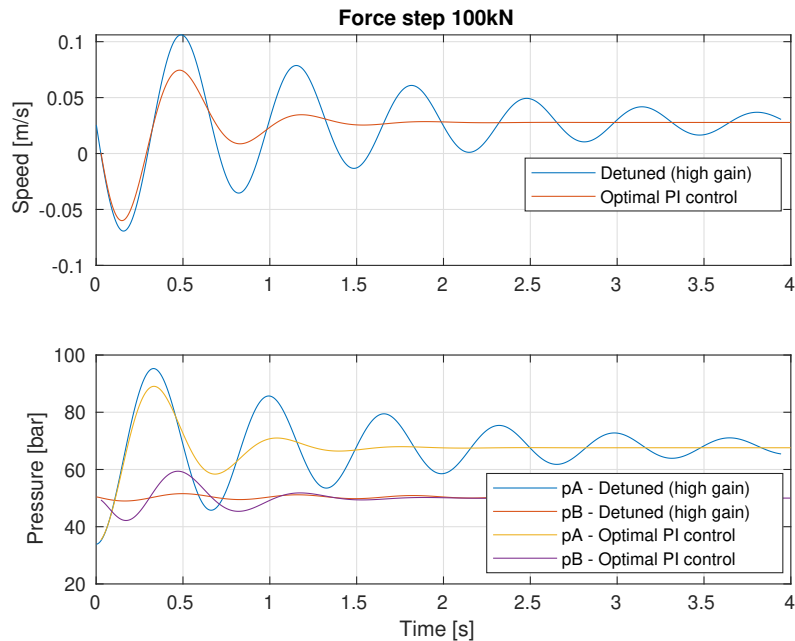


Figure 7: Step response of the simulated non-linear system

A second experiment is done according to the system in fig. 2 in Matlab®/Simulink® with a non-linear system. A constant oil flow is maintained with a fast proportional valve and a flow controller. For the downstream pressure controller also such a valve is used. The set value p_0 is 50 bar, the power supply pressure is 200 bar. The force step is delayed to allow the system to settle before the experiment. Figure 7 shows the speeds and the cylinder pressures over time.

6 Summary and Conclusions

In this work pressure feedback control in hydraulic actuators for motion control is investigated. Such loops are often used in individual metering systems to stabilise the pressure on the downstream side, while a flow controller governs the motion speed. Another well-known technique is the use of a hydro-mechanical pressure relief valve. This would be equivalent to an electronic P control with a very high gain and has a low damping contribution. Alternatively, electronic pressure feedback with a high-pass filter maybe applied to bring additional damping into the system. Since a control loop is also a kind of feedback, and the PI controller can be regarded as filter, the configuration can expose damping behaviour too. It turns out that the parameters can be optimised with respect to this property, and a design procedure for this is presented. A simulation experiment shows that this works, while the pressure stabilising feature still is in function.

The design is strictly connected with the physical system parameters and therefore is sensible against changes, for example drift during the operation. In comparison to this, the classical pressure feedback using a separate filter is not so sensible to parameter errors and can provide higher damping ratios. But it is shown, that there is an essential damping contribution by the PI controller, when the parameters are adjusted accordingly.

Nomenclature

Designation	Denotation	Unit
q_A	Constant (controlled) input flow	m^3/s
q_B	Downstream flow determined by pressure controller	m^3/s
q_{B0}	Steady motion flow to chamber B	m^3/s
q_N	Nominal oil flow of valve	m^3/s
p_N	Nominal pressure of valve	Pa, bar
p_A, p_B	Pressures in chamber A and B	Pa, bar
p_0	Set value for pressure control	Pa, bar
p_s	Power supply pressure	Pa, bar
A_A, A_B	Piston areas	m^2
C_A, C_B	Hydraulic capacitances	m^3/Pa
k_p	Proportional control gain	$\text{m}^3/\text{Pa s}$
k_B	Flow change due to pressure change (linearised)	$\text{m}^3/\text{Pa s}$
T_i	Integral reset time	s
v	Velocity of piston and load	m/s
v_0	Steady motion velocity of piston and load	m/s
F	Disturbing force applied to load	N
F_A, F_B	Force contributions of cylinder chambers	N
m	Mass of the load	kg
b_{fr}	Viscous friction coefficient	Ns/m
η	Valve opening ratio, 0..1	

Acknowledgment

This work was supported by the Ministry of Education and Science of the Republic of North Macedonia, project *Development of Concepts and Control Strategies With Improved Energy Efficiency for Hydraulic Systems in Heavy Machinery*, and by the Austrian WTZ programme, project ID MK 10/2018.

References

- [1] B Eriksson and J-O Palmberg. Individual metering fluid power systems: challenges and opportunities. *Proceedings of the Institution of Mechanical Engineers, Part I: Journal of Systems and Control Engineering*, 225(2):196–211, 2011.
- [2] B Eriksson, J Larsson, and J O Palmberg. Study on individual pressure control in energy efficient cylinder drives. In M Ivantysynova, editor, *4th FPNI-Ph.D. Symposium, FPNI'06*, pages 77–99, Sarasota, United States, 2006.
- [3] Eaton Hydraulics Group, Eden Prairie, USA. *CMA200 Advanced Independent-Metering Mobile Valve*, 2016. Technical guide.
- [4] G Rath G Stojanoski and M Gimpel. The effect of bulk modulus on the dynamics of hydraulic independent metering systems. In *The Sixteenth Scandinavian International Conference on Fluid Power, SICFP19 : Proceedings*, pages 276–290, Tampere, Finland, 2019.
- [5] Q Yuan, C Schottler, and J Y Lew. Electronic flow control valve (efcv) with pressure compensation capability. In *5th International Fluid Power Conference (5th IFK)*, Aachen, Germany, 2006.
- [6] P Krus and J-O Palmberg. Dampening of fluid power systems in machines with high inertia loads. In *Proc. SICFP*, Sweden, 1998.
- [7] R Rahmfeld and M Ivantysynova. An overview about active oscillation damping of mobile machine structure. *Internationl Journal of Fluid Power*, 5(2):5 – 24, 2004.
- [8] D Padovani. Adding active damping to energy-efficient electro-hydraulic systems for robotic manipulators - comparing pressure and acceleration feedback. In *2020 5th International Conference on Robotics and Automation Engineering (ICRAE)*, pages 175–181, 2020.

- [9] T O Andersen H C Pedersen and M R Hansen. Guidelines for properly adjusting pressure feedback in systems with over-centre valves. In *In Proceedings of the BATH/ASME Symposium on Fluid Power Motion Control*, Bath, UK, 2016.
- [10] A Alexander, A Vacca, and D Cristofori. Active vibration damping in hydraulic construction machinery. In A Plummer V Sverbilov, editor, *Proceedings of the 3rd International Conference on Dynamics and Vibroacoustics of Machines (DVM2016), Samara, Russia*, volume 176 of *Procedia Engineering*, pages 514 – 528. Elsevier, 2017.
- [11] N C Singer and W P Seering. Preshaping command inputs to reduce system vibration. *ASME Journal of Dynamic Systems, Measurement, and Control*, 112:76–82, 1990.
- [12] J Bhatti, A Plummer, P Iravani, and M Sahinkaya. Implementation of closed loop signal shaping in a hydraulic system. In *Mechatronics 2012: The 13th Mechatronics Forum International Conference*, 2012.
- [13] G Rath, E Zaev, and D Babunski. Oscillation damping with input shaping in individual metering hydraulic systems. In *2019 8th Mediterranean Conference on Embedded Computing (MECO)*, pages 561–565, Budva, Montenegro, 2019.

Concept, Simulation Studies and Design for a Novel Concept of the Hydraulic Binary Counter

Rudolf Scheidl and Matthias Scherrer

Institute of Machine Design and Hydraulic Drives, Johannes Kepler University Linz, Linz, Austria
E-mail: Rudolf.scheidl@jku.at, Matthias.scherrer@jku.at

Abstract

For the realization of compact and lightweight digital hydraulic cylinder drives for exoskeleton actuation the hydraulic binary counter concept was proposed and studied previously. This counter principle is based on hydraulically piloted switching valves which feature a hysteretic response with respect to the pilot pressure. In first prototypes of that counter bistable mechanical buckling beams realized the hysteretic response. Their performance suffered from high friction in the hinges and high local stresses. Furthermore, they require tight manufacturing tolerances not only of themselves but also of their bearing structure. In this paper, hydraulic feedback from the multi-chamber cylinders is proposed and investigated to realize the reset of lower order valves when a higher order valve switches. To make the hydraulic feedback independent from the system pressure feedback to the valve is done via spring compression. This principle makes bi-stable elements obsolete. The functioning of this principle for a small drive for exoskeleton use is proven by a simple mathematical model and its numerical solution by a MATLAB program. An exemplary embodiment design of the valves with the proposed feedback mechanism shows the feasibility of its practical realization. The application of this concept is not limited to small drives but can be applied for larger drives where multi-chamber cylinders are advantageous, such as for excavators, to save cost and installation space of the many solenoid valves required otherwise.

Keywords: Multi chamber cylinder, digital fluid power, hydraulic binary counter

1 Introduction

The use of a hydraulic counter principle for the control of a multi-chamber cylinder drive was first studied 2011 in [1] for the realization of a digital pendant of the analog linear hydraulic amplifier. This device transfers a low force mechanical input motion x_d into a proportionate output motion x_a against a high force F ; see Figure 1. x_d is input mechanically to the spool, x_a to the housing of a proportional valve which leads to pilot flows Q_{XI} and Q_{XP} into or out of the pilot line. The pilot flow and the resulting pilot pressure p_C make the four 3-2 way valves switching on or off in a consecutive, binary manner such that the number values of the binary states follow the natural number series to raise or lower the resultant force according to the cylinder pressures and cylinder areas. Q_{XI} leads to an integral behavior of the system, because it provides a stepping up or down of the resultant hydraulic force as long as x_d is larger or smaller than x_a . The proportional part of this feedback control mechanism given by Q_{XP} stabilizes the response behavior. Later, this concept was taken up to realize a hydraulic piloting actuation of multi-chamber cylinder valves for exoskeleton use to save weight of the relatively heavy solenoids [2, 3]. The counting principle studied in these papers was based on a hysteresis response of the four 3-2 way switching valves for the four cylinder chambers. This response manages the reset of all lower order bits when a certain bit performs the counting step. The snap through property of a buckling beam was selected as a passive mechanical realization but turned out to suffer from a too high friction in the joints [4]. Furthermore, the concept imposes narrow design rules for the valves of the different binary stages and tight tolerances, which

means an additional complexity for system design. The use of repulsive permanent magnets [5], a passive principle too, leads to a relatively complex and bulky design.

The binary counter principle can not only save weight and space but also cost of the solenoid valves, which is a high burden for the economically feasible realization of multi-chamber cylinder drives. For instance, cost is a major design criterion of small and mid-size range mobile working machines, for which these drives are seen a promising way for substantial fuel savings [7-9]. For the valve sizes required for such mobile machinery applications passive concepts of binary counting are not feasible because of the high flow and friction forces. Such valves may use an internal hydraulic feedback by additional metering edges, as already suggested in [1] and sketched in the left side drawing of Figure 2. However, those edges would cause difficulties for very small valves, as needed for hydraulic exoskeleton actuation.

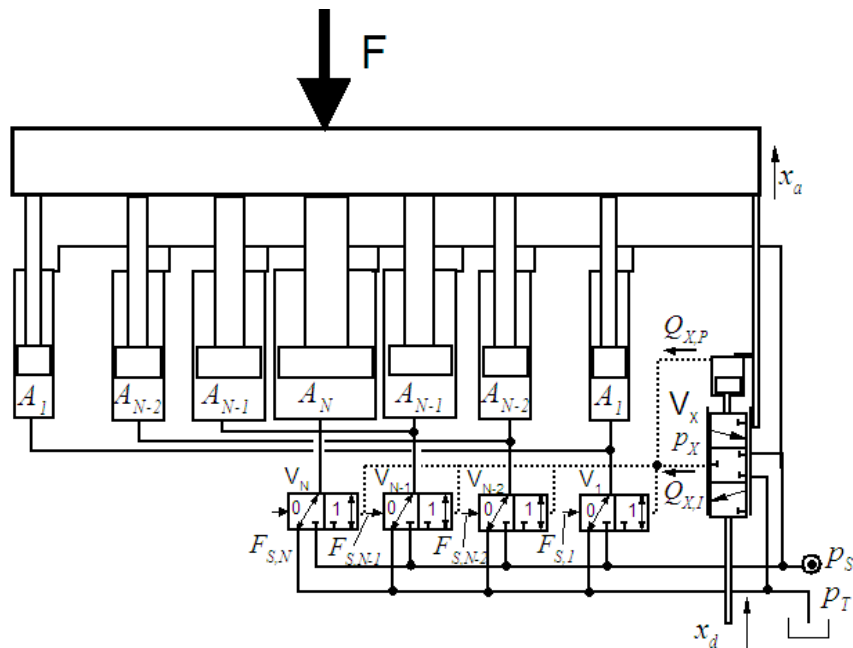


Figure 1: Linear digital hydraulic amplifier with a differential feed-back [1].

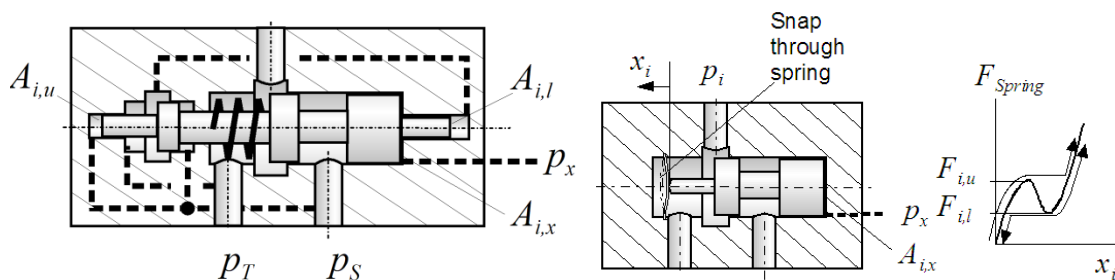


Figure 2: Exemplary embodiment designs of two concepts to realize a hysteresis behavior of a switching valve w.r.t. to a pilot pressure p_x ; left: hydraulic feedback by additional metering edges; right: snap through spring.

In this paper the feedback from the pressure of the multi-chamber cylinders is studied instead. It saves extra features of the valves and is applicable to any valve size. The concept is presented and its basic functioning and behavior are analyzed by a simple mathematical model. An exemplary embodiment design is presented to demonstrate the practicability.

2 Binary counting principle

The binary counter principle is given by a schematic in Figure 3. For a better comprehension of the functioning Figure 5 and Figure 10 are helpful. The purpose of the circuitry is adjusting a hydraulic actuation force F_H which

is a four bit equivalent of the pressure p_c in the pilot line. Thus, the counter can be also seen as a hydraulic analog-digital converter. For an equal force stepping the piston areas must follow a binary sequence. There are two solutions; both are given in (1); the first one is used in this paper.

$$A_1 : A_2 : A_3 : A_4 = \left\{ \left[-\frac{1}{8} : \frac{1}{4} : -\frac{1}{2} : 1 \right], \left[-\frac{1}{8} : \frac{1}{2} : -\frac{1}{4} : 1 \right] \right\} \quad (1)$$

A negative area is one that causes a negative hydraulic force. This convention eases the formulation of several equations.

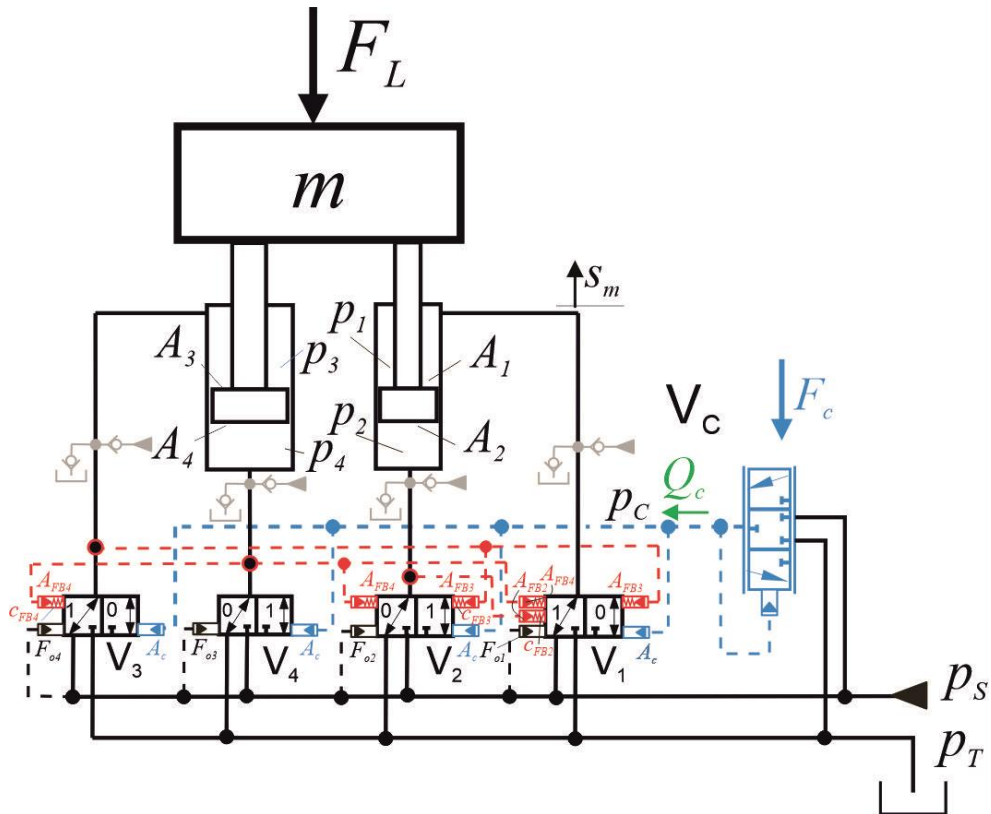


Figure 3: Hydraulic binary counting for the control of a four-chamber cylinder.

The force levels which the counter should realize and the corresponding switching positions of the four valve $V_1..V_4$ are depicted in Figure 4.

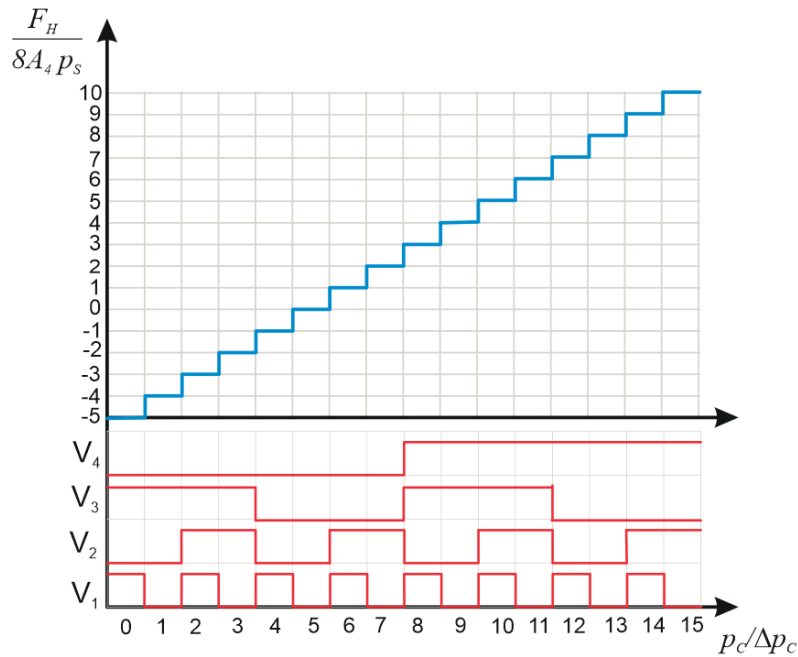


Figure 4: Intended AD conversion behavior of the binary counter and corresponding valve states.

If the pilot pressure is below the first threshold value ($p_C < \Delta p_C$) all four valves are in their initial states, as sketched in Figure 3. Δp_C are the pilot pressure increments, see Figure 4. The threshold values for the valves can be set hydraulically using the system pressure p_S – as shown in Figure 3 – or by spring preload. In the first case, the magnitude of these preload forces F_{O_i} , $i=1 \dots 4$ is adjusted by the active hydraulic displacement areas A_{O_i} , $i=1 \dots 4$. The values of F_{O_i} are given in Table 1.

Table 1: Values of the threshold forces F_{O_i} .

Valve	V ₁	V ₂	V ₃	V ₄
$\frac{F_{O_i}}{\Delta p_C A_C}$	5	6	4	8
$\frac{A_{FBk} p_S}{2 \Delta p_C A_C}$	~	2	4	8

The pressures in the cylinder chambers p_k are fed back to the valve V_i via areas A_{FBk} . Their sizes depend only on the chamber number k and not on the valve number i . Thus, the corresponding piloting units of order k can be realized in all valves identically. Valve V_i needs feedback only from the higher order valves $i+1$ ($2 \dots 4$). Valves V_1 and V_3 are controlling chambers with a hydraulic force in negative direction. Their initial values are 1, hence, the pressures in the related chambers are p_S . First switching of V_1 and V_3 cause a pressure change from p_S to p_T which is opposite to that of valves V_2 and V_4 . To handle this logic situation the feedback actuators of pressure p_3 are placed on the opposite sides. The corresponding initial forces are compensated by an increased value of F_{O1} and F_{O2} . This additional offset is $4\Delta p_C A_C$. Without this the values of F_{O1} and F_{O2} would follow the binary steps 1 and 2 as is the case for F_{O3} and F_{O4} since valves V_3 and V_4 are not affected by p_3 .

In order to keep the feedback forces in a narrow tolerance range even when the chamber pressure have some variation, a spring is placed between the feedback cylinders and the valve spools. The limited stroke of the feedback cylinder defines the feedback force via the spring constant. The areas A_{FBk} are such that these springs are fully compressed with a fraction of the system pressure. For the values shown in this paper that fraction is taken to be $p_k/p_S=1/2$. This explains the number 2 in the denominator of the expression in the second row of Table 1.

When p_C is raised and exceeds Δp_C V_1 starts to move from state 1 into state 0. The transition is continuous first, due to the continuous force changes of the springs in the feedback units. The lower these spring constants c_{FBk} , the steeper the rise of the valve transition with rising p_C , but the higher the compression stroke of the feedback units. Valve V_2 starts switching if $p_C > 2\Delta p_C$. When it reaches state 1, the pressure p_2 rises and puts a feedback

force F_{O2} on valve 1 which makes it switching back when it reaches $p_S/2$. At $p_C = 3\Delta p_C$ switching of V_1 starts again. At $p_C = 4\Delta p_C$ V_3 goes from state 1 to 0 which finally causes V_1 and V_2 to switch back to their initial states 1 and 0, respectively. Valve V_4 begins its transition to state 1 when $p_C = 8\Delta p_C$. Counting down, i.e. lowering the output force, happens in an analog way.

As will be demonstrated in Section 4 by simulation results, a monotonous rise of p_C does not mean a continuously positive pilot flow rate Q_C . For instance, if V_4 is switched the lower order valves $V_{1..3}$ switch back and displace three times the fluid which V_4 takes back to the pressure control valve V_C . Thus, in sum that event leads to a negative flow. That circumstance requires a control of p_C as indicated in the schematic of Figure 3. It shows as actual input a force F_C , which can be a manual or magnetic force. In the latter case V_C represents a proportional three way pressure control valve. Basically, it would be also possible to avoid flow reversal when a higher order valve switches, if the displacement volume of the pilot pressure actuation cylinder of V_i is larger than that of all lower order valves. That means an exponential growth of these displacement volumes whereas in the concept proposed here all valves $V_{1..4}$ differ only with respect to F_{oi} or A_{oi} , respectively.

The metering edges geometry (overlap or underlap) of the sealing lands decide on the transition between the two topologic different situations; to have an intermediate short circuiting from pressure to tank line or to happen fully separately. To avoid an intermediate blocking of the cylinder chambers or cavitation in the latter case check valves can be placed to both supply lines. These optional valves limit the pressures to the range $[p_T, p_S]$ and are shown in grey color in Figure 3. The problem of system transients due to switching and measures to avoid or limit unwanted dynamical effects are not studied in this paper.

3 Mathematical model of the counter

The validity of the concept and the influence of the design parameters on the properties are investigated by a simple mathematical model. It considers only effects relevant for the basic working principle and comprises the four valves and the pressure build-up in the four cylinder chambers. The following effects are disregarded:

- (1) inertias of the spools and pistons of the valve piloting pistons,
- (2) flow and friction forces in valves V_i ,
- (3) influence of motion of the driven system (\dot{s}_m) for the pressure build-up dynamics in the cylinder chambers.

Simplifications (1) and (3) are based on the assumption that there is a clear order of the dynamics of the motion of the driven system $s_m(t)$, the pressure build up dynamics in the cylinder $p_k(t)$, and the valve response dynamics $s_{vi}(t)$, with sufficient frequency gaps in between. Assumption (2) represents a requirement on valve design and dimensioning, particularly of the control force steps $\Delta p_C A_C$. This force increment must dominate all parasitic effects neglected according to this assumption.

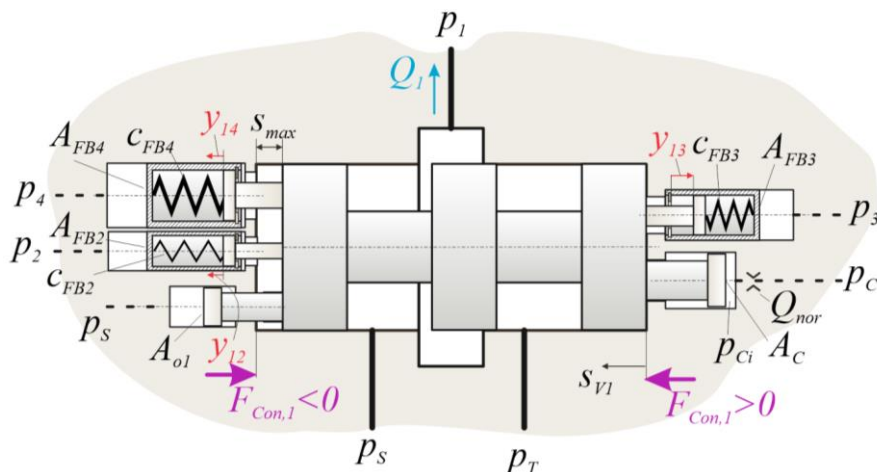


Figure 5: Model of valve V_1 ; other valves have lower number of feed-back actuators and different values A_{oi} .

The most complex valve is V_1 . A sketch of the main functional components is given by Figure 5. The spool has a maximum travel distance s_{max} which is identical for all valves. A perfect metering of the 3-2 way valves is assumed, the relation between spool travel s_{vi} and nondimensional valve position y_i is

$$y_i = -1 + 2 \frac{s_{Vi}}{s_{\max}}, \quad (2)$$

and for the flow rate Q_i over the valve V_i to the related cylinder chamber

$$Q_i = Q_N \left[sg \left(y_i \text{sign}(A_i) \right) \sqrt[4]{\frac{p_s - p_i}{p_N}} - sg \left(-y_i \text{sign}(A_i) \right) \sqrt[4]{\frac{p_i - p_T}{p_N}} \right]. \quad (3)$$

$$sg(x) = \max(0, \min(x, 1)); \quad \sqrt[4]{x} = \sqrt{|x|} \text{sign}(x)$$

The equilibrium of the up to five actuation forces for the spool valve V_i are

$$p_{Ci} A_C - F_{Oi} + F_{Con,i} - \sum_{k=i+1}^4 F_{FBk} \text{sign}(A_k) = 0. \quad (4)$$

The factor $\text{sign}(A_k)$ considers the feedback actuators' individual force direction. The forces are related to pressures and positions by the following rules.

$$F_{Oi} = A_{Oi} p_s; \quad F_{FBk} = \min \left[p_k A_{FBk}, (y_{ik} + y_{k0}) c_{FBk} \right] \text{sign}(A_k)$$

$$y_{ik} = 0 \quad \text{if } p_k A_{FBk} < y_{k0} c_{FBk}$$

$$y_{ik} = \begin{cases} s_{Vi} & \text{for } k = 2, 4 \\ s_{\max} - s_{Vi} & \text{for } k = 3 \end{cases} \quad \text{if } p_k A_{FBk} \geq y_{k0} c_{FBk} \quad (5)$$

$$F_{Con,i} \geq 0 \text{ if } s_{Vi} = 0$$

$$F_{Con,i} \leq 0 \text{ if } s_{Vi} = s_{\max}$$

$$s_{Vi} \in [0, s_{\max}]$$

The contact force $F_{Con,i}$ assures equilibrium if the spool is in one of its end positions $s_{Vi} = \{0, s_{\max}\}$. The pressure build-up equation for chamber i reads:

$$\dot{p}_i = \frac{E}{V_{i0} + A_i s_m} (Q_i - \dot{s}_m A_i) \quad (6)$$

The pilot flow Q_C and its integral V_{QC} are related to the control valve (V_C) equation.

$$\dot{V}_{QC} = Q_C = sg \left(\frac{y_C}{y_{C\max}} \right) Q_{NC} \sqrt[4]{\frac{p_s - p_C}{p_N}} - sg \left(-\frac{y_C}{y_{C\max}} \right) Q_{NC} \sqrt[4]{\frac{p_C - p_T}{p_N}} \quad (7)$$

$$y_C = \frac{F_C - p_C A_{CC}}{c_{CC}}$$

The pressure in the pilot line p_C is related to the difference of the inflowing oil volume and displacement by the valves V_i due to fluid compressibility in the pilot system, given by the hydraulic capacitance C_{Hp} .

$$p_C = \frac{1}{C_{Hp}} \left(V_{QC} - A_C \sum_{i=1}^4 s_{Vi} \right) \quad (8)$$

The speeds of the spool motions are related to the pressures $p_{Ci..4}$ in the displacement chambers of the pilot system by the following equation.

$$\dot{s}_{Vi} = \frac{Q_{Nor}}{A_C} \sqrt[4]{\frac{p_C - p_{Ci}}{p_N}}; \quad i=1..4 \quad (9)$$

The orifice between pilot line and the displacement chambers (specified by a nominal flow rate Q_{Nor}) are inserted to ease simulation. Otherwise p_C and s_{Vi} are not directly related to each other but only by (4) and (8) which involve the strongly nonlinear contact problems due to the contact forces $F_{Con,i}$. The solution of this set of equations requires methods to solve multidimensional contact problems.

The behavior of the system is studied for a ramp up and down of control input F_C . According to the simplifications specified above, the process is considered being so fast that no substantial change of the position s_m takes place in that time. Furthermore, the valves nominal flow rates Q_N are considered being large enough to keep the pressure losses small compared to system pressure p_S , a condition to cancel the term \dot{s}_m in (6). The reason for the simplifications is mainly to keep the analysis general and to keep the number of parameters which influence the results small. Then the whole system has the following state vector \mathbf{x} .

$$\mathbf{x} = [p_{1..4}, V_{QC}, s_{V1..4}]^T \quad (10)$$

It contains nonlinear constraint relations due to the contact forces $F_{Con,i}$ in (4). In order to keep the simulation model simple, these forces are modeled as elastic contact forces according to the following rule.

$$F_{Con,i} = c_{Con} (sg1(-s_{Vi}) - sg1(s_{Vi} - s_{max})); \quad sg1(x) = \max(0, x) \quad (11)$$

The vector describing the flow of \mathbf{x} is given by equations (6), (7) and (9) in combination with equations (4), (5), (8) to compute p_{Ci} and p_C . The model is implemented in a Matlab program. The differential equations system is stiff, therefore, solutions are computed numerically using Matlab's stiff ODE solver *ode15s*.

4 Simulation results

The counter's behavior is studied for an exemplary four chamber cylinder drive for exoskeleton use. The used system parameter values set are listed in Table 2.

Results are given by plots in the next figures. They show the working of the system. The response dynamics is illustrated for the switching from stage 3 to 4, when 3 valves change position, by the diagram in Figure 8. Despite the small nominal flow rate of the pressure control valve (see Q_{NC} in Table 2) valve V_3 needs only 3 milliseconds for switching. The lower order valves $V_{1,2}$ need much less due to the strong effect of the feedback mechanism.

The small changes of valve position at fully open or close positions, best to be seen for s_{V4} , results from the modeling of the elastic end stop with the spring constant c_{Con} and the effect of p_C . This is a modeling issue and has no meaning for the functioning of the counter.

Table 2: System and Matlab 'ode15s' options parameter values for simulation study.

Parameter	Value	Parameter	Value	Parameter	Value
A_C	10 mm ²	A_{CC}	2 mm ²	$A_{FB2..3}$	[1.6 3.2 6.4] mm ²
$A_{k \ k=1..4}$	[-.125 .25 -0.5 1] cm ²	$c_{FB1..3}$	[0.8 1.6 3.2] N/mm	c_{CC}	5.33 N/mm
c_{Con}	1000 N/mm	C_{Hp}	0.0643 mm ³ /bar	E	14 000 bar
$y_{k0 \ k=1..4}$	[10 10 10 10] mm	y_{Cmax}	0.3 mm	$F_{oi \ i=1..4}$	[20 24 16 32] N
Δp_C	4 bar	p_N	100 bar	p_S	5 bar
p_T	0 bar	Q_{NC}	1 lit/min	Q_N	3 lit/min
Q_{Nor}	0.5 lit/min	s_m	50 mm	s_{max}	0.5 mm
$V_{i0 \ i=1..4}$	[1.5 0.5 6.0 2.0] cm ³	options = odeset('RelTol',1e-4,'AbsTol',1e-8)			

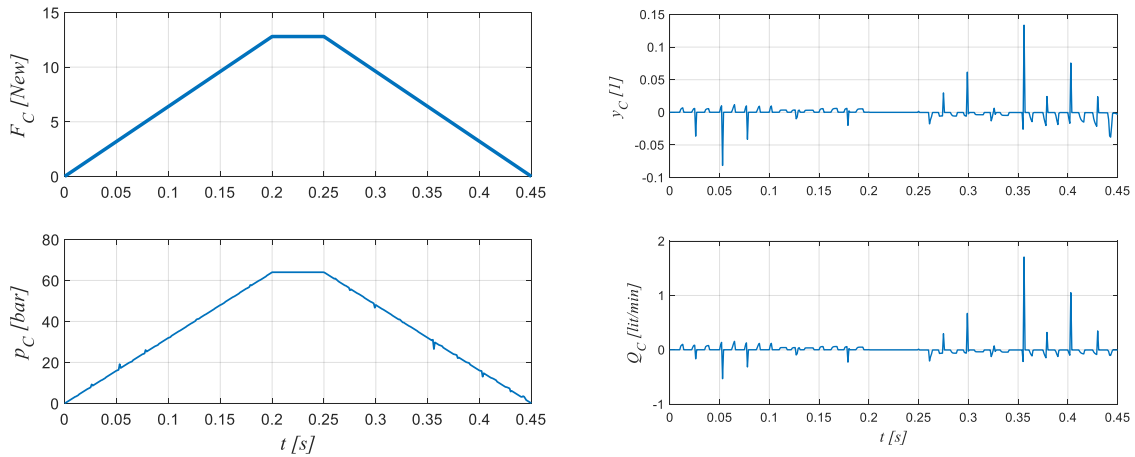


Figure 6: Results of a simulation of the digital cylinder drive controlled by a binary counter system; input force F_C , pilot pressure p_C , pressure control valve nondimensional opening y_C , and pilot flow Q_C .

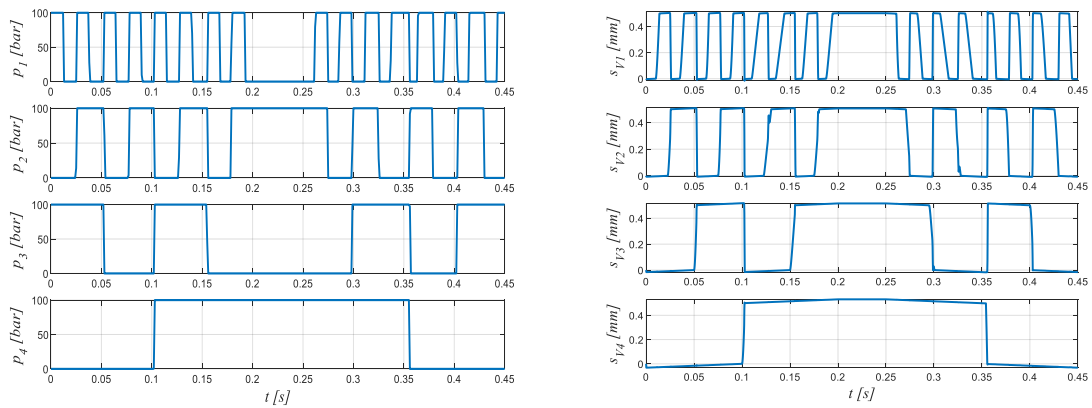


Figure 7: Results of a simulation of the digital cylinder drive controlled by a binary counter system; pressures in cylinder chamber p_i and valve positions s_{Vi} .

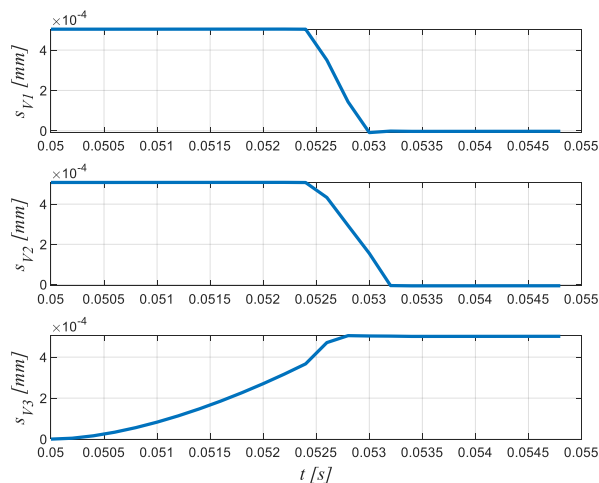


Figure 8: Magnified view on the response diagrams of valves $V_{1..3}$ when the counter switches from stage 3 to 4.

The system with the parameters of Table 2 can also follow faster changes of the system input F_C . Figure 9 shows the response in terms of valve position and chamber pressures for a ramp on and off time of 50 milliseconds. The system is probably at its limits when counting down, even though the cylinder pressure p_1 follows the counting sequence better than the spool of valve V_1 .

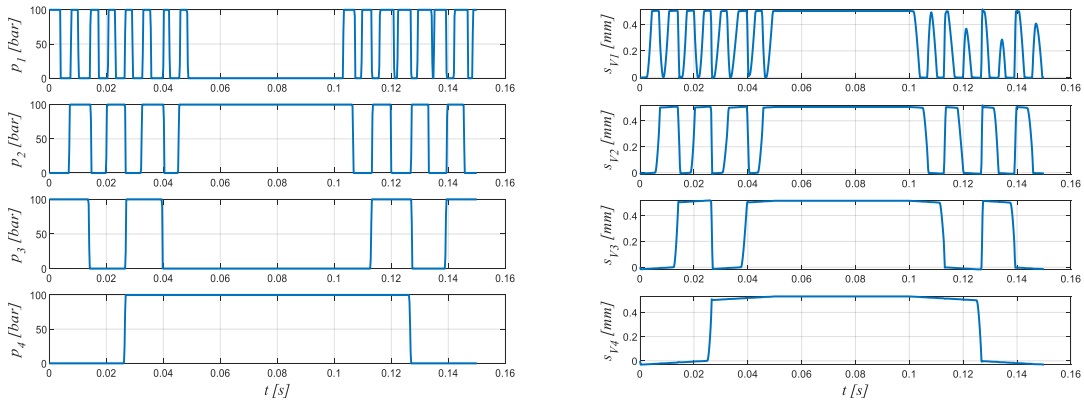


Figure 9: Results of a simulation of the digital cylinder drive controlled by a binary counter system for a ramp time of 50 milliseconds; pressures in cylinder chamber p_i and valve positions s_{V_i} .

5 Valve design

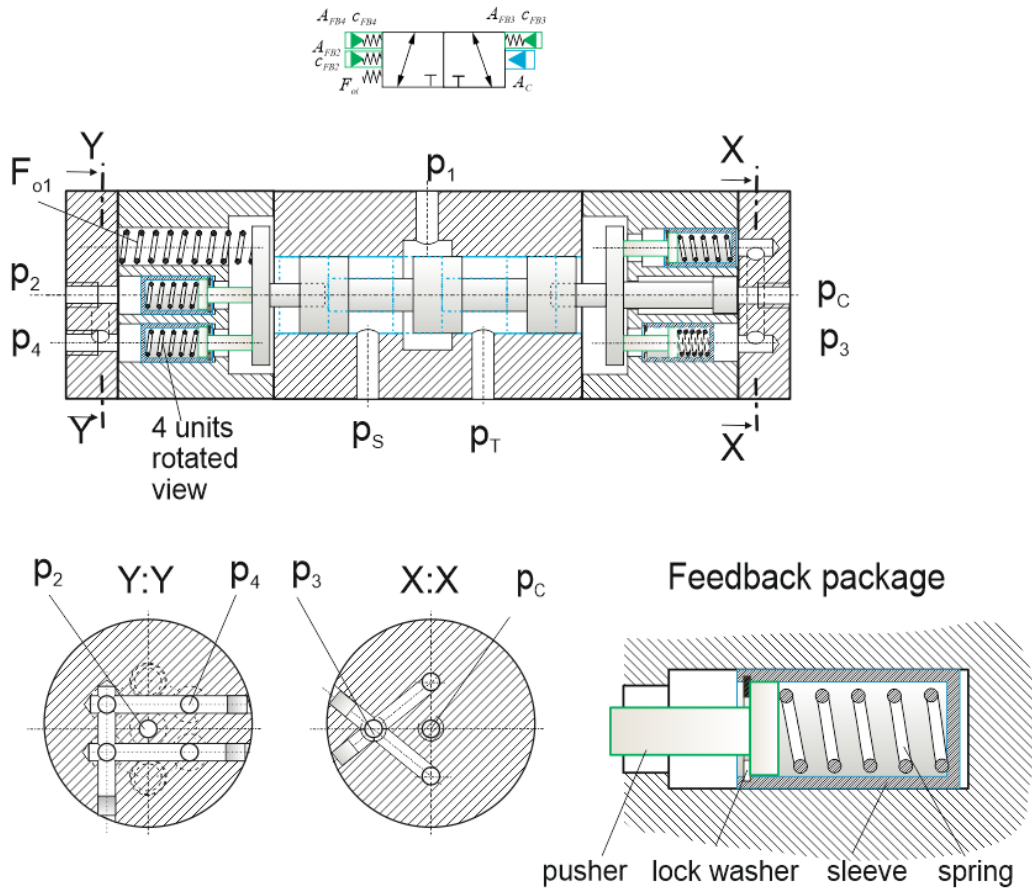


Figure 10: Exemplary design of valve V_1 .

The valve consists of a standard 3-2 way valve w.r.t. the main stage but needs an elaborate piloting system with up to five separate inputs. To judge on the feasibility of a practical realization an exemplary embodiment design is presented in this section.

Figure 10 shows such a design of valve V_1 which is the most complex one. Higher stage valves can be widely identical. The piston areas A_C and all cylinder pressure feedback units are identical for all valves. Higher order valves need fewer number of feedback units, V_2 from p_3 and p_4 , V_3 only from p_4 , and V_4 none. All valves could be equipped with all feedback units and only the required ones are actually connected to the cylinder chambers or unneeded units are skipped. The feedback units of each valve are only made of one feedback package, consisting of bore, sleeve, lock washer and pusher. The higher forces of the higher order feedback units – they

follow in value the power series of 2 – are realized by a higher number of feedback packages. p_2 has one unit, p_3 two units, and p_4 four units.

For a fast response of a valve when the pilot pressure reaches the corresponding value, the springs in these units should have a relatively large pretension. In the simulations a pretension $y_{k0\ k=1..4}$ of 10 mm was set which is twenty times the spool stroke $s_{max} = 0.5$ mm. In order to save space the concept with the sleeves which holds the pre-tensioned spring with the lock washer is recommended. Without this pretension sleeve the spring must be given the full pretension stroke to avoid a force on the spool when the related feedback pressure is zero. That increases the valve size unnecessarily. Furthermore, that would cost more fluid from the cylinder chamber when the pressure switches from tank to system pressure. The only valve specific parameter is the threshold force $F_{oi\ i=1..4}$. In the design concept of Figure 10 it is realized via a spring, actually two springs in order to balance that force with respect to the centerline. The simplest way to realize the different force values ([20 24 16 32]) is by different pretensions (y_{Foi}) of relatively soft springs to guarantee $s_{max} \gg y_{Foi}$. Individual pretensions are best realized by different washers placed between spring and end cap. This washer is not shown in Figure 10.

6 Summary and conclusion

A concept to control a binary staggered four chamber cylinder system by a hydraulic binary counter was presented. It uses feedback of the pressures from the higher order chambers to accomplish the reset of the lower order valves if a binary jump of a certain order is to be made. That concept needs piloted 3-2 way valves and a pilot pressure control system, which transfers the desired force level into a corresponding pilot pressure. The counter transfers this pressure into an appropriate force level out of the sixteen possible force levels available of a four chamber cylinder system. The functioning of this concept was demonstrated by a numerical simulation of a simple system model. A small hydraulic actuator for an exoskeleton served as an example.

The paper does not yet present a study of the control performance of certain motion control tasks, for instance, of exoskeletons. This and a compact realization of the pilot pressure control valve will be tackled next.

The concept can be applied to larger hydraulic drives as well, for instance for the four chamber cylinders for excavators, brought into discussion in the last years. In this case, the system needs to be augmented by means for a continuous force control for certain operation modes, obviously by adding some throttling control. A hydro-mechanical concept which can do both, combined digital and throttling control when inevitable, and pure digital control whenever feasible, will be a topic of further research.

Nomenclature

Designation	Denotation
$A_{FBk\ k=2..4}$	Piston areas for pressure feedback to valve V_i by pressure p_k
A_C	Pilot piston area
A_{CC}	Pilot pressure feedback area of pressure control valve V_C
$A_{k\ k=1..4}$	Four chamber piston areas
$A_{Oi\ i=1..4}$	Piston areas for hydraulic realization of offset forces F_{Oi}
C_{Hp}	Hydraulic capacitance of pilot line
E	Compression modulus
$F_{FBki\ i=1..3, k=i+1..4}$	Feedback forces to spool of valve V_i from pressure p_i
F_C	Control input force to pressure control valve V_C
$F_{Con,i\ i=1..4}$	Contact force to spool at end stop positions
F_H	Hydraulic force of the four chamber cylinder
F_L	Load force
$F_{Oi\ i=1..4}$	Force to realize switching threshold value for pilot pressure
Q_C	Flow rate from pressure control valve into pilot system
Q_N	Nominal flow rate of valve main stages
Q_{NC}	Nominal flow rate of pressure control valve

Q_{Nor}	Nominal flow rate of orifice
$V_{i0} \ i=1..4$	Dead volumes of cylinder chambers for $s_m = 0$
V_{QC}	Displacement volume of Q_C
c_{CC}	Spring constant of pressure control valve
c_{Con}	Spring constant of contact force modeling
$c_{FBk} \ k=1..3$	Spring constant of pressure feedback units
i, k	Indices of valve and cylinder chamber numbers
m	Load inertia
$p_C, \Delta p_C$	Pilot pressure and its counting increment
$p_{Ci} \ i=1..4$	Pressure acting on pilot area A_C of at valve V_i
$p_k \ k=1..4$	Pressure in cylinder chamber k
p_N	Nominal pressure loss of valves or orifices
p_S, p_T	System and tank pressure
s_m	Cylinder travel
s_{max}	Spool stroke of valves
$s_{Vi} \ i=1..4$	Position of spool of valve V_i
\mathbf{x}	State vector of dynamical model
y_c	Position of pressure control valve
y_{cmax}	Stroke of pressure control valve
y_{ik}	Compression of feedback spring by pressure p_K in valve V_i
y_{k0}	Pre-compression of feedback spring

Acknowledgement

This work was done in the framework of the COMET K2 Center on Symbiotic Mechatronics, which is funded by the Austrian Federal Government, the State Upper Austria and by its Scientific and Industrial Partners.

References

- [1] Biedermann I., Scheidl R., Plöckinger A. (2011). A Linear Digital Hydraulic Amplifier, in: Proceedings of the Fourth Workshop on Digital Fluid Power, 21-22 September, 2011, Linz, Austria, pp. 75-89.
- [2] Scheidl, R., & Mittlböck, S. (2018). A hydraulic piloting concept of a digital cylinder drive for exoskeletons. In BATH/ASME 2018 Symposium on Fluid Power and Motion Control. American Society of Mechanical Engineers Digital Collection.
- [3] Scheidl, R., & Mittlböck, S. (2018). A mathematical analysis of a hydraulic binary counter for hydraulic exoskeleton actuation. International Journal of Hydromechanics, 1(2), 153-171.
- [4] Matthias Scherrer, Simon Mittlböck, Rudolf Scheidl, "Embodiment Design of a Hydraulic Binary Counter for Exoskeleton Use - Problems and New Solutions" : Proceedings of the 10th Workshop on Digital Fluid Power (DFP19), February 28th-March 1st 2019, Linz, Austria, 3-2019.
- [5] Matthias Scherrer, Erwin Hauser, Rudolf Scheidl, "Simulation study of permanent magnetic actuation for a hydraulic valve with hysteresis response behavior" : Proceedings of the 2020 ASME on Fluid Power and Motion Control FPMC2020 September 9-11, 2020, University of Bath, Bath, United Kingdom, 9-2020.

- [6] Linjama, M., Vihtanen, H. P., Sipola, A., Vilenius, M. (2009). Secondary controlled multi-chamber hydraulic cylinder. In The 11th Scandinavian International Conference on Fluid Power, SICFP (Vol. 9, pp. 2-4).
- [7] Norrhydro (2018). Amazing energy saving for hydraulic machines, <https://www.youtube.com/watch?v=qEUYtT-CWuo>, visited May, 12, 2018.
- [8] Dell'Amico A, Carlsson M., Norlin E., Sethson M. (2013). Investigation of a Digital Hydraulic Actuation System on an Excavator Arm. In 13th Scandinavian International Conference on Fluid Power; June 3-5; 2013; Linköping, Sweden, pp. 505-511.
- [9] Heybroek K. and Sahlman M. (2018) A hydraulic hybrid excavator based on multi-chamber cylinders and secondary control – design and experimental validation, International Journal of Fluid Power, DOI: 10.1080/14399776.2018.1447065

Simulating a high frequency piezo pump with disc reed valves

Nathan Sell , Andrew Plummer , Nigel Johnston , and Jonathan du Bois

Department of Mechanical Engineering, University of Bath, Bath, United Kingdom
E-mail: N.P.Sell@bath.ac.uk

Abstract

Piezo pumps provide an attractive alternative for driving small actuators (e.g. less than 100W) compared to traditional valve controlled cylinders powered by a central hydraulic supply. This provides the ability to distribute power electrically rather than hydraulically, which can bring both weight and efficiency savings. Currently the use of piezo pumps is severely limited by the maximum power and flows that can be provided. This paper documents the simulation of a new pump which makes use of disc type reed valves to rectify the flow generate by a single piezostack-driven piston. The proposed valves have the potential to overcome frequency limitations of more conventional poppet or ball type check valves. This enables the pump to operate at higher frequencies and thereby produce larger flows. Simulation results suggest that a pump capable of producing a no load flow in excess of 1L/min would be possible using an off-the-shelf piezo stack.

Keywords: Piezopump, micro-hydraulics, piezoelectrics, reed valve

1 Introduction

The application of an electrical field to a piezoelectric ceramic results in a strain being induced in the material. The magnitude of this strain depends on the specific piezoceramic strain coefficient and also the strength of the applied field. In practical applications this is around 0.1 to 0.15% [1]. Piezoelectric stacks consist of multiple layers of ceramic and electrodes and are commercially available with total lengths up to around 200mm giving strokes of around 300 μ m. The face area of the piezoceramic governs the force which it is capable of applying, and stacks with diameters of over 50mm are commercially available giving maximum forces of up to 70kN. This combination of high force and low stroke presents challenges in many applications which wish to take advantage of the small size, high reliability and lack of magnetic influence of piezoceramic actuators.

To overcome the stroke limitations various means of motion accumulation have been proposed. There are a number of commercially available mechanical accumulation methods including the PI walking drive (up to 125mm stroke and 0.75W output) [2], Noliac amplified actuators (upto 0.95mm stroke and 0.8W output) [3] and other methods currently being researched [4]. All these actuators generally have a maximum output power of less than 5W however meaning they are not competitive with even the smallest traditional hydraulic drives..

The piezoelectric pump concept (commonly contracted to “piezopump”), uses hydraulic motion accumulation instead of mechanical and has been shown to be capable of delivering larger powers. There are a number of different designs for piezopumps but all have a similar operating principle. A piezoelectric stack is used to drive a piston (or diaphragm) and a pair of valves are used to control the flow into and out of the piston chamber. Cycling the piston at high frequencies the small displacement can still result in appreciable amounts of flow. Figure 1 shows the operating cycle of a piezopump.

The operating cycle is made up of 4 stages. The first of these is the compression stage with the piezostack extending and compressing the fluid in the pumping chamber. When the pressure in the chamber is equal to that at the pump outlet the exhaustion stage begins as the outlet valve opens and any further extension of the piezostack is used to push fluid from the pumping chamber providing flow. Once the stack has reached the end of its stroke and begins retracting the expansion stage begins. As the stack retracts the pressure in the chamber drops towards the pressure at the inlet valve. When these pressures are equal the intake stage begins with the inlet valve opening and allowing fluid flow into the pumping chamber. As shown in Figure 1 there is often an accumulator on the pump inlet to both

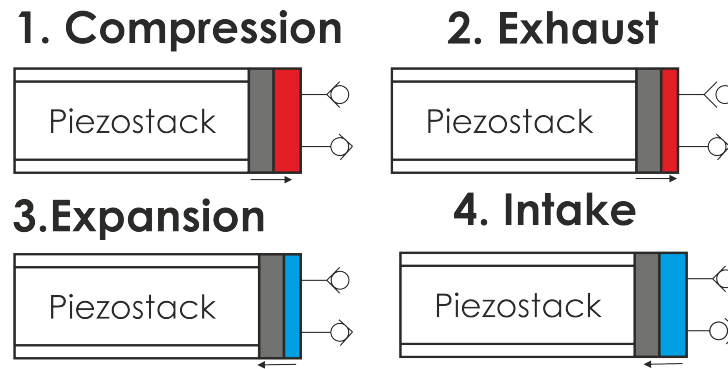


Figure 1: Operating principle of a piezopump

help with volume changes in the closed system (e.g. due to heating) and raise the net pressure of the circuit above atmospheric pressure in order to avoid cavitation at the inlet.

Small, low flow piezopumps (in the order of mL/s) are commercially available for applications such as medical dispensing [5] but currently only one commercially available unit with appreciable flow is known to exist [6].

An excellent review of piezopump technology was published by Chaudhuri and Wereley [7] in 2012. They suggest that most designs have 4 key limitations:

1. Actuator mechanical stiffness - if stiffer actuators were available then it should be possible to reduce the diameter of the actuators and still achieve the same blocking forces and thus reduce the size of piezopumps.
2. Fluid inertia and compressibility - as the driving frequency increases the inertia of the fluid becomes more important as it must be accelerated and decelerated each cycle. Given the small strokes associated with piezoactuators the compressibility of the working fluid also significantly limits pump performance as a considerable portion of the actuator stroke can be used compressing the fluid.
3. Bandwidth of driving circuits - performance may be limited by the ability of power electronics to provide full voltage at high frequencies.
4. Flow rectification using valves - Chaudhuri and Wereley argue that it is necessary to move towards active valves in order to increase operating frequency and therefore performance.

Since 2012 there have been a number of significant research papers including [8–15]. These papers suggest that instead of a movement to active valves as predicted by [7] researchers are starting to investigate reed valves and the possibility of using multiple discrete pumping units in order to achieve higher flows. The power electronics often proved to be a limiting factor suggesting that co-development of the pump and driver is likely to be required in order to significantly increase power.

This paper focuses on the simulation of a piezopump which features disc type check valves for both its inlet and outlet, and an off-the-shelf piezostack. The expected flow and pressure characteristics from such a device and frequency behaviour are predicted.

2 Piezopump modelling

2.1 Piezostack modelling

A Kinetic Ceramics D075080 stack is used in this simulation and its main parameters are given in Section 2.1.

The size was limited in order that commonly available amplifiers would be capable of driving the stack for future experimental work. The existence of hysteresis in piezoactuators is well documented and is simulated using the Bouc-Wen model [16] due to its tractability and ability to model a wide range of different hysteretic behaviours. Equation (1) shows this model where α, β and γ are tuneable parameters and x and z are the input and output respectively.

$$\dot{z} = \alpha \dot{x} - \beta |\dot{x}| |z|^{n-1} z - \gamma \dot{x} |z|^n \quad (1)$$

Table 1: D075080 stack parameters

Cross-sectional area	0.0003 m ²
Length	87mm
Maximum voltage	1000V
Free displacement (x_{max})	80 μ m
Blocking force (F_{block})	10kN
Capacitance	1.77 μ F
Natural Frequency	18kHz

A 10% effective voltage loss was assumed and the parameters set accordingly. The voltage available to drive the stack is converted to a force via a simple gain of 10N/V, and the force acting on the stack from the piston (due to pressure in the pump chamber) is subtracted from this force giving the total force available to extend the stack. The stack is then treated as a mass spring damper system with stack stiffness calculated as:

$$K_{piezo} = \frac{F_{block}}{x_{max}} \quad (2)$$

The stack is assumed to be critically damped (when fluid and seal damping are taken into account) and have an effective mass equal to 40% of the stacks actual mass [17]. The piston mass is added to this effective mass

The general form of the piezostack model is shown in Figure 2

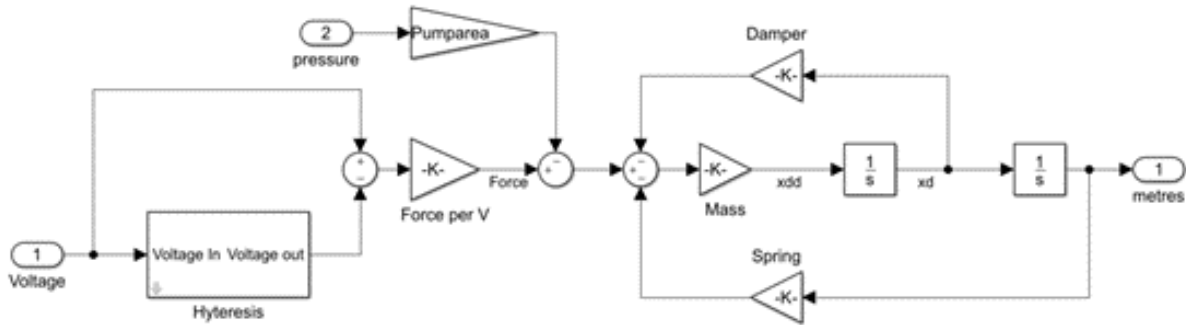


Figure 2: Piezoelectric actuator model

2.2 Pump chamber modelling

The displacement of this stack is assumed to be equal to the displacement of the piston. The sizing of the piston in piezopump is a trade off between flow and pressure performance. In the first instance the piston diameter will be assumed equal to the stack diameter but an exploration of its effect will be carried out. Multiplying the displacement of the stack by the area of the piston gives a volume change in the pumping chamber. This is combined with the volume change due to flow through the inlet (Q_{in}) and outlet (Q_{out}) valves to give a chamber volume change (ΔQ_{ch}) which can be multiplied by the pump stiffness (K_{pump}) to give a chamber pressure:

$$\Delta V_{ch} = x \cdot A_p - \int Q_{out} + \int Q_{in} \quad (3)$$

$$P_{ch} = K_{pump} \cdot \Delta V_{ch} \quad (4)$$

The pump stiffness is a combination of the fluid stiffness K_{fluid} , piezostack stiffness K_{piezo} and pump body radial K_{ra} and axial K_{ax} stiffness:

$$K_{fluid} = \frac{B}{V_{ch}} \quad (5)$$

$$K_{piezo} = \frac{k_{piezo}}{A_p^2} \quad (6)$$

$$K_{ra} = \frac{4E \cdot t}{\pi D_{ch}^3 L} \quad (7)$$

$$K_{ax} = \frac{E \pi D_{ch} t}{L A_{ch}^2} \quad (8)$$

$$K_{total} = \frac{1}{\frac{1}{K_{fluid}} + \frac{1}{K_{piezo}} + \frac{1}{K_{ra}} + \frac{1}{K_{ax}}} \quad (9)$$

where B is the bulk modulus of the working fluid and assumed to be 1.2GPa, V_{ch} is the initial volume of the pumping chamber which is another design trade-off that must be considered. Small chambers result in stiffer pumps (and therefore better performance) but they can also cause manufacturing or assembly difficulties and in the case of extremely small chambers severe flow restrictions from to the inlet and outlet valves. A chamber height of 5mm is chosen to balance these competing requirements. E is the Youngs modulus of the chamber wall material (assumed to be 207GPa for mild steel), t is the wall thickness (assumed to be 15mm)

2.3 Check Valve Modelling

The pressure in the pumping chamber dictates the opening on the passive disc reed valves whose flow rates are referenced in Equation (3). Currently it is assumed that the inlet and outlet check valves are identical and they are modelled to include the effects of valve and fluid inertia, valve bounce and context dependent opening times. The models are based on previous work conducted at Bath [18] for poppet type valves. Although disc reed valves will be used, experimentally derived coefficients are currently required in detailed reed valve models [19] making the models unsuitable for early investigations. It is proposed that a single-degree of freedom model with lumped mass and stiffness parameters is adequate, so that the disc reed valve can be treated in the same way as a poppet valve. 3 shows the diagram of the passive poppet type valve model.

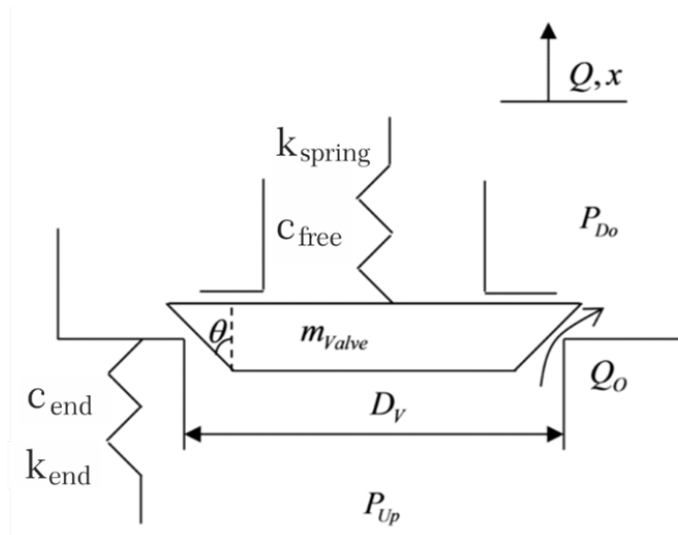


Figure 3: Check valve model [18]

The valve has a mass (m_{valve}) and is closed by a spring with linear stiffness (k_{spring}) and there is an associated damping (c_{free}):

$$c_{free} = 2\zeta \sqrt{k_{spring} m_{valve}} \quad (10)$$

When the valve reaches the end stop it is subject to a high stiffness (k_{stop}) and damping (c_{stop}) also changes as would be expected from Equation (10). The net force accelerating the the valve mass (F_{valve}) is a combination of

the spring and damper forces and the pressure difference across the valve face area. The net force can take one of three forms dependent upon the poppets position:

$$\begin{aligned} \text{Case 1 : valve fully open } (x \geq x_{stop}) \\ F_{valve} = A_{valve} C_f \Delta P - c_{stop} \dot{x} - k_{stop} (x - x_{stop}) - k_{spring} x - F_{pre} \end{aligned} \quad (11)$$

$$\begin{aligned} \text{Case 2 : valve partially open } (0 < x < x_{stop}) \\ F_{valve} = A_{valve} C_f \Delta P - c_{free} \dot{x} - k_{spring} x - F_{pre} \end{aligned} \quad (12)$$

$$\begin{aligned} \text{Case 3 : valve fully closed } (x \leq 0) \\ F_{valve} = A_{valve} C_f \Delta P - c_{stop} \dot{x} - k_{stop} x - k_{spring} x - F_{pre} \end{aligned} \quad (13)$$

where A_{valve} is the valve face area, C_f is the valve force coefficient and is a function of valve design and is fixed at 0.4 and F_{pre} is the preload force on the valve. Using this force the position of the check valve can be found from integrating:

$$\ddot{x} = \frac{F_{valve}}{m_{valve} + m_{fluid}} \quad (14)$$

where m_{fluid} is the “added mass” due to the fluid displaced as the valve moves. The flow through the valve is:

$$Q = Q_o + A_{valve} \cdot \dot{x} \quad (15)$$

$$(16)$$

where Q_o is the flow rate through the valve orifice, A_{valve} is the valve face area and \dot{x} is the velocity of the valve. A value for Q_o can be found by integration from the pressure change due to fluid inertia:

$$\Delta P_v = \frac{\rho}{2} \cdot \left(\frac{Q_o}{C_d \pi A_v} \right)^2 + \frac{\rho l}{a} \frac{dQ_o}{dt} \quad (17)$$

where ΔP_v is the pressure difference across the valve and so for the inlet valve is the pressure in the piston chamber minus the pressure at pump inlet, ρ is the fluid density (taken to be 850 kg/m^3), C_d is the valve discharge coefficient which is a function of valve design and assumed to be 0.72, l is the characteristic length of the fluid, and assumed to be the thickness of the valve and a is the valve opening area. An opening area lower limit of 1 mm^2 is set to model leakage and aid mathematical stability.

2.4 Reed Valve modifications

The actual form of the valve is shown in Figure 4.

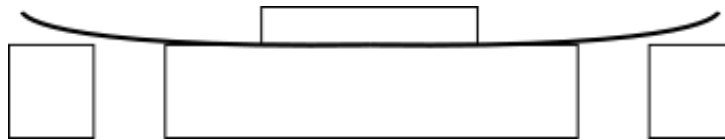


Figure 4: Disc type reed valve cross section

The valve opening area above will be calculated as:

$$a = \pi \cdot d_{orifice} \cdot x_{valve} \quad (18)$$

where x_{valve} is defined as the displacement of the disc at the outer edge of the annulus. The disc's mass is a function of its diameter:

$$m_{valve} = \frac{1}{3} A_{valve} (\rho_{valve} \cdot t_{valve} + \rho_{fluid} \cdot x_{valve}) \quad (19)$$

It is assumed that the deformation of the disc results in a triangular cross section and so the effective mass of the valve is a third of the valves mass plus the mass of fluid displaced by the valves motion. The stiffness of the disc can also be related to the dimensions of the valve by using Timoshenko's bending equation for a ring [20]. In order to apply this equation simplifications are made. Firstly it is assumed that all the opening force is located at the centre of the annulus. This is reasonable when the valve is closed. Secondly it is assumed that the centre of the ring is clamped. The tip displacement can then be calculated from:

$$x_{valve} = k_1 \frac{Pd_{orifice}^2}{2 \cdot Et_{valve}^3} \quad (20)$$

where k_1 is a coefficient dependent on the boundary conditions and ratio of valve diameter to hole diameter, E is the Young's modulus (assumed to be 207GPa). Using this displacement and the load force a stiffness can be found.

3 Sensitivity of pump performance to valve parameters

In order to investigate the effects of valve geometry it was initially assumed that an outer diameter equal to the piston diameter (19.5mm) and inner diameter of 6mm to allow for fastening of the valve to a seat and a thickness of $100\mu m$. It was assumed that the disc valves would be manufactured by chemical etching and as such they diameter of the disc could be easily adjusted but the thickness would be limited to standard sheet thicknesses.

Figure 5 shows the power delivered by the pump with different valve thicknesses. In order to measure this a small volume is connected to the pump's outlet and the pressure and flow through a $5 \times 10^{-5} m^2$ orifice connecting this volume back to the pump inlet is then calculated. The piezostack is excited by a 1kV sine wave at 1kHz.

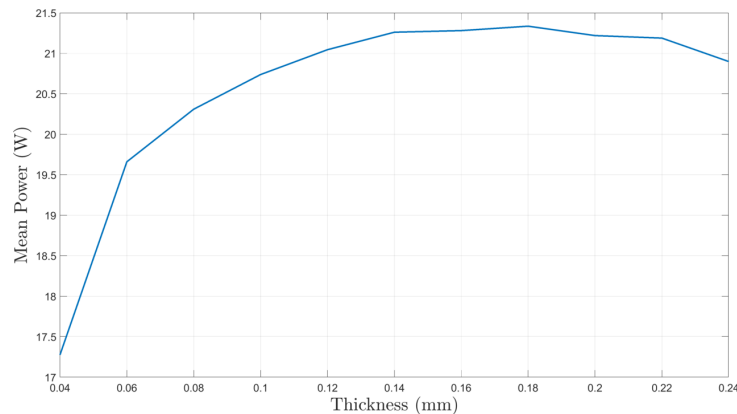


Figure 5: Effect of valve thickness on flow

A peak of 21W was found at 0.16mm with performance being reasonably consistent between 0.14mm and 0.22mm. As mentioned previously the valve thickness changes both stiffness and mass of the valve meaning the optimal flow conditions will be influenced by the operating frequency also. Operating the pump at 1kHz as this is sufficiently below the undamped natural frequency of the valve whilst also being in advance of frequencies attainable using traditional poppet style check valves. Looking at the effect of the valve outer diameter, Figure 6.

suggests that for a specific operating frequency there should exist an optimum set of valve dimensions and so a constrained optimisation was conducted on the valve thickness, inner and out diameters. This was carried out using the Matlab *fmincon* functions implementation of the interior-point algorithm [21]. The outer diameter was limited to 19mm in order to ensure the chamber volume was not increased and the ratio of inner diameter to outer diameter constrained to remain inside the range found in [20]. The minimum valve thickness was 0.1mm to ensure it could be etched from a standard sheet of metal which from Figure 5 is expected to be in the optimum range. Figure 7 shows the iteration history of this optimisation procedure where the aim is it maximise the mean pump power over its complete operating range from free flow to dead-headed.

The optimisation gave valve parameters of:

$$\begin{aligned} d_{valve} &= 12.3mm \\ h_{valve} &= 4.1mm \\ t_{valve} &= 100\mu m \end{aligned}$$

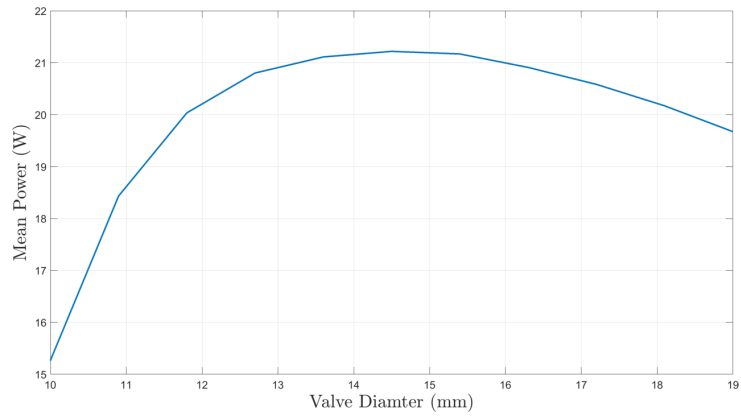


Figure 6: Effect of valve outer diameter on output power (100 μ m thickness)

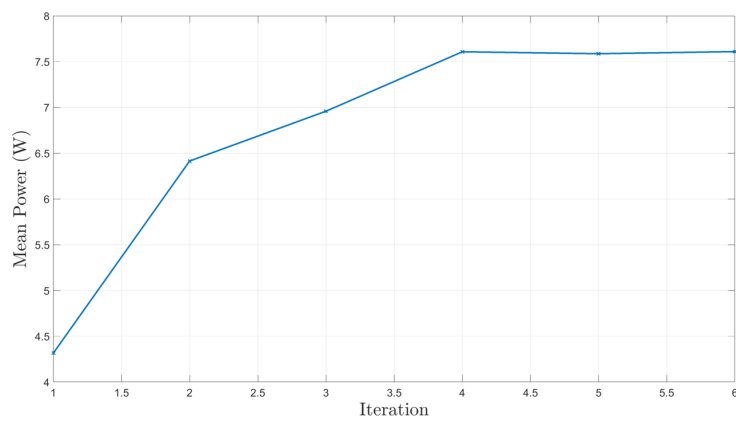


Figure 7: Optimisation of disc valve parameters

4 Performance of pump with optimised parameters

The simulated performance of the pump with these valve parameters at a range of driving frequencies and outlet pressures is shown in Figure 8.

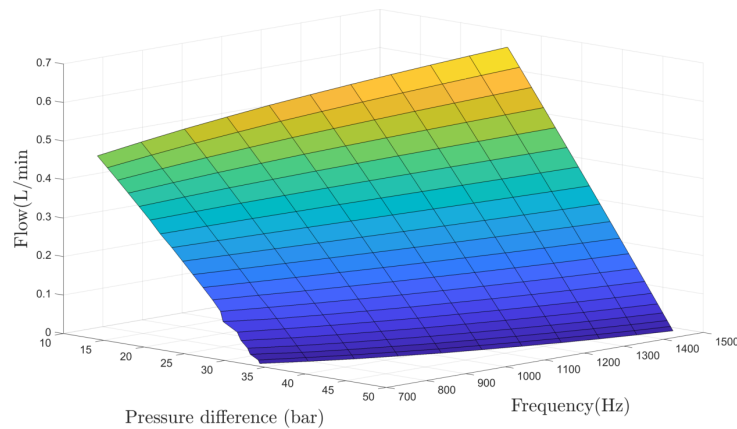


Figure 8: Simulated pressure flow behaviour of pump

As expected, the flow reduces with increasing pressure, due to reduction in stack displacement with increased force, and the need to overcome higher compressibility flow and the increase in performance as frequency increases drops off as the frequency itself increases. However, there is still some improvement in performance all the way up to 1500Hz suggesting that the valve bandwidth exceeds this.

5 Conclusions

The use of disc reed check valves offers a promising avenue to extend the operating frequency of piezo pumps, allowing them to be considered for higher power applications than previously possible. As a simple model for this style of valve does not exist, one is proposed based on previous work on poppet check valves and Timoshenko ring bending. The results of pump simulations using this model are promising, however, the model hasn't been validated and simplifies the bending of the valve into a simple tip deflection with no allowance for the deformed shape and so the exact numbers should be regarded with caution. However, it is clear that valve parameters such as disc diameter and thickness have a significant effect on pump performance. The flexibility and ease of prototyping given by chemical etching enables optimal disc valves to be manufactured for a particular size of pump. Preliminary experimental results confirm that this type of valve enables piezo pump operation at 1kHz or above; these results will be presented in a future publication.

References

- [1] Choi SB and Han YM. *Piezoelectric actuators: control applications of smart materials*. CRC Press, 2016.
- [2] LTD PI. Piezowalk actuators. <https://www.physikinstrumente.co.uk/en/products/linear-actuators/>. Accessed: 2020-04-08.
- [3] Noliac. Amplified actuators. <http://www.noliac.com/products/actuators/amplified-actuators/>. Accessed: 2020-04-08.
- [4] Tian X, Quan Q, Wang L et al. An inchworm type piezoelectric actuator working in resonant state. *IEEE Access* 2018; 6: 18975–18983.
- [5] Microfluidics D. Piezoelectric pump. <https://www.dolomite-microfluidics.com/product/piezoelectric-pump/>. Accessed: 2020-04-08.
- [6] Ceramics K. Solid-state pumps. <https://www.kineticceramics.com/products/solid-state-pumps/>. Accessed: 2020-07-15.
- [7] Chaudhuri A and Wereley N. Compact hybrid electrohydraulic actuators using smart materials: A review. *Journal of intelligent material systems and structures* 2012; 23(6): 597–634.
- [8] Larson JP and Dapino MJ. Reliable, high-frequency miniature valves for smart material electrohydraulic actuators. *Journal of intelligent material systems and structures* 2012; 23(7): 805–813.
- [9] Xuan Z, Jin T, Ha NS et al. Performance of piezo-stacks for a piezoelectric hybrid actuator by experiments. *Journal of intelligent material systems and structures* 2014; 25(18): 2212–2220.
- [10] Li Y, Le VT, Goo NS et al. High actuation force of piezoelectric hybrid actuator with multiple piezoelectric pump design. *Journal of Intelligent Material Systems and Structures* 2017; 28(18): 2557–2571.
- [11] Zhang Z, Chen S, Wang S et al. Performance evaluation and comparison of a serial–parallel hybrid multichamber piezoelectric pump. *Journal of Intelligent Material Systems and Structures* 2018; 29(9): 1995–2007.
- [12] Hwang JH, Bae JS, Hwang YH et al. Pressurization characteristics of a piezoelectric-hydraulic pump for uav brake systems. *International Journal of Aeronautical and Space Sciences* 2018; 19(3): 776–784.
- [13] Nguyen AP, Hwang JH, Hwang YH et al. Effect of check valve characteristics on flow rate of the small piezoelectric-hydraulic pump. *Journal of Aerospace System Engineering* 2018; 12(5): 54–68.
- [14] Woo J, Sohn DK and Ko HS. Experimental study on pressure pulsation in piezo driven reed valve pump. *Journal of Mechanical Science and Technology* 2019; 33(2): 661–667.
- [15] Woo J, Sohn DK and Ko HS. Performance and flow analysis of small piezo pump. *Sensors and Actuators A: Physical* 2020; 301: 111766.
- [16] Wen YK. Method for random vibration of hysteretic systems. *Journal of the engineering mechanics division* 1976; 102(2): 249–263.
- [17] Fox J and Mahanty J. The effective mass of an oscillating spring. *American Journal of Physics* 1970; 38(1): 98–100.
- [18] Johnston DN. Numerical modelling of reciprocating pumps with self-acting valves. *Proceedings of the institution of mechanical engineers, Part I: Journal of systems and control engineering* 1991; 205(2): 87–96.
- [19] Knutson AL and de Ven James D V. Modeling and experimental validation of disc and reed style check valves for hydraulic applications. In *Bath/ASME 2016 Symposium on Fluid Power and Motion Control*. ASME.
- [20] Timoshenko SP and Woinowsky-Krieger S. *Theory of plates and shells*. McGraw-hill, 1959.
- [21] Byrd RH, Hribar ME and Nocedal J. An interior point algorithm for large-scale nonlinear programming. *SIAM Journal on Optimization* 1999; 9(4): 877–900.

Multidimensional Trajectory Tracking for Numerically Stiff Independent Metering System

Goran Stojanoski , Dimitar Ninevski , Gerhard Rath , and Matthew Harker*

Chair of Automation, University of Leoben, Leoben, Austria

*Faculty of Engineering and Applied Science, Ontario Tech University, Ontario, Canada

E-mail: {goran.stojanoski, dimitar.ninevski, gerhard.rath}@unileoben.ac.at; matthew.harker@ontariotechu.ca

Abstract

This paper presents a new approach for solving an optimal control problem in a hydraulic system, using a variational calculus method. It uses a path tracking method of two different states with different units and of different magnitude. To ensure the uniqueness of the solution, two regularization terms were introduced, whose influence is regulated by regularization parameters. The system of differential equations, obtained from the Euler-Lagrange equations of the variational problem, was solved by a mass matrix method and discretized with linear differential operators at the interstitial points for numerical stability. This enabled the calculation of the control variables, despite the stiffness of the numerical problem. The results obtained show an energy-efficient performance and no oscillations. Finally, a Simulink model of the hydraulic system was created in which the calculated control variables were inserted as feed-forward inputs, to verify the results.

Keywords: Hydraulics, Optimal control, Independent metering, Euler-Lagrange.

1 Introduction

The theory of optimal control has existed for several centuries [1]. When applied to a hydraulic system, it dampens all vibrations at the end of the motion and still achieves the desired values [2]. However, due to the extremely non-linear dynamics its use in hydraulics is a challenge [3]. With the increasing demands for accuracy and performance in mining, especially for tunnel boring machines, the demand for new methods is also increasing. In addition, these new methods must deliver energy efficient control results and reduce the operating costs of the entire process. The new state of the art independent metering valves, which are an essential part of these systems, offer very flexible control strategies [4]. Since the valves move much faster than the natural frequency of the load system, the ODEs to be solved become numerically very stiff [5]. For this reason these systems cannot be solved with conventional solvers [6]. Rath in [5] shows that the use of exponential matrix results in unstable solutions for these type of systems. In this paper, the mass matrix method and interstitial derivatives are used to compute a stable numerical solution. Since tunnel boring machines have a given profile which has to be cut, optimal path tracking methods are suitable for these types of systems. Compared to conventional methods, optimal path tracking is often used for the navigation of mining equipment in mines. It increases efficiency and reduces working time, which in turn increases the safety of the process [7] [8]. In most cases, there is a given path that the system must follow [9] [10]. One of the methods that is frequently used is model predictive control (MPC) [11] [12] because it can take the constraints of the system into account [13]. Wang in [14] improves the efficiency of the ant colony algorithm to find the optimal path for barrier environments of varying complexity. Path tracking is also frequently used for control of multi-dimensional hydraulic manipulators. In [15], the trajectory of a one-armed hydraulic manipulator is tracked by a digital hydraulic system. Kalaiarassan also shows that the 5-bit digital flow control unit performs much better than the 4-bit system. Rudolfson [16] solves the kinematics of a crane for operation in the vertical plane. He uses the inverse to compensate and identify the non-linearity of the static dead zone input signals. A global least

squares method is used in [17] to determine the optimal control input for multi-dimensional path tracking of a hydraulic crane driven by electric drives. In [18], a new control law based on the sliding perturbation observer (SPO) is designed. Here the SPO is used to eliminate all disturbances that come from the environment, dynamic uncertainties and modeling errors. Chin in [19] presents a new type of contour tracking control which uses the force calculation for hydraulic parallel manipulators. Zhang in [20] uses the D-H (Denavit - Hartenberg) method to set the coordinates for the path of a hydraulic excavator. On the other hand, Kang [21] uses a PD controller with dead zone compensation to track the three-dimensional path. However, all of the above methods focus on tracking one or more parameters which have the same unit and magnitude and, in most cases, the position of the given system is tracked. Tunnel boring machines have very complex hydraulic circuits. In the case presented here, the valve is equipped with pressure and flow controllers that actuate the system. Since the external forces are very high, the set pressure value at the pressure controller is usually very high. This will increase the mechanical stiffness of the hydraulic system which in turn increases the mechanical stiffness of the overall system. However, the PID controllers normally used in these valves show a very oscillating behavior when the value of the pressure changes. In [22] it is shown that different pressure values during a motion can lead to an improved energy performance of these systems. The method proposed in this paper, which is based on the theory of optimal control, solves the tracking problem as a boundary value problem by means of variational calculus. The method is then applied to a simulated model of the actual system in order to show its potential.

The contributions of this paper are:

1. A novel linearized state space model for the system presented in fig. 1 is derived. For the first time the embedded valve controllers (flow and pressure) and the position controller (responsible for the position of the large mass) are included in the state space system.
2. A new method for multidimensional trajectory tracking of parameters with different units and magnitudes is presented on the basis of calculus of variations.
3. The mass matrix method and interstitial derivatives are used to calculate a stable numerical solution for this stiff numerical problem.
4. A simulation in Matlab Simulink is performed to verify the proposed control scheme.

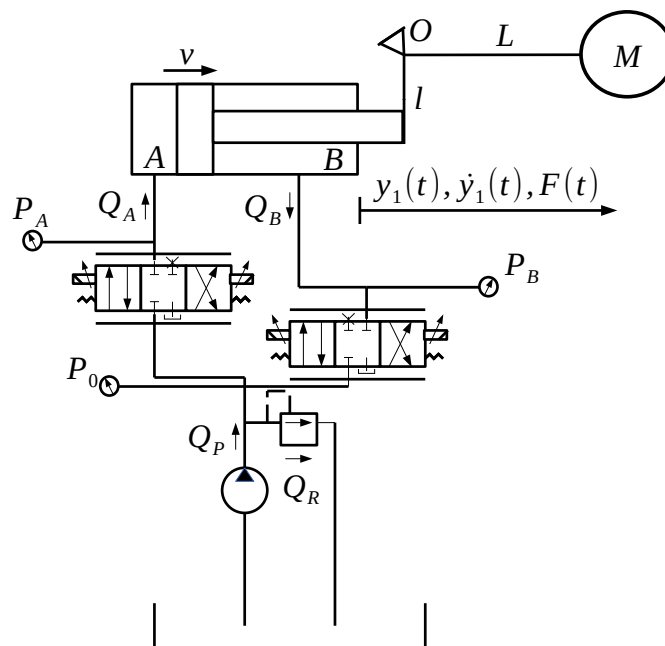


Figure 1: Simplified model of the hydraulic and mechanical system. The mechanical system is position controlled. The hydraulic system consist of two independent metering valves which are flow controlled (piston side) and pressure controlled (rod side). Auxiliary components, like pressure compensators and load sensing are not shown in this figure.

The results show that the system can always achieve the desired paths for position and pressure. Furthermore, despite the pressure changes significantly, there are no oscillations present during the motion.

2 SYSTEM MODEL

2.1 Mechanical System

The mechanical system consists of a large mass rotating around a point O (fig. 1) with a lever of length L . The hydraulic cylinder exerts the force F on a smaller lever of length l . If we assume that the system makes small movements around the fulcrum O, the effective mass of the system is

$$m = \left(\frac{l}{L}\right)^2 M. \quad (1)$$

If the position of the mass m in fig. 1 is labeled as y_1 , the equation of motion will have the form

$$m\ddot{y}_1 = P_A A_A - P_B A_B - b\dot{y}_1. \quad (2)$$

2.2 Hydraulic System

The hydraulic part of the system consists of a hydraulic pump, two independent metering valves and a hydraulic actuator. In this system the friction consists of several components. The oil flow through the valve orifice depends on the pressure which can cause damping. In addition, the movement of the load and the steel structure also contribute to the overall friction. The hydraulic cylinder has a highly non-linear friction behavior. A complete mathematical model of friction includes the Stribeck and stiction effect as well as Coulomb and viscous friction [23]. In the actual machine however, the greatest contribution comes from the rotating load that performs a cutting operation. Therefore, in eq. (2) the friction is assumed to be viscous with coefficient b .

2.3 Dynamics of the system

The displacement of the mechanical system is controlled by a position controller which actuates the two independent metering valves. The valves offer different operating modes for different load scenarios [4]. In this case it is assumed that the load on the system is passive when the movement is positive. This means that the actuating side of the system is flow controlled and the rear side is pressure controlled. The flows supplied by the valves are a function of the spool movement x_v and the pressures P_A, P_B [24],

$$Q_A = C_{q1} x_{v1} - C_{p1} P_A, \quad Q_B = C_{q2} x_{v2} + C_{p2} P_B \quad (3)$$

where $C_{q1}, C_{q2}, C_{p1}, C_{p2}$ are the valve linearization coefficients and x_{v1}, x_{v2} are the valves' spool positions. If eq. (3) is combined with the equations for the flow through the cylinder [25] the pressure equations are obtained:

$$P_A = \frac{C_{q1} x_{v1} - A_A v}{\frac{V_A}{\beta} s + C_{p1}}, \quad P_B = \frac{A_B v - C_{q2} x_{v2}}{\frac{V_B}{\beta} s + C_{p2}}, \quad (4)$$

where β is the bulk modulus of the oil, V_A and V_B the volumes and A_A and A_B the areas of the cylinder chambers. After deriving the linearized equations for the valve actuator system eq. (4), the controllers of the system can be applied. The independent metering valves presented in fig. 1 react much faster compared to the natural frequency of the load system. For this reason, no flow controller is implemented into the system in fig. 2. Here k_A and k_B are the proportional parts of the PID controllers for both sides. The system shown in fig. 2 is governed in state space form with mass matrix Π by the following equations

$$\Pi \dot{x}(t) = Ax(t) + Bu(t) \quad (5)$$

where,

$$\Pi = \begin{bmatrix} \frac{1}{\beta} & 0 & 0 & 0 \\ 0 & \frac{1}{\beta} & 0 & 0 \\ 0 & 0 & 1 & 0 \\ 0 & 0 & 0 & m \end{bmatrix}, x = \begin{bmatrix} P_A \\ P_B \\ y_1 \\ v \end{bmatrix}, u = \begin{bmatrix} y_{set} \\ P_{Bset} \end{bmatrix} \quad (6)$$

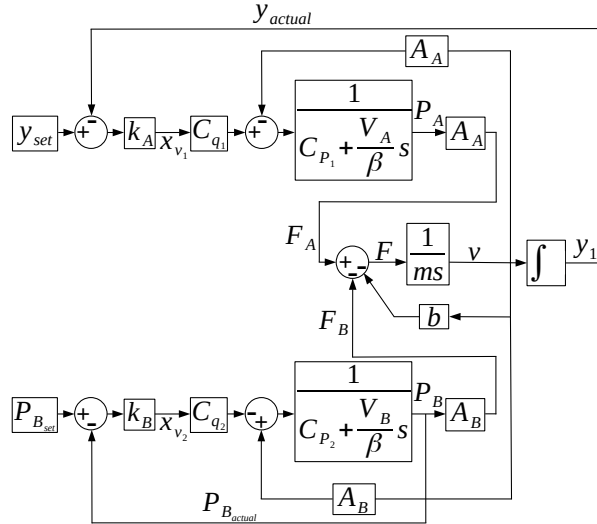


Figure 2: State of the art block diagram for the system presented in fig. 1. The system is controlled on both sides, where y_{set} and $P_{B,set}$ are the desired position and pressure values. Here k_A and k_B are the proportion parts of the PID controllers for both sides accordingly.

$$A = \begin{bmatrix} -C_{p1} \frac{\beta}{V_A} & 0 & -k_A C_{q1} \frac{\beta}{V_A} & -A_A \frac{\beta}{V_A} \\ 0 & -(k_B C_{q2} + C_{p2}) \frac{\beta}{V_B} & 0 & -A_B \frac{\beta}{V_B} \\ 0 & 0 & 0 & 1 \\ \frac{A_A}{m} & -\frac{A_B}{m} & 0 & -\frac{b}{m} \end{bmatrix} \quad (7)$$

$$B = \begin{bmatrix} k_A C_{q1} \frac{\beta}{V_A} & 0 \\ 0 & -k_B C_{q2} \frac{\beta}{V_B} \\ 0 & 0 \\ 0 & 0 \end{bmatrix} \quad (8)$$

In eq. (6), eq. (7) and eq. (8) the value of the bulk modulus β and the mass m are on both sides of the equations. Since β and m have very high values, a fraction of these values was stored in the mass matrix to ensure a numerically stable solution.

3 Solution of the problem

The path tracking problem can be formulated as determining the input vector u , so that a desired output of the system is achieved. This problem can be formulated in terms of variational calculus, as finding the optimal input vector u for which the cost function

$$\frac{\mu_1^2}{2} \int_{t_0}^{t_f} (x_2(t) - \xi_2(t))^2 dt + \frac{\mu_2^2}{2} \int_{t_0}^{t_f} (x_3(t) - \xi_1(t))^2 dt \quad (9)$$

is minimized. Note that because of the way the vector u is defined, x_2 tracks ξ_2 and x_3 tracks ξ_1 . The integrals quantify the least-squares differences between the states $x_2(t), x_3(t)$ and the desired paths $\xi_2(t), \xi_1(t)$ respectively. Since the states $x_2(t), x_3(t)$ are measured in different units of different magnitude, Pa and m respectively, a normalization of the least squares differences is necessary. This is done with the parameters μ_1, μ_2 . The previous equation can be rewritten as

$$\frac{\mu_1^2}{2} \int_{t_0}^{t_f} (e_2^T x(t) - \xi_2(t))^2 dt + \frac{\mu_2^2}{2} \int_{t_0}^{t_f} (e_3^T x(t) - \xi_1(t))^2 dt, \quad (10)$$

where $e_2 = [0 \ 1 \ 0 \ 0]^T$ and $e_3 = [0 \ 0 \ 1 \ 0]^T$ are coordinate unit vectors. In order to get a unique solution, a regularization parameter is also necessary [26], which in the case discussed here looks as follows:

$$\frac{\mu_3^2}{2} \int_{t_0}^{t_f} \dot{u}^T(t) \dot{u}(t) dt + \frac{\mu_4^2}{2} \int_{t_0}^{t_f} \ddot{u}^T(t) \ddot{u}(t) dt. \quad (11)$$

Finally, the functional which needs to be minimized will have the following form:

$$\begin{aligned}
J(x(t), u(t), \lambda(t)) = & \\
& \frac{\mu_1^2}{2} \int_{t_0}^{t_f} (e_2^T x(t) - \xi_2(t))^2 dt + \frac{\mu_2^2}{2} \int_{t_0}^{t_f} (e_3^T x(t) - \xi_1(t))^2 dt \\
& + \frac{\mu_3^2}{2} \int_{t_0}^{t_f} \dot{u}^T(t) \dot{u}(t) dt + \frac{\mu_4^2}{2} \int_{t_0}^{t_f} \ddot{u}^T(t) \ddot{u}(t) dt \\
& - \int_{t_0}^{t_f} \lambda^T(t) (\Pi \dot{x}(t) - Ax(t) - Bu(t)) dt
\end{aligned} \tag{12}$$

In eq. (12) only the ratio $\mu_1 : \mu_2 : \mu_3 : \mu_4$ is relevant, thus one of the parameters can be set arbitrarily. That is why μ_1 is set to be 1. The Euler-Lagrange equations [27] for this variational problem are as follows:

$$\begin{aligned}
e_2 e_2^T x - e_2 \xi_2 + \mu_2^2 e_3 e_3^T x - \mu_2^2 e_3 \xi_1 + A^T \lambda + \Pi^T \dot{\lambda} &= 0. \\
B^T \lambda - \mu_3^2 \ddot{u} + \mu_4^2 u^{(4)} &= 0 \\
\Pi \dot{x}(t) + Ax(t) + Bu(t) &= 0.
\end{aligned} \tag{13}$$

From these three equations the following system of differential equations is derived:

$$\begin{aligned}
\Pi^T \dot{\lambda} &= -E_{23}x + e_2 \xi_2 + \mu_2^2 e_3 \xi_1 - A^T \lambda \\
u^{(4)} &= -\frac{1}{\mu_4^2} B^T \lambda + \frac{\mu_3^2}{\mu_4^2} \ddot{u} \\
\Pi \dot{x}(t) &= Ax(t) + Bu(t)
\end{aligned} \tag{14}$$

where

$$E_{23} = e_2 e_2^T + \mu_2^2 e_3 e_3^T. \tag{15}$$

These equations can be written compactly in matrix form as:

$$\Pi_1 \dot{\gamma}(t) - V \gamma(t) - W \xi(t) = 0 \tag{16}$$

where

$$\begin{aligned}
\Pi_1 &= \begin{bmatrix} \Pi & 0 & 0 & 0 & 0 & 0 \\ 0 & \Pi^T & 0 & 0 & 0 & 0 \\ 0 & 0 & I & 0 & 0 & 0 \\ 0 & 0 & 0 & I & 0 & 0 \\ 0 & 0 & 0 & 0 & I & 0 \\ 0 & 0 & 0 & 0 & 0 & I \end{bmatrix}, \gamma(t) = \begin{bmatrix} x(t) \\ \lambda(t) \\ u(t) \\ \dot{u}(t) \\ \ddot{u}(t) \\ u^{(3)}(t) \end{bmatrix}, \xi = \begin{bmatrix} \xi_1 \\ \xi_2 \end{bmatrix}, \\
V &= \begin{bmatrix} A & 0 & B & 0 & 0 & 0 \\ -E_{23} & -A^T & 0 & 0 & 0 & 0 \\ 0 & 0 & 0 & I & 0 & 0 \\ 0 & 0 & 0 & 0 & I & 0 \\ 0 & 0 & 0 & 0 & 0 & I \\ 0 & -\frac{1}{\mu_4^2} B^T & 0 & 0 & \frac{\mu_3^2}{\mu_4^2} I & 0 \end{bmatrix}, W = \begin{bmatrix} 0 & 0 \\ e_2 & \mu_2^2 e_3 \\ 0 & 0 \\ 0 & 0 \\ 0 & 0 \\ 0 & 0 \end{bmatrix}.
\end{aligned} \tag{17}$$

3.1 Numerical Solution

Transposing eq. (16) one gets,

$$\dot{\gamma}^T(t) \Pi_1^T - \gamma^T(t) V^T - \xi^T(t) W^T = 0 \tag{18}$$

Now, for this system, the input vector is known (because it consists of the desired output) and can be solved numerically by discretizing with the methods described in [28]. The methods can be described as follows: note first that any state can be discretized directly as a vector,

$$\gamma_k = [\gamma_k(s_0) \quad \gamma_k(s_1) \quad \dots \quad \gamma_k(s_f)]^T \tag{19}$$

or, if the discretization is done at the interstitial points (the points t_i , between the samples s_i), one gets

$$\begin{bmatrix} \gamma_k(t_1) \\ \gamma_k(t_2) \\ \vdots \\ \gamma_k(t_f) \end{bmatrix} = J_0 \begin{bmatrix} \gamma_k(s_0) \\ \gamma_k(s_1) \\ \vdots \\ \gamma_k(s_f) \end{bmatrix} \quad (20)$$

$$J_0 = \frac{1}{16} \begin{bmatrix} 5 & 15 & -5 & 1 & 0 & \dots & 0 & 0 & 0 & 0 \\ -1 & 9 & 9 & -1 & 0 & \dots & 0 & 0 & 0 & 0 \\ 0 & -1 & 9 & 9 & -1 & \dots & 0 & 0 & 0 & 0 \\ \vdots & \vdots & \vdots & \vdots & \vdots & \ddots & \vdots & \vdots & \vdots & \vdots \\ 0 & 0 & 0 & 0 & 0 & \dots & -1 & 9 & 9 & -1 \\ 0 & 0 & 0 & 0 & 0 & \dots & 1 & -5 & 15 & 5 \end{bmatrix} \quad (21)$$

Using this, any vector of states γ can be discretized as a matrix in the following way

$$\Gamma^T = \begin{bmatrix} \gamma_1^T \\ \gamma_2^T \\ \vdots \\ \gamma_n^T \end{bmatrix} = \begin{bmatrix} \gamma_1(s_0) & \gamma_1(s_1) & \dots & \gamma_1(s_f) \\ \gamma_2(s_0) & \gamma_2(s_1) & \dots & \gamma_2(s_f) \\ \vdots & \vdots & \ddots & \vdots \\ \gamma_n(s_0) & \gamma_n(s_1) & \dots & \gamma_n(s_f) \end{bmatrix} J_0^T \quad (22)$$

Additionally, the derivative of a state can be discretized as

$$\dot{\gamma}_k \approx D\gamma_k, \quad (23)$$

where D is a differentiation matrix, with the following form

$$D = \frac{1}{24h} \begin{bmatrix} -23 & 21 & 3 & -1 & 0 & \dots & 0 & 0 & 0 & 0 \\ 1 & -27 & 27 & -1 & 0 & \dots & 0 & 0 & 0 & 0 \\ 0 & 1 & -27 & 27 & -1 & \dots & 0 & 0 & 0 & 0 \\ \vdots & \vdots & \vdots & \vdots & \vdots & \ddots & \vdots & \vdots & \vdots & \vdots \\ 0 & 0 & 0 & 0 & 0 & \dots & 1 & -27 & 27 & -1 \\ 0 & 0 & 0 & 0 & 0 & \dots & 1 & -3 & -21 & 23 \end{bmatrix} \quad (24)$$

where it is assumed that the discretization is done uniformly with step size h . Hence, a vector of first derivatives of states can be discretized as the following matrix

$$\Gamma^T = \begin{bmatrix} \dot{\gamma}_1^T \\ \dot{\gamma}_2^T \\ \vdots \\ \dot{\gamma}_n^T \end{bmatrix} = \begin{bmatrix} \gamma_1(s_0) & \gamma_1(s_1) & \dots & \gamma_1(s_f) \\ \gamma_2(s_0) & \gamma_2(s_1) & \dots & \gamma_2(s_f) \\ \vdots & \vdots & \ddots & \vdots \\ \gamma_n(s_0) & \gamma_n(s_1) & \dots & \gamma_n(s_f) \end{bmatrix} D^T \quad (25)$$

Finally, the discretized form of eq. (18) is

$$D\Gamma\Pi_1^T - J_0\Gamma V^T - J_0\Xi W^T = 0. \quad (26)$$

where Γ and Ξ are the matrices derived from the discretization of γ and ξ respectively. For more details, see [28,29]. Finally vectorizing the last equation, one gets

$$(\Pi_1 \otimes D - V \otimes J_0) \text{vec}(\Gamma) = (W \otimes J_0) \text{vec}(\Xi) \quad (27)$$

which is a linear system of equations and can be solved using standard methods for linear systems of equations, along with appropriate constraints (SVD, QR decomposition). In order to get a unique solution, an appropriate number of initial and final conditions need to be defined. From the system of 16 differential equations eq. (18), a

total of 16 initial and boundary conditions are given. ¹

$$\begin{aligned}
 \gamma_1(t_0) &= 0 \\
 \gamma_1(t_f) &= 0 & \gamma_{4-8}(t_0) &= 0 & \gamma_{10}(t_0) &= \xi_1(t_0) \\
 \gamma_2(t_0) &= \xi_2(t_0) & \gamma_{4-8}(t_f) &= 0 & \gamma_{10}(t_f) &= \xi_1(t_f) \\
 \gamma_2(t_f) &= \xi_2(t_f) & \gamma_9(t_0) &= \xi_2(t_0) & \gamma_{11-16}(t_0) &= 0 \\
 \gamma_3(t_0) &= \xi_1(t_0) & \gamma_9(t_f) &= \xi_2(t_f) & \gamma_{11-16}(t_f) &= 0 \\
 \gamma_3(t_f) &= \xi_1(t_f)
 \end{aligned} \tag{28}$$

The values in eq. (28) represent the real physical values of the tracked paths.

4 COMPUTATION AND RESULTS

4.1 Computation

The results of the path tracking algorithm were computed for an effective mass of $m = 4 \cdot 10^5$ kg, cylinder areas $A_A = A_B = 6 \cdot 10^{-2} \text{ m}^2$, friction parameter $b = 1.4 \cdot 10^7 \frac{\text{NS}}{\text{m}}$ and a bulk modulus of $\beta = 1.4 \cdot 10^9$ Pa. The value for the friction parameter b was identified during a cutting experiment. Furthermore, the values for the linearized terms C_{q1}, C_{q2}, C_{p1} and C_{p2} were calculated for the supply pressure of $300 \cdot 10^5$ Pa and it is assumed that the initial values for the pressures on the both sides will be $10 \cdot 10^5$ Pa. An oblique rectangular shape was chosen as the reference path for the pressure. This increased the overall stiffness of the system during the motion. For the position we have chosen a path that is followed by one of the cutting arms of the real machine. Due to the different dimensions and magnitudes of the two tracked states, the values of the normalization parameter μ_2 was assumed to be $\mu_2 = 10^4$. The values of μ_3 and μ_4 were experimentally determined to be $5 \cdot 10^{-5}$. The path tracking algorithm was firstly computed in MATLAB, where the control variables u_1 and u_2 were calculated. Then the system presented in fig.

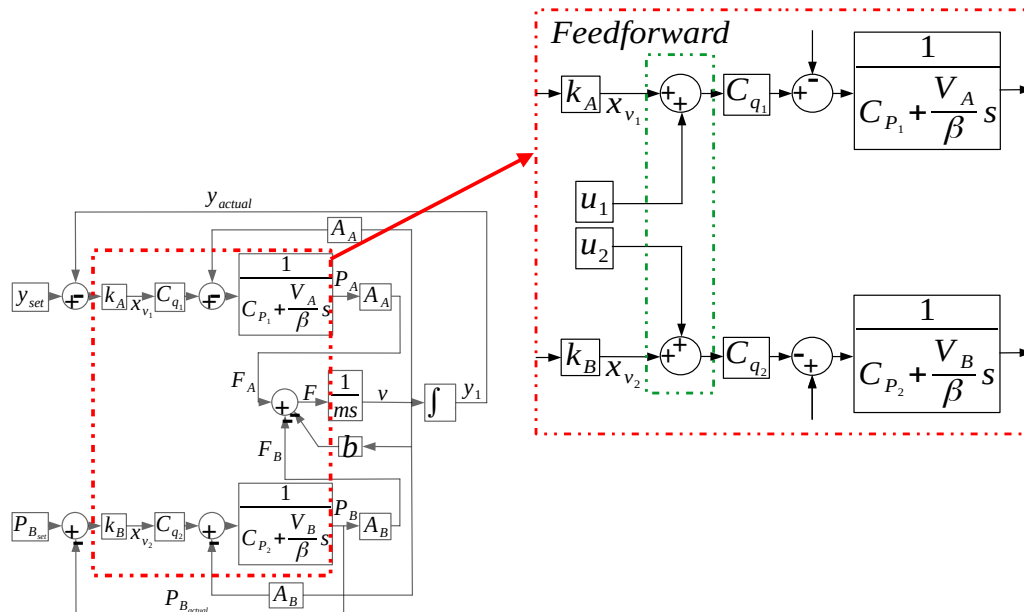


Figure 3: Implementation of the calculated control variables u_1 and u_2 into the simulation model of the system as a feed-forward.

2 was simulated in MATLAB Simulink where the control variables were inserted as feed forward inputs to the system (see fig. 3).

¹Due to the fact that some of the conditions are on the Lagrangian multiplier λ , only the conditions for the control variables need to be defined.

4.2 Results

The system presented in fig. 1 was simulated for two different time intervals, namely for $t \in [0,4]s$ and for $t \in [0,8]s$. In fig. 4 it can be seen that the system is following the given trajectories smoothly and precisely. The

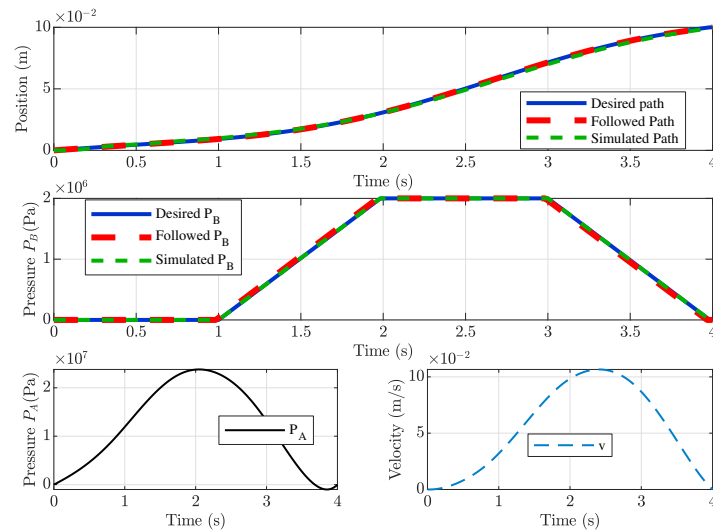
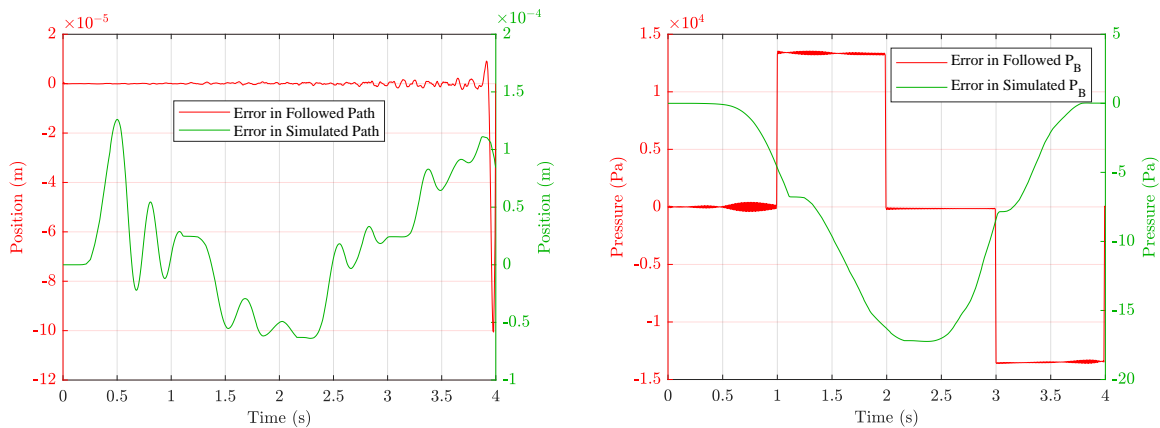


Figure 4: (Top and middle graph) - Results of the path tracking algorithm for time $t \in [0,4]s$. The states x_3 and x_2 (position and pressure respectively) are being tracked. The followed values and the simulated values deviate only slightly from the desired values. (Bottom graphs) - The behavior of the remaining two states of the system.

maximum value of the pressure on the rod side is set to $20 \cdot 10^5$ Pa. This increases the mechanical stiffness of the hydraulic system which will increase the mechanical stiffness of the overall system. Although the pressure



(a) Error curves for the followed and simulated positions in fig. 4. (b) Error curves for the followed and simulated pressures in fig. 4.

Figure 5: Error curves for the followed and simulated positions (left graph) and pressures (right graph) in fig. 4 accordingly. The maximum offset for the path tracking method is smaller than 1 %.

changes frequently during the time interval, there are no oscillations in the solution. This is not the case when using conventional controllers. The same applies for the position. The system reaches its maximum speed near the middle point of the path, demonstrating the energy efficient performance of this method. To be able to observe the accuracy of the new method, the error was observed for both the position and the pressure in fig. 5. It can be seen that the maximum offset for the position and the pressure is smaller 0.01 % and 1 % accordingly. This shows that the path tracking method has a very high accuracy. On the other hand in fig. 6, the system follows the same path for position and pressure but in double the time. Accordingly, the pressure on the piston side and the velocity are much smaller than in fig. 4. From fig. 7 it can be seen that the path tracking method shows even higher accuracy for longer paths. The maximum errors are in the magnitude of 0.005 %.

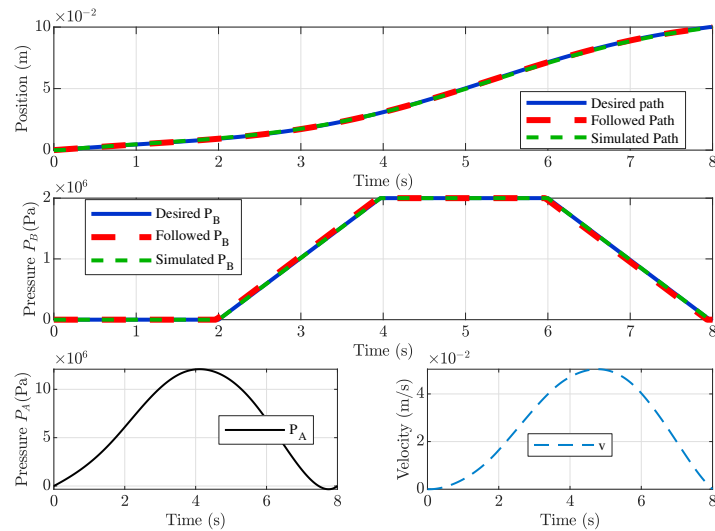
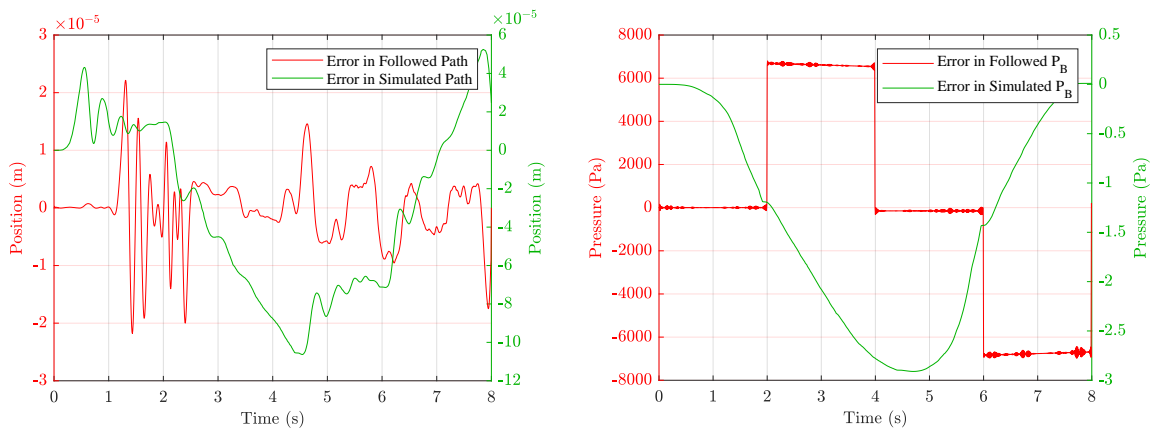


Figure 6: (Top and middle graph) - Results of the path tracking algorithm for time $t \in [0, 8]$ s. The states x_3 and x_2 (position and pressure respectively) are being tracked. (Bottom graphs) - The system is tracking the same distance over a longer period of time, which results in smaller pressure values on the piston side and a decreased velocity.



(a) Error curves for the followed and simulated positions in fig. 6

(b) Error curves for the followed and simulated pressures in fig. 6

Figure 7: Error curves for the followed and simulated positions and pressures in fig. 6 accordingly. Here the path tracking method shows maximum offset of 0.005 %.

5 CONCLUSIONS AND FUTURE WORKS

5.1 Conclusions

From the results obtained it can be concluded that the path tracking method can be used successfully to track states in different units and of different magnitudes. The calculated control variables, which were later used as feed forward inputs for the simulated system, provided paths with very small offset from the desired and the followed ones. Furthermore, the behavior of the other two states shows that the method is energy efficient for both tested scenarios.

5.2 Future Works

In this paper we use the mass matrix method and the interstitial derivatives to find stable numerical solution to a stiff numerical problem. Further we have implemented only P (proportional part of PID) controllers on the pressure and flow controlled side. In practice however, the valves have also I (integral part of PID) controllers. The numerical solution of the integro-differential equations for these systems could be a question of future work. Additionally, the further implementation of this method on the real system is of great interest.

References

- [1] H.J. Sussmann and J.C. Willems. 300 years of optimal control: from the brachistochrone to the maximum principle. *IEEE Control Systems*, 17(3):32–44, 1997.
- [2] Gerhard Rath and Emil Zaev. Optimal Control for Hydraulic System With Separate Meter-in and Separate Meter-Out. *The 15th Scandinavian International Conference on Fluid Power, SICFP'17, June 7-9, 2017, Linköping, Sweden*, pages 125–134, 2017.
- [3] Randal W. Bea. Successive Galerkin approximation algorithms for nonlinear optimal and robust control. *International Journal of Control*, 71(5):717–743, 1998.
- [4] B Eriksson and J-O Palmberg. Individual metering fluid power systems: challenges and opportunities. *Proceedings of the Institution of Mechanical Engineers, Part I: Journal of Systems and Control Engineering*, 225(2):196–211, 2011.
- [5] G Rath, M Harker, and E Zaev. Direct numerical solution of stiff ODE systems in optimal control. In *2017 6th Mediterranean Conference on Embedded Computing (MECO)*, pages 1–5, 2017.
- [6] Lawrence F. Shampine and Mark W. Reichelt. *The MATLAB ode suite*, volume 18. 1997.
- [7] B.J. Alshaer, T.T. Darabseh, and M.A. Alhanouti. Path planning, modeling and simulation of an autonomous articulated heavy construction machine performing a loading cycle. *Applied Mathematical Modelling*, 37(7):5315–5325, 2013.
- [8] B.J. Alshaer, T.T. Darabseh, and A.Q. Momani. Modelling and control of an autonomous articulated mining vehicle navigating a predefined path. *International Journal of Heavy Vehicle Systems*, 21(2):152, 2014.
- [9] Xuewu Ji, Yulong Liu, Xiangkun He, Kaiming Yang, Xiaoxiang Na, Chen Lv, and Yahui Liu. Interactive Control Paradigm-Based Robust Lateral Stability Controller Design for Autonomous Automobile Path Tracking With Uncertain Disturbance: A Dynamic Game Approach. *IEEE Transactions on Vehicular Technology*, 67(8):6906–6920, 2018.
- [10] Hans Andersen, Zhuang Jie Chong, You Hong Eng, Scott Pendleton, and Marcelo H. Ang. Geometric path tracking algorithm for autonomous driving in pedestrian environment. In *2016 IEEE International Conference on Advanced Intelligent Mechatronics (AIM)*, pages 1669–1674. IEEE, 2016.
- [11] Guoxing Bai, Li Liu, Yu Meng, Weidong Luo, Qing Gu, and Baoquan Ma. Path tracking of mining vehicles based on nonlinear model predictive control. *Applied Sciences (Switzerland)*, 9(7), 2019.
- [12] Jie Ji, Amir Khajepour, Wael William Melek, and Yanjun Huang. Path Planning and Tracking for Vehicle Collision Avoidance Based on Model Predictive Control With Multiconstraints. *IEEE Transactions on Vehicular Technology*, 66(2):952–964, 2017.
- [13] J M Maciejowski. *Predictive Control with Constraints*. Prentice Hall, England., 2002.
- [14] Tao Wang, Lianyu Zhao, Yunhui Jia, and Jutao Wang. Robot Path Planning Based on Improved Ant Colony Algorithm. In *2018 WRC Symposium on Advanced Robotics and Automation (WRC SARA)*, pages 70–76. IEEE, 2018.
- [15] G. Kalaiarassan and K. Krishnamurthy. Digital hydraulic single-link trajectory tracking control through flow-based control. *Measurement and Control (United Kingdom)*, 52(7-8):775–787, 2019.
- [16] Morten H. Rudolfson, Teodor N. Aune, Oddgeir Auklend, Leif Tore Aarland, and Michael Ruderman. Identification and Control Design for Path Tracking of Hydraulic Loader Crane. *IEEE/ASME International Conference on Advanced Intelligent Mechatronics, AIM*, pages 565–570, 2017.
- [17] Johannes Handler, Matthew Harker, and Gerhard Rath. Multidimensional Path Tracking With Global Least Squares Solution. *21st IFAC World Congress*, 21, 2020.

- [18] Jie Wang, Min Cheol Lee, Karam Dad Kallu, Saad Jamshed Abbasi, and Seokyoung Ahn. Trajectory tracking control of a hydraulic system using TSMCSPO based on sliding perturbation observer. *Applied Sciences (Switzerland)*, 9(7):1–17, 2019.
- [19] Jih Hua Chin, Yen His Sun, and Yuan Ming Cheng. Force computation and continuous path tracking for hydraulic parallel manipulators. *Control Engineering Practice*, 16(6):697–709, 2008.
- [20] Bin Zhang, Shuang Wang, Yuting Liu, and Huayong Yang. Research on Trajectory Planning and Autodig of Hydraulic Excavator. *Mathematical Problems in Engineering*, 2017:1–10, 2017.
- [21] Seonhyeok Kang, Jaemann Park, Seunghyun Kim, Bongju Lee, Youngbum Kim, Panyoung Kim, and H. Jin Kim. Path tracking for a hydraulic excavator utilizing proportional-derivative and linear quadratic control. In *2014 IEEE Conference on Control Applications (CCA)*, pages 808–813. IEEE, 2014.
- [22] Goran Stojanoski, Gerhard Rath, and Martin Gimpel. The Effects of Bulk Modulus on the Dynamics of Hydraulic Independent Metering Systems. *Sixteenth Scandinavian International Conference on Fluid Power*, pages 276 – 290, 2019.
- [23] Y F Liu, J Li, Z M Zhang, X H Hu, and W J Zhang. Experimental comparison of five friction models on the same test-bed of the micro stick-slip motion system. pages 15–28, 2015.
- [24] Herbert E. Merritt. *Hydraulic Control Systems*. John Wiley & Sons, Inc., 1967.
- [25] Peter Chapple. *Principles of Hydraulic Systems Design*. Momentum Press, vol. 2 edition, 2015.
- [26] Richard Belman. *Mathematical Optimization Techniques*. 1963.
- [27] I M Gelfand and S V Fomin. *Calculus of Variations*. Dover Books on Mathematics. Dover Publications, 2012.
- [28] Matthew Harker and Gerhard Rath. Discrete Inverse Problem Approach to Path Tracking in State Space Form. In *2018 International Conference on Applied Electronics (AE)*, pages 1–4. IEEE, 2018.
- [29] Matthew Harker. *Fractional Differential Equations: Numerical Methods for Applications*. Springer International Publishing, 2020.

Novel hydraulically relieved electromechanical direct actuation system for large scale switching valves

Tobias Vonderbank*, Pierre Marc Laßl Chavez, Katharina Schmitz

Institute for Fluid Power Drives and Systems, RWTH Aachen University, Aachen, Germany
E-mail: tobias.vonderbank@ifas.rwth-aachen.de*

Abstract

Extensive actuation forces and strokes are required for the actuation of large sized valves normally implemented in high power hydraulic systems. A hydraulic piloted operation is, as for now, the most suitable solution and the state of the art. However, recent research has shown that the application of new electromechanical valve actuation systems is possible in various cases. In this contribution a novel electromechanical valve actuation system for large sized 4/3-way directional control valves in a displacement controlled system is presented. The new actuation system is characterized by a hydraulic relief of the centering springs. Therefore, the springs are only active in safety-critical conditions, as in a power outage. Since the actuator is not working against the spring force during every displacement, the necessary actuation force is reduced drastically, so that common electromechanical actuators can be used. In case of a power outage, the spring relief is deactivated causing the stored energy to center the spool in neutral position. The performance of the novel actuation system is examined based on measurements, which are conducted on a manufactured demonstrator for valves of nominal size 25 with a flow rate of up to 600 l/min.

Keywords: Electromechanical actuation system, Large sized valves, Valve actuation system, Pilot operation, Flow controlled system

1 Introduction

Directional control valves are used to open or close flow paths of hydraulic systems [1–3]. Valves can be distinguished in their design (spool or seat valve), their adjustment (switching or proportional) and their actuation system [2]. To ensure the interchangeability of different valves the International Organization for Standardization has defined the dimensions and other specifics for mounting surfaces of four-port hydraulic directional control valves in the ISO 4401 [4]. This standard specifies six different nominal sizes with corresponding mounting surfaces which are distinguished by the position of the port holes and their maximum diameter. For industrial valves it is common practice that valves are classified by their respective nominal size.

The mounting surface for valves of nominal sizes 4, 6, 10, 16, 25 and 32 correspond to the six surfaces defined in ISO 4401. Valves of large nominal sizes possess higher possible port diameters and therefore allow for higher flow rates to develop. This correlation can be seen in Figure 1. The maximum possible flow rate of a specific valve series is displayed over the corresponding nominal size. Since the cross-section increases quadratically with the increment of the port's inner diameter there is, under assumption of a constant maximum flow velocity, an approximately quadratic progression between the nominal size and the maximum flow rate.

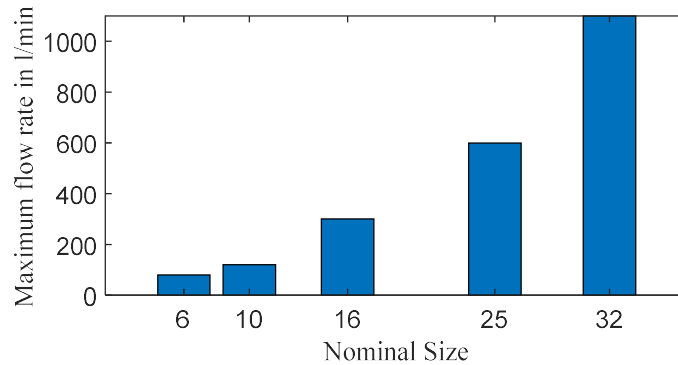


Figure 1: Maximum flow rate of a specific valve series over their nominal size. Data from [5]

Spool valves with a maximum flow rate larger than 80 l/min, which in practice are usually valves of nominal size 16 and larger, are normally actuated by a hydraulic pilot valve [1]. The performance of the whole actuation system depends on the pilot valve's hydraulic supply. Therefore, special attention must be paid to its design when using pilot operated valves. The pilot circuit can be supplied internally or externally by a separate hydraulic circuit. An external supply is essential for a faultless operation if pressure in the main line is able to drop below a critical value. In the literature, reference is made of a necessary minimum pressure of around 4 to 5 bar [1, 6]. The simplest external pilot supply consists of a fixed displacement pump supplying the pilot valve with a constant flow rate. Even if an improvement in efficiency through more complex pilot circuits is possible a trade-off between efficiency and expense must be made. Another way to potentially increase the efficiency is the application of electromechanical actuators, which represent a cost-effective alternative to hydraulic pilot systems. However, the necessary forces and large strokes which are required for larger valves to operate are challenging for common electromechanical actuators, like solenoids. During the movement of the spool, the actuator has to overcome various counter forces, as shown in Figure 2.

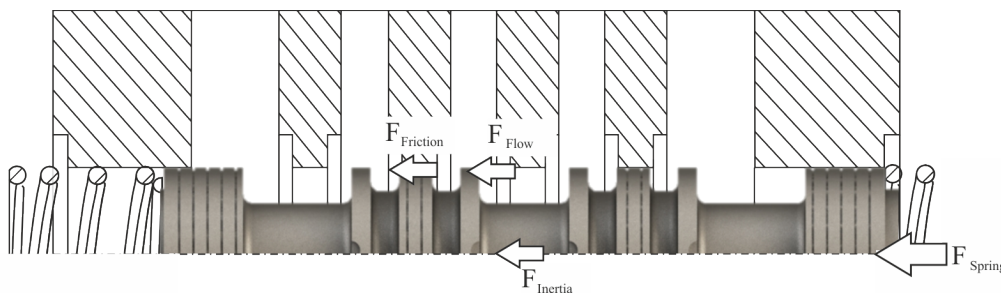


Figure 2: Applied forces on the spool according to. [7–11]

In the case of large valves, the most relevant forces acting during actuation are the flow and the spring forces. For valves with nominal size 25, previous research has shown that flow forces can reach values up to 800 N. Under operation in a flow-controlled system, a directional control valve faces considerably lower flow forces, when the flow rate of the system is reduced before the valve is switched. The observed reduction in flow forces results from a limited differential pressure and flow speed during valve switching. Due to the reduction of the occurring forces it is precisely in these systems that the implementation of electromechanical actuators is feasible and therefore an external pilot circuit would no longer be required.

The spring force represents the largest forces besides the flow forces. In 4/3-way directional control valves their function is to center the valve in the middle position anytime. Actuation systems that are capable of actively assume the center position could, in principle, leave out the spring centering. However, the springs fulfil a safety function, and are therefore necessary in the event of a power outage.

Aiming to reduce the necessary forces and therefore make the application of common electromechanical actuators possible an electromechanical actuation system is investigated in the following. It consists out of common solenoids and a hydraulic spring relief system, which is used to compress the springs during normal operations. Since the spring forces only act in case of failure, the driving electromechanical actuators only need to overcome friction and inertia related forces. In the case of a power outage, the spring relief system is deactivated, causing the springs to center the spool and fulfil the safety requirements.

The spring relief system, which is depicted in the lower branch of the functional structure, consist of two switches e), an energy transformer d) and the spring c). The switches e) serves to control the charging and discharging of the spring c). The spring c) can be charged with an alternative energy supply since the acceleration of the spool and the compression of the spring no longer happen simultaneously.

This concept of divided energy supply was realized in form of a hydraulically relieved electromechanical actuation system, which is sketched in Figure 5 and Figure 6. The actuation system is designed for a 4/3-way directional control valve of nominal size 25, which is implemented in a flow-controlled system. The design is able to apply higher forces than initially required, in order not to be completely limited to the application described in the introduction. Therefore, the actuator can also switch the valve under certain load.

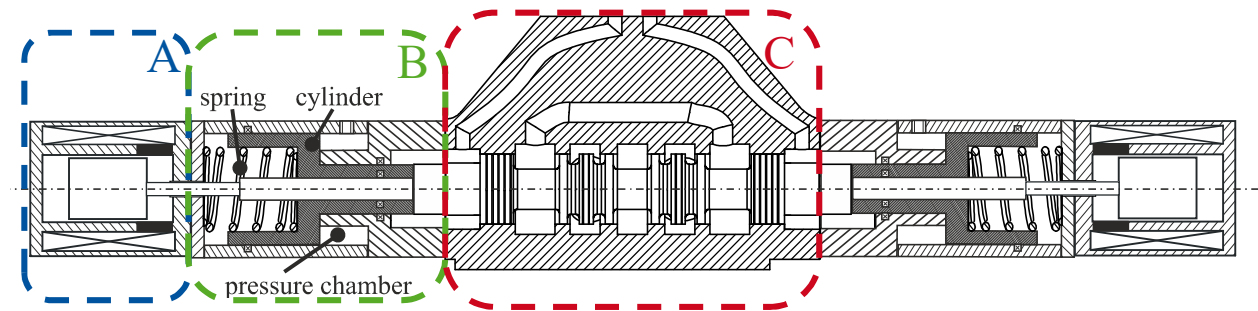


Figure 5: Technical sketch of the novel electromechanical actuation system. Spring relief not active.

The actuation system can be divided into three essential components. The component A represents a solenoid, which translates the electrical into mechanical energy. The hydraulic spring relief system B is located next to the solenoid. It is attached on both sides of the valve's housing C. To realize an active centering of the spool in neutral position a third solenoid is required, which is not sketched in. The hydraulic spring relief system depicts a spring returned cylinder in B, which centers the spool in case of a power failure. If the pressure chamber is pressurized, the cylinder will compress the spring until reaching the hard stop of the housing. Since the spool and the relief cylinder do not have a mechanically fixed connection, a gap is created between these two components. The spool is floating. This relieved state is shown in Figure 6.

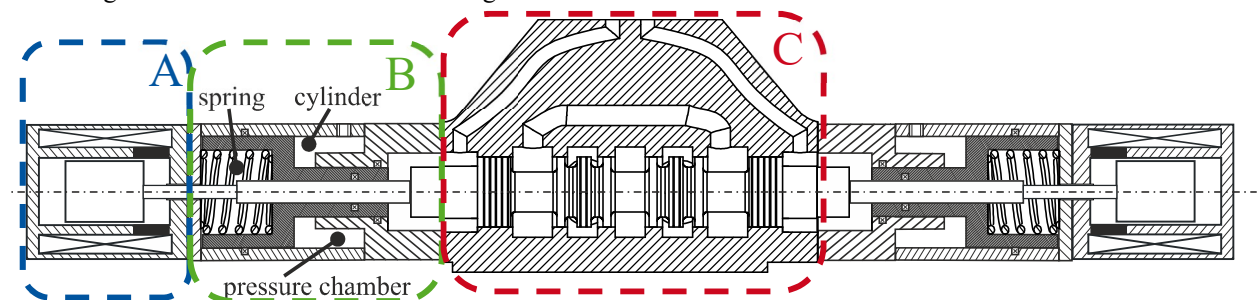


Figure 6: Technical sketch of the novel electromechanical actuation system in hydraulic relieved state

A rod, which connects the solenoid to the spool, is guided through the relief cylinder to transmit the force mechanically. In case of a power failure, the pressure chambers are relieved against the tank causing the spring to displace the relief cylinder. Thereby the spool also is centered in the middle position.

2.2 CAD of novel hydraulically relieved electromechanical direct actuation system for large scale switching valves

This new concept for a hydraulically relieved electromechanical direct valve actuation system was designed as a CAD model and was subsequently manufactured. The 3-D Modell is shown in Figure 7. To place the focus on the central aspect of the actuation system, namely the hydraulic relief system, the solenoids are not depicted. A hydraulic spring relief system is attached on each side of the 4/3-way directional valve.

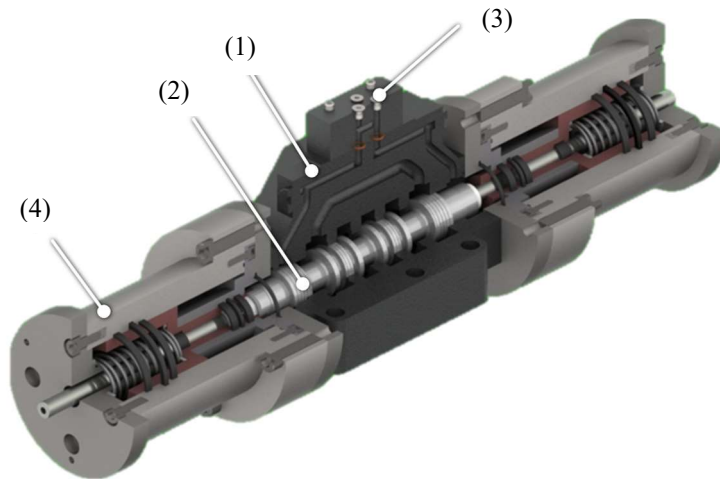


Figure 7: 3D-CAD model of the hydraulically relieved actuation system

The assembly consists of a valve housing (1), a spool (2) an adapter plate (3), which short circuits the pilot chambers to each other with an additional drain line to the tank, and two spring relief systems (4). This assembly is shown in detail in Figure 8. The hydraulic relief chamber (4.1) is formed by the housing (4.2), the relief cylinder (4.3), the spring (4.4) and the force cylinder rod (4.5). The connection port (4.6) represents the system's connection to the hydraulic system which will be explained in chapter 2.3.

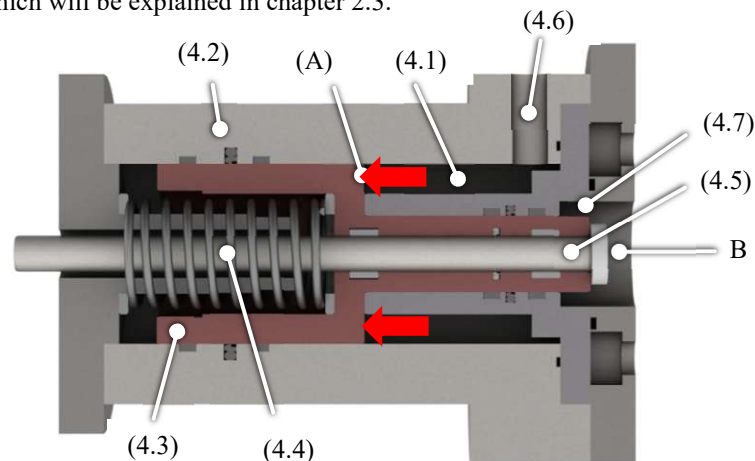


Figure 8: CAD model of the pressure relief system

Pressure builds up and acts on the area A of the relief cylinder (4.3) during the pressurization of the relief chamber (4.1). If the resulting force is larger than the preload force of the spring (4.4), the relief cylinder will be deflected and the spring will compress. The spool is not centered by the relief cylinder and can be moved freely. If the relief chamber is depressurized, the energy stored in the spring (4.4) will accelerate the relief cylinder (4.3) in closing direction. The stored energy must be sufficient to overcome all resistance forces, like friction or system inherent hydraulic resistance forces and accelerate the relief cylinder (4.3) fast enough to center the spool in sufficient time [9, 10].

During the reset of the process, fluid is displaced through the connection port (4.6) out of the relief chamber (4.1) and drained into the tank. As a result, a pressure difference between the chamber and the tank builds up, which poses a not negligible resistance force. Furthermore, the pressure in the pilot chamber (4.7) is also applied on the surface B, which leads to a further resistance force.

2.3 System design

The control of the relief system can be realized by two seat valves (1 & 2) arranged in a hydraulic circuit as presented in Figure 9. The control by two seats valves enables the charging and discharging of the relief system as well as the decoupling of the relief circuit from the main circuit. The novel direct electromechanical actuation system is drawn with standardized symbols for hydraulics in accordance with ISO 1219 [15]. The spring relief system can be interpreted as a spring returned cylinder (3), which is mechanically connected through a rod (4) to the spool of the valve. The designed actuation system is driven by three solenoids (5.1-5.3) which are drawn on

the bottom line of the valve. The solenoid on the left side can switch the spool to position A, the lower solenoid on the right side to position B and the solenoid above that (5.2) to neutral position.

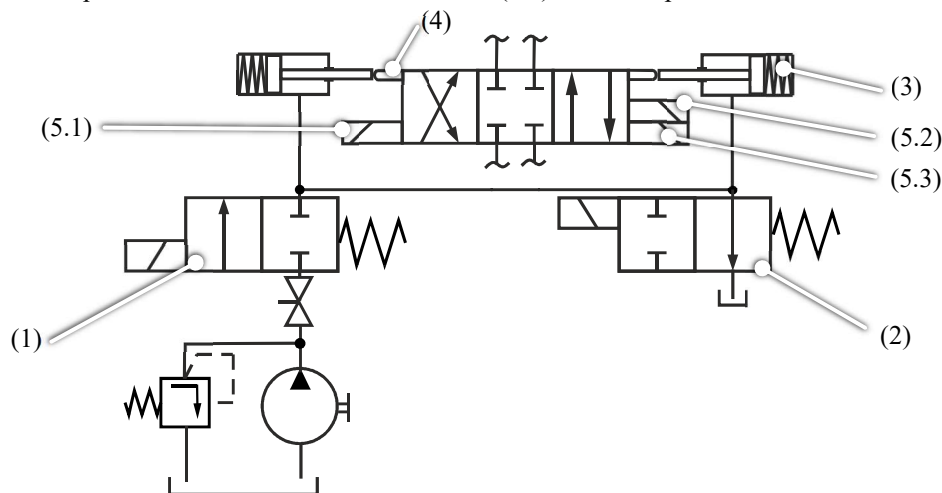


Figure 9 Hydraulic circuit to control the relief system

The solenoids on the right side are arranged with an offset to each other, so that only when (5.2) is energized the spool takes in the centered position. To fulfil a proper safety function, the loading valve (1) needs to be normally closed while the unloading valve (2) needs to be normally opened. To activate the relief system the loading (1) and the unloading valve (2) are energized simultaneously. After the system is initialized the spool is floating and the load valve (1) must be deenergized, so that the relief system is separated from the remaining hydraulic system and only leakage will lead to a pressure change. First measurements have been carried out to demonstrate that the pressure in the relief system does not drop rapidly while active. After the system was fully loaded a ball valve, located between the pump and the loading valve, was closed manually at a time of around 60 seconds. Sequentially the pressure in front of the load valve dropped down to 1 bar. In contrast, the pressure in the relief system could be maintained to nearly the same value for at least two minutes. Exemplary measurement results are displayed over time in Figure 10.

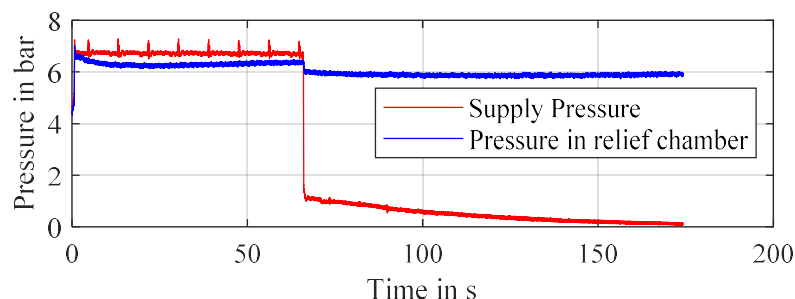


Figure 10: Measurements of the time dependent pressure drop in the designed accumulator

In case of an electrical power outage, the centered position cannot be attained actively by solenoid (5.2) anymore. The spool will remain in the deflected position requiring the relief system to be deactivated. Due to the operation modes (NC/NO) of the selected loading and unloading valve, this will occur automatically as long as the actuators and the relief system are energized by the same power source. In this case, both the loading and unloading valves will deenergize at the same time, causing the relief chamber to depressurize and therefore the springs to decompress. The spool is thereby accelerated to the neutral position, allowing the valve to take in its safe state.

When operating in industrial applications, the operation of the relief system must be adapted to the actual system. The simplest possible system design is shown in Figure 11. In this layout, the relief system is supplied by a separate pump. This system design still requires a pilot circuit and therefore possess no significant advantage against common pilot operated systems. If put in contrast to a hydraulic pilot control, the energy required to accelerate the spool and to compress the springs is no longer provided simultaneously. The compression of the springs can be realized before the switching process. Thereby the relief system can be supplied by the main pump without the possible eventuality that the pressure could drop below a critical value. The relief system can be integrated in the main circuit, as shown in Figure 12.

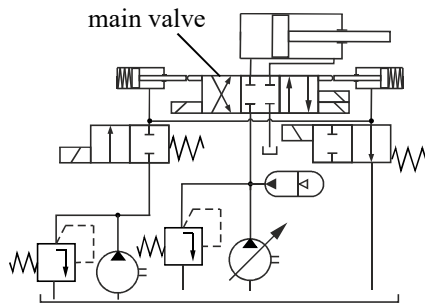


Figure 11: Hydraulic circuit for a new hydraulically relieved actuation system with external supply of the relief chamber

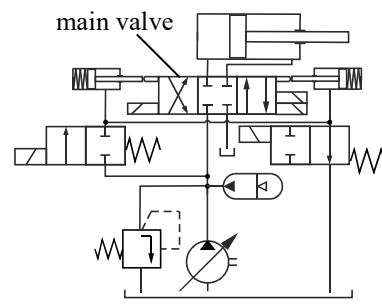


Figure 12: Hydraulic circuit for a new hydraulically relieved actuation system with integrated supply of the relief chamber

The relief system only can be loaded when pressure in front of the main valve is above a sufficient level. Once the main valve is closed, the delivered flow is relieved by the pressure relief valve directly to the tank. The pressure in the main line then is defined by the systems main pressure relief valve, so that maximum system pressure can be guaranteed. This way the relief system can be loaded by a short swing movement of the main pump. If necessary, a pressure reducing valve and a second pressure relief valve can be incorporated to prevent impermissibly high pressures in the relief system.

3 Experimental results

A test rig, according to Figure 13, was built at the ifas lab for experimentally testing of the hydraulically relieved electromechanical direct valve actuation system. The main circuit consists of a servo valve (SV), an adjustable pump (P₁), a pressure relief valve (PRV₁) and a directional control valve of nominal size 25 (V₁), at which the new actuation system has been attached. Additionally, six pressure sensors (p₁-p₆), two temperature sensors (T₁ and T₂) and a flow rate sensor (Q) has been incorporated into the main circuit. Two displacement sensors record the position of the force cylinder rods (4.5 in Figure 8), whereas five current sensors measure the currents of the three solenoids, as well as the loading and unloading valves. Two additional pressure sensors (p₇ and p₈) have been installed in the relief system circuit. For security reasons and since no burst test could be conducted previously, the power supply of the relief system was realized by an external hydraulic circuit, as shown in Figure 11. After the initial loading of the pressure relief system, its power supply was cut off by a manually operated ball valve. This step was made since beforehand demonstrations showed a reliable holding of pressure over a long period of time in the hydraulic relief system.

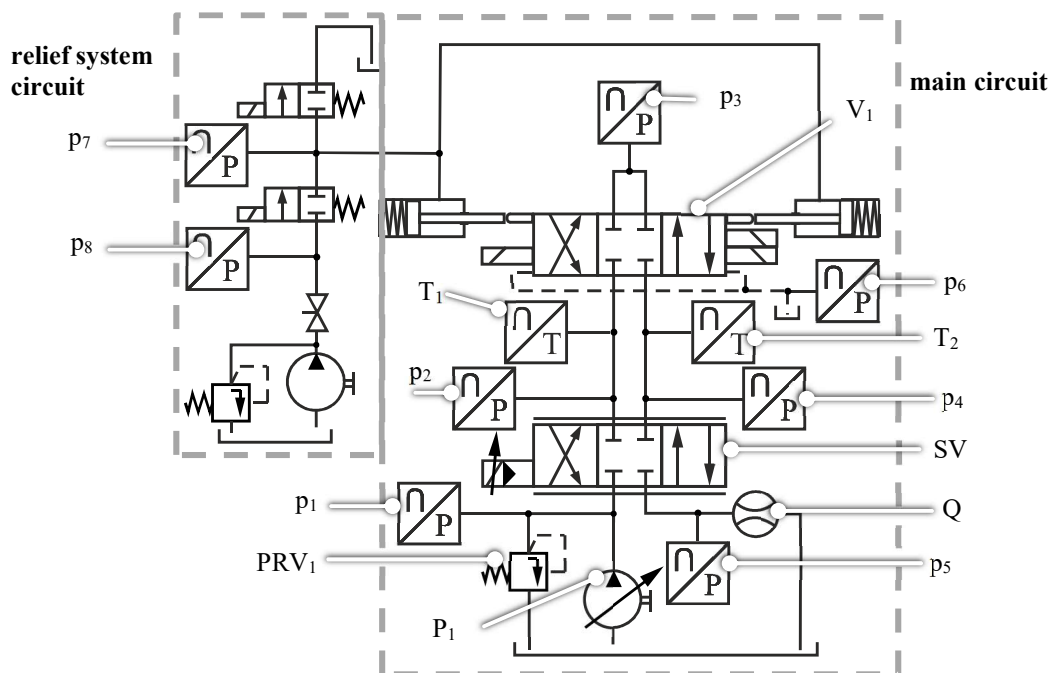


Figure 13: Hydraulic test rig

Beside the switching and the reset process also the static behavior of the actuation system during high flow phases is interesting, since high flow rates can lead to high flow forces [16–18]. Aiming to investigate these relevant states of operation two test cycles which can be seen in Figure 14 and Figure 15 have been defined. At the left y-axis the stroke of the actuator is displayed, which corresponds to the relative position of the actuator and its origin state.

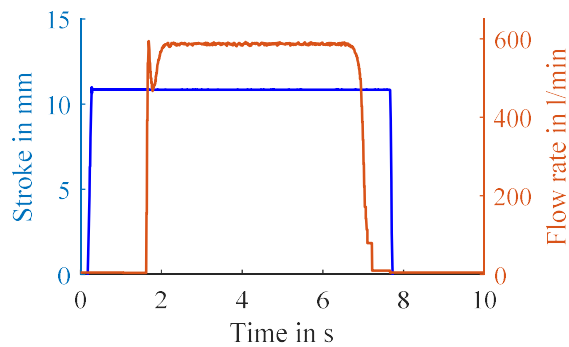


Figure 14: Switching process

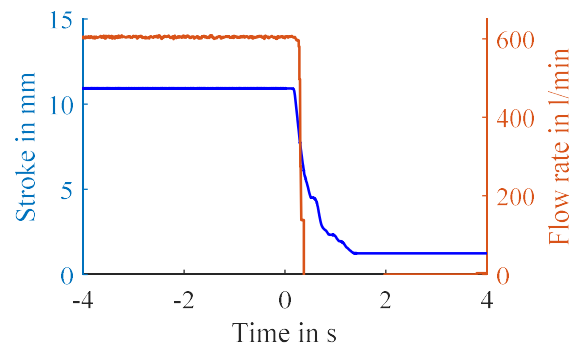


Figure 15: Reset process

In Figure 14 the test cycle for the investigation of the switching process and the static behavior is depicted. At the beginning of the test cycle the actuation system opens the valve abruptly. Since the servo valve is closed the actuation system always will switch the valve without applied pressure. After a defined time the servo valve is also opened and a flow rate can pass through the system. As the servo valve is opened rapidly a flow rate peak will occur. This will lead to high static and dynamic flow forces. As can be seen in Figure 14 the actuation system can hold the valve completely open even for flow rates up to 600 l/min. To analyze the reset behavior of the actuation system while different flow rates were passing the valve the second test cycle according to Figure 15 was defined. At the beginning the valve is fully opened, by a defined time the solenoids and the relief system are turned off ($t=0$ s).

3.1 Switching process

Switching times of common pilot operated valves are between 40 ms and 250 ms according to datasheets [19, 20]. An aimed switching time of 100 ms was defined for the novel electromechanical valve actuation system to be comparable to common pilot operated valves of nominal size 25. Multiple measurement series with different flow rates were conducted. During a measurement series the test cycle, explained before, was repeated 10 times. The measured stroke and current signal for the measurement series of 0 l/min (Figure 16 and Figure 18) and 600 l/min (Figure 17 and Figure 19) are displayed in the following graphs. The different measurements are shown in different colors.

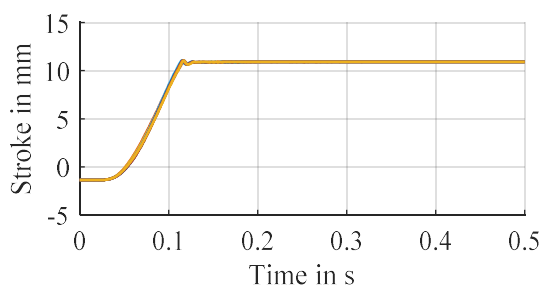


Figure 16: Stroke Signal for measurement series with 0 l/min

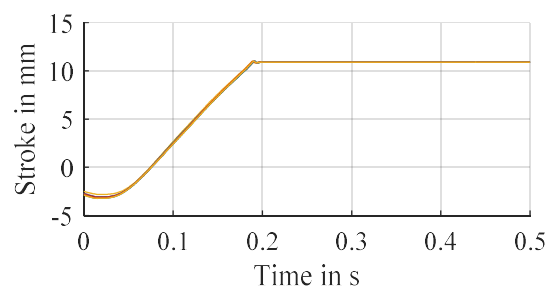


Figure 17: Stroke Signal for measurement series with 600 l/min

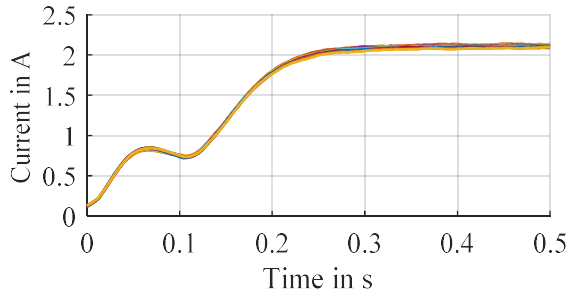


Figure 18: Current signal for measurement series with 0 l/min.

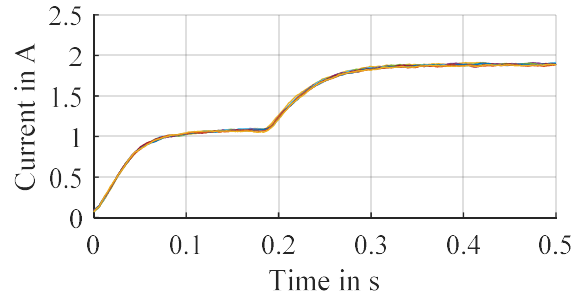


Figure 19: Current signal for measurement series with 600 l/min.

The switching time of the actuation system during the measurement series with 0 l/min is around 130 ms as shown in Figure 15. During the movement the solenoid consumes a current of around 0.85 A. Reaching the end stop the current drops down to 0.75 A due to counter induction. Afterwards the current increased to 2 A. Since the valve switches while the servo valve is in closed position, there is no flow rate passing through the testing valve during the switching process. Therefore, the testing valve should switch under the same conditions, regardless of the flow rate which passes the valve when it is opened. As can be seen in the measurement results, the stroke curves as well as the current curves differ from each other. In the measurement cycle with 600 l/min the switching times increased up to nearly 200 ms. Thereby the solenoid consumes a current of around 1 A and there is no decrease in the current signal like in the measurements with zero flow. Due to these differences there must be an effect of the high flow rate phase on the system's conditions during the switching process.

As a pressure is build up at the T port of the valve, a leakage flow over the sealing gap from the tank port to the pilot chamber develops. Therefore also the pressure in the pilot chambers increases. During the measurement cycle with 600 l/min a pressure between 1.5 and 2 bar was measured in the pilot chambers, which could explain the decreased performance by higher sealing friction forces compared to the measurement cycle with zero flow. Whereby the pressure in the pilot chambers was around 0 bar.

3.2 Reset process

Analyzing the reset times, the solenoids and the loading and unloading valve were deenergized while a flow rate was passing the valve. Again, multiple measurement series were conducted. Each series consists of 10 measurements evaluating the reset times during a given flow rate. The results of the stroke signal are displayed in Figure 20 and Figure 21. The measured pressures at the P and T port (p_2 and p_4) are displayed in Figure 22 and Figure 23.

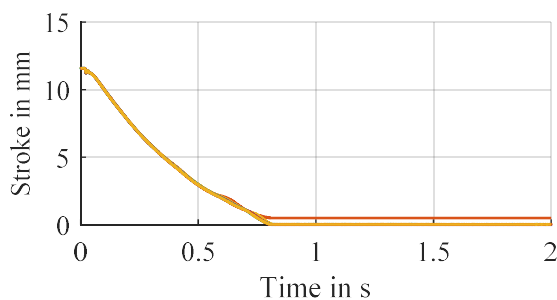


Figure 20: Stroke signal of reset process during a flow rate of 50 l/min

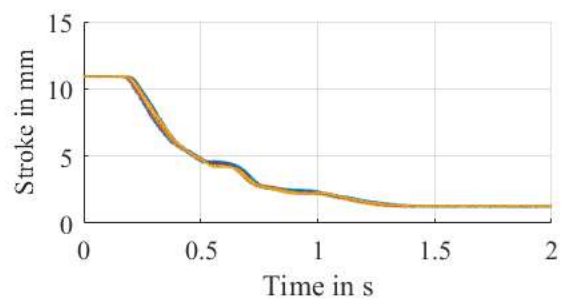


Figure 21: Stroke signal of reset process during a flow rate of 600 l/min

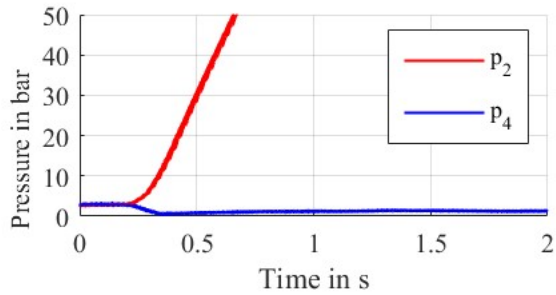


Figure 22: Pressure signal during the reset process with a flow rate of 50 l/min

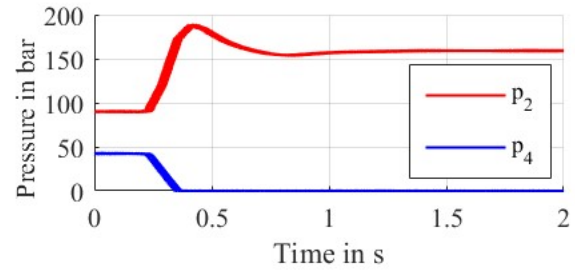


Figure 23: Stroke Signal for measurement series with 600 l/min

As can be seen in Figure 20, the reset time of the relief cylinder and therefore also the cylinder rod during a flow rate of 50 l/min is approximately 750 ms. Due to flow forces acting in closing direction and since there is no mechanical connection between the cylinder rod or the relief cylinder and the spool, the spool can move faster than the relief system. When closing the valve, the opening cross section is reduced, resulting in an increased pressure drop over the valve. Therefore, also the measurement results of the pressure signals p_2 and p_4 are displayed above. The safety-critical moment can be determined from the tank-sided pressure p_4 , at which the valve is completely closed with no pressure downstream of the valve. For both flow rates this point is reached after approximately 300 ms. Considering the positive overlap of the metering edges of 5 mm, pressure p_4 should drop to 0 bar at a stroke of approximately 5 mm. As flow forces are acting in closing direction they support the centering process of the spool and since they increase with small strokes it is likely that the valve spool tends to move faster than the relief cylinder. This can be especially observed in the measurement results of 600 l/min, since the pressure drops to zero bar before the stroke signal reaches a position of 5 mm.

Nevertheless, the relief system is still necessary. Without the relief system, the reset time would only depend on the flow forces. This would represent an issue, especially during phases with low flow rates and, since the deflected valve is nearly balanced in respect to the flow forces, also for large strokes. Friction forces may be larger than the flow forces and the spool would stay deflected. As can be seen in Figure 20 and Figure 22 the pressure p_4 drops down to 0 bar nearly by the same time as reaching a 5 mm stroke. In this case, the relief system is primarily responsible for the centering of the spool and therefore the relief system is necessary during low flow rates. And as can be seen in the measurement cycle with a flow rate of 600 l/min (Figure 21 and Figure 23 the closing process is initiated by the relief system and then self-amplifying by the increased flow forces. During the initial 200 ms, both pressures and stroke maintain their initial values. It is only after that time frame that the relief cylinder's stroke begins to decrease and shortly after the tank-sided pressure also drops. Therefore, it can be concluded that the closing movement is driven by the relief system.

3.3 Switching under load

Unlike previous measurements, the servo valve was opened before the test valve, which was thereby pressurized during the switching process. Therefore, the actuation system needed to overcome additional flow forces. The test cycle according to Figure 24 was repeated 10 times. The results of the flow rate (Figure 25), the stroke (Figure 26), the pressures (Figure 27) and the current of the active solenoid (Figure 28) over time are displayed below.

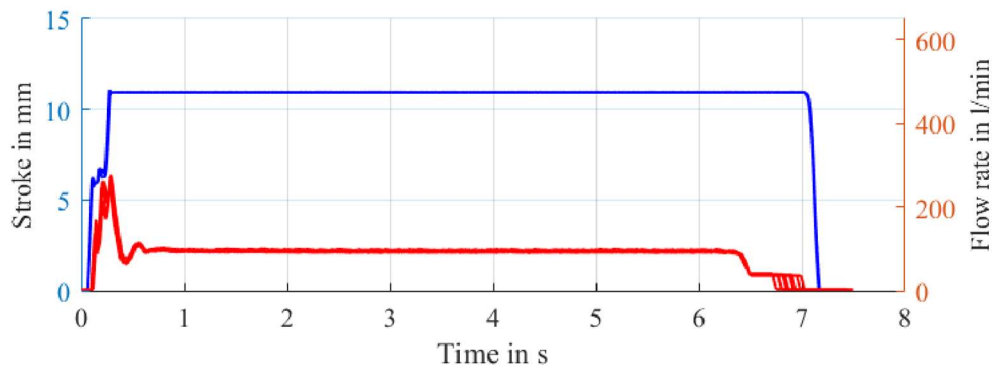


Figure 24: Measurement cycle for switching under pressure

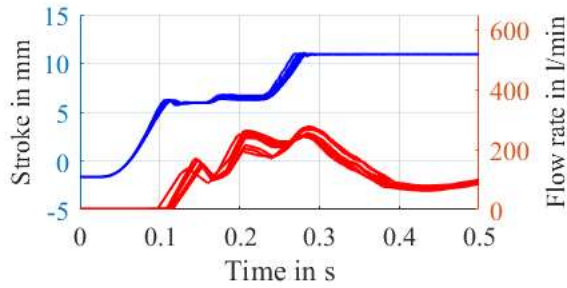


Figure 25: Flow rate with applied 100 bar and 100 l/min

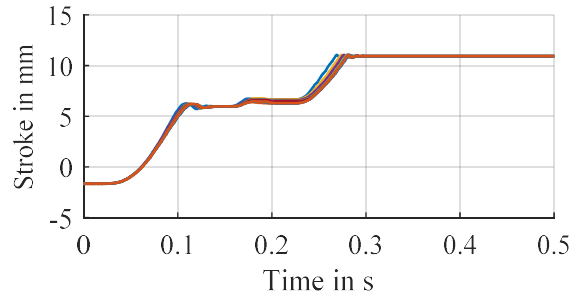


Figure 26: Stroke signal with applied 100 bar and 100 l/min

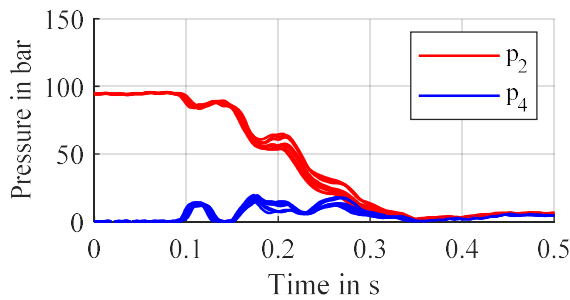


Figure 27: Pressure signal with applied 100 bar and 100 l/min

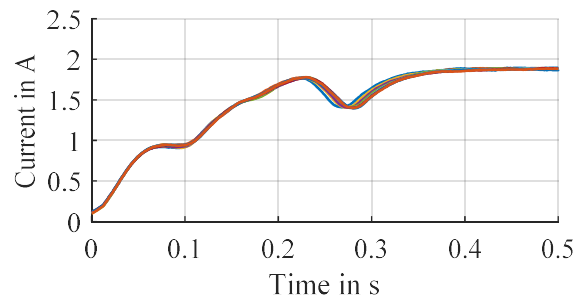


Figure 28: Current signal with applied 100 bar and 100 l/min

The system was supplied with a flow rate of 100 l/min and a pressure of 100 bar. The valve was operated in a constant pressure system, during which a flow rate peak of 250 l/min occurred. The thereby resulting flow force tends to close the spool. Compared to the stroke signal with no flow rate, a large plateau in Figure 26 can be identified between 0.1 and 0.25 s. During this phase, the force applied by the actuator is in an equilibrium with the flow force. The spool remains in the corresponding position until the flow rate decreases, so the actuation system can overcome the flow force. The gap of the metering edge has only a small opening, as can be seen in the stroke signal (considering the 5 mm positive overlap). At this point of operation, the flow rate is determined by the pressure drop over the valve. Since the occurring flow rate (up to 250 l/min) is larger than the adjusted flow rate of 100 l/min, the pressure before the valve starts dropping (Figure 27) during this operation. As the spool starts moving again, the pressure difference over the valve is reduced to a comparatively low value. Also, the current signal is significantly increased during the time range of 0.1 to 0.25 s. During this phase, power consumption compared to the previous measurements is increased and therefore higher forces are applied by the actuator. It can be assumed that the solenoid is applying maximum nominal force as the current nearly reaches the nominal value of approximately 2 A. The short-time reduced current demand at 0.28 s is due to the velocity-dependent counter-induction, which occurs when the solenoid armatures reaches its end position.

4 Discussion

The designed concept, which uses solenoid actuators, is able to realize strokes of around 11 mm with switching times of between 130 ms and 200 ms. It is therefore competitive with conventional pilot operated valves which achieve switching time between 40 ms and 250 ms. Nevertheless, the designed concept needs further improvement, since occurring internal leakage may affect the actuator's performance.

With regard to the reset times, the actuation system is not comparable with common valves, as these achieve considerably shorter reset times. Geometrical optimizations and adapted springs need to be implemented in order to improve the reset time. Even if the designed actuation system reaches reset time of 750 ms, they still can be reduced. It is noticeable that the flow supported spool is even faster at returning to the middle position than the relief system in test cycles with high flow rates. Nevertheless, hence a flow supported centering of the spool cannot be guaranteed, it is necessary to actively initiate the self-amplifying reset process, especially if low flow rates are passing the valve.

Although the concept has been adapted to an operation in a flow-controlled system where the pump is completely swung back during the switching process, existing systems may be few. Therefore, the switching process also was investigated while the valve was pressurized. The actuation system was used to switch the spool while a flow rate of 100 l/min was applied with a maximum pressure of 100 bar. In this case, switching times of approximately

250 ms were achieved. A time interval, during which the stroke signal was indifferent, suggests no movement of the spool. During that period of time, the acting flow forces in closing direction are in balance with the actuator force. Flow forces at this stage are high, due to the initially occurring flow rate peak. As the pressure before the valve decreases and the flow rate stabilizes, the flow forces decrease subsequently allowing the actuator force to accelerate the spool until reaching its full stroke. The application of the actuation system therefore is not limited to flow controlled systems. However, it should be considered that the switching performance and whether the actuation system can switch the valve is dependent on the hydraulic system and the operation condition.

As in measurements up to now the relief system was supplied by a separate hydraulic circuit the integration into a large hydraulic circuit as depicted in Figure 12 should be analyzed in further research.

5 Conclusion

As experiments on the concept show, the designed novel hydraulically relieved electromechanical direct actuation system for large scale switching valves is feasible. Switching times of around 200 ms and reset times of around 750 ms are achievable. The application of such a concept is particularly useful for systems, in which the main line pressure can drop below a critical value of 4 bar and therefore, an internal supply of the pilot valve is not possible. However, the hydraulic spring relief system needs to be controlled, therefore the integration into the main hydraulic system must be realized, exemplarily shown in Figure 12. Compared to common pilot operation systems, the dependency between the energy provision to overcome the spring forces and to accelerate the spool is resolved. Thus, the main pump can be used to compress the centering springs by supplying the relief system independently from the valve's switching process. Since the requirements for the actuation forces to shift the spool have been drastically reduced by the relief system, alternative applications of electromechanical actuators are possible.

The concept of a hydraulic spring relief system, which is embedded into an electromechanical valve actuation system, opens up new prospects for actuator implementations. Nevertheless, the design must be matched to the respective system operation profile. If the application in a constant pressure system is planned, the force of the electromechanical transformer needs to be adapted to the occurring flow forces.

6 Acknowledgments:

The IGF research project 20084/N of the research association Forschungskuratorium Maschinenbau e. V. – FKM, Lyoner Straße 18, 60528 Frankfurt am Main was supported from the budget of the Federal Ministry of Economic Affairs through the AiF within the scope of a program to support industrial community research and development (IGF) based on a decision of the German Bundestag.

7 Conflicts of Interest:

The authors declare no conflict of interest.

8 References

- [1] G. Bauer, *Ölhydraulik: Grundlagen, Bauelemente, Anwendungen*: Vieweg + Teubner, 2009.
- [2] W. Backé and W. Hahmann, *Grundlagen der Ölhydraulik: Umdr. zur Vorlesung*: Institut für hydraulische und pneumatische Antriebe und Steuerungen der RWTH (IFAS), 1972.
- [3] J. Watton, *Fundamentals of Fluid Power Control*. Cambridge: Cambridge University Press, 2009.
- [4] *Hydraulic fluid power - Four-port directional control valves - Mounting surfaces*, ISO 4401, International Organization for Standardization, Berlin, Jul. 2005.
- [5] Hydac International, *HYDAC Fluidtechnik: Industrial Valves* (accessed: Apr. 21 2021).
- [6] E. Kauffmann, *Hydraulische Steuerungen*. Wiesbaden: Vieweg+Teubner Verlag, 1980. [Online]. Available: <http://dx.doi.org/10.1007/978-3-322-85723-1>
- [7] N. Herakovič, J. Duhovnik, and M. Šimic, "CFD simulation of flow force reduction in hydraulic valves," *Tehnički vjesnik - Technical Gazette*, vol. 22, no. 2, pp. 453–463, 2015, doi: 10.17559/tv-20141128090939.
- [8] K. Schrank and H. Murrenhoff, "Beschreibung der Strömungskraft in Längsschieberventilen mittel Impulserhaltung," *O+P Journal*, no. 4, pp. 4–15, 2013.
- [9] Helmut Tatar, *Störkräfte bei elektromagnetisch betätigte Wegeventilen*. Aachen, 1974.
- [10] W. Backé and H. Tatar, *Untersuchung des Einflusses von Störkräften auf den Schaltvorgang bei Wegeventilen der Hydraulik*. Opladen: Westdt. Verl., 1975.
- [11] G. Schuster, *CFD-gestützte Maßnahmen zur Reduktion von Strömungskraft und Kavitation am Beispiel eines hydraulischen Schaltventils*. Aachen: Shaker, 2005.
- [12] N. Gebhardt and J. Weber, *Hydraulik - Fluid-Mechatronik: Grundlagen, Komponenten, Systeme, Messtechnik und virtuelles Engineering*: Springer Berlin Heidelberg, 2020.

- [13] H. Watter, *Hydraulik und Pneumatik: Grundlagen und Übungen - Anwendungen und Simulation*: Vieweg+Teubner Verlag, 2008. Accessed: Jan. 26 2021.
- [14] T. Vonderbank and K. Schmitz, “Design of Electromechanical Actuators for Large Sized Valves,” *Proceedings*, vol. 64, no. 1, p. 37, 2020, doi: 10.3390/IeCAT2020-08477.
- [15] ISO, “Fluid power systems and components - Graphic symbols and circuit diagrams: Part 1: Graphic symbols for conventional use and data-processing applications (ISO 1219:2012 + Amd.1:2016),” vol. 2012.
- [16] P. Bordovsky, K. Schmitz, and H. Murrenhoff, “CFD Simulation and Measurement of Flow Forces Acting on a Spool Valve,” in *10TH INTERNATIONAL FLUID POWER CONFERENCE*, 2016, pp. 473–484.
- [17] P. Bordovsky, *Evaluation of steady-state flow forces in spool valves: = Evaluierung stationärer Strömungskräfte in Schieberventilen*, 1st ed. Düren: Shaker Verlag, 2019.
- [18] N. D. Manring and S. Zhang, “Pressure Transient Flow Forces for Hydraulic Spool Valves,” *Journal of Dynamic Systems, Measurement, and Control*, vol. 134, no. 3, p. 193, 2012, doi: 10.1115/1.4005506.
- [19] Parker Hannifin GmbH, *Directly operated and pilot operated directional control valves: Series DIVW / DIDW / D3W / D3DW / D31DW / D41VW / D81VW / D91VW* (accessed: Apr. 21 2021).
- [20] Bosch Rexroth, *Directional spool valves, pilot-operated, with hydraulic or electro-hydraulic actuation: type WEH and WH* (accessed: Apr. 21 2021).

Non-reviewed Articles

The Hydraulic Infinite Linear Actuator for Efficient and Flexible Timber and Agricultural Logistics

Magnus Landberg, Magnus Sethson*, Petter Krus*

Landberg Solutions AB, Linköping, Sweden
E-mail: magnus.landberg@saabgroup.com, magnus.sethson@liu.se, petter.krus@liu.se
* Division of Fluid and Mechatronic Systems;
Department of Management and Engineering,
Linköping University, Linköping, Sweden

Abstract

In forestry and agriculture industry, robust and power-dense hydraulics have long played an important role for a rational and cost-effective logistics. In these fields there is a trend towards longer, larger and heavier vehicles and machines. Within the forestry business there is a need to develop transport vehicles with lower energy consumption. This can be done by improving the vehicles' aerodynamics. The air resistance of unloaded timber trucks and timber trains will be significantly reduced if stakes and banks are put together. Furthermore, there is a need to place banks and stakes at individual distances individually to accomplish different load combinations. In agriculture when sowing, it is an advantage to be able to flexibly position row units on a seed drill in optimal distances from each other to secure productive and sustainable farming. However, most present seed drills have fixed row distances and thus have a low adaptability for different crops or soil conditions. There is also a need for a faster transport of the seed drill between different fields.

Future actuation systems for forestry and agricultural vehicles and machines can be improved by utilizing a new sort of hydraulic linear actuator technology, the Hydraulic Infinite Linear Actuator (HILA). HILA technology also has an impact on heavy and dangerous manual steps when changing banks and stakes on timber vehicles. The adjustment can be controlled from the cabin, thus eliminating manual steps. Heavy bank elements on a timber vehicle can be positioned individually with high locking force. In the agricultural context, it is possible to quickly change between different inter-row spacing on a seed drill when using HILA technology, enabling a multi-purpose seed drill and inter-row cultivator. HILA long stroke capability also facilitates a smooth folding into a compact transport position. With the bills are gathered, a low center of gravity will be accomplished. This enables a more stable vehicle dynamics and enables a higher speed.

HILA is based on a well-known hydraulic clamping element technology, where the piston and the piston rod can be coupled and uncoupled by means of the clamping element. The HILA invention, in its simplest usage, provides new features to hydraulic cylinders, such as providing very long strokes and small chamber volumes, which means high stiffness and low capacitance. However, the invention also enables lower weight and volume of the actuator when compared to conventional hydraulic cylinders. This is a new way to generate and distribute mechanical linear movement and force by using hydraulic actuators in a cost effective way. The technology also represents a new sort of digital hydraulics. The technology is best suited for relatively slow dynamics and where the movement pattern is well-known.

Keywords: hydraulic actuator, incremental control, digital hydraulics, logistics

1 Introduction to HILA technology

The HILA technology combines two short-stroke cylinders with two engaging and disengaging clamping mechanisms into one actuator with long stroke length. The clamping mechanism, a sort of hydraulic membrane, is connecting the piston and the rod, when pressurised, see fig. 1. The friction between the clamping mechanism and the piston rod is $\mu = 0.1$ [3]. Spiral grooves in the clamping mechanism ensure that excess oil is removed in order to maintain the friction [3]. By using simple logic valves for pressurizing, the piston and rod can be connected and disconnected with a maximum secure and reliable clamping action in a fast way. The motion of each single short-stroke piston linked together by the clamping mechanisms creates the motion of the piston rod. For movements, one of the pistons is connected alternatively to the rod providing the drive. In this way the two pistons are moving the rod alternatingly in a kind of rope climbing motion.

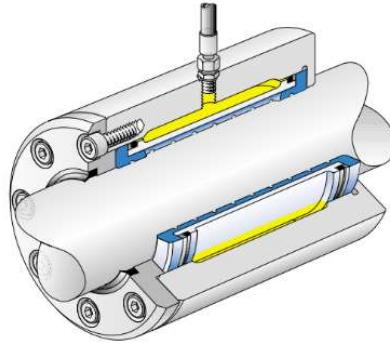


Figure 1. The clamping mechanism built into a hub [3].

In fig. 2 and 3 the actuation process of the cylinders is described. After step 7 the process will continue with step 2 (see also <https://www.youtube.com/watch?v=tVJkqC2w5ws>).

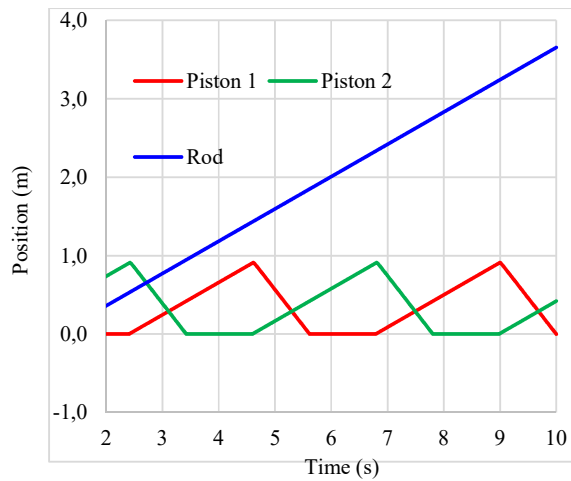


Figure 2. The positions of the pistons and piston rod during motion.

The actuator is the whole mechanism which is driving the load. It includes the piston rod, the hydraulic cylinders and its clamping elements and the position sensors. The shift of the load from one cylinder to the other is called load shift.

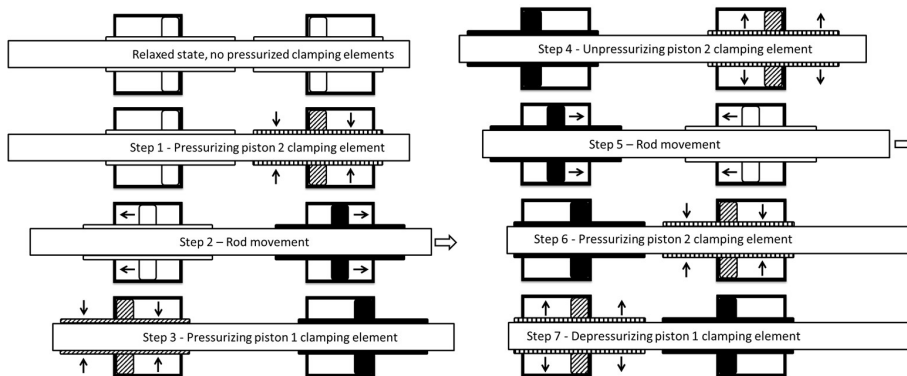


Figure 3. The actuation process of the cylinders.

The pressurization of the clamping element and thus the engaging can be implemented by a separate port through the piston (see fig. 4) and using a separate 3/2 valve. The purpose is to pressurise the small membrane volume and a minimal flow is needed. Thus a small and fast operating valve can be used. The piston and the clamping element are independently controlled by a timing procedure.

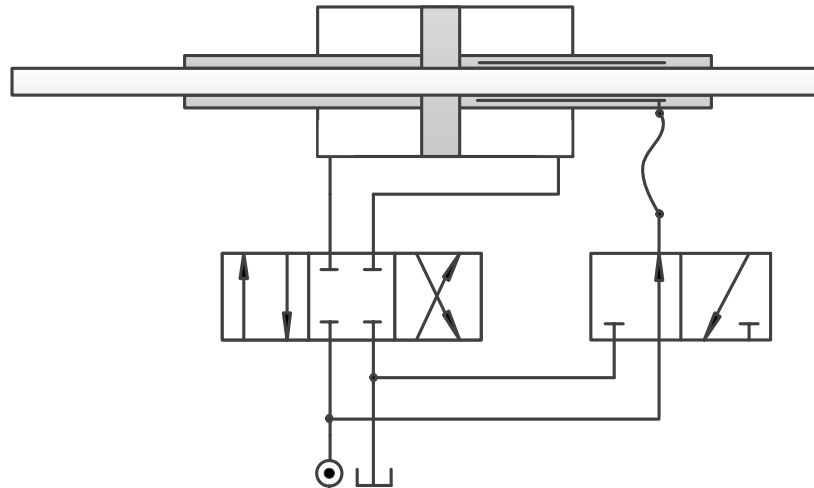


Figure 4. Separate pressurization of the clamping element.

In comparison with conventional long-stroke hydraulic actuators, HILA can offer shorter, more compact and easier-to-place solutions, especially on mobile vehicles and machines. Since the piston areas in the cylinders are symmetrical, marginal variation of the volume of oil in the system is obtained and a much smaller oil reservoir is required (see fig. 5). A challenge with this technology is to obtain a linear motion with a relatively low pulsation level. In many applications, however, smaller pulsations are acceptable. The technology is best suited for mobile applications with relatively slow dynamics and where the movement pattern is largely kinematic and well-known at beforehand.

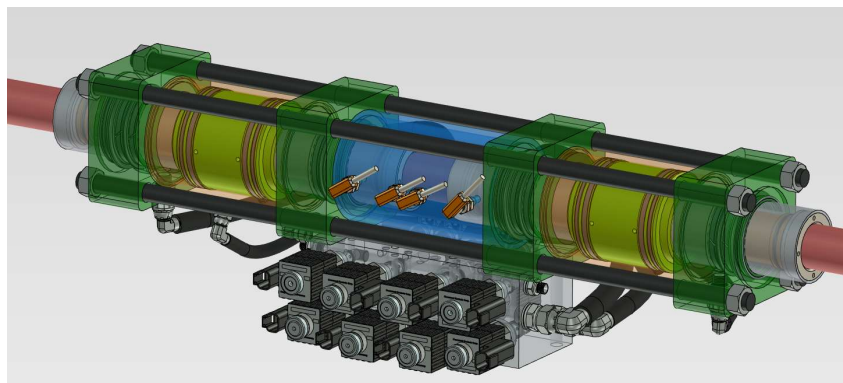


Figure 5. The HILA actuator. Illustration: Gustav Näslund, GN Tech.

1.1 Issues with long linear motion with conventional hydraulic cylinders

There are a few problems that occurs with long linear motion with conventional hydraulic cylinders. These are; buckling, hydraulic stiffness and hydraulic capacitance. Buckling is probably the main problem, limiting the stroke length of conventional hydraulic cylinders. It can be solved in some applications using a pulling cylinder instead.

Hydraulic stiffness and hydraulic capacitance affect the dynamic behavior and the controllability of the actuator system in an unfavorable manner. [4].

Long-stroke conventional hydraulic linear cylinders obviously have a number of difficult technical, economic and environmental problems. The advantages which normally are associated with the hydraulics; compactness and high power density diminish with increasing stroke length. The Hydraulic Infinite Linear Actuator (HILA) solves a number of the listed problem above. The HILA technology is characterized by providing very long strokes and high system pressure. The actuator has a higher stiffness compared to conventional hydraulic cylinders. Increased design pressure reduces the natural frequency of the system. These factors are favorable in actuator control design [1].

When using long stroke lengths of hydraulic cylinders, it is usually difficult to use high hydraulic pressure as it reduces the natural frequency in the system. It can be shown that the natural resonance frequency ω_h for an elevator cylinder is:

$$\omega_h \propto \sqrt{\frac{\beta_e}{L_{stroke} * p_{system}}} \quad (1)$$

where L_{stroke} is the stroke of the cylinder and p_{system} is the system pressure. Because the HILA cylinder has a much shorter stroke, a sufficiently high natural frequency can also be achieved at high system pressures [2]. However, the bulk modulus increases slightly with increasing pressure. The higher system pressure and small chamber volumes allows for an even more compact system design, with lower flow levels compared to low pressure systems, less energy losses in valves and a significant smaller reservoir volume.

Unique characteristics of the HILA actuator are the long strokes, the high system pressure and a compact and light actuator solution. It can be implemented in demanding environments, especially in mobile applications, where there presently are no alternative solutions. In contrast to ordinary ball screws or rack and pinion, HILA actuators also fit in applications used in tough environments, as forestry, agriculture and mining. In comparison with conventional long-stroke hydraulic cylinders, HILA can offer shorter, more compact and easier-to-place actuator solutions with long strokes. HILA is built on robust and cost-effective standard components. The technology is best suited for relatively slow movements and situations where the movement pattern is well known. The technology is patented.

Another advantage is that the system's need for hydraulic oil is only a fraction of what an ordinary hydraulic cylinder would require at the same stroke. Since the piston products in the cylinders are symmetrical. There is only marginal variation of the volume of oil in the system during feeding. The total volume of oil to minimal leakage of environmentally hazardous hydraulic oil into the vehicle.

Strokes of up to 7-8 m are possible depending on the piston rod diameter in horizontal applications, for pulling loads. Even longer strokes can be implemented in vertical applications, such as elevators. As the HILA technology needs a small cylinders and oil volumes is possible to design a very compact and long stroke electro-hydraulic actuator (EHA). The HILA technology also enables several active actuators to work on the same piston rod, which can be interesting for certain applications. This means that several processes can be performed in parallel instead of serially.

The disposition of the article is as follows. The first part is an introduction to the HILA technology and how heavy elements can be positioned with the technology. In the second part, it is showed how timber vehicles' aerodynamics can be significantly improved if stakes and banks are put together and a few other facilitating abilities for forestry logistics using HILA actuators. In the third part it is showed how agricultural can take advantage of the technology by flexibly position row units on a planter for optimal row distances from each other, to secure productive and sustainable farming.

2 Need for linear positioning of heavy elements

In some applications there is a need to position several heavy elements along a row, with high locking force either equidistant or with individual positioning. This need exists in several sectors, including agriculture, forestry, construction and logistics. For example, when you want to different bank and stakes for another load combinations (see fig. 6).



Figure 6. An unloaded timber trailer with banks and stake. Illustration: Gustav Näslund, GN Tech.

These elements need not be positioned by a dedicated actuator for each of the elements. Instead, a locomotive-carriage-like arrangement can be used, where the locomotive places the elements in the respective desired position. With the HILA actuator, several heavy elements can be placed and positioned in this desired way. These can be positioned with the actuator along the entire stroke. They are locked, for example, with a hydraulic clamping connection in the piston rod or in the surrounding fixed structure with an electromechanical lock.

One challenge, however, is to be able to position each element individually and in new patterns dynamically without having active locking mechanisms in each carriage element. An active locking mechanism that includes hydraulics or electromechanics means more potential fault modes compared to a passive solution, which has few possible fault modes.

If the distance between the elements in the extended position should always be the same, there is an easy way to access it with a passive method. By using fixed links between the elements, this need can easily be met. The weakness of this procedure means that manual intervention is required to change the length of the links. Another important aspect that must be considered is that when placing the elements along the linear path, they must be so attached to the fixed structure that drawer effects are avoided.

2.1 Passive locking mechanism

There is an easy way to create a passive locking mechanism. With a so-called friction coupling, the elements can be held in place. A friction joint is applied between the element and the linear path. The coefficient of friction is $\mu = 0.4$. A suitable frictional force is applied to the joint which is large enough for the application to hold the element in place. This type of passive locking mechanism has been used with good results on timber banks on timber vehicles for many years. An element coming out of its dedicated position can be detected by a sensor located on the element and be repositioned.

3 More efficient and greener timber trucks

There is a great need in forestry transport to reduce fuel consumption in order to keep variable costs and carbon dioxide emissions down. Already 20 years ago, the issue of forestry transport and its contribution to carbon dioxide emissions in Sweden was lively debated. One solution was to develop vehicles that could take more load and thereby reduce both fuel consumption and carbon dioxide emissions in terms of transport work performed [5]. The expected fuel savings of about 20% could be met by a good margin. There are still opportunities to reduce fuel consumption that have not been studied in more detail, among other things by improving the vehicles' aerodynamics. Air and rolling resistance are two of the most important factors for fuel consumption.

Truck manufacturers put a lot of effort into reducing air resistance through better aerodynamic design of cab and chassis on towing vehicles with limited gains. For the trailers, no similar development has taken place. A timber vehicle, on the other hand, is like two completely different vehicles, loaded or unloaded. In unloaded condition, there are several points where turbulence occurs, not just behind the cab. Above all, around the vertical stakes, but also around the horizontal banks to which the stakes are attached, strong turbulence arises. Studying aerodynamic solutions that reduce air resistance for both loaded and unloaded timber vehicles has, as far as is known, never been tried before.

Carried out wind tunnel studies show good opportunities to reduce air resistance [6]. Research is ongoing with the aim of developing, investigating and verifying the aerodynamic design of timber and wood chip cars that are heavier and longer than today's vehicles.

The simulation studies show that the biggest aerodynamic problems for unloaded timber trucks are partly the turbulence under the trailers that create air resistance, and partly stakes and banks that stand upright in the air stream. If these were bundled and assembled to one point, the air resistance would be significantly reduced. CFD (Computational Fluid Dynamics) simulations indicate reduced air resistance of around ten percent per measure, where the fuel savings can be estimated at 25–30 percent of the reduction in air resistance achieved, depending on the average vehicle speed. Today, there is no known technology or product on the market, for assembling banks and stakes on timber trucks [10].

There is a parallel to this with high aerodynamic resistance on unloaded timber train carriages. According to oral information an unloaded timber train gives a very large air resistance much due to the air turbulence that banks and stakes create [11]. Timber trucks may drive loaded and unloaded at 80 km / h (Sweden) but freight trains may drive unloaded at 100-120 km/h. The air resistance increases with the square of the speed, ie it is also very interesting to put together banks and stakes even on unloaded timber trains. Studies on unloaded open coal wagons have shown that covering the wagons can reduce air resistance by 42% [7].

The trend for timber vehicles is towards longer distances and higher average speeds in Sweden. This is due to fewer and larger sawmills and pulp mills. As the air resistance increases with the square of the speed, the need for assembled banks and stakes for reduced fuel consumption further increases.

In other countries, such as the USA and Canada, unloaded timber vehicles are driven at a higher maximum speed, over 100 km / h, i.e. the benefits of assembled banks and stakes are even greater here. .

The bundling of banks and stakes on timber trains is also interesting, especially given the higher speeds of the unloaded timber trains. There are no technologies or products on the market for this today.

3.1 Other needs in timber logistics

In addition to lowering air resistance and fuel consumption on unloaded timber vehicles, there are several other needs to be met in timber logistics. It is also important to keep the empty weight of the timber vehicle down.

Most timber vehicles that load with their own crane have a bank shifter, a hydraulic cylinder that moves the banks for the trailer's rear stack forward to enable loading. The crane has a limited range. Then the whole stack is pushed back so that another stack can be loaded. The bank shifter is a 4 m long hydraulic cylinder that weighs 400 kg. It also requires a large hydraulic tank. In addition, the bank shifter does not have sufficient stroke length to be able to assemble all the banks and stakes on a trailer. But with the compact HILA technology, it is feasible. The HILA system is estimated to weigh about 200 kg, i.e. half of today's bank displacements and a smaller hydraulic tank can be used.

Today's timber transports are characterized by great variation in timber length. The length of the stacks can be changed between each timber transport. There is also a need to be able to combine different long stacks, from 2.6 to 6 m long stacks on the same timber vehicle. Today, this means a great deal of manual work to have to push the heavy banks and stakes between the various positions. Being able to operate everything from the truck cab with the push of a button on a display would significantly improve ergonomics for drivers and save a lot of time.

3.2 HILA technology applied to timber trucks

With the HILA technology, several heavy bank and stakes on a timber vehicle can be positioned individually with high locking force, that improves aerodynamics and reduces fuel consumption for heavy unloaded timber vehicles. This is a major environmental benefit in terms of reduced emissions from fossil-fueled engines. With HILA technology, the vehicles' flexibility can significantly increase and open up for many more combinations that facilitate cost-effective and environmentally friendly logistics for both timber and complementary goods flow. HILA technology means that heavy and dangerous manual steps when changing banks and stakes on timber vehicles can be eliminated. The adjustment can be performed from the cab via keystrokes.

With the HILA actuator, the following functions can be implemented on towing vehicles and/or timber trailers (1-9):

1. **Bundling of banks and stakes for better aerodynamics.** The assembly of banks and stakes to one point on the trailer or behind the cab of the towing vehicle, will reduce air resistance, and fuel consumption and carbon dioxide emissions by about 5% [6], see fig. 7.

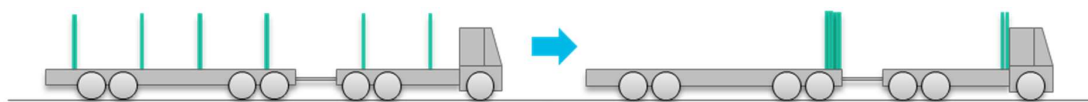


Figure 7. Bundling of banks and stakes

2. **Bank shifting.** Most timber vehicles that load with their own crane need to be able to move the rear stack of the trolley forward during loading. This bank shifting is done with a long stroke hydraulic cylinder. This can be solved just as well, but only with a predicted halved weight using the HILA actuator in comparison with today's bank shifters. This manoeuvre needs a high actuator force, up to 170 kN.
3. **Enable different bank and stakes combinations.** The HILA actuator enables to switch to bank combinations for different lengths of wood (see fig. 8). The combinations are based on the number of stacks and the length of wood on each stack. This is especially important when the length of wood on a stack is to be changed from 2.6 to 6 m. Timber trailers can have up to eight banks, which enables four stacks of short timber.

A large number of banks leads to higher air resistance and increased manual work when the banks are to be converted to fewer stacks. There are also risks in the working environment when this adjustment is done manually, especially in stressful situations.

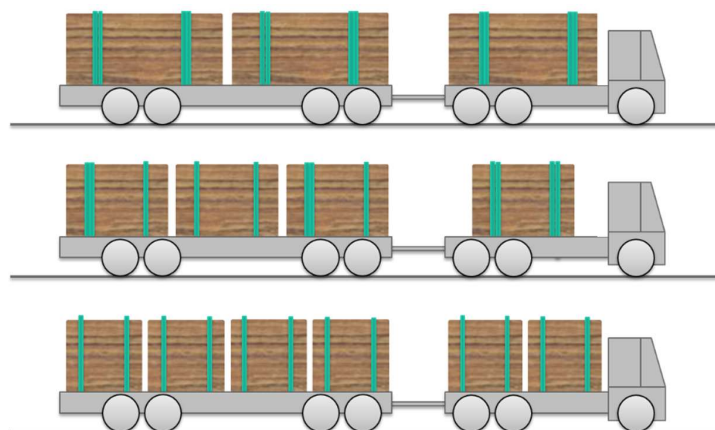


Figure 8. A timber vehicle with different load combinations.

With HILA actuator technology, adjustment between 2, 3 and 4 stacks combinations can be done smoothly simply with a push of a button in the cab. This saves time and creates a better working environment.

4. **Adjustable center of gravity.** Center of gravity balancing of stacks is important to get the right weight distribution and avoid overloading on any axis group.
5. **Gap-filling.** Minimizing gap between stacks, so-called gap filling, has two purposes; 1. to reduce the air resistance of a loaded vehicle, and 2. to improve the torsional rigidity of the trailer. The latter can be done by pressing the two stacks of the trailer together so that they go into each other and partially hook together.

6. **Easier inspection.** HILA can be used to disassemble stacks during inspection. For measurement of timber volume and quality control, it is important to have a certain distance between the stacks to be able to go in and measure with, for example, cameras [12].
7. **Easier to turn.** When banks and stakes are assembled in the middle of the trailer it will be easier to turn the vehicle in the woods. The risk of the stakes getting caught in trees and branches is thus reduced.
8. **Allows for complementary cargo.** Complementary freight flow for timber and container transport lead to savings with respect to time, costs and climate impact. With the HILA technology, towing vehicles and trailers can easily be rebuilt to carry 20'-40' containers (also applies to trains). This will create opportunities for valuable complementary freight flow and large savings with respect to time, costs and climate impact, especially on long transport routes (see fig. 9).

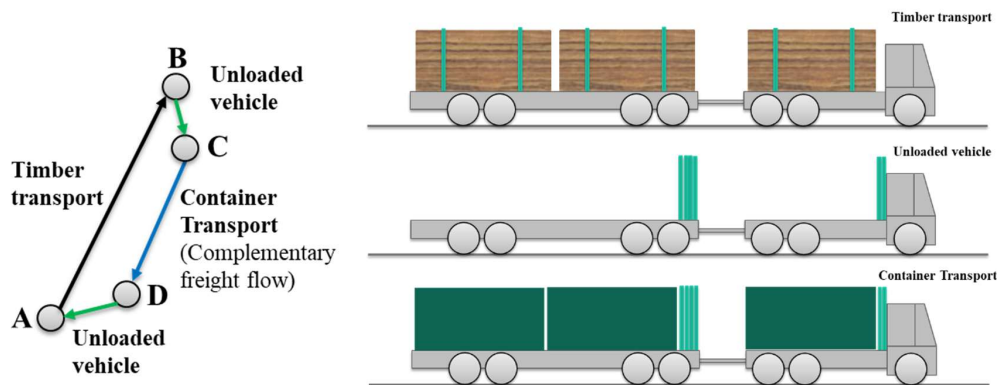


Figure 9. An example of a complementary freight flow schematic.

9. **Use on timber trains.** Bundling of banks and stakes on unloaded high speed timber trains can radically reduce air resistance and reduce energy consumption and in some cases also carbon dioxide emissions.

4 HILA technology applied to precision seed drills

Hydraulics has been important in agriculture since the 1940s and is still strategic. Today, hydraulics control a number of advanced functions. The hydraulics in turn are often controlled by advanced electronics in combination with sensors.

In the subject area of field machines in agriculture, since Jethro Tull's invention of the row seed drill around 1733, people have been interested in sowing, row cleaning and fertilizer filling etc. with different row distances [8]. Purely biologically, it is motivated to have different line spacings depending on crop or cultivation philosophy. But practical reasons have meant that you do not vary the distance in the way you would like due to lack of suitable actuators. Changing the row spacing is sometimes not even possible, and when possible, it takes time, which is rarely available and especially during spring sowing, as time is precious. Exceptions exist such as French Monosem [9], but their machine still has fixed positions and requires manual steps to change row spacing.

It can take two working days to manually rebuild a precision seed drill from 50 to 75 cm row spacing. This is a procedure that must be performed many times during a growing season by, for example, machine station owners. During the machine's lifetime of perhaps 20 years, the labor costs will exceed several 100,000s SEK. If the adjustment of line spacing can take place in a few minutes, this means large savings. Another way to solve the problem of variable row spacing today is to turn off certain row units so that 25, 50 or 75 cm row spacing is easily obtained. But driving around with a very high dead weight, for example at a line distance of 75 cm, is costly.

Fully flexible machines, however, still shine with some absence in the market, but there is a need for them. Another area of problems is how large wide carriages can be folded together to be transported on roads. Different countries have different rules for width, but usually the limit is 3 meters.

A key to secure productive and sustainable farming, is the placing of seeds at optimal distance from each other. However most, present seeders have fixed row distance and thus have low adaptability for different crops or soil conditions. With HILA technology, it is possible to implement a fast, efficient, and variable row spacing setting on machines for precision sowing, inter-row cultivation and crop harvesting. This means that the same machine can be used for different crops and meet farmers' demands for a common multi-purpose machine.

HILA technology enables quick shift between different inter-row spacings simply from a display in the tractor cabin. It is possible to choose which crop to sow from a display in the tractor cabin and HILA sets the desired inter-row spacing automatically. The HILA concept allows infinite possibilities of configurations for different sort of seeds and the spacing can be independently adjusted with high precision. With the possibility of being able to vary the distance on the drill units, it means that the working width also varies. Thus, there is also the need to be able to vary the arm width of the machine. How this is solved is not described in this article. There are several capabilities of the HILA technology that can be integrated in a seed drill or planters.

With the HILA actuator, the following functions can be implemented on a seed drill:

1. **Automatic change of row distance.** It is possible to quickly vary the distance between drill units from a display in the tractor cab, i.e., without having to leave the cabin. This also includes the opportunity of fine-tuning the inter-row spacing for a certain crops and soils (see fig. 10).

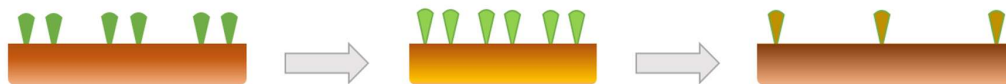


Figure 10. Different crops with different inter-row spacings.

2. **Optimal center of gravity during folding.** With HILA technology, it becomes practically possible to indirectly offer longer arms with a more optimal center of gravity during folding (see fig. 11). Another advantage is a simpler folding mechanism for changing 3-plex or 5-plex to 2-plex which gives opportunity to transport the row units a long distance. This also has potential to lower the folding time enabling faster moves between fields.

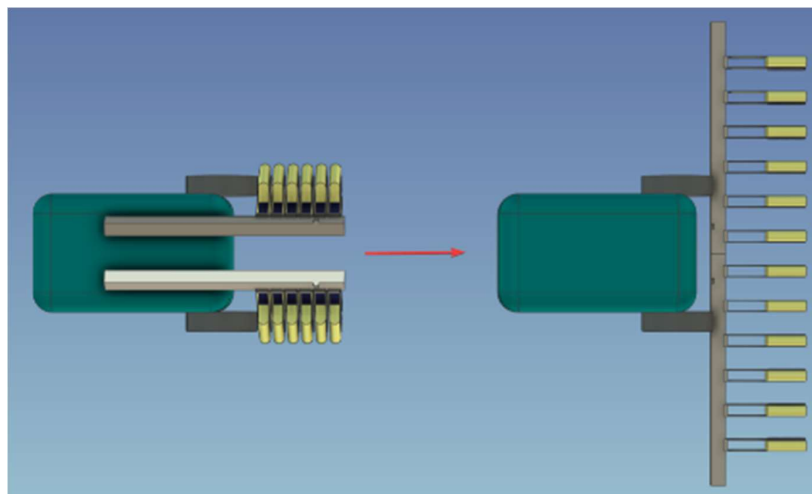


Figure 11. Unfolding the precision seed drill machine.

3. **Optimal center of gravity during transport.** With HILA it is possible to obtain a folding into a compact transport position, with the rows gathered with a low center of gravity of row units. This enables a more stable vehicle dynamics and that a higher speed can be allowed on the vehicle. This means a lot of valuable time saving when you must transfer between the fields.

4. **Reconfigure on the fly in case of row unit failure.** Being able to quickly reconfigure if a row unit fails, means that planting can continue without having to wait for a service technician. This contributes to higher productivity (see fig. 12).

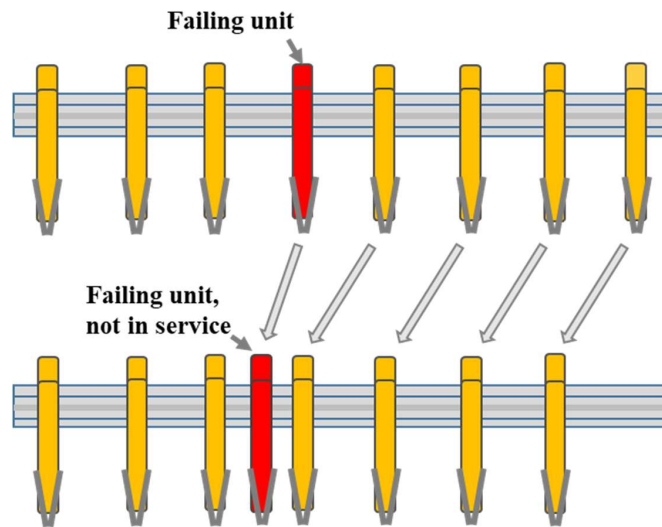


Figure 12. Reconfigure on the fly in case of row unit failure.

5. **Reconfigure for service mode.** During service or repair on a specific row unit, it is possible prepare large service space between the heavy row units, by pushing a button in the tractor cab (see fig. 13).

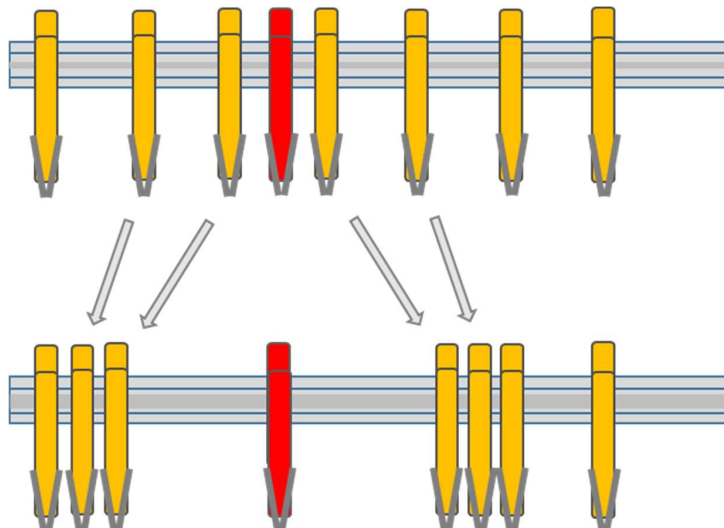


Figure 13. Reconfigure for service mode.

4.1 The HILA demonstrator



Figure 14. The HILA demonstrator¹. Photo: Per Frankelius. LiU

A demonstrator of the concept has been developed with the aim that an actuator of this type can perform the most central task: the actuator can be connected to the row units and position them individually (see fig. 14). The demonstrator has been successfully tested and meets the initial requirements regarding functionality. The next step will be to build a full scale seed drill. The demonstrator is a result of a collaboration within the innovation program Agtech 2030. The collaboration has been conducted between Saab Ventures, The Rural Economy and Agricultural Societies (Hushållningssällskapet), Linköping University, Landberg Solutions and GN Tech. The hydraulic research division (FLUMES) at Linköping University has been instrumental for this work².

5 Discussion

The HILA technology presented in this article shows several interesting applications in forestry and agricultural logistics. Several parallel development actions of HILA technology are underway in these sectors. In the forestry segment, a Vinnova-funded project is underway that aims to develop a first functioning HILA demonstrator for bundling banks and stakes that improves aerodynamics and reduces fuel consumption for heavy timber vehicles. In order to be economically viable, the chosen solution must also be able to completely replace the current bank shifting cylinder for load displacement. The project is primarily expected to provide a better understanding of the technology's functionality but also to get an indication of how energy consumption can be reduced for timber vehicles through better aerodynamics.

In the agricultural segment, a first demonstrator has been built and tested. It meets basic requirements for functionality. The actuator can be connected to the row units and position them individually. Subsequently, research has been carried out to gain a better understanding of the development needs and areas for improvement in sowing and mechanical weed control in agriculture and how HILA technology can improve current technology. The next step will be to develop a full-scale seed drill demonstrator based on this information. The purpose is to demonstrate the flexibility and robustness of HILA technology in the field.

Machine stations have a particularly large need to be able to offer different customers various row distances for sowing and mechanical weed control of different crops as well as quick transport between different fields. Semi-structured interviews with farmers and experts have been performed. This research work has provided a lot of new knowledge and insights about different needs that exist today to be able to conduct a rational agriculture.

Based on this newfound knowledge, several interesting new possibilities and abilities that the HILA technology enables have been identified. One area that has particularly attracted extra interest is a rational control of weeds. It is becoming increasingly difficult to control weeds with chemical methods. More and more growers are choosing to switch to mechanical weed control. For example, there are great financial benefits from being able to go from manual weed cleaning to mechanical weed control for vegetable growers. Much of the economy of vegetable

¹ The commercial name of the HILA technology is Flexrow, see also www.flexrow.com.

² See film on https://www.youtube.com/watch?v=cPK7-Wwx_mk

growing is determined by how effectively weed control can be carried out and how manual labor can be minimized. It is short periods of the year that sowing, and planting take place, respectively, row chopping. Everything happens under high time pressure. It must be easy and convenient to adjust the row spacing during inter-row cultivation.

When weeding in a row, there are two factors that are important to distinguish: partly the distance between the rows and partly the widths of row weeding. The technology for variable distance between the crop rows must be able to be combined with a variable width of the row harvester itself for it to be really effective. Different widths of row weeding are required for different times of the season. Field grown vegetables are weeded several times during the growing season and it requires narrower and narrower inter-row cultivation widths, as the crop grows.

It is important to enable inter-row cultivation as close to the crop as possible, in order to get the most out of the harvest. A key question in this context is how close to the crop you can do the inter-row cultivation without damaging the crop. That limit is dynamic, especially if there is large variation in how far the plants have come in their growing. It often occurs that large and small plants are damaged when the row weeding cannot have a dynamic width. With modern positioning technology based on RTK / GPS, it is possible to implement variable row weeding width with one or a few centimeters at a time and thus be able to get closer to the crop.

The assessment is that with HILA technology, inter-row cultivation with variable row weeding width can be realized; to be able to quickly change the distance between the row cultivating bills and the width of the row cultivating bills. Furthermore, row spacing, and weeding width can be set with high accuracy and resolution.

An interesting possibility with HILA technology is to be able to switch between sowing units and units of inter-row cultivation on the same machine. Thus, there are opportunities to obtain several capabilities in the same machine. Partly an efficient and flexible seed drill for different crops and partly an inter-row cultivation machine for different types of crops in different growing stages during the growing season.

6 Conclusion

In this paper a new hydraulic actuator technology has been presented, called HILA. HILA is based on a well-known hydraulic clamping element technology, where the piston and the piston rod can be coupled and uncoupled by means of the clamping element. The innovation, in its simplest usage, provides new features to hydraulic cylinders, such as providing very long strokes and small chamber volumes, which means high stiffness and low capacitance. However, the invention also enables lower weight and volume of the actuator. The technology also represents a new sort of digital hydraulics. The technology is best suited for relatively slow dynamics and where the movement pattern is well-known in mobile hydraulic applications. The technology enables hydraulic actuators in new applications and expands field-of-use for hydraulic actuators, especially in the mobile domain.

The HILA technology enables several heavy elements to be positioned along a row, with high locking force either equidistant or with individual positioning. In this paper, two promising applications have been identified in timber logistics and agriculture that require positioning of several heavy elements. With this technology, specific problems within these domains can be solved in a completely new way. Forestry needs to develop transport vehicles with lower energy consumption. This can be done by improving the vehicles' aerodynamics. The air resistance of unloaded timber trucks and timber trains will be significantly reduced if stakes and banks are put together. They can be positioned individually with high locking force using the HILA actuator. In the agricultural context, it is possible to quickly change between different inter-row spacing when using HILA technology, enabling a multi-purpose seeder and mechanical weeding machine.

An agricultural demonstrator of the concept has been developed with the aim that an actuator of this type can perform the most central task: the actuator can be connected to the row units and position them individually. The demonstrator has been successfully tested and meets the initial requirements regarding functionality. The next step will be to build a full scale seed drill.

Acknowledgement

Research funding from Sweden's innovation agency Vinnova, the research and innovation program Agtech 2030 at Linköping University and Agtech Challenge at Rural Economy and Agricultural Societies has been platform for parts of the research behind this article. Some of the illustrations have been produced by Gustav Näslund at GN Tech AB.

References

- [1] Magnus Landberg, Martin Hochwallner, and Petter Krus. "Novel Linear Hydraulic Actuator". ASME/BATH 2015 Symposium on Fluid Power and Motion Control (FPMC2015).
- [2] Martin Hochwallner, Magnus Landberg, and Petter Krus. "The Hydraulic Infinite Linear Actuator – properties relevant for control." The 10th International Fluid Power Conference (10. IFK), 2016.
- [3] ETP-OCTOPUS, ETP Transmission AB
- [4] Magnus Landberg, Robert Braun, Magnus Sethson, and Petter Krus. "The Hydraulic Infinite Linear Actuator Applied to Elevators in Mid-Rise Buildings". ASME/BATH 2018 Symposium on Fluid Power & Motion Control (FPMC2018).
- [5] Gunnar Svensson and Claes Löfroth, C. "ETT - Modulsystem för skogstransporter", Skogforsk, Arbetsrapport 758, 2012
- [6] Claes Löfroth and Olle Gelin. "A pilot study of aerodynamic design of forest vehicles", Arbetsrapport, Skogforsk nr. 870–2015, 2015
- [7] Watkins, S., J. Saunders, and H. Kumar. "Aerodynamic resistance reduction of goods trains". Journal of Wind Engineering and Industrial Aerodynamics Volume 40 (2), p 147–178, 1992
- [8] [https://en.wikipedia.org/wiki/Jethro_Tull_\(agriculturist\)](https://en.wikipedia.org/wiki/Jethro_Tull_(agriculturist)) (retrieved 210520)
- [9] <https://www.monosem.com/News/News/Multi-purpose-MultiSlide-frame>
- [10] Oral reference Joakim Eriksson, ExTe, 2020
- [11] Oral reference Owe Ljunghammer, ExTe, 2020
- [12] www.cind.se/timber-industry (retrieved 210520)

Benchmarking the performance of hydrostatic pumps

Robin Mommers , Peter Achten , Jasper Achten , and Jeroen Potma

Innas BV, Breda, The Netherlands
E-mail: rmommers@innas.com, pachten@innas.com

Abstract

In search for sustainable and clean solutions, the hydraulic industry is forced to develop more efficient alternatives to traditional systems. For mobile applications, battery driven machines are becoming an essential solution. But, electric driven hydraulic systems set completely different demands than classical systems. Since batteries are expensive and bulky, it is no longer acceptable that the majority of the battery stored energy is lost in the hydraulic system.

One of the promising solutions for efficiency increase is the application of electro-hydraulic actuators (EHAs). Aside from all the inherent control advantages, EHAs deliver energy to each load on demand. This makes them much more efficient than current valve controlled systems, at least in principle.

In practice, EHAs require both low and high-speed operation of pumps. Almost all hydrostatic pumps have high friction losses, strong wear and often also high volumetric losses at speeds below 500 rpm. Additionally, it is obvious that the pumps must have the highest efficiency possible.

Given these constraints and demands it is understandable that information is needed about the performance of pumps and motors. In the past years, Innas has measured and tested several positive displacement machines and published a comprehensive report about these measurements. This paper will analyse the outcome of the test results, with a special focus on the application in EHAs.

Keywords: pumps, performance, benchmark, efficiency, electro-hydraulic actuators

1 Introduction

Energy efficiency has become one of the most important topics for the hydraulic industry. The clear trend towards sustainable and clean solutions forces companies to develop more efficient alternatives to traditional systems. For mobile applications, battery driven (i.e. engine-less) machines are becoming an essential solution. According to the European Union "the objective is to progressively reduce the pollutant emissions and to phase out equipment with the most polluting engines" [1].

But, electric driven systems set completely different demands than classical systems. Since batteries are expensive and bulky, it is no longer acceptable that the majority of the battery stored energy is lost in the hydraulic system. Energy efficiency is no longer a question of fuel cost, but of battery costs i.e. initial investment costs.

One of the promising solutions for increasing efficiency is the application of electro-hydraulic actuators (EHAs). The basic concept of a linear electro-hydraulic actuator is shown in fig. 1. A variable speed electric motor is coupled directly to a constant displacement pump. The hydraulic flow generated by rotation of the pump is directed to a load, which in this case is a cylinder. To ensure that flow reaches the correct side of the cylinder, several auxiliaries can be used. A large number of recent studies has focussed on designing such auxiliary circuits to optimize efficiency, enable energy regeneration, and overcome problems related to the asymmetrical nature of standard single rod cylinders (for example [2–4]).

Control of the velocity at the load side of EHAs, like the cylinder shown in fig. 1, is achieved by controlling the speed of the electric motor. In practice, this means that EHAs require both low speed and high speed operation of pumps. The high speed capability corresponds with the demand for smaller and more efficient electric motors. On the other hand, the low speed capability is needed to achieve low load velocities. However, almost all hydrostatic

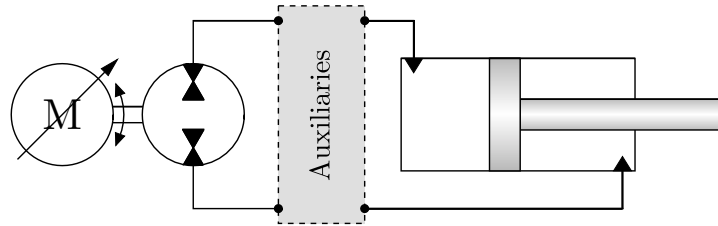


Figure 1: Simplified schematic of the basic concept of electro-hydraulic actuators (EHAs).

pumps have high friction losses, strong wear and often also high volumetric losses at speeds below 500 rpm. While there have been efforts to work around these minimum speed limitations of pumps, they typically depend on introducing new throttling losses via a variable leakage path [5, 6].

It is known, that there are almost no pumps available that meet both the high and low speed demands that are required for application in EHAs [7]. However, little to no information about the performance of pumps is available. Given these new constraints and demands it is understandable that this information is needed. In the past years, Innas has measured and tested several pumps and motors and published a comprehensive report about these measurements [8]. The report will be a living document, with new editions being published as soon as new pump (and motor) data will become available. In this paper, the outcome of the test results is analysed, with a special focus on the application in EHAs.

2 Tested devices

For the current study, five different hydrostatic devices were benchmarked: three piston pumps, and two gear pumps. Table 1 shows an overview of some of the key specifications of these devices. The piston-type units have a number of pistons (z) ranging from 7 to 24. From a physical point of view, the number of pistons in a piston-type machine is similar to the number of teeth in a gear pump. The geometric displacement volume, V_g , of each of the devices has been derived from volumetric measurements [9], and ranges from 23.7 to 32.7 cc per revolution. The volume ratio r_V describes the ratio between the amount of dead volume per piston, V_{min} , and displacement volume per revolution, as described in eq. (1).

$$r_V = \frac{zV_{min}}{V_g} \quad (1)$$

The value of r_V shown in tab. 1 has been derived from a combination of drawings and geometrical measurements of the devices. The maximum pressure and speed limitations, p_{max} and n_{max} respectively, are provided by the manufacturers of the devices.

The derived geometric displacement volume V_g is a scale for the size of the device. To operate a larger pump, more torque is required. In the case of EHAs, this means that a larger electric motor is needed. However, the movement of the cylinder in EHAs depends on the flow rate, which is the product of pump size and speed. In practice, the electric motor will almost always have a higher speed limitation than the pump. This means that a higher maximum pump speed will result in a larger maximum flow rate without the need to increase the size of the electric motor.

Table 1: Overview of the specifications of the tested hydrostatic pumps.

Pump name	Type	z	V_g [cc]	r_V	p_{max} [bar]	n_{max} [rpm]
Rexroth A4FO28	Axial slipper	9	27.87	0.78	400	3750
Moog RKP32	Radial slipper	7	32.66	0.08	350	2750
Eckerle EIPH3-025	Internal gear	13	24.31	0.17	330	3200
Marzocchi ELI2-D-25.7	External gear	7	25.41	0.00	210	3000
Innas FC24	Floating cup	24	23.65	0.85	500	5000

3 Measurement description

Each of the devices was benchmarked on the test bench at Innas BV [10]. This hydraulic test bench can operate pumps and motors at speeds ranging from 5000 rpm to less than 0.01 rpm, by using two different actuators. The

first actuator is a large electric motor, which is able to rotate the test device at any speed between 10 and 5000 rpm. This actuator is used to execute standard performance measurements in accordance with ISO4409:2019 [11].

The second actuator consists of a combination of a linear actuator and a sprocket, and is able to rotate the test device consistently at speeds from around 1 to less than 0.01 rpm. These extremely low-speed measurements provide useful information about the starting conditions of the different machines, which is very relevant for the use of these pumps and motors in EHAs. One of the benefits of EHAs is that the cylinder velocity can be controlled by the speed of the electric motor. In a typical load scenario, this means frequently switching between extraction and subtraction of the cylinder. This requires the pump to decelerate to a standstill and accelerate again.

The performance of each of the pumps was measured at a range of different discharge pressures. For the sake of conciseness, the following only shows the results of these measurements at a discharge pressure of 200 bar. The performance at the other pressure levels, as well as a more comprehensive description of the test bench, including pictures of the setup, hydraulic circuits, and sensor information, can be found in the full report [8].

4 Electric motor sizing

Before looking at any of the traditional results of the measured pumps, we want to be able to compare the devices when applied in an EHA. This will be done by looking at the relation between torque and flow rate. The electric motor delivers torque to the pump shaft in order to control the flow rate to the load. This flow rate can therefore be seen as the required output of the pump. The amount of torque required to achieve this flow rate, will correspond to the size of the electric motor: less torque generally means a smaller motor.

Figure 2 shows the measured torque on the pump shaft as a function of the discharge flow rate, at a discharge pressure of 200 bar. Each of the marked points is a measured operating speed. Due to the different pump sizes, the output flow rate and the torque varies for the different machines. This figure shows that the Moog, Eckerle, and Marzocchi pumps have a similar range of operation, with a maximum flow rate of about 75 lpm. To obtain this flow rate, the Eckerle only requires 85 Nm. On the other hand, the Moog pump needs an electric motor that can deliver a torque of 113 Nm, due to the difference in pump size. In other words, to obtain a flow of 75 lpm at 200 bar, a system with the Moog pump would need an electric motor that is roughly 40% larger.

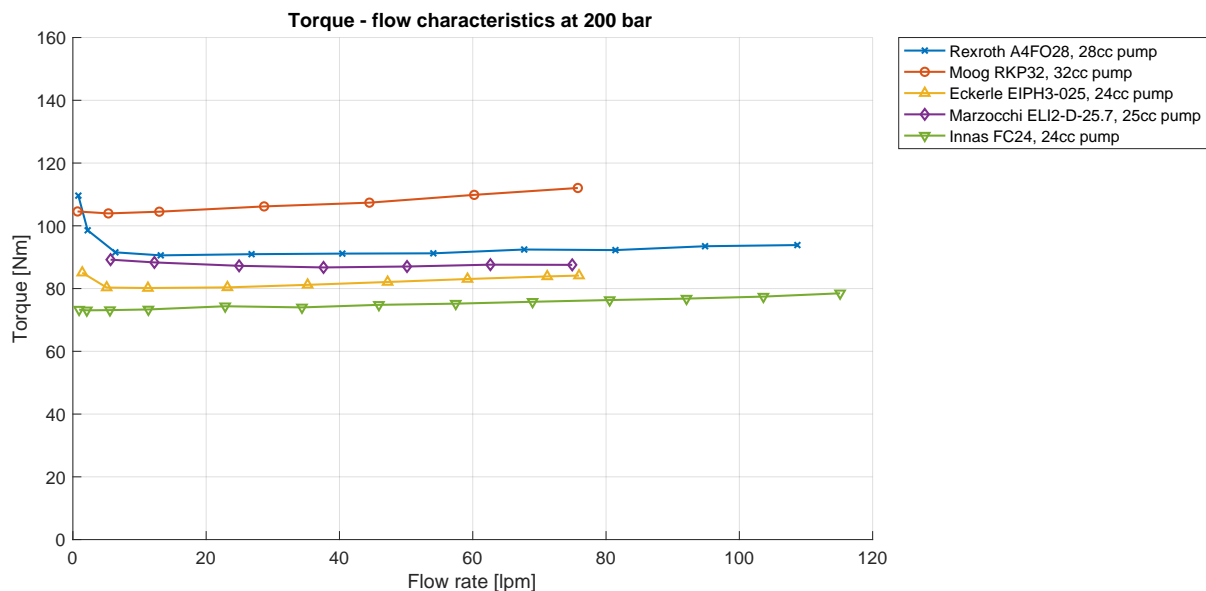


Figure 2: Measured torque as a function of the measured discharge flow rate, at a discharge pressure of 200 bar. Less torque means smaller electric motor.

The Rexroth and the Innas pump have a much higher maximum flow rate than the three other pumps. Suppose we want to design an EHA with a maximum output flow rate of 100 lpm at 200 bar. Since the maximum flow rate of the 27.9 cc Rexroth is roughly 110 lpm, we could settle for a pump that is 10% smaller than the tested unit: 25.4 cc. Furthermore, the torque of this smaller Rexroth pump is also expected to decrease with 10%, from 94 to 85 Nm. If we assume that the performance of these devices scales proportionally with the size of the pump, the torques and flow rates shown in fig. 2 scale equally. Figure 3 shows these scaled torques and flow rates of the five pumps.

From fig. 3, it is found that there is a large difference between the torque requirements of the tested devices when implemented in a 100 lpm EHA at a discharge pressure of 200 bar. The (scaled) Innas pump is expected to require the smallest electric motor, with a torque of roughly 70 Nm. The (scaled) Moog pump on the other hand requires roughly 150 Nm of torque to get the same amount of productivity.

Another difference between the different pumps is found when looking at the low speed operation in fig. 3. For most part of the operating range, roughly 85 Nm is required to operate the scaled Rexroth pump at 200 bar. However, when a lower output flow rate is required, the torque requirement for this unit increases rapidly. This is caused by an increase in torque losses at low speeds, which will be discussed in sec. 6.

Next to the difference in torque loss, fig. 2 also shows a difference in the minimum amount of flow that the pumps can output. For example, the Moog pump can deliver 0.70 lpm at 200 bar, while the Marzocchi pump has a minimum of 5.66 lpm at this pressure level. The inability to output low flow rates is caused by flow losses, and can lead to difficult control issues. This flow loss and its effects on the performance of EHAs in particular, will be discussed in sec. 7.

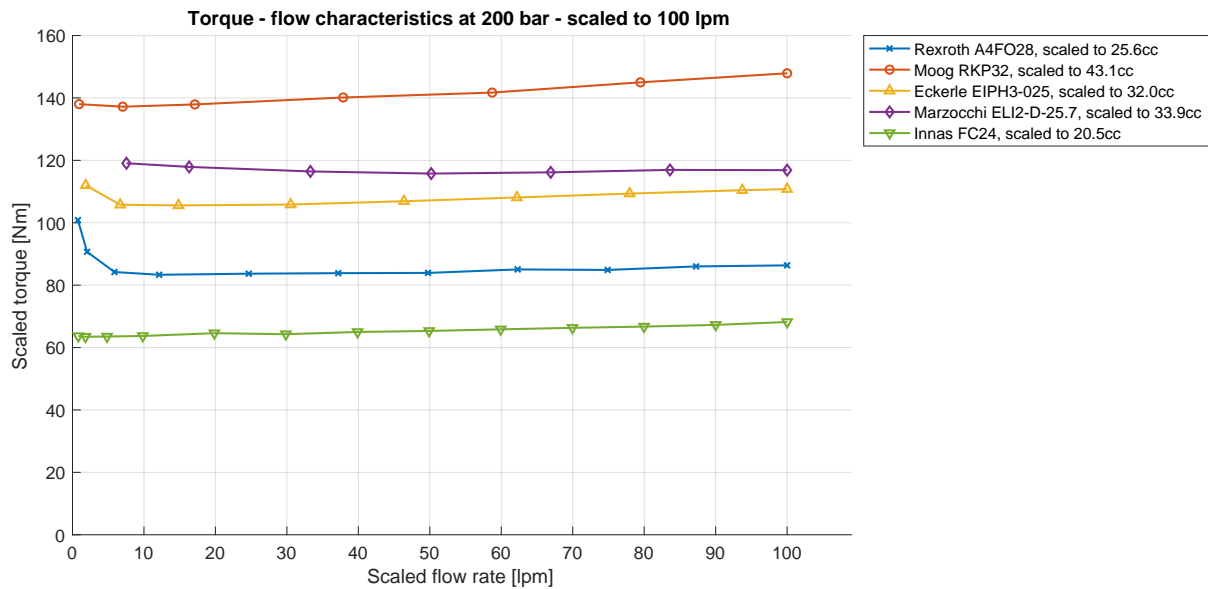


Figure 3: Torque as a function of the discharge flow rate at a discharge pressure of 200 bar, scaled to a maximum flow rate of 100 lpm.

5 Efficiency

Before looking at the individual torque and flow losses, we look at the efficiency of the different pumps. Since the goal of applying EHAs is to increase system efficiency, the pump efficiency is an important result of the high-speed measurements. Pumps are used to convert mechanical energy into hydraulic energy. In the case of EHAs, the electric motor is responsible for the mechanical power. Energy is therefore stored in bulky and expensive batteries. A higher efficiency primarily means smaller batteries can be used to get the same amount of work done.

Furthermore, when a pump has poor efficiency, the lost energy will increase the temperature of the oil. Managing the oil temperature will likely involve large cooling solutions that also require power from the battery pack. In other words, using a pump with higher efficiency also reduces the amount of energy needed to cool the oil in the system.

5.1 Definition

The rate at which mechanical power is converted to hydraulic power is defined as the efficiency, and can be calculated using eq. (2).

$$\eta = \frac{P_{hyd}}{P_{mech}} \quad (2)$$

In which η is the efficiency of the pump, and P_{mech} and P_{hyd} the measured mechanical and hydraulic power, respectively. According to [12], the mechanical power, P_{mech} , and hydraulic power, P_{hyd} , are calculated using eq. (3) and (4).

$$P_{mech} = T \omega \quad (3)$$

$$P_{hyd} = p_2 Q_2 a_P - p_1 Q_1, \quad \text{with } a_P = 1 + \frac{p_2}{2K_s} \quad (4)$$

In which T is the measured torque, ω the rotational speed, p_2 and Q_2 the pressure and flow rate at the high-pressure side of the device, and p_1 and Q_1 the pressure and flow rate at the low-pressure side. Furthermore, a_P is a correction factor to account for the compression energy in high pressure oil flow, with K_s the isentropic bulk modulus of the used oil. While traditional methods for calculating the hydraulic power ignore the compressibility effects captured in a_P , authors of several recent publications have concluded that these effects should be included when calculating the efficiency [12–14].

5.2 Results

The overall efficiency of all of the pumps was calculated using eq. (2). Figure 4 shows the results for different shaft speeds at an operating pressure of 200 bar. At low operating speeds, pumps are often unable to reach the required pressure level. In these cases, a second pump was used to ensure a correct circuit pressure. Since this second pump adds hydraulic energy to the system, eq. (4) no longer holds (i.e. a larger flow rate Q_2 will be measured). Therefore, it is not possible to determine the efficiency in these situations.

For all of the pumps, the efficiency in fig. 4 shows the same trend for an increasing shaft speed. At low operating speeds, the efficiency is low. As the machine starts rotating faster, the efficiency increases rapidly, until a maximum is reached somewhere between 1000 and 2000 rpm. As the shaft speed increases further, the efficiency decreases at a slower rate.

At this particular pressure level, the highest peak efficiency of almost 0.96 was realized by the Innas pump at 1000 rpm, while the Moog pump had the lowest peak efficiency of 0.87 at 1500 rpm. The other three pumps show very similar results to one another, all with a peak efficiency of 0.92 at 1500 rpm.

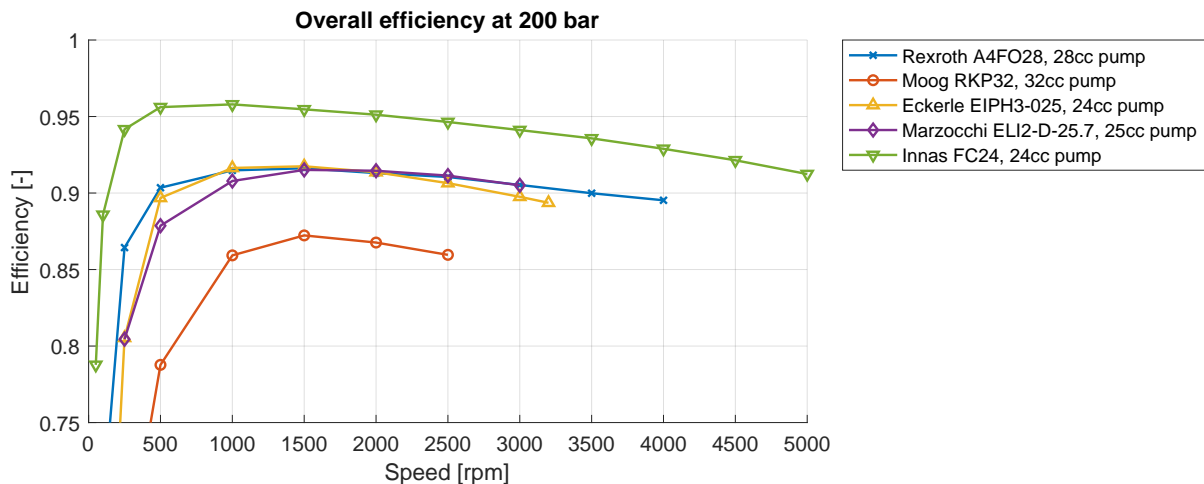


Figure 4: Comparison between the measured efficiency for all of the pumps at 200 bar.

6 Torque loss

Given the displacement size of a pump, it is possible to determine the torque that should theoretically be required to generate a certain amount of hydraulic power. However, since there is no such thing as a perfect pump, more torque will be required. Friction between moving parts, throttle losses due to limited flow areas, and improper commutation between the supply and discharge side, among other things, are all causes of torque loss inside of a pump. In the case of EHAs, higher torque loss means that a larger electric motor is needed to get the same amount of work done. Additionally, torque loss is a large contributor to the increase in oil temperature mentioned before.

At low operating speeds, coulomb friction greatly increases the amount of friction and resulting wear of the moving components in a pump. For this reason, classical valve controlled systems typically keep a pump rotating above a certain minimum speed. Closing a control valve will reduce the load velocity to zero. In speed controlled EHAs on the other hand, the pump will have to stop each time the load has to stop moving. To analyse the performance of the devices during starting and stopping, low-speed tests have been conducted.

6.1 Definition

The torque loss of a positive displacement machine can be defined as the difference between the measured torque T , and the theoretical torque T_{th} . According to [12], the theoretical torque can be calculated using eq. (5).

$$T_{th} = \frac{\Delta p V_g}{2\pi} a_T, \quad \text{with } a_T = 1 - \left(\frac{1}{2} + r_V \right) \frac{\Delta p}{K_s} \quad (5)$$

In which Δp is the pressure difference over the device ($p_2 - p_1$), and V_g is the derived displacement volume of the device as shown in tab. 1. Similar to the calculation of the efficiency, a_T is a correction factor to account for the compressibility of the oil. This correction factor can be determined using the volume ratio r_V (eq. (1), tab. 1). To be able to compare the torque loss of pumps of different sizes, the torque loss will be normalized by comparing it to the theoretical torque.

$$\hat{T}_{loss} = \frac{T - T_{th}}{T_{th}} \quad (6)$$

From eq. (6), the normalized torque loss can be seen as the additional amount of torque required to operate the pump, relative to the theoretical torque.

6.2 Torque loss during normal operation

The normalized torque loss of the five devices at an operating pressure of 200 bar is shown in fig. 5. In this figure, the same graph is shown on both a linear (left plot) and a logarithmic scale (right plot). The linear scaled plot mainly shows the losses at normal operating conditions, while the logarithmic plot provides some insight into the losses during low-speed and start-stop operation.

The logarithmic plot in fig. 5 shows that for a single device, for example the Moog pump, the torque loss is more or less constant at speeds up to 1 rpm. Between 1 and 250 rpm, the torque loss quickly decreases as the speed increases. At 250 rpm the pump reaches a minimum torque loss, which is the lowest of the pumps measured here. For speeds above 250 rpm, the torque loss increases again. This trend is similar for most of the devices that were benchmarked and is in accordance with the Stribeck curve. The three sections describe the transition from coulomb friction (boundary lubrication), to mixed friction, and viscous friction (hydrodynamic lubrication), respectively.

At this pressure level, the five pumps show some differences with respect to each other. Overall, it can be found that the Innas pump has the lowest torque loss, especially in the low speed range. This can be explained by the fact that this is a floating cup type pump, which has almost no contact between the piston and the cylinder, and thus very little coulomb friction. In the viscous friction section, the torque loss in the Rexroth, the Eckerle, and the Innas units increase at roughly the same rate. The torque loss for the Moog pump increases at a faster rate, while the torque loss of the Marzocchi seems relatively constant at higher operating speeds.

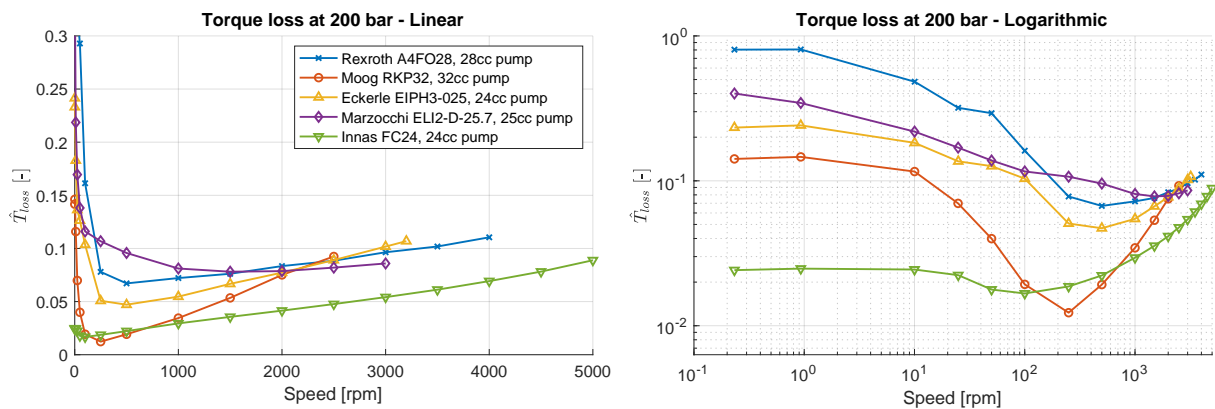


Figure 5: Comparison between the normalized torque losses for all of the devices at 200 bar.

6.3 Torque loss during low-speed operation

As mentioned before, the torque loss during measurements below 1 rpm is more or less constant, as it is mainly caused by coulomb friction. At these low speeds, the torque loss can be seen as the amount of breakaway torque that is needed (additionally to the torque required for operation) to start the pump from standstill, while the system is already pressurized. The results shown in fig. 5 show average values of the torque loss. However, at these low operating speeds there is a significant difference in torque loss between different angular positions of the shaft.

Figure 6 shows the torque loss, with respect to the angular position of the shaft, at a speed of 0.931 rpm and a discharge pressure of 200 bar. This figure shows reoccurring patterns caused by the limited number of pistons per device. The remaining variations between the individual piston patterns are caused by small differences in the tribological interfaces. These patterns are very reproducible, as is shown in the full measurement report [8].

Figure 6 shows that the Rexroth, on average, has a normalized torque loss of roughly 0.8. However, depending on the position of the shaft, this can be anywhere between 0.7 and 0.9. This means that almost double the amount of theoretical torque is required to breakaway. The other pumps require less additional torque, with the Innas pump requiring only a maximum of 0.02. From this figure, it becomes clear that not all of the tested pumps will be suitable for the stop-and-go kind of operation that is very common in several applications of EHAs.

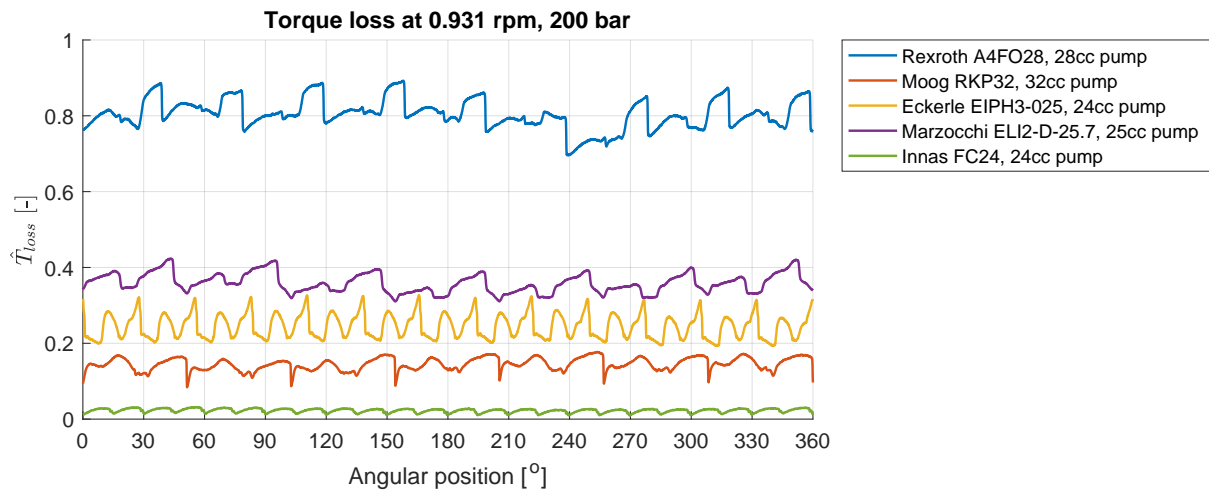


Figure 6: Torque loss as a function of the angular position for different pumps, at pressure 200 bar, speed 0.931 rpm.

7 Flow loss

Next to torque losses, hydraulic devices also experience flow losses. Based on the size of the pump, a certain flow rate is to be expected. However, since the moving parts inside a pump have a gap between them (albeit very small), oil will leak as soon as a pressure difference is present. Since flow occurs from high to low pressure volumes, the total flow loss will be a combination of several gaps.

First and foremost, oil can flow from the rotary group into the case. When a case drain line is available, this flow is directed back to the tank and can thus be measured. Most of this external leakage flow will come from the high-pressure side of the pump, since there is a large pressure difference between the pressure at the discharge port and the case pressure. However, since the case pressure is lower than the supply pressure, there will also be some leaked flow rate from the low-pressure side. Secondly, oil can also flow from the discharge side of the pump back into the supply side.

In case of EHAs, a pump with little to no flow loss is a very predictable device. Generally, this means that the control of such a device is fairly simple. In such a system, any change made to the speed of the electro-motor will result in a proportional change in velocity at the load. However, pumps often struggle to reach the desired pressure level at low operating speeds since all flow that the pump generates is lost before reaching the outlet port. In practice, this means that the control of the EHA has a dead-band. In the low speed region, a rotation of the electric motor does not result in movement of the load, leading to a non-linear system response. This undesirable behaviour will occur each time the load velocity switches direction, or the load has to stop and start moving again.

7.1 Definition

The flow loss of a positive displacement machine can be defined as the difference between the measured flow rate at the high pressure side Q_2 , and the theoretical flow rate $Q_{2,th}$. The theoretical flow rate can be calculated using eq. (7).

$$Q_{2,th} = \frac{\omega V_g}{2\pi} a_Q, \quad \text{with } a_Q = 1 - (1 + r_V) \frac{\Delta p}{K_s} \quad (7)$$

As was the case with hydraulic power and torque, correction factor a_Q is required to account for compressibility effects in the theoretical flow rate. To be able to compare the flow loss of pumps of different sizes, the flow loss

will be normalized by comparing it to the theoretical flow.

$$\hat{Q}_{2,loss} = \frac{Q_{2,th} - Q_2}{Q_{2,th}} \quad (8)$$

7.2 Overall flow loss

The normalized flow loss of all the devices at an operating pressure of 200 bar is shown in fig. 7. The left figure shows that the flow loss at speeds above 1000 rpm is less than 0.05 for most of the devices. Additionally, at higher speeds, the flow loss is relatively constant for these devices, which is beneficial for the control of EHAs. At speeds below 1000 rpm, the flow loss rapidly increases as is illustrated more clearly in the right plot of fig. 7.

In the right plot of fig. 7, we see that the minimum speed at which the flow loss is measured is different for the different pumps. For example, the minimum speed of Marzocchi pump is 250 rpm, while the minimum speed of the Rexroth pump is 50 rpm. Most manufacturers will address that their pump should be operated above a certain minimum speed. In an effective EHA however, the pump should be able to operated at near zero speeds. To this end, the minimum speeds in fig. 7 correspond to the ability of the pump to reach the desired pressure level (200 bar in this case).

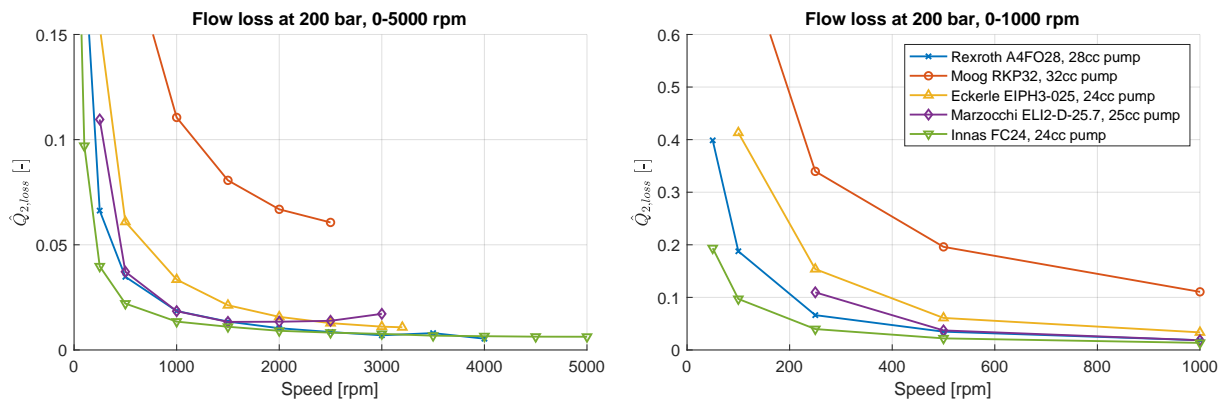


Figure 7: Comparison between the normalized flow losses for all of the devices at 200 bar.

7.3 External leakage

During the benchmark measurements, the external leakage from the rotary group to the housing of the devices is measured using a flow sensor. This flow rate is used to determine the flow rate at the low-pressure side of the device, which is standard practice [11]. The external leakage of three of the pumps at an operating pressure of 200 bar is shown in fig. 8. In the case of the two gear pumps, there is no external leakage port, so all flow loss will occur internally.

First and foremost, fig. 8 shows that the Moog pump has significantly more external leakage than the Rexroth and the Innas pump. This is likely caused by the different working principles (radial vs. axial), and the corresponding

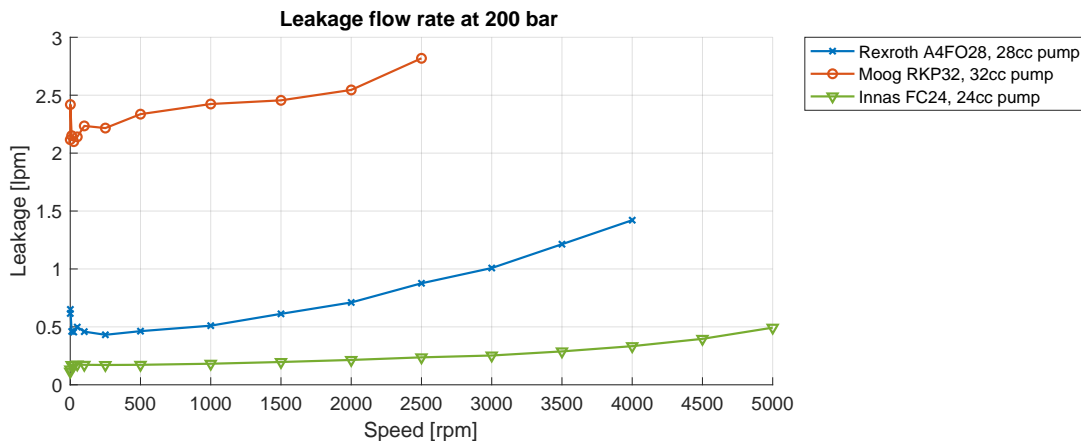


Figure 8: Comparison between the measured leakage flow rate for all of the device at 200 bar.

sensitivity to manufacturing tolerances. For the two axial units, it can be found that the leakage flow only slightly increases at the lower operating speeds. At larger operating speeds, the leakage increases for these devices. This could be the result of barrel tipping [15].

8 Conclusion

In electro-hydraulic actuators (EHAs), the integrated combination between electric motors and hydraulic pumps sets very different requirements for the hydraulic pump than in a traditional, valve-controlled circuit. While a lot of research is being conducted about the control, and auxiliary components required for EHAs, little to no information is available on the performance of the actual pumps. Therefore, five different pumps were measured on the Innas test bench. The main focus during the analysis of the results has been on the application of these pumps in EHAs.

The results have shown that it is difficult for many of the traditional pumps to meet requirements related to the use in EHAs. First of all, the maximum rotational speeds has been shown to be a limiting factor. Pumps that have a relatively low maximum speed, need to be larger in order to output the same amount of flow. This directly translates to a larger electric motor for the same output. For example, it was found that some pumps will require an electric motor that is roughly twice the size of a motor required for other pumps, while the output flow rate is the same.

On the other side of the range of operation, the pumps were tested during very low speed conditions. Since the load in an EHA is directly controlled by the speed of the pump, the pump will often be operated around zero speed. It was found that pumps can have very large amounts of torque losses at starting speeds, which will also increase the size of the required electric motor. Additionally, at these starting speeds, large amounts of flow losses result in dead-bands in the control strategies for EHAs, leading to non-linear system response.

Nomenclature

Designation	Denotation	Unit
Δp	Pressure difference over the device ($p_2 - p_1$)	Pa
η	Efficiency	-
ω	Measured rotational speed	rad/s
a_P	Compressibility correction factor for hydraulic power	-
a_Q	Compressibility correction factor for flow rate	-
a_T	Compressibility correction factor for torque loss	-
K_s	Isentropic bulk modulus (constant, $K_s = 1.76e9$)	Pa
P_{hyd}	Hydraulic power	W
P_{mech}	Mechanical power	W
p	Pressure	Pa
Q	Flow rate	m ³ /s
$\hat{Q}_{2,loss}$	Normalized flow loss	-
$Q_{2,th}$	Theoretical discharge flow rate	m ³ /s
r_V	Ratio between dead volume and displacement volume per piston (or tooth)	-
T	Measured shaft torque	Nm
\hat{T}_{loss}	Normalized torque loss	-
T_{th}	Theoretical torque	Nm
V_g	Displacement volume per revolution	m ³
V_{min}	Dead volume per piston	m ³
z	Number of pistons or driving teeth	-

Subscript	Port on device
1	Low-pressure side (supply)
2	High-pressure side (discharge)

References

- [1] European Commission. Non-road mobile machinery emissions. https://ec.europa.eu/growth/sectors/automotive/environment-protection/non-road-mobile-machinery_en. Accessed: 29-01-2021.

- [2] Ahmed Imam, Moosa Rafiq, Ehsan Jalayeri, and Nariman Sepehri. Design, implementation and evaluation of a pump-controlled circuit for single rod actuators. In *Actuators*, volume 6, page 10. Multidisciplinary Digital Publishing Institute, 2017.
- [3] Lasse Schmidt, Søren Ketelsen, Morten Helms Brask, and Kasper Aastrup Mortensen. A class of energy efficient self-contained electro-hydraulic drives with self-locking capability. *Energies*, 12(10):1866, 2019.
- [4] Søren Ketelsen, Giacomo Kolks, Torben Ole Andersen, Lasse Schmidt, and Jürgen Weber. Bootstrap reservoir concept for electro-hydraulic compact drives. In *12th International Fluid Power Conference*, 2020.
- [5] Haigang Ding and Jiyun Zhao. A new method of improving low-speed performance of variable speed hydraulic systems: by leaking parallel valve control. *Advances in Mechanical Engineering*, 6:967373, 2014.
- [6] Shaoyang Qu, David Fassbender, Andrea Vacca, Enrique Busquets, and Uwe Neumann. A closed circuit electro-hydraulic actuator with energy recuperation capability. In *12th International Fluid Power Conference*, 2020.
- [7] Martin Inderelst, David Prust, and Michael Siegmund. Electro-hydraulic swot-analysis on electro-hydraulic drives in construction machinery. In *12th International Fluid Power Conference*, 2020.
- [8] Innas BV. Performance of hydrostatic machines; extensive measurement report. <https://www.innas.com/assets/performance-of-hydrostatic-machines.pdf>. Accessed: 29-01-2021.
- [9] Gijsbert Toet, Jack Johnson, John Montague, Ken Torres, and José Garcia-Bravo. The determination of the theoretical stroke volume of hydrostatic positive displacement pumps and motors from volumetric measurements. *Energies*, 12(3):415, 2019.
- [10] Peter Achten, Jeroen Potma, and Sjoerd Eggenkamp. A new hydraulic pump and motor test bench for extremely low operating speeds. In *ASME/BATH 2017 Symposium on Fluid Power and Motion Control*. American Society of Mechanical Engineers Digital Collection, 2017.
- [11] ISO4409:2019. *Hydraulic fluid power, positive displacement pumps, motors and integral transmissions; Methods of testing and presenting basic steady state performance*. International Organization for Standardization, 2019.
- [12] Peter Achten, Robin Mommers, Takao Nishiumi, Hubertus Murrenhoff, Nariman Sepehri, Kim Stelson, Jan-Ove Palmberg, and Katharina Schmitz. Measuring the losses of hydrostatic pumps and motors; a critical review of iso4409:2007. In *BATH/ASME 2019 Symposium on Fluid Power and Motion Control*. American Society of Mechanical Engineers, 2019.
- [13] Christopher Williamson and Noah Manring. A more accurate definition of mechanical and volumetric efficiencies for Digital Displacement® pumps. In *BATH/ASME 2019 Symposium on Fluid Power and Motion Control*. American Society of Mechanical Engineers, 2019.
- [14] Perry Y Li and Jonathan Barkei. Hydraulic effort and the efficiencies of pumps and motors with compressible fluid. In *BATH/ASME 2020 Symposium on Fluid Power and Motion Control*. American Society of Mechanical Engineers, 2020.
- [15] Peter Achten and Sjoerd Eggenkamp. Barrel tipping in axial piston pumps and motors. In *Proceedings of 15th Scandinavian International Conference on Fluid Power, June 7-9, 2017, Linköping, Sweden*, number 144, pages 381–391. Linköping University Electronic Press, 2017.

Extremal Optimisation Approach to Component Placement in Blood Analysis Equipment

Magnus Sethson¹

¹Div. of Fluid and Mechatronic Systems (FLUMES),
Dept. of Management and Engineering (IEI),
Linköping University, Sweden

May 31, 2021

Abstract

This reports present an initial study on generative mechatronic design of equipment for blood analysis where the samples and chemicals are forwarded in thin single millimeter vessels. The system of vessels in the equipment transfers the fluids to different stations where chemical reactions and studies are performed. One of the stations is an optical inspection that requires controllable lighting conditions using an array of LEDs of different types.

The focus is on the generative design of the placement and configuration of the LEDs. The placement of the LEDs has been taken as a studying case for the method of Extremal Optimisation (EO) approach to mechatronic design. This method forms an opposing strategy to methods like genetic algorithms and simulated annealing. This is because it discriminate the individual parts or components of the configuration that underperform in a particular aspect instead of the more classical strategy of favouring good configurations from global measures. The presented study also relates to the class of many-objective optimisation methods (MaOP) and originates from the concept of self-organised criticality (SOC). The characteristics of avalanche barrier crossings in the parameter search space is inherited from such systems.

The test case used for the evaluation places occupying circles onto a quarter ring domain representing LEDs and circuit board. The fluid vessels are represented by lit up small domains that are also approximated by a circular disc. Some conclusion upon the methods capability to form a valid solution are made. A framework for describing a set of local flaw-improvement rules, called **D2FI** is introduced.

1 Background

This article reports the current state of an ongoing research project at Linköping University, where *Biomedical and Clinical Sciences* and *Management and Engineering* departments collaborate within the project CLOTRETRACT. The work presented here relates to some engineering aspects of defining and building mechatronic parts of a prototype machine for a new type of automated blood analysis. Most of the presented study relates to the Extremal Optimisation (EO) method and is carried out by the author at the Fluid and Mechatronic Systems division at Linköping University.

The general layout of the prototype and experimental machine for the blood analysis is shown in figure 1. Its overall structure goes from a particular camera in the base to the sample holder on the top. In the middle, there is a circuit board (PCB) holding several LEDs (Light Emitting Diode) for illumination of the six sample chambers at the top. The layout of this LED PCB is the focus of this article. Its configuration both in terms of shape, LED population, and component placement is delicate and affects the general performance of the automated analysis process. An external computer controls both the camera and LED synchronisation. The LED configuration act as an illumination source with angular characteristics to the optical axis through the machine. .

2 Introduction

The layout of PCBs is called auto-routing, most often solely related to generating the copper paths on different layers of the PCB so that the mounted components on the surfaces of the PCB are connected correctly. The routing process may occur with conditional requirements regarding the maximum current of the trace, high-frequency crosstalk, or other geometrical hinders. Most modern software packages (EDA) have auto-routing with conditions built-in today.

In this work, most of the component placement have stipulated boundary conditions set by external factors, and therefore the software available is not suitable for an automated design process of the PCB for this type of machine. By combining the external conditions into the automated design process, one needs to include geometry conditions from other levels than the PCB surface along the optical axis.

First studies on this indicated that setting up a general optimisation problem for such a design process was not achievable due to the difficulties of finding a reasonable starting condition. Both genetic algorithms and simulated annealing were tested. The problem proved to include some barriers that were very difficult or costly to cross. The search process was often stuck, or the progress was plodding, indicating that the approach used was not the correct one.

The problem at hand has the characteristics of both varying topology and combinatorics. The number of LEDs on the PCB is not given beforehand. Instead, a maximum surface area is provided and should include a particular mix of LEDs. The LEDs come in different sizes and have different emission angular openings and therefore need to be placed at a certain distance from the affected test chamber. The ranges also vary with the type of LED. The illumination from some LEDs is also believed to be more critical



Figure 1: The prototype machine is a vertical optical bench with a special camera at the base and an LED lightened sample holder. The blood sample box at the top consists of six test chambers called targets where some observations occur along with a particular passage for the blood flow.

than others and requires alignment along the optical axis. Some shadow effects are also required to avoid posing further restrictions on the LED placement. However, that is not included in this work. Several academic studies using Extremal Optimisation were found in the search for methods to deal with problems like this, see the next section.

This report focuses on finding a valid starting point for a design problem using Extremal Optimisation (EO) techniques. The presented results do not represent an optimal configuration of the PCB, but more of a starting point from where established optimisation methods can be applied successfully. Primarily simulated annealing is believed to be the way forward in that. The method described here is the author's first interpretation of the Extremal Optimisation technique for solving combinatorial problems within the generative design. It has been found useful, and it is believed it can serve as a good tool for further studies on generative design or even automated

design, especially where the problem size and topology are part of the search.

This report is organised as follows:

- Sec. 3: General presentation of Extremal Optimisation.
- Sec. 4: Formulation of the test problem by transforming it from 3D to 2D.
- Sec. 5: Introduction of the concept of design flaw-improvement pair rules, **D2FI**.
- Sec. 6: Conceptual PCB rules.
- Sec. 7: Test results.
- Sec. 8: Discussion, observations, and software.
- Sec. 9: Conclusions.

3 Extremal Optimisation

By academic search services, one gets a clear view that Extremal Optimisation (EO) was an unknown business up until about 2000 when the early work of Boettcher et al. [1] started to get attention. Today one can see that most of the efforts using this search technique take place in China. Recent work indicates that EO could be a way forward in training certain types of neural networks for classification problems within the business of machine learning, [2]. Also, it seems that EO was first established as a heuristic approach to deal with some combinatorial problems within physics. Therefore, it is often referred to as a practical problem-solving method based on the statistical physics concept of self-organised criticality, SOC. The author has not studied the founding basis for SOC, but it seems fundamental to the mathematical description of natural phenomena like storms, earthquakes, granular piles, and even evolution itself.

A fundamental character of such a system is the built around barriers, obstacles that suddenly break down, resulting in avalanche progress of the system state. Furthermore, that is what attracts its principle for solving automated design problems as the progress of the solution often mimics such avalanche behaviour. The eye-opening article for the author was the first part of the article of Boettcher et al. [1] on re-partitioning network structures.

A wide variety of engineering problems have recently been addressed with techniques borrowed from EO. That includes load balancing in network configurations of both email communications systems and electrical grids [3] [4] [5] [6]. It also includes application within controller design [7]. It has also been studied for weight training in LSTM neural networks [8], which is interesting due to many parameters in such applications. The design of new proteins has been addressed using EO to overcome the extraordinary combinatorial problem size such biochemical engineering pose [9].

Most often are published academic work using EO in combination with more traditional optimisation methods. That is true for genetic algorithms [10] and particle swarm methods [11]. EO forms a way of addressing many-objective optimisation problems (MaOP) applications in combination with other methods [12]. Particularly in mechatronics, engineering problems are often found to include objectives from widely different fields [13].

4 Test problem formulation

The actual design problem for the prototype machine is still under a patenting process and therefore not revealed in detail here. The presented problem is an interpretation of the problem for the sole purpose of exemplifying Extremal Optimisation (EO) techniques for the combinatorial problem of placing electronic components onto a circuit board (PCB) with the restriction imposed by other mechanical, hydraulic, and optical restrictions in the machine prototype. The trace routing between the components is not included in the test problem but is a separate and later process. The electric current requirements of the PCB are less dominant, and therefore the width of the nest net traces are in the range of 12-20 mil and are believed to fit in between the component placed on the surface easily. The LEDs used have a significant overhang due to their optical lens size and then provided plenty of routing space beneath its footprint.

A record vector describes each LED and component according to:

$$(\mathbf{p}_{LED}, d_{LED}, R_{LED}, E_{LED}) \quad (1)$$

where \mathbf{p}_{LED} denotes the (x, y) -coordinate of the component. d_{LED} is the component size, its diameter. R_{LED} is its operative range. It is further described bellow, but relate to the light emitting angular cone of the LEDs. E_{LED} is the emitting power in normalised form from each LED.

To simplify the coding of all components, they are treated equally, resulting in that the LED driver IC and the adjustment resistors (see figure 2) have no emitting power ($E_{LED} = 0$) and an range equal to a world size constant ($R_{world} = 100mm$). However, the emitting powers E_{LED} are not a part of the EO problem formulation but just included for further optimisation steps involving a global objective of equalising the received illumination at the six test chambers.

During the EO step sequence, the position \mathbf{p}_{LED} of one component is updated based on some selection criteria, see section 5 below.

4.1 From 3D problem to a flat 2D description

To simplify the problem from a fully 3D problem based upon the placement of each LED in relation to the six test chambers, some approximations have been made.

Projecting LED cone: The LED has an emitting cone of light. These are deliberately selected to be of both wide-angle and narrow spotting types. Values go from 9° to 110° . Assuming the distance between the PCB surface and the test chambers is constant during the design, one can transform this property into an emitting range (R_{LED}) of each LED. This is the radius of the zone that is illuminated by the LED.

Neglecting optical axis extent: The test chambers have a significant extension in the optical axis direction. Chambers extent has been compressed into a set of six flat circles, as can be seen in the middle of the opening in 2. Further, the test chambers are considered only by their centers $\mathbf{p}_{c,n}$ where $n = [1..6]$.

LEDs aligned to optical axis: All LEDs are aligned with the optical axis, resulting in that the LEDs may very well be approximated with a circle and an omnidirectional equal emitting radius, as described in figure 2.

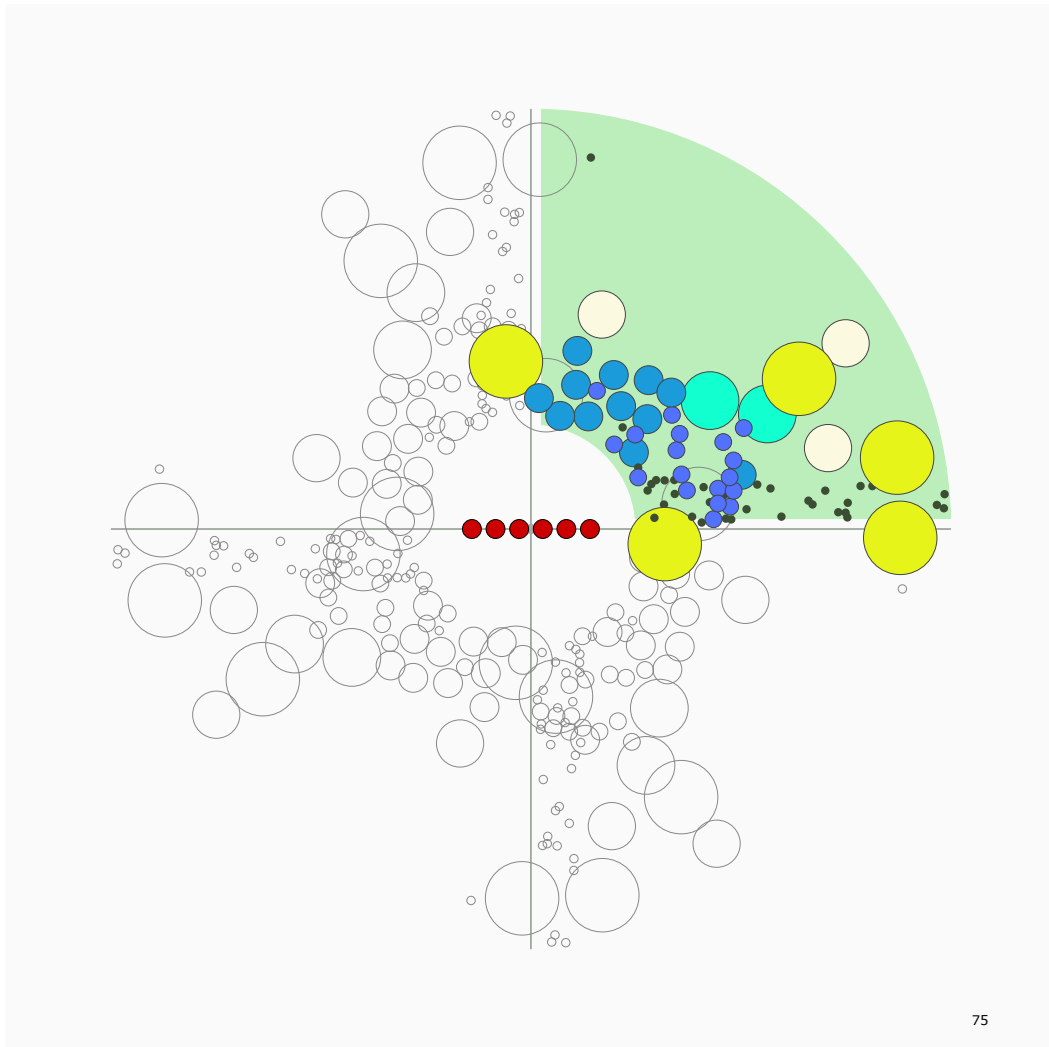


Figure 2: This is an intermediate result from a test run using EO. The problem is formulated onto a 2D quarter of a PCB surface with a hole in the middle for the optical axis. Symmetry is used for the PCB and is indicated by contours for quadrants 2-4. In the center are six test chambers placed, marked by red circles. The valid zone is the quarter-shaped segment in green, and the varying population of LEDs is seen in bluish color. The yellow circle marks LED driver IC-circuits that need to be in close vicinity of the LEDs connected and the small black dots represent current adjustment resistors that should go along each LED. In this view, a non-optimal layout has been reached.

5 Flaw-Improvement pair Rules, D2FI

In this work, the interpretation of Extremal Optimisation has been to improve the bad individual parts instead of the more classical approach in optimisation of promoting the good global solution. The algorithm used here can be described by two steps: identifying a flaw in the design and a corresponding improvement of that flaw. The pair of a design flaw and design improvement is called **D2FI** and forms a set of rules applied to the single design configuration repeatably.

The process may be described by two parts, a single topology and a multi-topology generative design process. The first focuses on reorganising a design with all its design variables defined at the beginning of the algorithm, and the second extends the procedure to make the topology of the design problem variable or scan multiple topologies sequentially.

5.1 Single Topology

Each flaw is identified sequentially by its type and a normalised score of flaw level. The number of possible types of flaws is fixed from the start, and they have a priority order between them, meaning some flaws are more significant than others and takes presence when it comes to the second stage of improvement. The flaws are ranked within each type class by the score of flaw level. In each step of the algorithm, one part of the design (one LED) is selected based upon its flaw score and is then improved based upon the priority of the type and flaw score level. This algorithm may get stuck in a local loop of **D2FI**-pair selections, but that is hindered by **not** selecting the flaw with the highest score each time. Instead, a probability density function is applied in the selection process favouring the most erroneous flaws for further improvement in most cases.

The overall algorithm is shown in algorithm 1 below. $C(\mathbf{x})$ represents the design space with the configuration $C()$ and its design variables \mathbf{x} . There are at most N design variables. The set of rules \mathbf{R}_s denotes the possible identifiable design flaws f_s and their corresponding improvement action a_s . The design rules may be variable over the iteration of the algorithm, but the rules in the set \mathbf{R}_s always remain normalised in the same fashion. There are at most $s \leq S$ design rules.

Algorithm 1 D2FI

Require: $C(\mathbf{x})$ $x = [x_1..x_N]$, $\mathbf{R}_s(f_s : a_s)$

Ensure: $N \geq 1, S \geq 1$

$n \leftarrow 1$

repeat

$\text{sort}(C(\mathbf{x}), \mathbf{R}_s)$

$(f_i : a_i) \leftarrow \text{select}(\mathbf{R}_s, p_s(n))$

$\text{improve}(C(\mathbf{x}), a_i)$

$n \leftarrow n + 1$

until $f_s = 0, s \in S$

Of course, some other termination criteria may apply when trying to reach zero flaw score on all flaw types for all design variables. The iteration number n may be used or some threshold on some lower-priority flaw type.

The flaw score is in this algorithm assumed to be a scalar number between 0 and 1. It is seen in the following example that it is a bit of a challenge to encode the score in such a way. Moreover, the algorithm does not fail if the flaw score extends beyond this range, but it has proved important that all design parameters are bounded or have a limit based on an equation describing a parameter boundary.

The set of design rules S is evaluated sequentially, making one take precedence over the other in a falling scale of importance. It is believed that there will always be a way to establish an order among the possible design flaws, from devastating flaws to less catastrophic.

This hierarchy of rules and the introduction of a normalised value for the individual flaw levels form the main contribution in this study. This approach forms a difference from other rule-based search methods.

5.2 Multi-Topology

The multi-topology sequential search is a simple extension to the single topology evaluation described in the previous section. It adds or removes one specific set of design parameters if, and only if, the previous step of a single topology search results in a total design flaw of zero. Once the repetitive process of topology changes can not reach a zero design condition, the overall process stops, and the previous topology from the last being tested is taken as the result of the process. On the way, one gets a sequence of increasing or decreasing design complexity solutions.

6 The PCB design example

This section is an example of how to apply the algorithm 1 presented above. The following sub-sections are design flaws presented along with the related improvement implemented in this test case. Also, the normalisation of the flaw score is given. All parts are transformed into the 2D space limited by a maximum coordinate value of R_{world} .

6.1 Outside outer boundary

A circle represents the edge of the outer boundary. The design flaw score is represented by the red part of the component area compared to its total area (see figure 3). In position a is the component entirely outside the boundary used for identifying the design flaw. The flaw score may either be represented by the red circular area solely or combined with the projected light red area towards the boundary. In position b , is the component partly correctly placed and therefore the flaw score may be in the range $[0..1]$. In this case, a suitable flaw score is defined by the red part of the total circular area of the component. Finally, in position c the design flaw score is 0 since the component is entirely inside the valid zone.

$$f_i = \frac{4A_{outside,i}}{\pi d_{LED,i}^2} \quad (2)$$

Placement of a component making it cross the boundary in figure 3 will result in some geometric expression giving the area of the out of boundary part of the component circle (coloured red). The normalised score in eq. 2 then represents the flaw made by design configuring the component at position (x_c, y_c) on the x-y-plane. The score may be extended by the almost rectangular area seen in position a in figure 3. This is a minor deviation from the general idea of having all design flaw scores normalised to the range [0..1] but will be useful for quickly move far outplaced components into the valid zone.

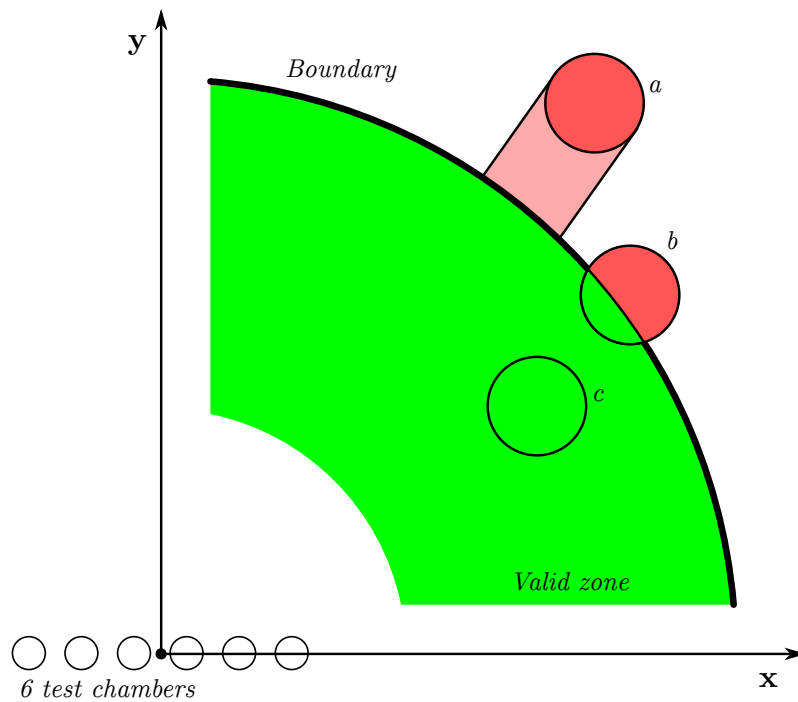


Figure 3: The quarter-shaped area forms the valid zone for component placement. Here one component is represented by its potential three positions a , b and c . Down to the left are the six test chambers indicated just for reference. That is where the blood flow passes through the machine. Symmetry is used, and the quarter-shaped zone is repeated by rotation to the other quadrants.

Once the flaw score has been selected and a component's position (x_c, y_c) has been selected for an update using this type of flaw, a position updating rule is applied.

$$(x_c, y_c) \leftarrow K_{f1} \times (x_c, y_c) + \mathbf{w}(n) \quad (3)$$

where $\mathbf{w}(n)$ represents a small random 2D vector to avoid cyclic behaviour of the algorithm further. Since the natural attractor for the improvement, in this case, is the PCB center, the value of K_{f1} is typically in the range of [0.80..0.99].

6.2 Inside inner boundary

In a comparable fashion as the outer boundary, a design flaw score may be established. In this case, the outer world maximum distance R_{world} does not need to be considered, and instead, the corresponding factor K_{f2} should be in the range of [1.01..1.20]. In this example, the largest component circle size is 14mm compared to the PCB center hole of 40mm. Due to the difference in these two measures, there might be a problem with the applied randomness through a $\mathbf{w}(n)$ addition. An extended design flaw value related to the rectangular-shaped area in figure 3 position a has not been used or tested.

6.3 Outside left boundary

This flaw and improvement pair is slightly more straightforward to implement than the previous ones. Only the x_c coordinate of the position of the component needs to be considered. Some geometric mathematical expressions are needed to deal with components close to the corners of the quarter-shaped zone, but overall the expressions are simple. The improvement update function is relatively straightforward:

$$x_c \leftarrow d_{f3} + x_c \quad (4)$$

where d_{f3} represent a small scalar value in the range of [0.01..0.10].

6.4 Outside bottom boundary

This is similar to the boundary violation rules set above, except the objective coordinate is y_c instead, hence the improvement update function become:

$$y_c \leftarrow d_{f4} + y_c \quad (5)$$

where d_{f4} mimics the characteristics of d_{f3} above for symmetry reasons.

6.5 Overlapping avoidance

This rule differs from the first flaw and improvement pairs above since it involves the relation between one LED and the others on the board. Apart (LED or another component) is selected $((x_c, y_c))$ based upon the amount of overlaid interferences from other components. It is then very straightforward; first, it searches for the closest neighbour in terms of center-to-center distance (x_n, y_n) that interfere with its boundary. Then both the nearest neighbour and the selected part are moved away by a small amount based on the direction given by the center-to-center vector. This neighbouring search can be costly and violates the idea of only considering design parts individually, but it is used here for simplicity and can be replaced by local search methods. The

total overlapping area is normalised towards the component's area, meaning that the flaw score may become greater than one but is still bounded by all the LEDs' total area. This mimics the normalising process from the rules presented above.

$$(x_c, y_c) \leftarrow k_{f5} ((x_n, y_n) - (x_c, y_c)) \quad (6)$$

A scaling coefficient k_{f5} is used to affect the rate of convergence in this flaw-improvement pair. This set of rules will be the most used in the process, hence the importance of this coefficient's convergence rate.

6.6 Evenly light distribution for test chambers

Once the LEDs start to organise, the positions reflect the characteristics of the individual LED. Each LED has a parameter for its operative range R_{LED} as described above. In a similar way to the flaw-improvement pair above (eq. 6) the selected LED's position is adjusted towards the targets if it has a flaw that indicates that its R_{LED} range is less than the distance to any test chambers. Only when it reach 3 different chambers it is assumed not to have a flaw anymore concerning test chamber lightning. The improvement rule then becomes:

$$(x_c, y_c) \leftarrow k_{f6} ((x_{st}, y_{st}) - (x_c, y_c)) \quad (7)$$

where the parameter st indicates one of the six targets. The target with the minor light emitted to it is selected by st . This varies with the position of the selected LED $((x_c, y_c))$ and the emitting power from all other LEDs. The enlightenment level for the targets is updated continually during the process. It is calculated by a radius-square relation for all six test chambers ($n = [1..6]$):

$$P_{target,n} = \sum_{k=1}^{N_{LEDs}} \frac{E_{LED,k}}{((x_t, y_t) - (x_c, y_c))^2} \quad (8)$$

Here the normalised flaw only takes values in the set of $(0, 1, 2, 3)$ so no area-based normalising takes place.

7 Evaluation tests

This section describes a test run of the algorithm on the PCB design for a machine described in the introduction. There are several LEDs marked as coloured circles in the following diagrams. The largest circle describe the LED driver circuit and has no light emission but is instead a regular IC. Its occupancy area is still treated as a circle even if it has a rectangular shape. The valid PCB-surface is pictured in light green and forms the valid design space. The overall design space is a square with $100mm$ sides.

7.1 Single Topology Example

The example results come from a test run with a fixed number of LEDs, a single topology. It runs for 500000 state changes or steps. In each step, one LEDs is selected, most often the one with the worst total flaw score, but 0.5% of the times the second-worst is selected, and 0.005% of the steps is the third worst selected. This is to make the algorithm not get stuck in a bistable scenario.

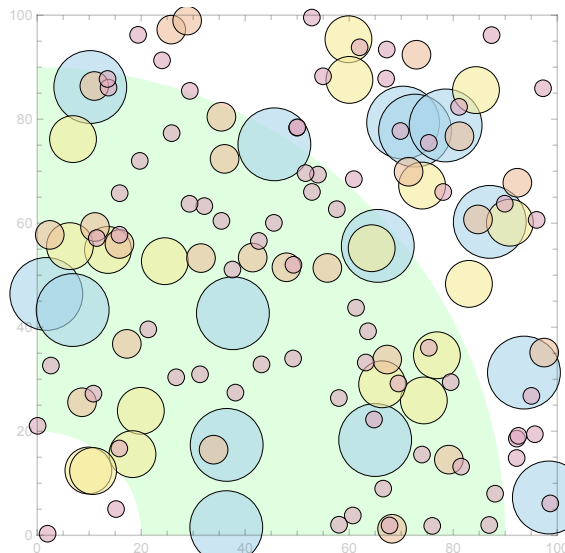


Figure 4: Starting topology from the beginning of the algorithm. The set of LEDs are randomly placed and selected from three categories. 72 pcs of 3mm LEDs (red small circles), 24 pcs of 5mm LEDs (orange larger circles), 18 pcs of 8mm LEDs (yellow large circles). To balance this, a number of LEDs 16 pcs of driving circuits, is added as well (blue largest circles). In the background, one can see the valid PCB surface in light green. This board layout forms step 1 in the process of 500000 steps.

Observations: The exemplified test run takes 50 seconds on average to complete using an Intel i7 CPU at 4.6GHz. The memory footprint is tiny.

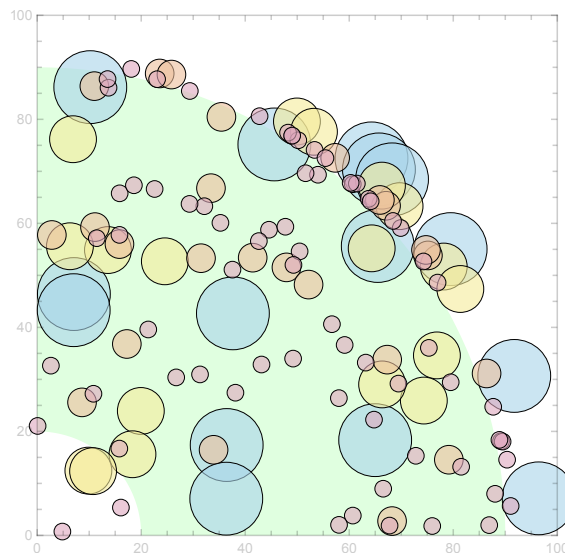


Figure 5: This is step 924, and the hierarchy of flaws can be observed in that the outliers are drawn into the valid PCB-area first. The LEDs placed inside the green area have only minor position adjustments, while those outside the PCB have moved onto or close to the PCB border. Some minor changes on the left and bottom border can also be observed.

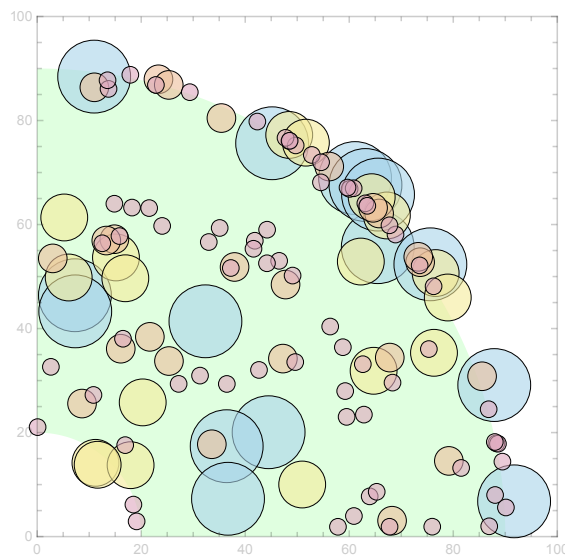


Figure 6: This is step 1852 and the set of flaw-improvement pair rules \mathbf{R}_s have been applied equally many times, bringing the process further. Some effects of the overlay flaw can be observed since some larger circles have bounced off the other border of the PCB. At the same time, the other borders have attracted outliers more.

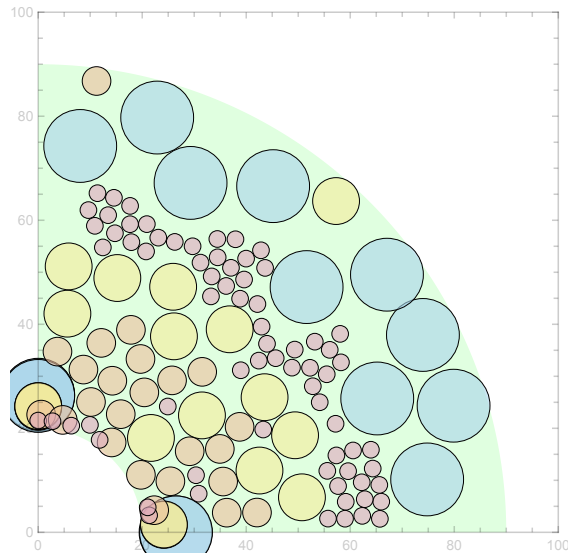


Figure 7: This is step 66983, and some ordering among the LEDs can be seen. This is the last flaw-improvement rule coming into more application forwarding light emission onto the targets situated near origo in the figure.

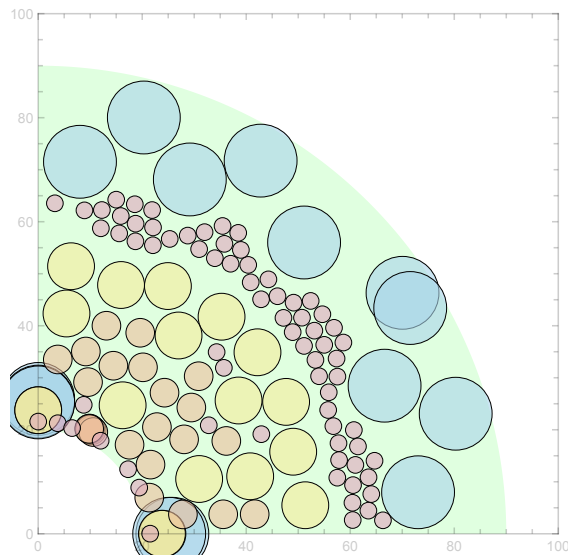


Figure 8: This is step 196264, and further order can be observed. Still, some overlay flaws are noticed especially close the corners of the inner circle of the PCB area.

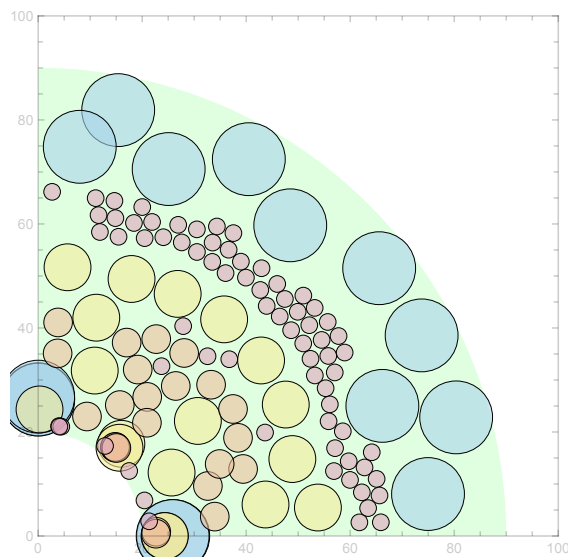


Figure 9: This is the final step 500000, and the process terminates. The overlapping issues remain for the circles in the close vicinity of the driver circuits (blue large circles). Still, the current state of the layout could serve as a good starting point for a optimisation using some global scheme like genetic algorithms or simulated annealing.

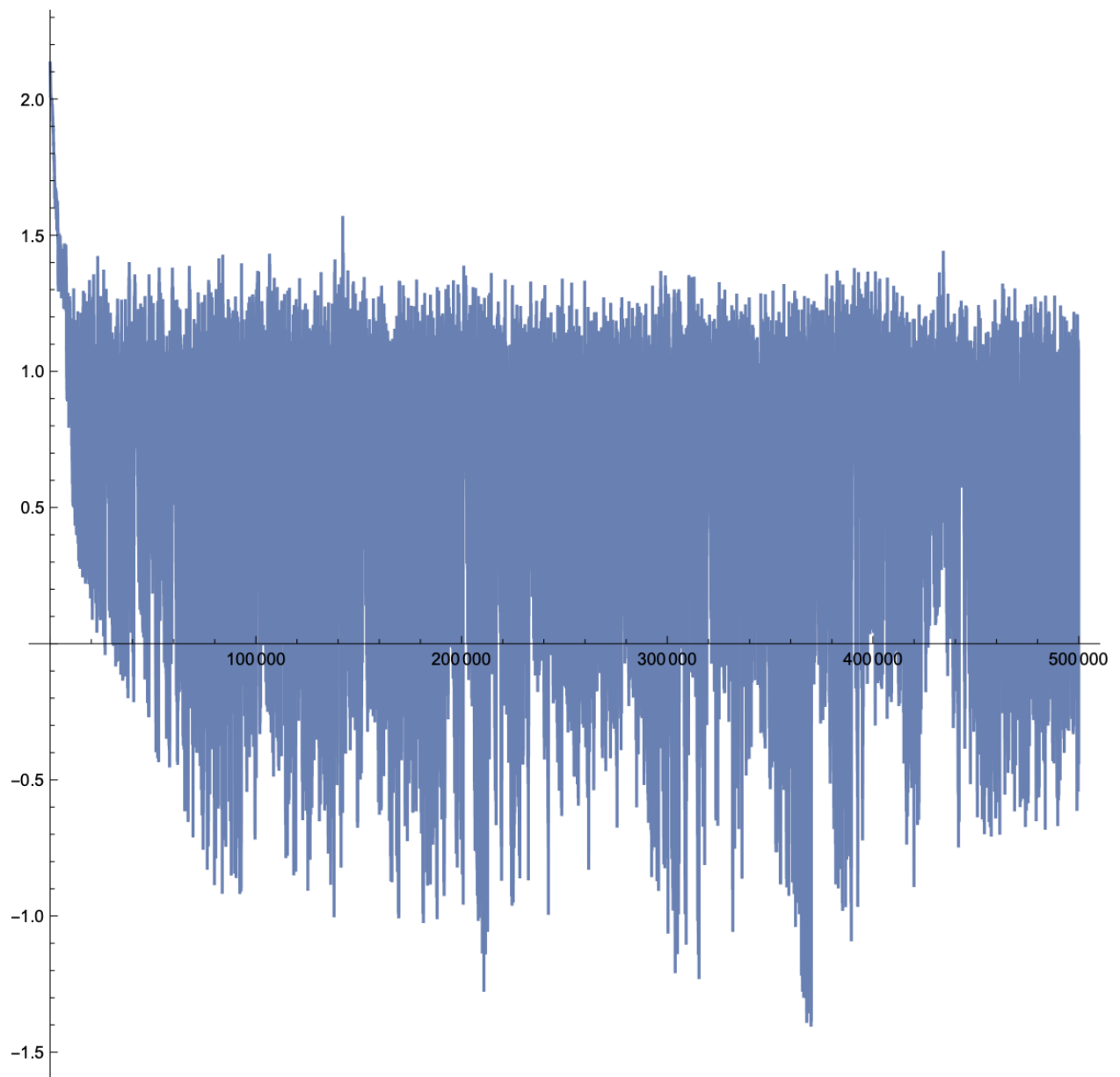


Figure 10: This is the total flaw score of the test run, where the score value is presented as a \log_{10} value. It is not to be interpreted as a global design error value, revealing some 4 orders of magnitude reduction in the design flaws but is just presented as an indication that the algorithm works as a search method using flaw-improvement rule pairs. Most noticeable is that several deep pockets of very low total flaw scores are passed during the test run. Some thousand tests have been carried out, all converging to a result similar result to this diagram.

8 Discussion

This short and preliminary study has led to many observations. It is worth mentioning that the study is intended as a search method for finding robust start conditions for further optimisation of the machine's LED layout and **not** as an optimisation method on its own. The idea is also to be able to start with a rather broad parameter search space. Similar to other academic works presented related to EO techniques.

The overall procedure is intended to support a flexible and quick method to re-configure the machine's performance during the prototype development process. The lighting conditions of the test chambers or targets are the LED PCB's objective and need to be varied during different prototype stages. An alternative procedure to the one presented here could have been used applying modern CAD software in combination with optimisation tools. Several commercial tools exist for that.

It is noticeable that the algorithm 1 has a similar look as a classical genetic algorithm with the `sort()-select()-recombine()` structure. This may be extended in future versions to include branches in the search space, making the LEDs positions not only just being shifted by a small step on the PCB but moved away to a new area entirely.

Such movement needs to take all other LEDs into account, which violates the proposed method's character to only evaluate individual components attributes when looking for the highest design flaw score in each step. A small violation of that has already been made since the search for the most overlapping design flaw evaluates all LEDs relation to each other. Nevertheless, there exist ways to reduce this $O(n^2)$ search by modern algorithms. The unique approach in this algorithm to only evaluate each component's design flaw individually encourages parallel execution. Still, in this early stage, the program has been implemented as a single-threaded program unit using C++14 template structures, and no parallelism has been applied.

The total flaw score seen in figure 10 above indicates that the organising of the LEDs' position works. A considerable number (1000+) of similar test runs have been carried out, and none have got stuck in a limiting loop. This is due to the introduction of small randomness when selecting the individual with the highest flaw score, as described in section 7.1 above. The results presented in figure 10 are not to be interpreted as a minimised design error even if it looks like the flaw goes down with an increased number of steps. Instead, the correct interpretation of it is that the search of the design space works. One can see from the logarithmic values that the total flaw score goes down from around 130 to 0.04, a drop of ca 3300 times or nearly four orders of magnitude.

One may find many steps in the algorithm, and the presented example uses 500000 steps, overwhelming. However, consider that a standard global optimisation method usually requires 1000 to 10000 steps for a 150-variable optimisation problem. That also results in some state changes among variables in the range of millions.

Finally, a more subjective remark can be made on this work. To make this flaw-improvement pair ruleset work, one needs to have an algorithmic approach to describing the problems at hand. This may differ from standard optimisation methods where one formulate mathematical equations that are to be minimised. Perhaps one can find it more challenging to establish this set of rules than defining a global mathematical

expression, and also, the computational performance of the method depends highly on the implementation of the rules. The selection of high-performance computer languages like C++ has become very fruitful, just by chance. However, languages like Haskell maybe even more suitable for future studies.

8.1 Next step

The presented method is going to be used further in the project of creating this blood analysis machine. It has been combined with simulated annealing with promising results already, but some more analysis on the combined results is still needed.

8.2 Software release

The software created in this project has been made available for public use with the restriction of no commercial use and attribution according to the Creative Commons license model. The use of it is described in the attached LICENCE file. Please notice that it is highly specialised and requires some good C++ insight.

GitHub link: https://github.com/magse/pcb_layout_demo_eo.

8.3 Referencing

Attributing this work is primarily done by referencing the indicated scientific work as indicated on the https://github.com/magse/pcb_layout_demo_eo site.

8.4 Acknowledgment

The author presented this report at the SICFP21 online conference in June 2021. The author happens to be the conference's information system organiser, controlling the peer-review process in detail. For that reason, no peer-review process has been carried out on this contribution.

9 Conclusion

This report presents preliminary results from the mechatronic design process of a blood analysis machine that combines engineering from highly diverse fields like chemistry, electronics, fluid power, optics, and computers. This report focuses on the pre-processing stages for optimising the layout of LEDs onto a PCB surface. The following observations were made:

- Combining design flaws and their related improvement/updating actions into a pair forms a good structure for algorithmic generative design and possible for automatic design.
- The process of updating a mechatronic design stepwise is done by selecting one action from a hierarchical set of rule pairs where the most severe design flaw score takes presence over the rest, on a falling scale of severeness.
- The algorithm's performance indicates that the avalanche barrier crossing characteristics found in self-organised criticality (SOC) systems are inherited into the presented **D2FI** algorithm. The search for such characteristics was the initial driver for this study.
- A set of six rules organised hierarchically has proved to work when each rule flaw is normalised into a value of $[0 .. 1]$.
- Bounded deviations of the normalising flaw score are allowed and do not affect the overall performance, just the sequencing of the improvements taken.
- The procedure has been exemplified upon a combined mechatronic design problem of optics and target lightning conditions where the original geometric 3D problem has been reduced to a flat 2D domain.
- The algorithm have been executed many times without any observation of being stucked in a loop condition, mainly due to some randomness in the flaw selection step.
- Further investigation on the combination with a following global optimisation procedure is still needed.
- The current state of demonstration software using the proposed approach has been made available through GitHub.

10 References

References

- [1] Stefan Boettcher and Allon G. Percus. Extremal optimization: Methods derived from co-evolution. 1999.
- [2] F. Zhao, G. Zeng, and K. Lu. Enlstm-wpeo: Short-term traffic flow prediction by ensemble lstm, nnct weight integration, and population extremal optimization. *IEEE Transactions on Vehicular Technology, Vehicular Technology, IEEE Transactions on, IEEE Trans. Veh. Technol*, 69(1):101 – 113, 2020.
- [3] Ivano De Falco, Eryk Laskowski, Richard Olejnik, Umberto Scafuri, Ernesto Tarantino, and Marek Tudruj. Dynamic load balancing based on multi-objective extremal optimization. *2020 19th International Symposium on Parallel and Distributed Computing (ISPDC), Parallel and Distributed Computing (ISPDC), 2020 19th International Symposium on*, pages 134 – 141, 2020.
- [4] Noemi Gasko, Mihai Alexandru Suciuc, Tamas Kepes, and Rodica Ioana Lung. Shapley value and extremal optimization for the network influence maximization problem. *2019 21st International Symposium on Symbolic and Numeric Algorithms for Scientific Computing (SYNASC), Symbolic and Numeric Algorithms for Scientific Computing (SYNASC), 2019 21st International Symposium on*, pages 182 – 189, 2019.
- [5] Yi-Yuan Huang, Min-Rong Chen, Liu-Qing Yang, Kang-Di Lu, and Guo-Qiang Zeng. An electric load forecasting model based on bp neural network and improved bat algorithm hybridized with extremal optimization. *2019 Chinese Automation Congress (CAC), Chinese Automation Congress (CAC), 2019*, pages 4673 – 4678, 2019.
- [6] Jing-Liao Sun, Xiao-Qing Xie, Ru Xiong, Guo-Qiang Zeng, Huan Wang, and Yu-Xing Dai. Binary-coded extremal optimization based fractional-order frequency control of an islanded microgrid. *2017 36th Chinese Control Conference (CCC), Control Conference (CCC), 2017 36th Chinese*, pages 10679 – 10685, 2017.
- [7] Guo-Qiang Zeng, Xiao-Qing Xie, Min-Rong Chen, and Jian Weng. Adaptive population extremal optimization-based pid neural network for multivariable nonlinear control systems. *Swarm and Evolutionary Computation*, 44:320 – 334, 2019.
- [8] Min-Rong Chen, Bi-Peng Chen, Guo-Qiang Zeng, Kang-Di Lu, and Ping Chu. An adaptive fractional-order bp neural network based on extremal optimization for handwritten digits recognition. *Neurocomputing*, 391:260 – 272, 2020.
- [9] Keiichi Tamura, Hajime Kitakami, Tatsuhiro Sakai, and Yoshifumi Takahashi. A new distributed modified extremal optimization for optimizing protein structure alignment. *2015 IEEE 8th International Workshop on Computational Intelligence and Applications (IWCIA), Computational Intelligence and Applications (IWCIA), 2015 IEEE 8th International Workshop on*, pages 109 – 114, 2015.
- [10] F. Pistolesi, B. Lazzerini, M.D. Mura, and G. Dini. Emoga: A hybrid genetic algorithm with extremal optimization core for multiobjective disassembly line balanc-

- ing. *IEEE Transactions on Industrial Informatics, Industrial Informatics, IEEE Transactions on, IEEE Trans. Ind. Inf.*, 14(3):1089 – 1098, 2018.
- [11] Fleford Redoloza and Liangping Li. A comparison of extremal optimization, differential evolution and particle swarm optimization methods for well placement design in groundwater management. *Mathematical Geosciences*, 53(4):711 – 735, 2021.
- [12] Min-Rong Chen, Guo-Qiang Zeng, and Kang-Di Lu. Constrained multi-objective population extremal optimization based economic-emission dispatch incorporating renewable energy resources. *Renewable Energy*, 143:277 – 294, 2019.
- [13] Leandro dos S. Coelho, Viviana C. Mariani, Rafael B. Grebogi, Emerson H. de Vasconcelos Segundo, Mauricio V. Ferreira da Luz, Jean V. Leite, and Roberto Z. Freire. Diversity-guided generalized extremal optimization for transformer design problem. *2017 IEEE Symposium Series on Computational Intelligence (SSCI), Computational Intelligence (SSCI), 2017 IEEE Symposium Series on*, pages 1 – 6, 2017.

Control Strategies for a Dual AC Motor Pump System in Aircraft Hydraulic Power Packages

Nils Trochelmann and Frank Thielecke

Hamburg University of Technology, Institute of Aircraft Systems Engineering, Hamburg, Germany
E-mail: mailto:nils.trochelmann@tuhh.de; frank.thielecke@tuhh.de

Abstract

Hydraulic power packages (HPP) integrate electric motor-driven pumps (EMP) and hydraulic equipment to supply (on demand) hydraulic power to specific functions. To achieve a high operational availability two redundant EMPs are installed per HPP. To produce maximum output power, the EMPs need to operate in parallel. In the first part of this paper a baseline pressure control strategy is developed that enables the parallel operating mode. It has to cover the performance requirements and it is crucial to avoid stability issues of today's aircraft multi-pump hydraulic systems, induced by slightly differing pump characteristics. A central pressure controller, which calculates the total (cumulated) control effort and allocates it evenly to both EMPs, is selected as the basic controller structure. A loopshaping approach, where the requirements are mapped on target loop shapes, is applied. The control design is verified by non-linear simulation and by experiments using representative aircraft prototype EMPs. Their slightly differing characteristics are utilized for an implicit proof of robustness. The second part of this paper makes use of the low utilization of the EMPs during most parts of the flight to achieve secondary objectives (efficiency, dynamic performance) and to improve the handling of operational constraints (e.g. electric input power limit). A model predictive control allocation (MPCA) algorithm flexibly allocates the total control effort to the EMP units. The allocation is derived from the solution of an optimization problem with the operational limits as constraints. Non-linear simulations of two exemplary scenarios show that the MPCA algorithm minimizes power losses by increasing the utilization of the more efficient unit. In addition, the MPCA algorithm improves the dynamic performance in case of an asymmetric performance degradation by prioritizing the unit with better performance capability. The potential for improvement increases with the difference between the units and therefore offers advantages in dynamic allocation in particular for fault-tolerant operation.

Keywords: Hydraulic Power Package, Electric Motor-Driven Pump, (Model Predictive) Control Allocation, Parallel Pump Operation

1 Introduction

The electrification of the aircraft secondary power systems is a major approach to increase future aircraft efficiency, reliability, and to reduce operating cost. Under the guiding concept of More Electric Aircraft (MEA) different electrical system architectures have been investigated since the 1980s [1]. However, electric systems require electric actuation concepts. The main candidates are electro-mechanical actuators (EMA) and electro-hydrostatic actuators (EHA). Both still have issues that inhibit their frontline operation. For EMAs these are in particular prediction of jam-probability in safety critical functions, jam-tolerant control, high weight and complexity in case of large power applications (like landing gear actuation). For EHAs pump reliability and heat rejection are the main concerns. In this situation, electro-hydraulic systems that supply hydraulic power from electric-motor-driven pumps (EMP) to conventional hydraulic actuators are a promising alternative.

1.1 Decentralized Electro-Hydraulic System Architectures

In particular, decentralized architectures, as shown in fig. 1, are considered. They replace the central hydraulic system by a number of smaller zonal systems. Hydraulic power is generated by hydraulic power packages (HPP) and routed to the consumers of a specific zone through a local pipe network. This architecture eliminates the maintenance intensive central pipe system and allows proven and jam-free hydraulic actuation technology with high power density to be retained.

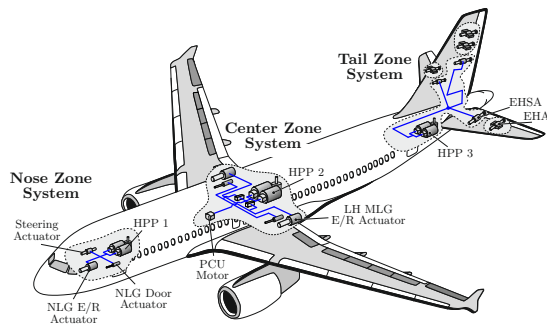


Figure 1: Decentralized Electro-Hydraulic System Architecture of a More Electric Aircraft

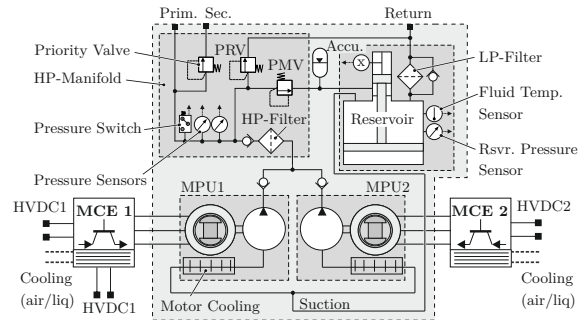


Figure 2: Exemplary Hydraulic Power Package Schematic

1.2 Hydraulic Power Package

The HPP is a key technology of new electro-hydraulic architectures. It integrates the EMP(s) and the hydraulic system equipment (accumulator, valves, filters, reservoir, sensors, etc.) in a compact easy-to-replace module. HPPs can be pre-assembled and pre-tested which permits quicker installation and cost savings. The HPP hydraulic schematic is illustrated in fig. 2. Two redundant EMPs are necessary to ensure the availability target [2]. For industrial purposes both EMPs are the same size. Check valves downstream of each pump avoid backflow to an inactive unit. For mass reduction, the EMPs are not sized for the maximum flow demand each. The EMPs are of type speed variable fixed displacement (VSFD), comprising a speed controlled permanent magnet synchronous motor (PMSM) and a fixed displacement pump. Electric power is modulated by the motor control electronics (MCE). The MCEs have a communication interface to the aircraft’s avionic system.

For feedback pressure control and monitoring two redundant pressure sensors are installed. Pressure control is supported by a system accumulator covering transient flow peak demands that exceed the quasi-static maximum flow demand. The fluid is stored in a self-pressurizing bootstrap reservoir (pressurized air from the pneumatic system may not be available in the considered MEA scenarios [1]). A pressure maintaining valve (PMV) keeps a minimum reservoir pressure during pump start-up.

1.3 Motivation and Objectives

The HPP has to operate both EMPs in parallel to provide maximum hydraulic output power. Parallel pump operations can lead to undesired oscillations, e.g. triggered by (slightly) differing pump characteristics. A robust controller is developed that overcomes this issue and enables the stable parallel operation (duplex mode). The development steps concept synthesis, control, design, and experimental verification are presented.

Maximum output power is needed only for a short time during a typical flight mission, so that the dual EMP system is oversized most of the time. This opens up the potential to include additional/secondary goals, like minimization of power losses, and to handle operational constraints (e.g. power limitations) through dynamic control allocation of the two pump speeds, when the maximum output power is not requested. The development of a dedicated optimized control algorithm is the second objective of this contribution. First, chapter 2 gives an overview of existing multi-pump control concepts.

2 Aircraft Multi-Pump Systems

Many aircraft hydraulic systems operate multiple pumps, e.g. to increase availability or dissimilarity of hydraulic power sources. Mostly inline piston pumps with variable displacement and hydro-mechanical pressure compensators are used. For example, the AIRBUS A380 runs four engine driven pumps (EDP) per hydraulic system (a comprehensive overview is provided in [3]). Systems with multiple EMPs, like the HPP, are less common. One

example is the BOEING 787 center system with two parallel EMPs. Though, the EMPs are normally not operated in parallel. The second EMP is activated only during phases of higher demand and/or to balance usage [4], [5].

Experiences with with parallel operations of pumps with hydro-mechanical compensation and associated findings are described in [6]:

- **Pump-Flow-Fight:** Pumps with slightly different characteristics attempt to dominate each other. This results in flow-fighting (crosstalk) and pressure oscillation. Pump-flow-fighting can be mitigated by different check valve pre-loadings or pressure compensator settings.
- **Resonance:** The superposition of pump pulsations can lead to resonances in the delivery line. This is avoided by (slightly) different pump speed settings.
- **Instability:** Instability due to a very low fluid volume can occur when a check valves is closed. This issue is more severe for pumps with low internal leakage (like the compensated IGP) and thus lower damping. Either compromising the compensator design and/or a redesign of the plant (e.g. increasing pump internal leakage, different check valve installation location) is necessary.
- **Blocked Pump:** In the above situations one pump could be blocked by the other and produce very low output flow. This leads to high internal pump temperatures and undesired, very low pump speeds in case of a speed variable pump.

The state of the art control solutions for multiple pump systems are limited to hydro-mechanical approaches. Electronically controlled pumps are not yet being used in commercial aircraft hydraulic systems [7]. A fighter aircraft hydraulic system with two parallel variable displacement pumps and electronic control is considered in [8]. The authors, however, do not detail the dual-pump control concept. A parallel configuration of two speed variable EMPs, which is very similar to the present application, is used for pump controlled landing gear actuation [9] and [10]. A closed loop pressure control with a dedicated pressure controller for each EMP is proposed. It should be mentioned that the pressure is sensed between check valve and pump so that the point of regulation is located directly at the pump's high pressure port, similar to a hydro-mechanical compensator. This arrangement is prone to the stability issues discussed above.

Multi-pump systems can also be found outside aerospace. In [11] the problem of an asymmetric loading of the pumps with hydro-mechanical compensators in a vessel hydraulic system is addressed. Electronic control concepts for pump controlled cylinders using multiple speed variable pumps, e.g. for moulding machines, can be found in [12], [13], [14]. These approaches cannot be transferred directly, because the EMPs are not redundant but control different process parameters (e.g. cylinder position, cylinder chamber pressure). To avoid inefficient part load phases dual-pump configurations are investigated that replace a single main pump by two smaller variable displacement pumps [15] or by a smaller primary pump and a VSFD EMP (operated in open loop) [16]. Last, energy efficient control strategies of parallel speed variable pump systems parallel centrifugal pumping systems were investigated in [17].

3 Reference System

The HPP concept from fig. 2 is emulated by the arrangement of two parallel EMPs. This is the reference system for the control development and verification in this paper. The test rig set up and the corresponding non-linear model are detailed below.

3.1 Test Rig

The test rig set up of the dual EMP system is depicted in fig. 3. Two aircraft prototype motor pump units (MPU) are supplied by industrial MCEs (Siemens SINAMICS). The combination of a MPU and MCE represents an EMP. The test rig hydraulic circuit includes the required utilities like accumulators, filters, pressure relief valves, and reservoirs. The consumers are emulated by a number of load valves (servo valves, flow control valves). The control and monitoring functions run on a dSPACE realtime platform, which basically provides the control inputs to the MCEs and valves, resp. reads the sensor signals.

The MPUs are nominally identical but their characteristics are slightly different due to different wear:

- The volumetric efficiency of pump 1 is slightly degraded. Its maximum output flow at nominal speed is only 431/min and lower than that of pump 2 (451/min).
- Compared to pump 2, the hydro-mechanical losses of pump 1 are increased by ca. 10%

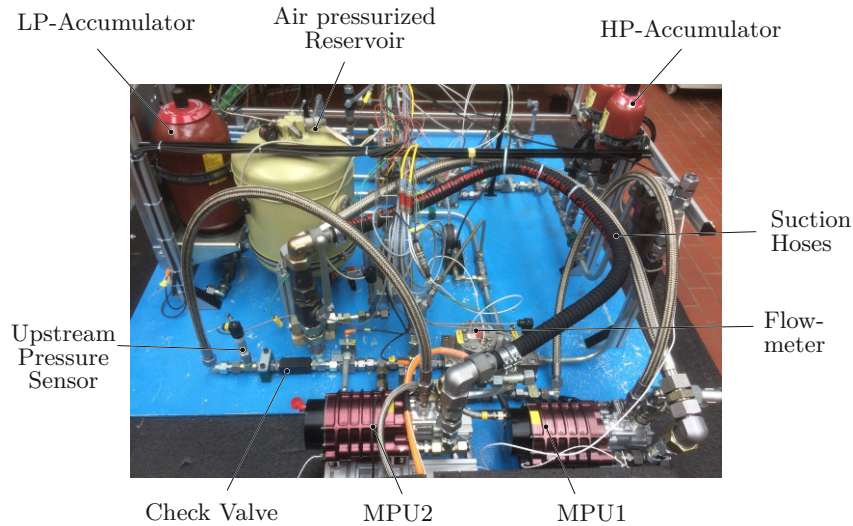


Figure 3: Experimental Dual EMP System Set Up

- Due to the power limitation of MCE 1, MPU1 maximum speed (9500 1/min) and current 95 A are below the nominal limits (10350 1/min, 105 A).

Notice that a comparison of the MPU power losses is illustrated in fig. 13.

The hydraulic integration of the pumps in the test rig follows the design of the HPP in fig. 2. The installation of check valves avoids mutual interferences. Pressure is measured upstream and downstream of the check valves. So, both sensor locations are available for regulation. The (combined pump) flow is measured downstream of the flow summing point and upstream of the accumulator. The suction line is splitted. The hydraulic jacket coolings are integrated in the separate line sections.

3.2 Nonlinear Model

A block diagram of the non-linear system model is illustrated in fig. 4. It comprises the two non-linear VSFD EMP models and a lumped system representation. The hydraulic consumers are represented by a load flow demand Q_L . The model (plant) inputs are the voltage set points $u_{q,c,i}$. The output is the pressure in the downstream system p . The non-linear plant model is implemented in MATLAB/SIMULINK.

The VSFD EMP model follows the approach detailed in [18] which achieved high accuracy. In this model the MCE dynamics, i.e. the time to set the commanded voltage, is modeled by a first order approximation of [19]. The PMSM is modeled as typical two phase system applying the park transformation [20]. The d- and q-axis currents i_q, i_d are calculated by the stator voltage equations. The resulting electromagnetic torque is obtained from resulting currents and the linked flux. The rotor speed ω_m is derived from the mechanical equation.

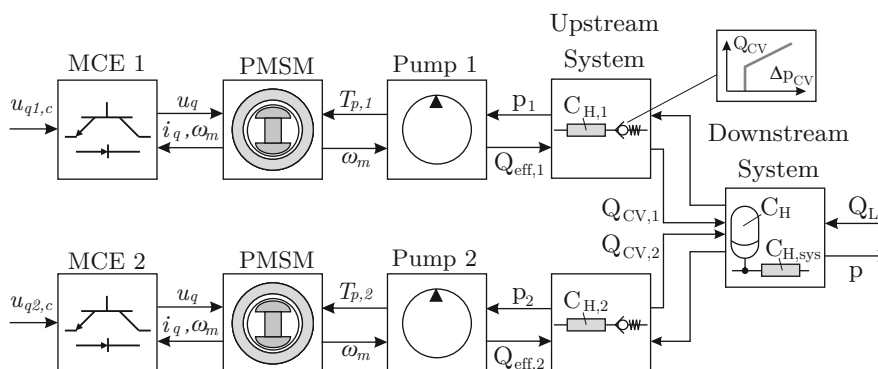


Figure 4: Non-Linear Duplex EMP Control Design Model

The pumps are modeled as combinations of ideal fixed displacement pumps and volumetric, resp. hydro-mechanical loss models, which are functions of speed, pressure, and fluid temperature, derived from measurements. The

pumps output the effective flows $Q_{eff,i}$ and require the drive torque $T_{p,i}$. The pipe segments between pump and check valves, referred to as the upstream system, are represented by lumped capacities $C_{H,i}$. The pressure build-up in the upstream capacities $C_{H,1/2}$ is described by

$$\dot{p}_{1/2} = \frac{Q_{eff,1/2} - Q_{CV,1/2}}{C_{H,1/2}} \quad (1)$$

where $Q_{eff,1/2}$ are the effective pump output flows and $Q_{CV,1/2}$ are the check valve flows. In the open position these are calculated by the orifice equation

$$Q_{CV,1/2} = B_{CV,1/2} \cdot \sqrt{p_{1/2} - p_{sys}} \quad (2)$$

with the orifice coefficient $B_{CV,1/2}$. The pressure build-up in the downstream system capacity, which is formed by the lumped accumulator and downstream pipe system capacities, yields

$$\dot{p}_{sys} = \frac{Q_{CV,1} + Q_{CV,2} - Q_L}{C_{H,sys}} \quad (3)$$

where $C_{H,sys}$ is also a function of the pressure (compare [18]). Solving eq. (2) for $p_{1/2}$, inserting the result and (3) into eq. (1) yields the expression

$$Q_{CV,1/2} = Q_{eff,1/2} \cdot \frac{C_{sys}}{C_{H,sys} + C_{H,1/2}} + (Q_L - Q_{CV,2/1}) \cdot \frac{C_{H,1/2}}{C_{H,1/2} + C_{H,sys}} \quad (4)$$

which describes the cross-coupling between the two check valve flows. The coupling is mainly characterized by the fraction of the system and upstream capacities. In particular, the coupling is strong for large $C_{H,1/2}$ which yields

$$\frac{\partial Q_{CV,1/2}}{\partial Q_{CV,2/1}} = -\frac{C_{H,1/2}}{C_{H,1/2} + C_{H,sys}} \approx -1 \quad (5)$$

The coupling is weak for large $C_{H,sys}$, respectively. So, to reduce mutual interferences

- $C_{H,sys}$ should be designed large in comparison to $C_{H,1/2}$
- and the variations of $Q_{CV,2/1}$ should be compensated by adjusting $Q_{eff,1/2}$, e.g. by a flow synchronization.

4 Baseline Controller Synthesis

This section develops a baseline pressure controller for the duplex operation mode. After the specification of the requirements and the selection of a suitable control structure, a linear design model is created. The subsequent design and tuning apply a loopshaping design method, presented in [18]. The control design is verified and validated by non-linear simulation and an experiment.

4.1 Requirements Specification

The main task of the pressure controller is to maintain the required supply pressure by tracking the reference pressure and reject disturbances with zero steady state error. The stability of the closed control loop shall be ensured by satisfying a maximum gain margin $GM \geq 6$ dB and a minimum phase margin $PM \geq 60^\circ$. High frequency noise has to be blocked from entering the feedback loop. A general objective is to keep design simple and transparent for low complexity and certification effort.

Pressure control performance requirements are stated by SAE AS 595 [21]. In particular, the performance is specified by a pressure response to a load step from minimum to maximum flow demand and vice versa, as illustrated in fig. 5. It is characterized by the parameters of tab. 1. These are minimum and maximum pressures $p_{min/max}$, the response times (t_1, t_2), and the settle time t_3 . The response time specifies the time to transit from minimum to maximum output flow and vice versa. The settle time is the time for the pressure to settle back to the rated level. Note that there is no explicit requirement for p_{min} , so it is assumed to be symmetric to p_{max} .

The EMP speed must stay within the operating limits. The SAE AS 595 recommends to not exceed 115 % of the rated speed as upper limit. In addition, a minimum speed limit of 500 1/min (well above the physical limit) is applied, to be conservative. Further, to limit wear effects, acceleration shall not exceed ± 50.000 rpm/s.

Table 1: Dynamic Requirements

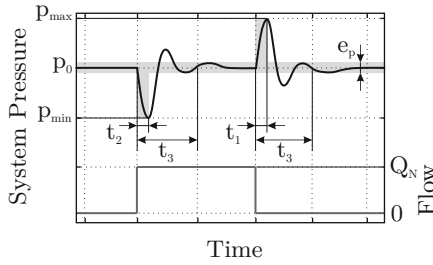


Figure 5: Step Response

Parameter	Description	Value	Unit
p_0	Nominal System Pressure	206	bar
t_1	Response Time	50	ms
t_2	Response Time	100	ms
t_3	Settling Time	1	s
p_{max}	Max. Transient Pressure	257.5	bar
p_{min}^*	Min. Transient Pressure	154.5	bar

Last but not least, to avoid the issues of duplex operation mentioned in section 2, the control shall offer robustness against dissimilar EMP characteristic.

4.2 Pressure Control Concept Selection

A cascaded control, in which the speed control loops and their subordinate current controllers have already been suitably designed, is taken as basis. Then, the task of the pressure controller is to calculate the required motor speeds $\omega_{c,1/2}$, for which different concepts are possible by varying the following properties:

- The **point of regulation** is defined by the location of the pressure sensor. The pressure sensors can be either installed upstream or downstream of the check valves. It has a significant impact on the controller performance and structure.
- The **hierarchy** defines the EMP role. In the related field of electronic synchronizing distributed electric drives ([22], [23], [24]) the following concepts are distinguished:
 - Peer-to-peer (P2P): All (electric) drives have (almost) equal authority. Decentralized and centralized controller structures are possible.
 - Master/Slave: One leading drive represents the master, which follows the commands of a supervisory level controller. The other drives (slaves) track the reference signal of the master.

The resulting concepts are illustrated in fig. 6. Concepts I-III are discarded because the upstream pressure sensor location was found to be disadvantageous for stability and performance, mainly due to the non-linear behaviour of the check valves. The downstream concepts IV-VI avoid these issues in principle since opening and closing of the check valves has low impact on the downstream pressure. In addition, the downstream sensor arrangement is advantageous for disparity monitoring.

In concept VI the slave EMP tracks the master EMP speed, so it adapts to the master EMP automatically without complex monitoring. Yet, this approach decreases the overall performance because the tracking is non-ideally fast. Another drawback is that the slave EMP does not compensate for a degradation of the master EMP. The M/S concept is also discarded.

The remaining P2P concepts IV and V have different controller structures. In concept IV a centralized pressure controller commands a cumulated total speed which is allocated to both EMPs. In concept V the speed commands are calculated by two decentralized pressure controllers, which receive the same reference and feedback. The main advantage of the central controller (concept IV) is the simple (re-)configuration between simplex/duplex mode and the possibility to flexibly allocate the total effort. That is why concept IV is chosen.

4.3 Design and Tuning

The detailed design of the selected pressure control concept is illustrated in fig. 7. Based on the control error $e_p = p_c - p$ the pressure controller C_p calculates a total control effort v , which represents the total required speed. The EMP speed commands $\omega_{c,i}$ are determined by the allocation algorithm (allocator) via

$$[\omega_{c,1} \ \omega_{c,2}]^T = [\alpha_1 \ \alpha_2]^T \cdot v \quad , \quad (6)$$

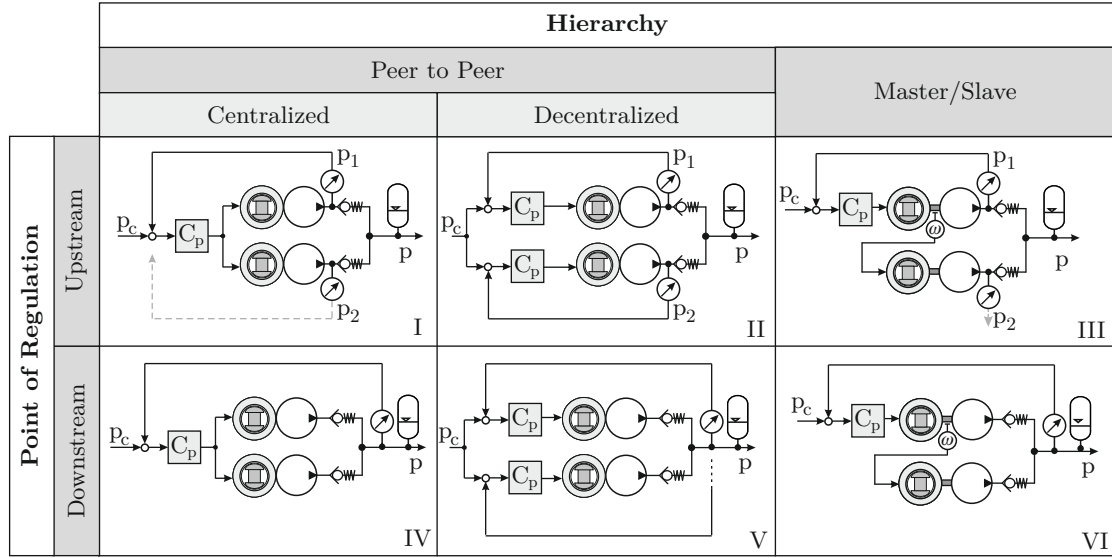


Figure 6: Classification of Control Concepts

introducing the allocation factors $\alpha_{1,2}$. In the nominal case, which is considered here, the effort is allocated evenly $\alpha_1 = \alpha_2 = 0.5$. Note, that simplex operation is achieved by simply setting $\alpha_{1/2} = 1$ and $\alpha_{2/1} = 0$. In the following a linear design model is derived.

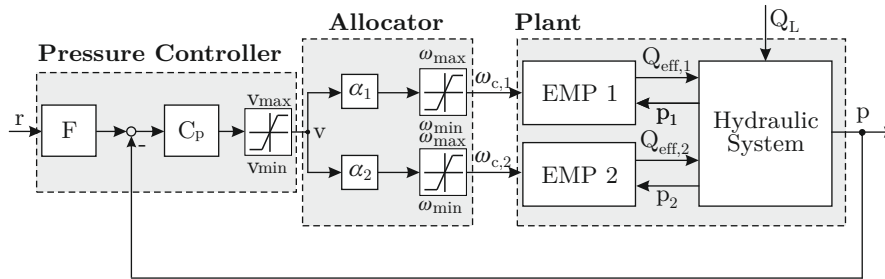


Figure 7: Detailed Design of the Dual EMP Baseline Control Concept

4.3.1 Linear Design Model

The plant block diagram representation is illustrated in fig. 8. It comprises the closed speed control loops, which are represented by second order transfer functions $T_{\omega,cl}$. The pump transfer function is $G_{p,i}$, where $k_{le,\omega,i}$ denotes the linear coefficient of speed-dependent leakage. The concatenate $T_{\omega,cl} \cdot G_{p,i} = G_{MPU,i}$ yields the MPU transfer function. The check valves and the upstream capacities are neglected. This approximates the open check valve and is a reasonable assumption for the nominal operation. The system pressure build-up is modeled by the system transfer function G_{sys} , where $k_{le,p,i}$ represents the pressure-depending internal pump leakage and C_{sys} is constant. Note that G_{sys} is identical to the disturbance transfer function P_d , which describes the relation between disturbance Q_L and output p .

For the nominal system it is assumed that both MPUs are identical, introducing $G_{MPU} = G_{MPU,1} = G_{MPU,2}$. This simplifies the plant to a SISO system shown in fig. 9.

For the controller design the allocation factors are set to $\alpha_i = 0.5$, which yields the loopgain to be

$$L(s) = C_p(s) \cdot T_{\omega,cl} \cdot G_p \cdot G_{sys} = C_p(s) \cdot P(s) \quad , \quad (7)$$

where $P(s)$ is the SISO system plant.

4.3.2 Loopshaping Design and Tuning

The simplification to a SISO system enables the application of the loopshaping method proposed in [18]. It facilitates a systematic design and a low order controller. The principal idea of classical loop-shaping is to *shape*

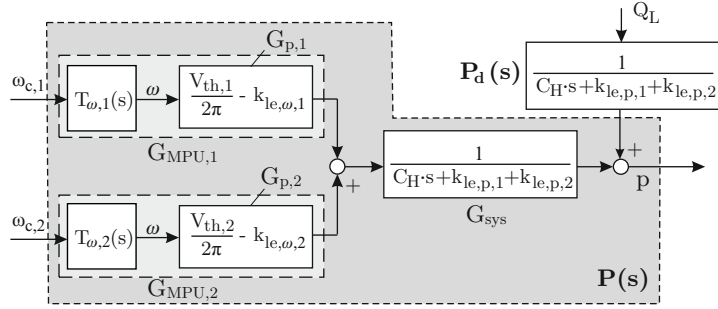


Figure 8: Block Diagram of the Plant

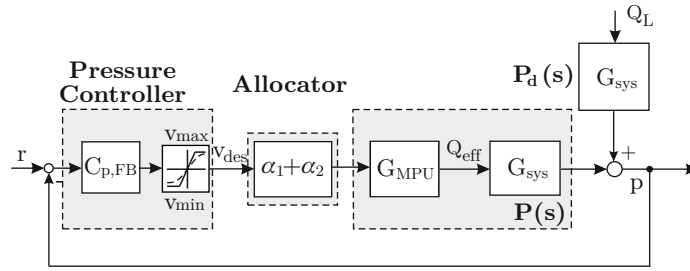


Figure 9: Simplified Closed Loop System in SISO Configuration

the open loop transfer $L(s)$, specifically its magnitude to a defined (target) loop shape. In parallel, stability margins can be evaluated from the phase. In the following the performance requirements are mapped onto target loop shapes.

Specification of Target Loopshapes The performance requirements and constraints have to be mapped onto specific closed loop transfer functions. For this purpose the following set of closed loop transfer functions is introduced:

$$S(s) = \frac{1}{1+L(s)}, \quad T(s) = \frac{L(s)}{1+L(s)}, \quad SP_d(s) = \frac{P_d(s)}{1+L(s)} \quad (8)$$

$$CS(s) = \frac{C(s)}{1+P(s) \cdot C(s)}, \quad CSP_d(s) = \frac{C(s) \cdot P_d(s)}{1+P(s) \cdot C(s)} \quad (9)$$

The sensitivity S characterizes the impact of a disturbance, acting on the output of the plant. The complementary sensitivity T describes the closed loop transfer function from reference to output. Ideally $S(s)$ shall be small for a small control error. At the same time $T(s)$ shall be small for low noise sensitivity [25], which is a typical design conflict. Further, $SP_d(s)$ denotes the disturbance sensitivity transfer function, which characterizes the transfer of a (load) disturbance on the output. The disturbance rejection requirements, defined in sec. 4.1, are mapped onto a target loop shape for $P_d S(s)$, as proposed in [18]. In general, $SP_d(s)$ should be low at low frequencies, to limit the impact of disturbances. It should also be low at high frequencies to attenuate noise. The maximum magnitude corresponds to the overshoot requirement, whereas its frequency - in good approximation - corresponds to the bandwidth. The controller sensitivity $CS(s)$ describes the transfer from the reference or the noise input to the controller output u . Its magnitude should be high at low frequencies for a responsive controller but low at high frequencies to attenuate the noise. The controller disturbance sensitivity $CSP_d(s)$ characterizes the impact of a disturbance on the control signal. An upper bound on $CSP_d(s)$ limits the maximum speed command due to the maximum disturbance. Moreover, an upper bound on $CSP_d(s) \cdot s$ limits the corresponding rate. The resulting target loop shapes W_i (grey lines) are illustrated in fig. 10 (b).

Tuning Result The tuning is carried out using MATLAB's `sisotool`. Both, design targets and resulting loop-shapes are illustrated in fig. 10. The controller is designed primarily to meet the stability and disturbance rejection

performance requirement ($W_{SP_d}(s)$). As a result a PI control law is obtained to be a suitable choice, which matches most of target loopshapes.

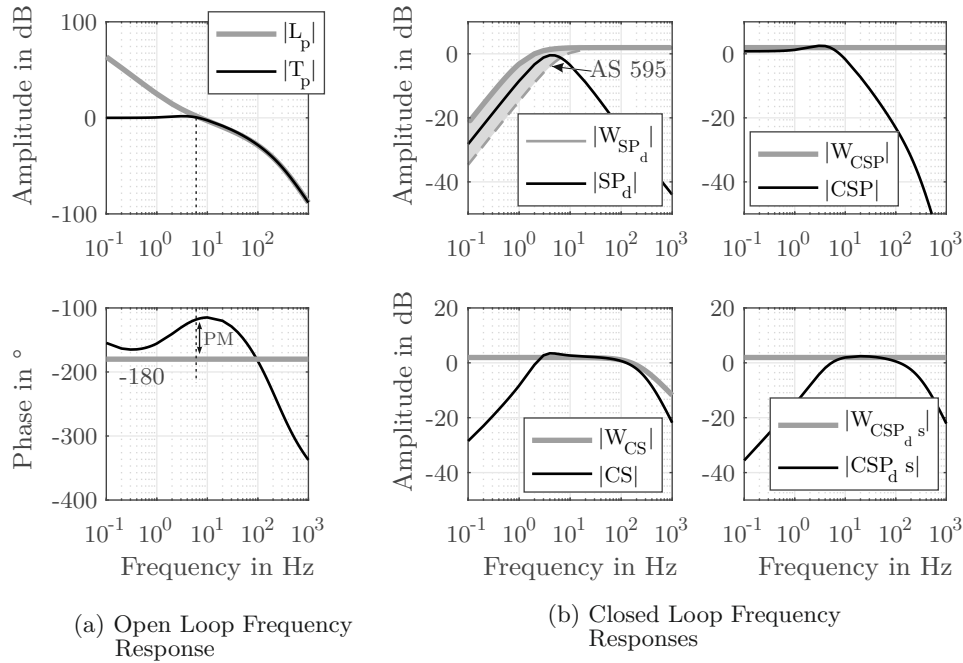


Figure 10: Target Loopshapes and Controller Tuning Results

The evaluation of the phase angle (115°) at the crossover frequency ($\omega_{L,0} = 8 \text{ rad/s}$) implies that the design has sufficient stability margin ($PM = 65^\circ$). In terms of performance the $SP_d(s)$ magnitude reveals that the overshoot requirement is satisfied, while the response time requirement cannot be met. The magnitudes of $CSP_d(s)$ and $CSP_d(s) \cdot s$ indicate that speed and rate limits are satisfied, so the system is at the design limit here.

4.4 Design Verification

The controller design is verified regarding stability and dynamic performance (disturbance rejection capability). Figure 11 compares the simulation of a load step with the nonlinear model to the experiment. Initially, the system is compensating the static flow demand of 101/min. Here, the most essential finding is that the pump speeds are synchronized well and that no oscillations are present. After one second a load step to 801/min (maximum considered load) is applied. The controller compensates the load by increasing the speed command. Both EMPs accelerate at their maximum rate. The details reveal that the EMP 1 acceleration is slower (by ca. 10000 (1/min)/s) due to the limited performance. Yet, no fighting or instability is observed. This is an implicit proof of the robustness against dissimilarities. During the load step back to 101/min both EMPs have the same performance, because of the aiding hydraulic load torque. The minimum pressure (170 bar) and the maximum pressure (250 bar) stay within the limits. This shows that the controller satisfies the performance requirements and avoids the issues of multi-pump systems with hydro-mechanical compensation. Last but not least, simulation and experiment show an acceptable match. So, the model of the duplex system appears suitable for further model based investigation.

5 Flexible and Optimal Control Allocation

During flight maximum hydraulic power is needed only temporarily. This means the dual EMP system is oversized and thus overdetermined most of the time. During these phases the low utilization opens up potential to include secondary objectives (efficiency, dynamics) and/or to handle varying operational constraints (e.g. power limitations of electric supply system) through dynamic allocation. This section develops and investigates a flexible control strategy based on a model predictive control scheme.

5.1 Potentials of the Low Utilization

Flexible dynamic allocation is possible when the available total flow exceeds the demand $Q_{MPU,1,max} + Q_{MPU,2,max} > Q_L$ and neither MPU is saturated ($Q_{MPU,i} < Q_{MPU,i,max}$). Then, it is possible to satisfy secondary objectives and/or to handle specific operational constraints. In this paper the following objectives and constraints are considered.

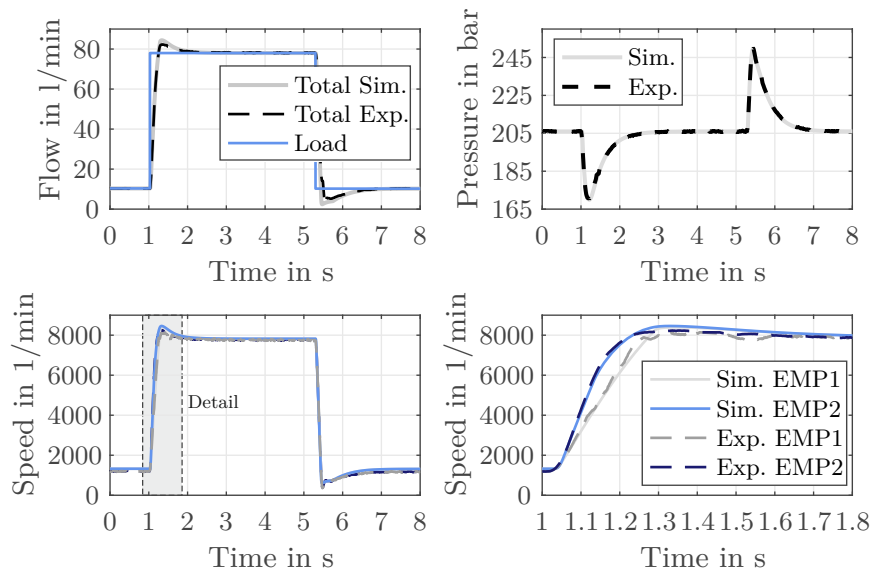


Figure 11: Control Design Verification and Model Validation

5.1.1 Secondary Objectives

In addition to the primary control objective, i.e. to ensure the required output power, the controller shall consider the following secondary objectives:

- **Minimization of power losses:** The requested hydraulic output power is provided at maximum efficiency, i.e. with minimum power losses.
- **Maximization of dynamic performance:** A useful measure of the dynamics is the gradient dQ/dt . Since $Q_i \sim \omega_i$, in this paper maximizing dv/dt is used as a suitable approximation (neglecting the impact of different internal pump leakage).

The approach could be extended to include additional objectives, for example minimization of operating noise or reducing wear, e.g. by balancing the usage and by penalizing fast accelerations.

5.1.2 Operational Constraints

The operation of the HPP is subject to numerous boundary conditions, which are imposed by the inherent monitoring functions and by adjacent systems. A controller with flexible allocation can improve the restriction handling resp. enable it at all. This is illustrated by the following examples:

- **Health and Usage Monitoring (HUMS):** The HUMS monitors the health condition and usage of the system. In order to compensate for the degradation of a component, the HUMS could require the controller to adapt the EMP operating limits or to balance their usage by prioritizing one unit. Then, certain operating points (e.g. very high or low speed or certain frequency bands) may have to be avoided.
- **Failure Monitoring:** This function detects failures in the hydraulic system and triggers a dedicated reaction. For example, a detected reservoir low pressure condition could require to limit the speed or rate to prevent from cavitation.
- **Electric Power Management:** The electric power system is an important adjacent system. Specifically, the electric power management may impose limitations on the available HPP input power. For example, in an emergency a limited amount of power has to be shared among different (electrical) functions. Then, the voltage level and/or current available for the HPP may be reduced. A reduced voltage in turn limits the maximum speed and a reduced current limits the maximum torque (and consequently dynamic performance).

5.2 Concept Definition

Based on the above considerations the optimized control concept shall offer the following capabilities: optimization of the operating behavior with respect to secondary objectives, handle varying operating constraints. This section

selects and defines a suitable control strategy. For that, the tasks of (higher-level) pressure control and control allocation, shall be separated, in order to retain the proven pressure controller. This is expected to be advantageous in terms of transparency and acceptance, as the system can recover to the baseline control any time by fixing the allocation. Then, the control task narrows down to a typical control allocation problem.

A comprehensive overview of different control allocation methods is given in [26]. In this paper a model predictive controller (MPC) is used to solve the allocation problem, which is referred to as model predictive control allocation (MPCA). This approach calculates the control allocation by optimization of the predicted behaviour over a finite horizon. The main advantage of MPCA over simple algorithms - like direct allocation or daisy chaining - is the ability to explicitly take into account the actuator (here EMP) dynamics as higher order models and the systematic handling of actuator limits. MPCA is widely used in process industry [26], but also applied for braking torque blending in vehicle control [27] or in flight control [28]. For usage of MPC to optimize hydraulic process controls refer in particular to WILLKOMM [29]. An approach to reduce the computational effort (by structured MPC) is presented for a cylinder drive in [30].

Figure 12 illustrates the proposed structure of the HPP control including the MPCA. The (high-level) pressure controller computes a required total control effort v . The main objective of the MPCA algorithm is to ensure that this control effort is produced (jointly by all EMPs) at all times, while meeting the secondary objectives and satisfying the constraints.

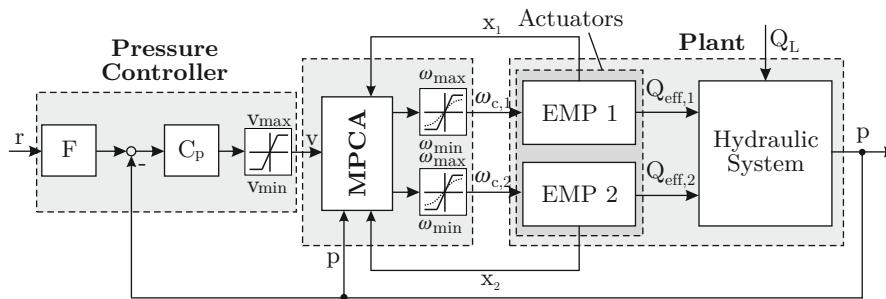


Figure 12: HPP Control Concept including MPCA

5.3 Implementation and Optimization Problem

The MPCA implementation used is based on the MPC formulation in [31]. Specifically, the objective of the MPC is to find a finite horizon of N_c (control horizon) control inputs u_k that minimize an objective function and satisfy the constraints over the prediction horizon N_p . More specifically, here $u_k = \omega_{c,k} = [\omega_{c,1,k}; \omega_{c,2,k}]$ is a vector that contains the two control commands, which are the decision variables of the optimization problem. The objective function is

$$J = \min \left\{ \lambda_v \cdot \sum_{k=1}^{N_p} (y_{ref,k} - y_k)^2 + \lambda_{\Delta u_k} \cdot \sum_{k=0}^{N_c-1} \Delta u_k^2 + \lambda_{P_V} \cdot \sum_{k=1}^{N_p} P_V(x_{m,k}, \Delta u_k) \right\} \quad (10)$$

It is formed by different terms to account for different objectives, which can be blended by the weighting factors λ_i . The first term minimizes the error between the set point $y_{ref} = v$ and the predicted output $y = \omega_1 + \omega_2$. The second term penalizes the control effort. The third term minimizes the total power losses $P_V = f(\omega_1, \omega_2, p, \vartheta_{fl})$ to optimize the efficiency. The power losses are a function of speed, pressure, and fluid temperature, which are based on experimental measurements, as is detailed in sec. 5.4. The optimization is subject to the following constraints

$$u_{i,min} \leq u_i \leq u_{i,max} \quad , \quad \Delta u_{i,min} \leq \Delta u_i \leq \Delta u_{i,max} \quad , \quad (11)$$

which allows physical limitations of the system to be incorporated. In this paper the speed limits and rate (acceleration) limits are considered as constraints because current and voltage limits are satisfied by the subordinate control loops. Note that current and voltage limits can be formulated implicitly by speed and rate limits, too. The constraints are provided by the supervisory control level. The prediction of system states x_k and outputs y_k uses a discrete time state space representation

$$x_{k+1} = A \cdot x_k + B \cdot \Delta u_k \quad (12)$$

$$y_k = C \cdot x_k \quad (13)$$

which includes not only the EMPs but also the system, because the pressure retroacts on the motors via the pump torque. Notice that the input is $\Delta u_k = u_k - u_{k-1}$ and A, B, C represent an augmented model with an integrator. The augmented state vector $x_k = [\Delta x_{m,k}^T y_k]^T$ is formed by the state increments $\Delta x_{m,k} = x_{m,k} - x_{m,k-1}$ (motor currents, speeds, and pressure) and the output y_k . The objective function is solved at each time step, to obtain the optimal sequence of Δu , resp. of u . Only the first element of Δu is commanded to the motors. This procedure is repeated at each sample instant (receding horizon control).

5.4 Evaluation

The performance and potential of the MPCA strategy are evaluated in comparison to the baseline concept, using efficiency and dynamic performance as examples.

5.4.1 Energy Efficiency

The efficiency optimization requires to minimize the power losses, while ensuring the allocation of the total speed. To achieve this objective the power loss term is activated in the objective function by setting $\lambda_v = \lambda_{P_v} = 1$. In addition, including the control effort in the objective function ($\lambda_{\Delta u_k} = 1$) is necessary to avoid high frequency variations of the control output. The power loss function is evaluated exemplarily for 206 bar and 30°C fluid temperature in fig. 13 over v and ω_1 , where implicitly $\omega_2 = v - \omega_1$. An offline optimization yields the optimal ω_1 for each v . It shows a prioritization of unit two, in particular at higher speeds, which is in line with the increasing delta between the power losses in fig. 13 (b).

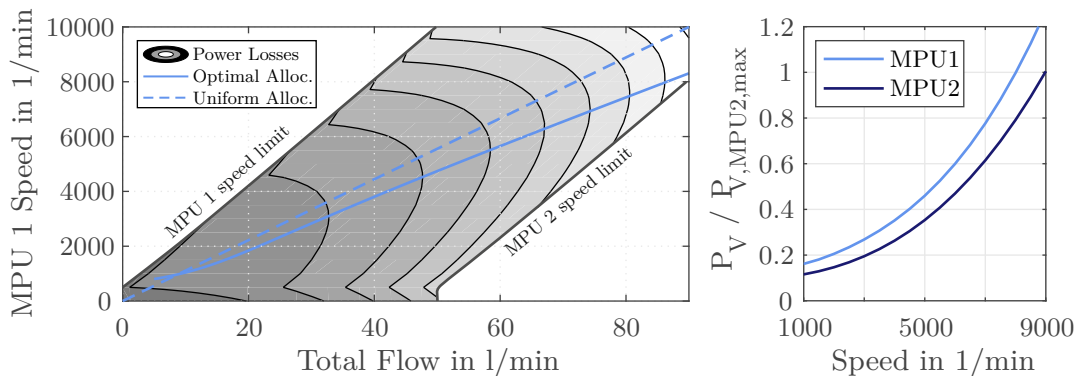


Figure 13: Comparison of Power Losses and Static Offline Efficiency Optimization

For the evaluation of the efficiency optimization a test scenario is defined, which includes different load conditions of a potential HPP operating profile. The pressure controller maintains a constant system pressure of 206 bar. The nominal limitations are applied as constraints. The simulation results for the baseline and the MPCA control concept are compared in fig. 14. From the top to the bottom the plot depicts the consumer flow demand (load) and total pump output flow, system pressure, pump speeds, and the delta energy loss between MPCA and baseline. Comparing the pressure regulation quality, no dynamic performance differences are visible over the entire sequence. So, the MPCA approach does not lead to adverse system behaviour here, which is an essential prerequisite.

Comparing the speed allocation, the MPCA scheme makes slightly more use of the second (more efficient) unit at low speed. However, considering the energy loss, the potential savings are low here, because the increased loss at an increased speed appears to cancel out the savings at the less efficient unit. For low flows energy savings are possible by switching off the unit with poorer efficiency, which is not detailed here. At higher flow demands the situation is different. The more efficient EMP 2 is prioritized considerably (e.g. at the flow demand of 80 l/min the delta between the commanded speeds is about 1000 1/min) as the different efficiencies have a greater impact here. During dynamic phases increased motor current, required for acceleration, causes additional losses in both units. So, both units are accelerated similarly. The dynamic loss fraction is however low compared to the static fraction. In conclusion, the MPCA approach enables the same dynamic performance while a slight improvement

of the efficiency is possible. Qualitatively it can be expected, that the potential energy savings increase for greater differences in the efficiencies.

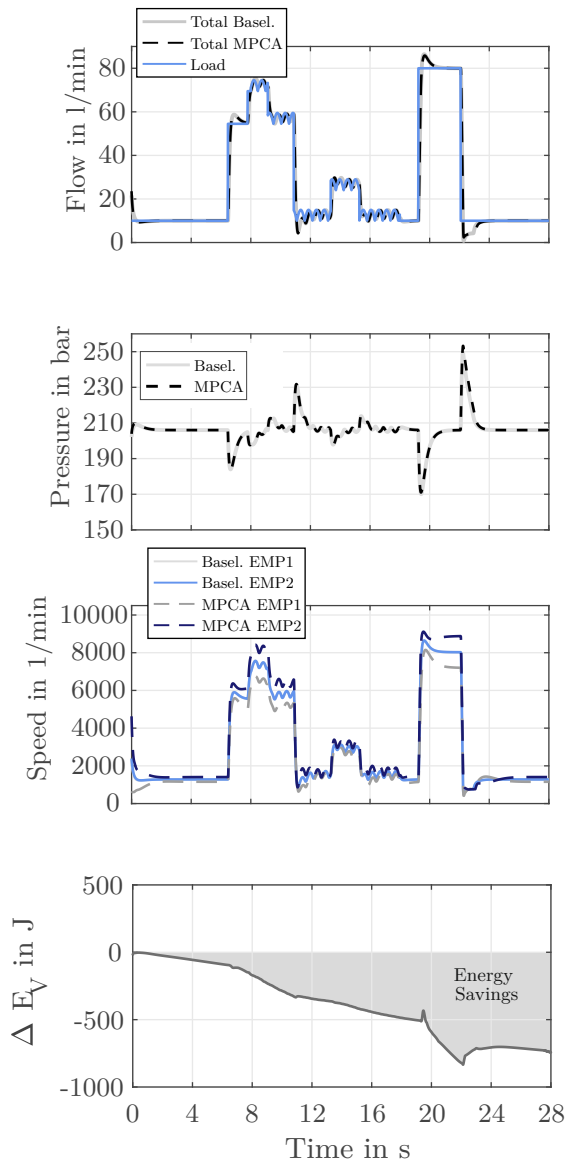


Figure 14: Result Efficiency

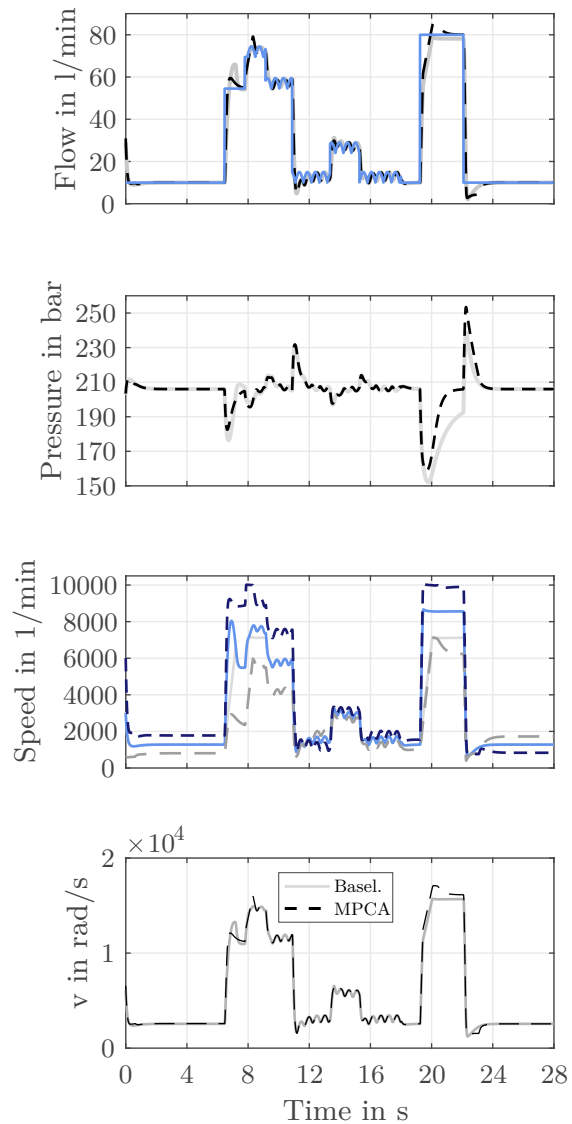


Figure 15: Result Dynamic

5.4.2 Dynamic Performance

According to the definition given above, the optimization of the dynamic performance is equivalent to eliminating the error between v and $\omega_1 + \omega_2$ as fast as possible. This objective is pursued by prioritizing the first term of eq. 10. Again, the second term is kept for damping, so that $\lambda_v = \lambda_{\Delta u_k} = 1$ and $\lambda_{P_V} = 0$ (no efficiency optimization).

In case of two units with identical dynamic performance the best overall dynamic performance is achieved by a uniform allocation. Then each single unit has to accelerate to a relative lower target speed. In this case there would be no optimization potential for the MPCA algorithm. The situation is different for two units with (asymmetrically) degraded dynamic performance. Then, the MPCA algorithms can generate an advantage by preferring the better unit. This potential becomes apparent by considering a worst case scenario for MPU1:

- The HUMS detected a significant degradation of the hydraulic pump efficiency. Specifically, the friction torque is increased by 10%.
- The electric power management requests to limit the EMP1 power consumption (e.g. in an emergency condition). Specifically,

- the input voltage is reduced to 75 %,
- the maximum current is limited to 80 %.

The combination of lower maximum current and increased friction torque reduce the acceleration capability to 15 % of the nominal capability. The reduced voltage level limits the maximum nominal speed and flow. Limited speed and rates of EMP 1 are taken into account by the MPCA by adapting $\Delta u_{i,max}$, $u_{i,max}$. The simulation result is illustrated and compared to the baseline in fig. 15.

The potential for improvement of the MPCA already becomes clear in the first load step. The MPCA algorithm allocates almost the entire speed to the non-degraded EMP 2. This partly compensates the degradation of EMP1, which improves the pressure control quality considerably (lower pressure undershoot, shorter settling time). During the subsequent load reduction no difference is observed, since negative acceleration is aided by the hydraulic pump torque.

The performance difference becomes also clear in the second load step. Here EMP 1 is driven into the (reduced) speed limit. The MPCA algorithm compensates the saturation by increased utilization of MPU2. This improves the pressure control quality. Again, there is no principle difference during load reduction. The baseline controller pressure overshoot is lower only because the pressure had not been fully recovered before the load step. In summary, the exemplary analysis showed that the MPCA algorithm is able to compensate for asymmetric characteristics, resp. operational constraints. This allows the system to maintain improved performance even in a degraded state.

6 Conclusions and Outlook

In the first part of this paper an electronic pressure controller for a hydraulic power package (HPP) with two redundant speed variable electric motor-driven pumps (EMP) was developed. A central pressure controller, which calculates a total speed and allocates it evenly to both units, was selected. A robust control was designed applying a loopshaping method, where requirements and constraints are mapped on target loopshapes. The control design was verified in non-linear simulation and by an experiment on a dedicated test rig. It meets the specified performance requirements and offers robustness against slightly asymmetric EMP characteristics. This is an important result, as oscillations due to slightly differing pump behaviours are a well-known issue in today's aircraft multi-pump systems.

In the second part of this paper a model predictive control allocation (MPCA) was developed, to take advantage of the low utilization during most parts of the flight. The MPCA algorithm solves an optimization problem, which minimizes a cost function for a secondary objective and satisfies control limitations as constraints, to calculate the speed allocation. A first test case showed that the algorithm improves the efficiency by preferring the more efficient unit. The improvement is, however, rather low but increases with increasing differences between the units. In a second test the MPCA algorithm was demonstrated to improve the dynamic performance in case of asymmetrically degraded units by prioritizing the better one. This is a promising result to enable fault-tolerant control.

Overall, the MPCA algorithm provides the baseline for the implementation of a holistic and integrated HPP operating strategy. Future investigations need to verify the MPCA strategy on the test rig. This should also include the investigation of additional optimization objectives, e.g. the minimization of noise emissions, wear and tear effects. Furthermore, the MPCA algorithm needs to be coupled to the HUMS, which provides the essential plant information (like pump efficiencies, limits) and the potential of integrating also the pressure controller into the MPC formulation should be explored.

Acknowledgement

This work was funded by the German Federal Ministry of Economic Affairs and Energy (BMWi) within the MODULAR project (contract code: 20Y1910G) in the national LuFo VI-1 program. Their support is greatly appreciated.

The authors would further like to thank Liebherr-Aerospace Lindenberg GmbH for their support, provision of the prototype EMPs, and funding of the test rig. It has received funding from the Clean Sky 2 Joint Undertaking under the European Union's Horizon 2020 research and innovation programme under grant agreement No 807097.

Thanks also go to Jonathan Jobmann, who made an important contribution to the conceptualization of the basic control structure as part of his master's thesis. Last but not least, the authors would like to thank Liesa Voges, whose work provided an important basis for the MPCA concept development.

References

- [1] R. I. Jones. The more electric aircraft – assessing the benefits. *Proceedings of the Institution of Mechanical Engineers, Part G: Journal of Aerospace Engineering*, 2002.
- [2] N. Trochelmann, T. Rave, F. Thielecke, and D. Metzler. An investigation of electro-hydraulic high efficient power package configurations for a more electric aircraft system architecture. In *Deutscher Luft- und Raumfahrtkongress, Munich*, 2017.
- [3] SAE International (Publ.). *Aerospace Information Report (AIR) 5005 - Commercial Aircraft Hydraulic Systems*. Society of Automotive Engineers (SAE), 2015.
- [4] Boeing (Publ.). 787 No-Bleed Systems: Saving Fuel and Enhancing Operational Efficiencies. *AERO magazine*, 2007.
- [5] Boeing. Dynamic activation of pumps of a fluid power system, 2018.
- [6] SAE International (Publ.). *Aerospace Information Report (AIR) 4553B - Aerospace Hydraulics and Actuation Lessons Learned*. Society of Automotive Engineers (SAE), 2010.
- [7] S. Guo, J. Chen, Y. Lu, Y. Wang, and H. Dong. Hydraulic piston pump in civil aircraft: Current status, future directions and critical technologies. *Chinese Journal of Aeronautics (CJA)*, 2019.
- [8] J. E. Spencer. Development of Variable Pressure Hydraulic Systems for Military Aircraft Utilizing the Smart Hydraulic Pump. In *ImechE*, 1993.
- [9] W. Davidson and J. Roizes. Electro-Hydrostatic Actuation System for Aircraft Landing Gear Actuation. In *Workshop on Aircraft System Technologies*, 2015.
- [10] N. Elliott, S. Linforth, and C. Moore. Thermae ii (main landing gear & door eh actuation system) integration and testing. In *Recent Advances in Aerospace Actuation Systems and Components, March 16-18, 2016, Toulouse, France*, 2016.
- [11] A. Banaszek and R. Petrovic. Problem of non proportional flow of hydraulic pumps working with constant pressure regulators in big power multipump power pack unit in open system. In *Technical Gazette 26, 2(2019), 294-301*, 2019.
- [12] I. Rühlicke. *Elektrohydraulische Antriebssysteme mit drehzahlveränderbarer Pumpe*. PhD thesis, Technische Universität Dresden, Institut für Fluidtechnik, 1997.
- [13] T. Neubert. *Untersuchungen von drehzahlveränderbaren Pumpen*. PhD thesis, TU Dresden, 2002.
- [14] A. Helbig. *Energieeffizientes elektrisch-hydrostatisches Antriebssystem am Beispiel der Kunststoff-Spritzgiessmaschine*. PhD thesis, TU Dresden, 2007.
- [15] K. Ritters, L. Roos L., and L. Frerichs. Efficiency Studies on Double Pump Supply Units. In *11th International Fluid Power Conference, Aachen*, 2018.
- [16] L. Roos, J. Untch, and L. Frerichs. Effizienzsteigerungen durch 2-Pumpen-Versorgungseinheiten. In *Hybride und energieeffiziente Antriebe für mobile Arbeitsmaschinen*, 2015.
- [17] J. Viholainen, J. Tamminen, T. Ahonen, J. Ahola, E. Vakkilainen, and R. Soukka. Energy efficient control strategy for variable-speed driven parallel pumping systems. In *Springer Energy Efficiency Journal*, 2013.
- [18] N. Trochelmann, P. Bischof, F. Thielecke, D. Metzler, and S. Bassett. A robust pressure controller for a variable speed ac motor pump – application to aircraft hydraulic power packages. In *Bath/ASME 2018 Symposium on Fluid Power and Motion Control (FPMC)*, 2018.
- [19] R. Krishnan. *Permanent Magnet Synchronous and Brushless DC Motor Drives*. Taylor and Francis Group, LLC, 2010.
- [20] D. Schroeder. *Elektrische Antriebe – Regelung von Antriebssystemen*. Springer-Verlag Berlin Heidelberg, 3 edition, 2009.
- [21] SAE International (Publ.). *Aerospace Standard (AS) 595 - Pressure Compensated variable displacement aircraft pumps - Revision D*. 2010.

- [22] M. Franke. *Intelligente Antriebe im Systemverbund – Ein Beitrag zur Untersuchung des Betriebsverhaltens von dezentralen feldbusgekoppelten Antrieben*. PhD thesis, TU Dresden, 1999.
- [23] H. Niemann. *Synchronisierte Regelung dezentraler Antriebe über einen Feldbus*. PhD thesis, University Erlangen-Nürnberg, 2001.
- [24] H. Geilsdorf. *Modellbasierter Entwurf der Synchronisationsregelung und Fehlerüberwachung elektrischer Einzelantriebe in Landeklappensystemen*. PhD thesis, TUHH, 2009.
- [25] S. Skogestad and I. Postlethwaite. *Multivariable Feedback Control*. Prentice Hall (ACHTUNG: TBD), 2005.
- [26] T. A. Johanssen and Thor I. Fossen. Control allocation – a survey. In *Automatica*, volume 49, pages 1087–1103, 2013.
- [27] C. Satzger, R. d. Castro, and T. Bünte. A model predictive control allocation approach to hybrid braking of electric vehicles. In *IEEE Intelligent Vehicles Symposium*, 2014.
- [28] M. Hanger, T. A. Johanssen, G. K. Mykland, and A. Skullestad. Dynamic model predictive control allocation using cvxgen. In *9th IEEE International Conference on Control and Automation (ICAA)*, 2011.
- [29] J. Willkomm. *Modellprädiktive Optimierung drehzahlvariabler Verstellpumpen*. PhD thesis, Technical University of Darmstadt, 2016.
- [30] F. Bakshande, M. Spiller, Y.-L. King, and D. Söffker. Computationally efficient model predictive control for real time implementation experimentally applied on a hydraulic differential cylinder. In *21st IFAC World Congress*, 2020.
- [31] L. Wang. *Model Predictive Control System Design and Implementation Using MATLAB*. Springer-Verlag Londong Limited, 2009.

